

Airborne and ground-based holographic
measurement of hydrometeors in
liquid-phase, mixed-phase and ice clouds

Dissertation zur Erlangung des Grades "Doktor der Naturwissenschaften"

am Fachbereich Physik, Mathematik und Informatik der Johannes
Gutenberg-Universität in Mainz

vorgelegt von
Oliver Schlenczek
geboren in
Bad Hersfeld

Mainz, Oktober 2017

D77 - Mainzer Dissertationen

Tag der mündlichen Prüfung: 18. Januar 2018

Erstgutachter:

Zweitgutachter:

Zusammenfassung

In dieser Arbeit wurde ein neues Instrument zur Messung von Hydrometeoren entwickelt, das zum Einsatz auf Forschungsflugzeugen bestimmt ist. Es basiert auf dem Prinzip der digitalen Einstrahl-Holografie und liefert sechsmal pro Sekunde eine Aufnahme des Interferenzmusters aus einem Messvolumen von ca. 35 Kubikzentimetern. Mithilfe von numerischer Rekonstruktion wird daraus die Position und ein fokussiertes zweidimensionales Bild eines jeden Partikels berechnet, das zum Zeitpunkt des Laserpulses im Volumen war. Aus den rekonstruierten Bildern werden schließlich die Partikelgröße sowie Volumen und Oberfläche bestimmt. Dieses neue Instrument "HALOHolo" wurde mittels verschiedener Messungen im Labor bezüglich Genauigkeit der Größenbestimmung und Detektierbarkeit der Partikel kalibriert. Ein Vergleich mit anderen Instrumenten während mehrerer Messflüge konnte die zuvor ermittelten Zusammenhänge im Wesentlichen bestätigen.

- Aus drei verschiedenen Flugzeugmesskampagnen auf zwei unterschiedlichen Flugzeugen wurden Messungen in Flüssigphasenwolken, Eiswolken und Mischphasenwolken durchgeführt. Bei den Messungen in Flüssigphasenwolken, es handelte sich um arktische Stratocumuluswolken, wurde der Zusammenhang zwischen der Variabilität in der Anzahlkonzentration der Tropfen und dem mittleren Tropfendurchmesser untersucht. Die viel größere Variabilität in der Anzahlkonzentration lässt auf inhomogene Vermischung zwischen Wolkenluft und Umgebungsluft schließen.
- In einem sich entwickelnden tropischen Regenschauer konnte die mikrophysikalische Entwicklung während des Vereisungsprozesses dokumentiert werden. Von besonderem Interesse war die lokale Umgebung von Eiskristallen in der Mischphasenregion. Dort konnte festgestellt werden, dass die meisten Messungen für eine homogene Durchmischung zwischen Eis und Wolkentropfen auf räumlichen Skalen von wenigen Millimetern bis Zentimetern sprechen. Außerdem konnte gezeigt werden, dass große bereifte Eiskristalle (Graupel) häufig zusammen mit deutlich kleineren, säulenförmigen Eiskristallen auftreten, dies wurde bevorzugt in starken Aufwinden beobachtet.
- Abschließend wurden Strukturen auf einer Größenskala von 30 m bis 300 km in hohen Eiswolken (Zirren) inspiziert. Diese Wolken haben manchmal eine bimodale Größenverteilung der Eiskristalle, welche vornehmlich durch Mischungsprozesse entstehen. In einigen Fällen konnte ein Zusammenhang zwischen mikrophysikalischen Eigenschaften und dynamischer Ursache gefunden werden. Bei der Untersuchung der Eiswolken konnte auch gezeigt werden, dass sich die Gesamtgrößenverteilung durch die Addition von Lognormalverteilungen für die jeweilige Kristallform erklären lässt.

Insgesamt konnte gezeigt werden, dass das neue Instrument Daten aus mehreren Flugkampagnen liefern konnte, die über den Umfang der Daten konventioneller Wolkenmessinstrumente (Forward Scattering Spectrometer Probe, Cloud Imaging Probe, Cloud Droplet Probe) hinausgehen. Für alle drei mikrophysikalischen Wolkenklassen (Flüssigphasen-, Eis- und Mischphasenwolken) konnten Fallstudien gefunden werden, die neue wissenschaftliche Erkenntnisse über die Mikrostruktur der Wolken liefern.

Abstract

A new cloud particle spectrometer has been developed in this work with the purpose of obtaining in-situ measurements on different research aircraft. It is based on the principle of digital in-line holography and delivers six images per second of the recorded interference pattern from the laser background and particles suspended in the approx. 35 cubic centimeter large sample volume. Particle position and two-dimensional in-focus images of particles are determined via numerical reconstruction based on Fraunhofer diffraction pattern analysis. Particle properties such as diameter, area and mass are calculated from the reconstructed images. This new instrument, called "HALOHolo", has been calibrated in the laboratory w.r.t. particle detectability and sizing accuracy. An instrument inter-comparison with other cloud particle spectrometers confirmed the determined instrument characteristics in general.

- Measurements in liquid-phase, mixed-phase and ice clouds were obtained from three airborne field campaigns where HALOHolo was operated on two different aircraft. The liquid-phase clouds measured were Arctic stratocumulus clouds, where the connection between variability of particle number concentration and mean volume diameter was investigated. The measured data were indicative of inhomogeneous mixing between the cloud and the surrounding air.
- A developing tropical rain shower was sampled in the process of glaciation and its microphysical evolution has been characterized. The local environment of ice crystals surrounded by supercooled liquid water droplets was studied and the spatial distribution of ice crystals and droplets was found to be a uniform random distribution for the majority of measurements in the rapid glaciation zone of the cloud. In addition, the simultaneous occurrence of small columnar ice crystals among larger rimed particles (graupels) has been documented in a variety of cases, which were most likely to be found in strong updrafts.
- Finally, the spatial structure of cirrus clouds has been investigated on scales between 30 m and 300 km. These clouds did sometimes exhibit bimodal distributions of particle maximum dimension, which were supposedly induced by mixing processes. In some of the cases, a connection between dynamics and microphysics could be established from the holographic measurements and the meteorological data recorded by the aircraft. It could also be shown that the size distribution of ice crystals can be described as a superposition of log-normal distributions from each individual particle habit.

In this thesis, it could be shown that the new instrument is capable of delivering scientifically useful data, which extend beyond conventional instruments like the Forward Scattering Spectrometer Probe, the Cloud Imaging Probe or the Cloud Droplet Probe, and it could even provide new insights in some aspects of cloud physics in all three microphysical classes of clouds. While the majority of the data analysis is able to run automatically, some critical steps like particle classification are still semi-automatic.

Contents

Contents	iv
1 Introduction	1
2 Background	4
2.1 Principle of holography	5
2.2 Airborne particle sampling strategies	7
2.3 Basic cloud microphysical properties	9
<hr/>	
Part I Technical developments	
<hr/>	
3 Holographic instruments for measurement of cloud hydrometeors	14
3.1 Design considerations	15
3.2 The first generation: GipfelHolo 1 and 2	16
3.3 The second generation: HALOHolo	19
3.3.1 Instrument design	19
3.3.2 Calibration	21
3.3.3 Sizing accuracy	24
3.3.4 Position accuracy	28
3.4 Summary	29
4 Algorithms behind image processing and data analysis	31
4.1 Hologram preprocessing and reconstruction	32
4.1.1 Hologram reconstruction	34
4.1.2 Threshold calculation	39
4.1.3 Threshold adaption for improved sizing accuracy	42
4.1.4 Focus plane estimation	43
4.1.5 Calculation of geometric particle properties	45
4.1.6 Particle sizing via sign-matched filtering	47
4.2 Particle classification	49

4.2.1	Ice crystal habit classification	51
4.3	Post processing	56
4.3.1	Analysis of spatial distributions	56
4.3.2	Detection and removal of particle shattering	58
4.4	Instrument modeling	63
4.5	Summary	65
5	Instrument and software limitations and sources of uncertainties	68
5.1	Determining the volume of uniform detectability	69
5.1.1	Estimation of the effective sample volume from airborne measurements	69
5.1.2	Validation of observed trends via instrument modeling	73
5.2	Particle shading	77
5.3	Particle shattering	81
5.4	Particle counting uncertainties	82
5.5	Particle sizing uncertainties	82
5.5.1	Sizing accuracy for droplets	83
5.5.2	Sizing accuracy for ice	85
5.5.3	Sizing accuracy of the sign-matched filter method	86
5.6	Discussion and summary	91
<hr/>		
Part II Results from field measurements		
<hr/>		
6	Local variability and mixing in Arctic stratocumulus clouds	94
6.1	Introduction	95
6.2	Data and methodology	98
6.2.1	Mission strategy, instrumentation and data of the RACEPAC field experiment	98
6.2.2	Statistical analysis methods for cloud microphysical properties	101
6.3	The influence of different sampling strategies on microphysical quantities derived from two contrasting cloud cases	104
6.4	Mixing between two particle modes in the cloud top entrainment zone	107
6.5	Inter-histogram variability of cloud properties	111
6.6	Investigating the spatial structure of mixing processes in extended stratiform cloud decks	116
6.7	Discussion and summary	120
7	Bulk and local microphysical properties in cumulus clouds	124
7.1	Introduction	124
7.2	Data and methodology	127
7.3	Trends in microphysical properties during the process of glaciation	129
7.4	The local environment of ice crystals and water droplets	135

7.5	Connections between dynamics and microphysics	138
7.6	Investigating the local environment of rimers and splinters in the Hallett-Mossop zone	140
7.7	Discussion and summary	143
8	Mesoscale and microscale structures in cirrus clouds	145
8.1	Introduction	146
8.2	Data and methodology	149
8.3	Mesoscale and microscale structures in wave cirrus during COSMICS Flight B889	151
8.4	Explaining additional modes in WCB cirrus and warm front cirrus by habit segregation	156
8.5	Vertical structure of three contrasting cirrus clouds	161
8.6	Recent measurements of cirrus clouds in the tropical tropopause layer	164
8.7	Discussion and summary	169
9	Discussion and conclusion	171
9.1	Advances in the development of cloud particle spectrometers	172
9.2	Advances in image processing algorithms	172
9.3	Advances in cloud microphysics	173
9.4	Future work	175
<hr/>		
Part III Appendix		
<hr/>		
A	Ground-based measurement of ice crystal precipitation at the Jungfraujoch research station during CLACE 2013	180
B	Technical details of HALOHolo	180
B.1	Optical properties	181
B.2	Electronics unit	183
B.3	Size calibration	184
C	Details of the hologram analysis software	186
C.1	Particle metrics	187
C.2	Particle reconstruction after shattering	189
D	HALOHolo characteristics and uncertainties	191
D.1	Spatial dependence of signal strength	192
D.2	Derivation of an instrument response function for HALOHolo	195
D.3	Intercomparison of particle size from CAS and HALOHolo	196
D.4	Performance analysis of the sign-matched filter algorithm	197

E RACEPAC campaign overview and additional data	198
E.1 Overview of the aircraft instrumentation	199
E.2 Instrument intercomparison	200
E.3 Flight overview	201
E.4 The impact of sampling on noise in HALOHolo power spectra.....	202
E.5 Calculation of neighbor distance statistics from two distinct particle modes	205
E.6 Mixing diagrams from other flights	206
E.7 Spatial distribution analysis of selected cloud passes	207
F ICE-D campaign overview and additional data	209
F.1 Determining the spatial overlap of the cloud passes	210
F.2 Meteorological overview of Flight B926	212
F.3 Additional figures of the cloud passes	215
F.4 Estimation of particle terminal velocity	220
F.5 Spatial distribution of ice among droplets	222
G COSMICS campaign overview and additional data	229
G.1 Meteorological overview of COSMICS Flight B889, B890 and B895	230
G.2 Horizontal and vertical structure of the flights	233
G.3 Time series data of COSMICS Flight B889, B890 and B895.....	236
G.4 Size distribution intercomparison	239
G.5 Particle size distributions and fit parameters	244
List of Acronyms	254
List of Symbols	256
List of Figures	259
List of Tables	278
References	285

Introduction

In the past century of cloud physics, the main objective was to understand the physical processes in clouds to the point of successful numerical simulations. These processes include the formation and dissipation of clouds as well as the development of rain, snow and other forms of precipitation. The main difficulty was to build the bridge from the large-scale dynamics down to the small-scale processes which happen in subvolumes of the cloud that are only a few cubic centimeters large. While the effect of several dynamical aspects on the microphysical scales can be derived somehow via investigation of parameters related to thermodynamics and turbulence, the direct analysis of these tiny cloud volumes was not possible for decades. Knowing the distances between particles is crucial for the calculation of precipitation-related processes such as collision and coalescence. With the technique of holography, it is possible to access these scales and to investigate important precipitation-relevant processes. One of the key players in broadening of the cloud droplet size spectrum is mixing. The physically correct representation of the mixing process in clouds might be an answer to the question why it is still so difficult to predict cloud coverage and precipitation accurately over a time period of more than a few hours. However, other influences from turbulence on the cloud droplet size spectra need to be considered as well (Grabowski and Abade, 2017).

Since the beginning of the operational usage of holography as an airborne in-situ measurement technique, knowledge about the relevant microphysical processes is growing rapidly. A recent study by Beals et al. (2015) has already demonstrated that the classic assumption of spatial homogeneity in terms of mixing is a smooth and straightforward way for numerical implementation but clouds in the real atmosphere tend to mix *inhomogeneously* with the surrounding air.

The main purpose of a holographic particle spectrometer is the investigation of spatial distributions among populations of droplets, droplets and ice crystals, or populations of ice crystals. However, a holographic instrument can also deliver bulk properties from each recorded sample as other state-of-the-art instruments can do. The disadvantage is that the hologram analysis is nontrivial as the numerical reconstruction of one second of flight data takes approximately three hours on a single node of a supercomputer in 2017. The technical developments in this work and also the examples of science which can already be done with holography should be able to provide a big leap of motivation for using this technology in future studies.

This work is subdivided in two major parts: Part I contains the methodology and technical specifications of a holographic instrument (Chapter 3), a description of the image reconstruction and data analysis (Chapter 4) and an estimation of uncertainties from both the instrument and the software in a qualitative and quantitative way (Chapter 5). Some scientific aspects are already briefly addressed in Part I and investigated in depth in Part II. Each of the three chapters in Part II will provide insights into the local environment of hydrometeors from three microphysical types of clouds, which are liquid-phase clouds (Chapter 6), mixed-phase clouds (Chapter 7) and ice clouds (Chapter 8). As each cloud type has its own microphysical structure, the subject of each chapter was carefully se-

lected to address recent questions in cloud physics. In the case of liquid-phase clouds, the connection between scales of ten meters and larger with the local microphysical scale, which ranges from some millimeters to about 10 centimeters, is studied. A case study from a convective cloud in the process of glaciation provides the chance to examine and quantify the effect of primary and secondary ice production in mixed-phase clouds on the small scales. Finally, the process of sedimentation and mixing and its effect on the microphysical structure of ice clouds is analyzed. Technical details of the instrumentation and data analysis and additional information on particular field campaigns and cloud cases beyond the ones described in the main chapters are included in the Appendix (Part III). Recent results from ice particles measured in a convective outflow in the subtropics during the StratoClim 2017 field campaign, obtained in August 2017, are shown in Subsection 5.5.2 and Section 8.6.

Background

In this chapter, the basic principles of holographic measurements, sampling strategies used in airborne in-situ measurements of clouds, and the main cloud microphysical properties are explained. The principle of holography is crucial for understanding the technical details and methodology of the Chapters 3 and 4. In terms of error discussion, which is the main content of Chapter 5, the sampling strategy is another important aspect. Finally, the commonly used cloud parameters and their relationship among each other need to be introduced as the results of Chapters 6, 7 and 8 depend on them.

2.1 Principle of holography

Holography, initially discovered and described by Gabor (1948), was in the first place a theoretical method to enhance the resolution of electron microscopes without the usage of ultra high precision electron lenses. Instead of obtaining a crisp in-focus image, holography uses the interference of a reference wave and a wave scattered or diffracted by an object, which requires *coherence* of the source. After the invention of the laser, this method has been extensively used for electromagnetic waves in the optical spectrum. In the following explanation, the "beam" or "wave" could be either from an electron source or a coherent light source (usually a laser).

A hologram¹ is made when a reference wave interferes with an object wave and the interference pattern is captured on film (analog) or on an image sensor (digital). For recording a hologram of objects in motion, it is recommended to either use a very short exposure time of the camera and / or a pulsed laser to minimize the effect of motion blur. While the interference pattern itself is a complex field, the holographic medium is only able to capture the intensity of the interference pattern, integrated over the exposure time.

Let $E(x, y, t) = \Re \{E(x, y, t)\} + j\Im \{E(x, y, t)\}$ be the optical field (denoted as electric field in the unit of V m^{-1}) with $\Re \{\dots\}$ and $\Im \{\dots\}$ the real and imaginary parts at the lateral location x and y at time t . The dependence of E , strictly spoken it is $E = E(x, y, z, t)$, on the position z along the optical axis is ignored here as E is discussed at a fixed, arbitrary z . By using Euler's formula, the field $E(x, y, t)$ can be decomposed into the field amplitude $U(x, y, t) = |E(x, y, t)|$ (in V m^{-1}) and the phase $\phi(x, y, t)$ (in rad), which is defined via $\tan(\phi(x, y, t)) = \Im \{E(x, y, t)\} / \Re \{E(x, y, t)\}$. In case of both the real and imaginary part of $E(x, y, t)$ being equal to zero, the phase $\phi(x, y, t)$ is zero by definition.

The measured intensity $I_{meas}(x, y, t)$ is proportional to $U^2(x, y, t)$. Usually, $I_{meas}(x, y, t)$ is obtained during the *exposure time* τ (in s) and can be written as an integral mean of the light intensity at each detector pixel over time. Here, it is assumed that the time stamp t is the time when the image has been recorded. In practical use, the integral is often ignored as typically more than 90 % of the recorded light intensity are deposited on the holographic medium in a laser pulse of *pulse duration* Δt , which is typically much

¹Here, the term *hologram* is used for the whole image containing the interference pattern of the reference wave and particle wave(s).

smaller than τ . For the holographic systems used in this work, typical values of τ are 10^{-3} s and typical values of Δt are 10^{-9} s.

$$I_{meas}(x, y, t) = \frac{1}{\tau} \int_{t-\tau}^t |U(x, y, s) \exp(j\phi(x, y, s))|^2 ds \quad (2.1)$$

From the structure of the integrand in Eq. 2.1 it is obvious that the phase information is lost upon recording. However, the phase can be reconstructed numerically by using Fourier transforms (e.g. the algorithm from Raupach (2009a)). To understand the formation of a hologram, the amplitude value of the reference wave $U_r(x, y, t)$ and the amplitude value of a diffracted particle wave $U_p(x, y, t)$ need to be considered in Eq. 2.1. The superposition of the two components yields four terms in Eq. 2.2. The first term $U_r^2(x, y, s)$ can be identified as the background intensity, the second term $U_p^2(x, y, s)$ can be identified as the light intensity scattered by the particle. These two terms do not require any coherence of the source. The two terms of major interest are the mixed terms $U_r^*(x, y, s)U_p(x, y, s)$ and $U_r(x, y, s)U_p^*(x, y, s)$, which resemble the *virtual* and *real image* (Fugal et al. (2004), their Eq. 3). The "*" denotes the complex conjugate of the original term. An assumption which is very often implicitly involved in digital hologram reconstruction under far field conditions is setting the background intensity to unity and the scattered intensity to zero. The assumption of almost zero scattering intensity requires that either the area cross section of scatterers in the sample volume is no more than 1 % of the detector area or the particle diameter is less than approx. 100 μm (Fugal et al., 2004).

$$\begin{aligned} I_{meas}(x, y, t) &= \frac{1}{\tau} \int_{t-\tau}^t |U_r(x, y, s) + U_p(x, y, s)|^2 ds \\ &= \frac{1}{\tau} \int_{t-\tau}^t |U_r^2(x, y, s) + U_p^2(x, y, s) + U_r^*(x, y, s)U_p(x, y, s) \\ &\quad + U_r(x, y, s)U_p^*(x, y, s)| ds \end{aligned} \quad (2.2)$$

The spatial coordinates of the holographic sample volume are the Cartesian coordinates x , y and z (in m). x and y are referred to as the *lateral coordinates* while z is pointing along the optical axis. Let z_p be the position of the particle along the optical axis of the system and z_H the position of the hologram plane in the reconstructed space. Then, an analog hologram is reconstructed by placing a coherent light source at $z = z_H - z_p$ and the particle will appear as bright spot at $z = z_p$ (cf. Fig. 4 in Borrmann (1991)). Depending on the optical alignment, the particle could be either illuminated by a point source (e.g. the tip of a single-mode fiber or a pinhole in case of optical holography) or by a collimated beam. Here, for the sake of simplicity, it is assumed that the beam is collimated and consists of plane wave fronts. Fig. 2.1 shows the concept of making an in-line hologram. Further mathematical details of holography, which are needed to perform the digital reconstruction and the estimation of instrument properties, are explained in

Goodman (2005). Details on applications to cloud physics are described in Borrmann (1991), Fugal and Shaw (2009), Beals (2013), Henneberger (2013) and others.

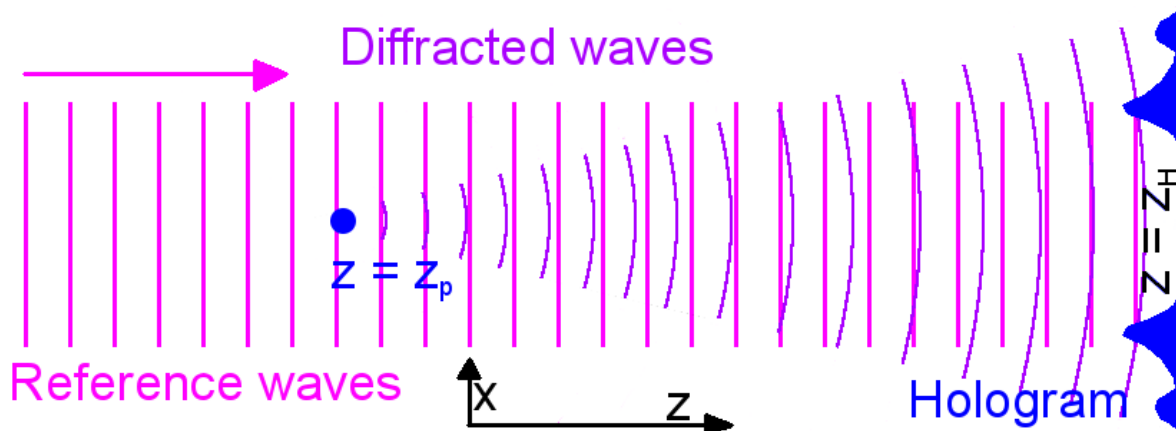


Fig. 2.1: Illustration of hologram recording. The reference wave is diffracted by the particle located at $z = z_p$. Both waves interfere and the interference pattern (which is the hologram) is recorded at $z = z_H$. The interference pattern contains all information necessary to reconstruct the 2D particle image and the 3D particle position. The pattern in blue resembles the intensity distribution at the hologram plane along x . The y axis is pointing out of the page.

2.2 Airborne particle sampling strategies

In contrast to conventional particle measurements, holograms cannot be taken continuously during a research flight with an aircraft. There is always a time lag Δt (in s) between two holograms, determined by the speed of the camera electronics. If the aircraft is flying at a speed v_a (in m s^{-1}), the spatial displacement ΔL (in m) of two subsequently recorded holograms is $\Delta L = v_a \Delta t$. If v_a is slow enough, it might be possible to obtain a three-dimensional overlap of the two sampled volumes of air via particle tracking. For a camera which records 6 frames per second and covers a width of 13 mm in direction of the particle flow, the critical particle velocity v_c needs to be smaller than 4 cm s^{-1} to warrant a 100 % chance of finding the same particle in the next hologram, if no collisions occur. The difference between individual three-dimensional snapshots of a particle ensemble via holography and the conventional sampling strategy, which is used in many other airborne cloud hydrometeor spectrometers, is illustrated in Fig. 2.2. The conventional sampling strategy is based on continuous particle by particle measurements in a very narrow area cross section along the direction of flight. A particular example of a conventional instrument is the Cloud Droplet Probe (CDP) from Droplet Measurement Technologies Inc. (DMT) which uses a focused laser beam to measure the size and number of cloud droplets particle by particle. The conventional sampling strategy introduces the need of accumulating over a defined sampling time t_s to obtain a size distribution of particles,

represented by the dashed black line in Fig. 2.2. In holography, each three-dimensional snapshot contains a particle size distribution (shown in green, blue and red in Fig. 2.2). The two sampling strategies are compared in the top right of Fig. 2.2, the gray line is the accumulated size distribution from the holographic cloud probe. One sees that the first sample contains small and large cloud droplets (the blue line in the bottom right of Fig. 2.2 shows a bimodal distribution). In contrast to this example, the subsequently measured volume contains mainly small and very few large droplets (red line) while the measurement after the red one contains only large droplets (green line). The fact that one particular measurement contains only small or only large particles is not resolved by the one second average from the CDP. The difference in the number of particles n by one order of magnitude is due to the sample volume of the holographic cloud particle spectrometer HALOHolo (described in Section 3.3 being ten times as large as the CDP sample volume at the given aircraft speed. It needs to be mentioned that the axis orientation in the holographic sample volume differs from the example shown in Fig. 2.2. During airborne operation, x points vertically upwards, y points along the direction of flight and z points into the plane spanned by x and y .

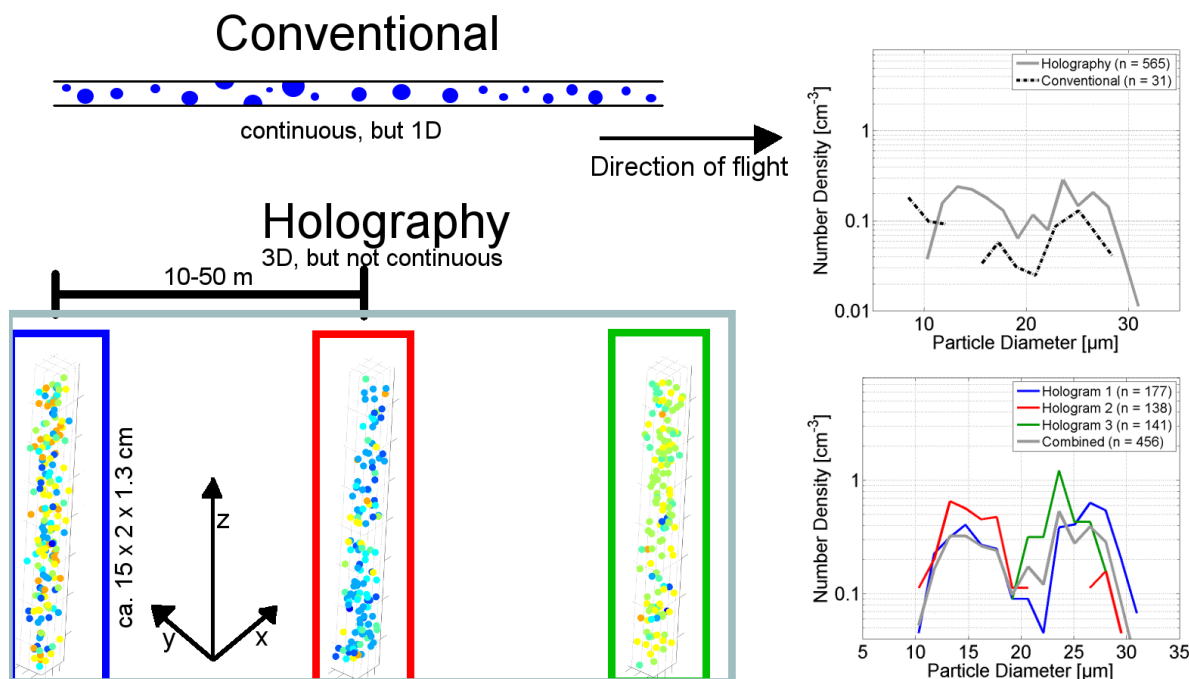


Fig. 2.2: Illustration of the conventional sampling strategy (here: a CDP) in contrast to holographic measurements (here: HALOHolo). Data were taken from Flight 6 of the airborne field campaign RACEPAC in Inuvik, Canada on 06 May 2014. The sample volume geometry as defined in the previous paragraph was rotated to allow for better visibility. The colors of the particles indicate particle size (blue / turquoise for small particles, green / yellow / orange for larger particles). A gap between 12 and 16 μm in the dashed black line (top right) indicates that particles of this size were not measured by the CDP.

2.3 Basic cloud microphysical properties

The visual appearance of clouds varies greatly between individual cloud types, sometimes even within the same cloud. These differences need to be understood in a quantitative way to allow numerical simulations of clouds or cloud systems, which are essential for weather and climate predictions. The quantities introduced and explained in this section are widely used in the cloud physics literature and can be found in Pruppacher and Klett (1997), Seinfeld and Pandis (2012) and others. While the basic definitions are most often identical, the authors of the mentioned textbooks might use different symbols or units as the ones used here.

We assume the measurement of n hydrometeors in a cloud volume V of some cubic centimeters². The first microphysical quantity obtained from this measurement is the *number concentration*, which is usually measured in the unit of cm^{-3} or L^{-1} .

$$N = \frac{n}{V} \quad (2.3)$$

Each of the n sampled hydrometeors, indicated by index i , has a diameter D_i . From the sampled hydrometeors, the *mean particle size* \bar{D} and the *size distribution width*³ $\sigma(D)$ (both in μm) can be derived (see Eq. 2.4 and 2.5).

$$\bar{D} = \frac{1}{n} \sum_{i=1}^n D_i \quad (2.4)$$

$$\sigma(D) = \sqrt{\frac{1}{n-1} \sum_{i=1}^n (D_i - \bar{D})^2} \quad (2.5)$$

In analogy to \bar{D} and $\sigma(D)$, the *geometric mean diameter* \bar{D}_g and *geometric standard deviation* σ_g can be used. The calculation is done straightforwardly by using $\ln(D)$ instead of D and taking the exponential of the results (see Eq. 2.6 and 2.7). Both D_g and σ_g are given in μm . D_i should be given in μm to minimize numerical errors.

$$\bar{D}_g = \exp\left(\frac{1}{n} \sum_{i=1}^n \ln(D_i)\right) \quad (2.6)$$

$$\sigma_g = \exp\left(\sqrt{\frac{1}{n-1} \sum_{i=1}^n (\ln(D_i) - \ln(\bar{D}_g))^2}\right) \quad (2.7)$$

²Unless otherwise noted, this volume V is the *sample volume* of the holographic instrument.

³After calculation of the arithmetic mean, there are only $n-1$ degrees of freedom left in the sample. Thus, the normalization factor is $1/(n-1)$ instead of $1/n$ (cf. Bevington (1969), his Eq. 2-10).

Another type of mean particle size is the *mean volume diameter* (or *volume mean diameter*) D_3 , which is used to quantify mixing processes in clouds. It is defined as the cubic root of the mean of the cubed particle diameters (see Eq. 2.8).

$$D_3 = \sqrt[3]{\frac{1}{n} \sum_{i=1}^n D_i^3} \quad (2.8)$$

Oftentimes, the size distribution does not follow a Normal or Log-normal distribution, which means that knowing N , \bar{D} and $\sigma(D)$ is not sufficient to reconstruct the size distribution. By binning the measured particle sizes in J size bins D_j (in μm), a frequency distribution of the particles is obtained. For the purpose of intercomparison with other measured cloud volumes, the histogram needs to be normalized. There exist two common definitions of volume density distributions in the literature. One of them, known as dN/dD , is the differential number concentration dN normalized by the bin width dD , given in the unit of $\text{cm}^{-3} \mu\text{m}^{-1}$. Another representation is $dN/d \log D$ in the unit of cm^{-3} , which is typically used for log-normal distributions⁴. The volume density distributions in Eq. 2.9 and 2.10 are referred to as *number-weighted size distributions*.

$$\frac{dN}{dD_j} = \frac{n(D_j \leq D < D_{j+1})}{V(D_{j+1} - D_j)} \quad (2.9)$$

$$\frac{dN}{d \log D_j} = \frac{n(D_j \leq D < D_{j+1})}{V(\log(D_{j+1}/D_0) - \log(D_j/D_0))} = \frac{n(D_j \leq D < D_{j+1})}{V \log(D_{j+1}/D_j)} \quad (2.10)$$

From the measured particle area cross section A (in mm^2) and the particle mass m (in mg), the corresponding area-weighted (in $\text{mm}^2 \text{cm}^{-3}$) or mass-weighted size distributions (in g m^{-3}) can be calculated. There exist several ways of calculating the area-weighted and mass-weighted size distribution directly from the number-weighted size distribution and the bin centers for spherical particles, but for ice it is more accurate to use the particle by particle sum of A or m . As the particle diameter is derived from its measured area and outline (see Chapter 4), it is recommended to use rather the measured area than the area from the spherical assumption. The mass is calculated from the particle area in two different ways: If the particle is spherical, it is assumed to be liquid water and the mass is calculated via Eq. 2.11. For a non-spherical particle, most likely ice, the area to mass relationship from Baker and Lawson (2006) is used (Eq. 2.12). $\rho_w = 1000 \text{ kg m}^{-3}$ at $T = 4^\circ\text{C}$ is the density of liquid water; the density of pure ice without any air bubbles is $\rho_i = 918 \text{ kg m}^{-3}$ at $T = 0^\circ\text{C}$ and implicitly included in Eq. 2.12. The units in the area to mass relation from Baker and Lawson (2006) are mm^2 for the particle area A and mg for the particle mass m .

⁴Here, the $\log(x)$ means the decadal logarithm, sometimes $\log_{10}(x)$ in the U.S. literature. The natural logarithm is labeled $\ln(x)$ here. The reference diameter D_0 , usually $1 \mu\text{m}$, is used to eliminate the unit in the logarithm.

$$m_{sph} = \frac{2}{3}\rho_w AD = \frac{\pi}{6}\rho_w D^3 \quad (2.11)$$

$$m_{ice} = 0.115A^{1.218} \quad (2.12)$$

Two additional bulk parameters can be calculated from the measured particles. The first one is the liquid water content LWC (or ice water content IWC , both in g m^{-3}), which is defined as the mass of liquid water (or ice) per volume of cloudy air. With the individual particle masses, the calculation of LWC and IWC is straightforward.

$$LWC = \frac{\sum_{i=1}^n m_i}{V} \quad (2.13)$$

Another quantity, which is related to radiative properties of clouds, is the particle effective radius r_{eff} (in μm). The definition from McFarquhar and Heymsfield (1998) uses the number density N for each particle size and defines r_{eff} as the ratio of two integrals. Ideally, the radius r is the radius of an equivalent sphere with the same area cross section as the particle. If the area cross section of the particle cannot be measured, the radius r needs to be calculated from the corresponding size bin of the particle.

$$r_{eff} = \frac{\int_0^\infty N(r)r^3 dr}{\int_0^\infty N(r)r^2 dr} \quad (2.14)$$

From the calculated individual particle area cross section A_i and particle mass m_i , the calculation can be abbreviated to Eq. 2.15.

$$r_{eff} = \frac{3}{4\rho_w} \frac{\sum_{i=1}^n m_i}{\sum_{i=1}^n A_i} \quad (2.15)$$

In particular for the purpose of instrument intercomparison, the uncertainties of the cloud properties mentioned above need to be calculated. A common assumption in experimental cloud and aerosol physics is that the particle measurement is interpreted as a Poisson process. Thus, the uncertainty ΔN of the particle number concentration N is expressed in terms of the total particle counts n (Eq. 2.16).

$$\frac{\Delta N}{N} = \frac{\sqrt{n}}{n} = \frac{1}{\sqrt{n}} \quad (2.16)$$

The error bars for each bin of a particle size distribution are calculated via Eq. 2.16. A straightforward way to calculate the uncertainties of the arithmetic mean diameter \overline{D} or geometric mean diameter \overline{D}_g , the so-called *standard error of the mean* is used in Eq. 2.17 and 2.18. For the uncertainties of the distribution width $\sigma(D)$ and $\sigma_g(D)$, error propagation in the sense of $\Delta\sigma(D)/\sigma(D) = \Delta\overline{D}/\overline{D}$ is assumed (Eq. 2.19 and 2.20).

$$\Delta\overline{D} = \sigma(D)/\sqrt{n} \quad (2.17)$$

$$\Delta\bar{D}_g = \sigma_g(D)/\sqrt{n} \quad (2.18)$$

$$\Delta\sigma(D) = \sigma(D)\frac{\sigma(D)}{\bar{D}\sqrt{n}} \quad (2.19)$$

$$\Delta\sigma_g(D) = \sigma_g(D)\frac{\sigma(D)}{\bar{D}\sqrt{n}} \quad (2.20)$$

For the other cloud properties (LWC , r_{eff}), the error estimation is more complicated. In general, it is recommended to use the Gaussian Law of Error Propagation if the error of a quantity composed of two or more independent variables needs to be estimated. The Gaussian Law of Error Propagation uses the partial derivatives of the quantity from which the error is calculated. For a variable R depending on the two variables A and B , the estimated error ΔR can be calculated from the errors ΔA and ΔB (similar to Eq. 4-9 in Bevington (1969)).

$$\Delta R = \sqrt{\left(\frac{\partial R}{\partial A}\Delta A\right)^2 + \left(\frac{\partial R}{\partial B}\Delta B\right)^2} \quad (2.21)$$

Let $R = A^n B^m$ with $n \neq 0, m \neq 0$ be the variable from which the error needs to be estimated. After some lines of algebra, Eq. 2.21 yields an easy to use formula for products and quotients, shown in Eq. 2.22.

$$\Delta R = R\sqrt{\left(\frac{n\Delta A}{A}\right)^2 + \left(\frac{m\Delta B}{B}\right)^2} \quad (2.22)$$

An application of Eq. 2.22 is the calculation of ΔLWC under the assumption that LWC is seen as a product of n and \bar{D}^3 . A reasonable approximation of ΔLWC is given in Eq. 2.23. The factor of 3 in the second term is due to the third power of D in Eq. 2.11.

$$\frac{\Delta LWC}{LWC} \approx \sqrt{\left(\frac{1}{\sqrt{n}}\right)^2 + \left(\frac{3\sigma(D)}{\bar{D}\sqrt{n}}\right)^2} \quad (2.23)$$

A similar approximation can be done for the error of the effective radius Δr_{eff} . As r_{eff} is expressed in terms of particle volume divided by particle area, the factor in Eq. 2.24 is 3/2. Eq. 2.16 to 2.20 and Eq. 2.23 and 2.24 are needed for the determination of the hologram-to-hologram consistency of cloud properties in Chapter 6.

$$\frac{\Delta r_{eff}}{r_{eff}} \approx \frac{3\sigma(D)}{2\bar{D}\sqrt{n}} \quad (2.24)$$

The cloud microphysical properties which were introduced in this chapter are essential for the interpretation of the results in Part II of this thesis. Methods used to describe spatial distributions mathematically are explained in Subsection 4.3.1 of Chapter 4.

Technical developments

Holographic instruments for measurement of cloud hydrometeors

The use of holography in Atmospheric Sciences started in the 1960s, just at the time when the first ruby lasers ($\lambda = 694 \text{ nm}$) became commercially available for research facilities. After Silverman et al. (1964) proposed a possible instrument setup for a holographic distrometer, the first in-situ measurements of cloud droplets were obtained by Thompson et al. (1966) and Kunkel (1971). It did not take long until the first holographic systems were used aboard aircraft, at least to provide a proof of concept for holography under these conditions. Trolinger (1976), Conway et al. (1982) and Brown (1989) made holography airborne and recorded holograms in different types of clouds. While Trolinger (1976) used a ruby laser, Conway et al. (1982) and Brown (1989) used a frequency-doubled Nd:YAG laser ($\lambda = 532 \text{ nm}$). Numerous studies of cloud droplet spatial distributions in the 1980s and 1990s included ground-based holographic measurements based on a ruby laser system (Kozikowska et al. (1984), Borrmann (1991), Borrmann and Jaenicke (1993), Borrmann et al. (1993), Borrmann et al. (1994), Vössing et al. (1998), Uhlig et al. (1998)).

However, it took almost two decades from the first airborne applications until the concept of holography was again applied to airborne atmospheric measurements, now with a small and light-weight laser system (frequency-doubled Nd:YAG, $\lambda = 532 \text{ nm}$) and a digital camera (Fugal et al., 2004). Apart from numerous laboratory studies, digital holography was also applied to ground-based in-situ measurements of clouds around the same time (Raupach et al. (2006), Raupach (2009b), Henneberger et al. (2013)). Since the development of HOLODEC (Fugal et al., 2004), optical and imaging technology has improved, pushing the limits even further (Spuler and Fugal, 2011). The second version of HOLODEC, described in Spuler and Fugal (2011), uses a frequency-tripled Nd:YAG laser with $\lambda = 355 \text{ nm}$. Although the smallest practically resolvable particle diameter remained around $10 \mu\text{m}$, the increase in sample volume size and camera speed allows a more detailed investigation of clouds from the lowest centimeters of the boundary layer to more than 20 km above sea level in the stratosphere with the new instrument HALOHolo.

3.1 Design considerations

A holographic particle spectrometer which is designed for operation in a harsh airborne environment needs to fulfill a list of criteria for successful measurements. The main optical and design requirements for a holographic cloud probe, which are a large enough range of temperature and pressure, a compact design and low power consumption, are described in Spuler and Fugal (2011). Some additional requirements and issues are listed below:

1. Some electronic parts must be kept dry and in a temperature range that is safe for operation. The computer and power supply need to be operated at air temperatures below 40°C , camera and laser head may not get colder than 10°C .
2. Daylight adds noise to the holograms. A lens system in front of the camera helps to exclude indirect light via baffling.
3. Fluctuations in the temperature or density of the medium in which the particles are dispersed add high levels of noise to the holograms. Large temperature gradients near

the instrument windows need to be avoided whenever possible. This is also the reason why one should not use "compressed air" from a so-called "dust-off" can as propellant for calibration beads.

4. Pulsed lasers as the one built in GipfelHolo 1 (see Section 3.2) provide a very high peak power of the light field (typically some 10 kW over 1 ns). Most single-mode fibers that were commercially available before 2013 were not designed to withstand such high peak power and routinely failed if the beam was not dimmed by a neutral density filter. Thus, the intensity of the laser pulse has to be reduced by using neutral density filters, which decreases the signal to noise ratio of the holograms (see Section 3.2, first paragraph).

3.2 The first generation: GipfelHolo 1 and 2

GipfelHolo 1

The first holographic instrument, built as an imaging system prototype of HALOHolo, was the GipfelHolo version 1 ground-based holographic hydrometeor probe (GipfelHolo 1). It used a frequency-doubled 532 nm Nd:YAG laser from CryLaS GmbH with 30 μ J pulse energy over 1.5 ns at a repetition rate of 1 kHz, and used a fiber to bring light from the laser to the sample volume. The laser is directed via a single-mode fiber towards the tube with the collimation optics, where the beam is expanded to approximately 5 cm in diameter. The expanded beam is then reflected by a mirror and propagates through the volume between the two windows. The background light wave and possible diffracted waves, caused by particles in the sample volume, is captured by a SVS-Vistek hr29050 FLGEA camera, located behind a 532 nm interference filter. The camera can record up to 6 images per second, which are 6576×4384 pixels large, with a pixel length and width of 5.5 μ m. The sensor is placed close to the camera window location and also captures daylight which adds noise to the holograms. So, usable holograms can only be recorded during nighttime. Fig. 3.1 shows the setup of GipfelHolo 1 and examples of reconstructed particle images from melting snowflakes measured at Mt. Zugspitze on 01 October 2012 during the field experiment ACRIDICON-Zugspitze. The reconstructed particle images are between 100 μ m and 2.5 mm long.

GipfelHolo 2

In preparation of the next field campaign, which was the Cloud and Aerosol Characterization Experiment 2013 (CLACE2013) at the Jungfraujoch in Switzerland, several properties of the instrument were changed to obtain a better quality of data (Schlenczek et al., 2017). First, the fiber optics were replaced by a pinhole-lens combination in a cage system. This modification allowed operation at much higher laser intensities, which reduced the necessary gain factor of the signal from the image sensor significantly. Another change was the usage of $\lambda = 355$ nm, which is the same as in HALOHolo. The shorter

wavelength leads to a lower influence from sunlight as the solar spectral irradiance is higher at $\lambda = 532\text{ nm}$ than at $\lambda = 355\text{ nm}$. Also, the heating of the tips was modified to reach temperatures up to 50°C . The optical setup of GipfelHolo 2 and some results from an individual reconstructed hologram are shown in Fig. 3.2.

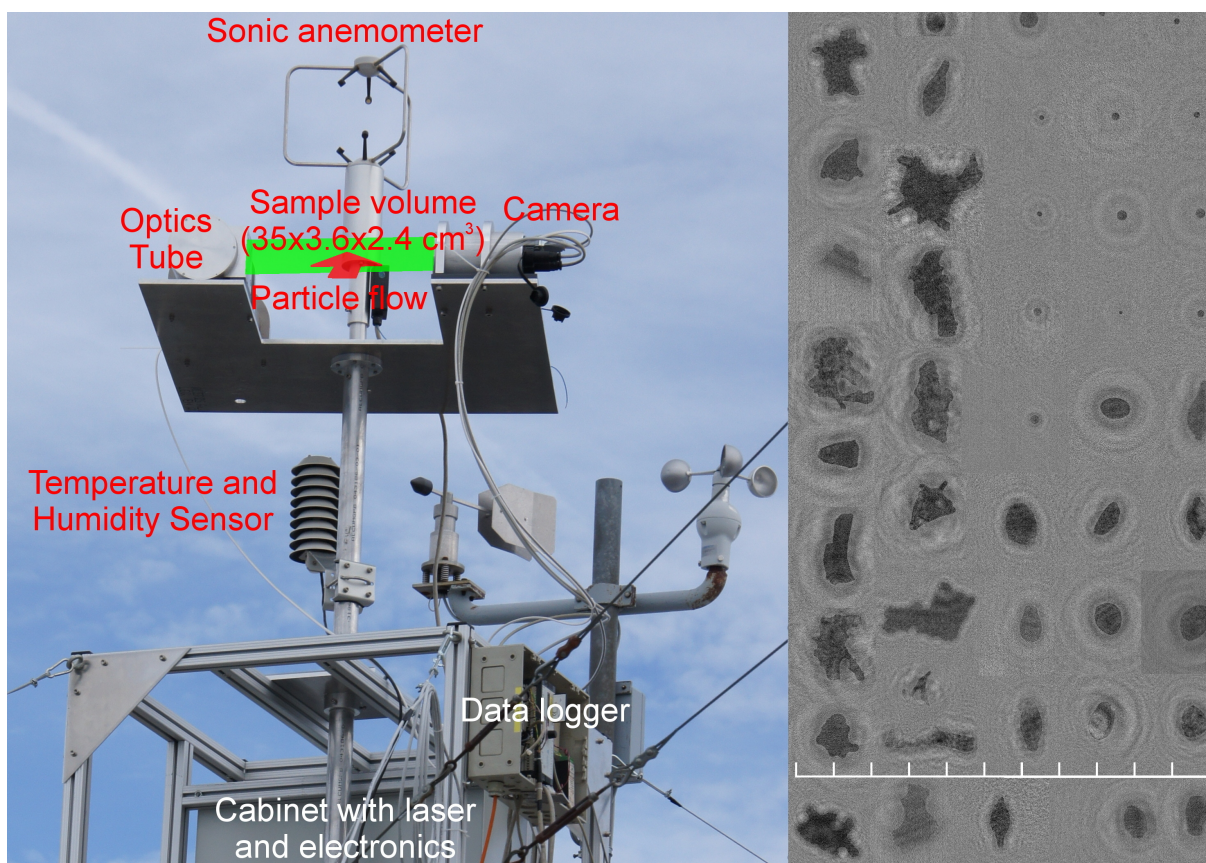


Fig. 3.1: Left: Photograph with description of GipfelHolo 1 on Mt. Zugspitze in September and October 2012. Right: Example of reconstructed hydrometeors from 01 October 2012 during a snow shower. Scale bar increments are 1 mm each.

Ice and snow on the windows were not a problem anymore but too much heat created another distorting effect to the measurements: Large temperature gradients in the vicinity of the sapphire windows can lead to convection and induce time-dependent fluctuations of the index of refraction. Thus, the background pattern changes faster than the holograms are recorded and the background filtering algorithm is unable to estimate a background hologram that is effective for filtering. Remaining time-dependent parts of the background pattern severely impair automatic reconstruction and the holograms used for publication (Schlenczek et al., 2017) needed to be reconstructed with the user in loop to search for particles. The operator had to visually search for the particle in the reconstruction before the focal plane could be determined automatically with a better accuracy. In addition to the optical setup of GipfelHolo 2, Fig. 3.2 shows three deliverables from one hologram:

Particle size distribution (top right), in-focus particle images (middle right) and the spatial distribution of particles in the sample volume (bottom).

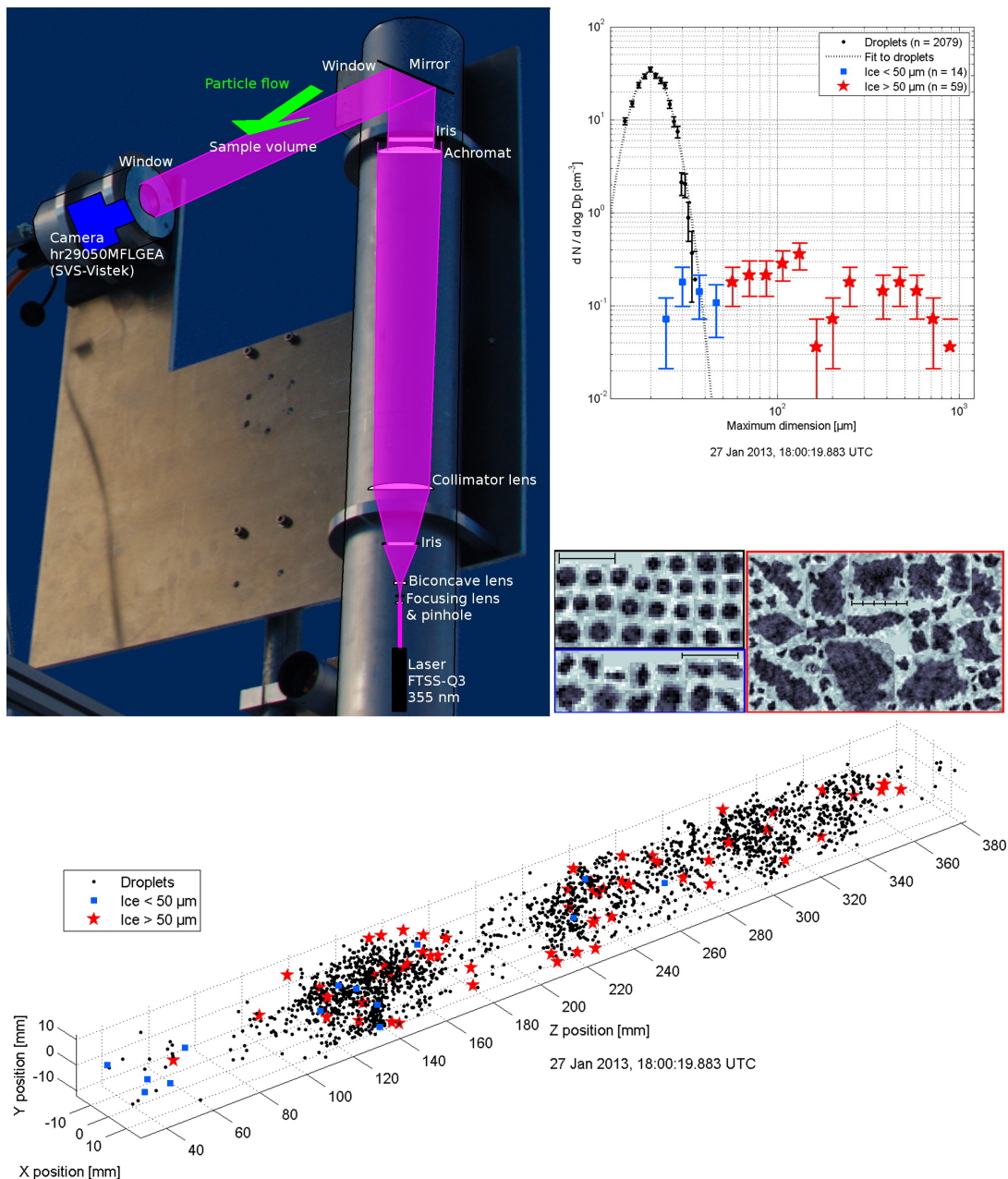


Fig. 3.2: Top left: Photograph with description of GipfelHolo 2 on Jungfrauoch in January and February 2013. Top right: Example of size distributions of cloud droplets and ice particles from a precipitating Nimbostratus cloud and corresponding particle images of droplets (black frame), small ice (blue frame) and larger ice (red frame). Scale bar increments are 100 μm each. Bottom panel: Spatial distribution of frozen hydrometeors and droplets from the same hologram. Modified from Schlenczek et al. (2017).

3.3 The second generation: HALOHolo

GipfelHolo was designed for measurements on mountain-top stations where an aerodynamic, low power consumption and light-weight design is not crucial for its operation. These requirements are fundamentally different for an airborne instrument.

3.3.1 Instrument design

The basic design of HALOHolo is similar to HOLODEC (Spuler and Fugal, 2011) and other cloud hydrometeor underwing probes where the electronics are stored behind the instrument head in a so-called "Particle Measurement Systems (PMS) canister" and the active sensing unit is located in or nearby the instrument tips. The instrument windows allow the laser beam to enter the sample volume and the imaging lens system and keep the interior of the instrument free of moisture and dust. The laser beam is focused through a 10 μm Fort Wayne Wire Die single crystal diamond pinhole, which acts as a spatial filter to keep the TEM₀₀ mode and remove higher-order modes of each laser pulse. From the pinhole, the diverging beam is expanded by a biconcave lens and then collimated by two plano-convex lenses close to the laser-side tip of the instrument. A turning prism is used to direct the collimated beam towards the sample volume. After traversing the sample volume, the beam with the superimposed diffraction pattern from the particles in the sample volume is directed towards the imaging lens system by another turning prism. The imaging lens system is a 9-element doubly telecentric lens system. It places the object plane of the camera close to the location of the camera-side sapphire window and provides a magnification of $1.87 \times$ for an effective pixel size around 3 μm on a 5.5 μm pixel CCD sensor. In order to avoid a space-dependent distortion of the particle images, effects from spherical aberration had to be kept as small as possible. The individual properties of the optical components are summarized in Table B.1 and B.2 of Appendix B.1. An overview of HALOHolo with the overlaid schematic of the optical components is shown in Fig. 3.3. A higher resolution schematic of the imaging system is shown in Fig. B.1 in Appendix B.1.

HALOHolo has been designed to work in an autonomous mode but can also be remotely controlled via an Ethernet connection. The fully automatic operation mode is required for aircraft like the M-55 Geophysica or the helicopter-borne sensor shuttle ACTOS. The remote control or remote monitoring is useful in particular for laboratory measurements or aboard an aircraft like the BAe-146 from the British Facility for Airborne Atmospheric Measurements (FAAM) or the Polar 6 from the Alfred Wegener Institute (AWI).

To make HALOHolo autonomous, it needs to have (a) a temperature control unit to avoid overheating or freezing of critical instrument components, (b) fail-safes to preclude malfunction of individual components, and (c) data acquisition scripts that are executed automatically. Also, HALOHolo has diagnostic abilities, which allows a faster error detection in case of an instrument failure. It uses 28 V DC for operation and 115 V AC for

heating. To minimize the influence of shattering as described in Korolev et al. (2011), HALOHolo is equipped with so-called "Korolev tips" as did HOLODEC.

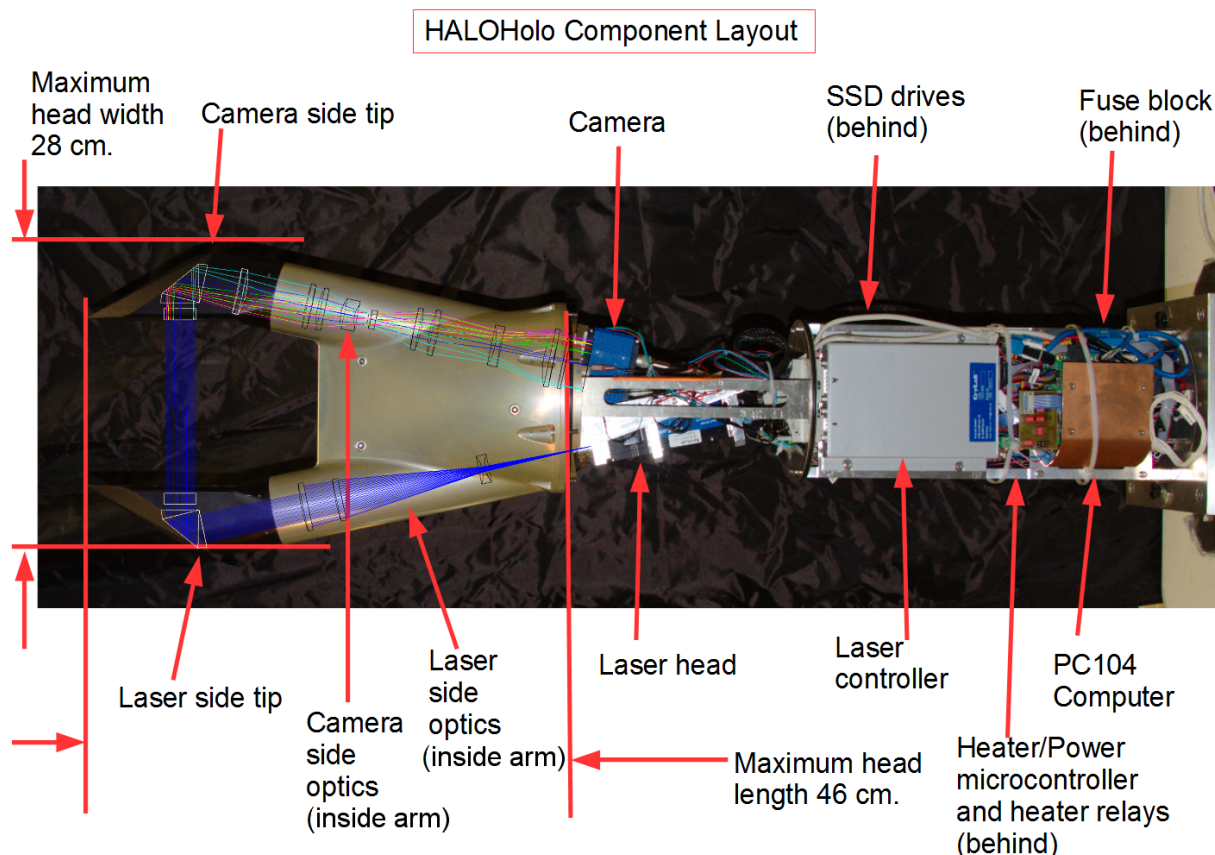


Fig. 3.3: Photograph of HALOHolo with labeled components of the instruments. A schematic of the optical components is overlaid to illustrate the working principle of the laser side and camera side lens system. The colored rays in the camera side lens system indicate that the magnified image is not inverted.

The camera of HALOHolo delivers up to 6.2 8-bit images with a size of 27.5 MB per second (approx. 600 GB per hour), which requires a writing speed of 171 MB per second. Thus, the data storage needs to be fast and large enough for flights that are up to 5 hours long⁵. As large hard disk drives (HDDs) are considerably slow and also not designed to be operated at a pressure as low as 70 hPa, the data storage in HALOHolo is based on solid state drives (SSDs), either a large single SSD or a group of SSDs arranged in RAID 0 configuration. From 2014 to 2016, a group of 3 SSDs with 1 TB was used. Since 2017, a single 4 TB SSD stores the holograms. Copying data from a 4-hour flight to a standard HDD needs approximately 12 hours and two of the 4 TB SSDs are used (one for the actual flight, one for the next flight). From this perspective it is possible to have several flight

⁵Here, an airborne field campaign with the M-55 Geophysica aircraft is assumed, which is among the toughest conditions HALOHolo and its operators have experienced so far.

days in a row with one flight per day. However, in such a scenario there is no time to make backups of the data.

3.3.2 Calibration

Pixel size calibration

The degree of collimation of the laser beam and the effective pixel size was measured with a ruler on a glass slide placed at the two window locations. With this setup, holograms were recorded and reconstructed. Counting the pixels and comparing the metric length L_m measured on the scale bar with their corresponding length L_p in pixels yields the (average) effective pixel size. The calibration results are shown in Table 3.1.

From the data set obtained on 10 February 2016, two holograms with the ruler were used on each of the two extreme positions of the sample volume to determine the pixel size. For one hologram, the ruler was held in a horizontal position and for the other, the ruler was turned by 90 degrees.

Table 3.1: Pixel size calibration of HALOHolo using a ruler at different positions along the optical axis. The measured length and pixel counts are presented along with their uncertainties. The uncertainty of the effective pixel size was determined by using Gaussian error propagation.

Z position [mm]	L_m [mm]	L_p [px]	Pixel size [$\mu\text{m}/\text{px}$]	Date
7.5 ± 0.1	19.00 ± 0.02	6396 ± 5	2.971 ± 0.004	10.02. 2016
19.9 ± 0.1	14.00 ± 0.02	4716 ± 5	2.969 ± 0.005	09.04. 2014
118.3 ± 0.1	12.00 ± 0.02	4059 ± 5	2.956 ± 0.006	09.04. 2014
158.7 ± 0.1	18.00 ± 0.02	6084 ± 5	2.959 ± 0.004	10.02. 2016

The individual results are shown in Table 3.2 and for both directions (x and y), a linear least-squares fit was performed. It should be noted that the input for fitting consists of only four data points each, which induces a low statistical significance. However, the very weak trend in effective pixel size as a function of z could be determined with an accuracy in terms of the error bars that is less than 50% of the value. As desired, it turns out that the effective pixel size dx in x direction and the effective pixel size dy in y direction are consistent within the error bars for both the measured and the fitted values. As dx and dy deviate by less than 0.1 %, the distinction between dx and dy in the notation is only for theoretical reasons. In practical use (such as hologram reconstruction), the assumption $dx = dy$ is made.

Table 3.2: Pixel size calibration of HALOHolo on 10 February 2016 under consideration of both x and y direction

Z position [mm]	L_m [mm]	L_p [px]	Pixel size [$\mu\text{m}/\text{px}$]	Direction
7.20 ± 0.05	14	4714 ± 5	2.970 ± 0.002	x
7.20 ± 0.05	12	4041 ± 5	2.969 ± 0.004	y
7.45 ± 0.05	19	6394 ± 5	2.972 ± 0.003	x
7.45 ± 0.05	11	3706 ± 5	2.970 ± 0.004	y
158.40 ± 0.05	14	4728 ± 5	2.961 ± 0.002	x
158.40 ± 0.05	12	4050 ± 5	2.963 ± 0.004	y
158.60 ± 0.05	18	6083 ± 5	2.959 ± 0.003	x
158.60 ± 0.05	12	4050 ± 5	2.963 ± 0.004	y

$$dx(z) = (2.971 \pm 0.004) \frac{\mu\text{m}}{\text{px}} - 10^{-5} \frac{\mu\text{m}}{\text{mm px}} \cdot (7.08 \pm 3.42)z \quad (3.1)$$

$$dy(z) = (2.969 \pm 0.002) \frac{\mu\text{m}}{\text{px}} - 10^{-5} \frac{\mu\text{m}}{\text{mm px}} \cdot (3.89 \pm 1.57)z \quad (3.2)$$

The measurements shown in Table 3.1 confirm that a change in the laser alignment on 09 February 2016 did not affect the effective pixel size. This result was expected as the beam collimation quality should not change if the laser position along the optical axis deviates from its ideal position (for perfect collimation) by a few millimeters. All other optical parts (except for the laser head) remained in place. From all individual measurements, a range of effective pixel sizes between 2.96 and 2.97 $\mu\text{m}/\text{px}$ is obtained, which means that the effective pixel size is determined with an accuracy of 0.5 %, even if the largest possible uncertainties are assumed. The minimum value (2.96 $\mu\text{m}/\text{px}$) was set as the effective pixel size for reconstruction. This setting introduces a sizing uncertainty of 0.3 % undersizing for particles close to the camera window. However, pixel counting uncertainties for particle size estimation are by far larger (typically 2 pixels or more, see Chapter 5) and this deviation would only need to be corrected if particles were larger than approximately 1.7 mm. Another fact to keep in mind is that large particles tend to be rather oversized than undersized if they have a very strong signal. In this case, the two sources of uncertainties might even cancel out. If desired, Eq. 3.1 and 3.2 might be used to correct the spatial dependence of the pixel size.

Resolution calibration with a USAF 1951 test target

Similar to Henneberger et al. (2013) and Spuler and Fugal (2011), a USAF 1951 test target was used to determine the minimum resolvable size at various axial distances within the sample volume. There are three major constraints which determine the minimum resolvable particle size: (1) the numerical aperture of the telecentric lens system in front

of the camera ($NA = 0.083$ for HALOHolo, yielding D_{lens}), (2) the effective pixel size, and (3) the resolution limit $D_{res,rec}$ from a particle reconstructed at a certain distance. While the first two are instrument-specific constants, the latter is dependent on the distance along the z axis. This dependence is given by Eq. 3.3 similar to Eq. 1 in Spuler and Fugal (2011) where D_{det} is the size of the detector. A table of the distances between the line pairs (which is identical with the line width) in each element and group of the USAF 1951 target is available online from the English Wikipedia or the website of optical manufacturers (e.g. Edmund Optics).

$$D_{res,rec}(z) = \frac{2.44\lambda z}{D_{det}} \quad (3.3)$$

Figure 3.4 shows the resolution limit D_{res} (in μm) as a function of distance z for HALOHolo. Obviously, the minimum d_{res} at small enough values of z is slightly above the pixel size dx . Particles as small as $3\mu\text{m}$ therefore can be seen at distances below approx. 30 mm. However, the distinction between particles and noise sets the effective detection limit at two pixels ($5.9\mu\text{m}$), which is a more conservative approach.

The theoretically smallest resolvable size from reconstruction $D_{res,rec}$ (in μm) is calculated from Eq. 3.3. As the detector area has a rectangular geometry, the detector size D_{det} used for the calculation of $D_{res,rec}$ is the "geometric mean diameter"⁶ of the detector and the minimum and maximum of the smallest resolvable size $\Delta D_{res,rec}$ are calculated by using either the detector width $D_{det,x} = N_x dx$ or the detector height $D_{det,y} = N_y dy$ as detector diameter. For the detection limit used in hologram reconstruction, the resolution calibration leads to the conclusion that even the smallest reconstructed particles ($D = 5.9\mu\text{m}$) can be seen at distances as far as $z = 120\text{ mm}$. Possibly due to spatial inhomogeneities of the signal to noise ratio, the measured resolution limit does not exactly follow the theoretical resolution limit. At shorter distances to the hologram plane, the measured resolvable length is larger than the theoretical limit, and for $z > 120\text{ mm}$, the smallest resolvable size is slightly smaller than the theoretical limit.

These values obtained from the resolution calibration are valid for laboratory conditions but during a research flight the background noise level is considerably higher. An in-flight calibration in terms of uniform detectability and sizing accuracy is therefore needed. This is achieved by an instrument intercomparison with a Cloud Droplet Probe (CDP) which is discussed in Chapter 5.

⁶Here, the geometric mean of a rectangular aperture is calculated, which is not the diameter of the inscribed circle.

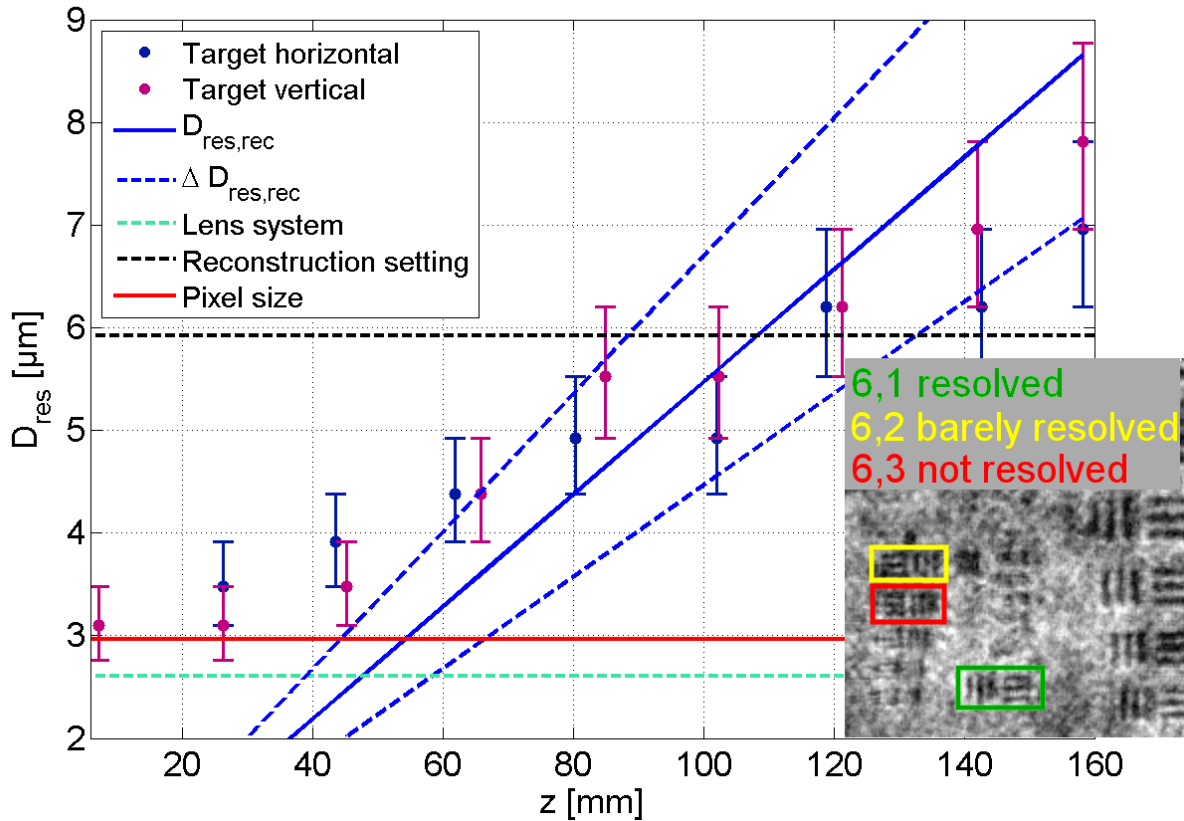


Fig. 3.4: Minimum resolvable size of HALOHolo as a function of distance along the optical axis for horizontal positioning (dark blue) and vertical positioning (violet) of a USAF 1951 test target placed at various z positions. In the lower right corner, a reconstructed hologram of the test target at the laser window position ($z = 158$ mm) is shown along with the clearly resolved (green), barely resolved (yellow) and barely not resolved (red) line triads (elements). The distances between a pair of lines in the green and red element define the error bars. The expected resolution limit from reconstruction $D_{res,rec}$ (solid line) and its range of uncertainties (dashed lines) is shown in blue. Further constraints shown in the plot are the resolution limit from the imaging lens system (turquoise), the pixel size (red) and the smallest allowed particle diameter in the reconstruction settings (black).

3.3.3 Sizing accuracy

Some calibration runs with glass beads of known size have been performed at various positions along the optical axis across the entire lateral range. The test bead sizes were 30 μm , 15 μm and 8 μm . This test was done to get an impression of the sizing accuracy as a function of the particle position in the sample volume.

As the detectability is a nonlinear function of the signal-to-noise ratio⁷, this effect needs a thorough investigation with both laboratory and field measurements. The results from

⁷The nonlinear behavior is due to the cutoff at a certain threshold.

the measurements should then be compared with results from numerical simulations (as instrument model).

The validity of the manufacturer information of the glass beads has been tested by using a calibrated ruler and a microscope to determine the size of the beads visually. From each particle, the width D_x and height D_y was measured and the arithmetic mean of the two was used as particle size D . From the individual particle sizes, a cumulative size distribution was obtained for each bead sample and fitted with a Normal distribution. The fits performed well with a coefficient of determination $r^2 = 0.99$ and a root mean square error $RMSE < 0.02$. The individual fits returned mean values and standard deviations with a high accuracy, shown in Table 3.3. All of the measured bead sizes were slightly too large in comparison with the manufacturer information, but still within the estimated uncertainty from the manufacturer. The magnification factor used for the microscopy was already at the limit of the microscope and for an effective pixel size of the microscope camera, which was $\approx 0.9\mu\text{m}$, the pixel size is only about 1.5 times the maximum wavelength from the illuminating light source (which was a white LED). Fig. 3.5 shows a photograph of the glass beads under the microscope. Many of the beads appear to be clustered and some of the $8\mu\text{m}$ or $15\mu\text{m}$ beads might be fragmented, which may lead to particle sizes deviating from the manufacturer information.

Table 3.3: Measured bead size in comparison with the manufacturer information. The mean and standard deviation values (STD) as well as the corresponding uncertainties were obtained from Normal distributions fitted to the cumulative particle size distributions. n is the number of particles in each sample. Additional parameters are listed in Table B.3 of Appendix B.3

Sample Nominal diameter	Best before	Manufacturer info		Measured		n
		Mean [μm]	STD [μm]	Mean [μm]	STD [μm]	
8 μm beads	12/2002	7.9 ± 0.8	1.5	8.25 ± 0.04	1.43 ± 0.06	225
15 μm beads	08/2009	14.5 ± 1.0	1.7	15.38 ± 0.05	1.72 ± 0.07	225
30 μm beads	01/2019	29.5 ± 1.0	1.9	30.04 ± 0.07	2.06 ± 0.10	225

The calibration results using the test beads are shown in Fig. 3.6. For this purpose, three independent methods of particle size estimation were used: The (standard) thresholding method (details described in Subsection 4.1.2), a variant of the standard thresholding which uses a relative threshold (also described in Subsection 4.1.2) and the application of the size estimation method using *sign-matched filtering* after Lu et al. (2012) (details described in Subsection 4.1.6). It turned out that the standard thresholding method yielded much larger particle diameters than expected⁸, most likely due to the very low noise level in the holograms obtained under laboratory conditions. Examples are shown

⁸In case of the $30\mu\text{m}$ beads, the mean particle diameter obtained as equivalent size or area-derived diameter via the standard thresholding method exceeded the nominal bead diameter ($30\mu\text{m}$) by $10\mu\text{m}$.

in the top row of Fig. 4.9 in Subsection 4.1.6. Thus, the particle size estimation for this particular analysis was done with the relative thresholding method and the sign-matched filter algorithm.

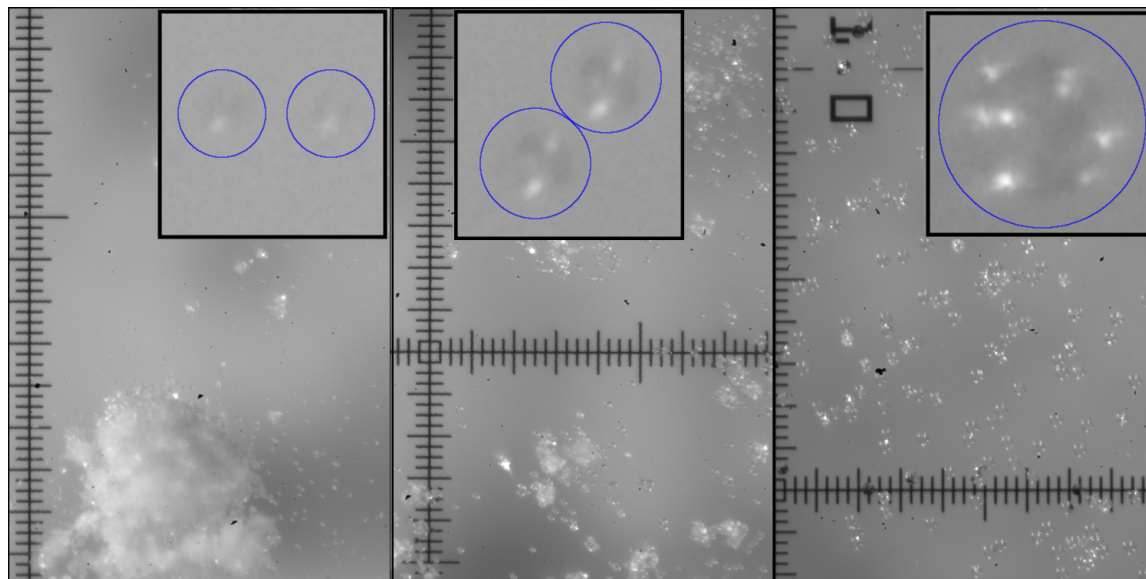


Fig. 3.5: Glass beads under the microscope. Left: 8 microns. Middle: 15 microns. Right: 30 microns. The scale increments of the ruler are $25\ \mu\text{m}$. For each of the images, the same magnification factor was used. The black boxes are closeups of 1 or 2 beads (marked with blue circles), digitally magnified by a factor of ten.

The usage of a relative threshold led to a better agreement with the expected particle diameters. It is apparent in the bottom row of Fig. 3.6 that the usage of the *equivalent size* (shown in black), which is the arithmetic mean of the *major axis length* and *minor axis length* of each particle, yields a reasonable agreement with the size distribution expected from the manufacturer information of the beads (shown in green). A similarly good agreement is achieved for the usage of the *area-derived diameter*, which is defined as the equivalent diameter of a circle with the same area cross section as the particle. The entirely threshold-independent sizing method based on the sign-matched filter from Lu et al. (2012) is in agreement with the two other particle diameter estimators.

The comparison of the two size estimators (equivalent size and area-derived diameter) obtained from the relative threshold application with the results from the sign-matched filter and the size distribution derived from the manufacturer information of the beads becomes more complicated when looking at the $15\ \mu\text{m}$ beads in the middle row of Fig. 3.6. While the two threshold-based methods yield a good agreement with the expected size distribution, there are notable deviations found for the sign-matched filter method. As the total number of particles was larger than 1500, these deviations cannot be explained by effects solely arising from counting statistics. Possible convergence issues of

the sign-matched filter algorithm in case of small particle diameters are examined further in Subsection 5.5.3.

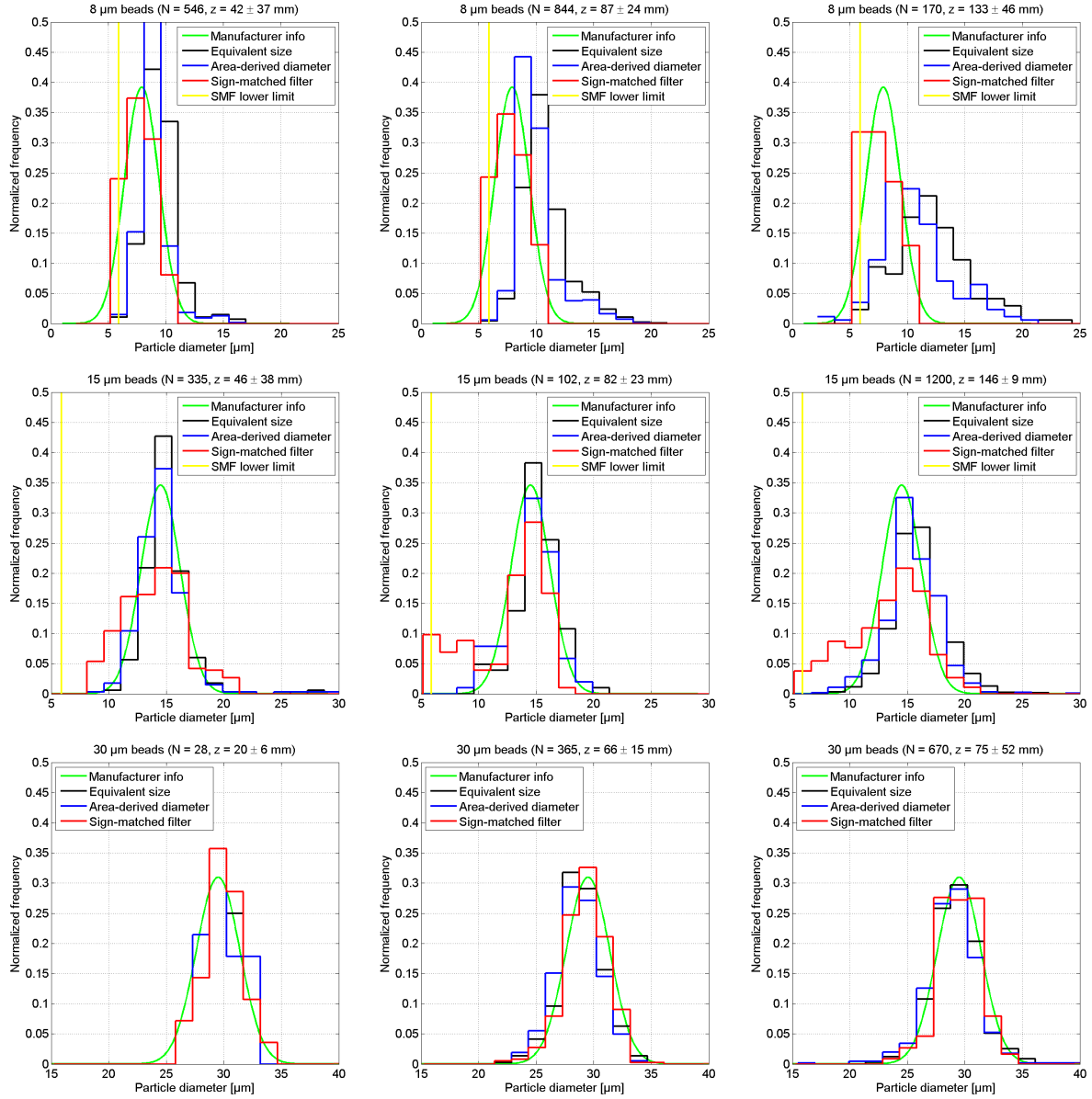


Fig. 3.6: Reconstruction results of holograms with calibration glass spheres. The spheres had a nominal diameter of $8\ \mu\text{m}$ (top row), $15\ \mu\text{m}$ (middle row) and $30\ \mu\text{m}$ (bottom row) as described in Tab. 3.3. Their corresponding size distributions given by the manufacturer (green) are shown in comparison with the "Equivalent Size" (black) and the "Area-derived Size" (blue), explained in Chapter 4. The "sign-matched filter" (red) is used as a threshold-independent reference method if the particle is larger than $5.9\ \mu\text{m}$ (SMF lower limit, yellow lines). The filter accuracy was set at $0.74\ \mu\text{m}$ (0.25 pixels). A typical value of the particle sizing uncertainty via determining the number of pixels for the object is $1.5\ \mu\text{m}$ (0.5 pixels). The mean z position of the beads in the sample volume increases from left to right where the mean and STD of z are given in the title of each plot.

Finally, the glass beads with a nominal diameter of $8\ \mu\text{m}$ were examined. Here, it turned out that the performance of the sign-matched filter method was superior to the threshold-based size estimation, though this was not the case for the $15\ \mu\text{m}$ beads. The threshold-based sizing methods tended to overestimate the particle diameter with an increasing bias and an increasing distribution width towards larger values of z . This effect of both increasing mean particle diameter and increasing distribution width is likely caused by the resolution limit effect, which is expressed by Eq. 3.3. Concerning the small deviations between the sign-matched filter algorithm and the manufacturer information for the $8\ \mu\text{m}$ beads in contrast to the larger deviations for the $15\ \mu\text{m}$ beads, further research is needed. Thus, a thorough investigation of the accuracy of the sign-matched filter algorithm based on synthetic holograms was performed and is discussed in Subsection 5.5.3 of Chapter 5. Table B.3 in Appendix B lists the individual fit parameters for the methods and metrics used for particle size estimation of the calibration beads.

3.3.4 Position accuracy

In particular for the analysis of spatial distributions it is crucial to know the uncertainties in determining the particle position. For this purpose, a series of synthetic holograms (each containing 100 particles) was analyzed to determine the deviation between the estimated particle location after reconstruction and the exact particle location. For the simulation, particle sizes between $6\ \mu\text{m}$ and $21\ \mu\text{m}$ were used, located at $z \approx 7\ \text{mm}$ (near the camera-side window) and $z \approx 157\ \text{mm}$ (near the laser-side window). Apparently, the lateral deviation is most often smaller than the pixel size of $2.96\ \mu\text{m}$ while the z position estimation is less accurate (see Fig. 3.7).

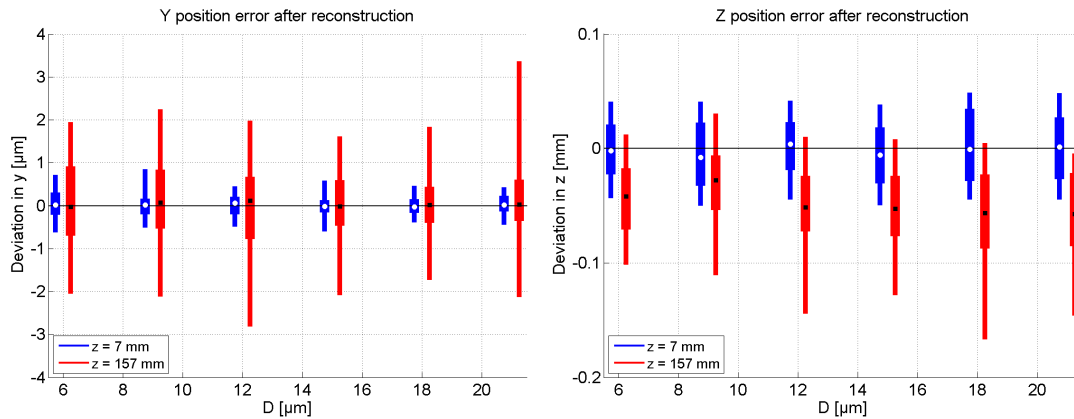


Fig. 3.7: Box plots of particle position uncertainties determined from synthetic holograms. Left: Error in y position for the holograms at short distance (blue) and long distance (red) to the hologram plane. Right: Error in z position with same color code as in the left panel. The wide boxes represent the inner 50 % of the distribution, the narrow boxes represent the inner 90 % of the distribution. The white circles / black squares indicate the median of each distribution. The x position error (not shown) looks the same as the y position error.

With a reconstruction setting of $dz = 100\ \mu\text{m}$, the z position error is usually within the distance between two reconstruction planes. While the lateral error (here for the y position) shows an increasing standard deviation for increasing z position without a trend in the mean or median value, there is a decreasing trend in the median value of the z position error for increasing z . This trend seems to be virtually independent of the particle size and suggests that the estimated focal plane is closer to the hologram plane than the actual focal plane (the median deviation of z is negative). It still needs to be verified that the decreasing trend in the z position error is not a possible artifact from numerical uncertainties in making the synthetic holograms. The magnitude of the errors might be different for particle holograms obtained in airborne measurements where the contrast is lower and particles are more difficult to detect.

3.4 Summary

The new airborne cloud particle spectrometer HALOHolo has similar optical properties as HOLODEC (Spuler and Fugal, 2011) but a larger detector area (27.5 instead of 16 million pixels) and a faster camera (6 fps instead of 3 fps). Apart from a higher volume sampling rate and a higher spatial resolution, HALOHolo has some more advances in comparison with HOLODEC: HALOHolo can be operated in a fully automatic mode and has enough storage capacity on board for a flight duration up to 6 hours. Measurements have been performed in the laboratory, during ground-based tests and during several airborne field campaigns aboard of four different airborne platforms (Polar 6 from the Alfred Wegener Institute (AWI), BAe-146 from the Facility for Airborne Atmospheric Measurements (FAAM), M-55 Geophysica from the Myasishchev Design Bureau (MDB) and the helicopter-borne turbulence measurement platform ACTOS). For each of the platforms, a customized solution had to be found to adapt to the individual requirements in terms of power supply and deployment. The measurements included the atmospheric boundary layer and mid troposphere from the subtropics to the Arctic, and the subtropical stratosphere. Severe failures leading to whole campaigns with no data did not occur. Some individual flights had a lack of data due to software or electronics issues (two flights of RACEPAC and several flights of ICE-D) and thermal issues (one flight of StratoClim 2016 and 2017). From all of the field campaigns, a data base consisting of several million holograms (approx. 20 TB of data) could be built.

The pixel size of HALOHolo could be determined to $dx = 2.96\ \mu\text{m}$ with an accuracy of 0.5 % along the range of z positions in both horizontal and vertical direction. The maximum usable sample volume is $V_s = 38.9\ \text{cm}^3$. For the practical use, a restricted volume is used to avoid the impact of shattering. Therefore, the lower and upper boundary of z is adapted, which yields $V_{s,r} = 35.4\ \text{cm}^3$ for $9.5\ \text{mm} < z < 149.5\ \text{mm}$ and $V_{s,r} = 30.3\ \text{cm}^3$ for $20\ \text{mm} < z < 140\ \text{mm}$ respectively. The latter is used in flights through mixed-phase clouds with high ice concentration or cirrus clouds, where the data set is heavily

influenced by shattering. Independent of the aircraft speed, the volume sampling rate is either $233 \text{ cm}^3 \text{ s}^{-1}$, $212 \text{ cm}^3 \text{ s}^{-1}$ or $182 \text{ cm}^3 \text{ s}^{-1}$.

The resolution limit was determined with the same method as in Henneberger (2013) and Spuler and Fugal (2011) and depends on the z position. The smallest particle size which is resolved in the entire sample volume is $D \geq 8 \mu\text{m}$. Smaller particles can be detected but are not accurately sized. Effects on particle sizing uncertainties in the size range between 8 and $10 \mu\text{m}$ are discussed in the section on convergence of the sign-matched filter algorithm in Chapter 5. Glass beads of 8, 15 and 30 microns dispersed across the sample volume could be sized with an accuracy of $0.3 \mu\text{m}$ (for the $30 \mu\text{m}$ beads), $1.3 \mu\text{m}$ (for the $15 \mu\text{m}$ beads) and $0.4 \mu\text{m}$ (for the $8 \mu\text{m}$ beads) when using the sign-matched filter algorithm for diameter estimation. Fragmentation of the beads or clustering may have played a role.

An investigation of the cross-sensitivity error, which is the instrument response to a monodisperse particle spectrum, needs to be performed with a model of the optical properties of HALOHolo as monodisperse calibration beads were not available. However, the spectral broadening can be estimated from the enhancement of the distribution width from the nine samples of calibration beads. The broadening of the size distribution STD with the pixel-counting particle sizing methods was highest for the $8 \mu\text{m}$ beads at distances around $z = 140 \text{ mm}$. Instead of $1.4 \mu\text{m}$, as indicated from the microscopic examination, the measured standard deviation was close to $3 \mu\text{m}$, which is a broadening by approximately half the pixel width. For this particular series of measurements, the probability of erroneously attributing a particle of size D_i to size D_{i+1} is 100 % for a bin width ΔD of 0.5 pixels (or $1.48 \mu\text{m}$). For the $15 \mu\text{m}$ and $30 \mu\text{m}$ beads, the spectral broadening was less than $0.4 \mu\text{m}$ for the pixel-counting methods. Thus, the derived particle size distributions, usually calculated with a bin width of 0.5 pixels, have an error bar in D of approximately the same size as the bin width for sizes of $8 \mu\text{m} < D < 15 \mu\text{m}$. For larger sizes, the cross-sensitivity error is likely below $1/3$ of the bin width. Thus, care has to be exercised when measuring size distributions. It is recommended to define the size bins $D_{i+1} - D_i$ wide enough such that cross sensitivity is not an issue.

Considering the calibration results and the geometric properties of the instrument, HALOHolo is able to measure particles in a size range from approx. $8 \mu\text{m}$ up to a maximum of 13 mm . Results from different field campaigns have shown that the measurement altitude does not affect the instrument properties. The cross-sensitivity error is size-dependent and maximized for $D < 10 \mu\text{m}$. In practical use, trustworthy particle size distributions can be obtained from approx. $10 \mu\text{m}$ up to 2 mm of particle diameter. Numerical simulations have shown that the lateral particle position error is typically less than 1 pixel and the z position error is most often less than $100 \mu\text{m}$. These errors are small enough to be neglected when discussing spatial distributions of particles. A further discussion of the usable range of particle sizes and a particle size intercomparison during airborne measurements are included in Chapter 5.

Algorithms behind image processing and data analysis

In the days of analog holography, a laser with a similar wavelength as the holography laser was used to illuminate the hologram, usually recorded on a glass plate. Bright spots appeared at the focus position of each particle and their position and size was determined in a laborious procedure by using a video camera that could be moved around with individually adjustable motors on micropositioning tables (Borrmann and Jaenicke, 1993).

Nowadays, computers are powerful enough in terms of floating point operations per second to perform digital reconstructions in a reasonable time, usually minutes to hours for a single hologram with a z position accuracy of 100 microns. Even analog holograms can be reconstructed via digital reconstruction after they have been scanned and digitized. In this chapter, the routines are explained which are needed to turn a raw hologram into deliverables in terms of atmospheric data. Additionally, the advances of this work in the big picture of previous studies of holography in atmospheric sciences are discussed.

4.1 Hologram preprocessing and reconstruction

The outcome of GipfelHolo, HALOHolo or any other holographic instrument from a single measurement covering the entire sample volume, introduced as *hologram* in Chapter 2, contains the information of the entire imaged particle ensemble which is needed for the calculation of LWC, IWC, size distributions or other cloud microphysical properties. To access the geometric particle properties and the location of the particle, the raw hologram needs to be reconstructed. The reconstruction procedure is fully automatic and has run on several servers and supercomputers, including MOGON⁹ from the University of Mainz. This constitutes the single most major step forward in the technology as previously only manual or semi-automatic extraction methods were available, which were extremely labor intensive. To reconstruct one hologram, it takes approximately 25 minutes per node. If 50 nodes are available (which is a quite realistic scenario), the reconstruction of an entire four-hour flight with 86,400 holograms (long RACEPAC flight or typical StratoClim flight) takes approximately one month (144,000 CPU hours). The resulting *particle data files* are saved to disk and need to be refined in further processing steps.

After the reconstruction, the semi-automatic process of *classification* to make a training data set for later machine learning is required to separate noise in form of laser speckles, out-of-focus interference fringes and checkerboard background patterns from water droplets and ice crystals. A sequence of reconstructed holograms is then loaded into the classification software tool *carft* (Schledewitz, 2016) where supervised machine learning assists the observer in separating spherical (*round*) from aspherical (*nubbly*) *particles* and for excluding patterns from noise (so-called *artifacts*). Depending on the desired accu-

⁹MOGON stands for "Mogontiacum", which is the Latin word for "Mainz". It consists of 555 nodes with four AMD Opteron 6272 CPUs and at least 128 GB of RAM per node. Each CPU has 16 cores (64 cores per node, 32 of them usable for floating point processing), which yields a total of 35,520 cores with a computational capability of 298 TFlops.

racy of the data products, classification can easily take one or more working days for five minutes of holograms.

The accuracy of the *classified particle data* is determined by the user, recommended are at least 80 % accuracy in terms of correctly detected particles and correctly rejected noise. However, further post processing is desirable to refine the data set. One very important step, in particular for measurements obtained in ice clouds, is the *shattering detection*. There exist several methods with different amounts of user interaction to remove or correct shattering. A detailed description is given in Subsection 4.3.2.

After the shattered particles have been removed, a further step in data post processing is the calculation of additional geometric properties (if desired) and, if there is a significant amount of ice, the ice crystal habit classification. There are two possible pathways for ice crystal habit classification, either via `carft` by adding more particle classes to the standard scheme or via "user-in-loop" where the observer chooses the classes by pushing the respective button of the keyboard after the particle image was shown. This is the closest the digital methodology gets to the fully analog semi-automated procedures of e.g. Borrmann et al. (1993). This step is usually much faster than the first classification procedure as the number of objects is generally much lower (of order 10^3 instead of 10^6). Towards final data products, another very important step is needed. The sample volume needs to be determined, which might depend on the mean particle size (see Section 5.1 for details), and the time axis of the HALOHolo data needs to be synchronized with meteorological data and data from other instruments. Usually, synchronization is done fully automatically via Network Time Protocol (NTP) over Ethernet or another data protocol delivering reference timestamps (e.g. UCSE in M-55 Geophysica). However, these methods are not fail-safe and two fallback procedures based on lag correlation exist to fix possible time offsets. One fallback procedure uses the pressure time series from the HALOHolo housekeeping data and correlates it with the static pressure measured by the aircraft. Another possibility is the usage of the time series data from cloud properties obtained by HALOHolo (e.g. N) which are correlated with the equivalent quantity from another cloud particle spectrometer. The other instrument may be a Cloud Droplet Probe (CDP) or a Cloud and Aerosol Spectrometer (CAS). Via maximizing the correlation coefficient between the two time series data, the time offset or lag is determined and the time axis is then corrected. During field campaigns with numerous other instruments and research groups involved, the synchronized data of the conventional instruments are typically available before the data from HALOHolo have been processed this far. The overall procedure for time axis synchronization and sample volume determination is considerably fast and rarely takes longer than a few minutes per flight.

With the previous preparation steps, the calculation of cloud properties as defined in Section 2.3 can be done almost fully automatically. Some individual data files need adaption (depending on the size and amount of ice, etc.) but the calculation itself is done with automated scripts. During this procedure, it is recommended to check the data quality and in particular the plausibility of the observations. Frequently observed mistakes

are for example the treatment of large deformed raindrops as nubby particles or "holes" in the time series due to failed reconstructions. After these issues have been ruled out, the final products are ready for scientific analysis connected with atmospheric research. A schematic of the individual steps is shown in Fig. 4.1. It should be mentioned that the final quality of the delivered data products depends on the operator who is responsible for the revision. The judgement by the operator is hidden in the particle habit classification, which may differ between two operators by more than 10 % of the habit fractions. Any other part with human intervention follows making training data sets due to less subjective definitions.

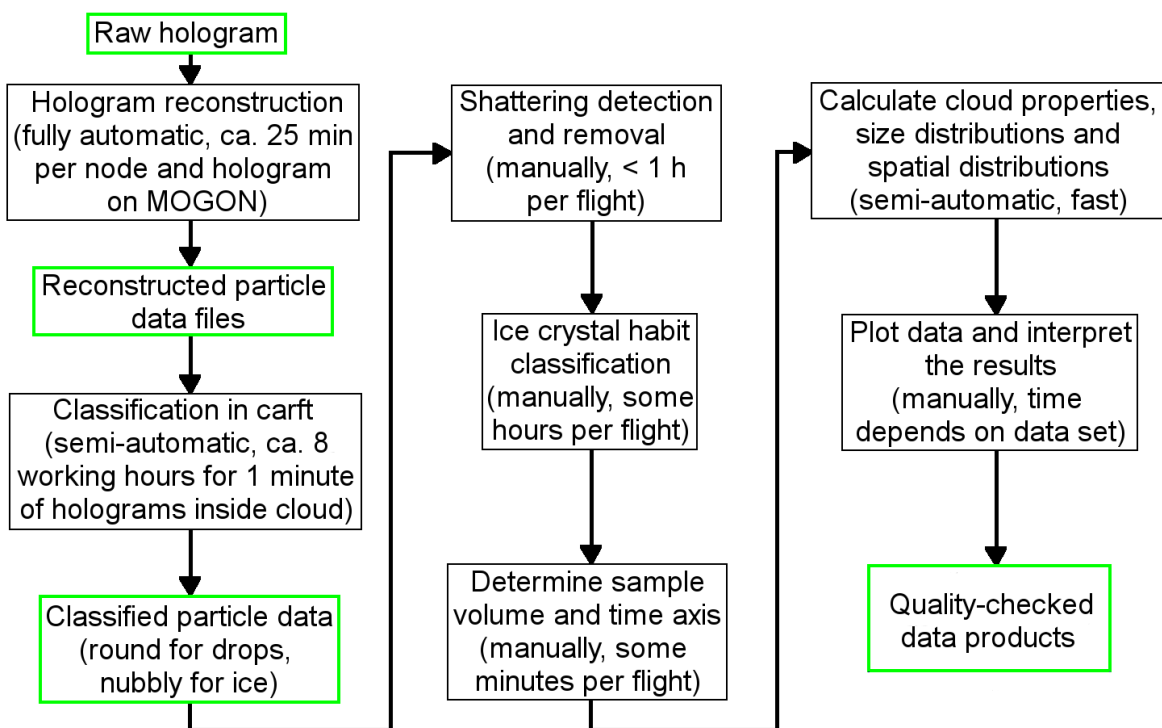


Fig. 4.1: Flow chart illustrating the data processing from the raw products leaving the instrument (HALOHolo, HOLODEC,...) to quality-checked high accuracy data products. The green boxes denote data products, the black boxes denote the processes involved to create them. There exist intermediate products in the chain from *classified particle data* to the *quality-checked data products*, which are not specified in the figure.

4.1.1 Hologram reconstruction

The fully-automatic reconstruction procedure of the top left black box in Fig. 4.1 consists of several steps that have to be taken to arrive at the *particle data files* which are the basis for higher order analysis. An overview is shown in Fig. 4.2. In the first place, the *raw hologram* needs to be filtered by using the *Background Median Divide* routine to minimize the influence of noise on the detection of particles and particle size estimation. The application of the Background Median Division is explained in Fugal et al. (2009).

In essence, a median brightness is computed for each pixel of the image from the actual hologram and an even number (usually six) of nearest neighbors, which estimates a background hologram by the assumption that consecutive holograms do not have particles at the same location. Then, the actual hologram is divided element-wise by the median brightness. After this division, most of the background pattern is removed from the hologram, which is now called a *filtered hologram* with almost equal brightness levels in the center and in the corners of the image. This step is essential for fully automatic hologram reconstruction. The difference between an unfiltered (raw) hologram and a filtered hologram is shown in the top row of Fig. 4.3.

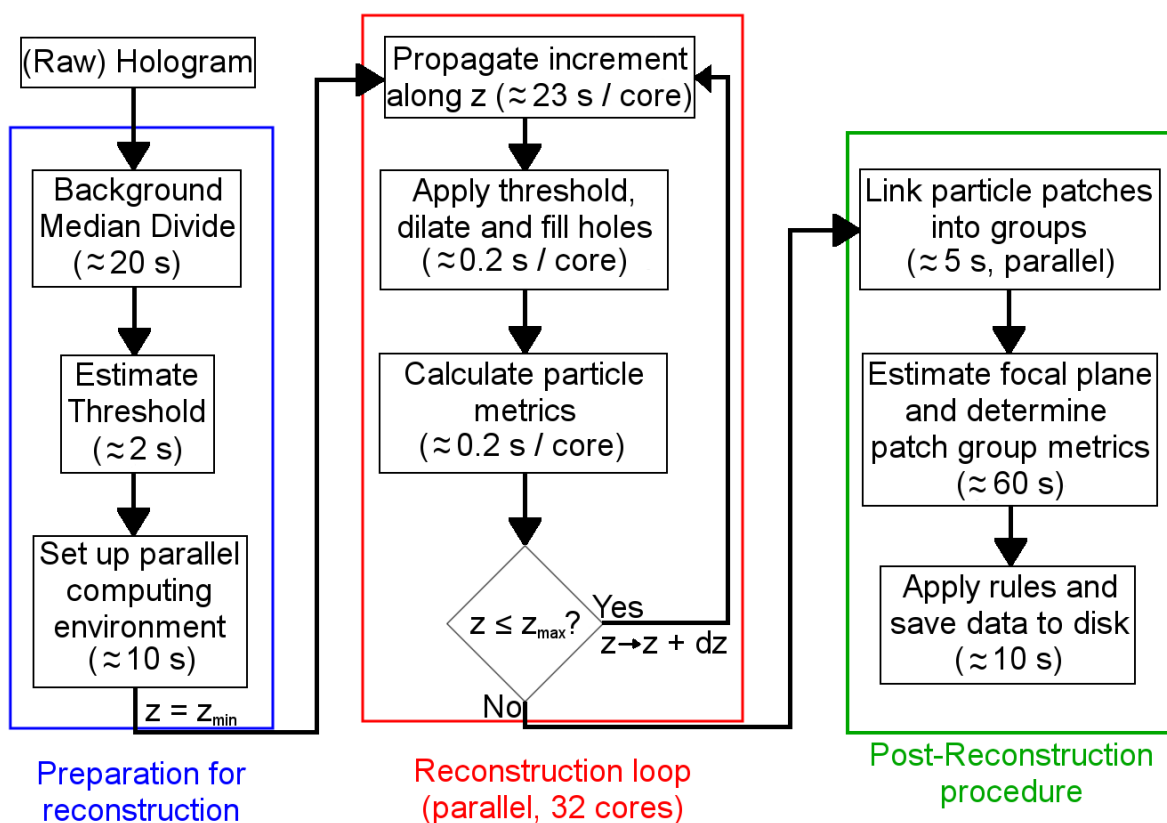


Fig. 4.2: Flow diagram of the hologram reconstruction software. The reconstruction software consists of a preparation segment (blue box), the main reconstruction segment (red box) and a post-reconstruction segment (green box).

Noise in holography has different origins, a common origin is the background pattern, which is the result of interference from multiple reflections on the optical surfaces (lenses, prisms, windows). While the stationary part of the background is removed via background filtering, the non-stationary part, which varies faster in time than the hologram recording rate, remains in the filtered hologram. However, the most important source of noise in particle holograms containing several hundred or thousand objects is speckle noise and

created by the particles themselves. In addition, the virtual image of large particles contributes to the total amount of noise in a hologram.

From the filtered hologram, an amplitude threshold is estimated, which is used to separate particles with a lower amplitude value from the background with higher amplitude values and to determine the particle area and size. A previous version of the hologram analysis software used a multiple of the amplitude standard deviation over the entire image, which is similar to the method in Malkiel et al. (2004). However, this simple approach did not prove to be sufficiently reliable for data from HALOHolo. Thus, the threshold estimation has been adapted to use not a factor that is based on the amplitude standard deviation but on the amplitude frequency distribution. Details are described in Subsection 4.1.2. Afterwards, the parallel computing environment is set up. In essence the imaged volume is subdivided into disjoint sets of independent reconstruction planes z . The sets of reconstruction planes are then "delegated" to different cores. A simple way of parallelization is to define a minimum z , called z_{min} and a maximum z , called z_{max} which set the range of z for each core as depicted in Fig. 4.3. However, the MATLAB-internal parallelization approach is more complicated than this simple description.

The *propagation* is done by using a FFT propagation kernel, which is derived from the Rayleigh Sommerfeld diffraction integral in the Fourier domain (Fugal et al., 2009). This FFT-based structure of the algorithm is crucial for the performance of the "reconstruction loop". An example of reconstructed particles and the original and filtered hologram from which the particles were reconstructed is shown in Fig. 4.3. In the reconstruction software package, the "reconstruction loop algorithm" is executed in a parallelized loop. This is one possible way to do the parallelization. There might exist other ways that could be even faster.

Additional steps are needed to segregate particle pixels from the background pixels. At first, the amplitude threshold is applied to find objects with an amplitude value that is less than the threshold. Secondly, the regions below the threshold are *dilated*. Dilation means that the pixels surrounding the thresholded region are also included in the region. Sometimes, there are individual pixels within the dilated region which have a higher brightness level than the threshold and would be excluded from the region. To avoid these "holes" in the region, the region is *filled*. An example where filling holes is essential for correct particle size and area estimation is a transparent plate-shaped ice crystal. This overall procedure is summarized by the term "Apply threshold, dilate and fill holes" in Fig. 4.2.

In a further step, all contiguous regions after thresholding, dilation and filling holes are determined and their complex-valued reconstructed field is stored in a two-dimensional array, which is hereafter called *particle patch*. It should be noted that this procedure is done for every patch at any z plane, not necessarily the focus plane of the particle.

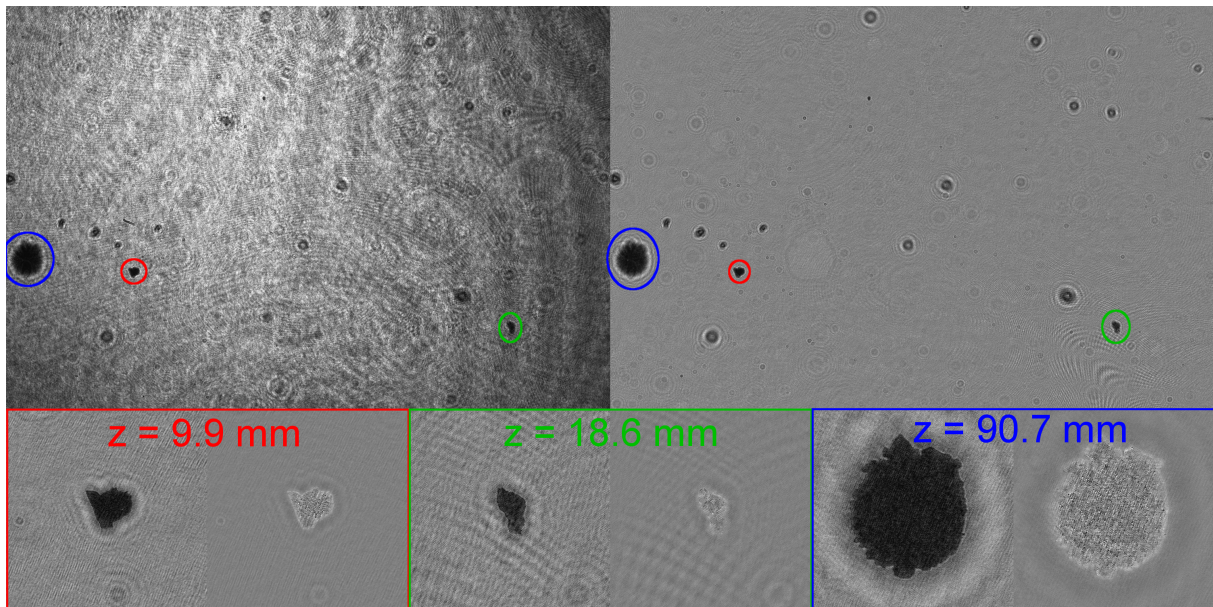


Fig. 4.3: Raw hologram (top left) and filtered hologram (top right) from measurements in a cumulonimbus cloud (Flight B926 of ICE-D). The particles which are marked with a red, green and blue circle are shown at their in-focus position in the bottom row. The left particle image in each panel shows the amplitude of the hologram field, the right shows the phase information. The image width of each particle image in the bottom row is 1.5 mm. Shown are a frozen raindrop with an attached columnar ice crystal (left), an irregular ice particle (middle) and a graupel (right). The focus position of each particle is written on top.

The particle patches are required to calculate the *particle metrics*, which are geometric or statistical properties of each particle patch. For the calculation of the statistical part of the particle metrics, standard embedded functions of MATLAB can be used to determine maximum, minimum, arithmetic mean and standard deviation of the particle patch amplitude, phase or one of the three gradient values (amplitude gradient, phase gradient, gradient of complex field). The statistical particle metrics play an important role for the focal plane estimation and the classification. However, the geometric particle metrics are of major interest for calculation of cloud properties. The function `regionprops`, which is part of the MATLAB Image Processing Toolbox, is used to calculate the center x and y position of the largest contiguous area within the particle patch that has an amplitude value below the threshold (defined in Subsection 4.1.2). Additional parameters derived from this refined thresholded and dilated object are the number of pixels (which yields the *particle area* A), the *major axis length* $majsiz$ ¹⁰ (used as maximum particle dimension), the *minor axis length* $minsiz$, the *particle perimeter* P and the *major axis orientation* ψ . These parameters are calculated for each particle patch at any and every arbitrary

¹⁰Determining major and minor axis length of an image region in `regionprops` is done in the following way: At first, the covariance matrix of the region is calculated. From this covariance matrix, the eigenvalues and eigenvectors are computed. While the eigenvectors determine the orientation of the ellipse, the major and minor axis length is given by the corresponding eigenvalues.

z. Further steps are needed to determine the focal plane, i.e. the precise position of the particle in space along z .

After the reconstruction loop is finished, the particle patches need to be *linked* into *linked patch groups*. This step makes three-dimensional particle objects out of two-dimensional particle patches. For two particle patches i and j with the lateral center coordinates x_i , x_j , y_i and y_j and their z location z_i and z_j , the weighted distance $d_{i,j}$ is calculated after Eq. 4.1. dx is the pixel size (2.96 μm for HALOHolo) and dz is the distance between two reconstruction planes (100 μm for HALOHolo).

$$d_{i,j} = \sqrt{(x_i - x_j)^2 + (y_i - y_j)^2 + \left(\frac{dx}{dz}\right)^2 (z_i - z_j)^2} \quad (4.1)$$

$d_{i,j}$ is calculated for every pair of particle patches and from the particle diameter D_i and D_j , the mean particle size is estimated, which yields the critical distance $d_{crit} = 0.5(D_i + D_j)$. All pairs of particle patches with $d_{i,j} < d_{crit}$ are linked together.

Each linked patch group has so-called *particle metric traces*, which are basically the particle metrics of the patches within the group put into vectors (one for each metric) and sorted by their z position. The information of the complex field is stored in a data structure that is equivalent to a three-dimensional array.

The traces of two selected statistical metrics, which are the standard deviation of the amplitude gradient¹¹ and the standard deviation of the complex gradient, are then examined to find their maximum peak. The focal plane of a particle is typically associated with an increase of edge sharpness (cf. Guildenbecher et al. (2013)) and therefore the z position with the maximum value of the gradient standard deviation is most likely to be the focal plane of the particle. The particle metrics, evaluated at the estimated focal plane, are then referred to as *patch group metrics*. However, this assumption is not perfect and there exists a variety of exceptions (particles far away from the detector and close to the edges, very large particles close to the detector) where this simple focus estimation routine tends to return invalid results.

Another step involved before saving the data to disk is the application of *rules*. The term *rules* means that specific conditions of the patch group metrics have to be met to consider the current linked patch group as a valid particle candidate. An example is the requirement of a minor axis length greater than or equal 2 pixels (5.9 μm) to exclude the very small objects, which cannot be firmly distinguished from noise and most of them are likely noise. In addition, another common rule is to require at least five reconstruction planes within the linked patch group, which is equivalent to a particle depth of field of at least 0.5 mm for the standard reconstruction settings. The patch groups which survive this selection process are saved to disk in a so-called *particle data file*. This is then the final

¹¹Here, the term "gradient" means the absolute value of the Sobel gradient filter in both directions, applied on the particular field (amplitude, phase, complex field).

product which contains the valid particles and potential artifacts from one reconstructed hologram.

Three of the steps involved in the reconstruction routine need to be discussed in further detail as they deviate significantly from the routines described in Fugal et al. (2009). These routines are (1) the threshold calculation, (2) the focus plane estimation, and (3) the calculation of geometric particle properties. Another nontrivial step is the combination of particle patches to linked patch groups, where the basic principle has been explained in this subsection.

4.1.2 Threshold calculation

The reconstructed amplitude and phase values are calculated for every pixel location x and y of the image throughout the entire range of z positions, for a total number of N_z reconstruction planes¹². As the memory is not large enough to keep the entire reconstructed field for all possible x , y and z positions, only the reconstructed field of the particles should be saved. Thus, it is necessary to separate pixel locations belonging to a particle (so-called *particle pixels*) from those which do not belong to a particle (so-called *background pixels*). After smoothing the background via the Background Median Division algorithm, the easiest way to separate particle pixels from background pixels is the application of a global threshold. In digital in-line holography, particles produce shadows at their projected location and thus the threshold is defined such that it separates the particles with lower amplitude values from the background with higher amplitude values. The threshold has to be just strict enough to preclude the accumulation of too many artifacts in the particle data files and just generous enough to avoid particles being subdivided into two or more fragments - or small faint particles from getting missed.

The reconstructed amplitude values of each pixel at a fixed z position are taken as one sample, from which a smoothed histogram is calculated. This smoothed histogram is typically bell-shaped, close to a Normal distribution. In order to determine a robust amplitude threshold, the bell-shaped histogram curve is approximated by a parabola with a finite positive maximum. Fig. 4.4 illustrates the actual histogram (in black), the fitted parabola (in blue) and the threshold derived from the particular fit (in red).

Apparently, from looking at the maximum value of histogram counts right at the calculated threshold value, it can be concluded that this threshold (indicated by the red line in Fig. 4.4 in the upper left panel) is likely too generous, which leads to an inclusion of too much noise. This could lead to particle sizes which are too large. The second idea was to obtain the same parabolic fit for the logarithm of the histogram counts as a function of amplitude. Taking the arithmetic mean of the threshold determined from the logarithm of the histogram and the threshold determined from the original histogram turned out to be very close to the ideal location to separate between particles and noise. However,

¹²Usually, the range of reconstructed z positions uses a separation distance $\Delta z = 100 \mu\text{m}$, begins at $z = 3 \text{ mm}$ and ends at $z = 160 \text{ mm}$, yielding $N_z = 1571$. This setup includes the inner surfaces of the camera window and laser window relative to the sample volume.

another issue comes into play for the logarithm of the histogram, which is the presence of a secondary mode (obvious in the upper right panel of Fig. 4.4). Ideally, the threshold would just cut the distribution at the mode separation amplitude value. In reality, the presence of the secondary mode disturbed the fit (which was designed for a monomodal distribution) and yielded an unphysical result of an amplitude threshold below zero amplitude. This issue could be fixed by forcing the algorithm to take only the histogram values above the 80th percentile into account for fitting¹³. Though the changes in the amplitude histogram are marginal (compare the position of the red lines in the bottom left and top left panel of Fig. 4.4), a significant improvement was achieved for the logarithm of the histogram counts. The position of the red line in the bottom right panel of Fig. 4.4 is much more reasonable than in the top right panel. With this adaptation, the automatic threshold estimation is almost 100 % fail-safe, even for holograms containing very large (millimeter-sized) ice particles. The threshold calculation procedure has been tested on several thousand holograms prior to integration into the reconstruction software.

The calculation of the actual value of the threshold is performed in the following way: Let $H(U)$ be the histogram of the amplitude values U and $\log(H(U))$ the logarithm of the histogram counts. The histogram $H(U)$ is then fitted using Eq. 4.2 to determine the coefficients a_0 , a_1 and a_2 and the same is done for $\log(H(U))$ in a subsequent step.

$$H(U) = \begin{cases} -a_0(U - a_1)^2 + a_2 & , -a_0(U - a_1)^2 + a_2 > 0 \\ 0 & , \text{otherwise} \end{cases} \quad (4.2)$$

The threshold TH is the first root of the fitted parabola and can be calculated directly from the coefficients a_0 , a_1 and a_2 .

$$TH = a_1 - \sqrt{a_2/a_0} \quad (4.3)$$

After TH has been determined from both the amplitude histogram $H(U)$ and the logarithm of the amplitude histogram $\log(H(U))$, both thresholds, hereafter labeled TH_{lin} for the amplitude histogram and TH_{log} for the logarithm of the amplitude histogram are combined to yield the actual threshold TH_{act} , which is defined as the arithmetic mean of the two (Eq. 4.4).

$$TH_{act} = 0.5(TH_{lin} + TH_{log}) \quad (4.4)$$

In order not to rely on one particular reconstruction plane, the actual threshold for the detection of particle patches and calculation of the particle metrics is chosen as the maximum of the individual thresholds taken from ten equally spaced reconstruction planes between $z = 3$ mm and $z = 160$ mm. This (global) threshold is used for all reconstruction planes of the particular hologram.

¹³This method of using a "cutoff percentile" was used in 2016 and early 2017. Recently, the coefficient a_1 is fixed at the amplitude value of the histogram mode and the coefficient a_2 is fixed at the histogram value of the histogram mode.

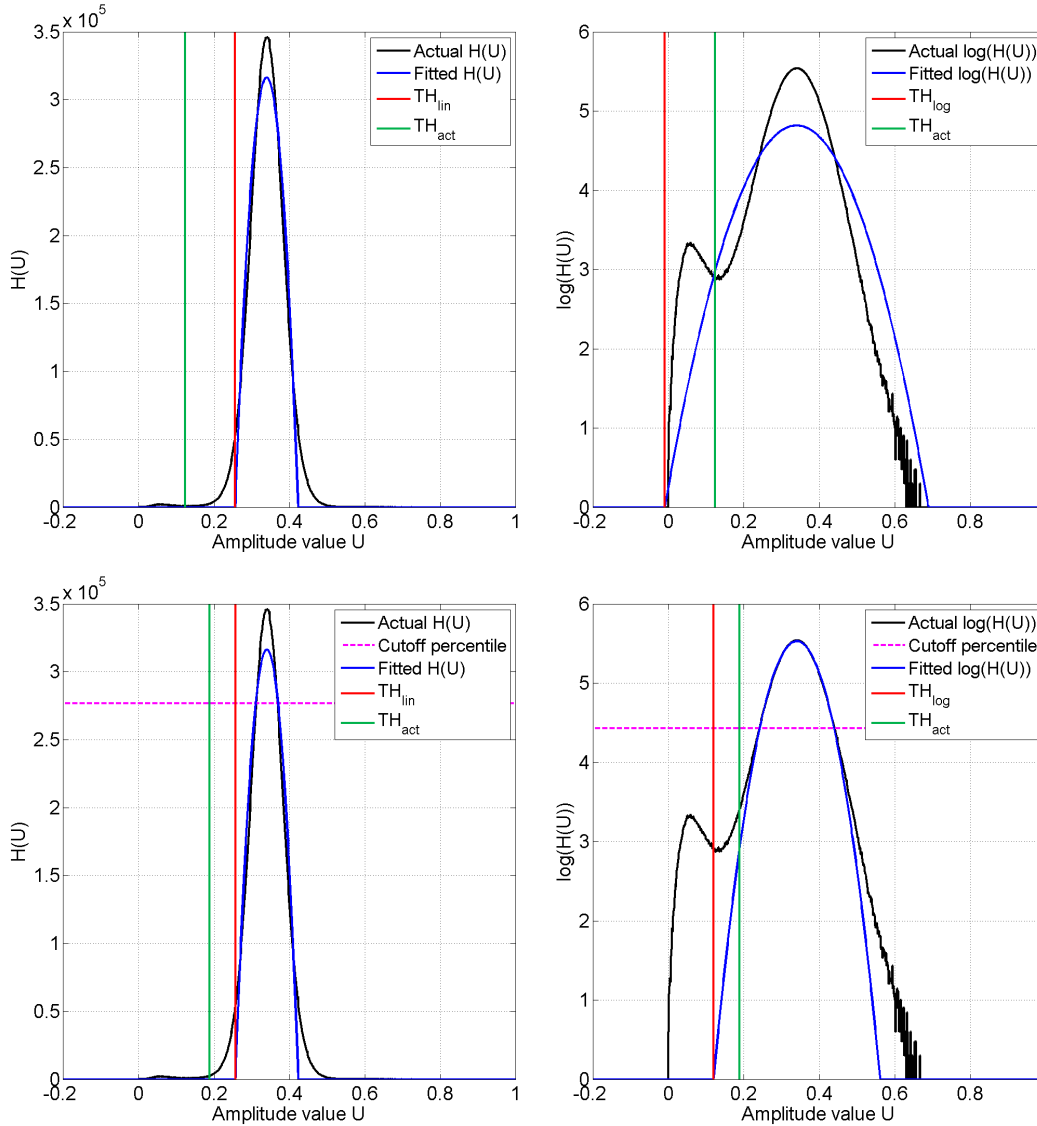


Fig. 4.4: Threshold calculated from the histogram of the amplitude reconstructed at a fixed z from a hologram containing large raindrops (Flight B926 of ICE-D). The histogram $H(U)$ is shown in the two left panels, the logarithmic histograms $\log(H(U))$ are shown in the two right panels. The threshold calculation in the top row was done via Eq. 4.2. For the bottom row, the range of the histogram to fit has been restricted to 80 % of the global maximum and greater ($H(U)$ above the dashed magenta lines). The bimodality in the logarithmic histograms is due to a significant number of dark pixels, probably from the raindrops. The actual threshold TH_{act} used for particle detection is shown in green, the corresponding threshold for the actual histogram (either TH_{lin} or TH_{log}) is shown in red. Apparently, the probability of missing particles or underestimating their size is reduced in the restricted case due to a less strict threshold (bottom row).

A major achievement of the described threshold calculation is that the threshold works for particle sizes between $5.9 \mu\text{m}$ and several mm and for many different noise levels. Some issues might be encountered for very clean holograms under laboratory conditions or for transparent particles.

4.1.3 Threshold adaption for improved sizing accuracy

For most holographic data sets, the contrast of particles in their focal plane is strong enough that the segmentation threshold TH_{act} is also used to determine the particle area and size. However, very clean holograms as obtained in the laboratory (low noise, low particle concentrations) have a contrast which is much stronger as in holograms from airborne measurements. While TH_{act} works well for particle size estimation under conditions during airborne operation (see Subsection 4.1.6), the segmentation threshold tends to be too generous for determining the size of particles measured under laboratory conditions. For this purpose, a relative threshold is used, which depends on the amplitude value U of the particle and the surrounding background pixels. Unfortunately, there is no general setting which can be used for any data set and the particular percentiles for the *background level* BL and for the *particle level* PL need to be adapted to the specific set of holograms. The assumption used for the relative sizing threshold is that the percentiles are proportional to the square root of the number of particle pixels or background pixels. The calculation of the background level and particle level is done via the percentiles BL and PL as defined in Eq. 4.5 and 4.6. n_{BP} is the number of background pixels and n_{PP} is the number of particle pixels. However, the maximum and minimum is bounded at 0.05 and 0.95 respectively. A calculation example is given in the following paragraph.

$$BL = 0.01\sqrt{n_{BP}} \quad (4.5)$$

$$PL = 0.02\sqrt{n_{PP}} \quad (4.6)$$

Assume a particle patch with a size of $25 \times 40 = 1000$ pixels with $n_{PP} = 100$ and $n_{BP} = 900$. The square root of the number of particle pixels is $\sqrt{100} = 10$, the square root of the number of background pixels is $\sqrt{900} = 30$. Using Eq. 4.5 yields $BL = 0.3$ and Eq. 4.6 yields $PL = 0.02 \cdot 10 = 0.2$. From these two values, the critical amplitude of the background U_{BL} and the particle U_{PL} is estimated. Here, U_{BL} is the 30th percentile of the amplitude values U which belong to the background pixels. The corresponding value of U_{PL} is the 20th percentile of the amplitude values U which belong to the particle pixels. With these two values, the normalization of U is done (Eq. 4.7). In case of very dark pixels in the center of the particle, the numerator in Eq. 4.7 is less than zero. Therefore, U_{new} is set to zero if $U < U_{PL}$. As $U_{BL} > U_{PL}$, the denominator in Eq. 4.7 is always positive.

$$U_{new} = \frac{U - U_{PL}}{U_{BL} - U_{PL}} \quad (4.7)$$

Now, the rescaled amplitude is segregated into the particle pixels ($U_{new} \leq 0.5$) and the background pixels ($U_{new} > 0.5$). A comparison of the two thresholds applied on reconstructed particle images from laboratory measurements in terms of particle size estimation is shown in Fig. 4.5. Obviously, the application of the relative threshold leads to fewer

background pixels included in the particle object, which yields a more accurate particle size estimation.

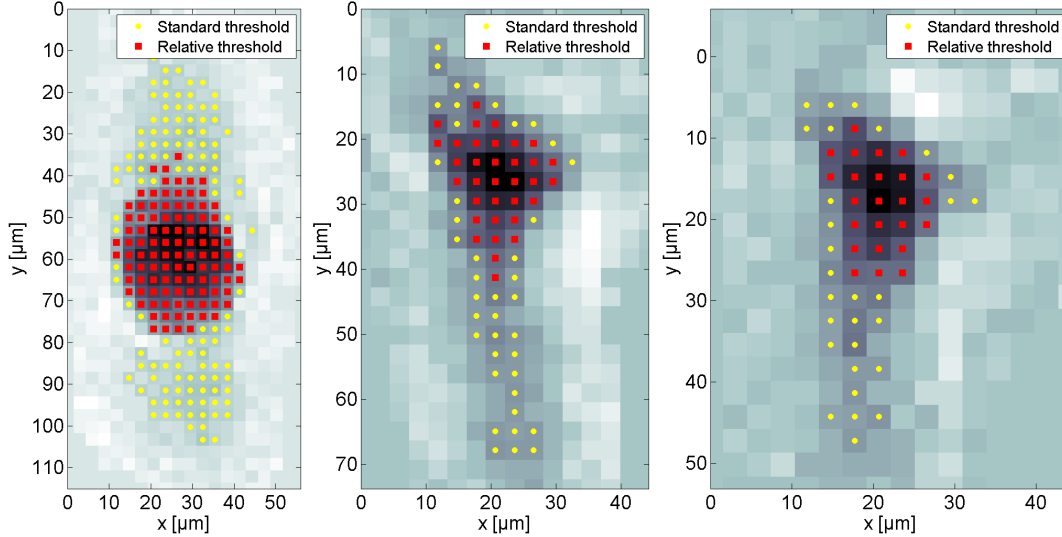


Fig. 4.5: Images of the amplitude of three particles measured in the laboratory. The yellow dots represent the pixels below the threshold if the standard threshold is used. The red squares represent the pixels with $U_{new} < 0.5$. All three particles were located close to the edge and at large distance to the detector, which led to the darker background pixels along the y axis.

4.1.4 Focus plane estimation

After a series of reconstruction planes have been obtained for a particle, an automatic algorithm is needed to estimate the focus position along the z axis of the particle. Edge sharpness is a commonly used parameter for the focus plane estimation (Guildenbecher et al., 2013). Here, a Sobel gradient filter as in Fugal et al. (2009) is applied on the amplitude field is used for quantification of edge sharpness. However, the maximum value of the Sobel gradient of the entire particle patch amplitude (as a function of the z position) is not reliable to determine the correct focal plane. A better way is to use the standard deviation (STD) of the Sobel gradient over the entire particle patch for several z positions and search for a maximum peak of the standard deviation of the Sobel amplitude gradient (hereafter abbreviated as *stdampg*). An example is shown in Fig. 4.6.

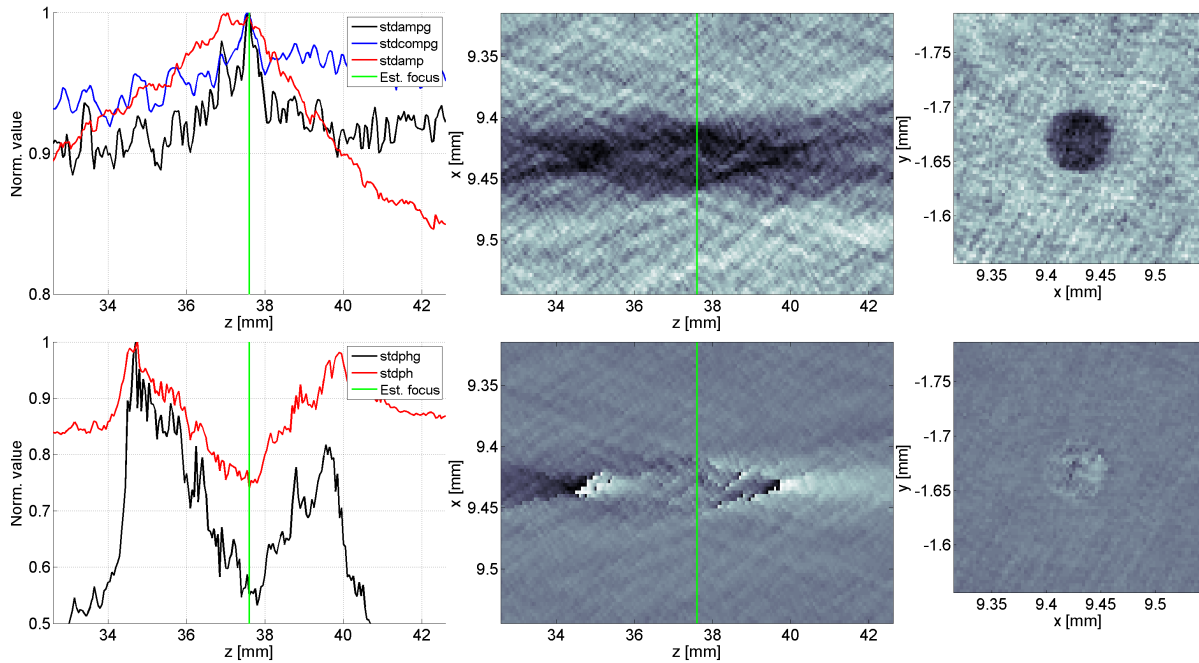


Fig. 4.6: Top row: Traces of STD of Amplitude Gradient (stdampg, black), STD of Amplitude (stdamp, red) and STD of Complex Gradient (stdcomp, blue) along z of a particle with approx. $60\ \mu\text{m}$ diameter (left), x - z cross section of the reconstructed amplitude (middle) and the in-focus amplitude image (right). Bottom row: Traces of STD of Phase Gradient (stdphg, black) and STD of Phase (stdph, red) in the left panel, x - z cross section of reconstructed phase (middle) and in-focus phase image (right). The estimated focal plane in the left and middle panels is shown in green.

Some exceptions might occur if the particle is some hundred microns large and its focal plane is close to the hologram plane or close to the lateral edge of the sample volume. In this case, there is a strong superimposed signal from the virtual image, which often distracts the thresholding and particle selection routine from selecting only the particle (without its halo). As a result, stdampg shows spikes close to the camera window plane, which are erroneously treated as the maximum peak (and therefore the focal plane of the particle). Usually, this exception is most likely for particles with a diameter of 100 microns or larger. In some flights, up to 50 % of these particles are found out of focus. An example of a complicated amplitude trace and the resulting misinterpretation of the focal plane is shown in Fig. 4.7. For these cases it is recommended to use an additional metric (e.g. the STD of Phase or STD of Phase Gradient) which is independent from the amplitude traces used for focal plane estimation. Recently, none of the additional metrics turned out to be perfect in terms of focus plane estimation. Thus, further research is needed to understand under which conditions the exceptions occur and how they could be detected if machine learning is not able to solve this issue.

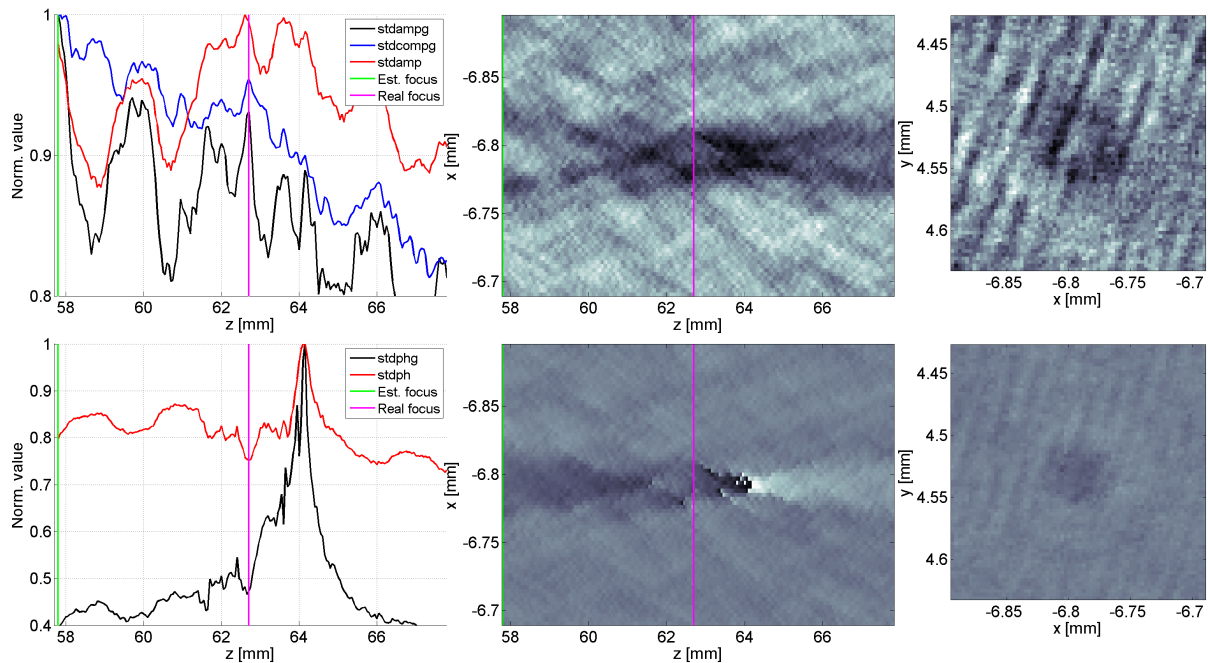


Fig. 4.7: As in Fig. 4.6 for an out-of-focus particle with the estimated focal position at the beginning of the reconstructed block (green line). The in-focus position would be located at $z = 62.7$ mm. One possible hint at the correct position of the focal plane (magenta line) is provided by the phase traces: Stdph and stdphg show a local minimum near the global maximum where the focal plane is located.

4.1.5 Calculation of geometric particle properties

A variety of geometric properties¹⁴ is already included in the patch group metrics (Subsection 4.1.1). Additional metrics are calculated after the classification. As Wu and McFarquhar (2016) have shown that the definition of the "maximum dimension" D has an influence on the particle size distributions and cloud microphysical properties derived from the particle size, it is recommended to calculate several measures of particle size. Some measures of particle size are best suited for aspherical particles (ice, mineral dust) while spherical particles should rather be measured with a different sizing algorithm. Here, five different measures of D are discussed in more detail, with application examples shown in Fig. 4.8.

1. Major axis length (*majsiz*)
2. Mean of Major axis length and minor axis length, hereafter *Equivalent size* (*eqsiz*)
3. Diameter of smallest enclosing sphere (D_s after Wu and McFarquhar (2016))
4. Area-equivalent diameter (*eqdiam*), defined as $D_A = 2\sqrt{A/\pi}$
5. Mean of maximum dimension in x direction (D_x) and y direction (D_y), hereafter D_r

¹⁴The calculation of *majsiz* and *minsiz* in *regionprops* is done via determining the covariance matrix of the region, which is equivalent to fitting a multivariate Normal distribution to the region. The covariance matrix is then diagonalized to determine *minsiz* and *majsiz* from the eigenvalues.

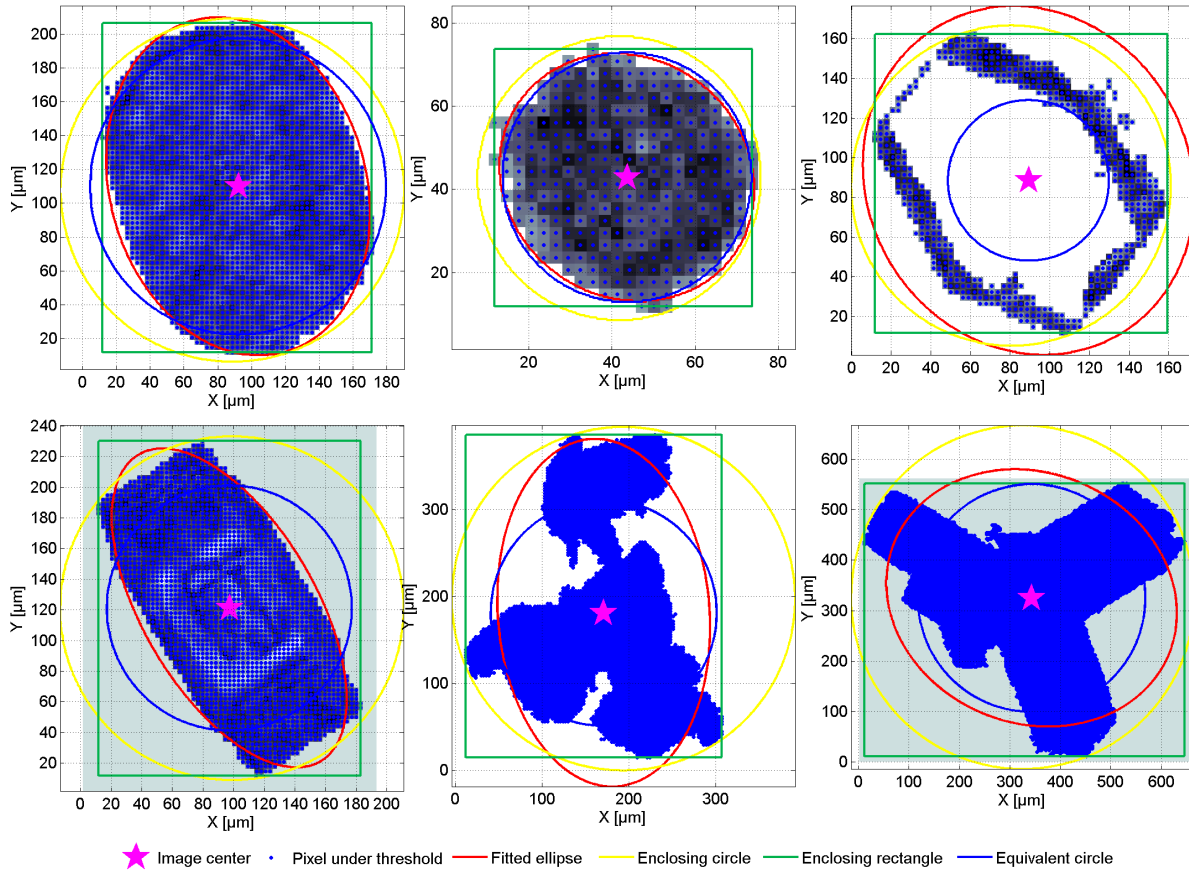


Fig. 4.8: Measures of particle diameter applied on particles of different habits. Shown are the thresholded pixels (blue circles), the fitted ellipse which defines $majsiz$ and $minsiz$ (red), the smallest enclosing circle which defines D_s (yellow), the smallest enclosing rectangle which defines D_x and D_y (green) and the area-equivalent circle (blue). The displayed habit categories are Spheroids (top left, top middle), Plates (top right), Columns (bottom left), Aggregates (bottom middle) and Rosettes (bottom right).

From the inspection of individual particles, it turned out that especially rosette-shaped particles tend to be undersized when using $majsiz$ as maximum dimension. Spherical particles, however, should be measured with D_r as erroneously larger aspect ratios resulting from darker background pixels are commonly observed, which lead to a too large $majsiz$. To get consistent results for all ice particle habits, the usage of D_s is recommended, which was suggested by Wu and McFarquhar (2016).

For spheroids, the deviation between the different measures is rather small (Fig. 4.8 top left). The largest deviations tend to occur in case of columns, aggregates and rosettes (bottom row of Fig. 4.8). Also, the probability of either oversizing or undersizing based on $majsiz$ in comparison with the true particle outline is habit-dependent. While rosettes and some aggregates tend to be undersized, columns and plates are more often oversized. Fig. 4.8 also illustrates another issue: Plates are sometimes transparent which leads to a difference between the actual particle area and the thresholded area. In case of

transparent particles, the entire area which is enclosed by the particle outline needs to be used for calculation of derived particle properties such as particle mass via the power law relationship from Baker and Lawson (2006).

4.1.6 Particle sizing via sign-matched filtering

Another idea of estimating the diameter of a *spherical* particle is the usage of an inverse modeling technique. There is an analytical solution for the Fraunhofer diffraction pattern produced by a spherical or a square aperture (cf. Goodman (2005), Chapter 4). If the fringe pattern of the analytical solution for a particle of diameter D_F (hereafter called *filter diameter*) is used as a filter in the Fourier domain, the particle with the diameter D_p will have a sharp and pronounced maximum amplitude at its exact focus position if $D_F = D_p$. This algorithm was developed by Lu et al. (2012) and is here applied on holograms obtained by laboratory and airborne measurements. To determine the optimum value of D_F , a complicated iterative procedure needs to be executed.

After the consistency of the filter results has been proven for particles of known size measured in the laboratory (see Chapter 3), this method was applied on airborne measurements. One hologram (it is from Flight 6 of RACEPAC) has a well-defined bimodal droplet size distribution and the other hologram (from Flight B933 of ICE-D) has a broad monomodal size distribution of cloud droplets, raindrops and ice crystals. A comparison between the standard sizing routine and the sign-matched filter method is shown in Fig. 4.9 and leads to the conclusion that the sizing method returns valid results for the airborne data. It is still questionable whether the low noise conditions in the laboratory or changes in the thresholding method led to the substantial deviation in case of the calibration beads.

However, the signal strength decreases with decreasing particle size and at a certain point, the particle diameter estimation, which is done via linear optimization of the z position and the filter diameter D_F , does not converge anymore. At a particle size below 2 pixels, the filtered amplitude is indistinguishable from the unfiltered amplitude, so the absolute lower limit of the sign-matched filter is at a particle size below 5.9 microns (in the case of HALOHolo). There is a size range between "convergence is assured" and "convergence will never be reached", which depends on the noise in the holograms and the particle position in the sample volume. The restrictions for applicability of the sign-matched filter are discussed in Subsection 5.5.3.

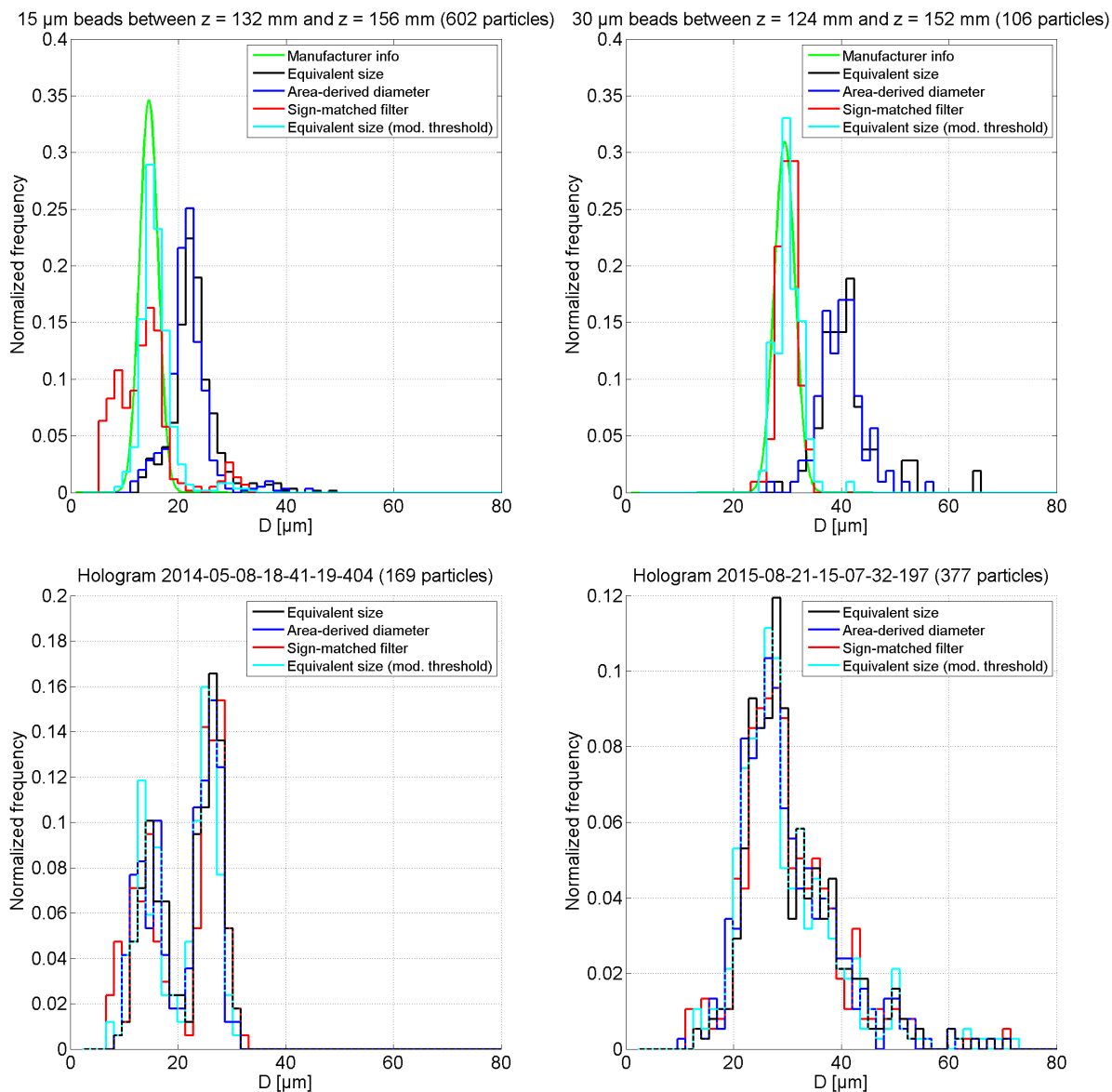


Fig. 4.9: Sizing performance of the Equivalent size (black) and Area-derived diameter (blue) from the standard threshold, the Equivalent size with modified threshold (cyan) and the sign-matched filter algorithm (red) for two holograms taken in the laboratory with 15 μm and 30 μm glass beads (top row, estimated bead size from manufacturer information in green), for one hologram from airborne measurements aboard Polar 6 (RACEPAC Flight 6, bottom left) and for one hologram from airborne measurements aboard the BAe-146 aircraft (ICE-D Flight B933, bottom right). While the "standard" and "modified" threshold seem to perform equally well on the airborne data, this is not the case for the laboratory measurements.

4.2 Particle classification

Finally, the linked patch groups with their geometric properties need to be classified in order to separate *artifacts* (out-of-focus fringes, parts of the background pattern, "ghost particles") from droplets and ice crystals. The classification is done with the software package `carft`, which is described in detail in Schledewitz (2016) and Gilles (2016). The working principle of `carft` is supervised machine learning: A subset of the objects is classified by eye (the *training data set*) and the remaining objects are then "predicted" by the computer. In subsequent steps the computer-based prediction is refined via visual inspection of the predicted particles. To illustrate the classification procedure, it is helpful to define some verification-related quantities. One of the commonly used methods to display results from a verification process is the *contingency table*. An example is given in Table 4.1.

Table 4.1: Explanation of a contingency table. The columns contain the information of the predicted class of the actual object, the lines contain the information about the actual class of the actual object. The combination "Predicted Particle" = "Particle" is called *hit*, the combination of "Predicted Particle" = "Artifact" is called *false alarm*, the combination of "Predicted Artifact" = "Particle" is called *miss detection* and the case of "Predicted Artifact" = "Artifact" is called *null event*.

	Predicted Particle	Predicted Artifact
Particle	Hit	Miss Detection
Artifact	False Alarm	Null Event

From the four realizations in the contingency table, measures of the forecast / classification *skill* can be derived. Three commonly used *skill metrics* are the *Probability of Detection* (POD), the *False Alarm Rate* (FAR) and the *Critical Success Index* (CSI). Their definitions are summarized in Eq. 4.8, 4.9 and 4.10.

$$POD = \frac{\text{hits}}{\text{hits} + \text{miss detections}} \quad (4.8)$$

$$FAR = \frac{\text{false alarms}}{\text{hits} + \text{false alarms}} \quad (4.9)$$

$$CSI = \frac{\text{hits}}{\text{hits} + \text{miss detections} + \text{false alarms}} \quad (4.10)$$

Two basic possibilities exist to optimize the classification for a low number of miss detections and a low number of false alarms. The first option is the "semi-automatic" classification, which starts the classification with the largest objects, followed by smaller particles with a less intense signal. The predicted particles are classified by eye into particles and artifacts until no particles are predicted in the subsequent update of the decision

tree. Then, the smaller objects are examined in the same procedure. This classification possibility usually reveals the highest CSI but it is the most expensive in terms of working hours. A typical application of this method is the analysis of holograms in cirrus clouds where particle number concentrations are usually no more than a few per hologram.

In case of optically thick clouds containing droplets, it is recommended to sort out only those objects which are very likely artifacts and to classify a large enough random sample of the remaining objects by eye. Usually, it makes sense to classify at least \sqrt{N} objects if N is the total number of objects in the data set. It is crucial to have a balance between artifacts and particles to yield reasonable predictions (ideally 50 % each) as the sample size of each object category determines the range of the patch group metrics, which are used to predict whether the current patch group is a particle or an artifact. After classifying several hundreds of objects, it is recommended to randomly classify a certain number of predicted particles and also a certain number of predicted artifacts. While classifying these objects by eye, the number of false predictions is noted for each class, which allows a quantitative estimation of the classification accuracy. The classification of data from RACEPAC (typically 10,000,000 particles per flight) was terminated after the CSI was on average around 90 %. The total number of particles saved after classification contains the predicted particles (here: 9,990,000) and the classified particles (here: 10,000). To judge the classification quality, it makes sense to introduce quality control measures based on the CSI of predicting particles:

- QC0: Plausibility checked raw data, $\text{CSI} \geq 50\%$, acceptable for so-called "quicklooks" to identify time periods of interest
- QC1: Improved raw data, $\text{CSI} \geq 80\%$, good enough for instrument intercomparison of particle size distributions
- QC2: "Technically pure" data, $\text{CSI} \geq 90\%$, minimum standard for bulk analysis of spatial distributions and size / concentration variability
- QC3: High quality data, $\text{CSI} \geq 95\%$, may contain miss detections from uncorrected out-of-focus particles
- QC4: Maximum purity data, $\text{CSI} \geq 99\%$, all out-of-focus particles corrected. Recommended standard for very sensitive spatial distribution analysis.

The data used for the scientific analysis in Part II of this thesis are QC2 or better, which means that, on average, up to one out of ten particles may be an artifact. At particle sizes below approximately 15 microns, it is much more likely to miss particles than to have too many artifacts predicted as particles. In essence, the QC4 level can only be reached if the actual data set does not contain too many particles as approximately 90 % of the objects need to be inspected by eye. Long cloud passes through liquid-phase clouds can rarely be classified better than QC2 (several million particles per flight minute, which is 12.7 L of sampled air) while it is not as labor-intensive to classify a cirrus cloud pass at QC4 (1,000 - 10,000 particles per flight minute or 12.7 L of sampled air).

4.2.1 Ice crystal habit classification

The distinction of ice crystal habits allows a better understanding of the microphysical processes which were involved in nucleation and growth of the individual ice particle. Ice crystal habits are dependent on temperature and ice supersaturation (Bailey and Hallett, 2009). Here, eight basic habit categories were defined for the most abundant habits. Two of them are specifically defined for mixed-phase clouds (Frozen Drops) and ice clouds (Rosettes).

- Columns: Particles with a predominant four-fold symmetry with a length-to-width ratio greater than 1. Both ends do not need to have a plane vapor-grown surface. Splinters, sheaths and bullets are incorporated in this habit category.
- Plates and Dendrites: Particles with a predominant six-fold symmetry, sometimes tilted. Some plates might develop into dendrite shapes.
- Rosettes: Aggregates which consist of multiple columns originating from a common center, usually found in cirrus clouds. These particles may not contain any other crystal type and are usually not rimed.
- Spheroids: Particles which cannot be reliably distinguished from ideal spheres. Tiny columns or plates (typically smaller than 30 μm) in cirrus clouds, shortly after nucleation (sometimes referred to as "droxtals", cf. Ström et al. (1997)), are often attributed to this habit class. In mixed-phase clouds, these particles are attributed to supercooled cloud droplets.
- Frozen Drops: Deformed particles, usually found in mixed-phase clouds, which are close to spherical. Some of them might have developed spicules during freezing as observed by Rangno (2008), Leisner et al. (2014) and Lawson et al. (2015). Frozen drop fragments are incorporated in this category. Heavily rimed Frozen Drops are classified as Rimed Aggregates.
- Irregular: Particles which cannot be attributed to plates, columns, spheres, frozen drops or (rimed) aggregates.
- Aggregates: Particles which are obviously composed of multiple ice crystals, e.g. columns and plates stuck together on a single particle.
- Rimed Aggregates: Aggregates which have half-spherical protuberances between approx. 10 and 40 microns in diameter on their outer shell which very likely resulted from freezing of supercooled cloud droplets on the particle. Graupels are also classified as Rimed Aggregates.

From the definitions above, the distinction between columns, plates, spheroids and rosettes should be straightforward, yielding the least probability of misclassification. Fig. 4.10 demonstrates the habit segregation for the four first categories which are the easiest to distinguish. Towards the classification of the other habits, the identification of rime is crucial. To demonstrate the appearance of a rimed vs. an unrimed particle, some representative examples were selected in Fig. 4.11.

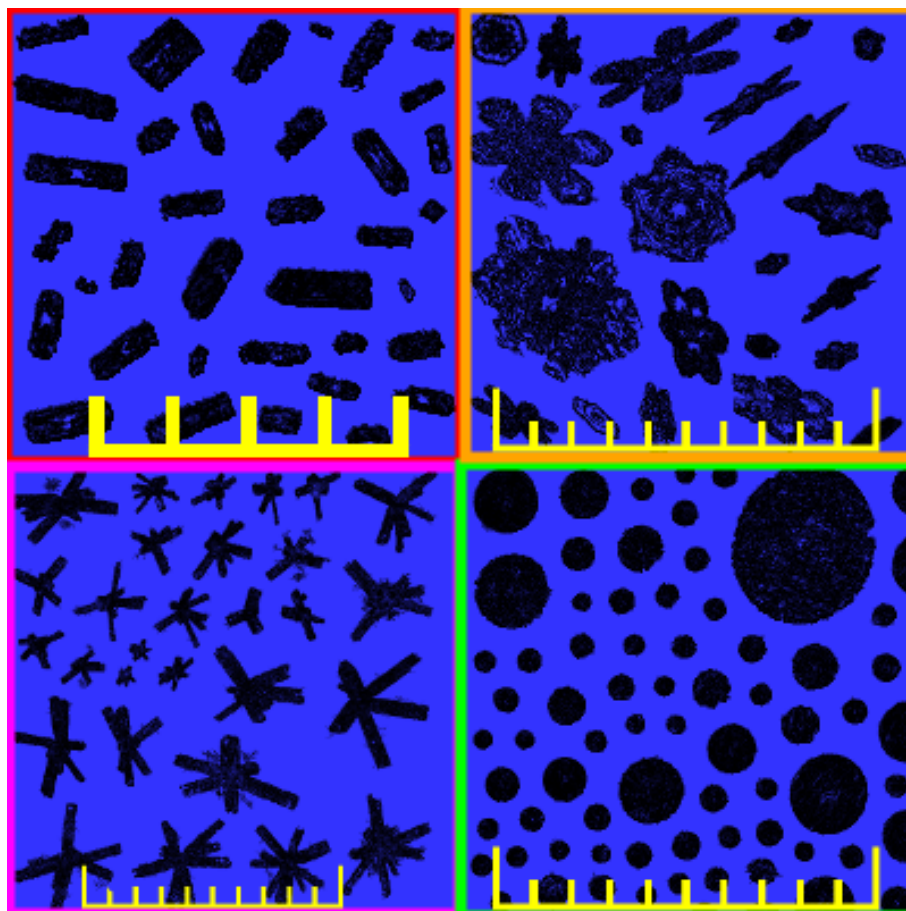


Fig. 4.10: Examples of columns (top left), plates and dendrites (top right), rosettes (bottom left) and spheroids (bottom right). The scale is only preserved within the individual panels. Scale bar increments are $100\ \mu\text{m}$ each. Data taken from ICE-D Flight B926 and COSMICS Flight B889.

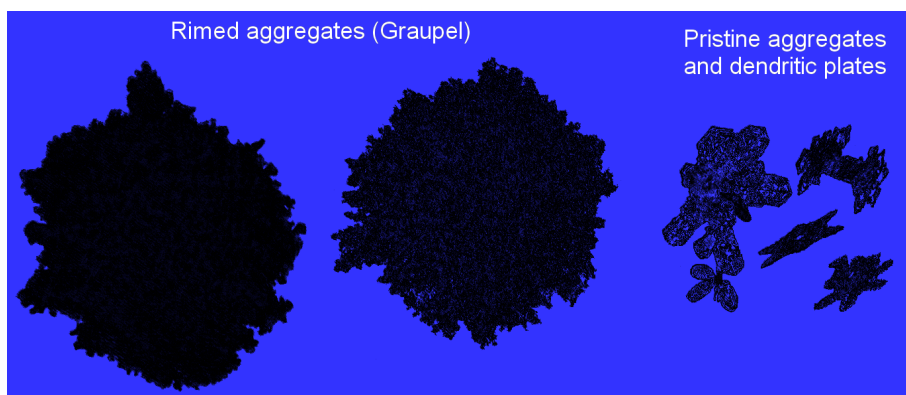


Fig. 4.11: Example of rimed aggregates vs. pristine (unrimed) aggregates. The rimed particles show numerous spherical protuberances on their outline, which are absent in case of pristine aggregates and dendritic plates. Data taken from ICE-D Flight B926.

It is important to distinguish between rimed and unrimed particles because of implications on cloud physics. Particles containing protuberances of 10 to 50 microns in width are classified as rimed particles. As sizes and shapes of the protuberances tend to vary, this is not a 100 % objective criterion and misclassification may occur more often than in the case of the "easier" habits.

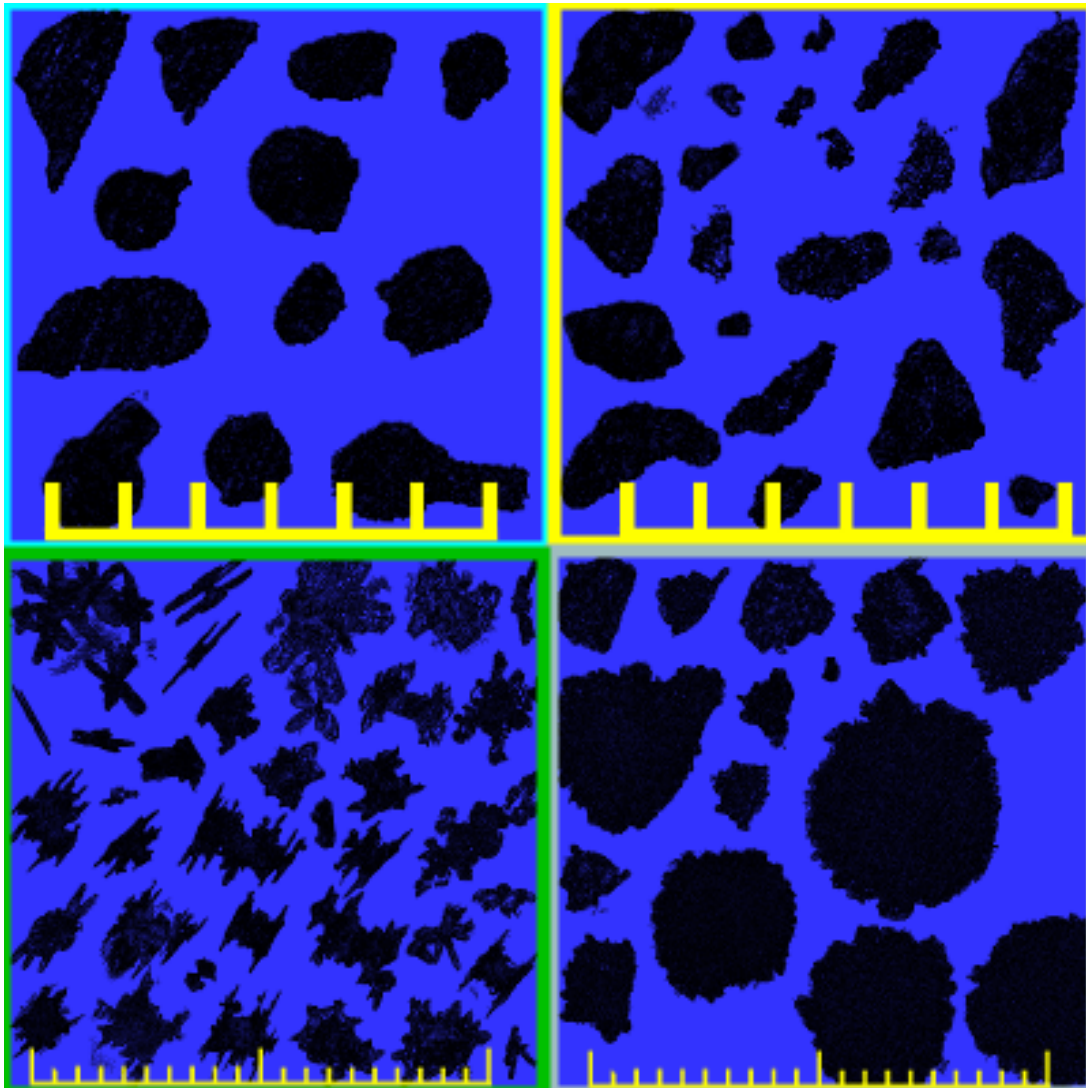


Fig. 4.12: Examples of frozen drops (top left), irregular particles (top right), pristine aggregates (bottom left) and rimed aggregates (bottom right). The scale is only preserved within the individual panels. Scale bar increments are 100 μm each. Data taken from ICE-D Flight B926.

Concerning the classification uncertainties, even the "easy" habit classes (spheroids, plates and dendrites, columns, bullet rosettes) are not 100 % accurate. Korolev et al. (2017) discussed the issue of small hexagonal plates (5 to 20 pixels in diameter) being almost indistinguishable from spherical objects. In particular small, barely aspherical ice particles

are very often misclassified as droplets. In addition, the orientation of the particle c axis of a hexagonal prism in the sample volume introduces classification uncertainties between columns and plates. Some "extreme cases" in terms of particle orientation are shown in Fig. 4.13.

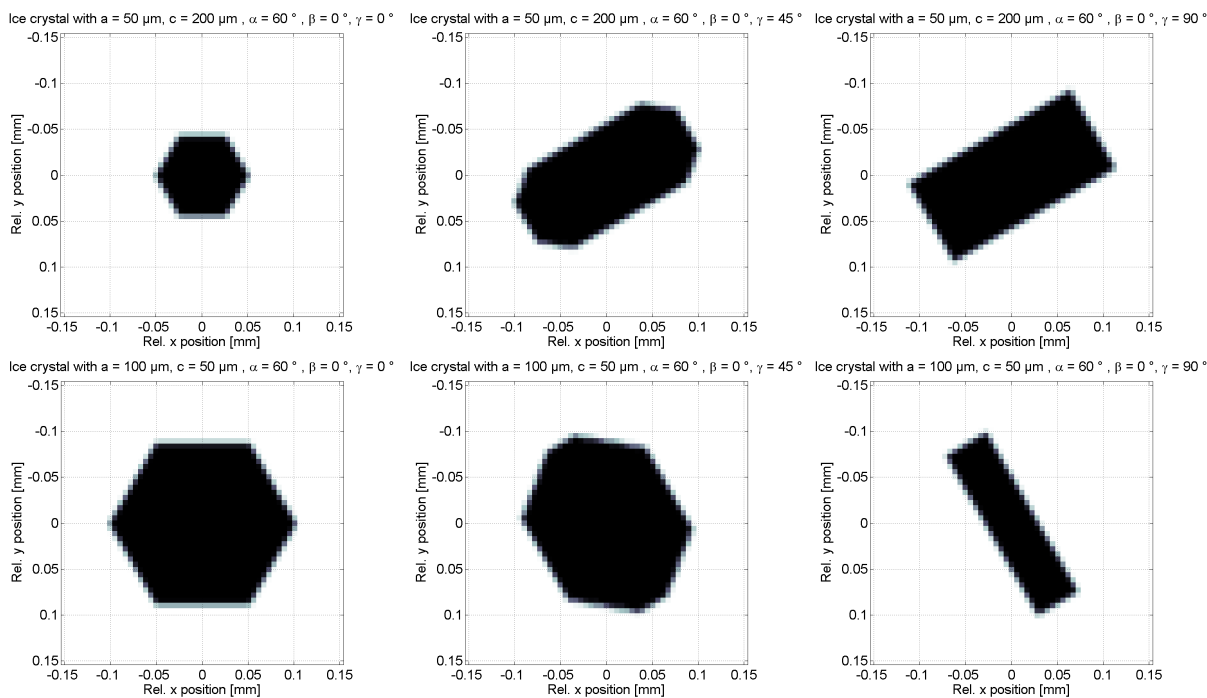


Fig. 4.13: Simulated shadowgraphs of columnar (top row) and plate-type (bottom row) crystals viewed under different angles. The rotational angle α around the z axis and the rotational angle β around the y axis were kept constant ($\alpha = 60^\circ$, $\beta = 0^\circ$) while the rotational angle γ around the x axis was 0° (left), 45° (middle) and 90° (right). The geometry is similar to the geometry of HALOHolo (the z axis points into the plane spanned by x and y). The pixel size used for the simulations was $dx = dy = 5.5 \mu\text{m}$ as in GipfelHolo.

Each of the particles is a hexagonal crystal with a hexagonal edge length a and a columnar axis c . The shadow images are simulated by rotating the particle in the 3D space (with the angles α , β and γ) and obtaining the front-view area cross section. The column in the top row has $a = 50 \mu\text{m}$ and $c = 200 \mu\text{m}$, the plate in the bottom row has $a = 100 \mu\text{m}$ and $c = 50 \mu\text{m}$.

The impact of the particle orientation on accurate size and mass estimation was examined further via seven simulation sets containing 10,000 hexagonal prisms with a uniform random orientation in space. With a constant hexagonal side length $a = 25 \mu\text{m}$, the length of the c axis was varied from $c = 25 \mu\text{m}$ to $c = 250 \mu\text{m}$ between the sets, which yields an *aspect ratio* $\delta = \frac{c}{2a}$ from 0.5 (plates) to 5 (long columns). From the area cross section of the simulated shadow image, the mass was calculated via the power law relationship from Baker and Lawson (2006). Fig. 4.14 left shows the disparity between the actual c axis length and the determined major axis length as well as the actual minor axis length in

relation to the hexagonal diameter $2a = 50 \mu\text{m}$. Though the maximum observed disparity between c and major axis length can reach $200 \mu\text{m}$, this particular case is very rare as it requires a direct front view on the hexagonal facet of the column. Moreover, the median major axis length, indicated by the white circles in Fig. 4.14 left, exceeds the actual length of the c axis by approximately 10 %. Under small rotation angles, one or both crystal facets are at least partially projected on the two-dimensional image and make the hexagonal prism appear longer.

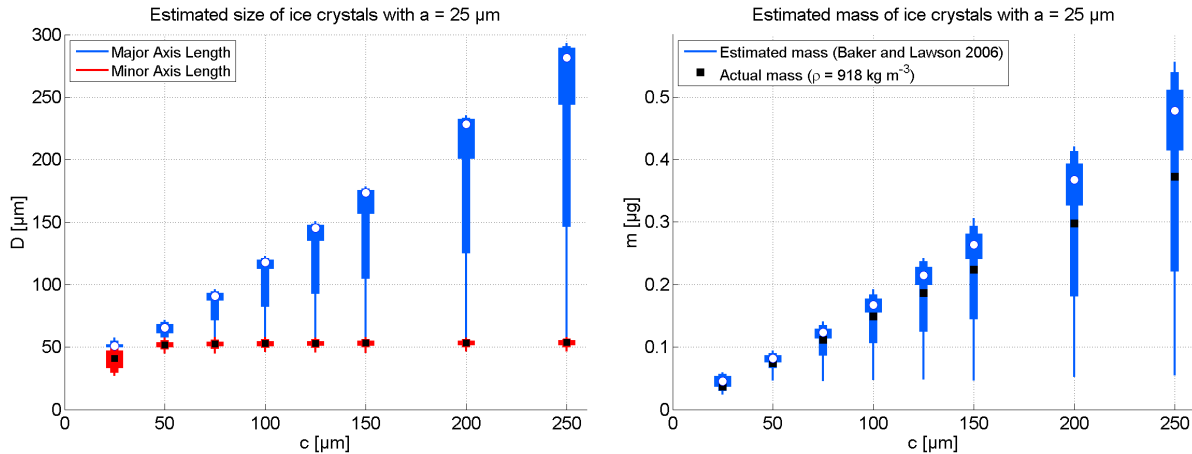


Fig. 4.14: Left: Major axis and minor axis length shown in box and whisker plots as a function of the c axis length for simulated hexagonal prisms with $a = 25 \mu\text{m}$. The three orientation angles α , β and γ were varied such that each angle had a uniform random distribution within its respective range (180° for α and β , 90° for γ). The median of the major axis length (white circles) and minor axis length (black squares) are shown along with the inner 50 % of each distribution (wide boxes), the inner 90 % of each distribution (thick lines) and the minimum and maximum (thin lines). Right: Estimated particle mass (white circles and blue boxes and whiskers) versus actual particle mass calculated from hexagonal geometry for the same simulated particles as in the left panel.

Another consequence arising from overestimation of the particle size is an overestimation of the particle mass calculated from the particle area. Fig. 4.14 right shows the actual mass calculated from the hexagonal prism versus the estimated mass from the area-to-mass power law relationship of Baker and Lawson (2006). While the mass median exhibits little deviation from the actual mass in case of plates and short columns ($0.5 \leq \delta \leq 2$), particle mass is often overestimated for long columns ($\delta \geq 3$). In addition, errors in particle mass estimation may occur as the amount of air within an ice crystal is uncertain. Via in-situ digital particle imaging, it is difficult to distinguish between hollow columns and solid columns. To summarize the results of this numerical study, it can be concluded that particle size and particle mass is more likely to be overestimated than underestimated in case of long columnar crystals. The relative error is between 10 and 30 % for the maximum particle dimension and also for the estimated mass if the median from all possible orientations is considered. However, a significant underestimation may also occur

if a plate is seen from the side or a column is seen from the front. In practical use, the case of underestimating particle size and particle mass should be quite rare as only a few realizations in terms of the particle orientation exist where the minimum area cross section is imaged. This is reflected by the thin lines in the box and whisker plots, which correspond to the minimum and maximum value in each set of simulations.

4.3 Post processing

4.3.1 Analysis of spatial distributions

Neighbor distance statistics

Measuring the spatial uniformity of a particle population can be done - among other ways - by the analysis of the neighbor distance distributions for the first neighbor particles, second neighbors, etc. This method is described in Raasch and Umhauer (1989) and has been used by Borrmann et al. (1993) and Uhlig et al. (1998) to examine the spatial distributions of cloud droplets. The only tricky part of this method is the treatment of particles close to the walls.

A straightforward approach for taking wall proximity effects into account is to restrict the volume within which neighbor distances are measured. A useful assumption is to use only 2/3 or even 1/2 of the lateral dimension of the sample volume for the neighbor distances which are analyzed. The neighbors of the selected particles do not need to be within the restricted volume. With this approach, a significant fraction of the sample volume is lost (and also many particles, which reduces the data quality in terms of counting statistics) but no assumption about the particle population needs to be made. If the particles follow a uniform random distribution in space, their normalized neighbor distance follows a theoretical distribution, which was derived by Raasch and Umhauer (1989) for a three-dimensional Poisson distribution. For the n -th neighbor of the particles, the density distribution of a uniform random dispersion is given in Eq. 4.11, which is equal to Eq. 18 in Raasch and Umhauer (1989). $s_{1,n}$ (in mm) is the distance of a particle to its n -th neighbor, $s_k = N^{-1/3}$ (in mm) is the normalization distance, which is the inter-particle distance on a cubical grid and $\phi_{n-1}(s_{1,n}/s_k)$ is the density distribution for a uniform random distribution of $s_{1,n}/s_k$ for the corresponding neighborhood ($n = 2$ for first neighbors, $n = 3$ for second neighbors, etc.). The particle neighbors in Eq. 4.11 are not necessarily pairs of each other. If only the first neighbor particle pairs are considered, Eq. 4.12 (Eq. 28 in Raasch and Umhauer (1989)) needs to be used.

$$\phi_{n-1}(s_{1,n}/s_k) = \frac{4\pi}{(n-2)!} \left(\frac{4}{3}\pi(s_{1,n}/s_k)^3 \right)^{n-2} (s_{1,n}/s_k)^2 \exp\left(-\frac{4}{3}\pi(s_{1,n}/s_k)^3\right) \quad (4.11)$$

$$\phi_0(s_{1,2}/s_k) = \frac{27}{4}\pi(s_{1,2}/s_k)^2 \exp\left(-\frac{9}{4}\pi(s_{1,2}/s_k)^3\right) \quad (4.12)$$

Subvolume (Fishing) test

The assumption of a Poisson distribution in case of a uniform random spatial distribution of particles can also be tested by a different approach, which is more closely related to the nature of the Poisson distribution. The idea is to subdivide the holographic sample volume V in J subvolumes V_j and to count the number of particles n_j in each subvolume. If the average number of particles per subvolume is \bar{n} , then the so-called Fishing statistics F after Baker (1992) are calculated after Eq. 4.13.

$$F = \left(\frac{\frac{1}{J-1} \sum_{j=1}^J (n_j - \bar{n})^2}{\bar{n}} - 1 \right) \sqrt{\frac{J-1}{2}} \quad (4.13)$$

An example of the two techniques for analysis of spatial distributions is shown in Fig. 4.15 with a hologram that is close to a uniform random dispersion, obtained from RACEPAC Flight 2, and another hologram with evidence of filamentation recorded in a laboratory experiment with the cloud chamber WINK (Gilles, 2016). It is obvious that both neighbor distance statistics as well as the Fishing test are able to identify the non-uniform dispersion in the filamented case (right column of Fig. 4.15). While the neighbor distance statistics only show the consistency with a uniform random distribution for the RACEPAC case, the Fishing test can resolve some structural information on a length scale of 4 mm.

The expectation value of F is zero and the variance of F is 1. According to Baker (1992), the null hypothesis "The spatial distribution of the particles follows a Poisson distribution" can be rejected at the 99 % confidence level if $F > 3$. This test is usually performed for an increasing number of gradually smaller sub-cubes. If inhomogeneities do exist on a certain spatial scale, the values of F vs. cube length a (in mm) will have a local maximum at this length scale. Its name "Fishing test" is probably due to the fact that beyond a certain length scale it is unlikely to "catch" a particle (most sub-cubes are empty). A recommendation mentioned in Uhlig et al. (1998) is to define the smallest box size as the length scale where the probability of finding a particle is theoretically 100 % for a uniform random distribution ($a \geq N^{-1/3}$). The upper limit of the sub-cube size is either determined by the number of the cubes which fill one lateral dimension completely, or by the error bars from counting statistics. Here, the relative statistical uncertainty is represented by \sqrt{J}/J . Both analysis methods for spatial distributions, neighbor distance analysis and Fishing test, are used in Chapters 6 and 7.

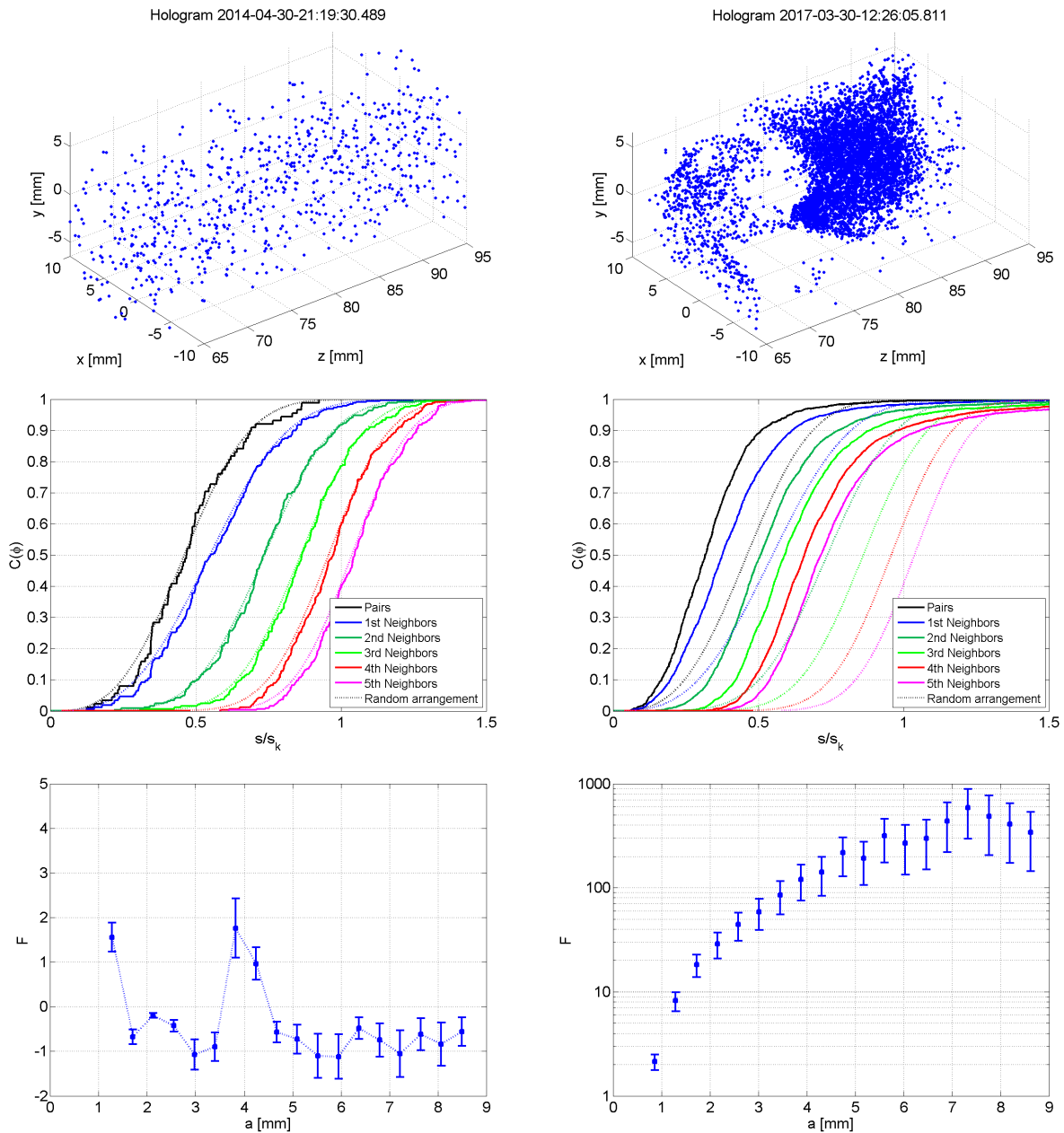


Fig. 4.15: Spatial distributions (top row), neighbor distance statistics (middle row) and F statistics from a Fishing test (bottom row) of two selected holograms. The hologram in the left column was obtained from RACEPAC Flight 2 (airborne hologram from a stratocumulus cloud in the Arctic) and the hologram in the right column was from a laboratory experiment in WINK where a jet flow was investigated. The two contrasting examples demonstrate the ability of the previously described algorithms of detecting spatial inhomogeneities.

4.3.2 Detection and removal of particle shattering

Particle shattering is easy to identify if the average particle number per hologram is low. Shattered particles tend to appear as spatial clusters with anomalously high local concentrations, usually near the instrument windows because of flow conditions. A typical

order of magnitude is a local concentration of several ice particles per cubic centimeter compared to an average number concentration of ten per liter. There exist two preferred locations in the HALOHolo sample volume where shattering occurs, which are the vicinity of the camera window ($6 \text{ mm} < z < 20 \text{ mm}$) and the vicinity of the laser window ($140 \text{ mm} < z < 160 \text{ mm}$). Outside this range of z , shattering is so rare that it does not need to be considered for HALOHolo. Two examples of obvious shattering are shown in Fig. 4.16. It should be noted that the majority of shattering events is much less spectacular than the examples in Fig. 4.16. Some of them had only two or three fragmented particles in close vicinity. It needs to be considered that a single particle with a possible fracture in one of the preferred locations for shattering might be a shard, but this hypothesis is impossible to prove.

Shattering removal, as briefly addressed in Section 4.1, can be done with a variety of methods. Each method has its advantages and disadvantages as the degree of necessary information and also the degree of human interaction varies. A summary of methods used in this work is listed in Table 4.2. The two basic ideas are either to throw away the shattering fragments (Method 1, 2 and 3) or to "glue" them together to estimate the geometric properties of the particle before shattering (Method 4). Method 1, called the "chop-off" method, is the easiest method to apply as no knowledge of the holograms affected by shattering and no human interaction is required. Via cutting away the regions of the sample volume where shattering tends to occur ($z < 20 \text{ mm}$ and $z > 140 \text{ mm}$ for HALOHolo), the remaining sample volume of each hologram is considered as "free of shattering". Method 1 is the only shattering removal technique that reliably works for mixed-phase clouds as it is extremely laborious to distinguish between clusters of droplets and shattering in holograms containing several thousand particles. Discarding all particles beyond the above limits of z might introduce a significant loss of particles, which can be problematic for cases of thin cirrus clouds or similar cases.

Less restrictive is Method 2, hereafter called the "throw-away" method. This method requires human interaction as the holograms affected by shattering need to be identified. Here, the entire hologram is discarded if it is supposedly affected by shattering. The overall particle loss introduced by the "throw-away" method is lower than in the "chop-off" method but there are still particles thrown away which are likely no shards. This disadvantage is avoided in Method 3, called the "SV surgery" method. Method 3 is in principle similar to Method 2 but from a hologram affected by shattering only the subvolume containing the shards is discarded. This method yields the minimum loss of particles from all the described methods based on discarding the shards, but it needs more human interaction and complicates the sample volume calculation. When determining particle concentration or size distributions, the removed subvolumes have to be subtracted from the total volume of the actual cloud event.

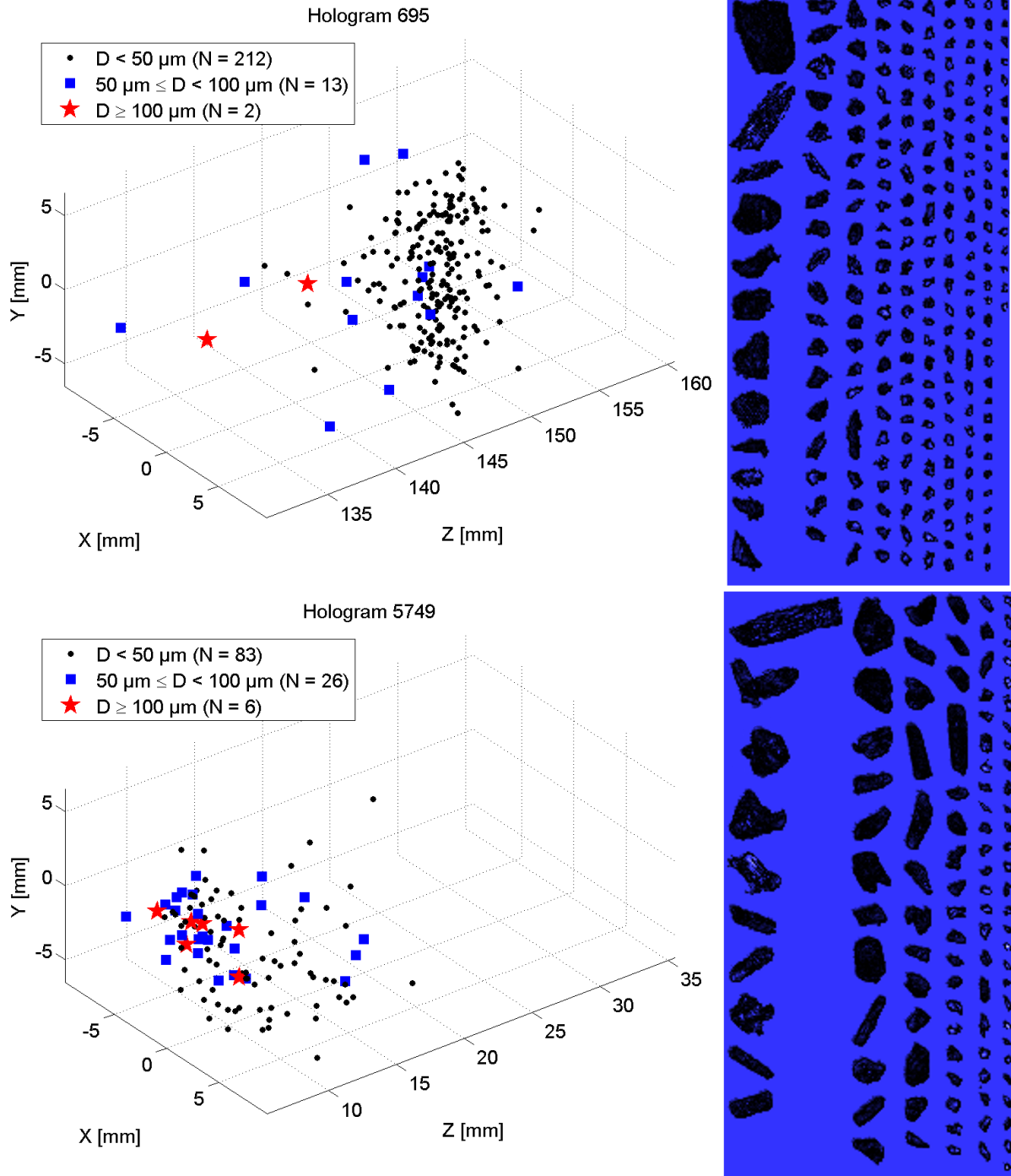


Fig. 4.16: Examples of shattering near the laser window at $z = 160$ mm (top row) and near the camera window at $z = 6$ mm (bottom row). The location of particles is shown in a pseudo-3D distribution plot in the first column. The particle image galleries are shown in the second column. Each image gallery has a height scale of 1 mm, the particle sizes are true to scale. All these images are images of shards. Data taken from COSMICS Flight B890.

Table 4.2: Short description of shattering removal techniques. The method names and corresponding numbers are used in the further discussion of each method. As the labor required from the user increases from left to right, the typical speed decreases (Method 1 is the fastest, Method 4 is the slowest).

Method	1	2	3	4
Short name	Chop-off	Throw-away	SV surgery	Particle repair
User in loop?	No	Yes	Yes	Yes
Needs knowledge of holograms with shattering	No	Yes	Yes	Yes
Needs knowledge of shattered particle location	No	No	Yes	Yes
Needs knowledge of shattered particle size and area	No	No	No	Yes

Shattering artifacts appear very often as irregular particles or columns with broken-off tips. A thorough comparison of Method 1 and Method 3 applied on data from COSMICS Flight B890 shows that both methods perform almost equally well in terms of the resulting particle size distribution (see Fig. 4.17). The applied method for shattering removal in most flights analyzed in Chapter 6 and 7 is Method 1 ("chop-off") as counting statistics were not critically impaired by a few missing particles. For the analysis of cirrus clouds in Chapter 8, the "SV surgery" (Method 3) was used.

If the number of particles is very limited and each particle adds significant value to the data, one should think about the "particle repair" method. A possible application is the measurement of very few ice or nitric acid trihydrate (NAT) particles in polar stratospheric clouds. Fortunately, shattering events are rarely observed for small particles occurring at low concentration. However, many assumptions need to be made for the "particle repair" method (Method 4), which are hard to verify. The assumptions are:

1. All particle fragments are located in the sample volume
2. The fragments broke apart from the original particle isotropically ($\frac{2}{3}$ of the area sum of all the fragments yields the total area cross section before shattering)
3. The largest fragment is the one from which the others broke off
4. The aspect ratio of the original particle is identical with the aspect ratio of the largest fragment

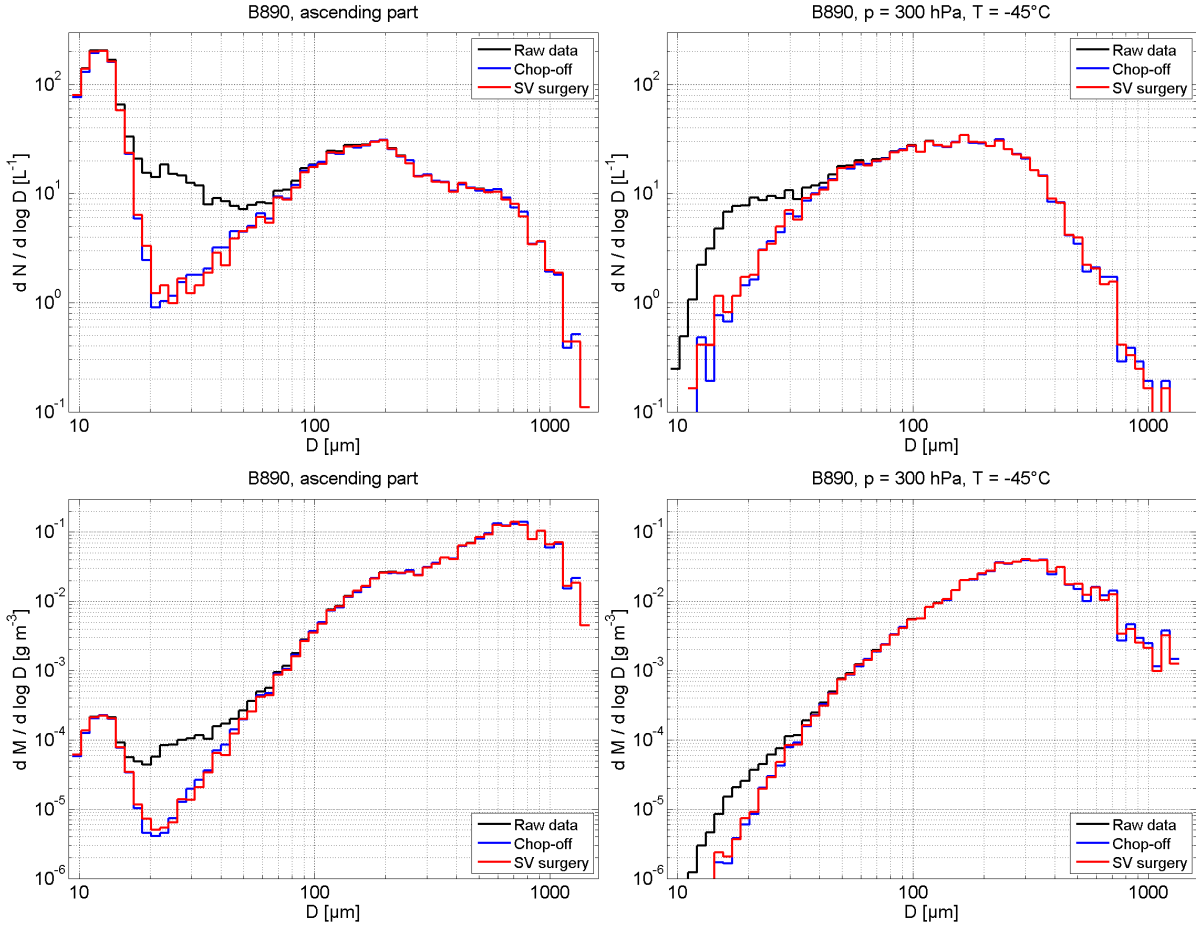


Fig. 4.17: Intercomparison of two shattering removal techniques for number-weighted (left column) and mass-weighted (right column) particle size distributions from COSMICS Flight B890. The top row shows the ascending flight leg where a zone with possible supercooled droplets was encountered, the bottom row shows the flight leg at constant altitude (at $p = 300$ hPa, $T = -45^\circ\text{C}$). Shown are raw data (which include shattering, black curve), shattering removed with Method 1 ("chop-off", blue curve) and shattering removed with Method 3 ("SV surgery", red curve).

Thus, the following equations can be derived where k is the index of the largest fragment and i is the index of any other fragment from the total number of shards N_{shards} . Eq. 4.14 is for the total area cross section A_{tot} (the factor of $1/3$ is due to the fact that A_k also appears in the sum over all A_i), Eq. 4.15 is for the estimated minor axis length $D_{min,tot}$ and Eq. 4.16 is for the estimated major axis length $D_{max,tot}$. A possibly more realistic assumption is a quasi-spherical particle with an area-derived diameter $D_{A,tot}$ calculated via Eq. 4.17. It is highly questionable that all these assumptions are fulfilled. Thus, the relative uncertainty of the particle area A_{tot} and the reconstituted particle size can be 50 % or larger. The derivation of Eq. 4.14 - 4.17 is discussed further in Appendix C.2.

$$A_{tot} = \frac{1}{3}A_k + \frac{2}{3} \sum_{i=1}^{N_{shards}} A_i \quad (4.14)$$

$$D_{min,tot} = 2\sqrt{\frac{A_{tot}D_{min,k}}{\pi D_{max,k}}} \quad (4.15)$$

$$D_{max,tot} = D_{min,tot} \frac{D_{max,k}}{D_{min,k}} \quad (4.16)$$

$$D_{A,tot} = 2\sqrt{\frac{A_{tot}}{\pi}} \quad (4.17)$$

Applying the three equations to the shattering examples in Fig. 4.16 yields $A_{tot} \approx 0.072 \text{ mm}^2$, $D_{max,tot} \approx 365 \text{ }\mu\text{m}$, $D_{min,tot} \approx 252 \text{ }\mu\text{m}$ and $D_{A,tot} \approx 303 \text{ }\mu\text{m}$ for Hologram 695 and $A_{tot} \approx 0.085 \text{ mm}^2$, $D_{max,tot} \approx 632 \text{ }\mu\text{m}$, $D_{min,tot} \approx 173 \text{ }\mu\text{m}$ and $D_{A,tot} \approx 330 \text{ }\mu\text{m}$ for Hologram 5749. Further research is needed to investigate the validity of the assumptions for the "particle repair" method and to determine the preferred cloud types, particle sizes and concentrations for shattering. A wind tunnel experiment similar to those performed by Korolev et al. (2011) would be adequate. Ideally, the particles are of known mass, size and area cross section.

4.4 Instrument modeling

An instrument model was developed to create synthetic but realistic holograms in terms of the signal to noise ratio in order to verify the results from the image processing algorithms. The model code uses the analytical solution from Fraunhofer diffraction of plane wave fronts on a spherical aperture as described in Goodman (2005). Its working principle is summarized in Fig. 4.18.

The main purposes of the instrument model are:

- Validation of particle reconstruction and size estimation routines discussed in this chapter
- Sample volume characterization (see Subsection 5.1.2)
- Investigation of the conditions for convergence of the sign-matched filter algorithm for particle size estimation (see Subsection 5.5.3)

The instrument model is initialized with a number of optical and particle parameters. Key parameters for calculation of the diffraction pattern are the laser wavelength λ in nm, the detector width N_x in pixels, the detector height N_y in pixels, the pixel width dx in μm , the pixel height dy in μm , the minimum and maximum z position z_{min} and z_{max} (both in mm) which limit the sample volume in direction along the optical axis, and the particle position (x,y,z) and particle diameter D_p . For the simulation of realistic camera noise, the camera gain factor G is also included. Other parameters such as the electron well depth of the imaging sensor and the read noise standard deviation are "hard-wired"

into the software as these properties were taken from the KAI 29050 imaging sensor, which is the sensor of the camera in HALOHolo. The typical spatial frequency of noise that simulates a nonuniform laser background is also "hard-wired" into the software. Via adding¹⁵ the particles one by one to the background, realistic speckle noise is also present in the simulated holograms, depending on number and size of the particles.

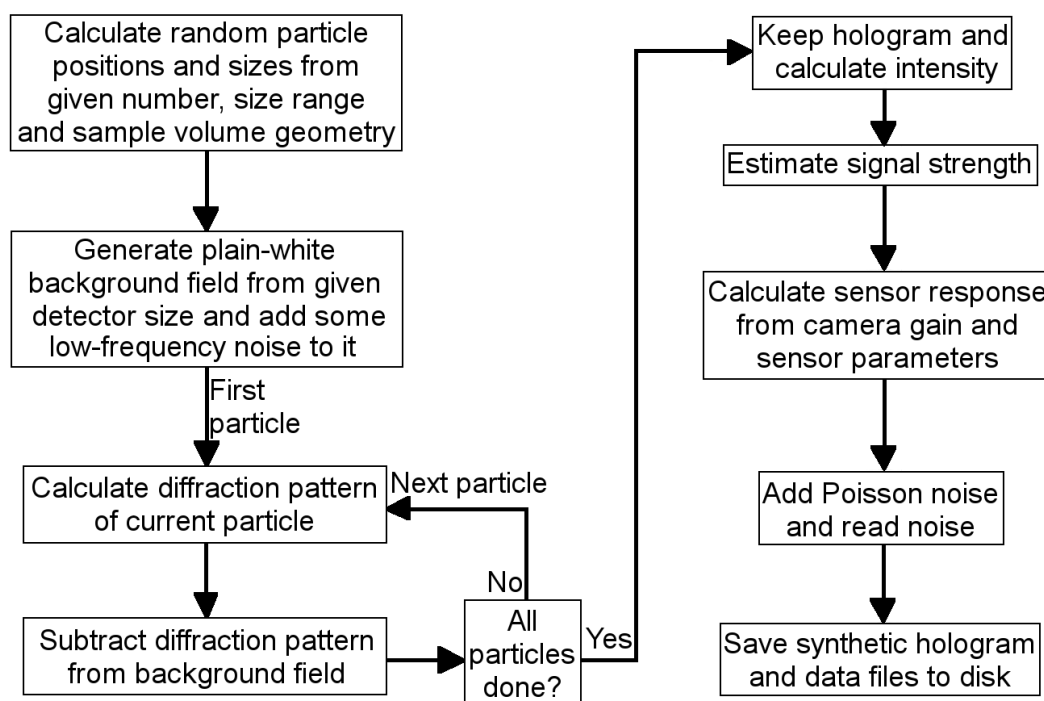


Fig. 4.18: Flow diagram of the instrument model main routine. Starting with optical parameters, sample volume parameters and particle parameters, synthetic holograms with realistic signal to noise ratio are created. The added low frequency noise in the background field emulate the effect of imperfect background filtering.

After initialization of the program, a random generator is used to emulate a uniform random distribution of particles in the sample volume defined by the initialization parameters $(N_x, N_y, dx, dy, z_{min}, z_{max})$ and the number of particles N_p . The particle diameter can be either fixed ($D_{p,min} = D_{p,max}$) or within a range spanned by $D_{p,min}$ and $D_{p,max}$. Via configuration of the initialization data file (which is a configuration text file similar to the configuration files used for hologram reconstruction), it is possible to create synthetic holograms with a well-defined size distribution of particles other than uniform random or monodisperse. In this case, vectors of particle number, minimum diameter and maximum

¹⁵In Fig. 4.18 is is a subtraction, but this is due to the fact that the calculated diffraction pattern yields bright spots where the particles are. Here, the particles should appear as dark spots as in digital in-line holography.

diameter need to be created and stored in the configuration file. A major advantage of the model is the ability to examine the practical limits of the cross-sensitivity error from particle size estimation with the same routines as used for the analysis of data measured in the field. This allows the calculation of purely software-based constraints in the particle size estimation accuracy, which may be compared with the total accuracy from laboratory measurements to disentangle the role of the instrument hardware and the role of the software in terms of sizing accuracy.

The main loop of the instrument model calculates the diffraction pattern from each particle and subtracts its complex field from the previously defined background field. The background field is a plain white background with some superimposed low-frequency noise on it. This loop is executed until all particles have been considered. The complex field is stored in memory and saved for future simulations where only camera parameters such as the gain factor G or the electron well depth are modified.

On the way from the almost clean hologram to a realistic (noisy) grayscale image, two additional steps are involved. The first one is to take the square of the absolute value of the field to convert from the complex field into intensity. Then, the effective electron well depth is calculated from the gain factor G and the actual electron well depth of the sensor to emulate the pixel-wise response of the sensor to the incident (simulated) light. After the pixel response has been determined, the actual integer number is rounded according to a Poisson distribution (to emulate random fluctuations during readout). In addition, the read noise standard deviation is added (with typical decimal values between 4 and 8 for an 8 bit integer number) and the 8-bit image is exported in a lossless compressed format (PNG). Along with the image, the estimated signal strength (which is the sum of the pixel-wise intensity that originates from all the particles in the clean hologram) is saved to disk.

4.5 Summary

In this chapter, the processes involved in getting from raw holograms to publishable data have been explained and discussed. While numerous algorithms have been mentioned in Fugal et al. (2009) and Beals (2013), their adaption to the new data set from HALOHolo and modification to improve the performance in terms of speed and accuracy was crucial for an adequate data quality. In addition, new routines for determining the particle detection threshold, semi-automatic out-of-focus correction, optimization of the sizing threshold and an independent sizing algorithm were implemented and successfully tested. Furthermore, particle reconstruction and size estimation has become fully automatic now and determines the focus position in more than 9 in 10 cases correctly. The focal plane of small particles is easier to determine and the percentage of out-of-focus particles with $D < 30\mu\text{m}$ is most often negligible. However, the presence of the superimposed virtual image impairs the correct focus estimation for larger particles, where approximately 20

% of the particles larger than 100 microns are out-of-focus. One future task is to reduce the number of large out-of-focus particles by using a better estimator of the focal plane. When determining the particle size, up to six different measures of particle diameter can be chosen in the described software package. It turned out that the one which is among the simplest to calculate (i.e. the major axis length) yields a good agreement of the size distributions in comparison with other instruments such as the Cloud Droplet Probe for droplets (see Chapters 5 and 6) and the 2D-S for ice (see Chapters 7 and 8). However, particular data sets such as cirrus cloud particles dominated by bullet rosettes and large cloud droplets as in cumulonimbus clouds show less accuracy in the instrument intercomparison for *majsiz*. Here, it is recommended to use the diameter of the smallest enclosing sphere for ice and the mean of the maximum dimension in x and y direction for droplets. Nevertheless, even with *majsiz* the disparity in size is less than 3 microns. Particular care has to be taken for transparent ice particles, which do most often occur in cirrus clouds. If the perimeter is not correctly determined, the calculated area is by far too small and the mass of these particles is underestimated by a factor of up to 100 % of the actual value.

When area- or mass-weighted size distributions need to be calculated, it is recommended to calculate the area and mass particle by particle and then sum up the individual areas and masses. This procedure reduces the uncertainties which would arise from using just the geometric mean diameter of the size bins and assuming spherical geometry. While the measurable error in the area-weighted size distributions can be reduced to the absolute uncertainty of measuring the particle area, the error within the mass-weighted size distributions is approximately 50 % of the value due to imperfections of the fitted area to mass relations, e.g. from Baker and Lawson (2006). This issue was already discussed in Frey (2011).

The calculation of quantities related to the analysis of spatial distributions has been explained and its performance has been demonstrated in two contrasting examples. However, the effect of shading might impair the performance of determining whether a spatial distribution is uniform random or not. This particular case is discussed in Chapter 5.

The bottleneck of the data analysis procedure is recently found in the classification of droplets, ice particles, out-of-focus particles and artifacts. With suitable training data sets, obtained from the manual part of the classification towards the scientific results of this work and other publications, it should be possible in the near future to allow for a much higher degree of automation in the classification step.

After the classification between spherical and aspherical particles has been done, another non-trivial step is involved to determine the ice crystal habits. This procedure is not yet automated but the same technique as in the first step of classification can be used towards a computer-aided manual classification. There exist algorithms to distinguish between pristine ice crystal shapes and others, e.g. the analysis routine used in Lawson et al. (2006). Other studies such as O'Shea et al. (2016) use neural networks to distinguish

between different ice particle shapes. It is not yet clear which technique is better suited in terms of accuracy and performance.

The orientation of hexagonal prisms in the three-dimensional space has an impact on the accuracy of particle size and particle mass estimation. While the deviation between the actual mass and the estimated mass by using the power-law relationship from Baker and Lawson (2006) is negligible for particle aspect ratios between 0.5 and 2, the overestimation of particle area becomes an issue for particles with larger aspect ratios. In fact, the particle mass of hexagonal prisms with aspect ratios between 3 and 5 is most likely overestimated by 20 to 30 %. Another observation from the simulation of the projected shadow images of ice crystals is that the major axis length tends to exceed the actual c axis length by approximately 10 %, independent of the particle aspect ratio. If the facets of the crystal are also partly visible (for small rotational angles), the crystal appears to be longer than it actually is. This systematic error of overestimating particle size and particle mass needs to be taken into account for all cloud particle spectrometers which rely on particle imaging. With some effort it is possible to simulate shadow images of other particle habits.

Instrument and software limitations and sources of uncertainties

Although holography opens a gate towards a formerly inaccessible realm of cloud microphysics, there exist limitations as for any measurement technique. Some of the limitations are induced by optical or geometric properties of the sampling volume, others are due to imperfections in the raw and processed signal. In this chapter, the main sources of errors are discussed and their effects on holographic data sets are quantified. If possible, an equation is derived to quantify the error and / or to correct the data set.

5.1 Determining the volume of uniform detectability

The boundaries of the sample volume to assure (almost) uniform detectability are crucial for the data analysis which goes into the results in Chapter 6, 7 and 8. Ideally, the sample volume of holographic instruments would be the projected area of the camera times the distance between the instrument windows. However, this is only true for particles which are large enough to produce a sufficiently strong signal even at large distances to the camera (large values of z) and to the center of the imaging sensor (large values of x or y). From measurements with GipfelHolo, it could be confirmed that ice particles above approx. 100 microns are visible anywhere in the sample volume. The greatest challenge is a uniform detectability of cloud droplets as small as 10 microns. Two effects counteract uniform detectability across the sample volume of these particles: (a) the resolution limit effect (i.e. the camera sensor is not wide enough to capture the entire pattern of the forward diffracted light wave), and (b) the so-called "edge effect" (only a half circle or quarter circle of the diffracted wave is recorded by the imaging sensor). The resolution limit effect leads to a blurry appearance with reduced signal strength of small particles at a large axial distance and the edge effect leads to a reduction in signal strength and distortion of the reconstructed in-focus particle image. The discussion of the volume of uniform detection uses two basic parameters: Position z along the optical axis, and *distance to nearest edge* (abbreviated $d2ne$) as a measure of the lateral distance to the nearest edge or corner of the sample volume that combines x and y position. With the detector width $L_x = N_x dx$ and the detector height $L_y = N_y dy$ (both in mm), the distance to nearest edge $d2ne$ is defined in Eq. 5.1. For the geometry of HALOHolo ($N_x = 6576$, $N_y = 4384$, $dx = dy = 2.96 \mu\text{m}$), the center position ($x = y = 0$) is equivalent to $d2ne = 6.49 \text{ mm}$.

$$d2ne = \begin{cases} \left| y - \frac{N_y}{2} dy \right|, & \left| y - \frac{N_y}{2} dy \right| < \left| x - \frac{N_x}{2} dx \right| \\ \left| x - \frac{N_x}{2} dx \right|, & \text{otherwise} \end{cases} \quad (5.1)$$

5.1.1 Estimation of the effective sample volume from airborne measurements

The first question to answer in terms of detectability is the dependence of the detected particle concentration on z and $d2ne$. It needs to be considered that the effective detector dimensions used in the RACEPAC flights (in Chapter 6) were different from those used in

ICE-D and COSMICS. Here, the effective detector dimensions were given by $N_x = 5184$ and $N_y = 4320$, which yields a center value of $d2ne = 6.39$ mm. The discussion of the volume of uniform detection for a given particle size is done for the RACEPAC flights as neither the analyzed ICE-D flights nor the COSMICS flights had sufficient concentrations of droplets smaller than $30 \mu\text{m}$ where "sufficient" means at least a few hundred consecutive holograms (one minute or longer in cloud) containing small droplets at $N \geq 1 \text{ cm}^{-3}$.

The particle size distribution obtained from reconstructed holograms of a particular cloud pass is characterized by the geometric mean diameter D_g and the geometric standard deviation σ_g as defined in Section 2.3. It needs to be considered that typical values of σ_g in this study are between $1.1 \mu\text{m}$ and $1.5 \mu\text{m}$.

To determine the relative loss of particles, the range of $d2ne$ and z is binned and the particle concentration over the entire cloud pass is determined for each bin for the actual local sample volume. In order to measure detectability, a *reference concentration* is needed, which defines 100 % detectability for this particular cloud pass. This reference concentration could be the concentration in the image center for the smallest values of z , but this region is impaired by droplet splashing (similar to ice particle shattering) and therefore another solution is preferred. Thus, the reference concentration is defined as the maximum particle concentration over the actual cloud pass for $d2ne > 0.2$ mm and $15 \text{ mm} \leq z \leq 20 \text{ mm}$. From the actual concentration per bin and the reference concentration, the normalized concentration is obtained.

The normalized concentration, which is used as a proxy for detectability, is shown as a function of $d2ne$ and z in Fig. 5.1 where a linear fit (yet with a fixed intercept at $d2ne = 0$ mm) was performed for a normalized concentration of 70 %. The *critical slope* s_c (in mm m^{-1}) for cutoff at a normalized concentration of 70 % determines the critical value of $d2ne$ at a given z for which the sample volume is considered uniform in terms of detectability (Eq. 5.2).

$$d2ne(z) = s_c z \quad (5.2)$$

Particles having $d2ne < s_c z$ are filtered out and the effective sample volume V is calculated as a pyramidal frustum (Eq. 3-132 in Bronstein et al. (2001)) determined by the critical $d2ne$ and z via Eq. 5.3. Here, z_{min} and z_{max} are the minimum and maximum values of z that are practically used (usually, $z_{min} = 10$ mm and $z_{max} = 150$ mm). Here, the effective detector length $X'(z) = L_x - 2s_c z$ and the effective detector height $Y'(z) = L_y - 2s_c z$ are used. Eq. 5.2 and 5.3 were used in the sample volume calculation for Chapter 6. As the number concentration of particles smaller than $30 \mu\text{m}$ was significantly lower in the ICE-D and COSMICS flights, this correction did not need to be applied for Chapter 7 and 8.

$$V = \frac{z_{max} - z_{min}}{3} (X'(z_{min})Y'(z_{min}) + X'(z_{max})Y'(z_{max}) + \sqrt{X'(z_{min})Y'(z_{min})X'(z_{max})Y'(z_{max})}) \quad (5.3)$$

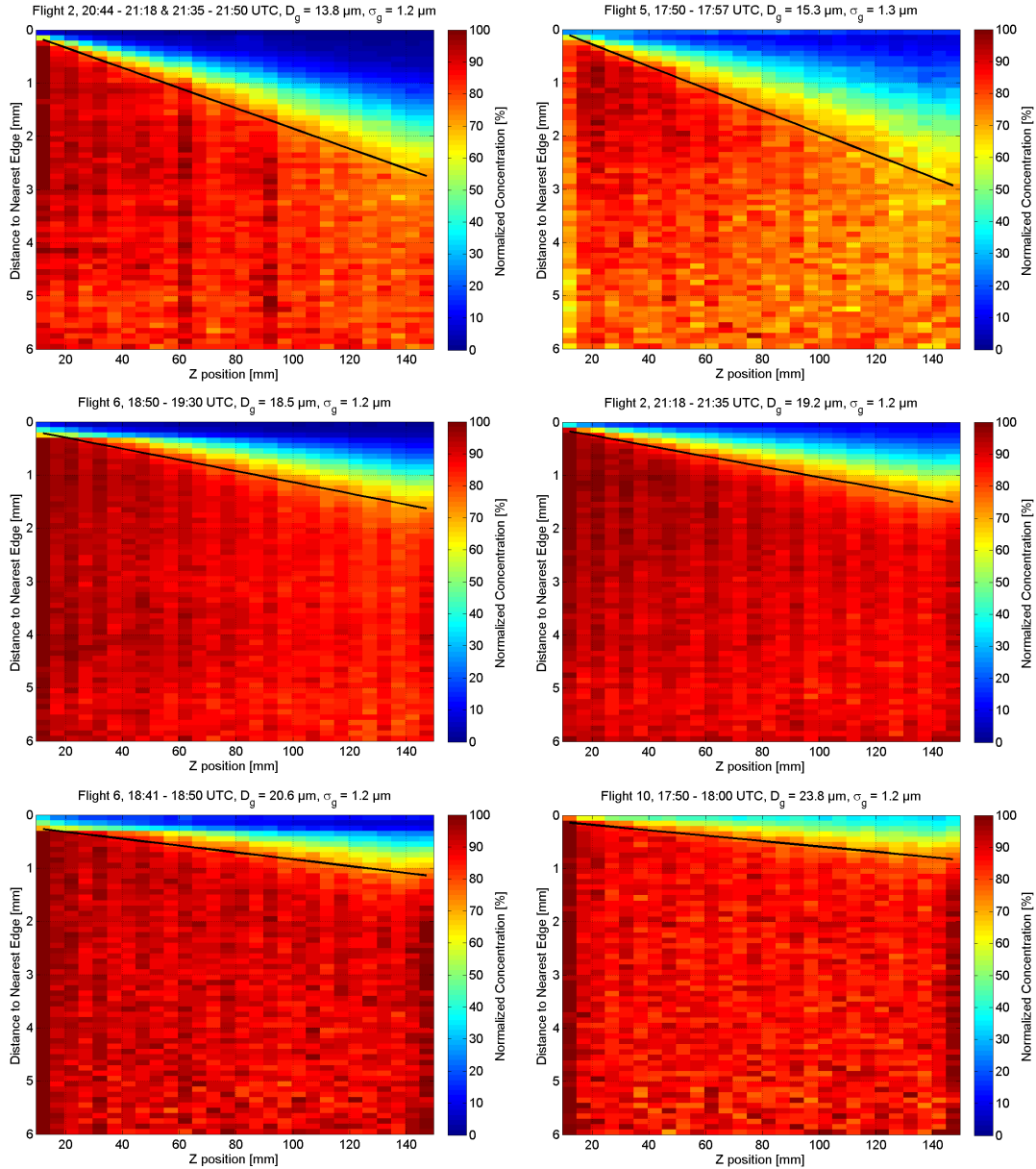


Fig. 5.1: Normalized number concentration as a function of particle z position and distance to nearest edge d_{2ne} for different cloud passes in RACEPAC Flight 2, Flight 5, Flight 6 and Flight 10 sorted by particle size in ascending order. The black line marks the cutoff threshold used to assure uniform detectability for the given size distribution. The calculation of the reference concentration is explained in the text. The ordinate axis is plotted in reverse direction, so the slope appears reversed in sign.

Apparently from Fig. 5.1, the slope s_c increases with decreasing D_g , which argues for a stronger resolution limit and edge effect in case of smaller particles (bottom left and top right panel of Fig. 5.1). The resolution limit effect can be written as in Eq. 5.4 (similar to Eq. (1) in Spuler and Fugal (2011)) where the particle diameter D and the along-axis position z are on the left-hand side, and a system-specific constant defined by λ , N_x , N_y and dx is on the right-hand side. The value of the system-specific constant is $61.8 \mu\text{m m}^{-1}$ for the detector dimensions in RACEPAC and $54.5 \mu\text{m m}^{-1}$ for the detector dimensions in ICE-D and COSMICS.

$$\frac{D}{z} = \frac{2.44\lambda}{\sqrt{N_x N_y} dx} \quad (5.4)$$

The results in Fig. 5.1 show that the slope increases with decreasing particle size. To examine the functional dependence, a linear least-squares fit was performed for the cutoff slope s_c as a function of the geometric mean diameter D_g (Fig. 5.2 left). The linear fit had a coefficient of determination $r^2 = 0.855$ and a root-mean square error $RMSE = 2.49 \text{ mm m}^{-1}$. However, it needs to be mentioned that this fit is derived from only six independent samples (each sample represents approximately one million particles).

Via Eq. 5.3, the effective sample volume V as a function of D_g was calculated from the actual data (blue symbols in Fig. 5.2 right) and from the fit (black line in Fig. 5.2 right). As V depends on s_c in the second power, the relative error of the effective sample volume is estimated as $2 \times$ the relative error of the fitted values of s_c at a fixed D_g . The slope of s_c as a function of D_g is negative, which is plausible as the $d2ne$ to be cut away increases with decreasing particle size. However, also for larger droplets it is recommended to stay at least 0.2 mm away from the walls or corners of the sample volume. While the overall agreement is acceptable for particle sizes $D_g > 17 \mu\text{m}$, the effective sample volume calculated from the fit seems to be approximately a factor of two too large for $D_g \approx 15 \mu\text{m}$. This disparity is examined in Subsection 5.1.2 where the instrument model is used to determine the volume of uniform detection from the signal strength in synthetic single-particle holograms.

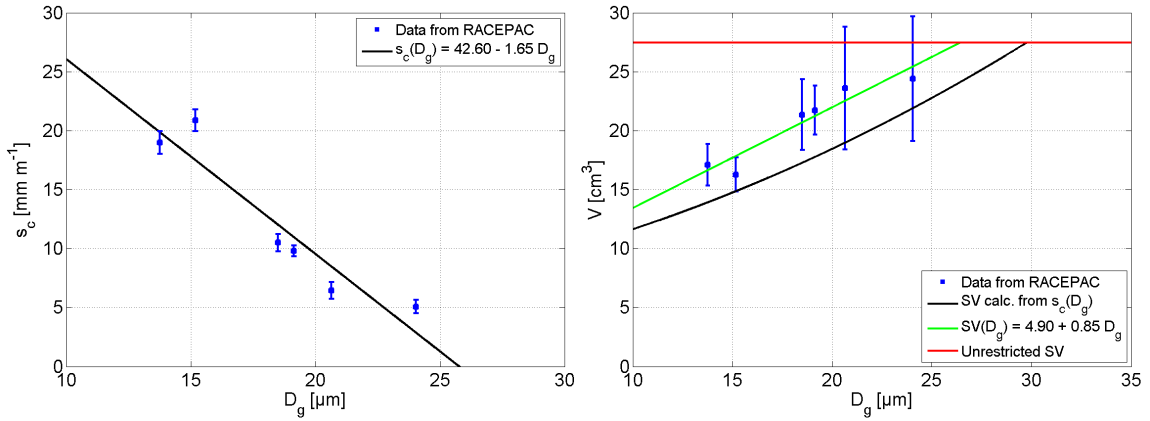


Fig. 5.2: Left panel: Cutoff slope s_c as a function of D_g for six cloud cases in RACEPAC. The actual values (blue symbols, error bars from fit parameters according to Eq. 5.2) are compared with a linear least-squares fit (black line, fit parameters given in the legend). Right panel: Effective sample volume V as a function of D_g calculated from the actual values (blue symbols, error bars from Gaussian error propagation) shown along with the sample volume calculated from s_c (black line) and a linear fit of the actual values (green line, fit parameters in the legend). The red line shows the unrestricted (maximum available) sample volume.

5.1.2 Validation of observed trends via instrument modeling

After the in-situ aircraft data were examined, the question is addressed whether the observed linear relationship of both $d2ne(z)$ and $s_c(D_g)$ can be explained by combined resolution limit and edge effects from the instrument geometry alone. Here, an agreement is assumed if the functional relationship from the in-situ data is the same as for the synthetic data.

Due to the fact that the signal to noise ratio in single particle holograms is extraordinarily high, it does not make sense to simulate single-particle holograms and estimate the detectability from the reconstruction results. A better way is to use the signal strength I from a single particle hologram as a proxy. The signal strength I is defined as the sum of the intensity deviation from unity over all pixels in the image as described in Subsection 4.4. I is proportional to the area cross-section of the particle and decreases if the particle location is far away from the lateral center and / or far away from the detector. In this numerical experiment, one particle was moved through the sample volume to measure the position dependence of the signal strength. At first, the most extreme case is tested where the particle x position is set to zero (right in the middle of the detector) and y increases from zero to the maximum height $N_y/2dy$ from the image center. Thus, the distance to nearest edge $d2ne$ is determined by the actual y position of the particle. Each simulation per particle diameter D consists of 65 values of $d2ne$ and 31 values of z from $z = 10$ mm to $z = 160$ mm. The value of I for $x = 0$, $y = 0$ and $z = 10$ mm acts as *reference intensity*, hereafter I_0 . In analogy to the procedure in Subsection 5.1.1, a critical value of the normalized signal strength is used to derive the cutoff slope s_c as in Eq. 5.2. Here, the *cutoff percentile* P_c was chosen at a value of $I/I_0 = 90\%$, which yields values of s_c close

to those determined from the 70 % detectability in the airborne in-situ data. Fig. 5.3 confirms the linear relationship of the decrease in relative signal strength for larger values of z at a fixed $d2ne$. The same kind of fits as in Fig. 5.1 was performed in the synthetic hologram study. Fig. 5.3 shows two examples of synthetic particles.

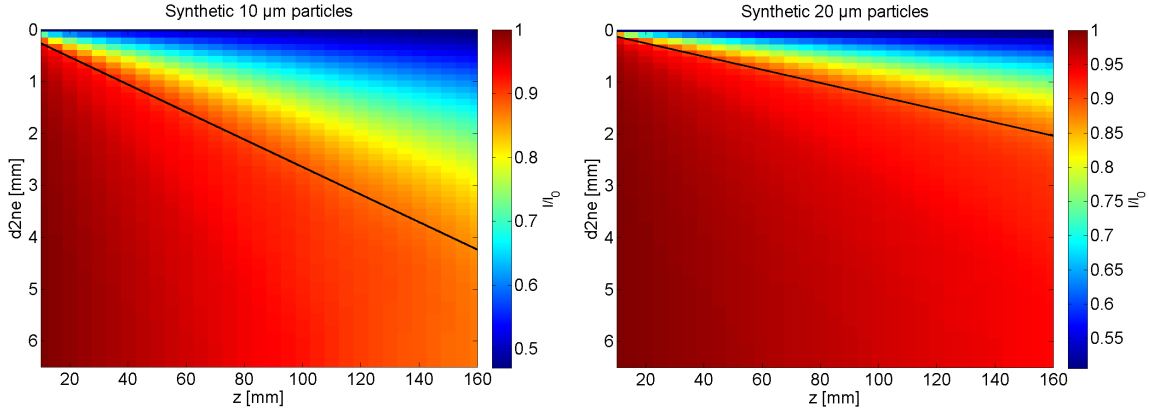


Fig. 5.3: Normalized signal strength I/I_0 as a function of $d2ne$ and z for synthetic monodisperse 10 μm (left) and 20 μm (right) single-particle holograms. I_0 is the reference intensity at $d2ne = 6.4$ mm and $z = 10$ mm.

In contrast to the airborne in-situ data, the synthetic droplet spectra are monodisperse. The overall quality of the fits was reasonable ($r^2 > 0.92$ for $70\% \leq P_c < 90\%$ and $6 \mu\text{m} \leq D \leq 26 \mu\text{m}$). A detailed summary of this analysis with the individual fit parameters is shown in Appendix D. The figures in Appendix D also show that the relationship between the cutoff threshold s_c for $d2ne$ at a fixed *cutoff percentile* P_c and z tends to become less linear for decreasing particle sizes. This is supposedly due to the relative importance of the resolution limit effect for small enough particles. For the smallest size of the test particles (which was $D = 6 \mu\text{m}$), it is not recommended to use the maximum range of z for determining the volume of uniform detectability. Table 5.1 shows typical values of the maximum relative signal strength at the maximum value of z for several particle sizes D . In practical use, the sample volume is often restricted to $z_{max} = 150$ mm to cut away possible locations of shattering. From the results in Table 5.1, the minimum particle size that can be uniformly detected up to this value of z is between 12 μm and 13 μm . This value of the critical diameter for the required detectability is in accordance with the results in Fig. 5.1 where the top right panel ($D_g = 15.3 \mu\text{m}$) and top left panel ($D_g = 13.8 \mu\text{m}$) contain values of the normalized concentration below 70 % also close to the center of the image.

Table 5.1: Maximum relative signal strength I/I_0 at the maximum z position within the sample volume as a function of particle size D . In addition, the actual z position is given at which a value of $I/I_0 > 90\%$ can be found.

D [μm]	$I/I_0(z = 160 \text{ mm})$ [%]	$z(I/I_0 \geq 90\%)$ [mm]
6	78.9	75
7	82.4	85
8	84.4	100
9	85.9	110
10	87.2	120
11	88.3	130
12	89.1	145
13	89.7	155
14	90.6	> 160

However, the exact value of D for being observable in the entire volume is not the only quantity which is somehow different in the model compared to the airborne in-situ data. Also, the functional relationship between the determined cutoff slope s_c and the particle size D differs. While a linear relationship with a negative slope was the result for s_c versus D_g for the airborne in-situ data, the synthetic data rather suggest a hyperbolic relationship between s_c and D , which is easy to verify on the log-log plot (Fig. 5.4 right).

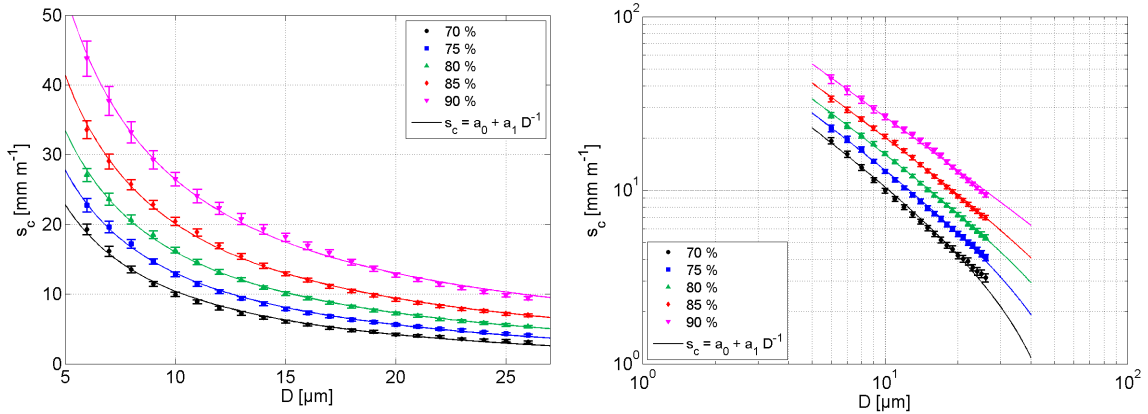


Fig. 5.4: Linear (left) and double logarithmic plot (right) of the cutoff slope s_c as a function of particle size D for five different cutoff percentiles P_c . The solid lines show a fitted hyperbola according to Eq. 5.5. Error bars are calculated from the 95 % confidence level of s_c determined from the individual fit.

Tests with a different setup (keep y at zero and vary x or go from the image center to an image corner) confirmed the results of the "standard" test conditions used in the simulations. It turned out that the fit quality decreased for $P_c > 90\%$ and therefore larger cutoff percentiles have not been examined further. For the fits, Eq. 5.5 was used.

$$s_c(D) = a_0 + a_1 D^{-1} \quad (5.5)$$

In conclusion, the influence of the combination of the edge effect and the resolution limit effect on particle detectability has been investigated and a functional relationship between the geometric particle mean diameter D_g and the cutoff slope s_c has been derived from RACEPAC data to determine the effective sample volume as a function of particle size. While the study from the instrument model showed a different functional relationship, this highly idealized setup did likely not contain all possible disturbances in the signal, which are found in real measurements. From the synthetic hologram analysis, a functional relationship of the critical $d2ne$ (here $d2ne_{crit}$) for a given particle diameter D , cutoff percentile P_c and z position is derived in Appendix D.2 and shown in Eq. 5.6.

$$d2ne_{crit}(z, D, P_c) = 10^{-3} \cdot \left(-1.95 + 0.003(P_c - 68.9)^2 + (5.33P_c - 248.7) \frac{1 \mu\text{m}}{D} \right) z \quad (5.6)$$

As the critical value of $d2ne$ as a function of the cutoff percentile, the z position and the particle diameter has been derived, it is now possible to provide a functional relationship for the effective sample volume SV_{eff} . It is helpful to define the effective x length $X'(z)$ and the effective y length $Y'(z)$ for a fixed D and P_c . If the critical $d2ne$ becomes larger than $Nydy/2$, z needs to be restricted such that the smallest value of $Y'(z) = 0$. The effective detector width and height $X'(z)$ and $Y'(z)$ are given in Eq. 5.7 and 5.8.

$$X'(z) = Nxdx - 2 d2ne(z, D, P_c) \quad (5.7)$$

$$Y'(z) = Nydy - 2 d2ne(z, D, P_c) \quad (5.8)$$

The two base areas A_1 and A_2 can be expressed in terms of detector width L_x , detector height L_y and detector area $A_D = L_x L_y$.

$$\begin{aligned} A_1 &= (L_x - 2 d2ne(z_{min}))(L_y - 2 d2ne(z_{min})) \\ &= 4d2ne^2(z_{min}) + A_D - 2(L_x + L_y)d2ne(z_{min}) \end{aligned} \quad (5.9)$$

$$\begin{aligned} A_2 &= (L_x - 2 d2ne(z_{max}))(L_y - 2 d2ne(z_{max})) \\ &= 4d2ne^2(z_{max}) + A_D - 2(L_x + L_y)d2ne(z_{max}) \end{aligned} \quad (5.10)$$

With the previously derived equations, the effective sample volume SV_{eff} can be calculated. z_{min} and z_{max} are defined as in the paragraph after Eq. 5.2 of Subsection 5.1.1. If $Y'(z) = 0$ for $z < z_{max}$, z_{max} needs to be adapted such that $Y'(z_{max}) = 0$. The volume is calculated as the volume of a pyramidal frustum as in Eq. 5.3 with the lower base area

A_1 and the upper base area A_2 . However, a simplification of Eq. 5.3 by the usage of Eq. 5.9 and 5.10 is not really useful.

To get a more realistic estimation of the signal strength in densely populated holograms in future simulations, one could add random noise to the signal strength I , which reflects the disturbance of the signal caused by the presence of other particles. In addition, the Gaussian-shaped profile of the laser beam might be considered as well.

5.2 Particle shading

There are two different influences which might be referred to as shading. One of them is that small particles are hidden by a larger particle which is located along z before or after the small particles at the same lateral location. This effect is hereafter named *direct shading* and its influence can be calculated as a function of particle size. The more complicated case is the so-called *indirect shading*, which is the effect of a very large particle disturbing the threshold estimation, leading to a large number of miss detections for small particles in the same hologram. Unfortunately, this effect is very hard to quantify. However, there is a possibility to check the hypothesized influence of indirect shading on a particular flight or cloud pass: By examining the correlation between the number of small particles per hologram and the number of large particles per hologram in a scatter plot, this effect will be reflected by a strong negative correlation between the number counts of small particles on the ordinate and the number of large particles on the abscissa. If the numbers of small and large particles in each hologram are uncorrelated or positively correlated for the particular cloud pass, the influence of the indirect shading is likely negligible except for a few possibly missing particles. In order not to erroneously attribute a shading effect to Wegener-Bergeron-Findeisen, this correlation study has to be done with holograms that do not contain large ice or large amounts of small ice. Cloud pass 1 from the ICE-D Flight B926 has been selected for this investigation as it contained virtually no ice but some millimeter-sized raindrops. The correlation between the number of small and number of large particles as well as the dependence between number concentration and maximum particle size and maximum vs. minimum particle size for a sample of 108 holograms is shown in Fig. 5.5.

It is visible that both slope and correlation between the number of small particles and the number of larger particles decrease if the separation diameter is increased from $50\ \mu\text{m}$ to $100\ \mu\text{m}$ (top row of Fig. 5.5). However, in none of the scenarios was there a strong negative correlation between the concentration of small and large particles to be seen. There is a weak negative trend when looking at minimum vs. maximum particle diameter from each hologram, and also between the total number concentration and maximum diameter.

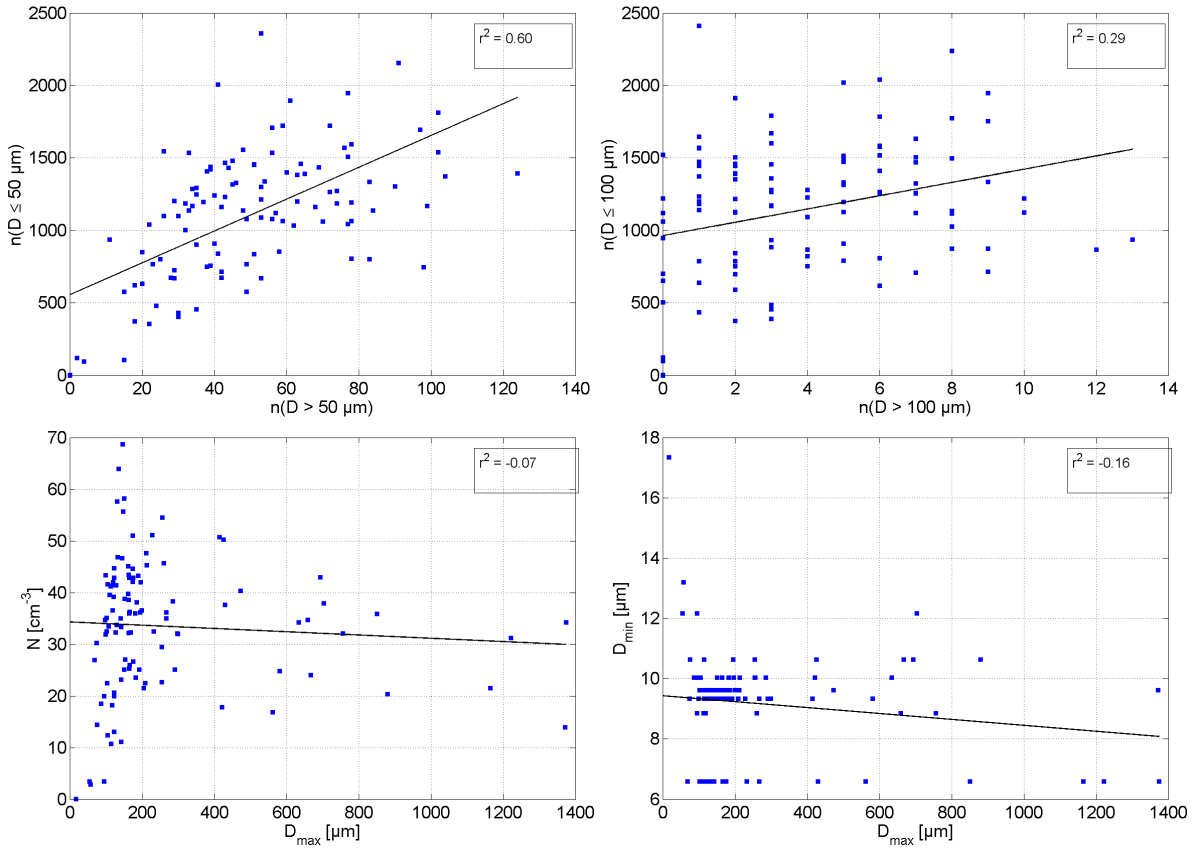


Fig. 5.5: Number of small particles vs. number of large particles for a separation diameter of 50 microns (top left) and 100 microns (top right) from ICE-D Flight B926, cloud pass 1. In addition to the data from 108 holograms (each data point belongs to one hologram), a linear fit (black line) is shown along with the correlation coefficient between the two quantities (text box in upper right corner). In the bottom row, the number concentration is shown as a function of maximum particle size per hologram (left) and the minimum particle diameter per hologram is shown as a function of maximum particle diameter (right).

From this limited sample with only about 100 data points it can be concluded that the effect of indirect shading does not lead to a strong influence on the data as the negative correlation expected from a shading effect is not significant and the slopes are very flat. This overall is due to the general low number density of particles within one hologram. Thus the objects seem sufficiently far from each other not to appreciably obstruct the detection of others.

To quantify the effect and the impact of *direct* shading on particle number concentrations, the minimum particle size to effectively hide other particles has to be determined. In Fig. 5.6 the z position difference is shown for large particles which have other particles in the same projected area at a different z position. Below a particle diameter of 200 microns, the fraction of particles which have another particle ahead / behind themselves is around 10 %. For larger particle sizes, this number gradually decreases to less than 1 %. However, two millimeter-sized raindrops had another particle along their projected area which was

detected. Thus, the impact of shading is likely negligible if the possible shader is smaller than 200 microns.

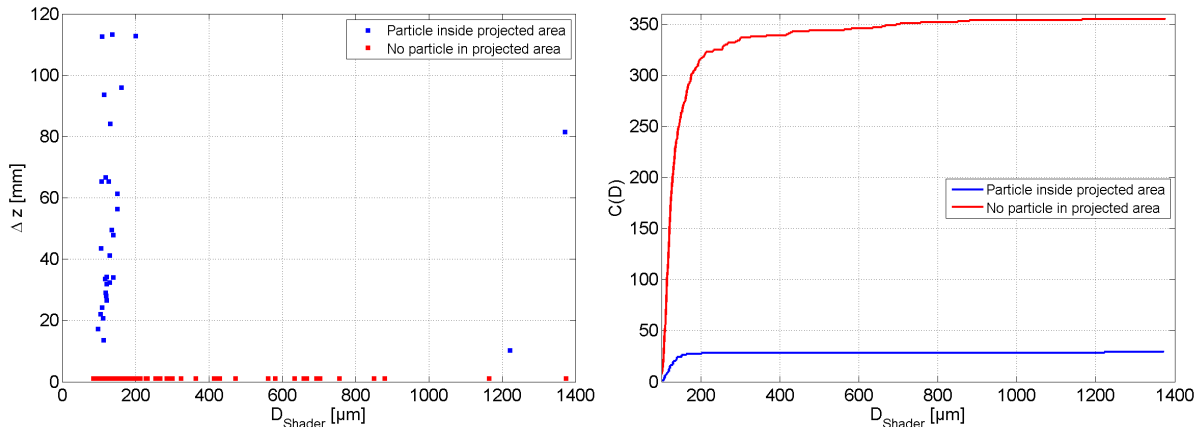


Fig. 5.6: Left: Distance between a possible shader and another particle in the same hologram along the optical axis z . Right: Cumulative distribution function of the particle diameter for large particles with another smaller particle in the same lateral range (blue) and others with no smaller particle in the projected area (red). The cumulative distribution functions reflect the overall number of particles of diameter D_{Shader} with and without other particles in the same lateral range.

The presence of particles ahead / behind a shading candidate is seen as a proof that particles are detectable in the same lateral area. In case of larger particles, it might make sense to correct the sample volume by subtracting the cylindrical projection volume of particles above 200 microns from the total sample volume when calculating the number concentrations and size distributions of smaller particles. From the examined cloud pass, 32 % of the holograms contained one or two particles larger than 200 microns. As the projected volume of a 1.4 millimeter sized raindrop, which is among the largest particles detected in the data sets used for this thesis, can be approximated as $V_d = \pi \frac{D_d^2}{4} (z_{\min} - z_{\max}) = 0.21 \text{ cm}^{-3}$ ($= 0.6$ % of the sample volume), the effect of shading is indeed negligible in terms of particle number concentration. Ten of the 1.4 millimeter sized raindrops would obstruct 6 % of the sample volume but such a high density of raindrops is unlikely to be measured.

The last question which remains to be answered is the impact of shading on spatial distributions. Therefore, a quantitative estimation of the possible reduction of detected particles is needed. For this purpose, an ensemble of synthetic particles was generated and a cylindrical removal of particles along the projected area of a hypothetical big raindrop was applied. Unfortunately, it is not possible to apply a correction without the possibility of introducing artifacts into the data when analyzing spatial distributions. This is due to the fact that certain assumptions (e.g. a uniform random distribution) would need to be made for possibly hidden particles. As first test attempts with shader diameters of 500 μm to 1 mm did not show any visible effect, an extreme simulation experiment

was considered by putting two 5 mm raindrops into the sample volume and removing all particles within the same lateral position as covered by the two shaders. The LWC of such a cloud volume would be more than 1000 g m^{-3} , which is highly unrealistic. Two values for the droplet number concentration N were used in the simulation, which were in the typical range as in real clouds with big raindrops or graupels: $N_1 = 20 \text{ cm}^{-3}$ and $N_2 = 80 \text{ cm}^{-3}$. The effect on the first neighbor distances from shading and also the effect on the F statistics from the Fishing test after Baker (1992) is shown in Fig. 5.7. In both cases of simulated shading, the particle population with shading tends to be more clustered than the unperturbed population (higher frequencies of shorter normalized neighbor distances in Fig. 5.7 top). For the Fishing test results, shown in Fig. 5.7 bottom, the frequency of significant deviations between the shaded and unperturbed case is concentration dependent.

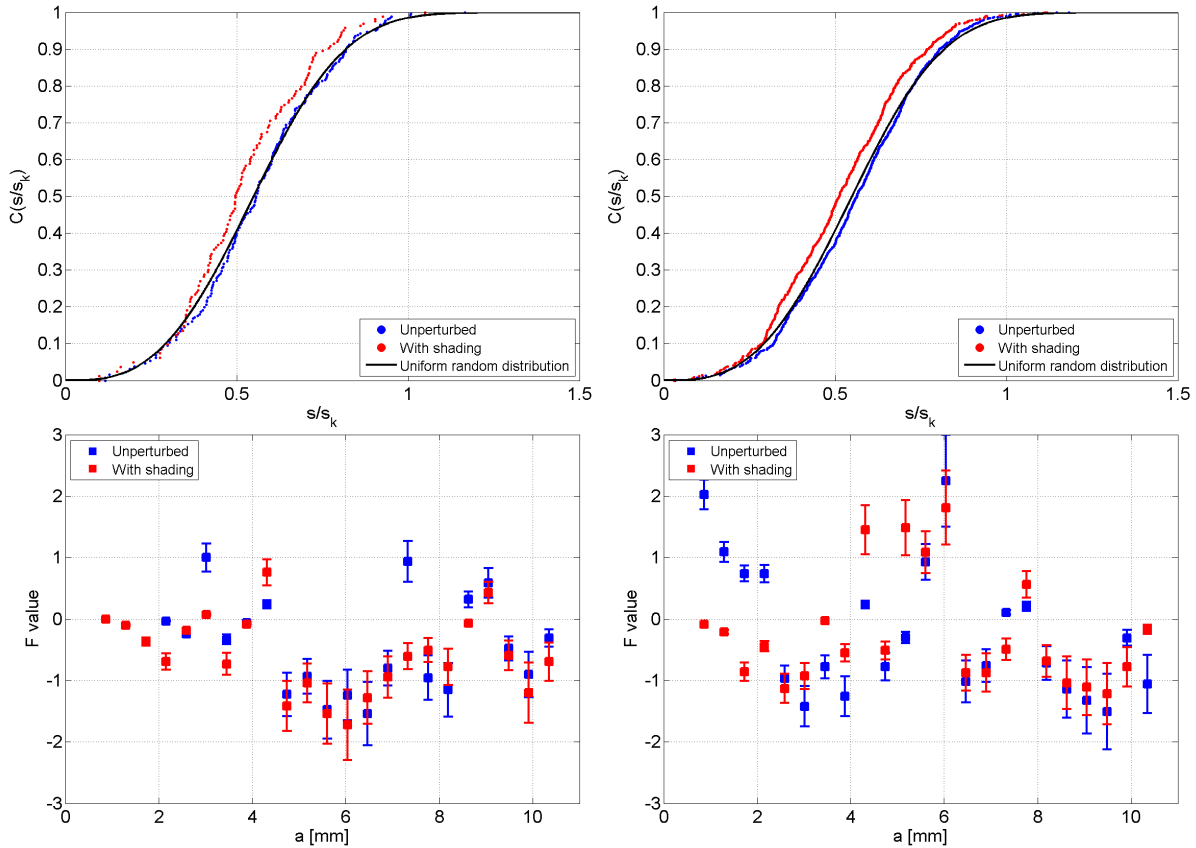


Fig. 5.7: Results from first neighbor distance analysis (top row) and Fishing test (bottom row) for synthetic data with $N = 20 \text{ cm}^{-3}$ (left) and $N = 80 \text{ cm}^{-3}$ (right). The effect of shading was simulated by artificially placing two spheres with 2.5 mm radius randomly in the projected plane and removing all particles within the lateral range of the sphere. No visible blue markers in the bottom row indicate that there is no difference between "unperturbed" and "with shading".

While the difference in F for the case with $N = 20 \text{ cm}^{-3}$ is significant for only five cube lengths, the number of cube lengths with a significant difference is 11 for the $N = 80 \text{ cm}^{-3}$ case. However, none of the F values was indicative of a significant deviation from a uniform random distribution ($\max(F) < 3$). This may be different for clusters of particles and needs to be assessed.

In conclusion, there is no significant effect of shading in terms of producing significant deviations from a uniform random distribution from the viewpoint of nearest neighbor distances. A similar result is seen for the F statistics from the Fishing test for several cube lengths a in the center part of the sample volume. Also here, the effect of shading is fairly small as only a few values have a significant deviation from the unperturbed population. But even this very strong and unrealistic case is not strong enough to smear out local inhomogeneities beyond recognition. The signal for local inhomogeneities on a scale of $a = 6 \text{ mm}$ in the bottom right panel of Fig. 5.7 is clearly visible in both cases. To summarize the results of the investigation of shading, it can be concluded that the effect arising from shading is likely smaller than other sources of uncertainties, except for possible miss detections of small ice particles.

5.3 Particle shattering

Shattering is a well-known issue of airborne in-situ particle measurements, especially in cirrus clouds. Korolev et al. (2011) addressed the disparity of the measured concentrations of small ice particles and the possibility that the majority of them might originate from this type of instrument artifact. Data from optical array probes (OAPs) are corrected for shattering by inspection of the particle inter-arrival times. The basic assumption, which is used, is that shattered particles occur as unusually high concentrated clusters of particles and therefore have very short inter-arrival times. If shattering is really an issue for a particular flight, the histogram of inter-arrival times will have a main mode which corresponds to the average particle concentration, and a secondary mode, which is found for inter-arrival times that are three or four orders of magnitude smaller. In holography, the spatial cluster identification method as in Fugal and Shaw (2009) is used to detect shattering. This is done by calculating the nearest neighbor distances of all particles in one hologram. Before applying a minimum distance threshold (analog to a maximum concentration threshold), a critical concentration needs to be defined. A reasonable first guess for pure-ice clouds is a minimum allowed distance of 1 mm between two particles (which corresponds to a concentration of 1000 cm^{-3}). From the data obtained in the CIRCCREX flights B889, B890 and B895, the preferred region of shattering could be determined to be located at $z < 20\text{mm}$ and $z > 140\text{mm}$. The technique used for shattering removal, and also its performance, has been discussed in Subsection 4.3.2.

5.4 Particle counting uncertainties

Knowing the number of particles within the sample volume is the first step towards a quantitative understanding of the microphysical properties of a particular cloud. Similar to the procedure described in Lance et al. (2010), which is applied for a Cloud Droplet Probe (CDP) and also for optical array probes, the counting uncertainties are calculated from the assumption of Poisson statistics. Thus, the uncertainty in number concentration ΔN translates via Gaussian error propagation to Eq. 5.11 by using $\Delta n = \sqrt{n}$ for the particle counts n .

$$\frac{\Delta N}{N} = \frac{\sqrt{n}}{n} = \frac{1}{\sqrt{n}} \quad (5.11)$$

This error is present in any data set where particle counting plays a role in determining derived parameters. The only way to reduce the impact of the error from counting statistics is the usage of a larger sample volume.

However, there is another source of error in particle counting, which arises from imperfections of the data analysis software. Any classified data set cannot be interpreted as perfect in terms of containing all particles that were measured, and containing no false particles or false artifacts. To quantify the quality of classified data sets, a random sample of 100 predicted *particles* and 100 predicted *artifacts* (out-of focus fringes and background patterns) was taken and the number of false predictions was determined. Each of the data sets used in this work has a minimum quality level of QC2 as explained in Chapter 4, which means that up to 10 % of the particles might be artifacts, or completely missed. For data acquired in field experiments, there is no gold standard to determine the number of miss detections accurately, so it can only be estimated from selecting individual measurements of a particular flight / cloud pass with high concentrations of small particles, which are exceptionally sensitive to Miss Detections. The procedure to estimate the data quality is visual verification of semi-automatically determined results. A reasonable workaround for considering the fact that particles might be overseen is to apply the sample volume restriction according to the particle size as explained in Section 5.1 of this chapter and calculate the size distribution either from a subvolume close to the hologram plane or define the individual sample volumes for narrow ranges ($\Delta D \approx 1.5\mu\text{m}$ for HALOHolo) of particle size. However, even without this correction, a reasonable agreement in terms of N and D is found when data from HALOHolo are compared to another instrument measuring cloud droplets (CDP or FSSP or CAS).

5.5 Particle sizing uncertainties

As previously discussed in Chapter 3, HALOHolo has a sizing uncertainty as any other cloud particle spectrometer. There are two main contributors to an uncertainty in terms of particle size: First, the pixel size conditions a lower limit of sizing accuracy, which is

half the pixel width. A more precise estimation of particle size from pixel counting is not possible. However, the sign-matched filter analysis after Lu et al. (2012) works in the Fourier domain and may yield a particle diameter that is more accurate than the sizing accuracy from pixel counting. In that case, the actual uncertainty would depend on the background noise level in the particular hologram as the iterative approach to determine the optimum size estimate depends on the reconstructed amplitude. The maximum of the reconstructed amplitude has to be unique and well above the noise level for accurate results of the sign-matched filter algorithm. A critical quantity for sizing accuracy is the cross-sensitivity error, which is the error of spuriously assigning a particle of size D_i the size D_{i-1} or D_{i+1} for the size bin i . For particles larger than 15 microns, the cross sensitivity error was found to be within the distribution width of the calibration beads (see Fig. 3.6 in Chapter 3). This error can be determined by the analysis of monodisperse particle samples. As these particles were not available for the instrument calibration, the cross-sensitivity error will be estimated via instrument modeling. For this purpose, synthetic holograms with a random distribution of particles with a fixed size are generated and then the size is determined by using both pixel counting and the sign-matched filter method. The cross sensitivity error for a given particle size is represented by the distribution width $\sigma(D)$ of the measured sample of particle diameters D from a monodisperse population. For a monodisperse population, $\sigma(D) = 0$ is expected.

5.5.1 Sizing accuracy for droplets

An important question arises at this point of the instrument characterization study: Which estimate for the particle diameter is the best under which conditions? From the data processing software, four different size estimates are obtained: Major axis length, minor axis length, equivalent size and optical equivalent diameter as defined in Subsection 4.1.5. It has to be noted that the sizing accuracy of HALOHolo depends on the accuracy of the particle segmentation threshold (see Subsection 4.1.2), which is sensitive to the background noise level. For very clean holograms recorded in the laboratory, a substantial oversizing is observed frequently. However, during in-cloud flights the noise level is much higher due to vibrations and stronger temperature gradients, which shifts the particle segmentation threshold more towards an undersizing. A reasonable approach for finding the most accurate representation of the particle diameter is an intercomparison with an independent instrument that measured the same cloud at the same time and had a similar size resolution. In the case of RACEPAC, the Cloud Droplet Probe (CDP) was used as calibration tool for the sizing accuracy of HALOHolo. The CDP uses forward scattering of red laser light to estimate the particle size particle by particle from the intensity of the scattered light (Mie theory, cf. Lance et al. (2010)). Table 5.2 summarizes the results from an intercomparison between different size estimators of HALOHolo and the CDP. The arithmetic and geometric mean diameters \bar{D} and \bar{D}_g and the distribution widths $\sigma(D)$ and σ_g of the CDP were calculated from the total size distribution of a particular flight segment (the times are listed in Table 5.2). The number of sampled particles from

HALOHolo were $n = 7.8 \cdot 10^6$ for Flight 2, $n = 1.0 \cdot 10^6$ for Flight 5 and $n = 6.4 \cdot 10^6$ for Flight 6.

Table 5.2: Comparison of different diameter estimators for HALOHolo in RACEPAC Flights 2, 5 and 6 against each other and against a CDP. For all HALOHolo data, the sample volume was restricted according to the 70 % detectability threshold as described in Fig. 5.1. "majsiz" is major axis length, "minsiz" is minor axis length, "eqsiz" is equivalent size and "OED" is area-derived optical equivalent diameter. The times of the flights with data were 20:40 - 21:51 UTC for Flight 2, for Flight 5 and for Flight 6. The sample sizes were larger than 1 million particles for HALOHolo, which yields error bars less than 0.1 % of the value. Errors for \bar{D} , $\sigma(D)$, etc. could be provided but, based on the number of particles, were negligible.

Quantity	CDP	minsiz	majsiz	eqsiz	OED
Flight 2					
\bar{D} [μm]	16.9	14.2	18.2	16.2	14.8
\bar{D}_g [μm]	16.4	13.6	17.6	15.7	14.1
$\sigma(D)$ [μm]	4.4	4.7	4.8	4.6	4.6
σ_g [μm]	1.3	1.4	1.3	1.3	1.3
Flight 5					
\bar{D} [μm]	14.0	11.3	15.0	13.2	12.2
\bar{D}_g [μm]	13.7	10.7	14.6	12.7	11.7
$\sigma(D)$ [μm]	3.3	4.1	4.0	3.9	3.8
σ_g [μm]	1.2	1.4	1.3	1.3	1.3
Flight 6					
\bar{D} [μm]	19.4	15.9	19.3	17.6	16.3
\bar{D}_g [μm]	19.1	15.5	19.0	17.3	16.0
$\sigma(D)$ [μm]	3.2	3.4	3.4	3.2	3.3
σ_g [μm]	1.2	1.2	1.2	1.2	1.2

For the HALOHolo data, the corresponding values of \bar{D} , \bar{D}_g , $\sigma(D)$ and σ_g were calculated particle by particle after the sample volume restriction according to Section 5.1. Particular care was taken that both instruments had valid data during the examined time-frame and that particle sizes were measurable by both instruments ($10 \mu\text{m} \leq D < 50 \mu\text{m}$).

It turns out that the difference between the particle size estimator for HALOHolo and the CDP particle diameter depends on the particle size itself. The smallest particle mean diameter (14 microns) was found in Flight 5 where *majsiz* and *eqsiz* were almost equally close to the CDP particle mean diameter (the deviation from the CDP particle mean diameter is $1.0 \mu\text{m}$ for *majsiz* and $0.8 \mu\text{m}$ for *eqsiz*). For Flight 2 with a mean particle diameter of approx. 16.9 microns, the absolute difference between CDP and HALOHolo is smallest for *eqsiz* as the diameter estimate ($0.7 \mu\text{m}$ deviation). With a deviation of $1.3 \mu\text{m}$, *majsiz* is the second best size estimator for this data set.

For Flight 6, the agreement in terms of the distribution parameters is best for major axis length as particle size estimate. For the arithmetic and geometric mean, the values from CDP and HALOHolo are almost identical. The consistency between CDP and HALOHolo *majsiz* for $\sigma(D)$ is $0.2\ \mu\text{m}$, which is much smaller than the sizing uncertainty of HALOHolo. A similar attempt as for the CDP was also tried for the Cloud and Aerosol Spectrometer (CAS) inside NIXE-CAPS from the Forschungszentrum Jülich. However, the signal background for particle sizes below $15\ \mu\text{m}$ measured by the CAS was so high that it often exceeded the concentrations measured by the CDP by more than an order of magnitude. A qualitative intercomparison for particle sizes above $15\ \mu\text{m}$ showed an agreement with HALOHolo that was very similar to the agreement with the CDP. Table D.2 in Appendix D.3 summarizes the results of the intercomparison between HALOHolo and the CAS for $D > 15\ \mu\text{m}$. Because of the good overall agreement for particle sizes greater than $15\ \mu\text{m}$ between CDP, CAS and HALOHolo *majsiz*, the particle size estimator *majsiz* was chosen as basis for calculation of particle size distributions in the following chapters. It needs to be emphasized that the particle size and concentration in comparison to the CDP and the CAS are not a guarantee of accuracy, but give confidence of accuracy.

5.5.2 Sizing accuracy for ice

The size of ice particles is more difficult to be estimated by a CDP or a CAS due to the deviations from spherical geometry. Cloud probes which use particle imaging, e.g. the Cloud Imaging Probe (CIP) or the Precipitation Imaging Probe (PIP), are better suited to estimate the size of nonspherical particles. Here, a cloud pass from Flight 8 on 10 August 2017 during the StratoClim2017 airborne field experiment was selected to examine the particle sizing accuracy via instrument intercomparison. The instruments to compare with are a CDP and a CIP Grayscale (CIPgs) integrated in the Cloud Combination Probe (CCP), a stand-alone CIP and a PIP with their properties listed in Row 3-5 of Table E.1 in Appendix E.1. The selected flight targeted convective outflow near the cold point tropopause over Nepal and northern India. On a pressure level of $p \approx 86\ \text{hPa}$ ($T \approx 188\ \text{K}$), a cloud event with approximately 5,000 ice particles in the HALOHolo sample volume has been identified and the size distributions from the five instruments mentioned (HALOHolo, CDP, CIPgs, CIP and PIP) are compared. The size distribution intercomparison, which is shown in Fig. 5.8, yields a good agreement between HALOHolo, CIPgs and CIP and a still reasonable agreement for the larger bins ($D > 15\ \mu\text{m}$) of the CDP. It is thought that the deviation between the CDP and HALOHolo in case of large particles is due to counting statistics and the bin sizes of the CDP. For particles smaller than $12\ \mu\text{m}$, the detection limit of HALOHolo needs to be taken into account. A close inspection of the particle images revealed some aggregates larger than $100\ \mu\text{m}$, irregular shapes and columns. The low concentrations in the PIP data are due to particle sizes close to the minimum detectable size.

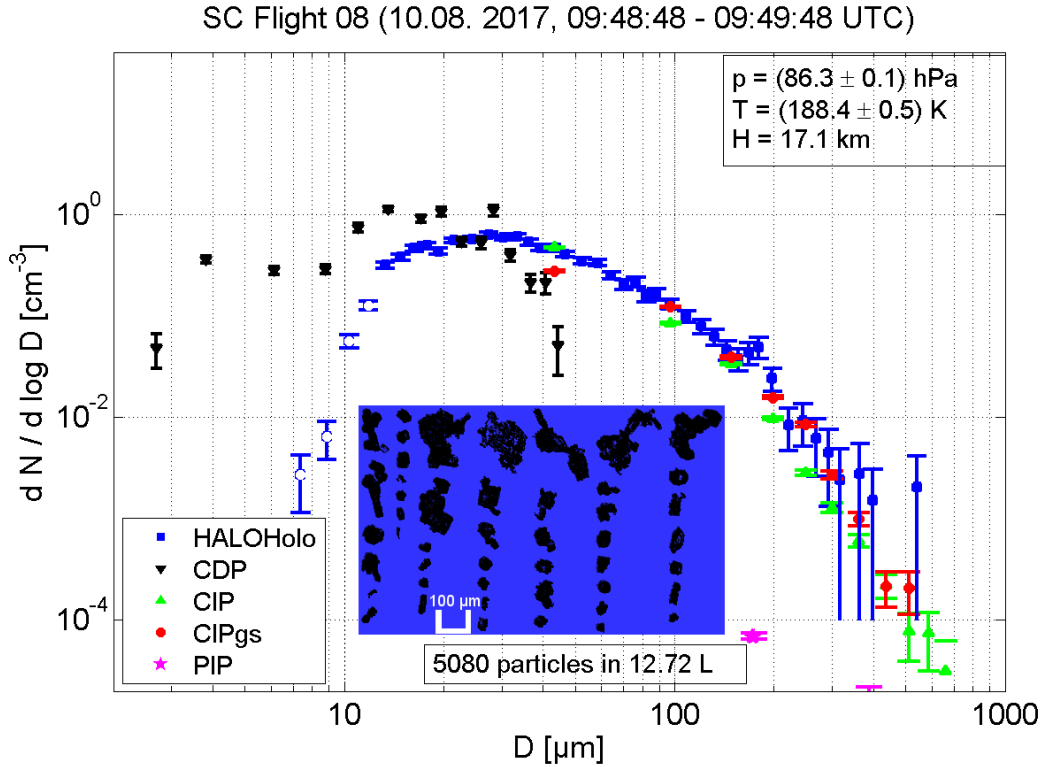


Fig. 5.8: Particle size distribution from a cloud pass during StratoClim 2017 Flight 8 (10 August 2017, 09:48:48 - 09:49:48 UTC). Shown are the number densities per bin for HALOHolo (blue squares), the CDP (black triangles), the stand-alone CIP (green triangles), the CIPgs (red circles) and the PIP (magenta stars) along with their error bars from counting statistics. In addition, pressure p , temperature T and altitude H are shown in the upper right corner and the number of particles detected by HALOHolo and the sampled volume of air are shown in the bottom line. White circles indicate that the concentrations measured by HALOHolo are likely underestimated due to detectability issues. The scale bar of the particle image gallery is 100 μm long.

5.5.3 Sizing accuracy of the sign-matched filter method

Small particles with $majsize < 15 \mu\text{m}$ are often smeared out at larger distances, which makes it difficult to determine their diameter accurately. Thus, the threshold-independent sign-matched filter algorithm after Lu et al. (2012) is used as an alternative approach to determine the particle diameter. The sign-matched filter algorithm returned valid results in accordance with the particle diameter obtained from pixel counting for the 15 μm and 30 μm glass beads (see Subsection 3.3.3). However, the results for the 8 μm beads looked right but after recognizing an implausible secondary size mode for the 15 μm beads at large z , it might be right for the wrong reason. Here, the instrument model is used to create two holograms with 100 randomly dispersed particles in a narrow range of z for a fixed particle diameter D_p .

The entire test series consists of two synthetic holograms with 100 particles concentrated in a depth range of 1 mm across the entire lateral range. The sign-matched filter is applied

on the data after reconstruction and classification of the particles. It would have been possible to use the positions from the synthetic hologram setup directly to start the sign-matched filter routine but in reality the particle position is unknown until the particle is reconstructed. In all cases, more than 90 % of the particle were found in the classification process after reconstruction.

The particle size estimation in the sign-matched filter algorithm is based on maximum search within the 3D reconstruction of the amplitude (which is a 3D array of the 2D amplitude values over the range of reconstructed z planes). Each so-called "amplitude block" has a corresponding filter diameter D_F , which is varied with a resolution about ten times smaller than the particle sizing uncertainty ΔD . The maximum accuracy which is achievable in the setup of the simulation is $\Delta D_F = 0.125 \mu\text{m}$. According to the description in Subsection 4.1.6, the maximum peak of the amplitude is searched over the range of the reconstructed slices at depth z . This maximum search is done over the entire range of filter diameters D_F . As the lateral error is fairly low, as discussed in Lu et al. (2012), the maximum search was done in the entire possible range of x and y within the particle, not necessarily in the particle center as determined from the reconstruction. The error of the sign-matched filter method is denoted as $|D_F^* - D_p|$ where D_p is the exact particle diameter used to make the synthetic holograms and D_F^* is the optimum filter diameter determined from the maximum search.

One rule that was applied to remove spurious results from the data set was to demand that the location of the maximum amplitude peak in the $z - D_F$ domain must not be the first or the last value of z and / or D_F . Most often, a maximum amplitude peak at the first D_F is indicative of too low signal strength, which happens in particular for small particles at large values of z . Some cases of the $7 \mu\text{m}$ series were strongly affected by this issue, which increased the error bars of the correctly sized particle fraction derived from counting statistics. The "worst case scenario" was encountered for the $7 \mu\text{m}$ series at $z = 40 \text{ mm}$, which had a total of 108 out of 200 particles as valid particles and 61 from the 108 were correctly sized. In terms of sizing accuracy, the fraction of correctly sized particles was $61/108 = 0.56$. Here, accurate size estimation by the sign-matched filter algorithm means that $|D_F^* - D_p|$ has to be smaller than $0.5 \mu\text{m}$, which is approximately $1/6$ of a pixel. An example of the dependence of correct particle size estimation on the lateral position, expressed as $d2ne$, and the z position is shown in Fig. 5.9. Each of the data points corresponds to one valid particle (the spurious ones have been removed previously).

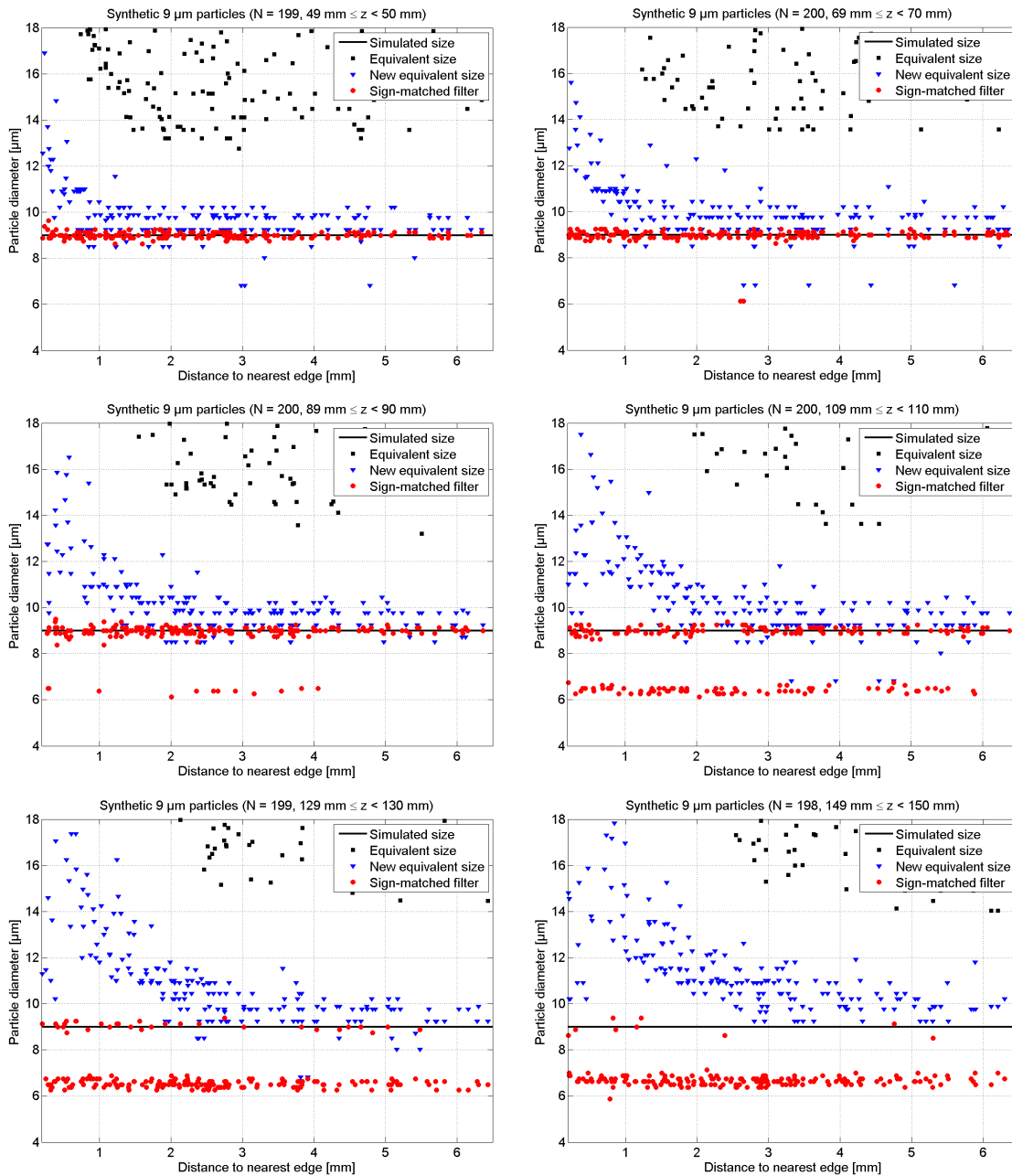


Fig. 5.9: Estimated particle size from sign-matched filter, equivalent size from reconstruction and equivalent size with relative threshold as a function of distance to nearest edge for synthetic particles with a diameter of $9 \mu\text{m}$. Each panel shows a small range of z positions from 50 mm (top left) to 150 mm (bottom right). The black solid line marks the expected particle size, the symbols represent the sizing result from each valid particle. A bimodal size distribution in the sizes from the sign-matched filter (apparent in the middle panels) is indicative of a violation of the conditions for accurate size estimation.

For the study of the sizing accuracy, four particle sizes were used at z positions within the HALOHolo sample volume geometry. The z positions range from 10 mm to 150 mm, the particle sizes were 7, 8, 9 and 10 microns. For particle diameters smaller than 2 pixels

(5.9 μm), the signal strength of the amplitude peak in the filtered cases is too weak to be distinguished from the unfiltered case. If the conditions for accurate size estimation are not fulfilled, there will be a smaller secondary mode in the particle size distribution (as visible in the middle row of Fig. 5.9). Also, the probability of accurate size estimation seems to be independent from the lateral distance, expressed as $d2ne$.

However, the trend in the probability of correct particle size estimation along z is significant and for the four particle diameters, the fractions of correctly sized particles could be fitted by using a Fermi-Dirac type distribution (Eq. 5.12).

The individual results for each set of simulations for a narrow range of z and a fixed D are shown along with the fits in Fig. 5.10.

$$f(z) = \left(\exp\left(\frac{z - z_0}{z_1}\right) + 1 \right)^{-1} \quad (5.12)$$

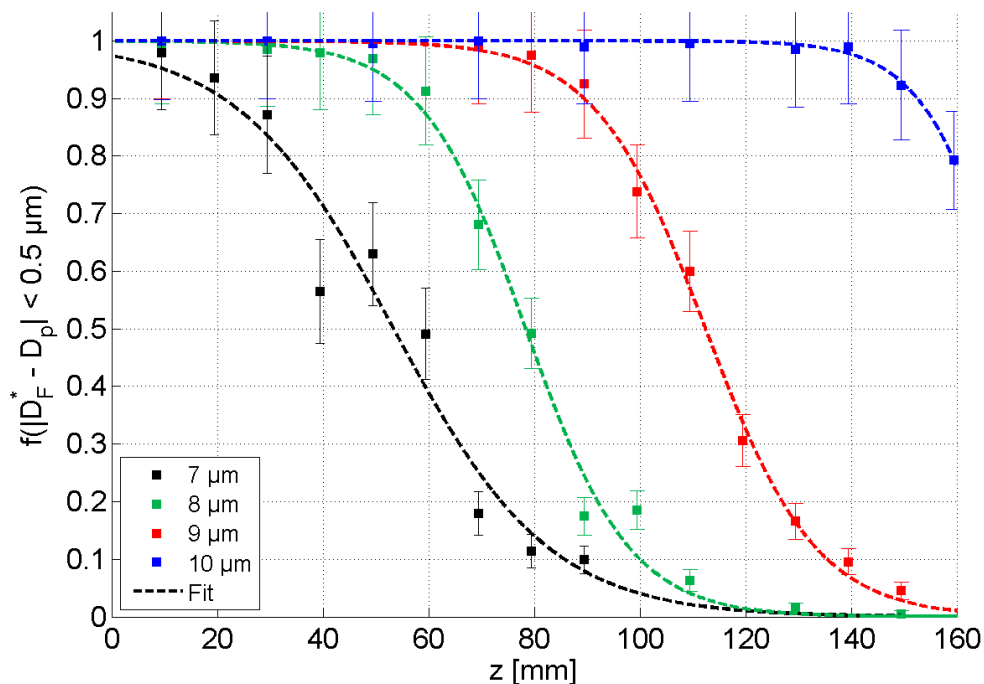


Fig. 5.10: Fraction of correctly sized particles with the sign-matched filter as a function of distance along the optical axis. The error bars were calculated from counting statistics and Gaussian error propagation, the fits were performed using Eq. 5.12.

One might ask why the accuracy of the algorithm is not given for larger z positions. The most likely explanation is the resolution limit effect as the signal to noise ratio decreases with increasing distance from the hologram plane. Spuler and Fugal (2011) discuss the resolution limit for a particle along the optical axis. Their Eq. 1 is shown as Eq. 5.13 here. The laser wavelength λ , detector width N_x and height N_y in pixels and pixel width

Δx are system specific constants. If the minimum resolvable diameter increases with increasing z , this leads to the effect that small enough particles are not resolved beyond a certain distance $z_{max}(D_p)$. From the geometry of HALOHolo, it turns out that z_{max} for the four test diameters is close to the 50 % sizing accuracy threshold in z only for the case of the 10 micron particles (see Table 5.3). Thus, the tradeoff in particle sizing accuracy for $D_p \leq 10 \mu\text{m}$ cannot be explained by the optical resolution limit.

$$z_{max}(D_p) = \frac{\Delta x \sqrt{N_x N_y} D_p}{2.44\lambda} \quad (5.13)$$

The cutoff threshold for 50 % accurately sized particles is z_0 , which is summarized in Table 5.3. From this synthetic hologram study it can be concluded that the sign-matched filter routine is suitable for particle sizes of at least 10 microns (or 3.5 pixels) throughout the entire sample volume of HALOHolo. This range of actual particle sizes can be seen as the "area for safe operation" of the sign-matched filter algorithm.

Table 5.3: Fit parameters of Eq. 5.12 applied on the frequency of correctly sized particles of size D with $|D - D_{test}| < 1 \mu\text{m}$. In addition, the values of z for 90 % correctly sized particles (hereafter z_{90}) and the optical resolution limit $z_{max}(D)$ are shown. For $D = 7 \mu\text{m}$, the value at $z = 90 \text{ mm}$ was ignored for fitting as it is obviously an outlier due to the resolution limit effect. The error bars of z_0 and z_1 were estimated from the 95 % confidence interval of the fit parameters.

Quantity	$D_p = 7 \mu\text{m}$	$D_p = 8 \mu\text{m}$	$D_p = 9 \mu\text{m}$	$D_p = 10 \mu\text{m}$
z_0 [mm]	53.3 ± 5.7	78.4 ± 2.1	112.4 ± 1.3	170.4 ± 2.3
z_1 [mm]	14.7 ± 5.4	9.8 ± 1.9	10.5 ± 1.1	8.2 ± 1.4
r^2	0.946	0.991	0.997	0.989
<i>RMSE</i>	0.081	0.040	0.023	0.007
z_{90} [mm]	21.1	56.8	89.5	152.5
$z_{max}(D)$ [mm]	128.0	146.3	164.6	182.9

Another constraint is given by the minimum size of D_F to yield a strong enough deviation between the filtered reconstruction slice and the unfiltered reconstruction slice. The critical value of D_F is approximately 2 pixels (which is $5.9 \mu\text{m}$ for HALOHolo). The most interesting range is located between the two constraints, where the exact position of the particle center relative to the pixel center determines whether the signal is strong enough for an accurate size estimation or not. In addition, the resolution limit effect comes into play. An influence from the edge effect is virtually ruled out as the probability of accurate size estimation in Fig. 5.9 seems to be independent from the distance to nearest edge d_{2ne} . From the results shown in Fig. 5.10, the recommended minimum particle diameter for using the sign-matched filter algorithm is $D \geq 9 \mu\text{m}$ where the application of the algorithm is safe throughout more than two thirds of the sample volume depth. An additional test using particle sizes of $7.5 \mu\text{m}$, $8.5 \mu\text{m}$ and $9.5 \mu\text{m}$ suggests that even

a particle size of $8.5\ \mu\text{m}$ is large enough to get valid results from the sign-matched filter algorithm. The test results are summarized in Appendix D.4 (Table D.3 and Fig. D.5). It needs to be mentioned that the values of z_0 in Table D.3 do not agree with the values of z_0 in Table 5.3. It is hard to believe that $z_0(D_p = 8.5\ \mu\text{m}) \gg z_0(D_p = 9\ \mu\text{m})$ and thus an error within the numerical simulations or the implementation of the particle size estimation algorithm is assumed. The reason for this behavior of the sign-matched filter algorithm is still unknown and needs further research.

5.6 Discussion and summary

With the aid of the instrument model using Fraunhofer diffraction to generate synthetic holograms, it has been shown that detectability of small particles is sensitive to particle size and position. The impact of both resolution limit and edge effect has been studied on a series of synthetic holograms to determine cutoff slopes for a definition of the uniform detection volume for particles of a given size. After a general equation for the HALOHolo geometry was derived and its free parameters have been determined, the results from the study of synthetic holograms was compared with cloud data obtained from field measurements in Arctic stratocumulus clouds. While the functional relationship between the cutoff slope as a function of z position was a hyperbola in case of the synthetic holograms, a linear function with a negative slope agreed better with the data from field measurements. The determined cutoff slope from the field measurements is further used in the analysis of the cloud data from RACEPAC in Chapter 6.

Another possible error source that has been critically discussed is the influence of large particles obscuring smaller ones, the shading. From both airborne measurements in clouds containing large raindrops and an idealized numerical experiment, it could be shown that the effect of shading is not critical for the interpretation of the analysis results of the spatial distributions. Its effect on determining the correct particle concentration was quantified to be less than 1 %, which is below the typical error from counting statistics for clouds with $N \leq 400\ \text{cm}^{-3}$. Particular care has to be taken if the position of the shader is exactly centered on the optical axis as only the center part of the volume is used for the calculation of the F statistics for the Fishing test.

The effect of shattering and its removal has already been demonstrated and discussed in Chapter 4. In particular the ice cloud data sets have to be examined and corrected for shattering artifacts, which tend to occur preferably in ice clouds containing high concentrations ($N > 100\ \text{L}^{-1}$) of large particles. If not corrected, shattering artifacts might be interpreted as a secondary particle mode in cirrus clouds. Fortunately, applying a z position threshold for minimum and maximum distance along the optical axis is as effective in removal of shattering as cutting away the volume affected by shattering manually. The examined examples in Chapter 4 had very similar particle size distributions for both techniques of shattering removal and the particular differences were in the same order of magnitude as the error bars from counting statistics. Nevertheless, the sample

volume surgery is the preferred method if only a small number of holograms did contain ice and every particle is a valuable addition to the statistics of the particular cloud pass. In cases with very few particles during the entire flight, it is possible to "repair" the shattered particle by using some assumption about the shards and the particle geometry. However the "repair method" should only be used as last resort as it introduces uncertainties of order 50 % to the particle size distributions from the repaired particles.

Yet another case exists where simplicity beats extensive manual investigation: From a data set containing approx. 10^7 cloud droplets, the particle sizing accuracy has been estimated via intercomparison with a CDP and a CAS. After applying the sample volume restriction as described in Subsection 5.1.1, a difference in mean particle diameter of less than $1\ \mu\text{m}$ was found for *majsiz* in comparison with the CDP particle diameter. For the *LWC*, the best agreement was found when using *majsiz* and spherical geometry to calculate the particle mass. Using *area* and *majsiz* for calculation of particle mass yields by a factor of two lower values of *LWC*. In addition, the mean aspect ratio of droplets, which is *majsiz* divided by *minsiz*, was between 1.2 and 1.5. A visual inspection of droplets with a large aspect ratio confirmed the expectation that imperfections in the threshold-based particle size estimation were likely responsible for missing pixels on the particle edges and yielding a too small value of *minsiz*. This effect needs to be considered when calculating cloud properties which are derived from particle size. It is recommended to use *majsiz* as particle diameter for all HALOHolo particle data from the RACEPAC field campaign.

In contrast to the results from the laboratory measurements with calibration beads, the sign-matched filter algorithm from Lu et al. (2012) had a reasonable agreement with *majsiz* for airborne cloud data in two selected sample holograms. Its performance has been studied by using synthetic holograms from the instrument model. While the accuracy was excellent for particle diameters above 3.5 pixels, the chance of accurate size estimation was very low for particle sizes smaller than 2.5 pixels. In between these two boundaries, a spatial dependence could be found and the 50 % accuracy cutoff distance could be determined for four different particle sizes along the range of z positions in the HALOHolo geometry. The critical distance was independent from the resolution limit of each particle size, only in case of the $10\ \mu\text{m}$ particles the cutoff distance was close to z_{max} . As the resolution limit effect alone is not able to explain the errors in particle size estimation, a critical signal to noise ratio in the holograms might be the answer. If the algorithm fails to return an accurate diameter, it yields a bimodal size distribution with one mode close to the expected size and another one close to a diameter of 2 pixels from an initially monodisperse droplet spectrum.

Results from field measurements

Connections between microphysical structure, local
microphysical variability and mixing in stratiform
cloud decks in the Arctic

6.1 Introduction

The degree and definition of "cloud uniformity", sometimes referred to as "cloud homogeneity"¹⁶, depends highly on the cloud type and the spatial scale that is looked at. Towering cumulus clouds with a strong and persistent updraft have a strikingly sharp interface from cloudy air to cloud-free air at their lateral boundaries. The horizontal extent of stratocumulus or stratus clouds is often some orders of magnitude larger than their vertical extent, in contrast to cumulus clouds with a width to depth ratio close to 1 (see Fig. 6.1). Marine stratocumulus cloud decks often cover an area of several thousands of square kilometers over the ocean and are of great importance for the local and global radiative balance. These clouds have been examined in numerous studies, one of the most recent is the study of bimodal droplet populations in Arctic stratocumulus clouds (Klingebiel et al., 2015).

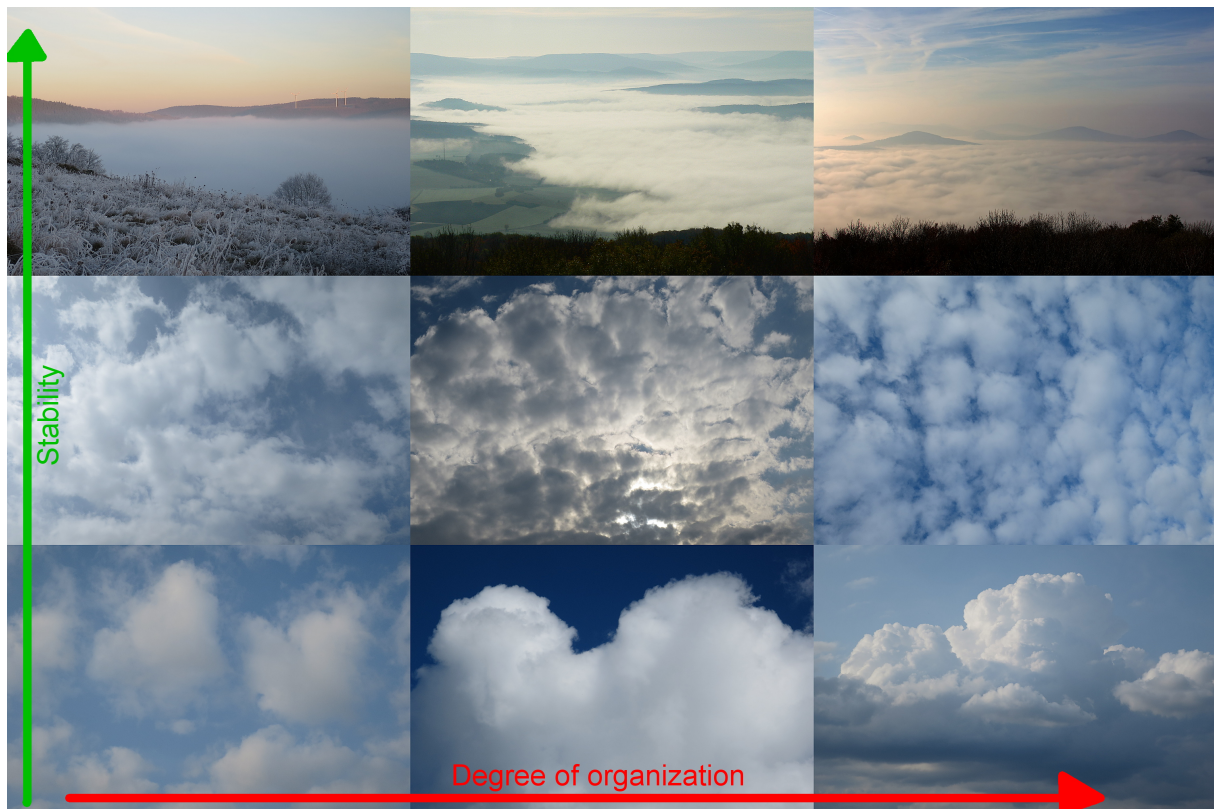


Fig. 6.1: Typical appearance of boundary layer clouds. Depicted are stratus (top row), stratocumulus (middle row) and cumulus (bottom row). The degree of stability decreases from top to bottom, the degree of organization increases from left to right. Photos taken from private collection of O. Schlenczek.

¹⁶The term "homogeneity" should be avoided when discussing intra-cloud variability as the terms homogeneous / inhomogeneous should be reserved for mixing processes. One purpose of this chapter is to establish a link between both phenomena.

The occurrence of bimodal droplet populations is usually associated with mixing processes between cloudy air and cloud-free air in the cloud top region. The theory of mixing is described in Beals (2013) and also in Kumar et al. (2014). Two basic principles of mixing are found in the literature: *Homogeneous mixing* means that the water vapor pressure field in the gas phase is spatially uniform and all droplets in the mixed volume of air respond in the same way to subsaturated conditions. Thus, the particles shrink and some of them might evaporate completely. As a result, the *number density* N as well as the *volume-weighted mean particle diameter* D_3 decrease towards the cloud edge. The opposite case, *inhomogeneous mixing*, assumes that the vapor pressure field is not spatially uniform and consists of local maxima and minima. Filaments of cloud-free air can be entrained into the cloud and keep their initial water vapor pressure for some time. As a result, small droplets close to the subsaturated filaments of air will tend to evaporate completely while the larger droplets further away from the filaments remain unchanged at first. In the diagram with N on the abscissa and D_3 on the ordinate, referred to as *mixing diagram*, inhomogeneous mixing is visible as a horizontal line as D_3 stays constant while N varies. A typical situation for the occurrence of mixing is the formation of eddies on the outer boundaries of cumulus clouds (Fig. 6.2 left), but also clouds which appear to be less turbulent can be subject to mixing at their edges due to local updrafts and downdrafts (Fig. 6.2 right). The distinction between homogeneous and inhomogeneous mixing, however, is complicated if the surrounding air is nearly water-saturated.



Fig. 6.2: Left: Mixing at a cumulus cloud edge. The red arrows indicate the position where cloud filaments were detrained by some ten to hundred meter large eddies. Right: Horizontal cloud structures mainly due to shallow convection in an altocumulus layer as seen from an aircraft. The clouds resemble the typical appearance of closed cell convection. Photos taken from private collection of O. Schlenczek.

Cumulus clouds were examined for their spatial uniformity by Brenguier (1993) using a modified version of the Forward Scattering Spectrometer Probe (FSSP), known as "Fast

FSSP" (Brenguier et al., 1993), aboard of an aircraft. Brenguier (1993) found sharp transitions from cloud-free air ($N < 1 \text{ cm}^{-3}$) to conditions in cloud interior ($N > 100 \text{ cm}^{-3}$) within a millisecond, which yields a spatial scale of approx. 10 cm at an aircraft true air speed (TAS) of approx. 100 m s^{-1} . However, diluted regions with number concentrations between undiluted cloud conditions and cloud-free conditions were also observed in Brenguier (1993). One needs to know that these measurements are continuous but they resolve inter-particle distances in only one dimension within a sample area that is only 0.5 mm^2 wide.

A detailed statistical analysis of cloud data was done by Davis et al. (1999) who analyzed the liquid water content (LWC) from airborne measurements of stratiform boundary layer clouds. In the power spectra of LWC , Davis et al. (1999) found inertial downscaling with the $-5/3$ power law for fully developed 3D turbulence on spatial scales between a few kilometers to approx. 10 m. A second regime with an exponent around -1 was found for scales from approx. 2 m to 8 cm, which was attributed to the LWC field being stationary. In between the two regimes, a scale break was found. The fluctuations on these scales exceed the variability from a Poisson process, which suggests that the "homogeneous" cloud segments in Baker (1992) were still more variable than a pure Poisson process. Gerber et al. (2001) found a similar relationship for cumulus clouds, yet some of them did not show the scale break and could be well-approximated by the power law from inertial downscaling ($-5/3$ exponent).

The scale break around 2 meters was also evident in the LWC power spectra from Siebert et al. (2015). The authors used laser Doppler interferometry to obtain particle size and radial velocity from clouds moving across the research station Schneefernerhaus (2656 m a.s.l.) at Mt. Zugspitze. Turbulence measurements confirmed their assumption that measurements obtained at this location can be compared directly with aircraft measurements as the conditions were close enough to free tropospheric conditions. The in-cloud LWC ranged from 0.1 to 0.6 g m^{-3} with fluctuations on time scales that were less than one second at wind speeds around 4 m s^{-1} (cf. Fig. 9 of Siebert et al. (2015)). Calculations of the droplet mean volume diameter and number concentration revealed evidence for inhomogeneous mixing.

Holographic measurements from Beals et al. (2015) were examined for mixing in cumulus clouds. The authors could show that inhomogeneous mixing provides the dominant signature in the mixing diagrams, which relate particle number concentration to mean volume diameter. From the aircraft speed, a spatial gap of approximately 50 m is found between the holograms. By combining the results of the studies mentioned, it seems plausible that the scale break in the LWC power spectra and inhomogeneous mixing are somehow connected. In addition, as the scale breaks were observed in stratocumulus clouds and cumulus clouds, it seems to be likely that a large fraction of stratocumulus clouds will also bear the signature of inhomogeneous mixing. In Section 6.3, the question regarding the compatibility of the two sampling methods from conventional sampling and holography is addressed. It might be possible that a continuous one-dimensional measurement of

cloud droplets yields a different result as three-dimensional snapshots. The microphysical variability of one particular cloud case sampled in different altitude levels is examined in Section 6.5 in order to shed light on this.

While cumulus clouds have been analyzed so far in terms of mixing (Beals et al., 2015), there is not much literature available for holographic measurements in stratocumulus clouds (Glienke et al., 2017). An investigation of the influence of mixing in the cloud top entrainment zone of Arctic stratocumulus was done by Klingebiel et al. (2015) via comparison of in-situ data from a CDP with direct numerical simulations. Klingebiel et al. (2015) could reproduce the observed bimodality in the particle size distributions with the model and relate it to entrainment in the cloud top region. Down to a spatial scale of about 6 cm, which was the lower limit given by the sampling rate of the CDP and the speed of the aircraft, these bimodal cloud segments seemed to be well-mixed, at least for a one-dimensional measurement. At this point, the question arises if the same is true for three-dimensional measurements on even smaller scales¹⁷, which are accessible with a holographic instrument. The question on how bimodal droplet populations are interspersed on spatial scales below 15 cm in three dimensions is investigated in Section 6.4 of this chapter. Section 6.6 will show the relationship between mixing and microphysical variability in extended arctic boundary layer clouds.

6.2 Data and methodology

6.2.1 Mission strategy, instrumentation and data of the RACEPAC field experiment

The dataset which was analyzed for cloud uniformity and mixing was obtained with airborne instruments during the field campaign RACEPAC, which stands for RAdiation and Cloud ExPeriment in the Arctic Circle. The field campaign took place in Inuvik, NWT, Canada in April and May 2014. During this field campaign, two aircraft from the Alfred Wegener Institute were used (the Polar 5 and Polar 6 aircraft, model Basler BT-67). In-situ measurements were obtained by the Polar 6 whereas the Polar 5 aircraft had remote sensing and radiation instruments on board. The Polar 6 aircraft flew at an average true air speed (TAS) of $v_a = 60 - 70 \text{ m s}^{-1}$ during the cloud passes discussed in this chapter. With two aircraft, the preferred measurement strategy was that the P6 flew at low altitude near cloud top while the P5 flew between some hundred meters and a few kilometers behind the P6 at higher altitude to measure the radiative properties of the cloud that had been sampled in-situ. A schematic of the flight strategy is shown in Fig. 6.3.

¹⁷The spatial scale which can be examined with airborne holographic cloud probes is between 1 mm and 15 cm.

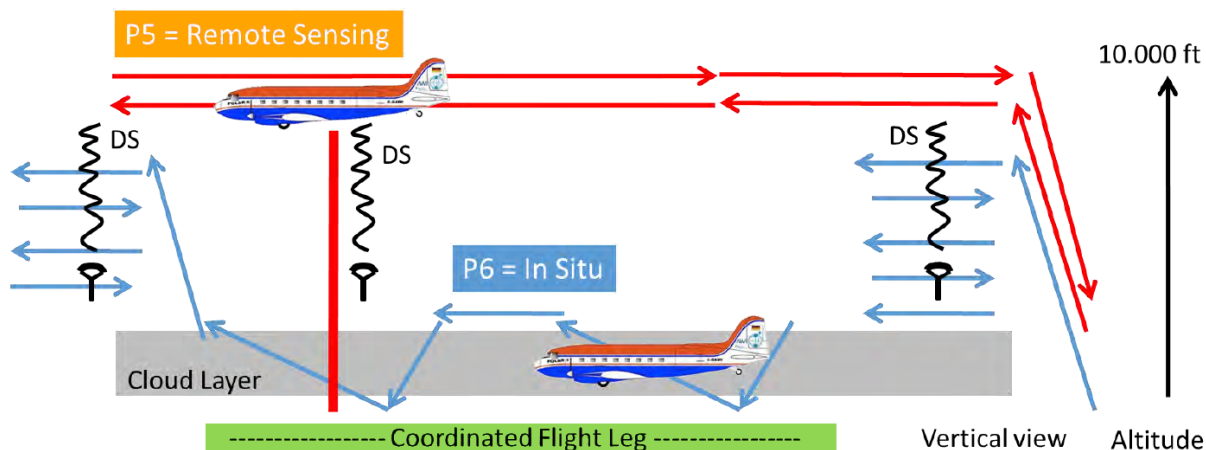


Fig. 6.3: Illustration of the sampling strategy during RACEPAC. While P5 is equipped with remote sensing instruments scanning the cloud layer from above and releasing dropsondes (DS), P6 performs in-situ measurements inside the clouds. Figure adapted after Ehrlich et al. (2015).

Usually, the P5 released a dropsonde some time during the flight to obtain a vertical profile of the thermodynamical variables and the wind. Apart from the dropsondes, each aircraft had instruments aboard to record meteorological data during the flight, which were an Aircraft-Integrated Meteorological Measurement System (AIMMS) plus other instruments). Cloud microphysical parameters were measured with four cloud probes from Mainz and Jülich, which were the Novel Ice Experiment Cloud and Precipitation Spectrometer (NIXE-CAPS) from Jülich, consisting of a Cloud and Aerosol Spectrometer (CAS) and a Cloud Imaging Probe (CIP), the Cloud Combination Probe (CCP), which consists of a Cloud Droplet Probe (CDP) and a Cloud Imaging Probe (CIP), the Precipitation Imaging Probe (PIP) and HALOHolo. For the flights with high enough concentrations of larger cloud droplets ($D > 100 \mu\text{m}$), an intercomparison was done for all of the mentioned instruments. Here, the examined cloud passes did not contain large amounts of ice or raindrops and therefore the instrument intercomparison was focused on HALOHolo, CDP and CAS. An overview of the instrument specifications with relevance for intercomparison are listed in Table E.1 of Appendix E.1, a size distribution intercomparison figure is shown in Fig. E.1. It should be noted that there is a significant discrepancy between HALOHolo and the CDP and CAS for particles smaller than approximately $12 \mu\text{m}$, which is mostly due to speckle noise from larger droplets impairing the detection of smaller droplets in the HALOHolo sample volume.

Temperature data came from a Rosemount RM 102 sensor, used was the deliverable called "static air temperature deiced". The static pressure data were taken from a Setra sensor, relative humidity was measured with a HMT333 and a Buck CR2 sensor, the HMT333 data set was used for the calculations in this work. Geographic latitude, longitude and altitude were obtained from the on-board GPS.

Measurement uncertainties and dynamic correction of temperature and pressure measured aboard an aircraft are described in Wendisch and Brenguier (2013). Typical uncertainties of the temperature measurements outside of clouds are $\Delta T = \pm 0.3^\circ\text{C}$. Much larger uncertainties are encountered in cloud as large cloud droplets or precipitation particles are deposited on the sensor and lead to evaporative cooling and other side effects that impair the measurements (Lawson and Rodi, 1992). Even more challenging is the accurate measurement of in-cloud relative humidity. There was a systematic disparity between the HMT333 sensor and the CR2 sensor by more than 5 % relative humidity in almost every flight, which argues for an overall uncertainty of the humidity measurements of at least this value. This issue needs to be discussed in terms of the analysis of the mixing diagrams. Relative humidity outside of the cloud is one of the parameters needed to calculate the homogeneous mixing curves. The aircraft data from the P6 are available at 1 Hz sampling frequency, i.e. one value recorded per second. Due to this relatively coarse temporal resolution (equivalent to a spatial resolution around 60 m at typical flight speeds of the P6), it is recommended to concentrate on rather long in-cloud measurement sections. In the two research flights, which are subject of this chapter, various stratiform boundary layer clouds were investigated. Flight 2 took place on 30 April 2014 and included three long cloud passes from a staircase flight pattern inside a thick stratus cloud. Flight 6 was performed on 8 May 2014 and had three long cloud passes with sampling in the cloud top region. "Long" means that each of the passes had an uninterrupted one-second average of $N \geq 5 \text{ cm}^{-3}$ over a distance $L \geq 5 \text{ km}$. Two other flights (Flights 5 and 10) did also contain long cloud passes but the cases of Flight 2 and 6 are better suited for the investigations in this chapter. Figures showing the spatial structure of the particle size distributions from the flights listed in Table 6.1 are presented in Appendix E.3.

Table 6.1: Cloud passes of the analyzed RACEPAC flights. Shown are Cloud number, date and time t , flight type, altitude h , temperature T , pressure p and cloud pass length L . For temperature and pressure, the mean and standard deviation are given. Clouds 1-3 were measured during Flight 2, Cloud 4 was measured during Flight 5, Clouds 5-7 were measured during Flight 6 and Cloud 8 was measured during Flight 10.

Cloud	Date	t [UTC]	Flight type	h [m]	T [$^\circ\text{C}$]	p [hPa]	L [km]
1	30 April	21:18 - 21:24	3-step up	366, 457, 518	-7.1 ± 0.4	958 ± 10	26.4
2	30 April	21:28 - 21:35	2-step down	579, 518	-7.0 ± 0.2	946 ± 5	27.6
3	30 April	21:35 - 21:37	Level flight	426	-9.4 ± 0.2	961 ± 1	8.0
4	06 May	17:50 - 17:53	Level flight	884	-3.2 ± 0.2	904 ± 1	11.7
5	08 May	18:41 - 18:46	Level flight	884	-5.6 ± 0.1	908 ± 4	18.9
6	08 May	19:11 - 19:14	Level flight	701	-6.4 ± 0.2	926 ± 1	9.0
7	08 May	19:22 - 19:26	Level flight	640	-6.4 ± 0.2	933 ± 2	14.2
8	14 May	17:51 - 17:53	Level flight	1189	-11.4 ± 0.6	886 ± 6	6.4

Fig. 6.4 shows the typical cloud structure that was encountered during Flight 2, 5, 6 and 10. The video stills shown here are from Flight 10 but the clouds in the other flights looked similar. Inside the cloud, there was no visible structure in terms of quasi-periodic changes in the brightness.

A summary of the flights is shown in Table 6.1. Cloud 3 from Flight 2 did not have valid CDP data and Flight 10 had issues with the measured TAS due to icing. The analysis is focused on Cloud 1, 2 and 3 from Flight 2, and Clouds 5 and 7 from Flight 6.



Fig. 6.4: Video stills from a GoPro camera aboard Polar 6 on RACEPAC Flight 10 (14 May 2014). Broken stratocumulus (top left) turns into overcast stratocumulus (top right) and later on, the cloud looks much more like a stratus (bottom left). Inside the cloud (bottom right), no structures are visible.

6.2.2 Statistical analysis methods for cloud microphysical properties

For the analysis of local variability, four main parameters were selected: Droplet number concentration N , droplet effective radius r_{eff} , geometric standard deviation of the size distribution $\sigma_g(D)$ and liquid water content LWC . Other parameters which reflect the particle size or size distribution width are not independent from the four selected parameters. A correlation analysis performed for the geometric mean diameter \overline{D}_g , N and LWC has shown that the overall time series pattern from HALOHolo is consistent with

the measurements from CDP and CAS (Table E.2 in Appendix E). While both particle size and number concentration contribute to the calculated LWC , the major dependence found for LWC is given by N .

The first analysis to perform is to examine the *consistency* of cloud microphysical properties along the flight path. *Consistency* is hereafter defined as a logical variable that describes the agreement between two subsequently measured quantities. The cloud property X in hologram i is compared with the same cloud property X in hologram j . If the two differ by no more than the joint error bars, Eq. 6.1 is satisfied and "hologram i and j are consistent in X ". This term will be used several times within this chapter.

$$|X_i - X_j| < |\Delta X_i| + |\Delta X_j| \quad (6.1)$$

To calculate the difference in X between the two holograms and the corresponding error bars, Eq. 2.3 - 2.7, 2.13, 2.15 - 2.20 and 2.23 - 2.24 from Chapter 2 are used.

The analysis of consistency in cloud microphysical properties from measurement i and measurement j is concentrated on two main questions:

- Are two neighboring holograms consistent in N , r_{eff} and LWC ? \rightarrow Variability on the 10 m scale
- If two subsequently measured volumes are not consistent w.r.t. the measured parameters, how far away is the next measurement that is consistent with the actual one?

In addition to the four scalar parameters which have been discussed, the individual particle size distributions are also examined. One hologram can be seen as one sample of particles in a statistical sense. Here, the random variable X of our sample is the particle diameter, which is either expressed as probability density function (PDF) or as cumulative distribution function (CDF). Both formulations are mathematically equivalent (PDF vs. CDF) and the one which is preferred depends on the method that is applied to the distribution. An advantage of the CDF is that it is not necessary to specify bins.

To quantify the consistency of a sample instead of a scalar value, a statistical hypothesis test needs to be used. Here, the Kolmogorov-Smirnov (KS) test was chosen as it is a nonparametric test which does not depend on a particular distribution shape of the sample. Other commonly used hypothesis tests, e.g. Student's t Test, require that the population is Normal distributed. The critical value for the test statistics K was calculated after Stephens (1970). The input of the KS test are two cumulative distribution functions (CDFs) $C_1(X)$ and $C_2(X)$ of a random variable X (here it is typically the cloud droplet diameter per sample) from which the test statistics K are calculated according to Eq. 6.2. Thus, the maximum absolute difference of the two cumulative distributions yields the test statistics K .

$$K = \max |C_1(X) - C_2(X)| \quad (6.2)$$

The KS test can be used to examine if the mean value of the two distributions $C_1(X)$ and $C_2(X)$ is statistically equal. Another application is to check if the two distributions have the same variance. To test for equality of the variance, the mean value needs to be subtracted from both samples which define $C_1(X)$ and $C_2(X)$. It needs to be mentioned that the maximum absolute difference for any particular bin of the CDFs defines K , which makes the KS test susceptible for outliers in the two distributions.

Another method of testing the statistical equality of two samples is the computation of the mean variance between two frequency distributions $n_{i,j}$ and $n_{k,j}$ (here typically the number of droplets per size bin) where $j = 1, 2, \dots, J$ is the corresponding size bin and i and k are the particular samples (holograms). In analogy to the definition of the variance, $n_{i,j}$ and $n_{k,j}$, the squares of the differences $n_{i,j} - n_{k,j}$ are summarized and normalized by the number of degrees of freedom, which is $J - 1$. The actual value of the so-called mean variance does not have a particular statistical meaning. Thus, the mean variance is compared with another measure of variance, which is the variance of n_i and n_k (the number counts in sample i and k) from the Poisson distribution. The observed variance $\sigma_{obs}^2(n_i, n_k)$ is compared with the "tolerable variance" $\sigma_{tol}^2(n_i, n_k)$ to qualify whether the observed variance can be explained by Poisson statistics or not. The definitions of $\sigma_{tol}^2(n_i, n_k)$ and $\sigma_{obs}^2(n_i, n_k)$ in Eq. 6.3 and 6.4 yield the "normalized root mean square error" $nRMSE(n_i, n_k)$ (Eq. 6.5). If the two frequency distributions n_i and n_k do not vary by more than the variance from the Poisson distribution, the value of $nRMSE(n_i, n_k)$ is less or equal to 1.

$$\sigma_{obs}^2(n_i, n_k) = \frac{1}{J-1} \sum_{j=1}^J (n_{i,j} - n_{k,j})^2 \quad (6.3)$$

$$\sigma_{tol}^2(n_i, n_k) = \sum_{j=1}^J (n_{i,j} + \sum_{j=1}^J (n_{k,j} \quad (6.4)$$

$$nRMSE(n_i, n_k) = \sqrt{\frac{\sigma_{obs}^2(n_i, n_k)}{\sigma_{tol}^2(n_i, n_k)}} \quad (6.5)$$

The time series data of the scalar cloud microphysical properties cannot only be examined in terms of consistency, but also in terms of spatial structure. For the analysis of the spatial structure, *power spectra* are calculated. There exist many realizations of power spectral density estimates in the literature. The methods in Davis et al. (1999) and Gerber et al. (2001) use a subdivision of the time series $Y(t)$ of length N_t into segments with a length of 2^k values. The spectrum ranges from $k = 1$ (wave number of the Nyquist frequency) to $k = \log_2(N_t)$ (maximum wavelength included in the time series). By averaging over the individual segments, the spectral uncertainties can be reduced for the sacrifice of spatial resolution. Finally, the power spectrum is averaged over wavenumber / wavelength bins with an octave spacing as described in Davis et al. (1996).

A more straightforward variant of the power spectrum analysis uses the so-called periodogram, which is calculated from the Fourier transform $F(Y(t)) = \tilde{Y}(\omega)$ of the time series $Y(t)$. The frequency ω is the variable in the Fourier space corresponding to the time t in the local space. In standard notation, the power spectral density $P(Y)$ is proportional to $1/\omega \left| \tilde{Y}(\omega) \right|^2$ in the unit of $[Y]^2 \text{ Hz}^{-1}$ where $[Y]$ is the unit of Y . The power spectral density $P(Y)$ is either displayed as a function of the frequency ω or, after multiplication with the speed v of the sample flow, as a function of the length scale L . Here, the length scale notation is preferred as the structures contained in the time series data from airborne measurements are rather spatial structures than temporal structures. Similar to the conversion of ω to L , the power spectral density can also be converted from $[Y]^2 \text{ Hz}^{-1}$ to $[Y]^2 \text{ m}$.

In addition to the other methods described in this section, spatial distributions of cloud droplets were analyzed by using two methods described in Chapter 4, which is the neighbor distance analysis and the Fishing test. The basis for the calculations is the set of particle locations as displayed in Fig. E.8.

6.3 The influence of different sampling strategies on microphysical quantities derived from two contrasting cloud cases

A suitable case for studying the influence of the sampling strategy on the outcome of the determined microphysical quantities is Flight 6 from RACEPAC. The targeted cloud system of this flight was an extended stratiform cloud deck with some parts of it over land and a large covered area over the Arctic Ocean. Three long cloud passes (Cloud 5, 6 and 7) were encountered in this flight where two of them (Cloud 5 and Cloud 7) had notable differences in the spatial structure of microphysical quantities.

The first cloud case discussed is Cloud 5 from Table 6.1, which had $\sigma^2(N)/\bar{N} = 3.9 \text{ cm}^{-3}$ and $\sigma^2(r_{eff})/\bar{r}_{eff} = 0.12 \text{ }\mu\text{m}$. In comparison with Cloud 7 from Table 6.1, the variance of r_{eff} was higher and the variance of N was lower. The corresponding values for Cloud 7 were $\sigma^2(N)/\bar{N} = 14.6 \text{ cm}^{-3}$ and $\sigma^2(r_{eff})/\bar{r}_{eff} = 0.025 \text{ }\mu\text{m}$. Though the mean value of N differs by almost a factor of two between the two cloud passes, the mean effective radius was very similar ($10.84 \text{ }\mu\text{m}$ for Cloud 5 and $10.48 \text{ }\mu\text{m}$ for Cloud 7).

In the first place, the spatial structure of N and r_{eff} is investigated in the time series data of the two cloud passes. To be fair in terms of the instrument capabilities, particle sizes larger than 50 microns in HALOHolo and particle sizes smaller than 8 microns in the CDP data were not considered in this comparison. The time series data of N and r_{eff} of the two cloud cases are shown in Fig. 6.5 and reveal a good agreement between the two instruments in terms of particle effective radius. In the case of Cloud 7, the agreement in terms of N seems to be better than in Cloud 5. While the one-second data of both instruments tend to show the same evolution of N and r_{eff} along the flight track, this is fundamentally different for the full-resolution HALOHolo data. At full resolution, the

variance is much higher and the question arises which processes of interest are hidden behind the one-second data of the CDP or the HALOHolo data accumulated over one second. Do the data from RACEPAC reveal a similar spatial scaling as the cloud data from Davis et al. (1999)? For this purpose, power spectra of N and LWC need to be calculated. The power spectra of N and r_{eff} are shown in Fig. 6.6 and confirm that the spatial structure in the time series data of the two instruments is consistent down to a scale around 400 m. The variance in the power spectral density could not be reduced substantially by averaging over larger frequency bins. When looking at the power spectrum of the effective radius, it is obvious that Cloud 5 has a stronger deviation from the white noise background (at approximately $10 \mu\text{m}^2 \text{m}$ in Fig. 6.6 bottom left) at scales of $L \geq 2 \text{ km}$. However, the power spectra of N show a similar trend in terms of contribution to the total power spectral density from larger scales. Though the mean value of N is higher in Cloud 7, most of the variability in Cloud 7 is found at smaller scales ($L \approx 1 \text{ km}$).

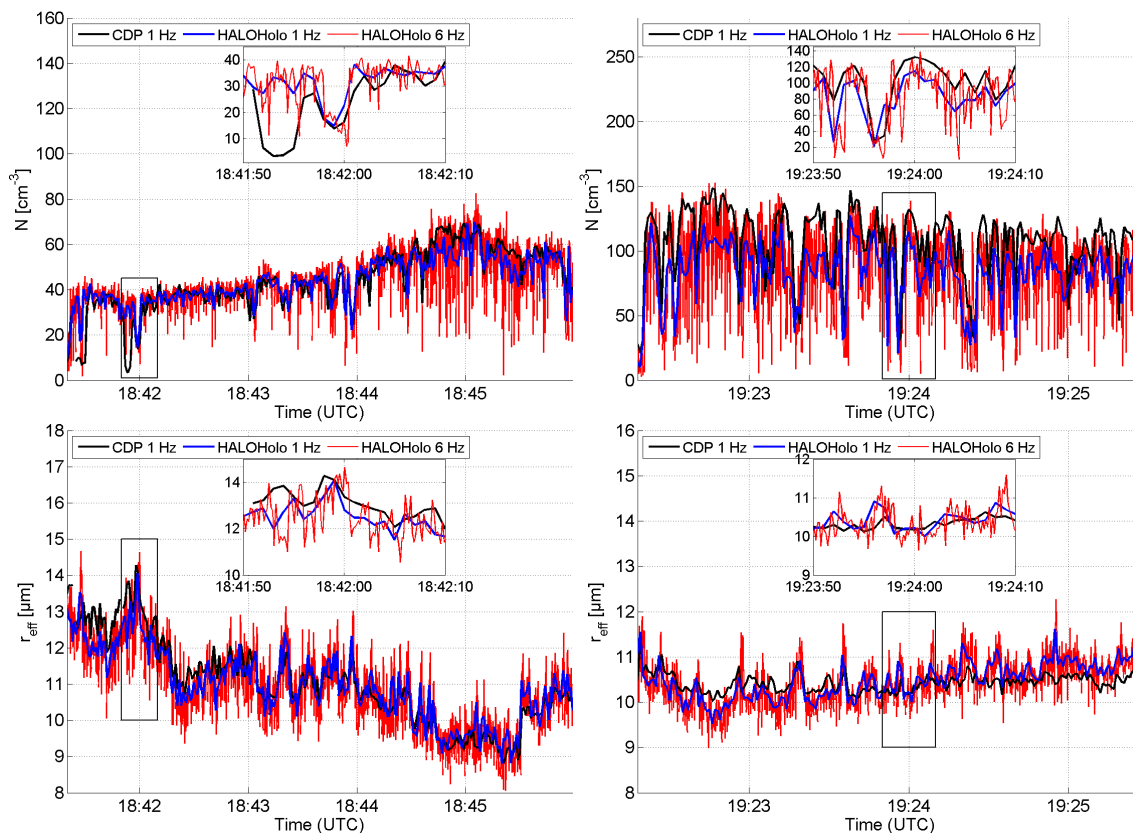


Fig. 6.5: Time series of N (top row) and r_{eff} (bottom row) from RACEPAC Flight 6 Cloud 5 (left) and Cloud 7 (right). Compared are the time series data of the 1 Hz CDP data (black), the 1 Hz HALOHolo data accumulated over one second (blue) and the full resolution HALOHolo data (red). The CDP data of each time series contain approx. 200,000 particles, the HALOHolo data contain approx. 1.4 million particles. Individual pieces of the time series data with strong variability are magnified (black boxes).

Not all peaks of the power spectral density from CDP and HALOHolo tend to overlap but the overall picture is fairly similar. Towards scales below 200 m, all spectra are dominated by white noise. Davis et al. (1996) argue that their observation of white noise is due to the sampling effect with a limited sample volume of the FSSP. This hypothesis has been tested with synthetic data and could not be confirmed for HALOHolo with both synthetic data of pure noise and sampling from a spectrum which follows the $-5/3$ power law of inertial downscaling (see Appendix E.4).

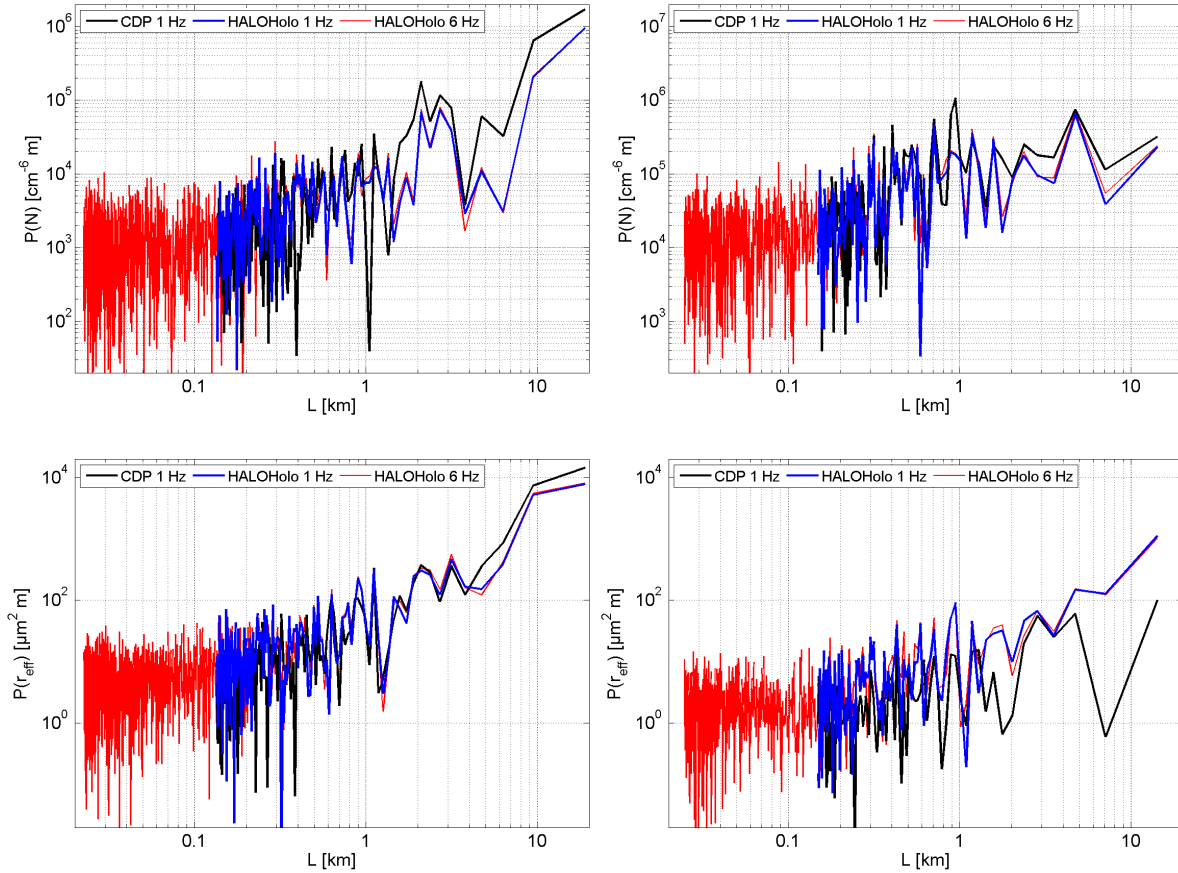


Fig. 6.6: As in Fig. 6.5 for the power spectra of N and r_{eff} . Shown are the power spectral densities $P(N)$ and $P(r_{eff})$ as a function of the length scale L . The high frequency structures show a nearly constant value of the power spectral density, which is indicative of white noise.

For typical particle number concentrations measured during RACEPAC, none of the synthetic tests (two examples shown in Appendix E, Section E.4) was able to explain the enhancement of noise. If an influence from the hologram background intensity or the threshold can be excluded, the noise is likely to have a natural origin, which contradicts the conclusion from Davis et al. (1996). To conclude this section, it could be shown that the difference arising from the sampling strategies of HALOHolo compared to the CDP is

considerably small in both correlation and absolute agreement of time series data as well as in the position and magnitude of internal cloud structures if the particle number concentration is at 10 cm^{-3} or higher. The limitations of the observed agreement still need to be found. Cirrus clouds with number concentrations typically below 1 cm^{-3} might yield a different result.

6.4 Mixing between two particle modes in the cloud top entrainment zone

Apart from the possible signature of shallow convection, there exist structures in the cloud top mixing zone where bimodal particle size distributions occur as a result of mixing. These structures have been analyzed by Klingebiel et al. (2015) by comparing particle by particle data from the CCP-CDP with direct numerical simulations. The primary particle mode was found at sizes above $20\text{ }\mu\text{m}$, the particles in the secondary mode induced by mixing were smaller than $20\text{ }\mu\text{m}$. The diameter separating the two modes (here: $20\text{ }\mu\text{m}$) is the so-called *mode separation diameter*. As Flight 6 from RACEPAC had a similar feature compared to VERDI Flight 11 which was used in Klingebiel et al. (2015), the same analysis technique was applied to the CDP data and compared with the spatial distributions measured by HALOHolo. A bimodal size distribution was detected by both instruments shortly before entering Cloud 5 in Flight 6. The CDP data in the bottom row of Fig. 6.7 show that there needs to be some degree of mixing between the modes, indicated by the black dots. HALOHolo sampled one hologram (Hologram A in Fig. 6.7) with an almost equal frequency of occurrence of droplets in both modes. At least on this spatial scale, the droplets of both modes in Hologram A seem to be randomly dispersed, which is in accordance with Klingebiel et al. (2015). The exact degree of randomness in the spatial distribution of the particles is investigated by a nearest neighbor analysis and a subvolume analysis.

This analysis was done for Hologram A, B and C in the black box of Fig. 6.7 as all three holograms contained a considerably large number of particles in the secondary (smaller sized) mode. The results from the first neighbor and subvolume analysis are presented in Fig. 6.8. Along the flight path, the number of droplets in the first mode was gradually decreasing. The top row of Fig. 6.8 shows the highest degree of uniformity in the observed spatial distributions among the two modes. On a length scale from 10 to 110 mm, the particles of the two modes are uniformly dispersed among each other.

However, at larger distances around $z = 120\text{ mm}$, there appears a cluster of larger droplets, followed by a relatively uniform dispersion at distances $z \geq 130\text{ mm}$ at the very end of the sample volume displayed in Fig. 6.8 top right. In the two other cases (Hologram B and C), the spatial distribution of the droplets appears less uniform: Hologram B (middle row in Fig. 6.8) has a particle cluster with preferably small droplets at $z < 50\text{ mm}$. Towards larger distances, the dispersion among the two modes and also the number of particles per subvolume is rather uniform. Hologram C in the bottom row of Fig. 6.8 shows a

structure that is similar to the filamented cloud volume shown in Beals et al. (2015). In this hologram, there were only eight particles in the primary mode and a "hole" is apparent in the spatial distribution around $z = 50$ mm.

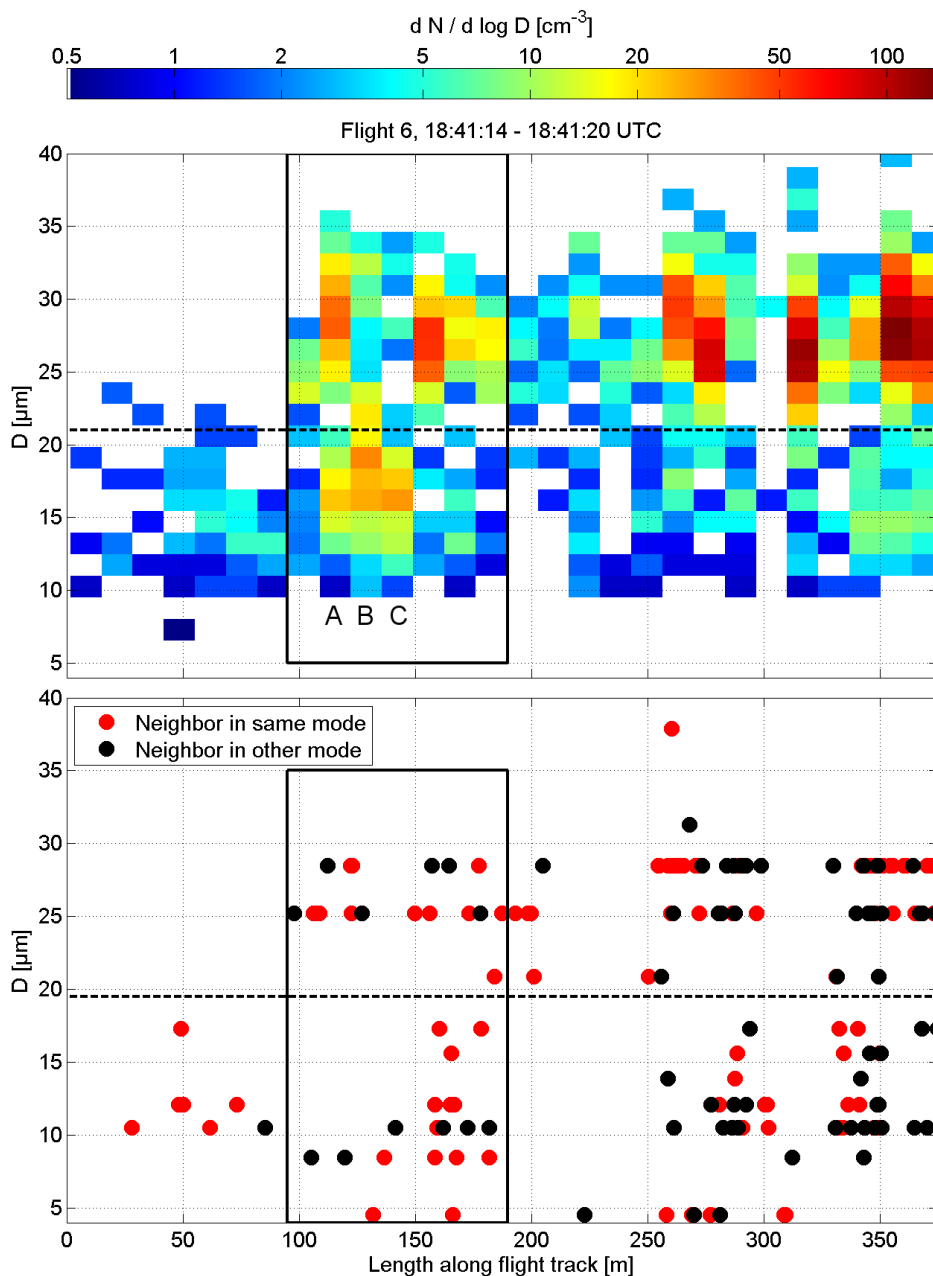


Fig. 6.7: Excerpt of a cloud pass from Flight 6 shortly before entering Cloud 5. Shown are the hologram by hologram particle size distribution from HALOHolo (top) and the particle by particle diameter along the flight path from the CDP (bottom) with color-coded first neighbors in same mode (red) or in the other mode (black) as in Fig. 8 of Klingebiel et al. (2015). The time axes were calibrated such that both instruments were synchronized and then converted into a length scale by multiplication with the aircraft TAS. The black box marks the bimodal feature observed in this flight segment. The mode separation diameter was found to be 21 microns for HALOHolo and 20 microns for the CDP.

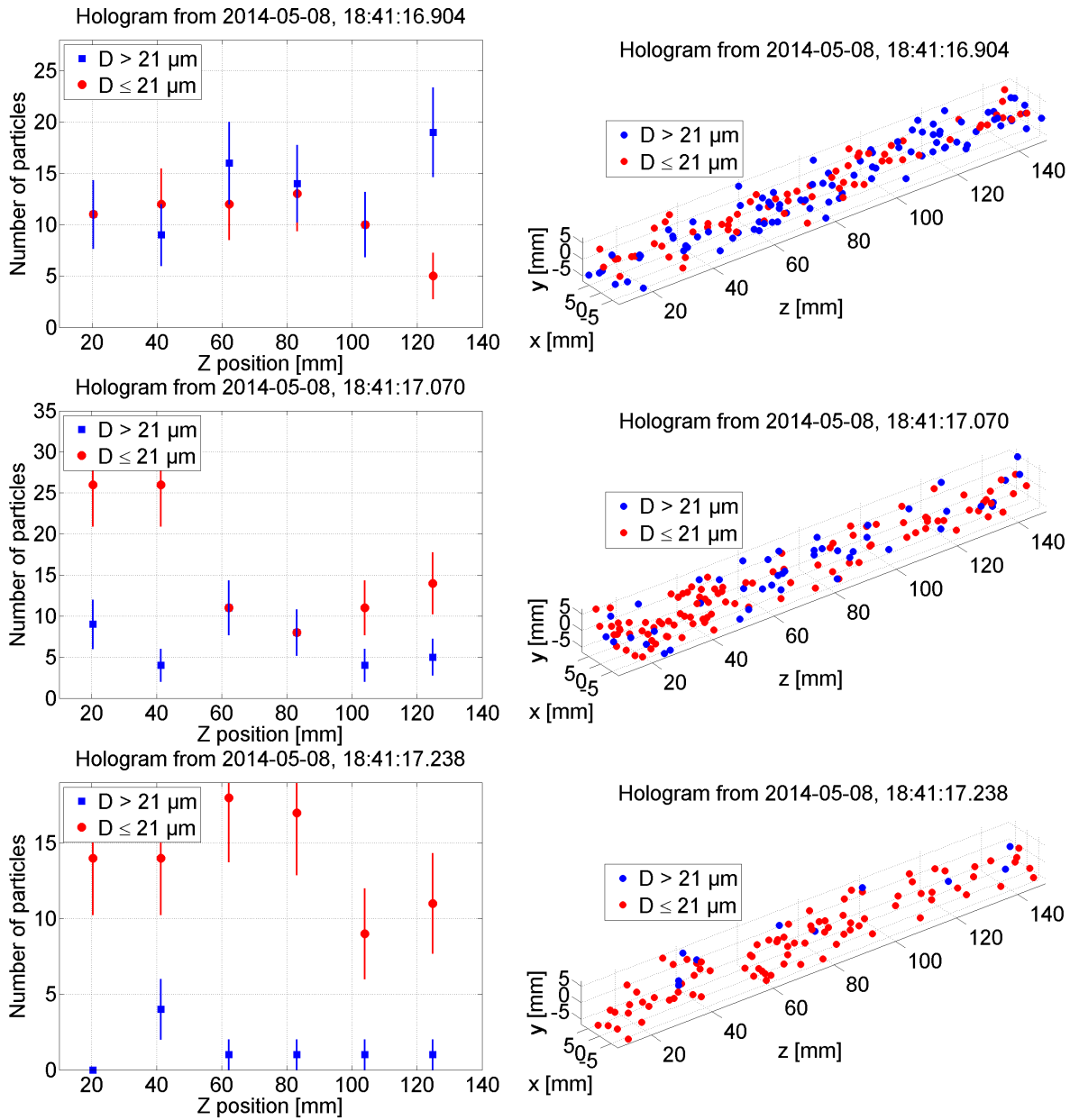


Fig. 6.8: Particle counts per subvolume (left) and Pseudo-3D display of particles in the sample volume of the holograms A, B and C of Fig. 6.7. The dispersion among the two modes appears to be close to a uniform random distribution in the first hologram, it appears clustered for the second hologram and filamented for the third hologram. At this time, the first neighbors in the CDP particle by particle data were close to a uniform random distribution in terms of dispersion among the two modes.

The degree of uniformity in terms of spatial dispersion among the two modes in the bimodal cloud segment is analyzed quantitatively in Table 6.2. The individual rows in Table 6.2 contain the number counts of particles in both modes for the total sample volume (unrestricted case) and the restricted sample volume where wall proximity effects

are absent (restricted case). In Table 6.2 the distribution of the particle neighbors among the three possible constellations large-large ($n_{1,1}$), small-small ($n_{2,2}$) and large-small ($n_{1,2}$) are compared with their corresponding expectation values computed from the number of large particles (n_1) and the number of small particles (n_2) via the rules of conditional probability.

The error bars for the expectation values of $n_{1,1}$, $n_{2,2}$ and $n_{1,2}$ are calculated via error propagation and assumption of Poisson statistics. If the actual value of $n_{1,1}$ is greater than the expected $n_{1,1}$ plus its corresponding error bar, the large particles are locally clustered. A clustering of small particles is found if the same relationship holds for $n_{2,2}$. Often, a significant enhancement of observed $n_{1,1}$ or $n_{2,2}$ is associated with a significant reduction of $n_{1,2}$.

Table 6.2: Hologram by hologram and CDP particle number in the first mode (n_1), particle number in the second mode (n_2) and particle neighborhood counts for particle and first neighbor in the primary mode ($n_{1,1}$), particle and first neighbor in secondary mode ($n_{2,2}$) and particle and neighbor in different modes ($n_{1,2} = n_{2,1}$). Results are shown for unrestricted (U) and restricted (R) sample volume ("restricted" means that only particles closer to their neighbors than to the nearest edge were counted to avoid wall proximity effects). The values in brackets denote the expectation value plus / minus uncertainty range from counting statistics after error propagation as derived in Appendix E.5. Bold-face values mark outliers that exceed the uncertainty from counting statistics. Hologram 2 is denoted as "A" in Fig. 6.7

Data	n_1	n_2	$n_{1,1}$	$n_{1,2}$	$n_{2,2}$
Holo 1 U	19	12	16 (12 ± 4)	6 (15 ± 3)	9 (5 ± 3)
Holo 2 U	92	70	64 (52 ± 9)	50 (80 ± 7)	48 (30 ± 6)
Holo 3 U	45	103	23 (14 ± 4)	31 (63 ± 7)	94 (72 ± 10)
Holo 4 U	10	89	2 (1 ± 1)	8 (18 ± 6)	89 (80 ± 10)
Holo 5 U	111	12	111 (100 ± 11)	7 (22 ± 6)	5 (1 ± 1)
Holo 6 U	39	23	37 (25 ± 6)	8 (29 ± 5)	17 (9 ± 4)
Holo 7 U	34	6	34 (29 ± 6)	2 (10 ± 4)	4 (1 ± 1)
Holo 1 R	4	2	3 (3 ± 2)	2 (3 ± 2)	1 (1 ± 1)
Holo 2 R	36	35	24 (18 ± 5)	28 (35 ± 5)	19 (17 ± 5)
Holo 3 R	11	51	8 (2 ± 2)	11 (18 ± 5)	43 (42 ± 8)
Holo 4 R	2	37	2 (0 ± 1)	4 (4 ± 3)	33 (35 ± 7)
Holo 5 R	45	1	44 (44 ± 7)	1 (2 ± 2)	1 (0 ± 1)
Holo 6 R	15	6	14 (11 ± 4)	1 (9 ± 3)	6 (2 ± 2)
Holo 7 R	6	2	6 (5 ± 3)	0 (3 ± 2)	2 (1 ± 1)
CDP 95 - 190 m	18	19	12 (9 ± 4)	12 (18 ± 4)	13 (10 ± 4)

Apparently, the large particles in the primary mode of the restricted case are more strongly clustered than expected in Hologram 2, 3 and 4 (which are Holograms A, B and C of Fig. 6.7). In the unrestricted case, their number fractions of $n_{1,1}$ and $n_{2,2}$ are even larger than

in the restricted case. This enhancement of particles with neighbors in the same mode (unrestricted) could be indicative of clustering but is here likely due to wall proximity effects. Though the number of particles is less in the restricted case, the enhancement of $n_{1,1}$ is statistically significant for Hologram 2, 3 and 4. In addition, Hologram 3 shows a significant depletion of the mixed fraction $n_{1,2}$ which supports the hypothesis of clustering in the first mode. The fraction of particles and neighbors in the second mode $n_{2,2}$ is very close to its expectation value for all three holograms discussed.

In the CDP data (bottom row of Table 6.2), the distribution of the particle neighbors among the three possible constellations large-large ($n_{1,1}$) and small-small ($n_{2,2}$) agree within the error bars with their corresponding expectation values. However, a total of 37 particles (18 particles in the first mode, 19 particles in the second mode) yields large error bars and complicates finding a statistically significant deviation. The large-small combination ($n_{1,2}$) was significantly less frequent than expected. Hologram A contained 36 particles in the first mode and 35 particles in the second mode if only the particles far enough away from the walls were considered. In terms of statistical significance, the error bars of the expectation value were barely exceeded for $n_{1,1}$ in Hologram A while the enhancement of $n_{1,1}$ in the CDP counts barely missed the limit for significance. The examined case from Flight 6 is very close to the limit of statistical significance. Fewer particles in Hologram A would have yielded an inconclusive result.

In this particular case of Flight 6, well-mixed cloud segments with a bimodal size distribution could be observed on the inter-particle scale in a cloud volume that is approximately 10 cm long. While the large-large and small-small combination in the CDP data barely support the hypothesis of a well-mixed droplet population, this hypothesis needs to be rejected for the measurement in Holograms A, B and C, even if the rejection was very close to the statistical limitations in this case. The reduction of the mixed neighborhoods ($n_{1,2}$) in the CDP data is barely significant. From the examined cases it can be deduced that number concentrations above approximately 5 cm^{-3} are required to yield a statistically significant clustering of either small or large droplets (or droplets and ice crystals) in the sample volume of HALOHolo. In the case of cirrus clouds, such high concentrations are rarely measured. More case studies are needed to investigate the frequency distribution of randomly dispersed vs. clustered and filamented volumes of cloud air on these local scales. Further statistical techniques in analogy to the Fishing test may be developed to quantify the degree of clustering between two distinct particle modes.

6.5 Inter-hologram variability of cloud properties

For the analysis of variability in microphysical properties, a different RACEPAC flight was selected. Flight 2 consists of two subsequently performed staircase flight patterns with 3 steps in cloud for the ascent and the descent (Cloud 1, 2 and 3 from Table 6.1). The region of the ascent and the descent overlap in space, yet with different altitudes of the cloud passes. Similar to Flight 6, the targeted cloud system was dominated by an

extended deck of stratocumulus. The main objective in this section is to quantify the variability of microphysical properties from one hologram to the next and to examine also the structure within a single hologram. The internal structure analysis is important to establish a possible connection between trends on the larger scales ($L \geq 10$ m) and the local environment of individual hydrometeors. At first, the inter-hologram consistency of the four selected parameters N , r_{eff} , $\sigma_g(D)$ and LWC is examined. Afterwards, the consistency of the particle size distributions is tested and finally the spatial distributions are investigated. Fig. 6.9 shows the flight track with the horizontal and vertical location of the individual cloud passes together with the size distribution averaged along each step. This three-step staircase pattern allows an investigation of the horizontal and vertical structure of the cloud.

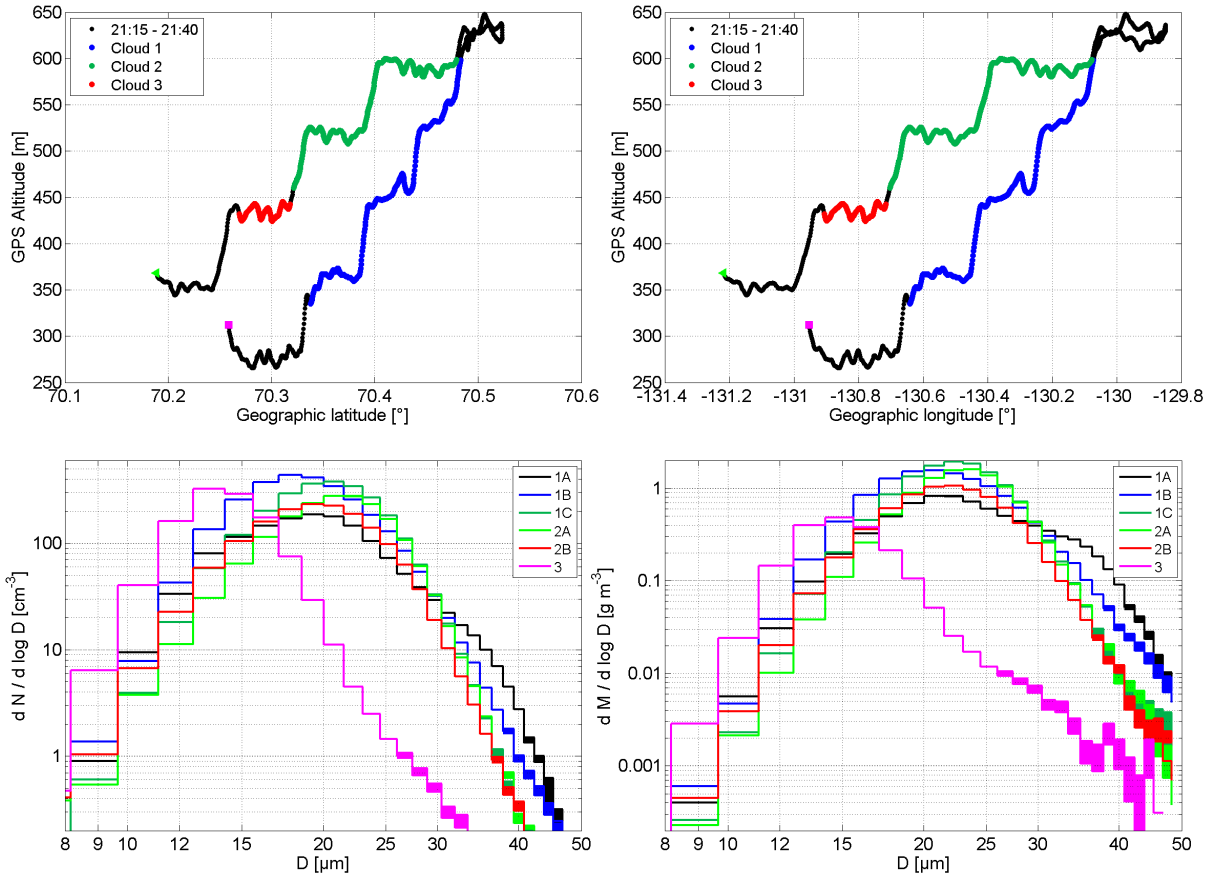


Fig. 6.9: Top row: Latitude and longitude of the flight track from RACEPAC Flight 2 with the cloud passes 1A - 3 highlighted. Bottom row: Number-weighted (left) and mass-weighted (right) particle size distributions of the six cloud passes from HALOHolo. Thick stairs indicate errors from counting statistics which are 5% or larger. Black lines indicate the flight track below or above the cloud.

When comparing the results of the size distribution analysis, it is obvious that the fractional agreement (the CDF value at the first step) of direct neighbors differs strongly between the two methods (KS test and normalized RMSE test). In particular for the case of Cloud 3, the normalized RMSE test is much stricter than the KS test. For the RMSE test, five size bins were used with a spacing of $\Delta x = 2.96 \mu\text{m}$, which is the effective pixel width of the detector. The five bins used were the ones remaining after filtering out the bins which contribute less than 5 % to the total number of particles.

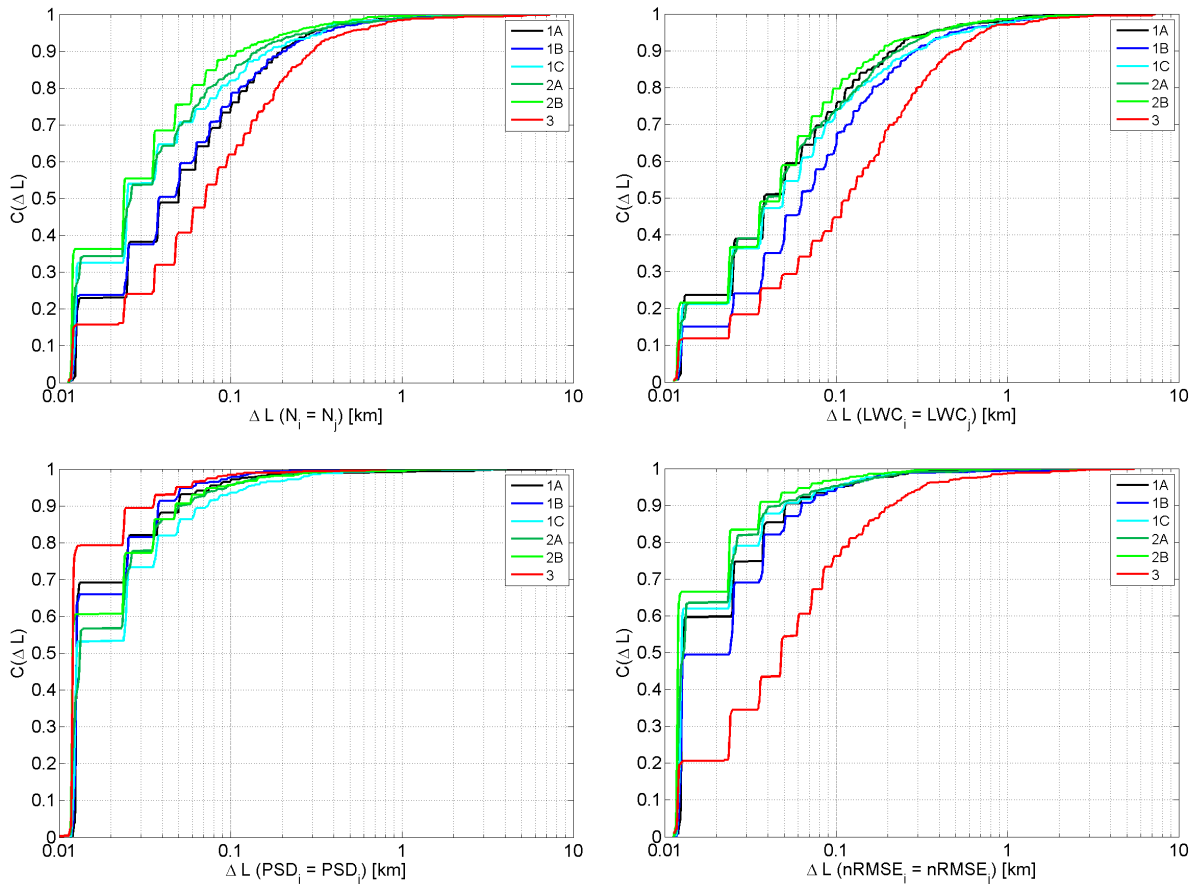


Fig. 6.10: Cumulative distribution of the distance ΔL between two holograms consistent in N (top left) and consistent in LWC (top right) of each cloud pass. In addition, the cumulative distributions of ΔL are shown for the size distribution agreement from the KS test between two holograms (bottom left) and the size distribution agreement from the normalized RMSE test (bottom right). The cloud passes are color-coded. Steps starting at values greater than zero on the ordinate (e.g. the red curve in the bottom left panel) indicate that there were holograms which did not agree with any of the others in terms of consistency in N , consistency in LWC or statistical equality of the size distributions.

The distributions of the distance to the nearest hologram which are consistent in N , shown in Fig. 6.10 top left, form three clusters: Cloud 1C, 2A and 2B (green and turquoise lines) are virtually identical, Cloud 1A and 1B are virtually identical and Cloud 3 differs

significantly from the others. From Fig. 6.9 it was visible that Cloud 1C and 2B were at the same altitude, also Cloud 1B and Cloud 3 were at the same altitude. However, Cloud 1C agrees better with Cloud 2A in terms of the distance between two holograms consistent in N . In terms of holograms that are consistent in LWC , all six cloud passes show a very similar distribution of the distances between two holograms consistent in LWC . This observation might be partially caused by assuming a constant error of particle size when calculating ΔLWC . However, the variability of N is also visible in the cumulative distribution of the length between two holograms consistent in LWC .

For the other cloud cases, the agreement between the two methods seems to be better. On average, about 60 % of the holograms in each cloud pass, except for Cloud 3, agree with their direct neighbor in terms of the particle size distribution. This number is large compared to the fractional agreement in terms of N (25 %) and LWC (35 %). However, in all of the examined cases were a few holograms where the next hologram with the same N , LWC or particle size distribution was more than a kilometer away from the actual one. This might be a pure stochastic effect, which means that after a certain distance L in the cloud the probability is high enough to find another sample with the same N , LWC or particle size distribution, even if the particular sample was an outlier w.r.t. to its neighbors.

Another question which remains to be answered is related to the spatial distribution of droplets within a particular hologram. Fig. 6.11 shows an overview of the fractional agreements of the quantities mentioned above (top left panel) and the hologram-specific quantities (top right panel). In addition to testing only the statistical equality of the first, second and third neighbor distance distributions with a uniform random distribution, the KS test was also used to examine the statistical equality of the neighbor distance distributions among hologram pairs of the same cloud pass.

In addition to the neighbor distance analysis, the Fishing test was performed where the maximum F value out of 23 different test cube lengths a was evaluated for each hologram and the fraction of holograms with $F_{max} < 3$ was determined. It turned out that the number of holograms which did not pass the definition of a uniform random distribution from the Fishing test was greater than the number of holograms which did not pass the neighbor distance consistency test. As the Fishing test is likely more sensitive to clusters or filaments than the neighbor distance statistics (cf. Fig. 4.15 in Chapter 4), this result is not really a surprise. However, the low number of outliers in terms of the F statistics shows that the majority of holograms has a uniform random dispersion of the cloud droplets. The two panels in the bottom row of Fig. 6.11 show the typical scales where the F values tend to reach their maximum.

For the small scales, $a = 2$ mm was chosen as a representative example as the probability of finding a particle in one of the cubes, derived from the particle number concentration, was at least 0.5. The representative for the larger scales was chosen such that 2/3 of the effective detector height after applying the sample volume restriction from Chapter 5 still fit into the cube, which yields a cube length of $a = 10$ mm. While the CDFs of the

six cloud passes did not show any significant disparity among each other in case of $a = 2$ mm, Cloud 3 is seen as an outlier for $a = 10$ mm. As the average particle diameter was smallest for Cloud 3, this might be an issue from detectability.

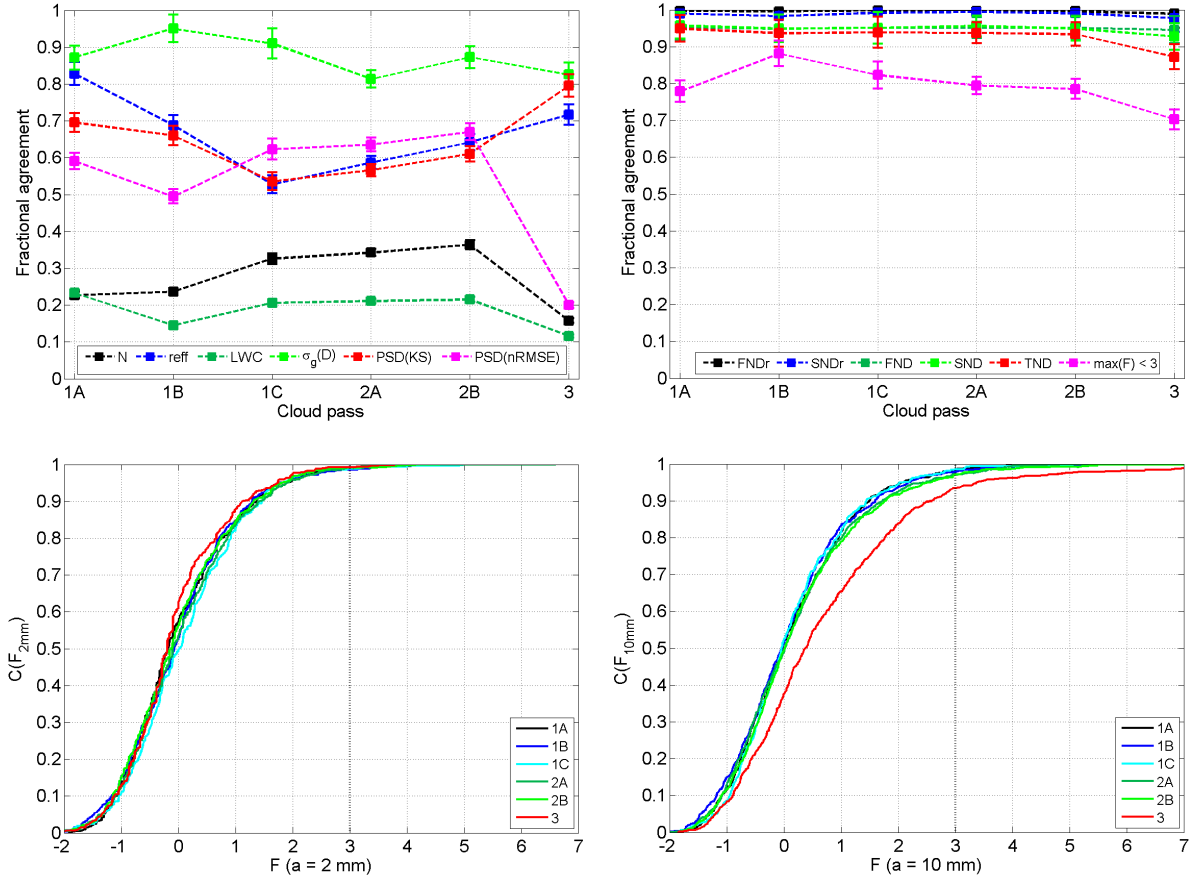


Fig. 6.11: Top left: Comparison of the inter-hologram pairwise agreement of N , r_{eff} , LWC , $\sigma_g(D)$ and the particle size distribution via KS test (PSD(KS)) and $nRMSE$ test (PSD(nRMSE)). Top right: Comparison of the agreement of the first and second neighbor distances with a uniform random distribution (FNDr, SNDr), the first, second and third neighbor distance among adjacent hologram pairs (FND, SND, TND) and maximum F values from the Fishing test below 3 ($\max(F) < 3$). Bottom row: Cumulative distribution functions of the F value from a Fishing test with $a = 2$ mm (left) and $a = 10$ mm (right).

A detailed look at the upper left panel of Fig. 6.11 shows that the inter-hologram consistency is somehow affected by the position relative to cloud base or cloud top. While the consistency of N and LWC between two holograms reaches its maximum in the cloud cases 1C, 2A and 2B, the agreement in terms of r_{eff} is reduced there. Also, the agreement of the particle size distributions, measured with the KS test, has a relative minimum in the cloud top cases 1C and 2A. This trend is significant w.r.t. the error bars from considering counting statistics of k holograms as the only error source. In conclusion, the

particle number concentration tends to be generally more consistent near the cloud top and more inconsistent near the cloud base while the effective radius and the particle size distribution are more consistent among two holograms in the cloud top region. One possible explanation of the higher variability of N and LWC in the cloud base region could be the presence of larger droplets ($D > 40 \mu\text{m}$) formed via collision and coalescence. These so-called *drizzlets* (cf. Glienke et al. (2017)) contribute to a large amount of the liquid water in the cloud and are present at fairly low number concentrations. However, Cloud 3 did not contain any drizzlets and had the same signature as Cloud 1A, which had a significant amount of drizzlets.

The presence of ice in these clouds is not able to explain the observations as the fraction of ice crystal number over droplet number N_{ice}/N_{liq} was of order 10^{-5} and the ice-to-liquid mass fraction m_{ice}/m_{liq} was between 10^{-4} and 10^{-3} with particle sizes between $40 \mu\text{m}$ and $150 \mu\text{m}$. Most of the larger ice was found below cloud base before Cloud 1 and after Cloud 3. 60 % of the ice crystals in Flight 2 were found outside of which was defined as long cloud passes. The higher variability of r_{eff} in the cloud top region might be a first evidence for the influence of mixing processes, which lead to highly variable spatial structures in terms of particle number concentration and size.

6.6 Investigating the spatial structure of mixing processes in extended stratiform cloud decks

As the previously performed study of the inter-hologram variability reflected a pronounced variability of the particle effective radius in the cloud top region, it needs to be investigated whether this might be a result from homogeneous mixing. According to the theory described in Beals (2013), the presence of either homogeneous or inhomogeneous mixing can be determined from so-called mixing diagrams, where the droplet mean volume diameter D_3 is analyzed as a function of particle number concentration N . The signature of inhomogeneous mixing would be a straight line with constant D_3 across the entire range of N . In the case of homogeneous mixing, the mean volume diameter would start to decrease with decreasing N after reaching a critical value of N . As the cloud top region is the preferred interface for mixing in stratocumulus clouds (cf. Klingebiel et al. (2015)), the ambient temperature and ambient relative humidity considered for calculation of the homogeneous mixing lines should be the values just above the cloud top. However, the accuracy of the humidity measurements during RACEPAC was not very high and therefore a range of plausible relative humidities ($RH = (95, 98, 99)\%$) was chosen as input to the mixing line calculation. With these assumptions, the most tricky case with almost 100 % relative humidity is examined. If the deviation from homogeneous mixing is evident for $RH = 99 \%$, it can be concluded that the observed mixing process has to be inhomogeneous mixing. The input variables are summarized in Table 6.3. The calculation of the normalized mean volume diameter $D_3/D_3(N_0)$ as a function of the normalized concentration N/N_0 is done via Eq. (4.1) to (4.9) in Beals (2013) where N_0 is the maximum

observed number concentration inside the cloud. Here, the normalization mean volume diameter $D_3(N_0)$ is computed as the median of all samples with $N/N_0 > 0.75$ to avoid bad scaling due to a possible outlier.

The mixing diagrams in Fig. 6.12 reflect a reasonable consistency with rather inhomogeneous than homogeneous mixing in 5 out of 6 cases. Cloud 1A was measured near the cloud base and its upper left portion in the mixing diagram (which corresponds to the beginning of the cloud pass) tends to follow the constant LWC line. This cloud pass did contain a significant amount of droplets larger than 30 microns, which barely induce a secondary mode in the mass-weighted size distribution of Fig. 6.9. The presence of a rather broad cloud droplet size distribution with $\overline{D}_g = 18.7 \mu\text{m}$ and $\sigma_g(D) = 1.28 \mu\text{m}$ - in contrast to $\overline{D}_g = 18.3 \mu\text{m}$ and $\sigma_g(D) = 1.23 \mu\text{m}$ in Cloud 1B - could be indicative of collision and coalescence forming drizzlets. These large droplets seem to be hardly influenced by being exposed to subsaturated conditions due to their large volume. The upper left panel of the mixing diagram therefore shows the cloud base region of a thick stratocumulus cloud in the process of creating precipitation.

Table 6.3: Thermodynamic variables used for calculation of the homogeneous mixing lines. The relative humidity was fixed at $RH = 99 \%$ for all six cloud cases. Listed are the mean and standard deviation of LWC , in-cloud temperature T_c and pressure p for the six cloud passes of RACEPAC Flight 2. The out of cloud temperature T_a was estimated from the vertical profile obtained from the aircraft where a value for below cloud base was used for Cloud 3 and values for above cloud top were used for the other five events.

Cloud	LWC [mg m^{-3}]	T_c [$^{\circ}\text{C}$]	T_a [$^{\circ}\text{C}$]	p [hPa]
1A	215 ± 83	-7.5 ± 0.4	-6.5	969 ± 1
1B	374 ± 106	-7.0 ± 0.2	-6.5	957 ± 2
1C	370 ± 122	-6.8 ± 0.1	-6.5	946 ± 1
2A	292 ± 122	-7.0 ± 0.2	-6.5	941 ± 1
2B	225 ± 89	-6.9 ± 0.2	-6.5	950 ± 1
3	80 ± 59	-9.4 ± 0.2	-9.0	961 ± 1

A fundamentally different picture is drawn by the subsequent cloud pass 1B in the top right of Fig. 6.12. It shows the classic signature of inhomogeneous mixing as a straight line from high to low number concentrations at a mean volume diameter around 20 microns. The maximum concentration is higher in comparison with Cloud 1A, and so is the minimum concentration, except for one outlier. The number of holograms containing relatively low number concentrations of particles is crucial to determine the difference between homogeneous and inhomogeneous mixing. In case of having a minimum number concentration of 80 cm^{-3} in Cloud 1B, the result would be inconclusive in terms of homogeneous vs. inhomogeneous mixing.

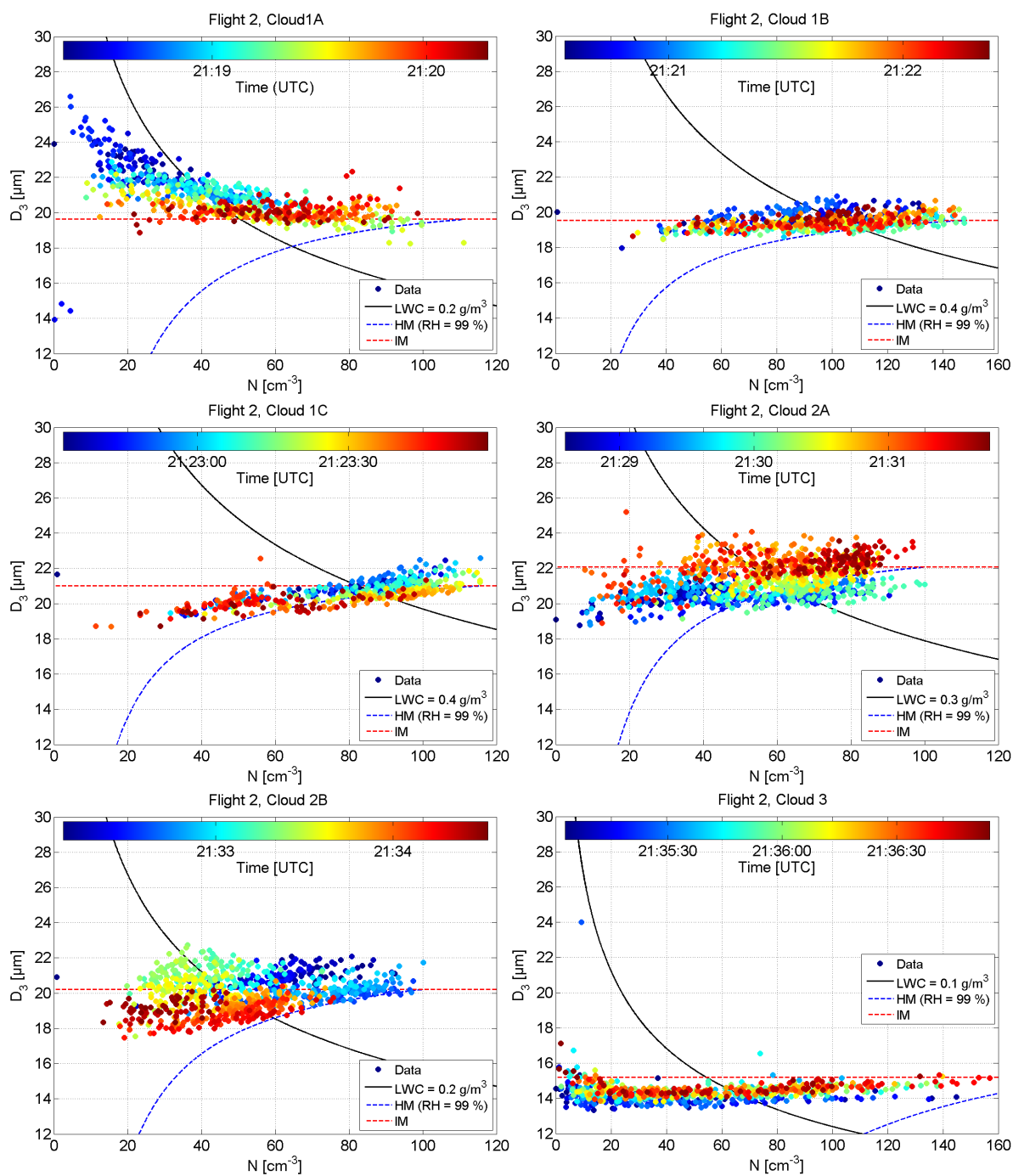


Fig. 6.12: Particle mean volume diameter as a function of particle number concentration for each hologram in Cloud 1A - 3. The time of measurement is color-coded. In addition, a black solid line of constant LWC is shown together with the calculated homogeneous mixing line (HM, dashed blue line) and the inhomogeneous mixing line (IM, dashed red line). The normalization diameter $D_3(N_0)$ used for rescaling the mixing lines was the median of D_3 from the holograms with $N/N_0 \geq 75\%$ where N_0 is the maximum observed number concentration in the particular cloud pass. Other examples can be found in Fig. E.6 of Appendix E.6.

The next case of Cloud 1C, which is a cloud pass through the cloud top region, is an example that is close to being inconclusive. Down to a number concentration around 50 cm^{-3} , the individual measurements follow the homogeneous mixing line. Towards lower concentrations, the number of measurements is significantly reduced and the majority of data points is in between the two extremes of homogeneous and inhomogeneous mixing. As discussed in Beals (2013), this particular case might be fractional homogeneous mixing, which means that a portion of the cloud volume has been mixed out and then re-entered the cloud. This case is an interesting particularity of inhomogeneous mixing as Beals (2013) suggested not to call secondary homogeneous mixing as homogeneous.

During the descending part of the staircase pattern on the return flight, a very similar signature as in Cloud 1C is encountered in Cloud 2A. However, the mean volume diameter is approx. $1 \mu\text{m}$ larger and more data points close to $N = 0 \text{ cm}^{-3}$ reveal this case as classic inhomogeneous mixing.

This signature is continued in Cloud 2B where disparities from homogeneous mixing appear at $N < 50 \text{ cm}^{-3}$. Interestingly, beginning and end of all the cloud passes except for Cloud 1A look virtually the same, which means that the pathway of mixing does not change along the cloud pass. Cloud 3 is, in contrast to Cloud 1A, another case of classic inhomogeneous mixing. The reason why the large particles are virtually absent in this region of the cloud is not yet clear. It might be a different cloud system where the formation of precipitation was not active during the time of the cloud pass. The six cloud passes did not fully overlap in space as seen in Fig. 6.9.

In an extended quasi-uniform cloud deck, one would expect a rather homogeneous cloud interior with little fluctuations in number concentration and also mean particle size. However, the mixing diagrams of Cloud 1B and Cloud 2B shown in Fig. 6.12 suggest that even the cloud interior is inhomogeneous in terms of the local number concentration. A possible explanation is the production of denser and less dense "cloud parcels" ascending from the cloud base as a result of convection and that the lifetime of the encountered cloud - until it was sampled - did not suffice to even out the variability. In other words, the observations in the cloud interior might be interpreted as "inhomogeneous mixing between droplet populations from a local updraft and droplet populations from the surrounding part of the cloud". A further analysis is needed to determine the time scales of convection and turbulent mixing in order to prove or disprove this hypothesis.

There is a way to get a zeroth-order approximation of the convective time scale, which is basically the cloud depth divided by the typical updraft velocity. The cloud in RACEPAC Flight 2 had a thickness of approximately 250 m (see Fig. 6.9) and w is typically between 1 m s^{-1} and 10 m s^{-1} . This yields a convective time scale $\tau_{conv} \approx 25 - 250 \text{ s}$. The more challenging part is to estimate the energy dissipation rate from turbulence (which yields the time scale of turbulent mixing) without knowing the three-dimensional wind field. If high-resolution data (3 Hz or better) of the static pressure p and / or temperature T are available, it is possible to estimate the energy dissipation rate from the power spectra of p

and T along a flight segment that was performed on constant altitude, which means that fluctuations in p can be related directly to local updrafts and downdrafts.

A transition from rather homogeneous to later inhomogeneous mixing is not found in the data. Other cloud passes from other RACEPAC flights do not substantially deviate from these six examples (see Appendix E). An interesting comparison would be achievable from very short cloud passes but the number of data points is likely too sparse to draw sophisticated conclusions. A future idea to investigate shorter cloud periods in terms of mixing is the usage of an airborne platform that is not as fast as an aircraft (e.g. the helicopter-borne measurement platform ACTOS).

6.7 Discussion and summary

Via intercomparison of full-resolution and one second combined cloud data from HALO-Holo and one-second average data from a CDP, it could be shown that the difference in the sampling strategies of conventional and holographic instruments does not lead to significant disparities in the analysis of cloud structure and bulk microphysics for the considered cases. The equality of both methods has been demonstrated by using data from RACEPAC Flight 6 of two contrasting cloud cases: One cloud case had a pronounced variability of particle size, the other had a pronounced variability of particle number concentration.

Below a spatial scale of approximately 400 m, the power spectra of all measured cloud properties tend to converge towards a white noise spectrum. While a similar effect has been documented and discussed by Davis et al. (1996), the reason for observing the same effect in holographic data sets needs to be different. Numerical tests have shown that the effect of sampling is insufficient by more than one order of magnitude to explain the high-frequency noise in the number concentration power spectra of HALOHolo. A detailed investigation of a possible connection between hologram brightness and / or the amplitude threshold with the observed variability of N is needed to finally confirm or reject the hypothesis that the measured noise is from a natural source. Amplitude threshold and N are correlated to some degree, the correlation coefficient is 0.35 for Cloud 5 from Flight 6 and 0.38 for Cloud 7 from Flight 6. A stronger correlation is found between the amplitude threshold and r_{eff} , which is approx. 0.47 for Cloud 5 and 0.63 for Cloud 7. However, the spectral components from threshold and N and threshold and r_{eff} are virtually uncorrelated in both cases. As the trends in N and r_{eff} were very likely no artifacts (as confirmed via intercomparison with the CDP), the changes in the amplitude threshold might be a result from the different amount of particle load in the holograms, and therefore a reaction on the cloud properties, not the other way round. Thus, the amplitude threshold for particle detection could have an influence on the number concentration of particles, but it is likely not the reason for the noise in the power spectra due to a lack of correlation between the spectral components taken from both time series by exactly the same calculation method. The selected cases of Flight 6 were no unique examples of this

effect; other flights did show the same trends. The results from this investigation would argue for a natural source being the more probable explanation than an instrument or data processing artifact. One way to gain more certainty about this question is to use a classified holographic data set of "maximum purity" (QC4) as described in Chapter 4 and repeat the power spectral analysis.

The investigation of an intersection through the mixing zone of the cloud top region provided insights into the local environment of cloud droplets in the mixing zone. After synchronizing the time axis of the CDP with HALOHolo, the particle by particle neighbor test as in Klingebiel et al. (2015) from the CDP data was compared with the spatial homogeneity and 3D first neighbor distance of the particles in the corresponding holograms of HALOHolo. While Klingebiel et al. (2015) found a uniform mixing in their cloud case from the VERDI campaign, this particular flight segment from RACEPAC is different. The CDP data suggest that the two particle modes, with a large mode above $21\ \mu\text{m}$ and a smaller mode below $21\ \mu\text{m}$ particle diameter, are well-mixed on the 10 cm scale in one dimension. However, the neighbor distance analysis of a hologram with an almost equal contribution of particles from both size modes revealed a spatial clustering of the larger droplets, indicated by significantly more large droplets with neighbors in the large mode than expected from a uniform random distribution. Even the maximum realistic particle sizing uncertainty is not able to remove the cluster. Though the counting statistics are borderline, the clustering of large particles in the rear part of the sample volume is statistically significant. Thus, the examined hologram (and also the subsequent ones) is uniformly interspersed between the two modes, but only on a maximum length scale of 8 centimeters. Other holograms in this flight segment had even stronger clustering of particles in one size mode, and also in total. Unfortunately, these transects through the mixing region are only a few ten to hundred meters long and the overall number of holograms is typically below 10. Nevertheless, this small amount of data was sufficient to examine the mixing between two particle size modes in a quantitative way. Again, the issue of the aircraft speed comes into play as a slower airborne platform would likely provide better statistics. As stratocumulus clouds do not reach altitudes above approximately 2 km, holographic balloon measurements might be able to provide high-quality data with a better spatial resolution.

In terms of microphysical variability on scales of about 10 m, most of the clouds sampled in RACEPAC Flight 2 had a large number of consecutive hologram pairs being consistent in number concentration and liquid water content. The highest fraction of a statistical agreement of a cloud property between two holograms was found in the size distribution width, which agreed in all cloud passes in approx. 90 % of the cases. The lowest fraction of hologram pairs being consistent was found for the consistency in LWC, which incorporates the high degree of variability in particle number concentration. It might be possible that the distribution of larger droplets among the samples led to strong fluctuations in the

LWC. However, the number of droplets greater than $50\ \mu\text{m}$ was low in case of the examined clouds and therefore the main contribution to the LWC came from the droplets smaller than $50\ \mu\text{m}$.

Only about 30, respectively 20 % of the holograms in each cloud pass had a neighbor hologram with a consistent N or LWC . The consistency of the effective radius between two holograms was dependent on the position of the cloud pass relative to the cloud top, where variability was strongest. Another observation that was made is that the first and second neighbor distances agreed in more than 90 % of the cases with a uniform random distribution. It could be shown that the Fishing test after Baker (1992) was more sensitive to inhomogeneities in the spatial distributions. However, the variability of the consistency in case of the Fishing test did not show a clear signal in terms of the position relative to the cloud top. On average, about 80 % of the holograms had a uniform random spatial distribution of particles according to the Fishing test. In conclusion, the observed trends in terms of inter-hologram consistency have shown that the variability of N increases towards cloud top while the variability of r_{eff} tends to decrease. However, the consistency of r_{eff} is still by a factor of two higher than the consistency of N in the cloud top region. Number concentration and liquid water content are most likely the microphysical properties which exhibit the highest degree of variability among all cloud properties used in the literature.

In the final section of this chapter, the role of mixing was investigated as one possible contributor to microphysical variability. Each of the cloud passes analyzed was dominated by the signature of inhomogeneous mixing. While one particular case of a cloud pass near the cloud top region might be explained by secondary homogeneous mixing, the others tend to follow either the straight line of constant mean volume diameter, or the mean volume diameter increases towards lower number concentrations, which would argue for a conservation of LWC . The latter was found near cloud base in a stratocumulus cloud with a significant amount of droplets larger than $40\ \mu\text{m}$, which already started to form a secondary mode in the mass-weighted size distribution. However, the presence or absence of inhomogeneous mixing was not correlated with the measures of intra-hologram randomness in terms of the spatial distribution. Holograms with particle clusters or particle filaments did occur sometimes and their position within the cloud pass seemed to be random. An inspection of the 3D distribution of particles confirmed that some of the extreme outliers from Cloud 2B and Cloud 3 in terms of the Fishing statistics ($F > 6$) were clustered or filamented (see Appendix E.7).

A very recent publication by Prabhakaran et al. (2017) has shown that nucleation of cloud droplets is possible in the wake of a large falling hydrometeor. Inducing the formation of small droplets in the wake of a large hydrometeor can lead to local inhomogeneities in particle number concentration. This mechanism could also explain bimodal size distributions with a small secondary mode in the cloud interior, but it requires considerably large particles (the large drops in Prabhakaran et al. (2017) were at least 1 mm in diameter,

the largest droplets in RACEPAC Flight 2 were smaller than 100 microns). In conclusion, the idea of Prabhakaran et al. (2017) might be able to explain some aspects of in-cloud variability, but not for the examined RACEPAC flights.

To summarize the results from the investigation of mixing and microphysical variability in Arctic stratocumulus, the following findings were considered the most important ones:

- The influence of the sampling strategy on both bulk microphysical properties as seen in a time series and their corresponding power spectra is considerably low. There are no substantial differences found between conventional sampling and holography on spatial scales as small as approx. 70 m. Some fine-scale structure below $L = 400$ m might differ, but below this length scale the spectra are in general dominated by noise.
- The hypothesis of the white noise in the high frequencies of the spectrum being produced by the effect of sampling has been investigated. It turned out that the observed noise cannot be explained by the effect of sampling. The time series data of the cloud microphysical properties from HALOHolo are partly correlated with the amplitude threshold used for particle detection and sizing. A reaction of the threshold becoming more liberal (higher values) on the presence of high LWC is more likely than the opposite direction.
- Number concentration and LWC were the two cloud parameters with the highest variance in the cases that have been investigated. The majority of subsequently measured cloud volumes has a uniform random distribution of particles, the normalized neighbor distances are consistent among each other and the particle size distributions agree most often. A trend could be determined for number concentration and effective radius, with an increasing variability of r_{eff} and a decreasing variability of N towards the cloud top.
- With better counting statistics than achievable with a scattering probe (FSSP or CDP), the cloud top entrainment zone of a stratocumulus cloud was examined. Local inhomogeneities in the distribution among the two particle size modes were found, which were present on spatial scales of approx. 8 cm. On smaller scales, the particles were randomly interspersed and the populations of the two size modes were well-mixed.
- Inhomogeneous mixing seems to be the dominant mechanism of mixing in stratocumulus clouds. All examined cloud passes followed more or less the corresponding inhomogeneous mixing line.

One future task should be the investigation of the other RACEPAC flights to back up the previously shown results with more robust statistics. Flight segments which targeted the cloud top entrainment zone are of particular interest as they could provide more insights into the dynamics of the spatial distributions of two distinct droplet populations in the process of mixing.

The evolution of bulk and local microphysical properties in glaciating cumulus clouds

7.1 Introduction

Convective clouds are distinguished from stratiform clouds by having a ratio of horizontal extent to vertical extent close to 1. Their vertical extent is mostly due to updrafts and downdrafts which easily exceed 1 m s^{-1} , sometimes even 30 m s^{-1} (Houze, 1993). Typical representatives of convective clouds are towering cumuli (cumulus congestus) and cumulonimbi. However, there exist individual types of stratocumulus, altocumulus, cirrocumulus and cirrus clouds which also fall into the category of convective clouds.

The simplest model of a cumulonimbus cloud is the so-called single-cell storm. Its initial stage, characterized by virtually pure updrafts and no downdrafts, is a cumulus congestus. After punching through the freezing level, ice formation may start as a result of freezing raindrops. If a considerable amount of ice is formed, the upper edge of the turret tends to lose its well-defined cauliflower-shaped boundaries and becomes more blurry and streaky. This stage, referred to as the cumulonimbus calvus stage, marks the transition from first ice to rapid glaciation. With increasing time, the upper parts of the cloud reach the level at which the buoyancy-delivered acceleration turns into deceleration and the vertical development of the cloud is terminated. Instead, the cloud top spreads out horizontally, forming an anvil (incus). At this stage, the cloud is recognized as a cumulonimbus incus, which is the mature stage of a thunderstorm. Both updraft and downdraft are fully developed and lightning activity is strongest in this stage. In an environment with little or no vertical wind shear, the cold air and precipitation from the downdraft reach the boundary layer, spread out in the horizontal and cut the supply of air with positive buoyancy for the updraft. As a result, the updraft gradually dissipates. If the water-saturated conditions provided by the updraft are not sustained anymore, the Wegener-Bergeron-Findeisen process will take effect and the upper parts of the cloud will glaciare. A remaining streaky anvil cloud with some fall streaks (recognized as cirrus spissatus cumulonimbogenitus) marks the final stage of this (former) convective storm. Figure 7.1 shows an example of convective storms in different stages of their life cycle.



Fig. 7.1: Convective storms during their life cycle. Upper image: Summertime convection with a developing storm (cumulus congestus, A1), a developing storm at glaciation (cumulonimbus calvus, B2) and a mature storm (cumulonimbus capillatus incus, C3). Lower image: Wintertime convection with a developing storm (cumulus congestus, A5), two mature storms (cumulonimbus capillatus incus, B3 and B4) and two dissipating storms (cumulonimbus capillatus, turning into cirrus spissatus cumulonimbogenitus, B1 and B2). Photos taken from private collection of O. Schlenczek.

Cumulonimbus clouds belong to the so-called *mixed-phase clouds*. Mixed-phase clouds as described in Korolev and Isaac (2006) consist of both solid and liquid-phase hydrometeors. These clouds are generally unstable as the saturation vapor pressure over ice is less than the saturation vapor pressure over liquid water at the same temperature. Thus, the ice grows at the expense of the droplets if the actual vapor pressure is between the

saturation vapor pressure over water and the saturation vapor pressure over ice. This situation is known as the Wegener-Bergeron-Findeisen effect (Korolev, 2006). However, under some circumstances a coexistence of both phases is observed for several minutes to hours. A stable mixed-phase cloud requires a continuous supply of supercooled droplets, which is provided via adiabatic or radiative cooling. A common way to retain the concentration of supercooled droplets is vertical lift through an updraft, either via convection or orographic forcing. Many orographic clouds developing next to a steep slope are stable mixed-phase clouds (Henneberger, 2013). Korolev and Isaac (2006) investigated the hypothesis of phase inhomogeneities in mixed-phase clouds ("ice pockets") via airborne measurements of relative humidity and IWC / LWC. They came to the conclusion that ice and water droplets should be well-mixed on spatial scales smaller than 100 meters. However, the measured data were available at a spatial resolution of 100 meters and were one-dimensional averages. Very small inhomogeneities might be averaged out in the calculation of the relative humidity as a function of ice water content (IWC) to total water content (TWC) partitioning. Here, the cloud composition in the mixed-phase region is examined on spatial scales of some mm to 10 cm with spaces between the measurements of approximately 30 m.

To form a mixed-phase cloud at temperatures below 0 °C, some of the supercooled liquid hydrometeors need to freeze. Freezing under atmospheric conditions is rarely observed at temperatures above -5 °C and cloud droplets can stay in the liquid phase at temperatures as low as -35 °C (Pruppacher and Klett, 1997). There exist four freezing mechanisms (deposition freezing, condensation freezing, immersion freezing and contact freezing) which can explain the formation of ice crystals. Larger drops tend to freeze at higher temperatures than smaller drops (Pitter and Pruppacher, 1973), therefore the freezing of supercooled raindrops is likely the beginning of the glaciation process.

However, the overall number of ice nuclei active at a temperature above -15 °C cannot explain the observed number of ice crystals in most clouds. Typical ice nuclei concentrations at a temperature as cold as -8 °C are below one per cubic meter (Mason, 1973). However, observed ice crystal concentrations in this temperature range often exceed 10 per liter, which is a discrepancy factor of 10^4 . Secondary ice production mechanisms can, in principle, be understood as contact freezing through an ice fragment as ice nucleus (Pruppacher and Klett, 1997). A fast reduction of the liquid water mass at particle sizes above $100 \mu\text{m}$ can be seen as indirect evidence of an active ice multiplication process. Large drops tend to produce small ice splinters when they freeze. The splintering process of freezing drops was investigated in the laboratory by Bader et al. (1974), who found an ice multiplication factor between 2 and 10 from this process.

From laboratory experiments (Hallett and Mossop (1974), Mossop et al. (1974)), it is well-documented that the freezing of supercooled cloud droplets on the surface of frozen hydrometeors, which is known as *riming*, releases tiny ice fragments (splinters), which then act as very efficient ice nuclei, or grow into larger ice crystals via water vapor deposition. The maximum efficiency of this so-called Hallett-Mossop process is found in a temperature

range between -5 and -8°C . In this temperature range, rime-splintering can easily explain a discrepancy between the number of ice crystals and the number of ice nuclei of a factor 100 - 1000.

Another pathway of secondary ice formation was discussed by Rangno (2008) and confirmed in laboratory experiments conducted by Leisner et al. (2014). If riming is not active, collision and coalescence can lead to the formation of large supercooled drizzle drops and raindrops. Raindrops typically freeze at higher temperatures than cloud droplets and during the freezing process, an ice shell grows from the drop surface towards the center, forming spicules on the freezing drop. Sometimes, a tiny ice particle is ejected from these spicules, which then starts the cascade of glaciation. Deformed frozen drops with spicules have been observed in-situ by Lawson et al. (2015) and other authors.

If there already is an abundance of approx. 100 ice crystals per liter, fracturing of fragile dendritic crystals can lead to ice multiplication at temperatures between approx. -12 and -16°C (Vali, 1980). This mechanism is active at temperatures where Hallett-Mossop is not efficient anymore, it does not require the presence of rimers and may account for a multiplication factor around 10. All of these processes were summarized and discussed in terms of their impact on cloud glaciation by Mossop (1985). However, a quantitative in-situ analysis of the individual ice multiplication processes (Hallett-Mossop, raindrop fragmentation and dendrite fracturing) on scales below a few hundred droplet radii has not been performed yet.

7.2 Data and methodology

The instrumentation used during the Ice in Clouds - Dust (ICE-D) field campaign was installed on the BAe-146 research aircraft from the Facility for Airborne Atmospheric Measurements (FAAM). For the measurement of cloud microphysical properties, four instruments were used besides HALOHolo: A Cloud Droplet Probe (CDP), a Two-Dimensional Stereo Probe (2D-S), a Three-View Cloud Particle Imager (3V-CPI) and a Cloud Imaging Probe with a $100\ \mu\text{m}$ pixel resolution (CIP-100) These instruments were operated either by FAAM, the University of Manchester or the University of Leeds. Data from the CDP and 2D-S were available for intercomparison with HALOHolo for Flight B926, which is discussed here. Aerosol measurements were conducted with a Passive Cavity Aerosol Spectrometer Probe (PCASP). Data from the PCASP for aerosol sizes above $0.5\ \mu\text{m}$ are used to estimate the number of ice nuclei after the parameterization from DeMott et al. (2010). Cloud hydrometeor and aerosol measurements were provided in data files with a sampling rate of 1 Hz.

Meteorological data were obtained from a variety of instruments: A five-hole turbulence probe is used to measure the three-dimensional wind components u, v and w at a sampling rate of 32 Hz with an accuracy better than $0.5\ \text{m s}^{-1}$, temperature T is measured with two Rosemount RM 102 sensors (32 Hz sampling rate), one of them is heated and delivers the static air temperature deiced, the other is not heated and acts as a backup. These sensors

have an accuracy of $\Delta T = \pm 0.3^\circ\text{C}$. Static air pressure p is measured as well as true air speed TAS with the aircraft air data system labeled "RVSM" in the aircraft data files at a sampling rate of 32 Hz. Humidity measurements are available from the General Eastern Chilled Mirror sensor (4 Hz sampling rate) and a Buck CR2 hygrometer (1 Hz sampling rate), both deliver the *dewpoint* T_d . In contrast to the temperature measurements, the humidity measurements have a much larger uncertainty, which is approx. $\Delta T_d = \pm 1^\circ\text{C}$. In the context of measuring the conditions for ice nucleation, accurate temperature measurements are of very high importance. The data sets from the Rosemount sensors were plausibility checked and corrected for known aerodynamically induced errors by FAAM, who provided the so-called "core data files". However, the windchill effect from the collection of cloud droplets or precipitation on the temperature sensor cannot be corrected in a straightforward way. Thus, the mean temperature shortly before and after a cloud pass on the same altitude should be used as the most probable estimate of the temperature inside the cloud, which is done here.

Flight B926 took place on 14 August 2015 south of Praia, Cape Verde, and targeted a developing mesoscale convective system over the Atlantic Ocean at about 13.6°N and 25.4°W . A satellite image with the cloud system and the location of the cloud passes is shown along with a Skew-T/log p diagram in Appendix F.2. An overview of the meteorological properties is listed in Table 7.1.

Table 7.1: Overview of the meteorological data of the cloud passes in ICE-D Flight B926. Listed are the cloud pass number, the time of the cloud pass, pressure p , temperature T , altitude z , cloud pass length L and number of holograms in cloud n_H . The temperature data are mean value and standard deviation before entering the cloud to avoid errors from a wet sensor which lead to measured temperatures that are by up to 5 K too low. The temperature after exiting the cloud was approximately 0.2°C lower than the mean temperature before entering the cloud. Temperature values marked with an asterisk (*) were taken from the non-deiced Rosemount RM 102 sensor due to a temperature drift of the deiced sensor. Altitude and pressure values are mean and standard deviation during the cloud pass. Each measurement of temperature, pressure and altitude used for calculating the mean and STD contains approximately 6,000 data points.

Pass	Time (UTC)	p [hPa]	T [$^\circ\text{C}$]	h [km]	L [km]	n_H
1	16:45:06 - 16:45:26	504 ± 1	-5.0 ± 0.3	5896 ± 5	2.8	111
2	16:48:25 - 16:48:49	485 ± 1	-6.3 ± 0.1	6214 ± 2	3.5	0
3	16:51:49 - 16:52:10	485 ± 1	-6.2 ± 0.2	6205 ± 9	3.1	120
4	16:55:37 - 16:56:00	475 ± 1	$-7.6 \pm 0.1(*)$	6373 ± 8	3.4	122
5	16:58:52 - 16:59:17	475 ± 1	-7.5 ± 0.1	6382 ± 3	3.9	0
6	17:03:34 - 17:03:59	455 ± 1	-10.1 ± 0.2	6710 ± 5	4.0	140
7	17:08:31 - 17:08:50	437 ± 1	$-12.5 \pm 0.1(*)$	7032 ± 5	3.0	107
8	17:14:31 - 17:14:55	409 ± 1	-16.0 ± 0.1	7525 ± 2	3.9	131
9	17:18:49 - 17:19:09	409 ± 1	-16.2 ± 0.1	7532 ± 2	3.3	0

One particular convective tower was penetrated in nine subsequent cloud passes where six of them had data from HALOHolo. The measured cloud passes cover the storm evolution from a cumulus congestus with almost no ice at $T \approx -5^\circ\text{C}$ to a dissipating cumulonimbus with a fully glaciated anvil cloud at $T \approx -16^\circ\text{C}$. From an analysis of the cloud passes and the advection of the cloud with the mean wind, which is discussed in Appendix F.1, it is very likely that it was the same cloud measured in nine subsequent cloud passes.

7.3 Trends in microphysical properties during the process of glaciation

In order to gain a better understanding of the situation that was examined, the cloud evolution in terms of the bulk microphysical properties is discussed first before the small-scale structures are analyzed. The first two cloud passes measured by HALOHolo were Pass 1 and 3. Both cloud passes with approximately 4 L of sampled air contained only a marginal amount of ice and raindrops up to a maximum dimension of about 1.5 mm were present, yielding a LWC up to 8 g m^{-3} in the one-second average during Pass 1. Typical values of the LWC in a cumulonimbus cloud are around 1 g m^{-3} , the very high values in this case are due to the considerably small (35 cm^3) sample volume containing one or two millimeter-sized raindrops. The highest LWC values were found in near-quiet conditions in terms of the updraft velocity w . The first ice particles detected in the temperature range of -5 to -6°C were between 40 and 100 μm large and most often found in the "small irregular" habit class, probably the result of freezing raindrop fragmentation. In terms of number concentration, these crystals contributed to only a small amount of the total (approx. 0.2 % of the number of hydrometeors greater than 40 microns). Also in terms of IWC the small ice particles in Pass 1 and 3 contribute only a negligible amount of the total mass. From the definition in Korolev and Isaac (2006), the cloud would be called a "liquid cloud" here. Fig. 7.2 summarizes the size distributions and time series data from Pass 1, a figure from Pass 3 showing a very similar partitioning of ice and liquid water with similar particle size distributions is included in Appendix F.

Also shown in Appendix F are the particle images of the large raindrops. In both cloud passes, the number concentration of ice and water is correlated with positive vertical velocity. Scatter plots showing the correlation between vertical velocity w and particle number concentration N for ice and liquid water are also shown in Fig. F.5 of Appendix F.3. Thus, it is probable that the observed ice crystals did not precipitate from higher regions of the cloud but formed at lower altitude / higher temperature.

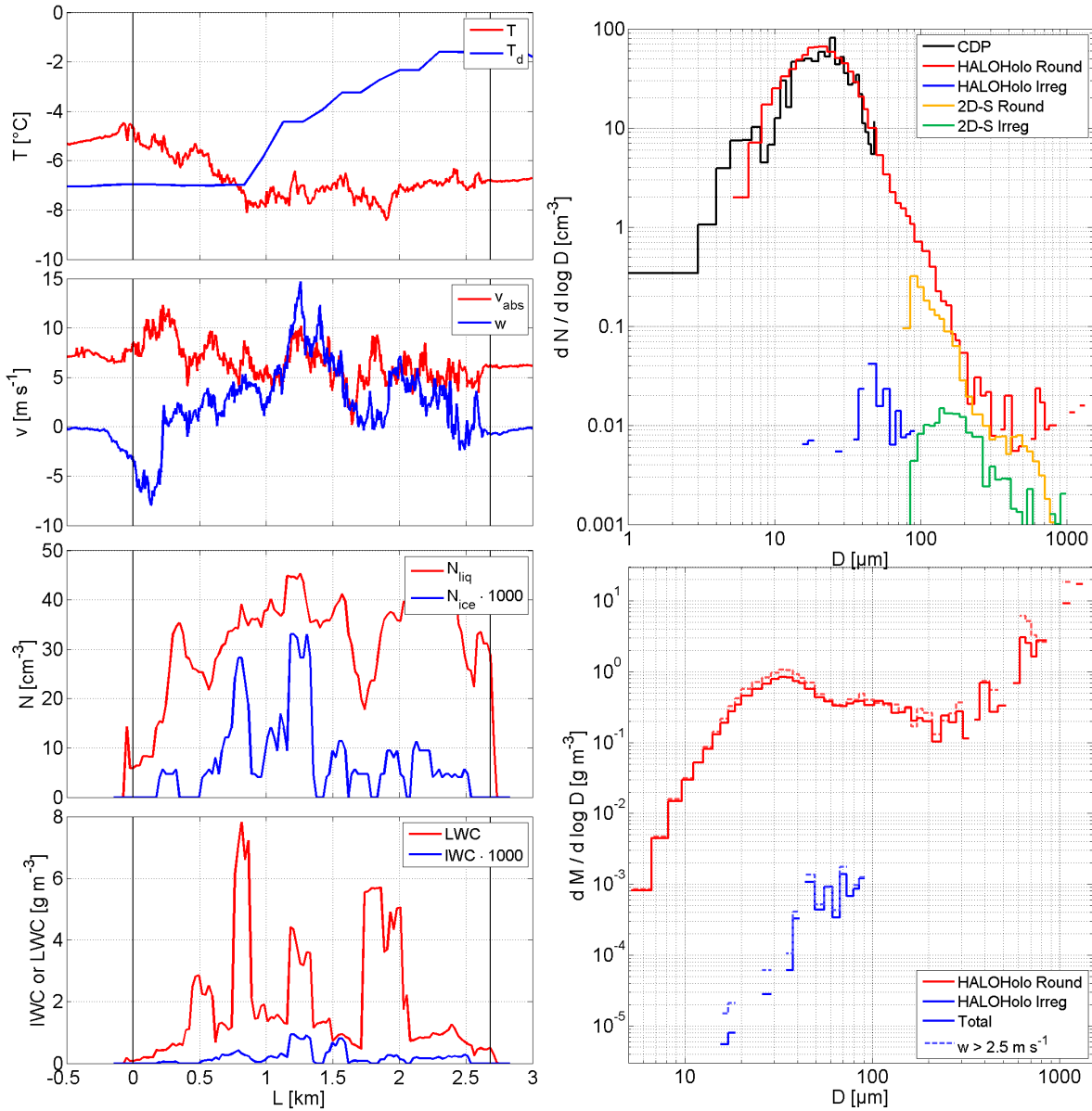


Fig. 7.2: Meteorological variables and cloud properties as a function of length along flight track (left column) and particle size distributions (right column) from Pass 1 of Flight B926. Shown are the temperature T (32 Hz) and dewpoint T_d (1 Hz, top row left, $T_d > T$ indicates water-supersaturated conditions), horizontal and vertical wind speed v_{abs} and w (second row left), number concentration of ice and droplets N_{ice} and N_{liq} (third row left, 1 s running average) and LWC / IWC (bottom row left, 1 s running average) along the cloud pass. The number-weighted size distribution (top right) includes data from the CDP (black), spherical particles from HALOHolo (red), aspherical particles from HALOHolo (blue), round particles from the 2D-S (orange) and irregular particles from the 2D-S (green). The mass-weighted size distribution (bottom right) is shown for spherical (red) and aspherical (blue) particles from HALOHolo. The solid lines represent the average size distribution over the entire cloud pass (Total), the dashed lines represent the stronger updrafts ($w > 2.5 \text{ m s}^{-1}$).

The overall picture changes significantly when looking at Pass 4, shown in Fig. 7.3. In comparison with Pass 1, the IWC has increased by almost a factor of 1000 while the maximum LWC decreased by a factor of 8. The large spherical particle mode with a mode diameter around 800 μm is gone and has been replaced by a large mode of ice. However, the size distribution of the spherical particles below 300 microns changed only marginally. The massive increase of IWC and massive decrease of LWC is indicative for an ice multiplication process which is capable of freezing the large raindrops in a very short time. Between Pass 3 and 4, the time difference was about 210s and the temperature decreased by less than two degrees. Also in this cloud pass, the maximum ice concentration and IWC is found in the updraft region. A closeup of the particle images (Fig. F.9 of Appendix F) reveals the presence of large rimed hydrometeors. Many of them are close to a spherical shape with numerous 20 to 80 micron wide protuberances on their outer shell. In the same cloud pass, there was a large fraction of columnar ice, which argues for the rime-splintering (Hallett-Mossop) process as the main contributor. A possible connection between the protuberances and the columns is discussed in Section 7.6. A very similar picture is seen in Pass 6, which was at $T \approx -10^\circ\text{C}$. For a better comparison of the cloud passes in terms of the ice to liquid water partitioning, number concentration and mass are listed in Table 7.2. *Cloud droplets* are spherical objects with $D < 40 \mu\text{m}$, *drizzlets* are spherical objects between 40 and 100 μm large and larger spherical objects are classified as *raindrops*. The two cloud passes 4 and 6 had a similar IWC/TWC ratio of approx. 40 %.

Table 7.2: Hydrometeor number and mass concentration for the cloud passes with data from HALOHolo. The number concentration of cloud droplets is given in cm^{-3} , the number concentration of the other hydrometeors is given in L^{-1} . In addition, the sampled volume of air V , the IWC/TWC fraction and the temperature are shown.

Pass	Number concentration [cm^{-3} or L^{-1}]				Mass concentration [g m^{-3}]				V [L]	$\frac{IWC}{TWC}$ [%]	T [$^\circ\text{C}$]
	Cloud droplets	Drizzlet	Rain	Ice	Cloud	Drizzlet	Rain	Ice			
1	29.8	2696	99	9	0.224	0.194	1.509	0.000	3.899	0.01	-5.0
3	9.8	663	42	5	0.066	0.055	0.433	0.002	4.215	0.37	-6.2
4	14.5	1469	24	165	0.123	0.093	0.053	0.203	4.285	42.96	-7.6
6	15.2	918	26	152	0.114	0.067	0.045	0.151	4.917	40.08	-10.1
7	3.7	321	7	131	0.023	0.023	0.008	0.181	3.758	76.81	-12.5
8	1.1	4	0	202	0.002	0.000	0.000	0.609	4.601	99.66	-16.0

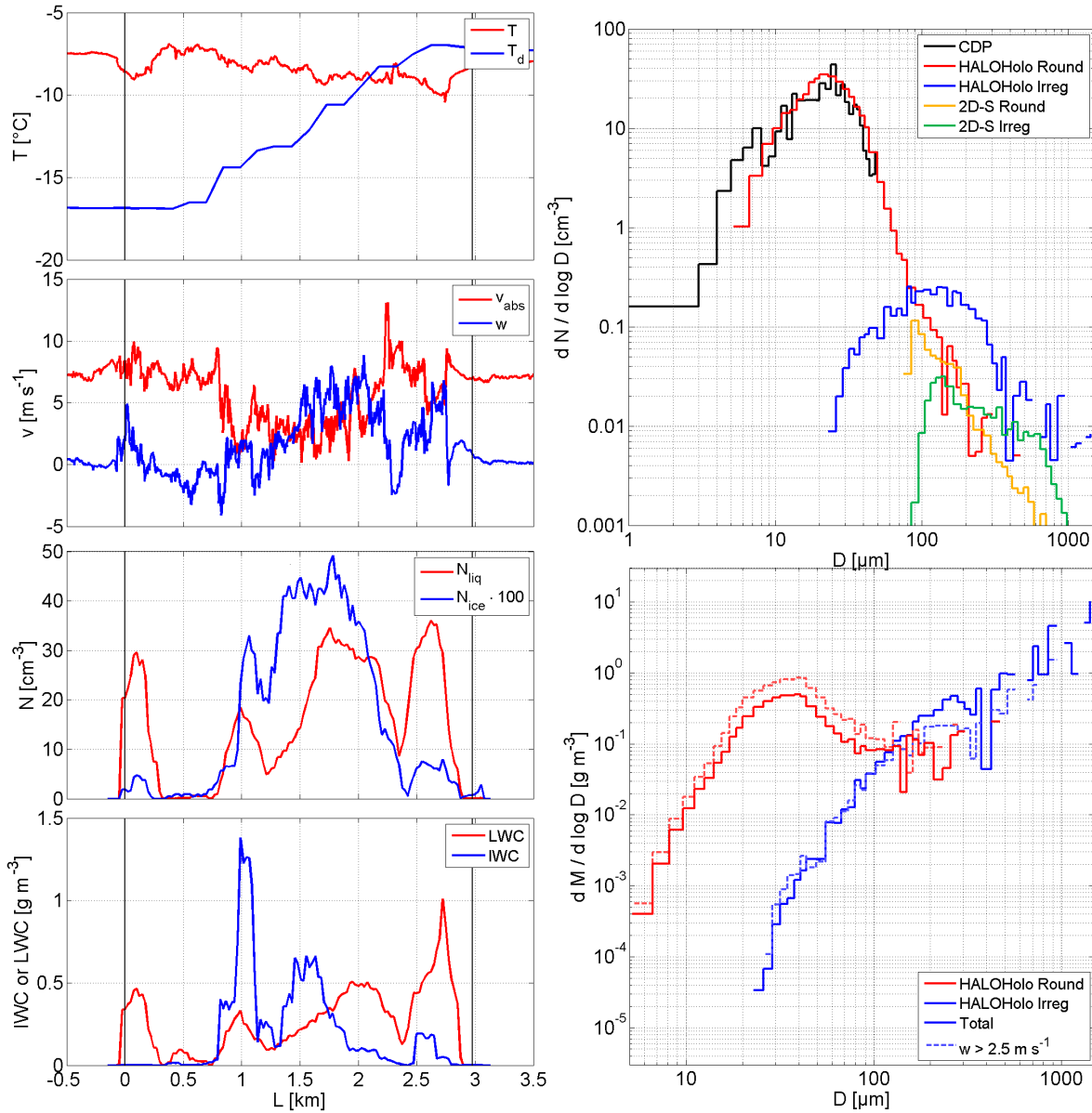


Fig. 7.3: As in Fig. 7.2 for Pass 4 as an example of the Hallett-Mossop zone.

Towards Pass 8, which was obtained at an ambient temperature of -16.2°C , the IWC/TWC ratio was close to full glaciation (over 99 %). A short episode of the cloud pass with spherical objects was encountered around 17:14:38 UTC in an updraft with $w \approx 5 \text{ m s}^{-1}$. Hence the maximum updraft velocity is reduced in comparison with the other cloud passes, the supply with supersaturated ascending air is weaker and the Wegener-Bergeron-Findeisen process may take effect. Outside the updraft core, there were virtually no droplets found. The ice crystals also tend to show different habits as in the previous cloud passes: While the dominant fractions were columns, frozen drops and rimed aggregates in the cloud passes 4, 6 and 7, aggregates of plates are most abundant in Pass 8. This is likely due to the regime change for particle growth as shown in Bailey and Hallett

(2009). Columnar growth dominates at high supersaturation down to a temperature of about -10°C .

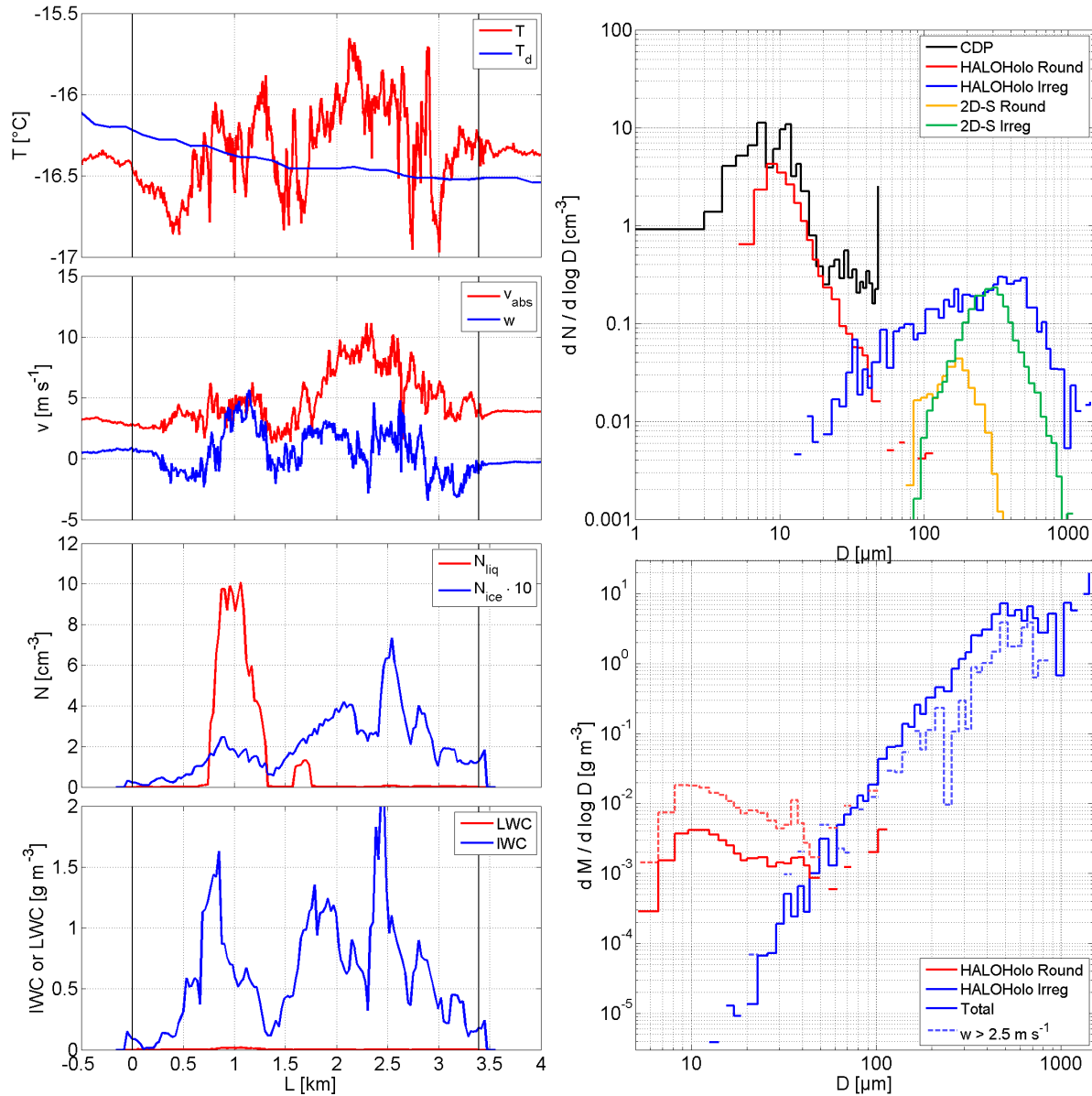


Fig. 7.4: As in Fig. 7.2 for Pass 8 as an example of the rapid glaciation.

In the measurements outside the cloud on the same altitude as in the cloud passes, the median and the quartiles of aerosol particle concentration from the PCASP for $0.5 \mu\text{m} \leq D \leq 2 \mu\text{m}$ were determined. The 25th and 75th percentiles were used as the "error bars" and the median as the actual value of the possible ice nuclei concentration. With the temperature data given in Table 7.1, the ice nuclei (IN) concentration was calculated after the parameterization of DeMott et al. (2010), given in Eq. 7.1. T is the cloud temperature in $^\circ\text{C}$ and $N_{aer,0.5}$ is the concentration of aerosol particles larger than 0.5

microns in cm^{-3} . The coefficients from the power-law fit in DeMott et al. (2010) are $a = 0.0000594$, $b = 3.33$, $c = 0.0264$ and $d = 0.0033$. $N_{IN}(T)$ is the number of ice nuclei per liter at the temperature T (in $^{\circ}\text{C}$).

$$N_{IN}(T) = a(0.01 - T)^b (N_{aer,0.5})^{(c(0.01-T)+d)} \quad (7.1)$$

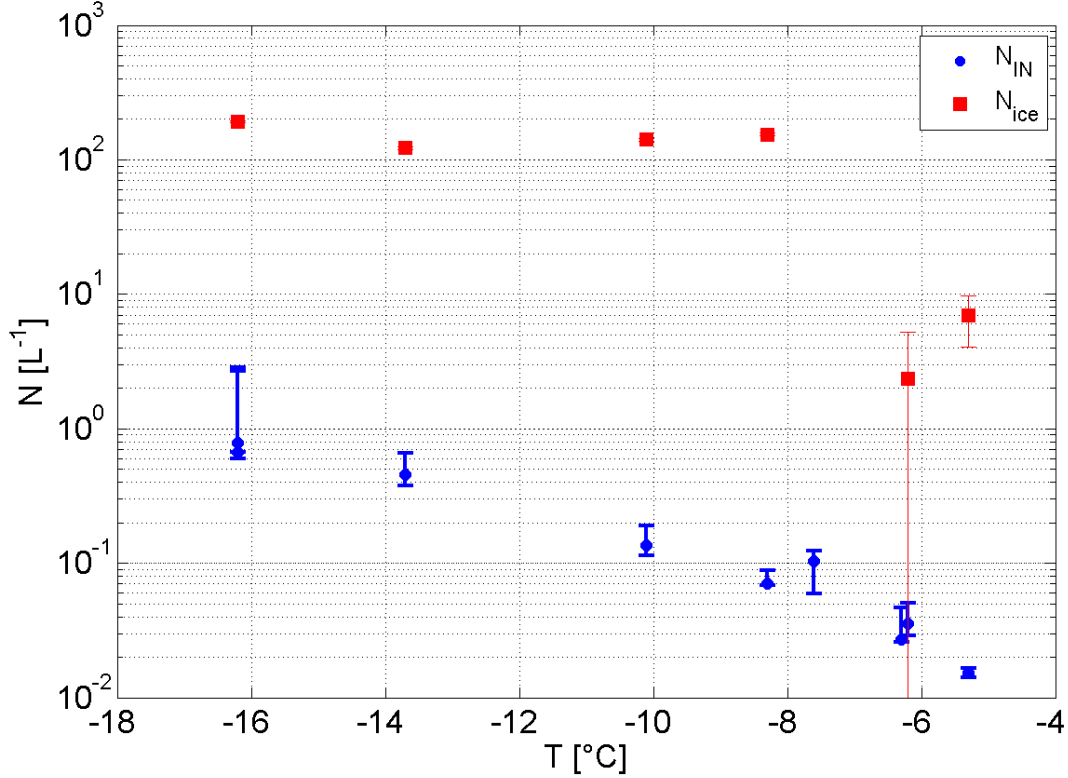


Fig. 7.5: Concentration of ice nuclei calculated from the PCASP aerosol measurements and the ambient temperatures via the parameterization of DeMott et al. (2010) (blue circles) vs. concentration of ice crystals larger than 40 microns measured by HALOHolo (red squares). Data base and error bar calculation are explained in the text. A notable change of regimes is seen between $T = -6^{\circ}\text{C}$ and $T = -8^{\circ}\text{C}$ where the Hallett-Mossop process is activated.

The values have been calculated for all cloud passes in Flight B926 and compared with the measured ice crystal concentration greater than 40 microns in HALOHolo. Due to the fact that miss detections of small ice particles do occur, the error bars of the HALOHolo ice crystal number concentrations reflect the uncertainty of one missed ice particle in ten holograms, which is a fairly realistic assumption. Fig. 7.5 shows the number of possible ice nuclei vs. the number of observed ice crystals for each temperature of the cloud passes (no data from HALOHolo for Pass 2, 5 and 9) and the disparity between the estimated IN concentration and the measured ice concentration reflects a high degree of secondary ice production. Even in the cloud passes 1 and 3, the difference between IN concentration

and observed ice crystal concentration is approximately a factor of 100. This finding suggests that secondary ice production was already active as no ice particle bigger than 100 microns was measured at all. From the absence of rimed particles in this time period of the flight, it is assumed that the mechanism responsible for secondary ice production is fragmentation of freezing raindrops after Rangno (2008), which was also the conclusion drawn by Lawson et al. (2015) who investigated very similar clouds. An enhancement of ice crystals by almost a factor of 100 is found in the transition from Cloud Pass 3 to 4, where a notable amount of rimed particles and possible splinters was discovered for the first time in this flight. Thus, it is thought that the previously active secondary ice production mechanism is boosted by almost a factor of 100 when Hallett-Mossop comes into play. A key question towards a better quantitative understanding of the secondary ice production mechanisms in convective clouds is the question about the local environment of ice crystals and water droplets as well as the local environment of rimers and splinters.

7.4 The local environment of ice crystals and water droplets

After the evolution of the ice and liquid water during cloud glaciation has been discussed in the previous section, the local environment of ice crystals and water droplets is inspected more closely. Therefore, the particle classes are compared for the first neighbors. In analogy to the examination of the bimodal size distribution in the RACEPAC clouds, the same method is applied but for the primary mode being water droplets (spherical objects) and the secondary mode being ice. For each hologram in the series, the number of droplets and the number of ice particles within the inner $2/3$ in both lateral directions of the sample volume are determined. A neighbor particle analysis is performed to determine the number of ice crystals being the first neighbors of droplets and vice versa, in addition to the particles and first neighbors in the same thermodynamic phase (ice or liquid water). The observed neighborhood frequencies ($n_{ice,liq}$, $n_{ice,ice}$ and $n_{liq,liq}$) are then compared with their expectation values from Poisson statistics in analogy to the analysis of the bimodal droplet populations in Chapter 6, Section 6.4. The actual values of $n_{ice,liq}$, $n_{ice,ice}$ and $n_{liq,liq}$ are listed in Table F.2 - F.9 in Appendix F.

From the analysis of the first neighbor distances, it was found that there were eight events in the cloud passes 4, 6, 7 and 8 where the number of droplets with an ice crystal as first neighbor (or ice crystals with a droplet as first neighbor) was significantly too low or too high in comparison with a uniform random distribution. This is a considerably small fraction, given a total of 148 holograms containing at least two droplets and at least two frozen hydrometeors. Thus, the significant reduction or enhancement of ice-droplet pairs could have been observed just by chance.

However, the frequency of ice crystals having an ice crystal as first neighbor ($n_{ice,ice}$) was occasionally enhanced beyond the limit of statistical significance for the actual sample. Pass 4 contained 2 holograms with significantly more ice-ice neighbors, Pass 6 had 4 of them, one was found in Pass 7 and two were found in Pass 8. An example of two

holograms from Pass 4 with two ice-ice neighborhoods that cannot be explained by a uniform random distribution is shown in Fig. 7.6. Both holograms have a significant amount of droplets and also of ice crystals, the upper was found in a downdraft region, the lower in the updraft.

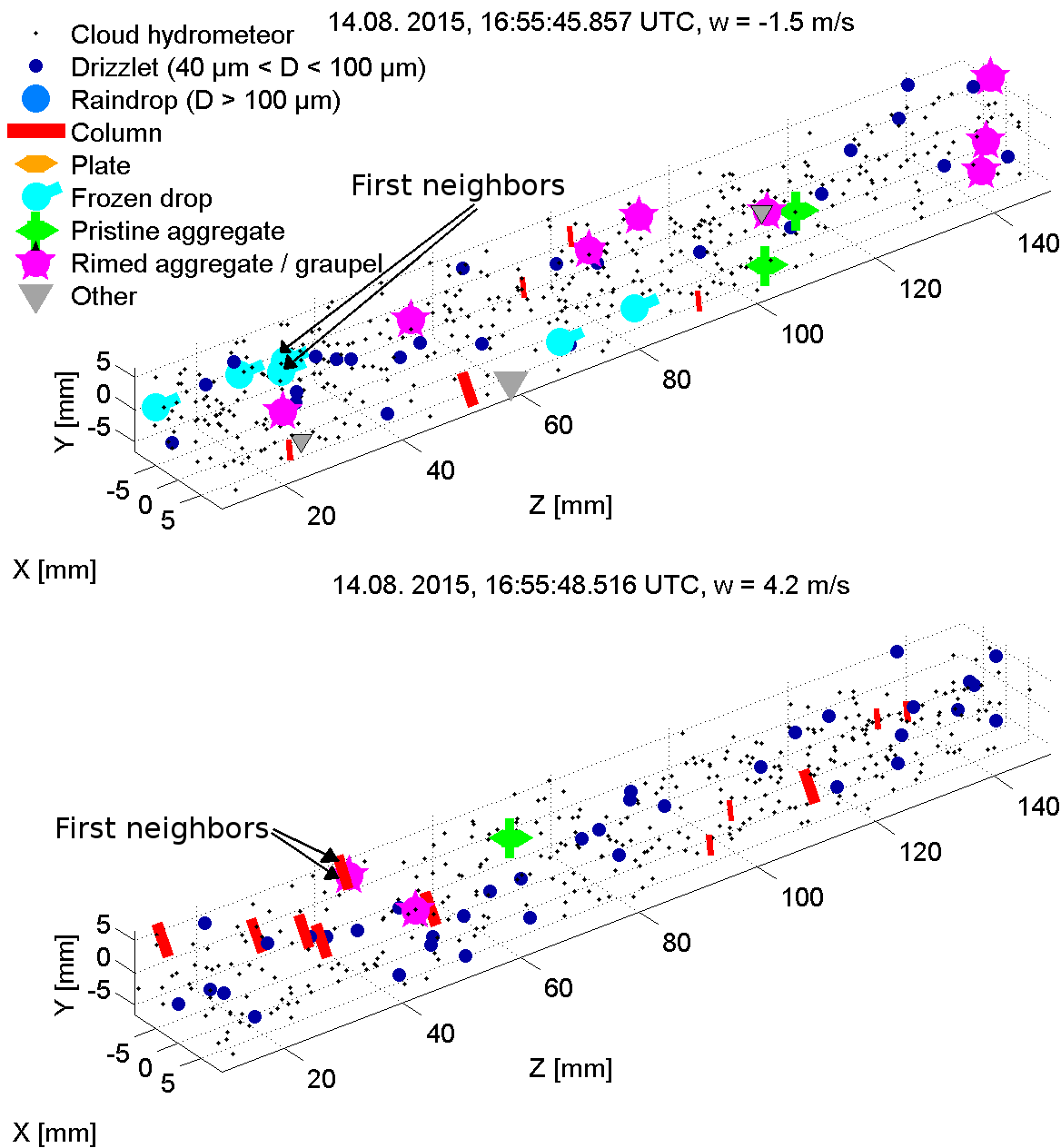


Fig. 7.6: Pseudo-3D display of frozen hydrometeors and cloud droplets, drizzlets and raindrops in two holograms from Pass 4 with two ice particles being neighbors of each other. The habits are expressed in different symbols and colors (see legend). The term "cloud hydrometeor" means spherical objects which are smaller than 40 microns. Other hydrometeor classes are explained in the legend. Vertical velocity and time of measurement are displayed in the title. Black arrows mark two ice particles being first neighbors of each other.

There is another example from Pass 6 where the number of ice crystals being neighbors of ice crystals was two or more in three holograms. Two of them are shown in Fig. 7.7. The examples from Pass 6 contain a large number of columns and are found in strong updrafts.

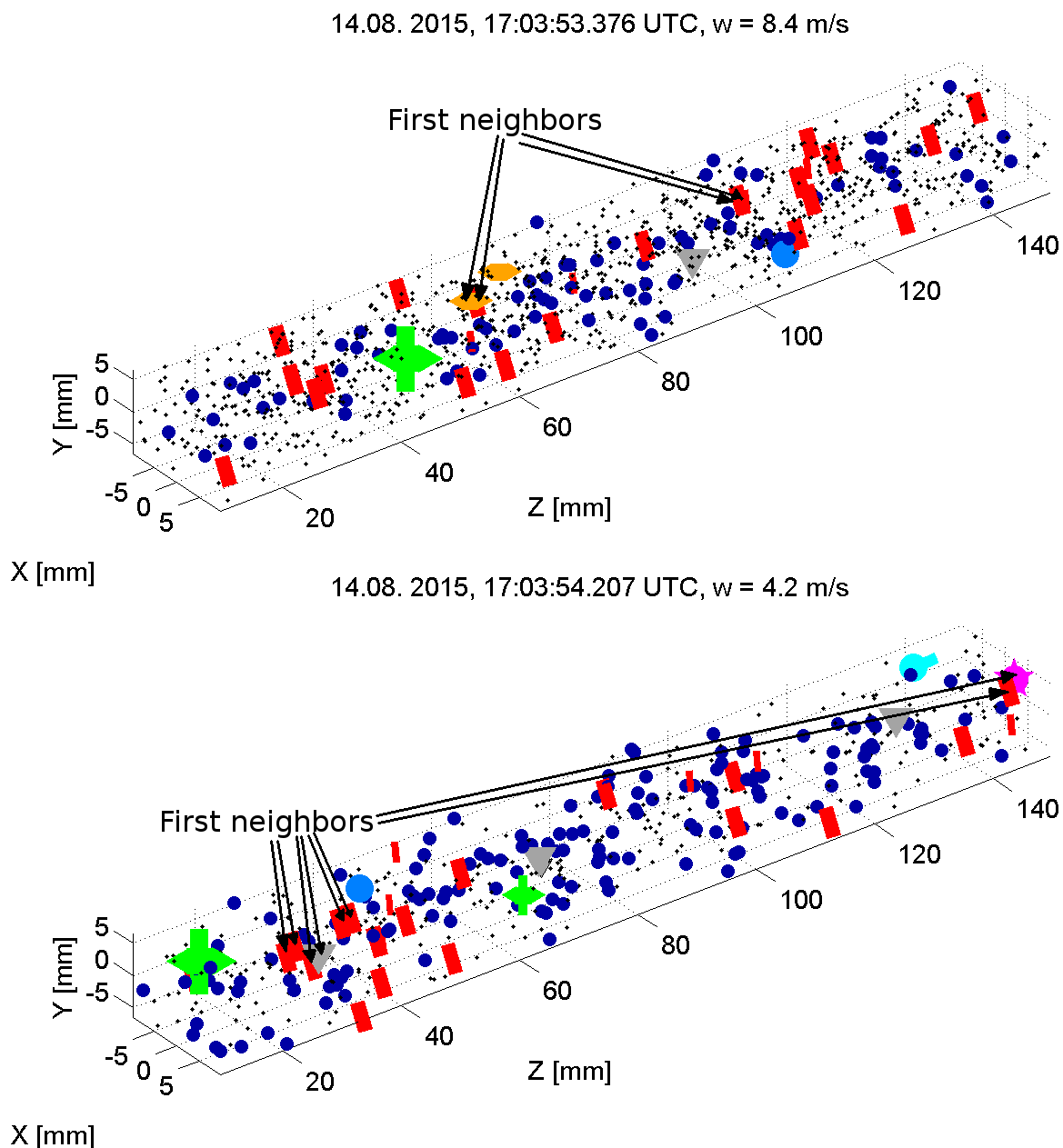


Fig. 7.7: As in Fig. 7.6 for two examples from Pass 6. Here, the number of drizzlets is considerably higher and the total number of ice particles is also larger.

One mechanism that is capable of creating a localized enhancement of ice is a gradient in terminal velocity of the particular ice crystal population. The very large graupel tend

to fall, even in strong updrafts, while the columns and small particles are transported upwards (see Appendix F.4). Due to the very low number of events, it seems plausible that the high local concentration of ice was an instant observation of a dynamical effect just at the right time.

Compared to the total number of holograms containing at least two ice particles and two droplets, the number of holograms with an observed clustering of ice particles is fairly small. Thus, the observed frequencies of holograms with ice particle clustering are 2/50 for Pass 4, 4/64 for Pass 6, 1/32 for Pass 7 and 2/13 for Pass 8. That means, the fraction of holograms with a local clustering of ice is between 4 and 6 % in Pass 4 and 6 (in the Hallett-Mossop) zone and between 3 and 15 % in the rapid glaciation region. In two cases, ice particles with ice as first and second neighbor can be found in Pass 6, but these holograms contained almost the same number of ice particles and droplets. The interesting cases are clusters of ice crystals surrounded by mainly droplets rather than ice crystals in the hologram. However, none of such clusters was found in Flight B926. The overall number of holograms in the examined cloud passes is too low to yield a statistical significance of the observed ice particle clustering. In addition, the observed "ice pockets" did rarely consist of more than two ice particles. The effect of shading as a possible influence on the results was analyzed in Chapter 5 and it is likely that shading did not have a substantial influence here. With the results from this investigation, the hypothesis from Korolev and Isaac (2006) that ice and droplets are on average well-mixed on small scales cannot be rejected.

7.5 Connections between dynamics and microphysics

A correlation analysis was performed between dynamical and microphysical quantities. All cloud passes have been checked in terms of correlation between the F values from the Fishing test at a cube length of $a = 10$ mm. Independent from the number of ice particles, the correlation was positive but very weak (typical values of the correlation coefficient were around 0.1).

However, a strong signal in correlation was found for particle number concentration as well as ice particle concentration with vertical velocity. An overview of the correlation coefficients of different parameters tested is shown in Table 7.3. A notable trend in the correlation between updraft velocity and cloud microphysical properties, an increasing trend of the correlation between w and LWC is seen with virtually no correlation in the all-liquid part of the cloud and higher correlation towards glaciation. In contrast to the LWC , IWC is almost uncorrelated with w for any cloud pass. The small correlation between IWC and w suggests that there are no preferred locations for the large ice particles within the cloud. The story is different when the number concentrations are examined. All cloud passes, except for Pass 3, have a correlation coefficient between N and w that is greater than 0.4. A similar observation is made for the number of ice crystals per hologram. The correlation between N_{ice} and w is maximized in Pass 6 and 4

and decreases towards higher IWC/TWC ratios and also towards lower IWC/TWC ratios. When considering the temperature, the maximum correlation is observed between -8°C -14°C , which suggests that the splinters that are likely produced by the Hallett-Mossop process could be important contributors to this enhanced correlation. A look at the table of particle habits (Table 7.4) confirms that the maximum correlation between w and N_{ice} is found where the number of columns was highest. When the correlation coefficients between w and $N_{columns}$ are inspected, there is a notable decrease from Pass 4 (0.619) towards Pass 8 (0.027), which suggests that the contribution from dynamics towards high local concentrations of columns weakens with decreasing temperature and increasing mean particle size.

Table 7.3: Hydrometeor number and mass concentration for the cloud passes with data from HALOHolo. $R(X, Y)$ denotes the cross correlation of the two samples X and Y .

Pass	$R(LWC, w)$	$R(IWC, w)$	$R(TWC, w)$	$R(N, w)$	$R(N_{ice}, w)$	$R(F_{10mm}, w)$
1	0.093	0.107	0.093	0.404	0.165	0.023
3	0.158	0.247	0.162	0.272	0.321	0.139
4	0.227	0.018	0.111	0.476	0.475	0.016
6	0.527	0.165	0.416	0.558	0.512	0.202
7	0.388	0.019	0.150	0.576	0.411	0.212
8	0.445	0.111	0.114	0.446	0.111	0.033

Table 7.4: Habit fractions from particle habit classification of the same cloud passes as in Table 7.3. Displayed are spheroids greater than 40 microns (sph), columns (col), plates (plt), frozen drops (FD), irregular particles (irr), rimed aggregates (RA) and pristine aggregates (PA).

Pass	sph	col	plt	FD	irr	RA	PA
1	10896	6	0	0	11	0	4
3	2973	2	2	0	3	1	1
4	6398	395	9	52	57	73	48
6	4644	374	17	88	26	109	45
7	1234	164	20	35	22	145	56
8	16	75	110	10	98	109	455

As already seen from the particle images in Appendix F.5, Fig. F.9, there seems to be a coincidence between columns and rimed aggregates / frozen drops, which tends to occur more frequently in strong updrafts (see Fig. F.13). The correlation coefficients of the number of particles per hologram of each habit reflect this observation. A generally enhanced correlation is found between columns and rimed aggregates in Pass 4, 6 and

7 (correlation coefficients between 0.356 and 0.537), columns and pristine aggregates for the same cloud passes (correlation coefficients between 0.332 and 0.625, monotonically increasing with decreasing temperature) and columns with rimed aggregates and frozen drops together (correlation coefficients between 0.400 and 0.527). The overall correlation between columns and frozen drops / rimed aggregates points towards a physical connection between them (raindrop fragmentation and / or rime-splintering) while the correlation between pristine aggregates and columns is likely just a coincidence without a direct interaction. There were no fragmented aggregates found, which would fit together with the columns. With the highest correlation between number of columns and vertical velocity (0.619) and a high correlation between number of columns and rimed aggregates (0.451), Pass 4 is selected for a detailed investigation of the Hallett-Mossop process.

7.6 Investigating the local environment of rimers and splinters in the Hallett-Mossop zone

After inspecting the particle images from individual holograms by eye, an attempt was made to find possibly matching columns and rimed particles / frozen drops, which are not too far away from each other and have a physically plausible displacement. The criteria which were tested were:

- The width of the column must be smaller than or equal the width of the source candidate
- The column must be displaced in positive vertical direction relative to the source candidate (as the source candidate is larger and has a higher terminal velocity)
- The candidate should not be another column
- The maximum distance between the two particles should not be larger than the detector height $N_y dy$

After applying these criteria, there was one candidate hologram found in Pass 4. This hologram contained one frozen drop and two columns in close vicinity to it. However, none of the columns would fit exactly to the spicule on the frozen drop. Pass 6 did not contain any possible candidate, nor Pass 7 did. Thus, a direct in-situ confirmation of columns breaking off from rimed hydrometeors cannot be drawn from the data. However, there are many holograms with a coincidence of rimed particles and columns. Also from the viewpoint of dynamics, a relationship between columns and rimed aggregates is evident. Both habits tend to occur together, preferably in strong updrafts (see Fig. F.13 in Appendix F.5). An example from Pass 4 is shown in Fig. 7.8. The statistical coincidence of columns and rimed particles is proven but it needs more to confirm that the underlying process is really the rime-splintering after Hallett and Mossop (1974).

If a direct confirmation is not possible, there are several ways to infer the presence of the Hallett-Mossop process indirectly. The first evidence shown in this chapter is the enormous discrepancy (factor 10^2 to 10^3) between the estimated number of ice nuclei and

the number of measured ice crystals per liter. Secondly, the ambient temperature was at -8°C , which is still within the range where Hallett-Mossop is active. Third, the two major ice particle classes in Pass 4 and 6 were columns and rimed aggregates / frozen drops.

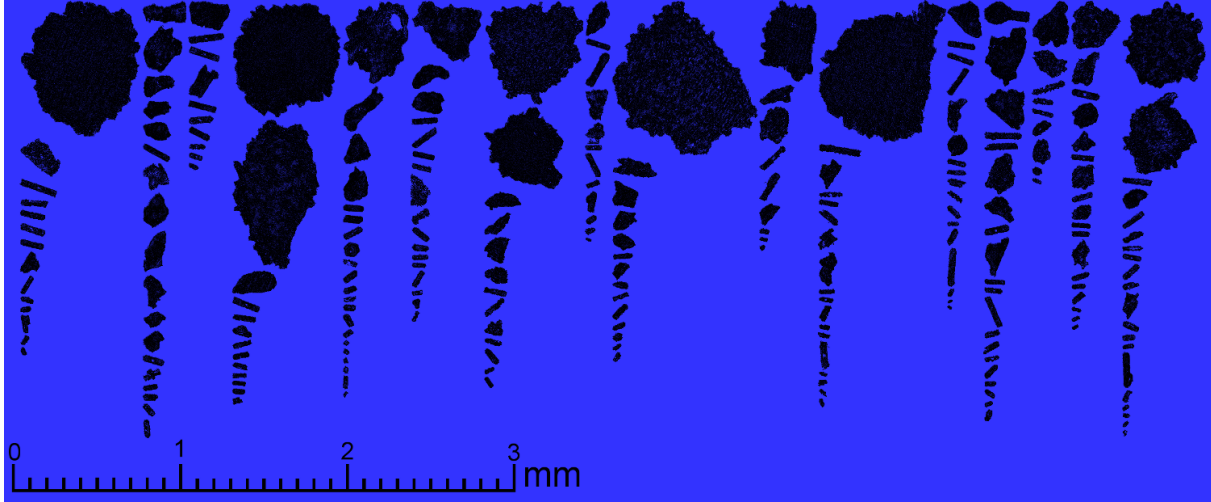


Fig. 7.8: Ice particle images from an excerpt of Pass 4. The particles which are stacked belong to the same hologram. The order in which the particles from the same hologram appear is from sorting the particles by their x size.

As the rimed particles and also the frozen drops often have small protuberances on their outer shell, a sample of 111 particles with visible protuberances from Pass 4 has been analyzed and the width of the spicules on the surface was measured. From the total number of spicules from all the particles of Pass 4, the spicule width distribution was obtained and compared with the distribution of the column width and the column length. This intercomparison is shown in Fig. 7.9 and reveals a reasonable agreement between column width and spicule width. The median spicule width ($31.86\ \mu\text{m}$) is in reasonable agreement with the median column width ($32.82\ \mu\text{m}$) and close to the droplet mean volume diameter ($30.06\ \mu\text{m}$). If the spicules and the columns have nearly the same distribution of width, the conditions where these particle grew were approximately the same. In addition, some of the spicules look very fragile and could easily break off from the rimed particle or frozen drop. Some of the holograms contain columns with a broken-off tip while the other tip seems to be vapor-grown. The number of spicules per particle N_{sp} is strongly correlated with particle size ($R(N_{sp}, D) = 0.759$) and a linear least-squares fit was performed to estimate the number of spicules on the projected area as a function of particle diameter. It needs to be mentioned that only two of three dimensions of the particle are visible and therefore the spicules in the third dimension are hidden. For the linear fit, the three smallest and three largest values of D were ignored in order to reduce the weight of the extreme values, which yields reasonably well results ($r^2 = 0.758$, $RMSE = 1.36$). From the fitted number of spicules as a function of particle size, it

is possible to estimate the approximate number of splinters that are generated by a rimed particle of the given diameter. To account for the not visible third dimension, it should be adequate to substitute $\tilde{D} = D^2$ for D in the fitted number of spicules per particle to transform the equation from the particle perimeter to the total surface area. From this local examination of the rimed ice particles, the "sources" and "sinks" are still missing to describe ice multiplication via breaking-off columns quantitatively, which are basically the number of spicules that break off per unit time and the growth rate of new spicules in the same time.

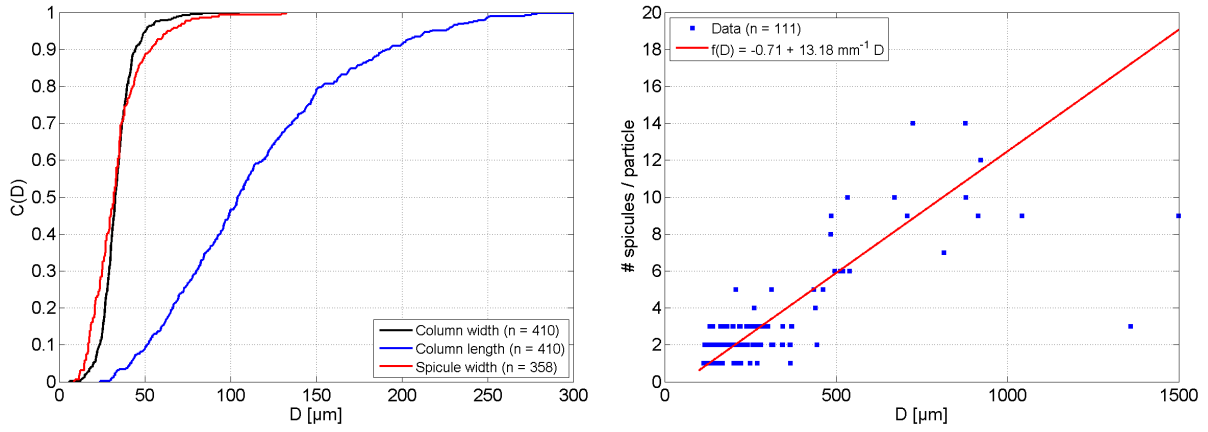


Fig. 7.9: Left: Cumulative distribution of the width and length of columns (black and blue curve) and the width of spicules on the surface of frozen drops or rimed aggregates (red). Right: Number of spicules as a function of particle size for frozen drops and rimed aggregates. The red line represents a linear least-squares fit of the data truncated by the three smallest and three largest values of D in the sample. The data were obtained from Pass 4 of Flight B926.

By using a modified version of the fit equation (Eq. 7.2), the number concentration of spicules N_{sp} has been estimated from the diameter of the n_{rimers} rimed particles (D_{rimer}). The square brackets indicate that the individual value was rounded to whole digits. For Pass 4, a value of $N_{sp} = 612 \text{ L}^{-1}$ has been calculated. Compared with the number concentration of rimed aggregates and frozen drops ($N_{rimers} = 32.7 \text{ L}^{-1}$), the estimated concentration of spicules is by a factor of 19 larger. The number concentration of columns was $N_{columns} = 95.7 \text{ L}^{-1}$ for Pass 4, which is by a factor of 6.4 smaller than the estimated number of spicules. Thus, the presence of spicules could explain the number of observed columns solely by breaking off of approximately 15 % of the spicules. If the same fit function from Pass 4 is also used for Pass 6, the numbers are relatively similar ($N_{sp} = 525 \text{ L}^{-1}$, $N_{rimers} = 45.1 \text{ L}^{-1}$, $N_{columns} = 78.7 \text{ L}^{-1}$).

Here, the spicules were defined as elevated regions on the particle surface which have a columnar shape and are at least two pixels high. Half-spherical shapes were excluded from this definition. Further studies should try to determine less liberal constraints and should use a more quantitative definition of the spicules to estimate the importance of

the Hallett-Mossop process versus other mechanisms in terms of generating secondary ice particles. As no in-situ splintering event was found in the data, the mechanism of tiny ice splinters being released during the process of riming described in Hallett and Mossop (1974) is much more likely to occur than the break-off of larger vapor-grown columnar protuberances on the outer shell of rimed hydrometeors.

$$N_{sp}(D_{rimer}) = \frac{1}{SV} \sum_{j=1}^{n_{rimers}} \max \left([(-0.71 + 13.18\text{mm}^{-1}D_{rimer,j})^2], 0 \right) \quad (7.2)$$

7.7 Discussion and summary

A convective cloud has been measured in nine subsequent cloud passes where six of them had usable data from HALOHolo. The bulk microphysical properties in the process of glaciation have been studied. During the glaciation process, the liquid water content gradually decreased while the ice water content increased. The increase in IWC had its maximum between -6°C and -8°C as the number concentration of ice particles increased by a factor of 10. A comparison of the observed ice crystal number concentration and the estimated number of ice nuclei after the parameterization of DeMott et al. (2010) revealed the presence of secondary ice production throughout the entire series of cloud passes. The discrepancy between ice nuclei and ice crystals stayed between a factor of 100 and a factor of 1000. In this cloud, there were two cloud passes (in the Hallett-Mossop zone) where the partitioning between ice and liquid water mass was almost equal ($\text{IWC}/\text{TWC} \approx 40\%$). At higher temperature, the IWC/TWC ratio was below 1% and at temperatures below -13°C the IWC/TWC ratio was above 75%. Thus, even in a developing convective cloud, the occurrence of almost equal ice to liquid water partitioning seems to be constrained to a rather narrow range of temperatures ($-14^\circ\text{C} \leq T \leq -6^\circ\text{C}$).

Afterwards, the connections between dynamics and microphysics were analyzed via correlation tests between dynamical variables and microphysical properties. Strongest was the correlation between the number concentration of droplets and vertical velocity but some cloud passes had an even higher correlation between the number concentration of columnar ice crystals and vertical velocity. This connection between enhanced number concentrations of some ice crystals and vertical velocity might be connected with the most likely secondary ice production mechanism in this cloud, which is the rime-splintering after Hallett and Mossop (1974). In laboratory studies, a velocity optimum around $2 - 3\text{ms}^{-1}$ was found to produce the highest number of splinters. However, the median vertical velocity of most cloud passes was in a range where large graupels could still reach lower altitudes while the smaller ice particles are carried further upwards.

This difference in terminal velocity could also explain the occasional observation of holograms with a more dense clustering of ice particles than expected from a uniform random distribution. The hypothesis of spatial homogeneity on scales smaller than 15 cm by Korolev and Isaac (2006) has been investigated from cloud passes 4, 6 and 7 of Flight B926

and could be confirmed within the statistical uncertainty of the measurements. The number of holograms which deviated from a uniform random distribution between droplets and ice crystals was below the statistical uncertainty given by the total number of holograms. An analysis of the results from the neighbor distance distributions and a Fishing test could show that the majority of holograms had a spatial distribution of particles which did not deviate significantly from a uniform random distribution. Detectability effects were taken into account by using only $2/3$ of the lateral range in x and y direction and by excluding the laser and camera window region in z . For the Fishing test, only the subvolumes along the hologram center $(x, y) = (0, 0)$ were used.

A direct proof of the Hallett-Mossop process via finding a hologram containing a rimed particle and several columns in close vicinity with a dynamically plausible orientation in the sample volume did not succeed. However, in many holograms, rimed aggregates or frozen drops and columns were present simultaneously, sometimes the number of columns exceeded 20 per hologram. In terms of the Hallett-Mossop process as a pathway to produce secondary ice, a connection between the mean column width and the mean width of spicules on frozen drops or rimed aggregates has been established. Furthermore, a reasonable linear relationship was found between the number of spicules on the particle perimeter as a function of particle diameter, which might argue for an additional ice multiplication process. This equation has been projected on the entire particle surface area and an estimate of the spicule concentration was calculated. From the calculated spicule concentration, it would be sufficient to explain the presence of the total number of columns if only 15 % of the spicules really broke off and formed small ice splinters. However, no in-situ splintering event could be detected in the examined data set of Flight B926. From laboratory experiments in a Paul trap (M. Weitzel 2016, to be published), similar to those of Leisner et al. (2014), the number of ejected particles could not be determined reliably with reasonable counting statistics. A possible future experiment, maybe performed in the Mainz vertical wind tunnel, should look at the size and number of ejected fragments from a riming graupel which is held at $T \approx -10$ °C and surrounded by droplets with approx. $30 \mu\text{m}$ of mean volume diameter at number concentrations around 50cm^{-3} . In addition, the number of spicules could be counted in all three dimensions to constrain the findings from the linear fit to the number of spicules vs. particle size on the projected perimeter.

**Observation of mesoscale and microscale structures in
ice clouds: The role of dynamics and microphysics**

8.1 Introduction

According to the World Meteorological Organization, cirrus clouds are defined as "detached clouds in the form of white, delicate filaments or white or mostly white patches or narrow bands". A "fibrous appearance or a silky sheen" is associated with these clouds which are "composed almost exclusively of ice crystals" (WMO, 2017). Cirrus clouds belong to the high clouds with a minimum height of 3 km in the polar regions and 6 km in the tropics, which separates cirrus clouds from other ice clouds, e.g. ice fog.

Three basic pathways of cirrus cloud formation are described in Voigt et al. (2017) and Krämer et al. (2016), each of them requires the existence of an ice-supersaturated layer (Krämer et al., 2009): (1) In-situ cirrus cloud formation via heterogeneous or homogeneous freezing¹⁸ in an ice supersaturated region, (2) Liquid-origin cirrus cloud formation via lifting of an air mass containing supercooled liquid water up to the cirrus temperature range where the droplets freeze heterogeneously or homogeneously, and (3) cirrus from aircraft condensation trails (contrail cirrus), where the ice crystals are produced by freezing of binary solution droplets consisting of water and sulfuric acid ($\text{H}_2\text{SO}_4/\text{H}_2\text{O}$) originating from the exhaust plume of an aircraft engine. The microphysical properties are fairly distinct between the three: Contrail cirrus has a pronounced maximum in the size distribution at small particle diameters (5 to 30 μm) and a much narrower size distribution than the two other (Voigt et al., 2017). Liquid-origin cirrus does also have a maximum at small sizes but often the size distribution is bimodal with a secondary mode around 200 μm which contributes significantly to the total number and IWC. In contrast to the liquid-origin cirrus, in-situ cirrus tends to appear monomodal (cf. Voigt et al. (2017), Fig. 7). The fact that contrail cirrus is well distinguishable from natural cirrus, even at an age of several hours, is likely due to the concurrent water vapor deposition on many small ice crystals, which reduces the individual particle growth rate and keeps the size distribution narrow.

The occurrence of secondary or tertiary modes¹⁹ in the particle size distributions has been documented in numerous studies of ice clouds, but only few investigations have been attempted to determine the physical process and its magnitude responsible for this effect. The presence of secondary size modes is often indicative of mesoscale²⁰ structures in an extended cloud deck. From the recent state of knowledge, four main dynamical effects may produce secondary size modes:

¹⁸The term "homogeneous freezing" means that no additional ice nucleus is needed for the phase transition from the (supercooled) liquid phase to the solid phase. "Heterogeneous freezing" takes place if an ice nucleus is responsible for the phase transition from the liquid phase or gas phase to the solid phase.

¹⁹Usually, the "main mode" of the particle size distribution in ice clouds is somewhere between 30 μm and 100 μm . Additional modes can appear as small mode (nucleation or sublimation mode, typically around 30 μm of particle diameter or smaller) or as large mode (aggregation or precipitation mode, particle diameter typically well above 100 μm).

²⁰"Mesoscale", according to Lin (2007), refers to spatial scales smaller than 2000 km and typically larger than 2 km.

- Mixing between cloudy air and cloud-free air or mixing between two different clouds due to various dynamical effects (e.g. wave breaking, mesoscale eddies), similar to the observations in Chapter 6 of this work
- Sedimentation of particles from cloud segments at higher altitude through either ice-subsaturated or ice-supersaturated layers (Lüttmer, 2017)
- Shallow convection in potentially unstable layers in the upper troposphere, often together with either sedimentation or mixing (Spichtinger, 2014)
- Freezing of cloud droplets in ascending (stratiform) mixed-phase clouds (liquid-origin cirrus after Krämer et al. (2016)), often observed in warm conveyor belts

To illustrate the underlying dynamical effects, a set of cloud photos, shown in Fig. 8.1, depicts cloud structures resulting from mixing, sedimentation and shallow convection. It needs to be mentioned that mixing and sedimentation are not strictly independent from each other. Most often, both processes occur together. Example 1 of Fig. 8.1 in the upper left corner shows the effect of wave breaking in undulating cirrocumulus. While some of the wave structures have one concentrated region with high optical thickness, other elements show two distinct regions of enhanced optical thickness and a transition region in between. The overturning circulation, which is sometimes present in these wave structures, leads to mixing between adjacent horizontal cloud segments or mixing between cloud base and cloud top region within one cloud segment.

Another case of wave cirrus is shown in Fig. 8.1 top right where no wave breaking is evident but the horizontally aligned cloud segments develop turrets which are indicative of shallow convection (i.e. the *castellanus* subtype of cirrus or cirrocumulus). Here, the driver for mixing within individual cloud segments is most likely the convection. Similar structures are frequently observed in long-lasting contrails.

The third example in Fig. 8.1 (bottom left) shows another case of shallow convection where mixing between different clouds probably occurred. In addition, the cirrus clouds are present at different levels and can influence each other via upward transport of nucleated ice crystals by convection or downward transport of larger ice crystals by sedimentation. In the last example (bottom right of Fig. 8.1), a large eddy ($L \approx 2\text{ km}$) stirs a fibrous cirrus cloud in the horizontal.

The effect of droplet freezing during the ascent of a mixed-phase cloud is usually not visible to an observer and acts within small volumes of the cloud. A fast realization of the droplet freezing process is the development of the anvil cloud in the transition from cumulus to cumulonimbus (see Fig. 7.1 in Chapter 7). However, anvil cirrus is most often treated as a different cirrus subtype and not as the "classic" liquid-origin cirrus.



Fig. 8.1: Examples of natural cirrus clouds that may contain bimodal size distributions. Shown are wave cirrus (cirrocumulus stratiformis undulatus) with wave breaking visible in the lower third of the first image (top left), a combination of wave structures and shallow convection in cirrocumulus castellanus undulatus (top right), another example of shallow convection in cirrocumulus floccus (bottom left), and mixing due to large eddies in cirrus fibratus (bottom right). Each of the underlying mesoscale processes is capable of producing a secondary mode in the particle size distribution. Photos taken from private collection of O. Schlenzcek.

After the dynamical effects have been discussed, the microphysical consequences need to be studied. In particular, the ice crystal habit of the primary and secondary size mode play a role as the particle habit provides at least some information about the particle origin. The habit distribution diagram in Bailey and Hallett (2009) shows zones where columnar

growth is preferred ($T < -35^\circ\text{C}$, $RH_i > 110\%$) and others where the particles rather tend to form plates. Below an ice supersaturation of about 10 %, it is hardly possible to estimate the temperature of the initial particle growth from the observed habit species as the dominant habit class is short columns with little variation in shape or aspect ratio (Bailey and Hallett, 2009).

A very unique habit class which is rarely observed in other clouds than cirrus is the *bullet rosette*, which can be seen as an aggregate of columns originating from a common center. The formation of bullet rosettes requires low temperatures (typically around -50°C) and sufficient ice supersaturation. An activated ice nucleus develops several active *c*-axes from which columnar growth is initiated. Most bullet rosettes are several hundred microns long and belong to the rather "old" ice particles as they require the longest time to grow in comparison with other habit types. The presence of bullet rosettes as a secondary mode in the size distribution is most often indicative of fall streaks from further above entering the sampled region.

Another habit type which often contains useful information in terms of determining its origin is the *sideplane aggregate*. These particles grow in the plate regime and are of similar size as bullet rosettes. The presence or absence of sideplane aggregates among bullet rosettes and other particles helps to draw a limit in terms of temperature where the particles grew.

Very small columns or plates are often classified as either Irregular or Spheroids due to the difficulty of distinguishing between a sphere and a small hexagon. This issue is discussed in Korolev et al. (2017) and in Subsection 4.2.1 of this work.

8.2 Data and methodology

During the field phase of the Cold-air Outbreak and sub-Millimetre Ice Cloud Study (COSMICS), which took place in Prestwick, Scotland in March 2015, a similar set of instruments as in ICE-D (see Chapter 7) was used aboard the BAe-146 aircraft from FAAM. Instead of the five-hole turbulence probe used in ICE-D, an Aircraft-Integrated Meteorological Measurement System (AIMMS) turbulence probe provided data of horizontal and vertical wind at an acquisition rate of 20 Hz and an accuracy of $\pm 0.75 \text{ ms}^{-1}$ ²¹. For the other instruments, the same time resolution and accuracy is valid as described in Chapter 7 for ICE-D.

A detailed intercomparison was done for all the instruments which measure water vapor or total water content. Under the assumption that the relative humidity from the chilled mirror should on average be close to the average of the AIMMS relative humidity and the relative humidity from the evaporator instrument, the "dewpoint" in the data files of Flight B889, B890 and B895 was considered to be the frostpoint instead. To dampen artificial over- and underestimations of the dewpoint from the duty cycle of the chilled

²¹In the description of the AIMMS set of instrument, there is no distinction made for the errors of the horizontal and the vertical wind speed.

mirror, the moisture data were filtered using a 150 s running average. An intercomparison with data from dropsondes for Flight B895 confirmed that the General Eastern hygrometer measured the frostpoint, not the dewpoint.

The particle size distributions of HALOHolo were fitted using a multimodal log-normal distribution, which is defined in Eq. 8.1. D_0 is the normalization diameter (usually 1 μm) to make the exponential unitless, and $n = 1, 2, \dots$ is the number of modes to include. The obtained fit parameters are the number concentration N_i , the mean particle diameter D_i and the geometric standard deviation σ_i . As already mentioned in Chapter 2, \log means the decadal logarithm and \ln means the natural logarithm.

$$\frac{dN}{d \log D} = \sum_{i=1}^n \left(\frac{N_i}{\sqrt{2\pi} \log(\sigma_i)} \exp \left(-\frac{(\log(D/D_0) - \log(D_i/D_0))^2}{2(\log(\sigma_i))^2} \right) \right) \quad (8.1)$$

When applying nonlinear least-squares fits, the number of modes should not be higher than 1/3 of the number of bins in the size distribution with non-zero counts, and the law of parsimony should be applied. However, it might be useful to fit a bimodal or even a trimodal log-normal distribution to a data set showing only one mode if the particular mode is very broad or otherwise deviating from a log-normal distribution. In that particular situation, the observed size distribution is explained by a superposition of up to three log-normal distributions. A rule of thumb, which is applied here, is that an additional mode is only considered to be valid if the goodness of fit measures (RMSE, r^2) show a substantial improvement after adding another mode. In particular, the new RMSE should be at least 10 % less than the previous RMSE, and fits with a coefficient of determination (r^2) below 0.5 should not be accepted.

Three cloud flights during COSMICS are discussed in this chapter: The first one was Flight B889 on 05 March 2015 where the jet stream region along a cold front was sampled. The cirrus clouds observed in this particular region looked like wave cirrus (see Appendix G, Fig. G.1 left). This cloud pass was characterized by in-cloud periods on a length scale between 3 and 30 km at constant altitude below the tropopause at $T \approx -52^\circ\text{C}$ and $p \approx 290$ hPa.

A contrasting case which was measured on the next flight B890 on 06 March 2015 targeted a deep stratiform cloud layer with cirrus clouds at the top. This cloud system was supposedly associated with a warm conveyor belt (WCB) and both profile flights as well as flight legs at constant altitude (so-called "runs") were performed (see Appendix G, Fig. G.1 right). In the beginning of the flight, a short cloud segment probably containing supercooled cloud droplets was encountered. The center part of the flight at a pressure of 300 hPa contained much fewer bullet rosettes in comparison with Flight B889 and some of the aggregates found in Flight B890 are possibly rimed.

Flight B895 on 13 March 2015 consists of a descending staircase pattern in a warm front cirrus that likely formed in-situ ahead of the front. A bimodal size distribution was encountered during the descent while the total appearance of the size distribution was rather monomodal with an increasing trend in both mean particle diameter and

distribution width towards lower altitudes. This is a typical example for sedimentation in a close to ice-saturated environment where sedimentation is important and particles are hardly influenced by sublimation. An overview of the individual cloud events in Flight B889, B890 and B895 is given in Table G.1 to G.3 in Appendix G.2.

Occasionally, the *potential temperature* θ is used as a vertical coordinate to compare cloud properties from different flights and / or different regions. θ is defined as the temperature a parcel of air would have if it was adiabatically brought to an ambient pressure of $p = 1000$ hPa (Liljequist and Cehak (1984), Eq. 9.29). In a stably stratified atmosphere, θ increases with increasing altitude. The tropopause in the polar regions and mid latitudes is often found at $\theta \approx 320$ K. In the tropics and subtropics, the tropopause is located around $\theta = 380$ K.

To determine the stability of an atmospheric layer, the *equivalent potential temperature* θ_e is used. As θ is conserved for (dry) adiabatic processes, θ_e is conserved for *moist adiabatic* processes. A vertical gradient of θ_e below zero is indicative of potential instability (Liljequist and Cehak, 1984).

8.3 Mesoscale and microscale structures in wave cirrus during COSMICS Flight B889

During the passage of several cirrus clouds with a length scale of typically no more than 30 km, four cloud events with at least partly bimodal size distributions were identified. Via hologram by hologram inspection of each particle ensemble, the structure of the bimodal segments was examined and presented in Fig. 8.2. The first bimodal event was Cloud 4 from the definition used in Fig. G.9 in Appendix G and had a mode separation diameter of approx. $35 \mu\text{m}$ and a spatial structure that was clearly discernible from a spatially uniform cloud. Starting with particle sizes around $100 \mu\text{m}$, the particle size gradually decreased along the cloud pass and increased again after the middle of the cloud pass. In the second half of this cloud pass, a mixture of particles smaller than $35 \mu\text{m}$ and larger than $35 \mu\text{m}$ is found, with 15 holograms containing at least one particle from both modes. This particular cloud structure was relatively persistent as the contiguous number of holograms with particles in both modes was 4, covering a spatial extension of $L = 120$ m. The small mode consists mostly of particles classified as "Spheroids", which are most likely *droxtals* as described in Ström et al. (1997) or small columns / plates. From the overall structure, the occurrence of this secondary mode might be due to wave breaking, but from the dynamical perspective it is hard to prove this hypothesis. Just at the location where the secondary mode appears to be most prominent, a relative downdraft was found in the time series data (Fig. 8.3 left), which was stronger than the surrounding descending motion. This feature is more a microscale than a mesoscale feature but its very distinct structure points towards a dynamical process that is likely different from just a randomly picked piece of a cirrus cloud segment with sedimentation. Unfortunately, there are no dropsonde data available from this flight.

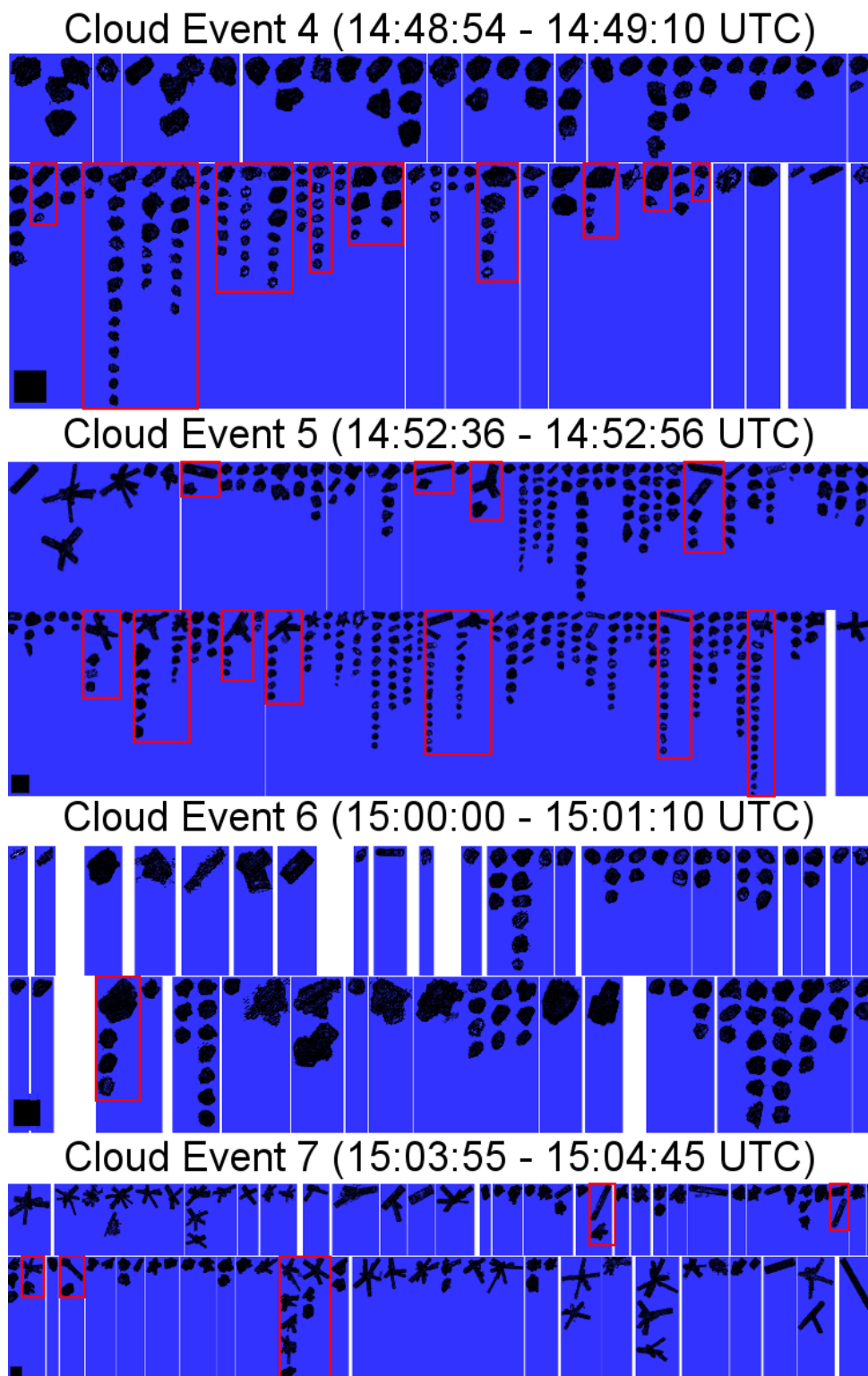


Fig. 8.2: Particle image gallery time series of Cloud Event 4, 5, 6 and 7 from Flight B899 on 05 March 2015. The time direction is from left to right, the thickness of the white lines is proportional to the number of empty holograms between two particle holograms. Particles occurring in the same hologram are vertically stacked. The black square in the bottom left of each image strip is 100 μm wide for size reference. A red frame marks events with simultaneous occurrence of particles in both modes of the size distribution. The selected segments contain 96 holograms (Cloud 4), 120 holograms (Cloud 5), 420 holograms (Cloud 6) and 280 holograms (Cloud 7).

Only the radiosounding from 5 March 2015 12:00 UTC at Castor Bay, Ireland²² (see Fig. G.2 left) could help to understand the thermodynamical conditions in the measurement region: A close inspection of the vertical profile of θ_e from the radiosonde reveals an unstable layer between $p = 300$ hPa and $p = 290$ hPa, which is close to the pressure of the measurement ($p = 288$ hPa). However, the decrease of θ_e with increasing altitude in this layer was only 0.1 K. In the same region, a very narrow zone with ice supersaturation was found. The wind measurements of the radiosonde showed a velocity around 34 m s^{-1} at the 300 hPa level, with a stronger jet streak (35.5 m s^{-1}) further above. The presence of high wind speeds together with wind shear and some potential instability would support the argument for wave breaking.

Another brief event with a bimodal size distribution was found in Cloud 6. From all selected bimodal events of Flight B889, this is the one with the lowest counting statistics (111 particles in total). Here, the mode separation diameter was around 90 microns and the cloud event started with a few small particles before only particles in the large mode appeared. Then, the small mode became dominant around the center part of the pass and one hologram appeared after a period with no particles where both modes appeared simultaneously. Though the size distribution of the entire cloud pass is bimodal, the particles of the two modes are not well-mixed. When comparing the one second combined particle size distributions in Fig. 8.3 right with the particle image gallery (third row of Fig. 8.2), it is obvious that the possible bimodal segment after the particular hologram is an artifact from averaging. The smaller and larger particles are almost perfectly separated from each other, so the following holograms contain either small or large particles but not particles from both modes.

Considering the dynamics of Cloud 6, it shows a completely different picture as Cloud 4. The occurrence of both modes was very close to the region with the strongest updraft ($w \approx 1.1 \text{ m s}^{-1}$) but there were no particles in the updraft center. The cloud events were located on the flanks of the updraft maximum with the small mode in the ascending branch and the small plus large mode in the descending branch. Right now, there is no conclusive explanation available for this separation of modes w.r.t. the mesoscale dynamics. It could be an effect from shallow convection, but that needs to be clarified with model simulations as done in Spichtinger (2014).

The third event of interest was Cloud 5 with a mode separation diameter of approx. $105 \mu\text{m}$. It covered a much longer distance than the other two cloud passes previously discussed, which was close to 30 km. When looking at the particle images in the second row of Fig. 8.2, it is apparent that larger particles mix with a persistent mode of smaller particles here. The occurrence of larger particles, either long columns or bullet rosettes, seems to be random as it cannot be attributed to a well-defined dynamical structure and the number of holograms in between two holograms with particles in both modes does

²²The radiosonde was launched approximately 3 hours before the flight and located about 150 km south and 100 km east of the center waypoint of the flight path.

not have a fixed period. A similar feature in comparison with Cloud 4 is the presence of the largest concentration of small particles in a stronger downdraft (see Fig. 8.4 left).

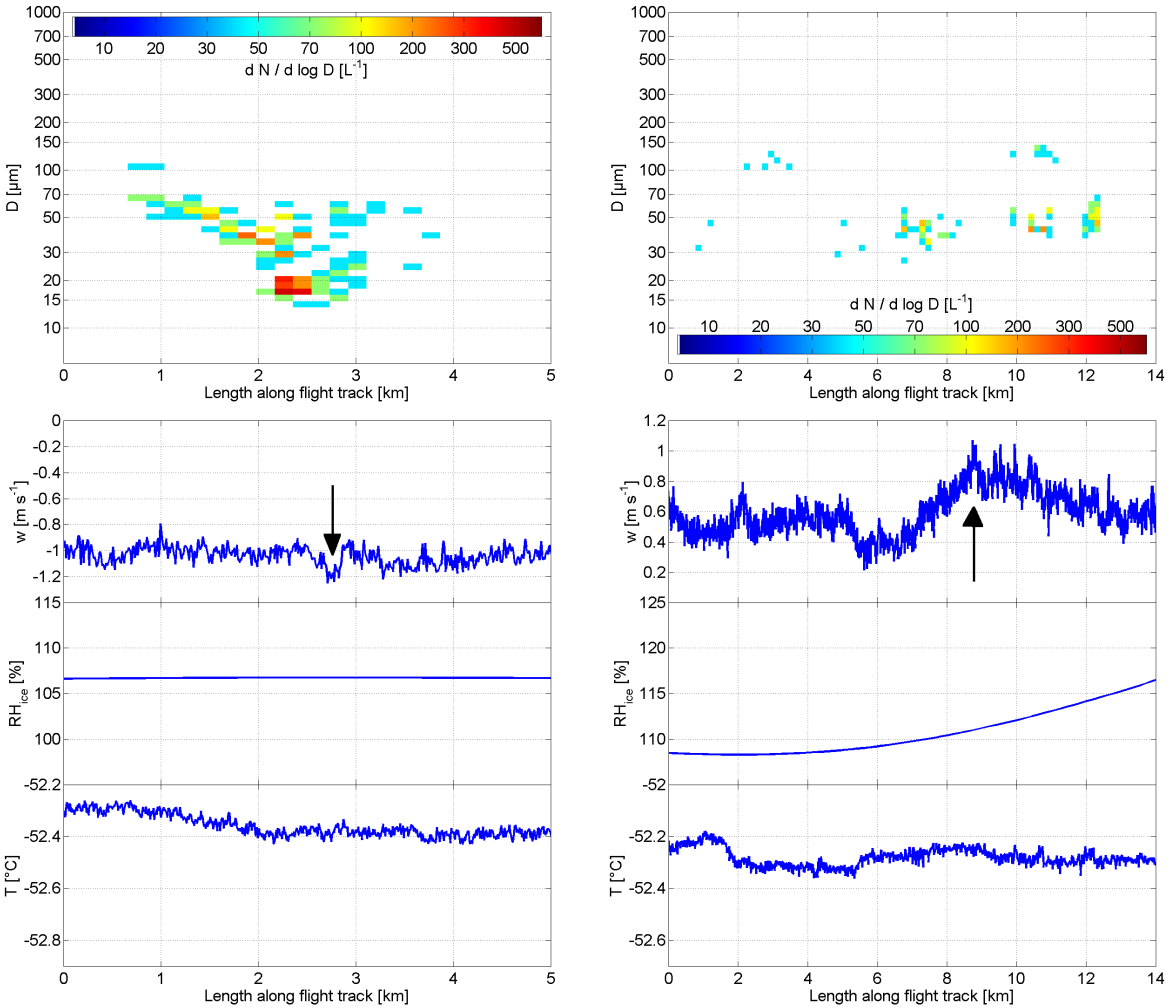


Fig. 8.3: One second combined particle size distributions (top row) and vertical velocity, relative humidity over ice and temperature as a function of distance along the flight path. The left case is Cloud 4 of Flight B889 on 05 March 2015 (14:48:50 - 14:49:14 UTC), the right case is Cloud 6 of Flight B889 (14:59:57 - 15:01:13 UTC). The regions of interest are marked with arrows.

As the flight was performed in a way that the aircraft returned after Cloud 6, the flight path through Cloud 7 targeted the same region as for Cloud 5, with a temporal displacement between 7:42 and 12:42 minutes. As calculated from the measured horizontal wind velocity, the cloud was displaced by advection by approximately 30 km in the meantime. Thus, it is likely that the microphysical conditions did not remain constant between the two subsequent cloud passes. In direct comparison with Cloud 5, the small mode between 20 and 50 μm is almost completely gone in Cloud 7. However, the bimodal feature of

larger particles possibly being seeded into a population of smaller particles could also be the case in Cloud 7 (see Fig. 8.4 right). Thus, the dynamical process involved in the secondary mode generation is likely the same in both cloud passes. Again, the majority of particles in the large mode are long columns and bullet rosettes. From this perspective, the idea of using habit-wise decomposition of the particle size distribution seems to be a useful tool for various cases of ice clouds. This assumption is tested on more complicated case studies of cirrus clouds in the following section.

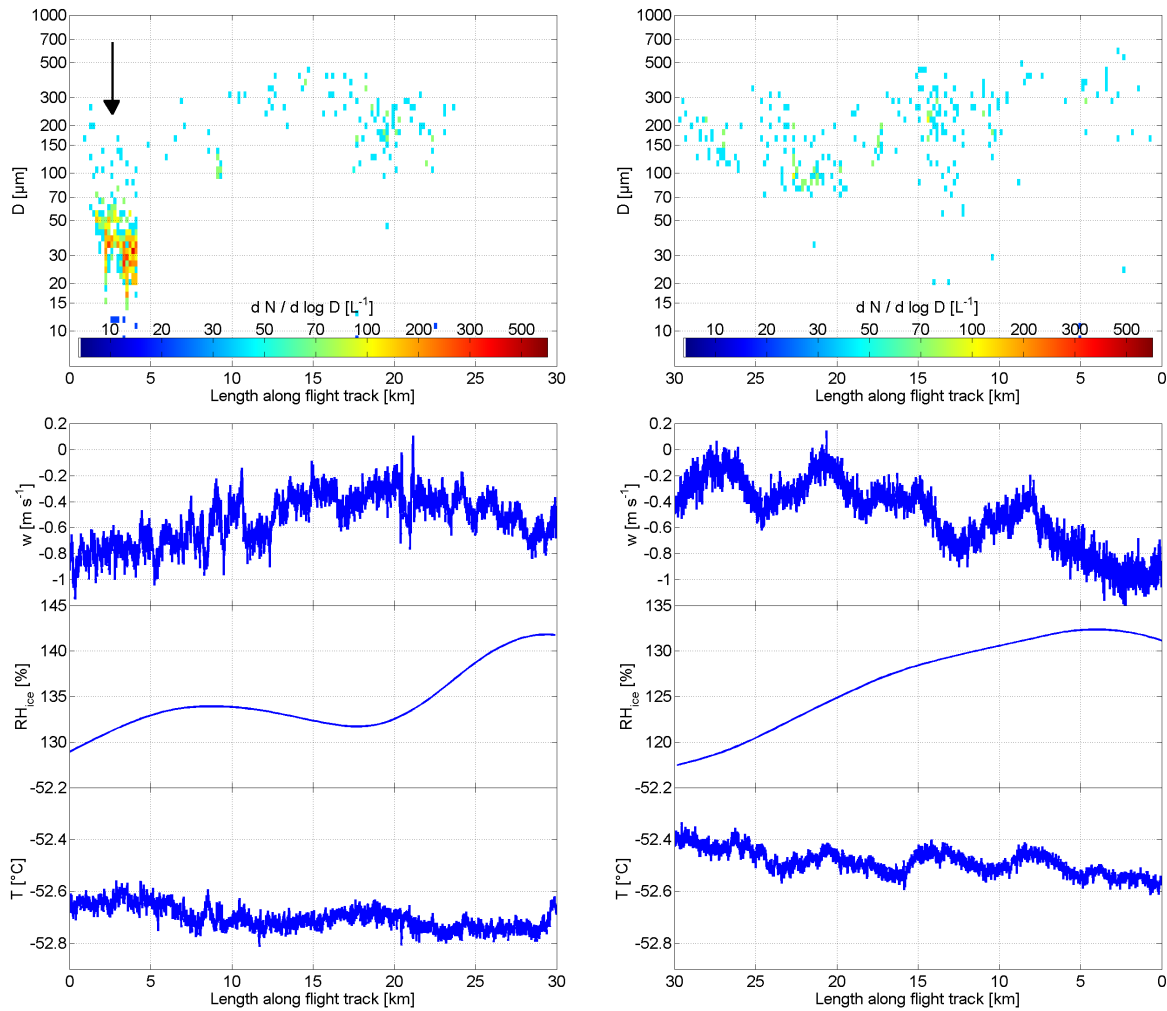


Fig. 8.4: As in Fig. 8.3 for Cloud 5 (14:52:29 - 14:54:40 UTC, left) and Cloud 7 (15:02:22 - 15:05:11 UTC, right) from Flight B899 on 05 March 2015. The direction of the abscissa in Cloud 7 was reversed to match the coordinates of Cloud 5 as Cloud 7 was the return flight along approximately the same line. The arrow marks the occurrence of the small mode in Cloud 5.

8.4 Explaining additional modes in WCB cirrus and warm front cirrus by habit segregation

In most cases of liquid-origin cirrus, it is not possible to define a mode-separation diameter in the particle size distribution. However, the total size distribution is not well-explained by a monomodal log-normal distribution. In a recent publication (Schlenczek et al. (2017), see Appendix A) it has been shown that a habit-wise decomposition is able to explain the total size distribution of an ice cloud as a superposition of log-normal distributions from individual particle habits. The case selected for demonstrating this method is Flight B890 which contains data from a liquid-origin cirrus. It is likely that the cirrus was found in a warm conveyor belt (WCB) as defined in Young et al. (1987). A fairly easy task is the separation of the droplet mode from the rest in Cloud Pass 1a, where the very small mode with a mode diameter around $8\ \mu\text{m}$ is likely from supercooled water droplets. This example is shown in Fig. 8.5 top left. For this case, most of the particle size distribution could be explained by the superposition of a log-normal mode from the droplets (spheroids) and two log-normal modes from the aggregates. The remaining particle habits did not contribute much to the total size distribution.

The rest of the first cloud pass (called Cloud Pass 1b), after the droplets were not measured anymore, does also show a bimodal size distribution of aggregates. While the smaller mode of Cloud Pass 1b ($D \approx 150\ \mu\text{m}$) overlaps with the smaller mode in Cloud Pass 1a ($D \approx 120\ \mu\text{m}$, compare Fig. 8.5 top left and top right), this is not the case for the larger mode. It is possible that the aggregates in Cloud Pass 1a could grow to larger sizes ($D \approx 700\ \mu\text{m}$ in Cloud Pass 1a compared to $D \approx 500\ \mu\text{m}$ in Cloud Pass 1b) due to the presence of droplets and possible riming. However, the large error bars due to low counting statistics in case of Cloud Pass 1a need to be considered in this intercomparison. In this case, leaving out the mode labeled as "Other particles" in Fig. 8.5 would induce a visible error when trying to explain the total size distribution by just a bimodal fit of the aggregates. A very different scenario is seen in the ascending flight leg towards the 300 hPa level, which is Cloud Pass 2 (bottom left panel of Fig. 8.5). During the ascent from the temperature regime of $-28\ ^\circ\text{C}$ to $-47\ ^\circ\text{C}$, two major observations were made: First, the appearance of bullet rosettes induced another mode in the size distribution, which partly overlaps with the aggregates. It has to be said that the fraction of rosette shapes in the "Other particles" class of the previous cloud pass was very small. Second, there is no mode separation diameter anymore, which means that all individual modes from the individual habit classes tend to overlap somehow.

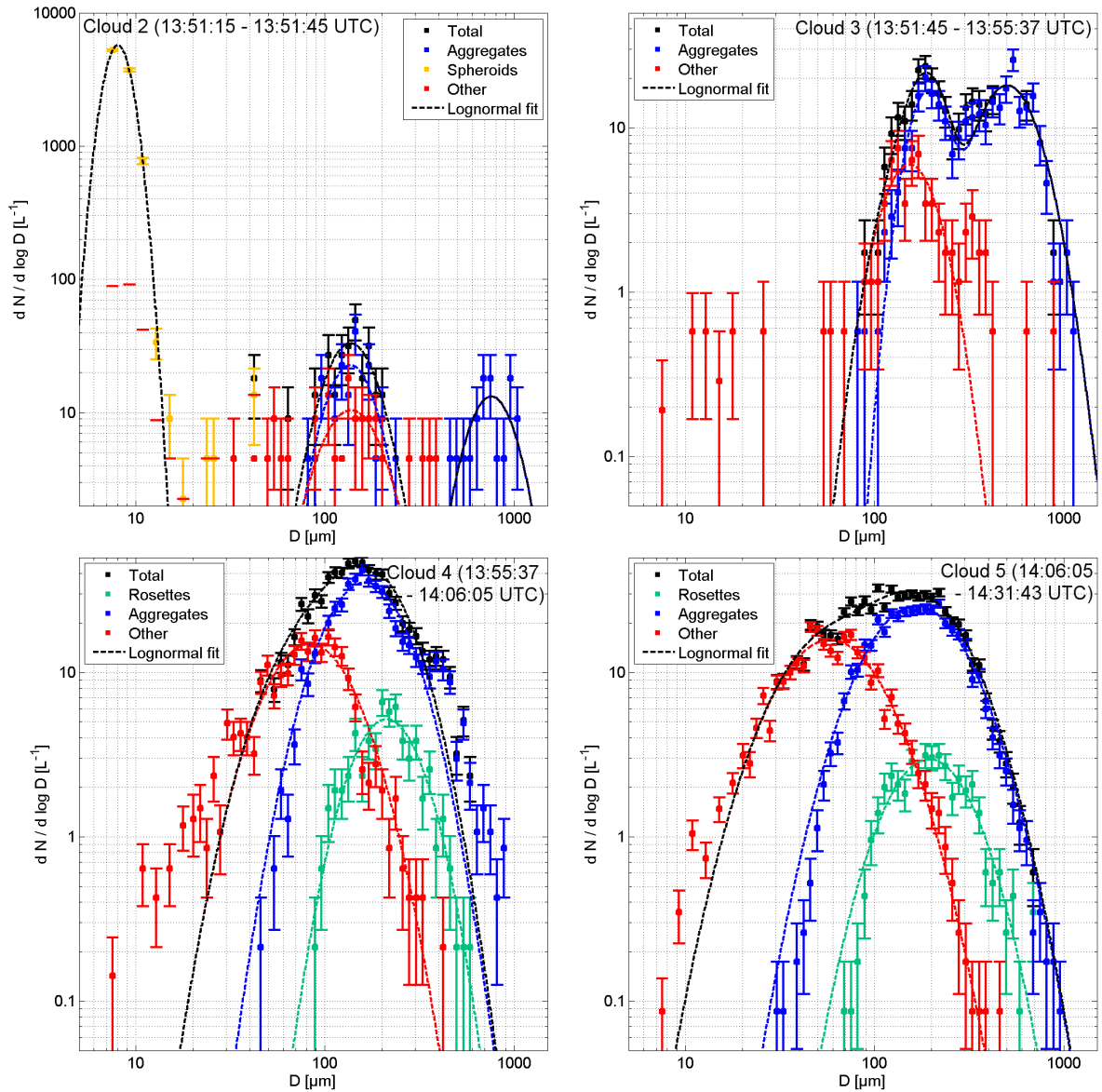


Fig. 8.5: Habit-segregated particle size distributions with individual monomodal or bi-modal log-normal fits. The fit parameters are shown in Appendix G, Table G.5. The cases shown are Cloud Pass 1a (top left), Cloud Pass 1b (top right), Cloud Pass 2 (bottom left) and Cloud Pass 3 (bottom right) from COSMICS Flight B890 on 06 March 2015.

A very similar picture is seen in case of Cloud Pass 3 (bottom right panel of Fig. 8.5), which was the longest in-cloud episode with almost 30 minutes ($L \approx 300$ km) at $T = -47^\circ\text{C}$. In both cases, an unambiguous distinction between the different particle modes just by their size is not possible and the question on the state of mixing between the mode arises. A first impression can be gained from looking at the particle images measured hologram by hologram in Cloud Pass 3, which are shown in Fig. 8.6.

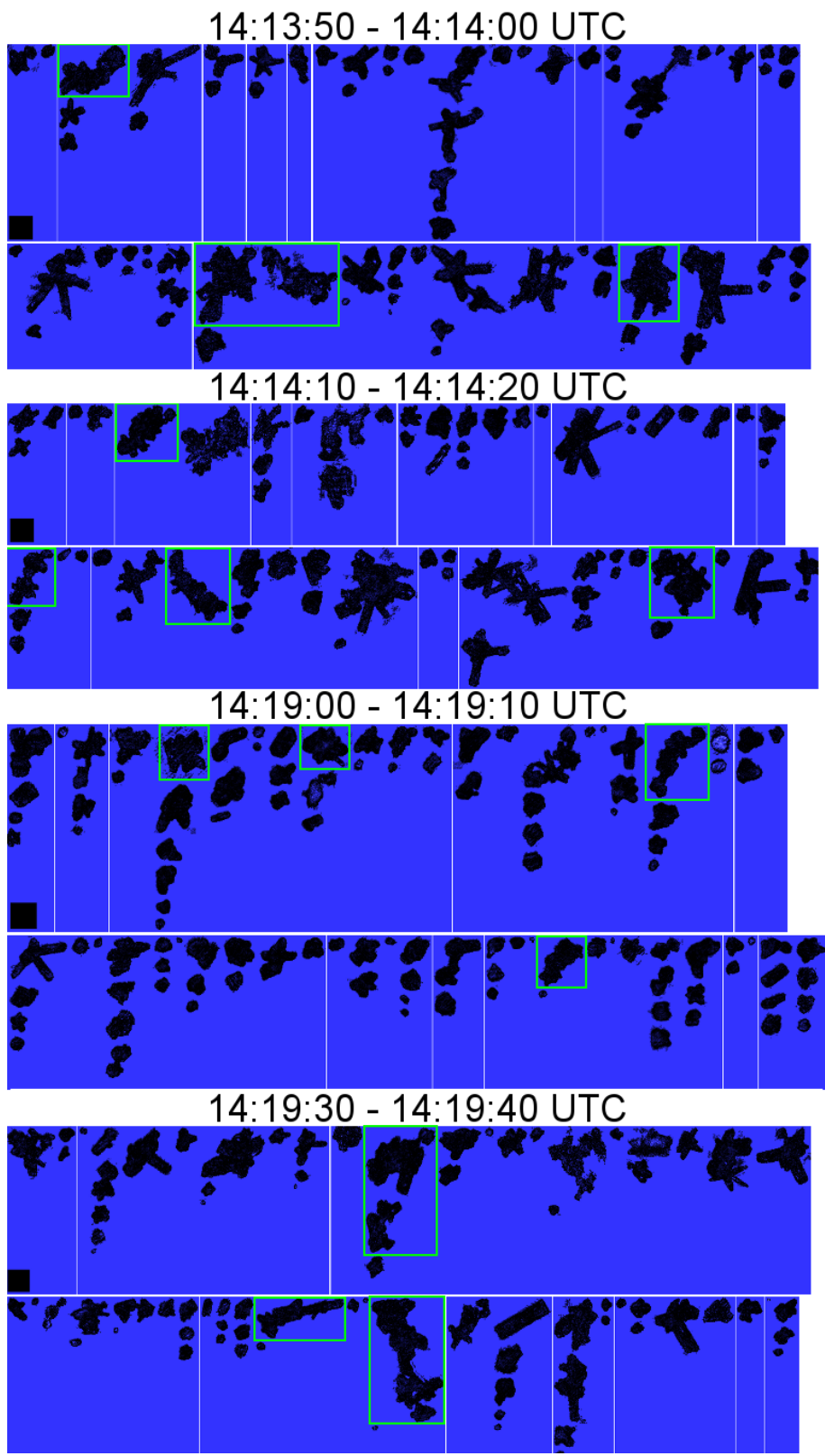


Fig. 8.6: As in Fig. 8.2 for Flight B890 on 06 March 2015 at the 300 hPa level (Cloud Pass 3). Each image strip represents 10 seconds of flight (60 holograms). Possibly rimed particles are marked with a green frame.

When compared with the data from Flight B889, the first striking difference in the particle image gallery is the presence of some possibly rimed particles. The presence of rime can be treated as a clear evidence that the corresponding ice crystal must have encountered supercooled droplets during some time of its life cycle. Thus, finding rimed particles is an evidence for a cloud that had at least in part a liquid origin. However, the absence of rime is a necessary but no sufficient criterion for a pure-ice origin. This conclusion can be drawn from Cooper and Vali (1981).

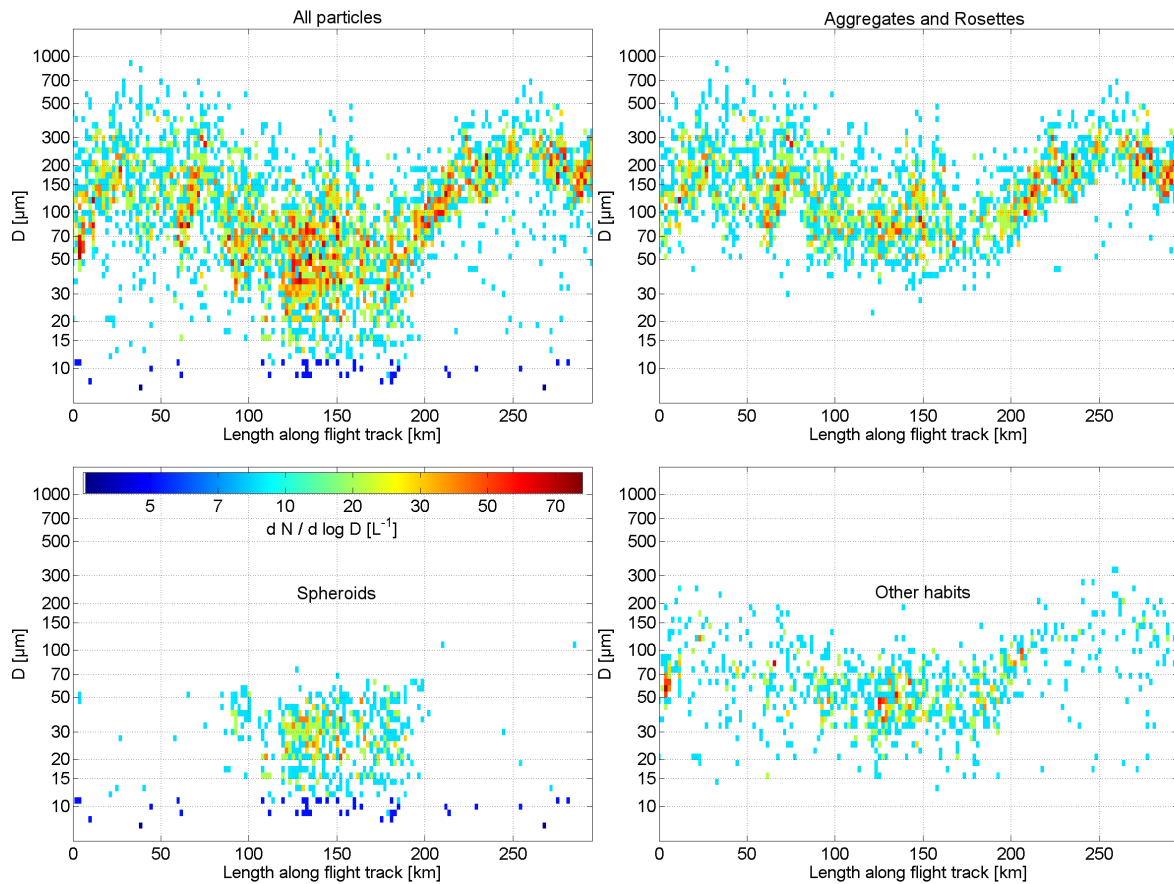


Fig. 8.7: Number-weighted particle size distribution from holograms combined over 10 seconds as a function of length along the flight track of Cloud 5 in Flight B890. Shown are the size distribution of all particles (top left), aggregates and rosettes (top right), spheroids (bottom left) and the remaining habits (bottom right). The color code shown for the Spheroids is valid for all four panels.

Another notable difference is the chaotic appearance of different particle habits from hologram to hologram. Particle sizes and habits tend to change within distances of less than 30 m with no well-defined underlying structure in either particle habit class, particle size or the dynamical variables T , RH_{ice} and w . Some individual cases of quasi-spherical particles or surface structures on the particle outline do not need to be produced by

droplet freezing or riming but may be produced by sublimation during the transition of an ice-subsaturated layer. To see if the partitioning of particle habits and sizes is really chaotic or if there is an underlying structure, the particle size distributions accumulated over ten seconds were examined by particle habit along the flight path. An overview of the size distributions in Cloud 5 along the flight path is given in Fig. 8.7.

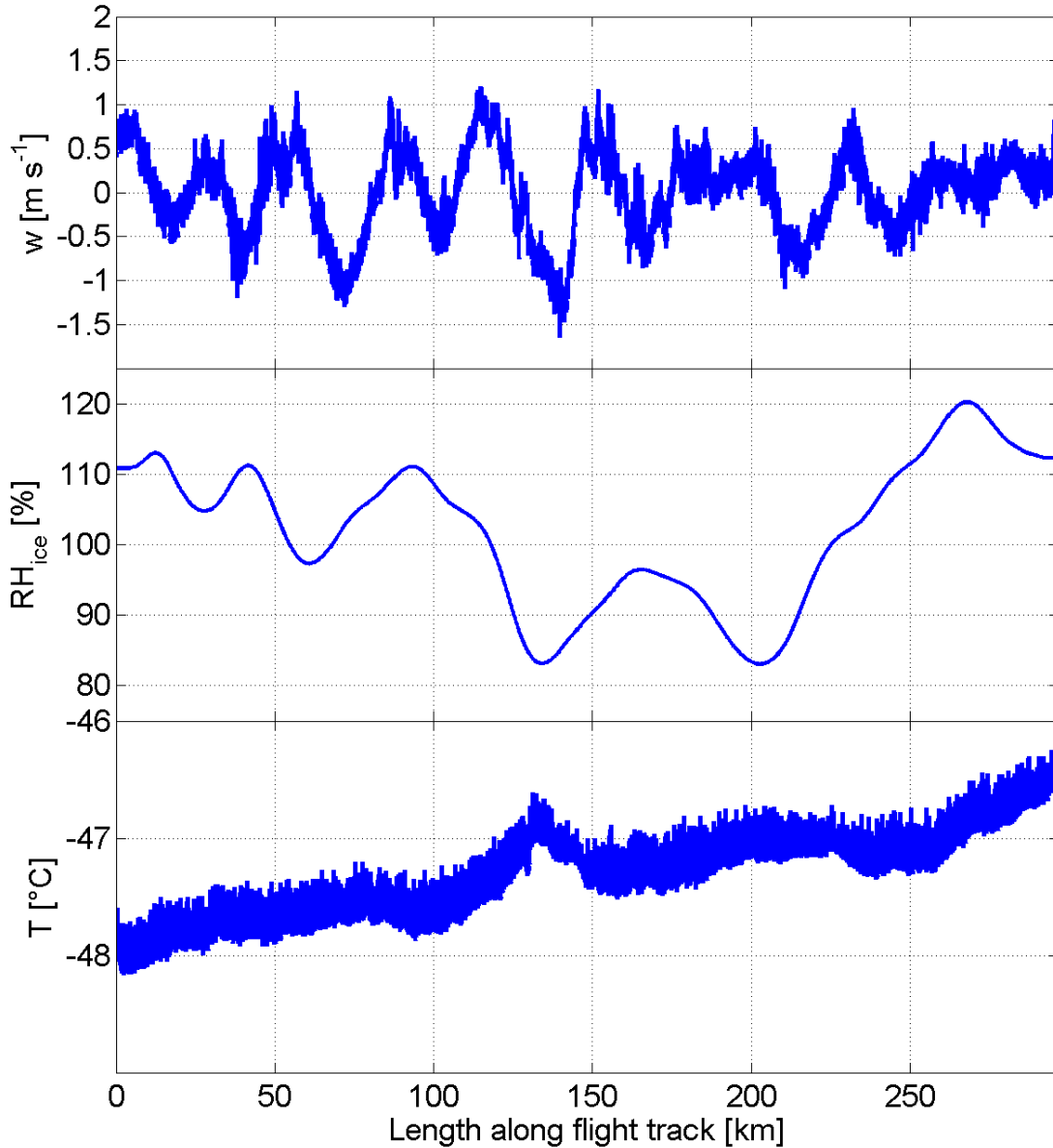


Fig. 8.8: Meteorological data along the flight path as in Fig. 8.3 for Cloud 5 of Flight B890.

Apparently, the majority of the total size distribution of particles larger than 70 microns is well-explained by the aggregates. Spheroids were preferably present in the center of the

flight leg between $L = 100$ km and $L = 200$ km. The spatial evolution of the aggregate fraction shows some minima and maxima in both mean particle size and particle concentration. Some of the local maxima in particle concentration and size seem to be correlated with w , which can be seen in Fig. 8.8. However, other maxima are not correlated with w and other dynamical variables (e.g. RH_{ice}) might play a role. The well-defined section with smaller aggregates and many spheroids and others is found in an ice-subsaturated region, which would argue for sedimentation as the process that brought the particles into the sampled region. For a detailed analysis of the process responsible for the different particle modes, a high-resolution trajectory analysis and a comparison with a cloud resolving model would be desired.

Flight B895, which targeted a cirrus cloud ahead of a warm front, had a similar overlap of particle size distributions from the different habit classes (shown in Appendix G, Fig. G.16), but virtually no rimed particles and a much higher abundance of bullet rosettes. An example of bimodal size distributions in the first descending flight segment, the second run and the third descending flight segment (labeled as Cloud 2, 3 and 4 in Fig. G.17) shows a mixture of habits and particle sizes which is nearly as chaotic as the one observed in Flight B890. From the knowledge that this cirrus cloud was measured in several descending staircase patterns, it is most likely that the mixture of habits and size modes is due to mixing and sedimentation. Thus, it is assumed that Cloud 5 and 7 from Flight B889 had the same or at least a similar background where the larger particle mode supposedly came from a sedimentation process.

8.5 Vertical structure of three contrasting cirrus clouds

After the structures and the habit segregation have been discussed, the vertical structure of the three cloud cases was examined in a very similar way as Frey (2011) did in her analysis of subvisual cirrus clouds in the tropics. The cloud data were binned in 0.5 K wide temperature and θ bins and for each bin, the cloud microphysical properties N , r_{eff} and IWC were calculated. The same was done for the meteorological properties related to dynamics, which were RH_{ice} , $|v|$ and w . The three flights are shown together in Fig. 8.9 and 8.10. When looking at the meteorological variables, it seems like RH_{ice} and v are strongly correlated in case of Flight B890 and B895. However, this might be an artifact from the binning as the scatter plots of v and RH_{ice} in Fig. G.5 of Appendix G.2 would argue for a more complicated relationship between the two variables. A decreasing trend in w towards higher altitude / lower temperature is visible in all flights. In the maps of θ , this trend is much weaker for Flight B890 in comparison with the other two flights. Generally, one of the main dynamical characteristics of the three flights was that Flight B889 had the highest horizontal wind speeds (with a maximum of 55 m s^{-1}), Flight B890 had the highest mean vertical velocity and largest range of altitudes with positive vertical velocity and Flight B895 had the lowest maximum in-cloud relative humidity. From the microphysical perspective, the main trend in effective radius (decreasing r_{eff}

for decreasing T / increasing θ) is in accordance with the results in Frey (2011) for tropical cirrus clouds. Klingebiel et al. (2017) presented a similar finding for cirrus clouds over the North Sea, i.e. an increase in particle mean diameter with decreasing altitude.

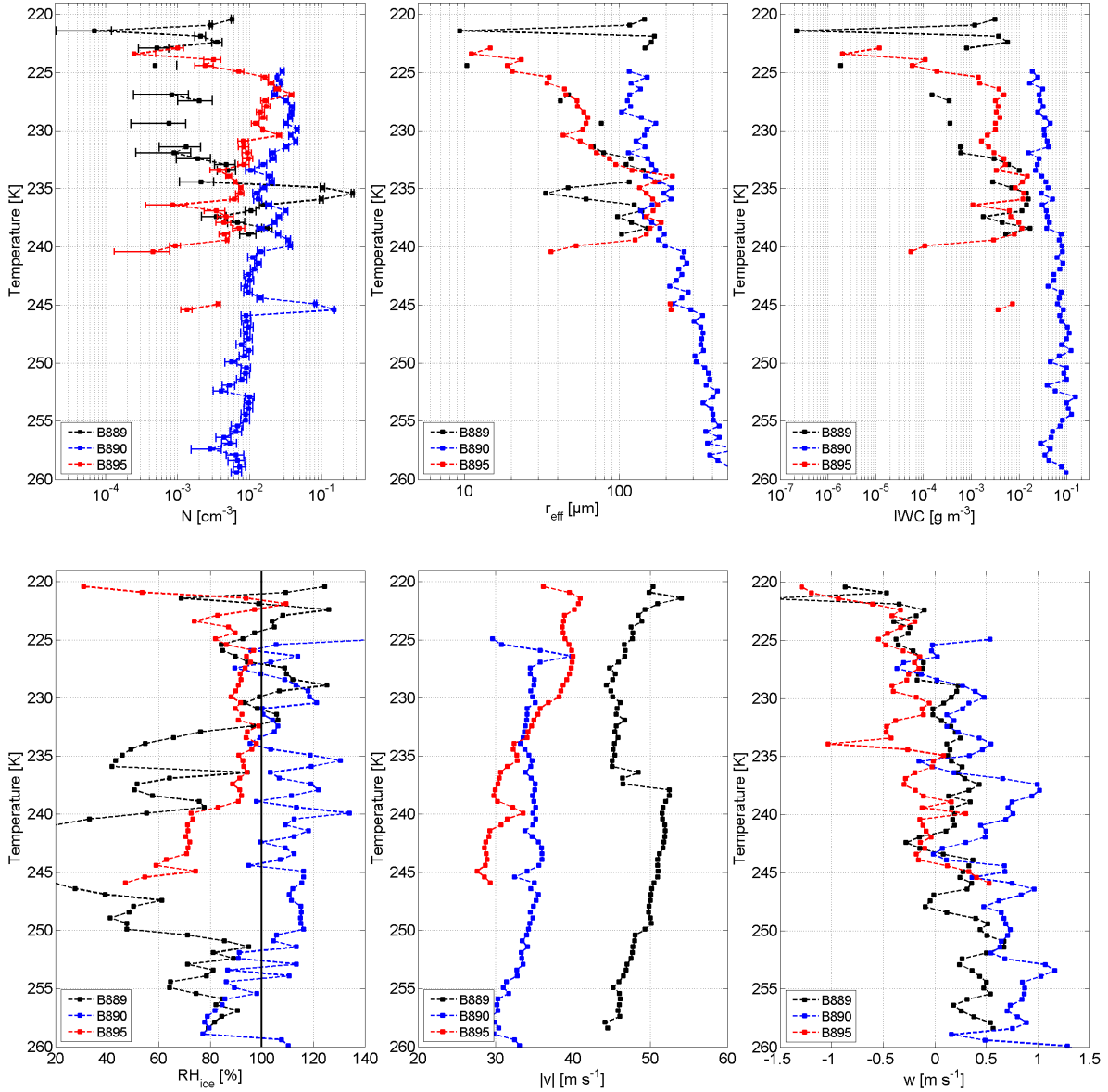


Fig. 8.9: Vertical profiles obtained from the microphysical properties measured by HALO-Holo. Shown are IWC (left column), r_{eff} (middle column) and N (right column). In the bottom row, the vertical profiles of RH_{ice} , $|v|$ and w , obtained from the aircraft, are shown. The bin sizes for T were 0.5 K. The error bars in N are calculated from counting statistics, typical uncertainties of IWC are a factor of two smaller / larger than the displayed value. The corresponding flights were Flight B889 (05 March 2015), B890 (06 March 2015) and B895 (13 March 2015).

When comparing the flights B890 and B895, the main difference at lower altitudes is found in a larger N for B890 and the main difference at higher altitude is a smaller r_{eff} for B895, both together yielding an almost constant difference in IWC of about a factor of three between 240 K and 235 K.

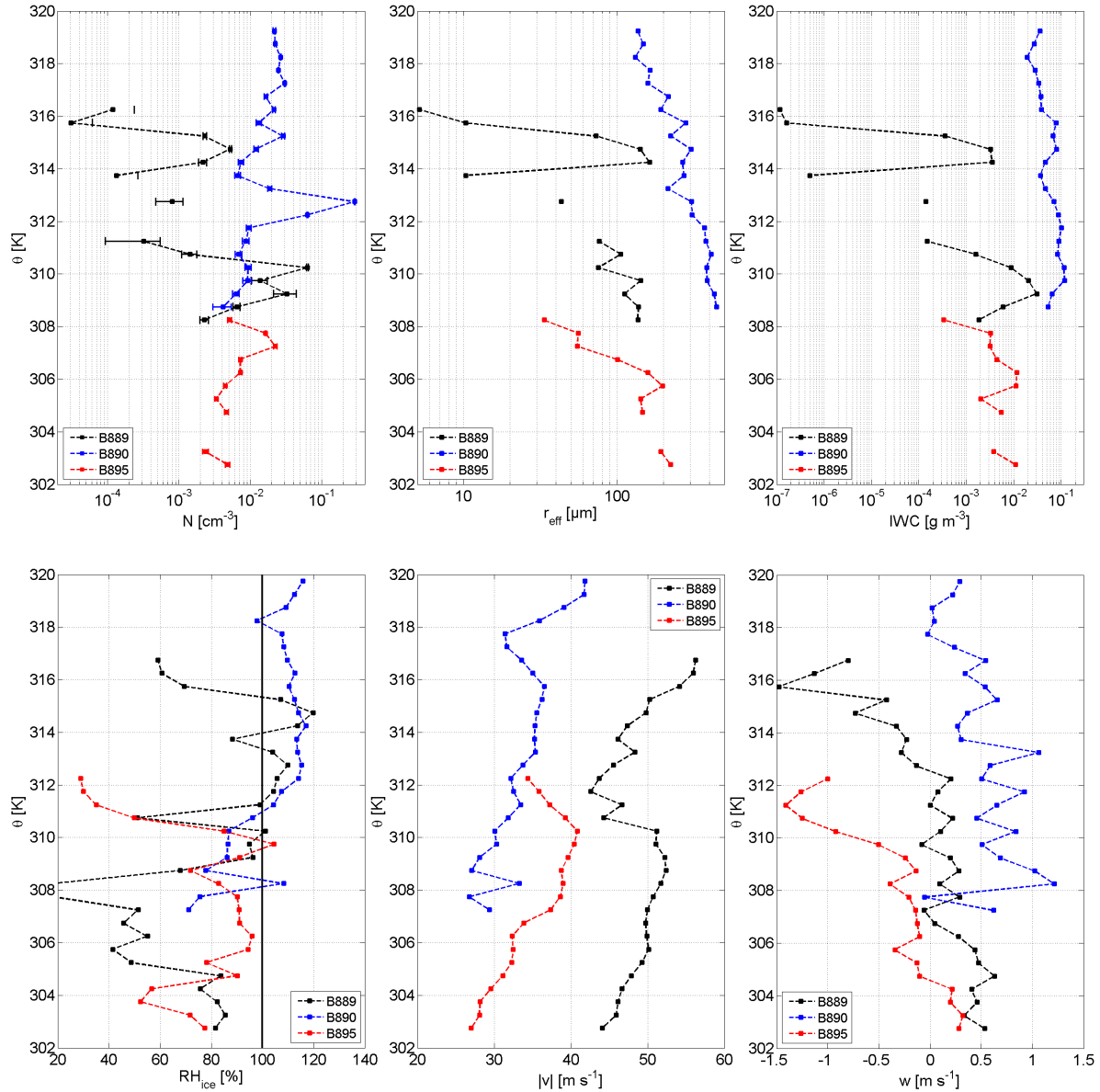


Fig. 8.10: As in Fig. 8.9 for θ as vertical coordinate. The direction of the ordinate is opposite to the direction of the ordinate in Fig. 8.9 such that the upper end of the ordinate resembles higher altitude. The corresponding flights were Flight B889 (05 March 2015), B890 (06 March 2015) and B895 (13 March 2015).

Flight B889 differs from the other two flights mainly in the presence of very sharp gradients in all three microphysical variables. N and IWC change by almost two orders of magnitude within half a degree of temperature near the 235 K and 222 K level.

In the theta-binned vertical profiles of dynamical and microphysical properties (Fig. 8.10), similar trends as in the temperature-binned vertical profiles can be found. However, the three flights had very different airmasses, which leads to significant changes in the altitude when comparing T and θ . An interesting feature in Fig. 8.10 is that the number concentration of Flight B895 at $\theta = 308$ K seems to be logically extended by the number concentration of Flight B890 at $\theta = 308.5$ K and above. However, in terms of particle effective radius there is a disparity between the two by one order of magnitude. The liquid-origin cirrus in Flight B890 differs significantly from the other two cirrus clouds (Flight B889 and Flight B895) in terms of effective radius and IWC . Though the decreasing trend with increasing altitude is apparent in both cases, the effective radius in B890 was on average four times larger at the same potential temperature as in Flight B889. In terms of IWC , the two in-situ cirrus cases are fairly consistent with a peak IWC around 10 mg m^{-3} for B895 and 30 mg m^{-3} for B889. In comparison, the liquid-origin cirrus had a peak IWC of 100 mg m^{-3} and stayed above 20 mg m^{-3} throughout the entire range of θ . These results agree well with the definition of liquid-origin cirrus in Krämer et al. (2016) where liquid-origin cirrus is characterized by an IWC that is typically between 10 and 100 mg m^{-3} . A main structural difference can be seen when comparing Flight B889 and B895: While the cirrus cloud in B895 was a rather thick and quasi-uniform cirrus cloud in terms of IWC , the clouds in B889 were confined to a narrow vertical range and appear as peaks in the IWC altitude profile.

8.6 Recent measurements of cirrus clouds in the tropical tropopause layer

In July and August 2017, the airborne experiments within the project StratoClim (Stratospheric and upper tropospheric processes for better climate predictions) were conducted in Nepalese, Indian and Bangladesh airspace, originating from Tribhuvan International Airport in Kathmandu, Nepal (ICAO code KTM). The main goal of the experiment was obtaining in-situ measurements of aerosol particles and trace gases in the upper troposphere / lower stratosphere within the Asian Monsoon Anticyclone. The airborne platform with which the in-situ cloud, aerosol and trace gas measurements were performed was the M-55 Geophysica with a maximum altitude of 21 km (ca. 60 hPa). Three successful flights with HALOHolo were conducted, one of them is Flight 8 on 10 August 2017 targeting the anvils of large convective systems and their outflows. One of the cloud events of this flight was found around 09:50 UTC at an altitude of 17.1 km and a pressure level of 86 hPa ($\theta = 379$ K). The temperature at this altitude was as low as 188.4 K, which is about the minimum temperature at the cold point tropopause in northern India at

this time²³. According to preliminary data of the Cryogenically Operated Laser Diode (COLD) instrument, this cloud event coincided with mixing ratio of carbon monoxide significantly above the background for the given altitude, which is indicative of a fast transport of air from the lower troposphere to the measurement location. Fig. 8.12 shows the number concentration, effective radius and IWC of ice particles measured by HALO-Holo as a function of distance L along the flight track. In addition, the particle size distribution is shown in intervals of one second ($L \approx 175$ m). Typical counting statistics were between 50 and 100 particles per second. Fig. 8.11 shows the typical shapes of the ice particles in the convective outflow. Most of the particles above a maximum dimension of 100 μm are either rimed aggregates or pristine aggregates. Plate- or column-shaped ice crystals do occur but they are not as abundant as the irregular shapes or aggregates. The habit distribution is in principle comparable to the habit distribution of Pass 8 in ICE-D Flight B926 (see Chapter 7) or the WCB cirrus of COSMICS Flight B890, which means a high abundance of pristine aggregates, some rimed aggregates and virtually no bullet rosettes.

The cloud measured over Northern India on 10 August 2017 has a very similar size distribution as the convective outflow region of a mesoscale convective system over Burkina Faso on 16 August 2006 (Frey et al., 2011), which is shown in Fig. 8.13. In particular the CIP and HALO-Holo data (black and dark blue markers in Fig. 8.13) between 150 μm and 600 μm particle diameter are in agreement with OF4 from Frey et al. (2011), which is shown in red. Between 10 μm and 150 μm , the number densities measured by the CDP or CIP and HALO-Holo (except for the four smallest bins) are larger than in the cases from Frey et al. (2011). However, the disparity is less than a factor of ten if the narrow bin around 27 μm of the CDP is ignored. Also, the other flights through a convective outflow region in Frey et al. (2011) have fairly similar size distributions. In comparison with the data from the convective outflow, the size distributions of subvisual cirrus are very different (see Fig. 8.13 bottom).

At the time this thesis was written, quality-checked data of NO_y , CO and CO_2 measurements were not available on the StratoClim database. When these data are available, a similar analysis as in Frey et al. (2011) needs to be done to determine the origin and age of the air mass containing the ice particles. It should be noted that the size distributions from Frey et al. (2011) were measured at altitudes between 11.5 km and 13.7 km at a potential temperature of 350 to 355 K; the size distributions from StratoClim Flight 8 were measured at 17.1 km altitude ($\theta = 379$ K), which is much closer to the tropical tropopause.

²³The minimum temperature found in the proximity radiosounding of Gorakhpur (26.75° N, 83.36° E) on 10 August 2017, 00:00 UTC was 188.8 K at 17.2 km altitude.

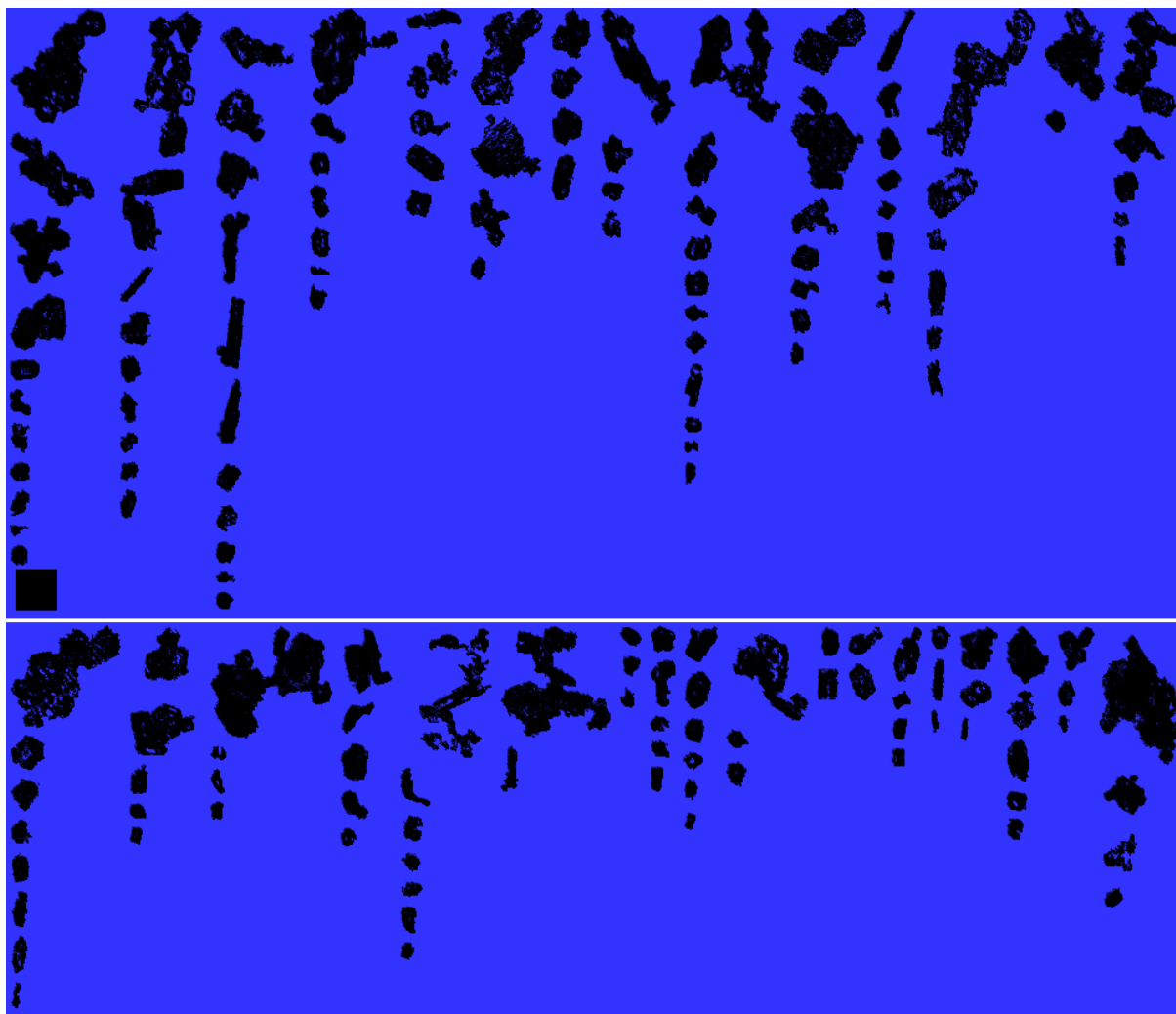


Fig. 8.11: Images of ice particles from StratoClim Flight 8 (10 August 2017) around 09:50 UTC. The black square in the middle left is 100 microns wide.

Other cloud passes from StratoClim should be analyzed to look for similarities and differences between convective clouds in the Asian Monsoon and convective clouds in the West African Monsoon. It might also be worth to compare the particle size distributions and trace gas concentrations from the StratoClim flights with those from the "Hector" storm system over Northern Australia measured during the SCOUT-O3 campaign (Vaughan et al., 2008) in November and December 2005.

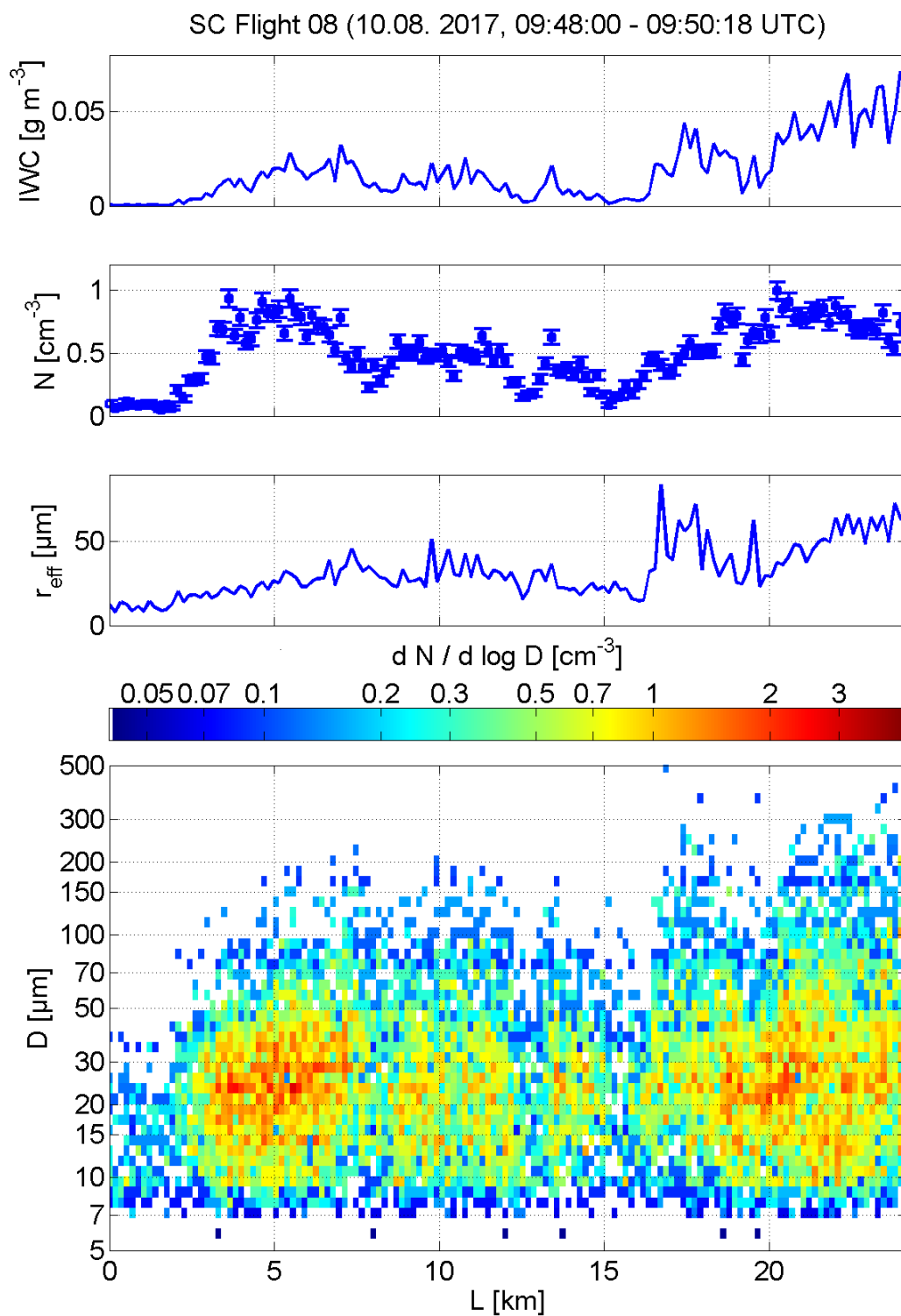


Fig. 8.12: Spatial structure of a cirrus cloud in a convective outflow region over Northern India measured during StratoClim Flight 8 (10 August 2017). Shown are the IWC (top), number concentration (middle) and effective radius (bottom) in the top panel and the color-coded particle size distribution in the bottom panel. The error bars of number concentration N were calculated from counting statistics over a sampling distance of approximately 170 m.

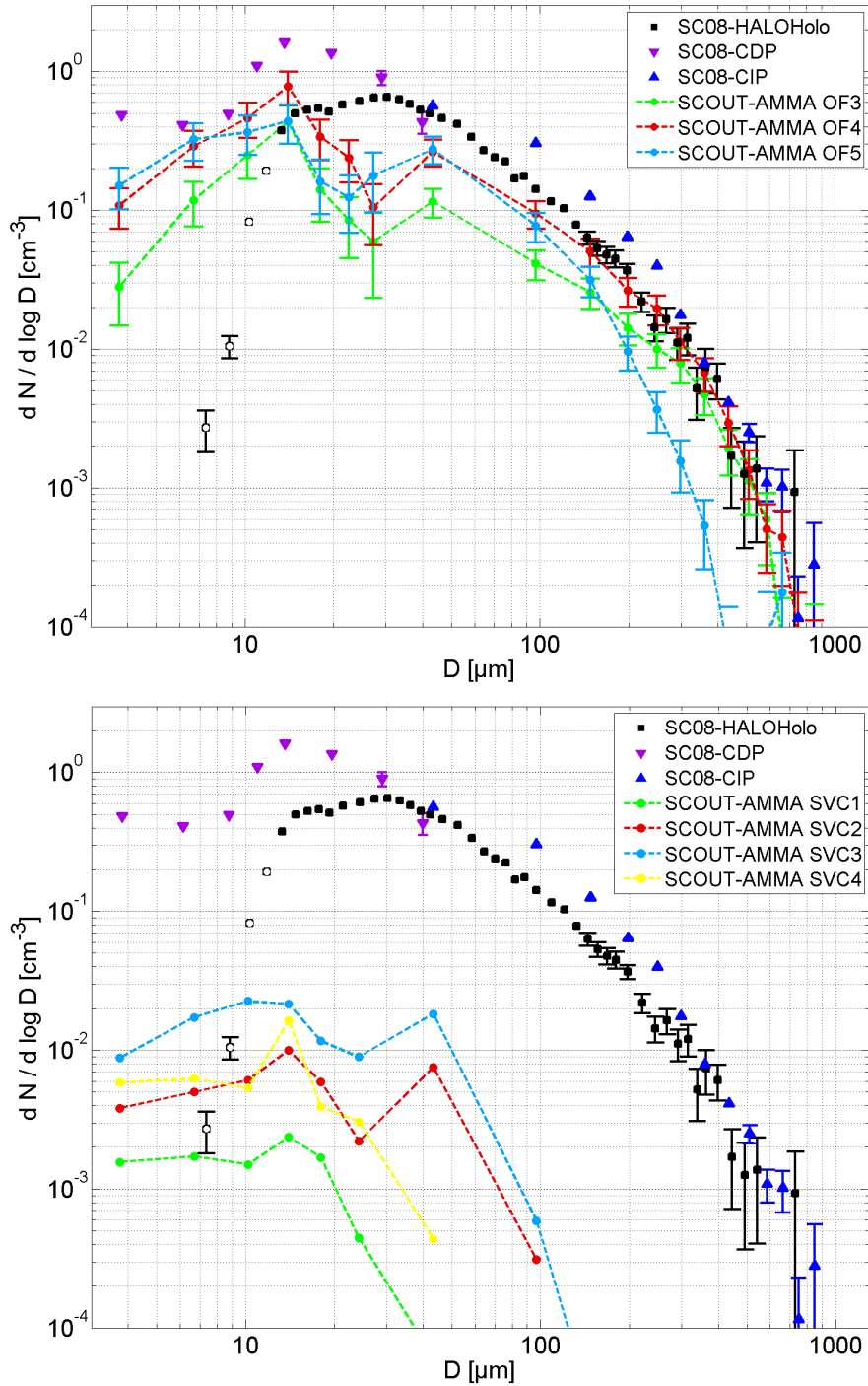


Fig. 8.13: Size distribution intercomparison of StratoClim Flight 8 (10 August 2017) 09:48 - 09:50 UTC (HALOHolo in black, CDP in violet, CIP in dark blue) and ice particles in a convective outflow on 16 August 2006 (top panel, data from Frey et al. (2011), OF3 in light green at 11.5 to 11.8 km, OF4 in red at 12.1 to 12.4 km and OF5 in light blue at 13.6 to 13.7 km altitude). Bottom panel: The same data from StratoClim Flight 8 compared with subvisual cirrus measurements over West Africa from Frey et al. (2011). Error bars of CDP, CIP and HALOHolo are shown for relative errors of 10 % or larger.

8.7 Discussion and summary

From the three measurement flights in cirrus clouds, horizontal structure, ice crystal habit composition and vertical structure have been examined. Four cloud cases in Flight B889, which targeted wave cirrus near a cold front, contained bimodal size distributions and the meteorological measurements and data from HALOHolo have been used to determine the dynamical background of these cloud segments. The first case that was investigated contained a very well-defined evolution of particle size along the flight track in the center region of a downdraft with $w \approx -1 \text{ m s}^{-1}$. Several holograms contained particles from both modes and from the presence of a shallow unstable layer in a region with high wind speeds, it has been concluded that the secondary mode was likely induced by wave breaking and subsequent mixing. Another rather short cloud pass showed a bimodal size distribution in the one second combined size distributions, which was found to be an artifact from averaging, except for one hologram containing particles from both modes. In this case, the particles of the two modes seemed to be almost perfectly sorted, which would argue for shallow convection as a possible mechanism. A major point which complicates the analysis is that the cloud status above the aircraft is unknown. No upward pointing lidar or radar measurements were available from the three flights and the video from the upward facing camera does not provide sufficient information for the particular clouds studied in this chapter. The two other cases were used to examine the stationarity of wave cirrus over time during the propagation of the cold front. Both cloud cases followed exactly the same track where the first passage and the return flight were separated by approx. 10 minutes in time, which yields approximately 30 km of cloud displacement due to advection. While a prominent small particle mode was found in the first passage of this cloud region, this was not the case on the return flight. The first passage of this cloud was bimodal in a way that occasionally large columns or bullet rosettes appeared in a population of small columns and irregular particles. A well-defined dynamical structure could not be found and therefore sedimentation is thought to be responsible for creating the small particle mode while the larger mode persisted through both cloud passes. Model simulations are needed to clarify this issue.

Two other flights have been studied where the occurrence of particular ice crystal habits, size and number concentration did not follow an underlying structure. The habit-wise analysis of the size distributions in Cloud Pass 3 of Flight B890 revealed spatial structures in the cloud. The presence of these structure argues, together with the observed decrease in relative humidity, for sedimentation as the most likely process for creating a smaller mode of particles in this cloud. Also, the habit-wise analysis was able to disentangle different log-normal modes of the size distributions and could provide insights into the changes in particle size and number concentration over time. This tool should be used in future studies when microphysically relevant processes need to be quantified in a very complicated ice cloud scenario. Flight B890 could be identified as a liquid-origin cirrus due to the presence of possibly rimed particles, along with a brief episode of holograms

containing droplets at a temperature around -28°C . A dissipating warm front cirrus in Flight B895, which has also been studied in O'Shea et al. (2016), did also have rather complicated size distributions with deviations from a log-normal distribution but no distinct mode-separation diameter. However, rimed particles were not present in this cloud case. Thus, an in-situ origin of this cloud is assumed as the maximum *IWC* was still within the range of in-situ cirrus as expressed in Krämer et al. (2016). In terms of ice crystal habits, the fraction of pristine bullet rosettes was highest in Flight B889, followed by Flight B895. Flight B890 contained only few bullet rosettes and much more sideplane aggregates or other aggregates (see Fig. G.18 and G.19 in Appendix G).

The three cloud cases have also been examined in terms of their vertical structure. A common finding in comparison with Frey (2011) was a decreasing trend in effective radius with increasing altitude. Also, it could be shown that the mean ice water content tends to remain fairly constant over the range of altitude in liquid-origin cirrus whereas the in-situ cirrus is often characterized by a strong decrease with increasing altitude. Differences between the vertical profiles expressed in temperature vs. the vertical profiles using θ as a vertical coordinate are likely due to the different airmasses in the three cloud cases and less variability in θ compared to T along the flight track. Dynamics likely play an important role for the development of the three cirrus clouds: The liquid-origin cirrus in Flight B890 with the highest *IWC* was found in an environment with fairly strong and persistent updrafts while the two other cases were dominated by downdrafts.

One cloud case from the StratoClim field campaign in Nepal (10 August 2017) was compared with the measurements of convective outflow cirrus over West Africa during the SCOUT-AMMA campaign in 2006 (Frey et al., 2011). While the altitude of the observation might suggest subvisual cirrus in the case of StratoClim Flight 8, the size distributions of the convective outflow agree reasonably well with the recently measured size distributions. Also, an enhanced mixing ratio of CO (60 - 80 nmol mol⁻¹ background at 17 km altitude, locally 110 - 120 nmol mol⁻¹ in cloud) argues for a recent convective outflow. Another intercomparison of the results from StratoClim Flight 8 with data from subvisual cirrus (also from Frey et al. (2011)) showed that the size distributions of ice particles in a convective outflow differ substantially from those of subvisual cirrus clouds in the tropics.

Discussion and conclusion

9.1 Advances in the development of cloud particle spectrometers

The first holographic particle spectrometer used for airborne in-situ measurements of cloud hydrometeors is called HOLODEC and was developed by Fugal et al. (2004) and updated by Spuler and Fugal (2011). While the optical arrangement of HALOHolo was designed in a very similar way as in HOLODEC, the camera in HALOHolo is faster and captures a larger lateral piece of the sample volume. The increase in sample volume and camera speed allows the investigation of more sparse droplet or ice crystal populations with a shorter length scale between each measurement.

Ground-based holographic instruments were developed by several groups in Europe, e.g. Raupach et al. (2006) and Henneberger (2013). HALOHolo is, however, the only European holographic instrument that has been designed for airborne operation and adds value to the existing gallery of the so-called "underwing probes". Its sampling strategy is unique due to its ability to provide particle size distributions, and also spatial distributions, from a single camera exposure like a snapshot. The technique of holography allows - in contrast to many other methods - a direct comparison of spatial and size distributions of particles from laboratory experiments with the same properties measured in-situ in the atmosphere. However, commercially available cameras are still not fast enough to allow a continuous three-dimensional measurement via particle tracking between two subsequent holograms, at least not for use on an aircraft. Several effects arising from averaging over a long and thin volume of sampled air (like for the CDP, FSSP, and similar instruments) do not need to be considered, and the sample volume, which is independent from the aircraft velocity, is always well-defined. Also, the detection of shattering is straightforward and it is possible to investigate the spatial characteristics of shattering or even try to "repair" a shattered particle numerically. The results from such an analysis would be a helpful guidance for the operators of other cloud microphysical instruments. In addition, it is questionable whether the effect of possible out-of-focus artifacts in the small particle mode of a 2D-S instrument would have been discovered if HALOHolo had not been operated on the BAe-146 aircraft during the COSMICS campaign.

9.2 Advances in image processing algorithms

With the recently developed, parallelized hologram analysis software, the analysis time needed to go from raw data to higher-order data has been reduced significantly. Besides the classification part, the hologram analysis works fully-automatic with the capability of reconstructing data from a whole flight within a few days on a supercomputer.

Recently, the bottleneck of the entire analysis procedure is the classification part, which needs human interaction to separate in-focus particles from artifacts and out-of-focus particles. After the advances in the use of neural networks, an automation of this step might be possible in the near future. Similar methods have already been implemented in data processing routines applied on images from optical array probes. After distinguishing

between particles and artifacts, the non-spherical particles can be classified by habit with a similar routine.

Some post-processing techniques can also be automated, an example is the detection of shattering. It has been shown that the rather crude approach of chopping off the possibly contaminated part of the sample volume is sufficiently accurate and much faster than inspecting individual holograms that were suspected for shattering. The final step which needs to be taken towards fully-automatic data analysis from the raw hologram to the final data product is the automation of the particle classification.

A numerical model simulating the instrument's response and properties has been developed, which is capable of producing synthetic but still realistic (not too clean) holograms. The impact of the resolution limit effect and the dark corner effect estimated from the model simulations agree in principle with the results obtained from in-situ aircraft measurements. Also, the particle sizing accuracy of two independent algorithms could be validated and a limit for the applicability of the more complicated algorithm (i.e. the sign-matched filter after Lu et al. (2012)) could be drawn. The intercomparison of both algorithms allowed a quantification of the bias in particle size estimation for small particles in very clean holograms. A corresponding particle sizing bias correction for very clean holograms has already been implemented by using a modified (local) threshold for particle size estimation.

9.3 Advances in cloud microphysics

Arctic low-level stratus clouds: The analysis of flights in stratiform cloud decks in the Arctic boundary layer provided first insights into the spatial variability of these clouds on scales below 10 cm. In particular, the spatial distribution of droplets among the two size modes in the cloud top entrainment zone has been examined. Previous investigations (Klingebiel et al., 2015) suggested a well-mixed state, even on the smallest scales. However, the measurements from HALOHolo could show that these segments are not always uniformly mixed and some cloud volumes have clusters or filaments of droplets from either the small or the large mode of the size distribution. One example was found where two droplet populations of distinct particle size were well-mixed on spatial scales up to 10 cm.

Another result from the measurements in Arctic stratocumulus clouds is the observation of high variability in particle concentration and liquid water content on spatial scales as small as ten meters. Almost empty holograms and very densely populated holograms did sometimes follow one another and the droplet number concentration was not correlated with the position relative to the cloud edge. Throughout the entire data set containing four flights and more than 100 km of flight distance in cloud, the signature of inhomogeneous mixing was dominant. After Beals et al. (2015) confirmed the presence of inhomogeneous mixing in cumulus clouds, this has now been accomplished for the sampled Arctic stratiform boundary clouds. The analysis done in this work yields strong reasons to assume

that inhomogeneous mixing is supposedly the dominant mixing process in the majority of clouds.

Glaciation of cumulus clouds in the tropics: In another field campaign, the microphysical evolution of tropical cumulus clouds in the process of glaciation has been examined. In accordance with results from another field campaign (Lawson et al., 2015), the beginning of ice formation could be attributed to small irregular ice particles, probably produced by freezing raindrops. Any of the cloud passes had ice crystal number concentrations which were by a factor of 100 or 1000 higher than the number of estimated ice nuclei. Also, the spatial distribution of ice crystals and cloud droplets in the rime-splintering zone of the cloud was analyzed. Here, the hypothesis of spatial homogeneity (i.e. the distribution of hydrometeor positions in three dimensional space of the holographic sample record) between the ice and liquid phase from Korolev and Isaac (2006) was examined. Local clustering of ice particles was observed in all cloud passes that contained a significant ($IWC/LWC > 0.1$) amount of ice, but it occurred on average in less than 10 % of the local cloud volumes examined.

High number concentrations of columnar ice crystals ($500 L^{-1}$ or more) were often measured in the same 35 cubic centimeters as heavily rimed particles. The width of columnar protuberances on the rimed particles was measured and compared with the width of the isolated columns, yielding an agreement of the size distributions of the two. In some rare cases, ice columns were found in a radius of less than two centimeters away from a rimed particle. It is possible that some of these columns might have been ejected by a rimed particle. The number of these spicules or protuberances per particle was determined for one cloud pass and due to strong correlation between particle diameter and number of spicules, a linear fit was performed. The empirical relationship derived from this fit was used to estimate the number concentration of spicules available for splintering, which was about a factor of seven higher than the measured concentration of columns. Thus, the number concentration of columns could be explained if only a fraction of 15 % of the spicules would produce a splinter. Although this application of in-situ holographic imagery provides hints for the occurrence of such processes in atmospheric clouds, nevertheless laboratory measurements are needed to quantify the frequency of splinters being created from a particle with spicules, and also the rate at which these spicules tend to grow and break off.

Different types of cirrus clouds: The spatial structure in cirrus clouds was analyzed on scales between some 100 m and some 10 km from data obtained during a flight through wave cirrus. From the four examples of mixing between two particle size modes, one could be related to possible wave breaking, another one is suspected for being induced by shallow convection and another one could be caused by sedimentation and partial sublimation of particles from another cloud layer aloft. These features vary on spatial scales of some kilometers. One cloud pass with a return flight along the same track had a much different microphysical structure than the return flight due to a nearly total absence

of the small particle mode. This flight was characterized by a high abundance of pristine bullet rosettes.

Two other flights of the same field campaign had different microphysical conditions. One flight could be attributed to liquid-origin cirrus in a warm conveyor belt with a persistent high ice water content in an environment that is characterized by relatively strong updrafts. The particle habit analysis could be used to identify a possible liquid origin by the presence of rimed particles. Also, the total number-weighted size distribution could be expressed as a superposition of log-normal distributions from the individual particle habits. The other flight was interpreted as in-situ cirrus ahead of a developing warm front. Its vertical structure was investigated in a descending staircase profile and it revealed similarities with the liquid-origin cirrus in terms of the vertical structure of particle number concentration.

Tropical convective anvil outflows: Ice crystals in a convective outflow sampled over Northern India had a very similar particle size distribution in comparison with data obtained from a mesoscale convective system over Western Africa. The comparison of the recent data (10 August 2017) measured at the cold point tropopause at 17km altitude with the anvil outflow from Frey et al. (2011) shows a good agreement of the particle size distributions. However, the subvisual cirrus clouds, also found in Frey et al. (2011), have a strikingly different particle size distribution in comparison with the anvil outflow over India. There are data available from two more flights under similar conditions which still need to be investigated in terms of their particle size distributions.

9.4 Future work

Besides the commonly mentioned necessity of additional measurements to support the actual findings, there are several very specific questions still to be answered.

Automation of hologram analysis: Recently, the analysis of holograms is fully-automatic except for the step of particle classification. In simple systems (monodisperse spectra of spherical particles) it is fairly easy to do the classification automatically as a method based on the analytic solution of the diffraction pattern from a spherical aperture can be applied to a number of hologram planes reasonably fast. Anything which is below a certain maximum amplitude value can be discarded as it is likely not a particle. However, this simple approach is impossible for a broader size spectrum and / or aspherical particles, and the pool of available methods is reduced greatly. The most promising candidate in recent advances of computer sciences is the usage of neural networks to obtain a fully-automatic particle classification scheme. It should be noted that a neural network needs to be fed with training data, which requires human interaction in the first place until the network is able to detect the right features for a reliable classification.

It might be possible that the process of automation can get even closer to the process of data acquisition. Digital signal processing is making considerable advances right now, and units similar to image processors in digital cameras might be used in future holographic

instruments to reconstruct the holograms instantly and store the processed holograms on disk.

Instrument characterization: Concerning the characterization of HALOHolo, there are still unresolved questions in terms of the particle detectability and its impact on derived data products. Occasionally, the hologram background changes over time and it is yet unclear how this change in the background translates into errors in terms of particle detection and sizing. While the measured data from several field campaigns and laboratory measurements delivered a solid foundation in terms of measuring plausible concentrations and sizes of particles (which are comparable to results reported from other types of instruments), small errors on the order of a few percent have not yet been quantified. A thorough calibration of the entire sample volume in terms of (a) particle detectability / visibility and (b) particle sizing accuracy is inevitable to push the limits further towards even higher data quality.

Analysis methods for finding clusters or filaments of particles are hard to calibrate as there is no known technique to generate an ensemble of water droplets or ice particles with well-defined spatial distributions. In a limited way it is possible to enhance the probability of particle filaments by choosing a suitable setup in a cloud or turbulence chamber. But the same drawback applies for these experiments as for atmospheric in-situ measurements: The experiment cannot be repeated with exactly the same outcome.

Limitations of airborne in-situ measurements in terms of measurement techniques: This paragraph is about the discussion of limitations in the measurement techniques to obtain particular data from an ensemble of cloud hydrometeors. There are two major remaining issues that are widely discussed in the scientific community where a solution would be considered as a very big leap towards a better understanding of clouds: The first issue is the phase discrimination, i.e. the distinction between ice and supercooled liquid water. As already stated by Korolev et al. (2017), the majority of instruments relies on particle shape to differentiate between ice and liquid water. This statement raises the question whether it is possible to distinguish a smooth, transparent quasi-spherical ice particle from a supercooled liquid water droplet. In fact, this is one of the toughest challenges in experimental Atmospheric Sciences. While it is possible to discern a difference between opaque ice particles or particles with a certain degree of surface roughness and a pure-liquid particle via forward scattering of light (cf. Ulanowski et al. (2014)), the distinction between the two becomes much more vague in case of a smooth, transparent and round ice particle. There are some peculiarities found in the light wave interacting with ice particles (cf. Raupach (2009b)) that might provide a possibility to make particle phase discrimination in holography easier. Until then, we have to deal with the fact that a reliable discrimination between ice and liquid water for small particles is not practical.

The second issue is the estimation of particle mass. While the usage of spherical geometry and a known density is great for estimating the mass of water droplets and tends to have error bars around three times the particle sizing uncertainty, this is much more

difficult for ice. Recently, power-law relationships from laboratory experiments are used to relate the particle mass to its area cross-section or its maximum dimension. The main unknowns, even in holography, are the particle outline in the third dimension and the possible containment of air inside the particle. While it is possible to determine the three-dimensional outline of a particle from crossed-beam holography as done by Raupach et al. (2006), the small size of the sample volume for stereo imaging is a drawback when it comes to the estimation of IWC and related quantities. The analysis of local cloud volumes in convective clouds (Chapter 7 of this thesis) has shown that LWC and IWC can fluctuate by two or more orders of magnitude between two adjacent samples. Thus, a major challenge is (a) to have the largest possible sample volume per sample and (b) to make the spatial gap between two neighboring sample volumes as small as possible. To estimate the volume of air enclosed in a particle, which is important to determine the particle density, is even harder. Thus, it appears likely that power-law relationships will play an important role in experimental cloud physics also in the following decade.

Unresolved questions in Atmospheric Sciences: The influence of the electromagnetic force on particles is well-understood for single particle systems in the laboratory but there are numerous open questions related to atmospheric electricity. One major desire is to know whether shallow cumulus clouds rather have a unipolar charge or a bipolar charge and also how the electromagnetic force interacts with an ensemble of cloud hydrometeors. The question behind the latter is "Are differences in the spatial distribution of cloud droplets measured in the atmosphere compared to numerical simulations due to inaccuracies of the initial conditions or due to a missing consideration of the electromagnetic force in the model equations?" A unipolar charge would likely lead to anti-clustering of particles as the same sign of charge on the particles acts as a repulsive force. In contrast to the unipolar case, particle clustering would be preferred in case of a bipolar charge as particles with a different sign of charge attract each other. Also, electric charge is known to stabilize water droplets in a water-subsaturated environment (Nielsen et al., 2011). Measuring particle mass in-situ is challenging, but measuring the charge distribution of particles in-situ is among the trickiest tasks in Atmospheric Sciences. However, the attractive or repulsive force due to particles being charged is likely a small effect as a back-of-envelope calculation with typical charge densities (about 100 electrons per particle and 20 microns of particle diameter) resulted in inter-particle distances of 1 micron or smaller to be on the same order of magnitude as gravity on Earth.

As mentioned before, it is highly desirable to measure not only position and size of particles, but also to gain information about the particle motion in all three dimensions and to close the gap between the intra-hologram scale and the inter-hologram scale. Thus, a holographic system with a very large detector size and a very fast camera is needed. Recently, this is a technological issue as the fastest solid state drives can handle about 2 GB per second in writing, but in a few years it might be possible to write ten times as fast. In terms of the maximum possible frame rate, the recently used solid state lasers can be operated in a very stable way at pulse repetition frequencies around 1 kilohertz,

so 1000 frames per second would already be possible with the recent laser technology. From the software side, efficient algorithms for particle tracking under non-uniform flow conditions are under development. Particle tracking is also a way to automate the process of classification as a major difference between particles and noise is that particles can be tracked. This method would increase the known parameters of a particle ensemble significantly as not only size, shape and position, but also velocity would be known. One possible way towards closing the spatial gap is the usage of a kite or a balloon, which remains stationary as the cloud passes by (similar to the ground-based measurements of clouds with GipfelHolo at the Jungfraujoch). For wind speeds not exceeding 10 m s^{-1} , a spatial inter-hologram resolution of about 1.5 m or less is possible with the hardware of HALOHolo.

From the investigation of two ice crystal precipitation events at the Jungfraujoch station, the easiest approach for high-resolution measurements of ice clouds or ice crystal precipitation is to perform ground-based measurements of diamond dust or precipitation from cirrus clouds aloft. Low-tropospheric ice clouds resemble similar microphysical properties as cirrus clouds and are easier to sample in-situ than cirrus clouds. However, they are more difficult to encounter in the limited time-frame of a field campaign. A continuously operating stand-by holographic instrument on a mountain top like the Jungfraujoch station would be a better suited approach as it could be operated anytime via remote control and interesting cloud cases could be targeted more specifically. In addition to the meteorological data and the holograms it would be nice to have additional sensors installed to measure turbulence-related quantities that could be related to the observed spatial distributions of particles.

Part III

Appendix

A

Ground-based measurement of ice crystal precipitation at the Jungfraujoch research station during CLACE 2013

This appendix is not shown in the online version of this work due to copyright restrictions. Access is provided by the publisher via the following link: <https://doi.org/10.1175/JAMC-D-16-0060.1>

B

Technical details of HALOHolo

B.1 Optical properties

The optical system in the camera-side lens tube of HALOHolo has to provide a magnification by $1.87 \times$ and is needed to move the hologram plane from the detector close to the camera-side instrument window. As a commercially built microscope objective with suitable optical properties (doubly telecentric, small enough numerical aperture, transparent at $\lambda = 355 \text{ nm}$) was not available, a customized optical design was needed. The optimum properties of the imaging lens system were obtained via simulations with the optical design program Zemax OpticStudio from Zemax LLC where the optical setup of HOLODEC (Spuler and Fugal, 2011) acted as prototype. Speckle effects introduced by reflections of the surfaces cause degradation of holograms (Borrmann, 1991) but these random patterns are removed by the digital filtering method described in Chapter 4.

Table B.1: Optical parameters of the elements within the laser side tube and camera side tube of HALOHolo. Displayed are the element type (lens, window, prism), element number (starting from the laser side, pinhole = element 0), center distance z to pinhole, the radius of curvature r_1 for the incident beam and r_2 for the exiting beam and the center thickness d . The two values of z marked with an asterisk correspond to the hologram plane (the first one at $z = 535.5 \text{ mm}$ equals $z = 0 \text{ mm}$ in hologram reconstruction). Positive values of r_1 indicate a concave curvature, positive values of r_2 indicate a convex curvature. Additionally, the lens diameter D and the glass type are listed. For the prisms and the windows, the aperture diameter is given for D instead. Unless otherwise noted, the surfaces have an accuracy of at least $\lambda/10$ w.r.t. 633 nm .

Element type	Number	z [mm]	r_1 [mm]	r_2 [mm]	d [mm]	D [mm]	Glass type
10 μm pinhole	0	0	∞	∞	0	10^{-2}	N/A
Lens	1	96.3	26.1	-26.1	2.6	25.4	Suprasil
Lens	2	227.1	∞	154.5	4.8	38.1	Suprasil
Lens	3	254.5	∞	154.5	4.8	38.1	Suprasil
Prism	4	365.5	∞	∞	42.0	34.0	PBM8Y
Window	5	375.5	∞	∞	10.0	28.4	Sapphire
Window	6	535.5*	∞	∞	10.0	28.4	Sapphire
Prism	7	561.5	∞	∞	42.0	34.0	PBM8Y
Lens	8	596.0	210.5	78.7	6.96	40.0	PBL25Y
Lens	9	652.4	-185.4	349.1	5.60	38.9	PBL25Y
Lens	10	660.9	-67.0	2425	6.68	37.4	PBM8Y
Lens	11	681.6	-31.5	-21.7	12.07	26.7	PBL25Y
Lens	12	698.1	41.3	-76.6	4.05	16.4	PBM8Y
Lens	13	735.3	-257.7	92.0	6.55	37.4	PBL1Y
Lens	14	747.2	-87.6	159.5	7.63	40.1	PBL1Y
Lens	15	800.8	47.2	-158.8	4.40	35.9	BSL7Y
Lens	16	844.1	-67.6	-1757	8.90	51.2	PBM8Y
Filter	17	856.1	∞	∞	4.0	50.0	Suprasil
Detector	18	873.2*	∞	∞	0.0	50.0	N/A

Table B.2: Parameters of the optical glasses as given in Table B.1 used for the optics of HALOHolo. Shown are the index of refraction n_{opt} and the linear thermal expansion coefficient α_L for each individual glass type. The data are valid for temperature $T = 20^\circ\text{C}$ and pressure $p = 1013\text{ hPa}$.

Glass type	n_{opt}	α_L [$\mu\text{m m}^{-1} \text{K}^{-1}$]
BSL7Y	1.538	6.80
PBL1Y	1.583	9.30
PBL25Y	1.623	8.70
PBM8Y	1.640	8.50
Sapphire	1.796	6.65
Suprasil	1.476	0.51

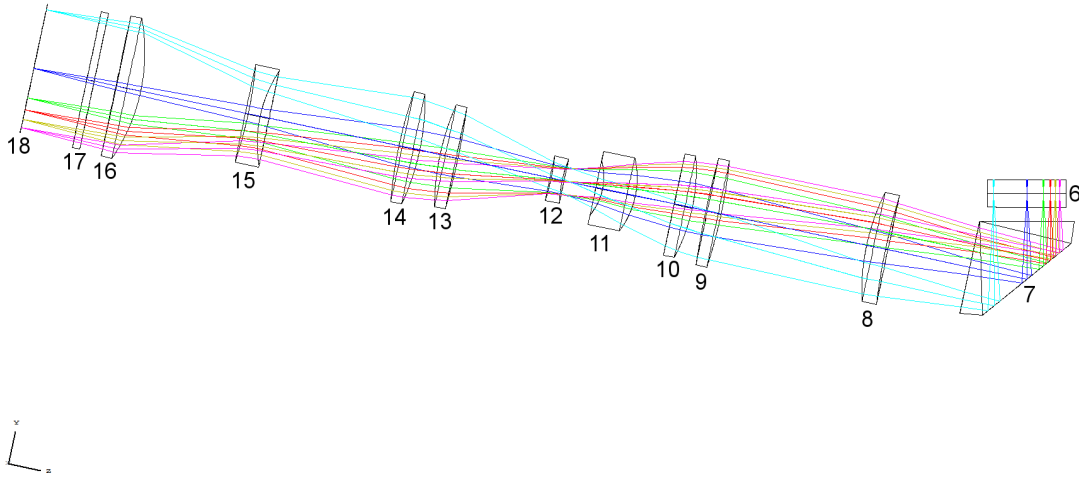


Fig. B.1: Optical design of the camera-side imaging system. The beam originates from the sapphire window before entering the prism (right) and then passes the system of nine lenses and a 355 nm interference filter before arriving on the detector (left). The lenses are spherical lenses. All optical elements are shown with their corresponding number as in Table B.1.

B.2 Electronics unit

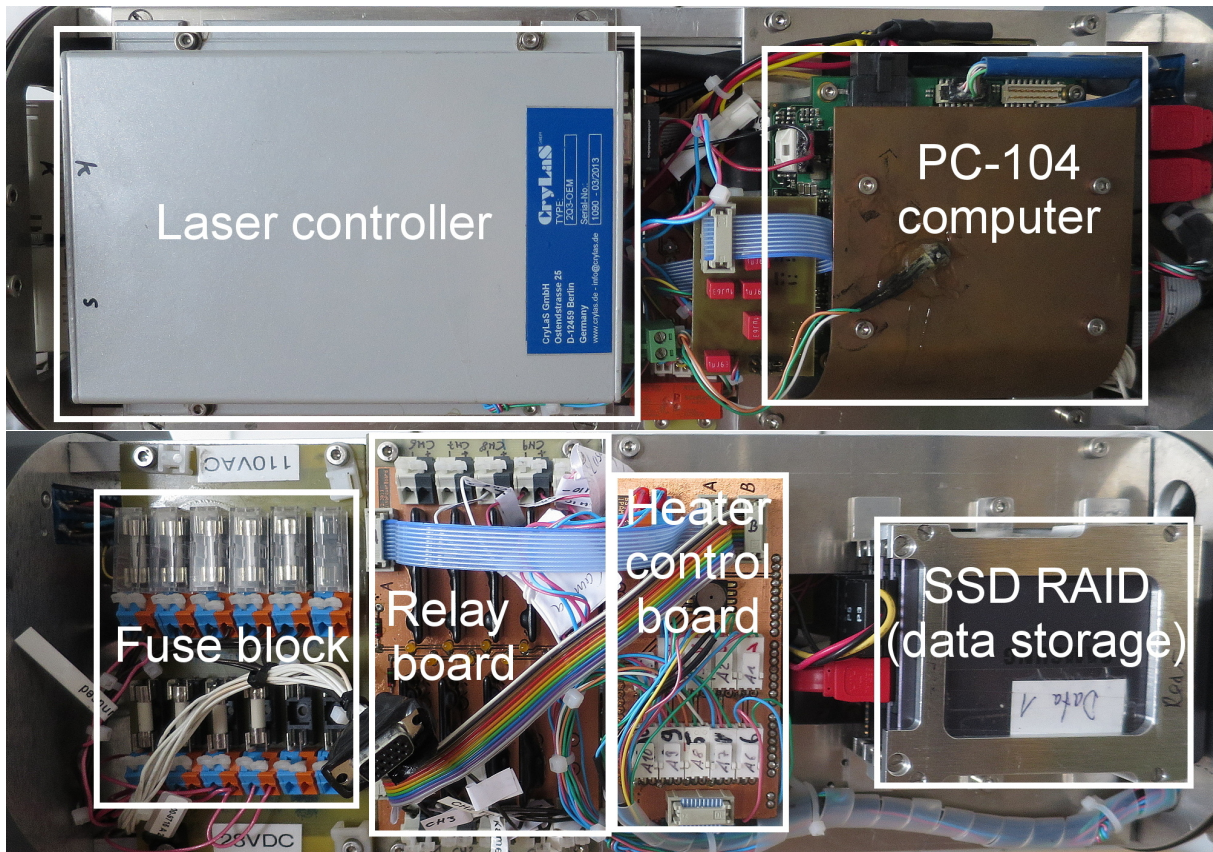


Fig. B.2: The electronics inside HALOHolo: The fuse block distributes the power to the components (110 VAC for the heater cartridges, 28 VDC for the other components). Ten independent temperature sensors measure the temperature of the instrument components and the components are switched off by the corresponding relay if the temperature range for safe operation is exceeded. The hologram sequences (captured by the camera and processed by the PC-104 computer) are stored on the SSD RAID.

B.3 Size calibration

Table B.3: Calibration results for HALOHolo using three different particle size estimators. The bead sizes displayed in the first line of each block (identical for "Far", "Middle" and "Near") were measured under a microscope via visual inspection and pixel counting (0.9 μm pixel height / width). The displayed Mean and STD as well as the error bars, r^2 and $RMSE$ were obtained from a nonlinear least-squares fit using a Normal distribution. n is the number of particles in each sample. The different size measures are the sign-matched filter algorithm (threshold-independent), Equivalent size (using a relative threshold) and Area-equivalent diameter (using a relative threshold) as defined in Subsection 3.3.3. The terms "Far", "Middle" and "Near" refer to the average z position where the beads have been dispersed in the sample volume. This table only lists the results for the 8 μm and 15 μm beads, the 30 μm beads are in Table B.4

Sample	Manufacturer info		Measured		n	r^2	$RMSE$
	Mean [μm]	STD [μm]	Mean [μm]	STD [μm]			
8 μm Far	7.9 ± 0.8	1.5	8.25 \pm 0.04	1.43 \pm 0.06	225	0.999	0.014
Sign-matched filter			7.42 \pm 0.09	1.65 \pm 0.13	170	0.989	0.034
Equivalent size			11.88 \pm 0.03	2.96 \pm 0.06	170	0.994	0.021
Area-equivalent diameter			10.30 \pm 0.10	3.04 \pm 0.15	170	0.997	0.021
8 μm Middle	7.9 ± 0.8	1.5	8.25 \pm 0.04	1.43 \pm 0.06	225	0.999	0.014
Sign-matched filter			7.62 \pm 0.05	1.53 \pm 0.09	844	0.996	0.023
Equivalent size			10.63 \pm 0.04	1.83 \pm 0.05	844	0.981	0.035
Area-equivalent diameter			9.55 \pm 0.14	1.69 \pm 0.19	844	0.991	0.035
8 μm Near	7.9 ± 0.8	1.5	8.25 \pm 0.04	1.43 \pm 0.06	225	0.999	0.014
Sign-matched filter			7.52 \pm 0.06	1.39 \pm 0.09	546	0.995	0.025
Equivalent size			9.55 \pm 0.03	1.18 \pm 0.05	546	0.989	0.03
Area-equivalent diameter			8.43 \pm 0.07	1.06 \pm 0.09	546	0.997	0.02
15 μm Far	14.5 ± 1.0	1.7	15.38 \pm 0.05	1.72 \pm 0.07	225	0.999	0.013
Sign-matched filter			13.13 \pm 0.10	3.37 \pm 0.15	1200	0.995	0.027
Equivalent size			15.91 \pm 0.01	2.13 \pm 0.02	1200	0.996	0.018
Area-equivalent diameter			15.14 \pm 0.04	2.05 \pm 0.05	1200	0.999	0.011
15 μm Middle	14.5 ± 1.0	1.7	15.38 \pm 0.05	1.72 \pm 0.07	225	0.999	0.013
Sign-matched filter			12.70 \pm 0.33	3.63 \pm 0.53	102	0.937	0.076
Equivalent size			14.99 \pm 0.02	1.71 \pm 0.05	102	0.995	0.022
Area-equivalent diameter			14.30 \pm 0.08	1.77 \pm 0.11	102	0.996	0.024
15 μm Near	14.5 ± 1.0	1.7	15.38 \pm 0.05	1.72 \pm 0.07	225	0.999	0.013
Sign-matched filter			13.70 \pm 0.07	2.79 \pm 0.11	335	0.996	0.021
Equivalent size			14.78 \pm 0.02	1.53 \pm 0.03	335	0.996	0.020
Area-equivalent diameter			14.18 \pm 0.05	1.58 \pm 0.07	335	0.998	0.016

Table B.4: As in Table B.3 for the 30 μm glass beads.

Sample	Manufacturer info		Measured		n	r^2	$RMSE$
	Mean [μm]	STD [μm]	Mean [μm]	STD [μm]			
30 μm Far	29.5 ± 1.0	1.9	30.04 ± 0.07	2.06 ± 0.10	225	0.998	0.019
Sign-matched filter			29.28 ± 0.04	1.71 ± 0.05	670	0.999	0.014
Equivalent size			29.25 ± 0.01	1.91 ± 0.01	670	0.999	0.007
Area-equivalent diameter			28.89 ± 0.03	1.95 ± 0.04	670	0.999	0.011
30 μm Middle	29.5 ± 1.0	1.9	30.04 ± 0.07	2.06 ± 0.10	225	0.998	0.019
Sign-matched filter			29.11 ± 0.05	1.72 ± 0.07	365	0.998	0.018
Equivalent size			28.92 ± 0.01	1.85 ± 0.02	365	0.997	0.015
Area-equivalent diameter			28.60 ± 0.03	1.93 ± 0.05	365	0.999	0.013
30 μm Near	29.5 ± 1.0	1.9	30.04 ± 0.07	2.06 ± 0.10	225	0.998	0.019
Sign-matched filter			29.78 ± 0.13	1.24 ± 0.23	28	0.981	0.049
Equivalent size			29.86 ± 0.07	1.61 ± 0.12	28	0.989	0.032
Area-equivalent diameter			29.61 ± 0.08	1.64 ± 0.14	28	0.990	0.033

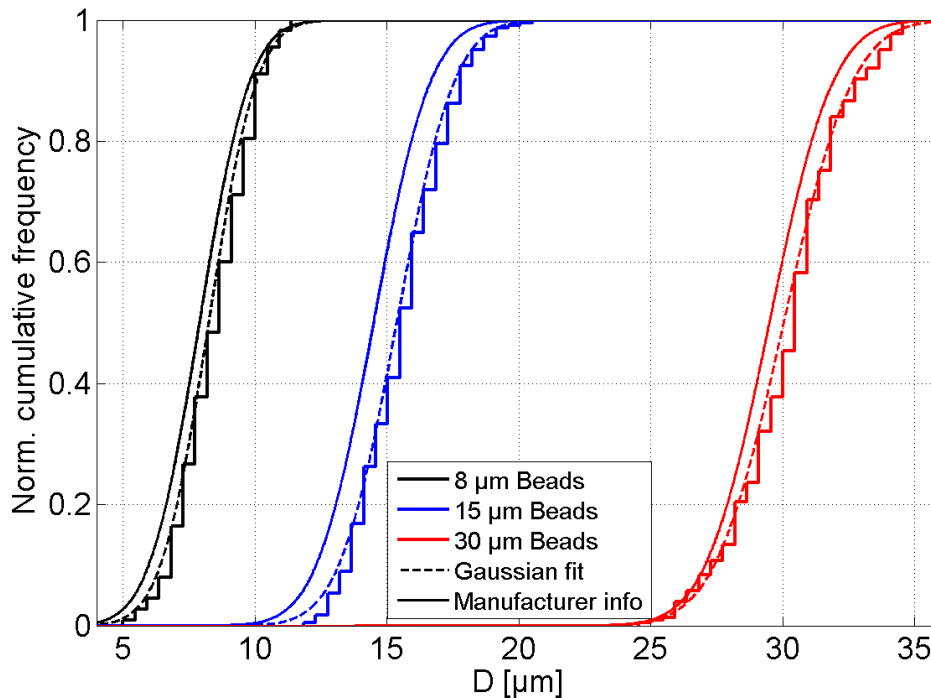


Fig. B.3: Cumulative size distributions from the glass beads examined under the microscope. The manufacturer info is shown as thin solid lines, the fitted Gaussian (Normal) distribution is shown as dashed lines. Each sample consists of 225 particles, which yields an overall error from counting statistics of $1/15$.

C

Details of the hologram analysis software

C.1 Particle metrics

Table C.1: List of the recently used particle metrics (in alphabetical order). Along with the acronym and the source where the metric is calculated from, a description of each metric is given. Table C.1 contains only the basic metrics. Metrics combined from other metrics are listed in Table C.3.

Acronym	Calculated from	Description
alvl	Amplitude value of pixels below threshold	Particle mean amplitude level of the particular particle patch
area	Number of thresholded pixels	Particle area obtained from counting the number of pixels below the threshold
asprat	Lateral distribution of thresholded pixels	Particle aspect ratio, defined as the major axis length divided by the minor axis length
balvl	Amplitude value of pixels above threshold	Mean background amplitude level of the particular particle patch
eqsiz	Lateral distribution of thresholded pixels	Particle equivalent size, defined as the arithmetic mean of particle major axis length and particle minor axis length
majsiz	Lateral distribution of thresholded pixels	Particle major axis length calculated from an ellipse fitted to the lateral distribution of thresholded pixels
maxamp	Amplitude values	Maximum of the amplitude value per particle patch
maxampg	Sobel gradient of amplitude values	Maximum of the amplitude gradient value per particle patch
maxcomp	Sobel gradient of complex field values	Maximum of the complex gradient value per particle patch
maxph	Phase values	Maximum of the phase value per particle patch
maxphg	Sobel gradient of phase values	Maximum of the phase gradient value per particle patch
meanamp	Amplitude values	Arithmetic mean of the amplitude value per particle patch
meanampg	Sobel gradient of amplitude values	Arithmetic mean of the amplitude gradient value per particle patch
meancomp	Sobel gradient of complex field values	Arithmetic mean of the complex gradient value per particle patch
meanph	Phase values	Arithmetic mean of the phase value per particle patch
meanphg	Sobel gradient of phase values	Arithmetic mean of the phase gradient value per particle patch

Table C.2: Table C.1 continued.

Acronym	Calculated from	Description
minamp	Amplitude values	Minimum of the amplitude value per particle patch
minampg	Sobel gradient of amplitude values	Minimum of the amplitude gradient value per particle patch
mincompg	Sobel gradient of complex field values	Minimum of the complex gradient value per particle patch
minph	Phase values	Minimum of the phase value per particle patch
minphg	Sobel gradient of phase values	Minimum of the phase gradient value per particle patch
minsiz	Lateral distribution of thresholded pixels	Particle minor axis length calculated from an ellipse fitted to the lateral distribution of thresholded pixels
numzs	Number of particle patches per linked patch group	Number of z slices of the actual linked patch group, proportional to the particle depth of field
orient	Lateral distribution of thresholded pixels	Orientation of the major axis relative to the x axis
ptcharea	Number of pixels in particle patch	Area of the particle patch
ptchngrps	Number of patches in patch group	Number of patches which define the actual patch group
ptchtharea	Number of pixels in particle patch below threshold	Area of the particle patch that is below the amplitude threshold
ptchxsiz	Patch width in pixels	Maximum width of the patch
ptchysiz	Patch height in pixels	Maximum height of the patch
stdamp	Amplitude values	STD of the amplitude value per particle patch
stdampg	Sobel gradient of amplitude values	STD of the amplitude gradient value per particle patch
stdcompg	Sobel gradient of complex field values	STD of the complex gradient value per particle patch
stdph	Phase values	STD of the phase value per particle patch
stdphg	Sobel gradient of phase values	STD of the phase gradient value per particle patch
thresh	Threshold value	Value of the amplitude threshold
xpos	Particle location	Particle x center position
ypos	Particle location	Particle y center position
zLInd	Location of focal plane	Local index of z for the focal plane of the particle
zpos	Particle location	Particle z center position (focal plane)

Table C.3: As in Table C.1 for the combined metrics.

Acronym	Calculated from	Description
d2c	xpos, ypos	Distance to the image center
d2ne	xpos, ypos, zpos	Distance to the nearest edge in lateral direction or z direction
d2nep	zLInd, numzs	Distance to the nearest end patch (in z direction)
dsqoverlz	numzs, eqsiz	Ratio of particle area to the number of slices in the actual linked patch group
pampdepth	alvl, balvl	Depth of the particle amplitude relative to the background amplitude
phfl	Traces of maxph and minph	Maximum difference of phase along z
rngamp	maxamp, minamp	Range of the amplitude value per particle patch
rngampg	maxampg, minampg	Range of the amplitude gradient value per particle patch
rngcomp	maxcomp, mincomp	Range of the complex gradient value per particle patch
rngph	maxph, minph	Range of the phase value per particle patch
rngphg	maxphg, minphg of phase values	Range of the phase gradient value per particle patch
underthresh	thresh, minamp	Minimum amplitude value below threshold

C.2 Particle reconstruction after shattering

Under certain assumptions it is possible to approximate the size, area and mass of a shattered particle from its shards. At first, it needs to be assumed that all shards entered the sample volume. Then, a useful assumption is that the largest fragment is likely the one where the others can be "glued to" in order to reconstitute the original particle. While the fragments can be seen in the volume affected by shattering, it is unclear from which part of the original particle they broke off. Thus, their overall contribution to the total area should be weighted by a factor of $2/3$ to account for the part that is hidden in the third dimension. With these assumptions, the total particle area A_{tot} can be estimated as the sum of the area from largest fragment (with index k) and all the other fragments (with index $i = 1, 2, \dots, N_{shards}$). These assumptions yield Eq. 4.14, here repeated as Eq. C.1.

$$A_{tot} = A_k + \frac{2}{3} \sum_{\substack{i=1 \\ i \neq k}}^{N_{shards}} A_i = \frac{1}{3} A_k + \frac{2}{3} \sum_{i=1}^{N_{shards}} A_i \quad (\text{C.1})$$

From the calculated area A_{tot} the mass is estimated via the power law relationship of Baker and Lawson (2006) (Eq. 2.12 in Section 2.3).

As the original aspect ratio is unknown, two commonly used assumptions are either spherical geometry or conservation of the aspect ratio of the largest fragment. The area-equivalent diameter $D_{A,tot}$ is calculated by assuming spherical geometry. Further research is needed to determine whether conservation of aspect ratio or spherical geometry gets closer to the actual particle maximum and minimum dimension. Estimating $D_{A,tot}$ is straightforward, shown in Eq. C.2.

$$D_{A,tot} = 2\sqrt{A_{tot}/\pi} \quad (\text{C.2})$$

Conservation of the aspect ratio means that the major axis length D_{max} divided by the minor axis length D_{min} of the largest fragment k is kept constant. Thus, the term A_{tot}/π in the root is weighted by the aspect ratio or its reciprocal to yield major and minor axis length $D_{min,tot}$ and $D_{max,tot}$ of the original particle (Eq. C.3 and C.4).

$$D_{min,tot} = 2\sqrt{\frac{A_{tot}D_{min,k}}{\pi D_{max,k}}} \quad (\text{C.3})$$

$$D_{max,tot} = D_{min,tot} \frac{D_{max,k}}{D_{min,k}} \quad (\text{C.4})$$

$$(\text{C.5})$$

The equations in this part of the Appendix should be used with care as none of the assumptions used for derivation of Eq. C.1 - C.4 is certainly fulfilled for an actual shattering event. Shattering experiments in the laboratory with particles of known shape, size and mass would be very helpful to quantify the uncertainties of particle reconstruction from a large number of fragments.

D

HALOHolo characteristics and uncertainties

D.1 Spatial dependence of signal strength

Here, the individual patterns of the spatial dependence of the signal strength for a variety of simulated particle sizes in synthetic holograms with the same geometry as for HALO-Holo are shown in Fig. D.1 to D.3. The size increment was $1 \mu\text{m}$, x was kept constant at 0, y was varied in 55 equally-spaced increments from 0 to half the detector minimum dimension. For the z position, an increment of 5 mm was used.

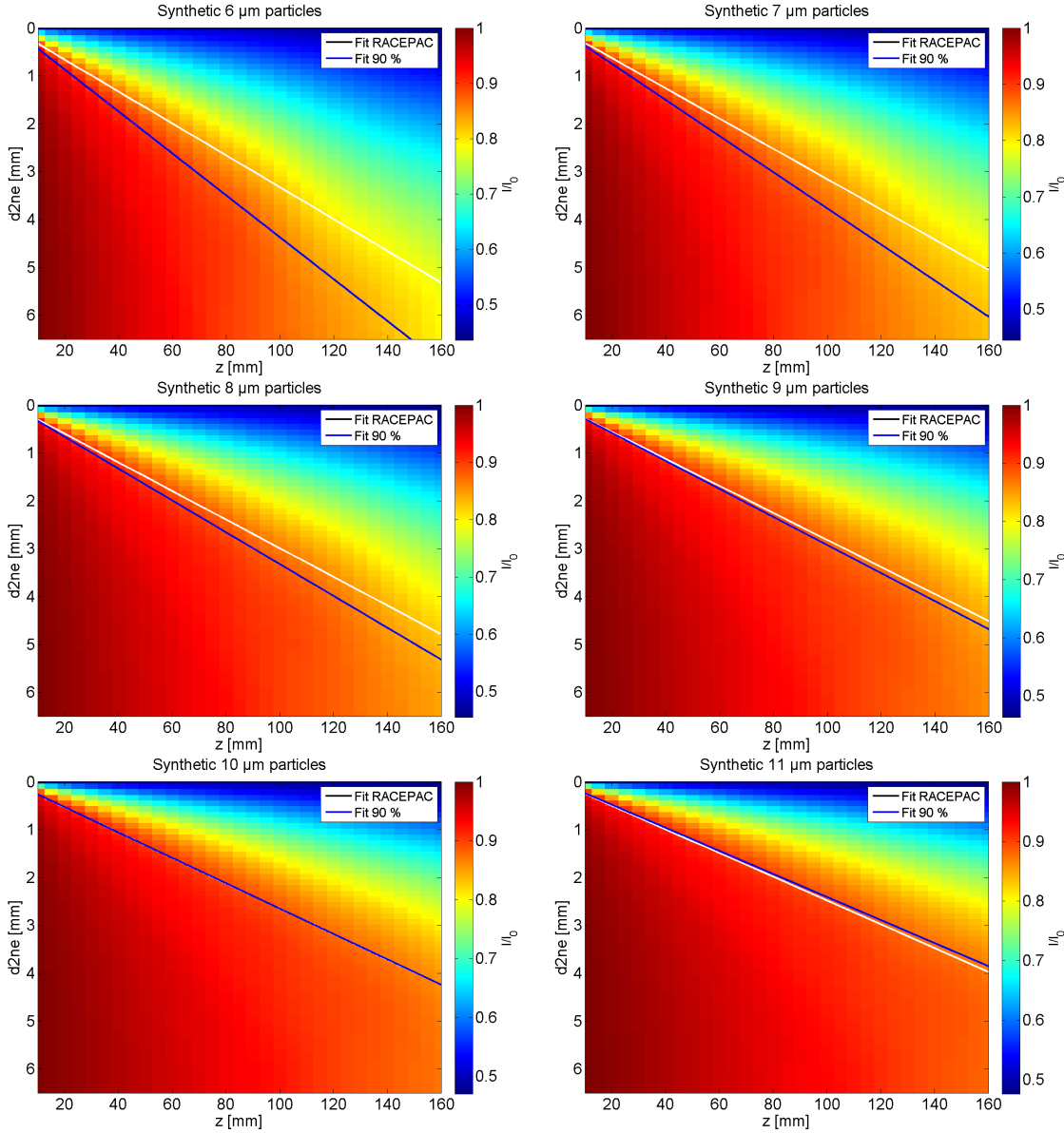


Fig. D.1: Spatial dependence of the relative signal strength for synthetic particles with diameters of 6 and 7 microns (top), 8 and 9 microns (middle) and 10 and 11 microns (bottom). The blue line (Fit 90 %) represents a linear fit of the 90 % signal strength threshold with forced zero offset. The white line (Fit RACEPAC, black in legend) represents the fit as obtained from airborne measurements during RACEPAC, using the equation in Fig. 5.2.

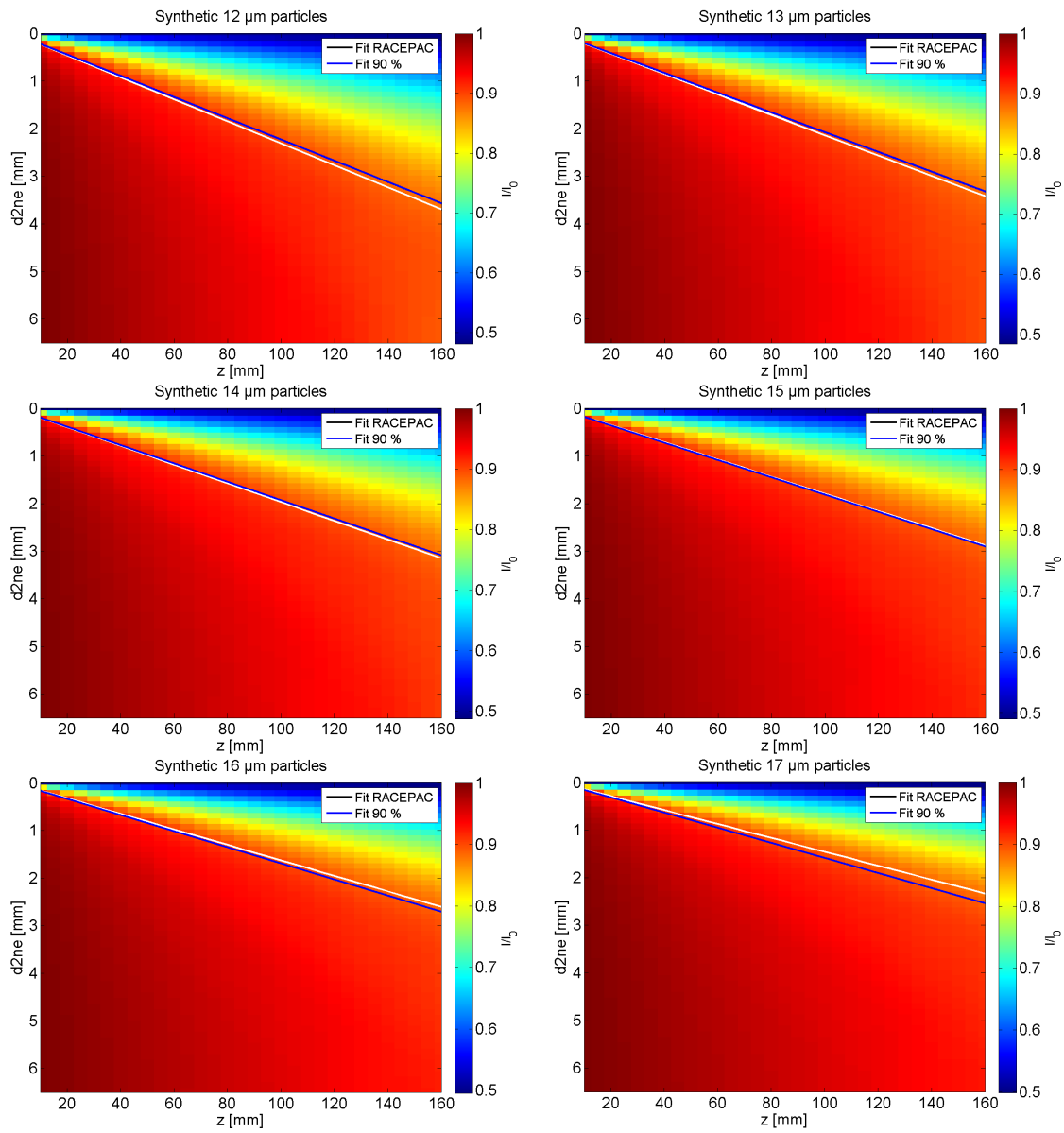


Fig. D.2: As in Fig. D.1 for particle sizes from 12 to 17 microns.

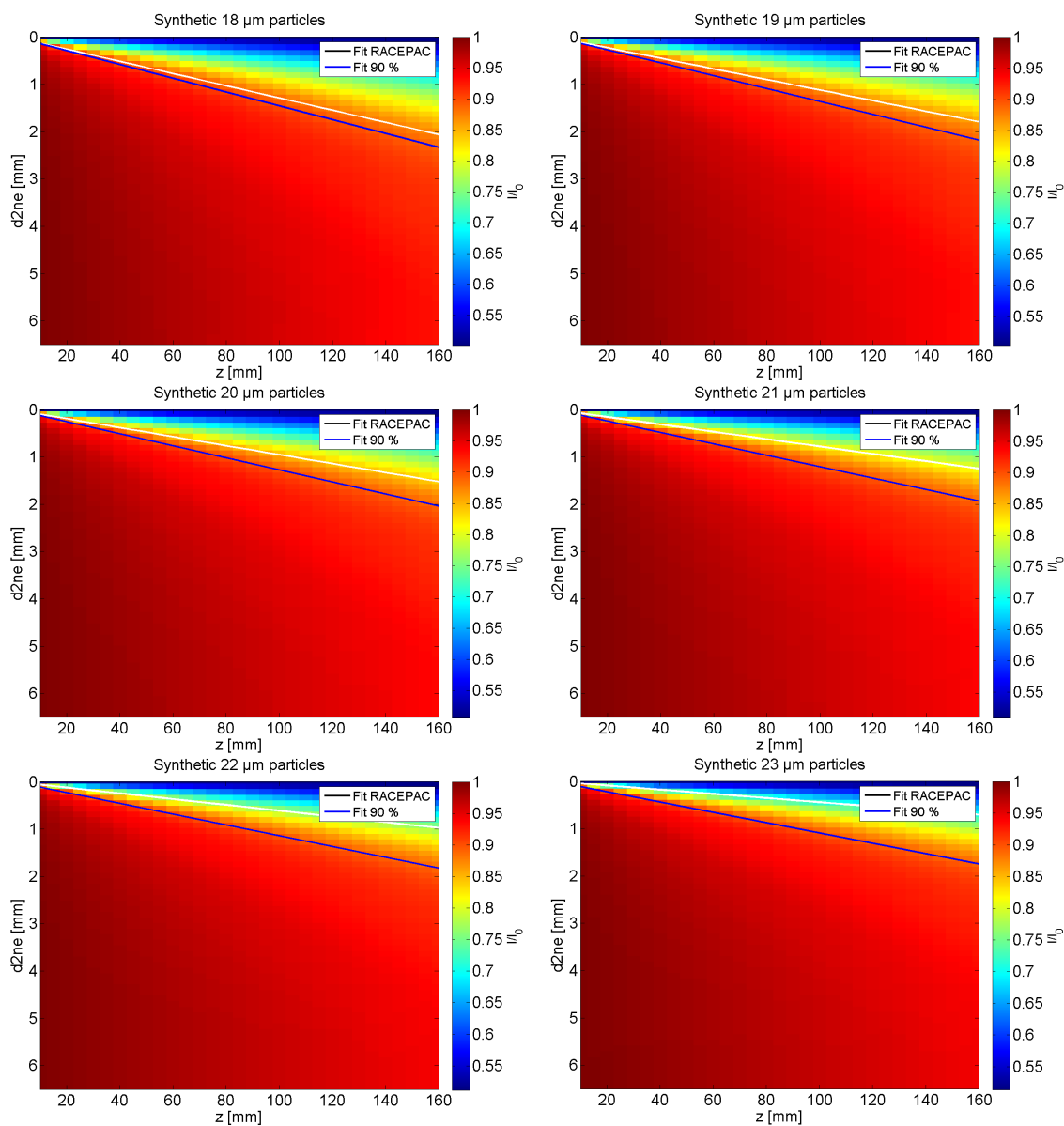


Fig. D.3: As in Fig. D.1 for particle sizes from 18 to 23 microns.

The individual fit parameters for 90 % of relative signal strength as a function of particle position are summarized in Table D.1.

Table D.1: Fit parameters for the 90 % relative signal strength threshold obtained from synthetic holograms.

D [μm]	s_c [mm m^{-1}]	r^2	$RMSE$ [mm]
6	43.78 ± 2.54	0.967	0.165
7	37.71 ± 2.07	0.967	0.168
8	33.24 ± 1.53	0.972	0.151
9	29.27 ± 1.33	0.971	0.144
10	26.50 ± 0.96	0.978	0.123
11	24.07 ± 0.99	0.971	0.146
12	22.30 ± 0.85	0.972	0.144
13	20.76 ± 0.78	0.971	0.148
14	19.30 ± 0.68	0.972	0.146
15	18.15 ± 0.58	0.976	0.137
16	16.93 ± 0.54	0.974	0.140
17	15.88 ± 0.51	0.974	0.133
18	14.58 ± 0.42	0.979	0.109
19	13.63 ± 0.36	0.981	0.095
20	12.74 ± 0.34	0.981	0.088
21	12.08 ± 0.29	0.984	0.075
22	11.40 ± 0.30	0.981	0.080
23	10.90 ± 0.25	0.986	0.065
24	10.29 ± 0.24	0.985	0.062
25	9.83 ± 0.24	0.983	0.062
26	9.40 ± 0.26	0.979	0.067

D.2 Derivation of an instrument response function for HALOHolo

From a variety of particle sizes D and cutoff percentiles P_c determined in Subsection 5.1.2, the dependence of the two fit coefficients from the hyperbola (a_0 and a_1 in Eq. 5.5) was investigated. While the assumption of a parabola was reasonable for a_0 , a_1 could be fitted linearly (see Fig. D.4). Between a P_c value of 60 % and 85 %, the fit agrees well with the data, yielding a $r^2 > 0.98$ for both fits. However, the increase of a_1 as a function of P_c becomes steeper after $P_c = 85\%$, and in this region above 85 %, the first signs of nonlinear behavior have been observed in the relationship between $d2ne$ and z for small D . Thus, the "idealized instrument response function for HALOHolo" (Eq. D.1, which summarizes the results of the study with the instrument model, should be used carefully if cutoff percentiles above 85 % or below 60 % are examined. The same holds for particle sizes which were not within the range of the tested diameters. The resulting $d2ne$ of Eq. D.1 has the same units as z for P_c in % and D in μm .

$$d2ne(z, D, P_c) = 10^{-3} \cdot \left(-1.95 + 0.003(P_c - 68.9)^2 + (5.33P_c - 248.7) \frac{1 \mu\text{m}}{D} \right) z \quad (\text{D.1})$$

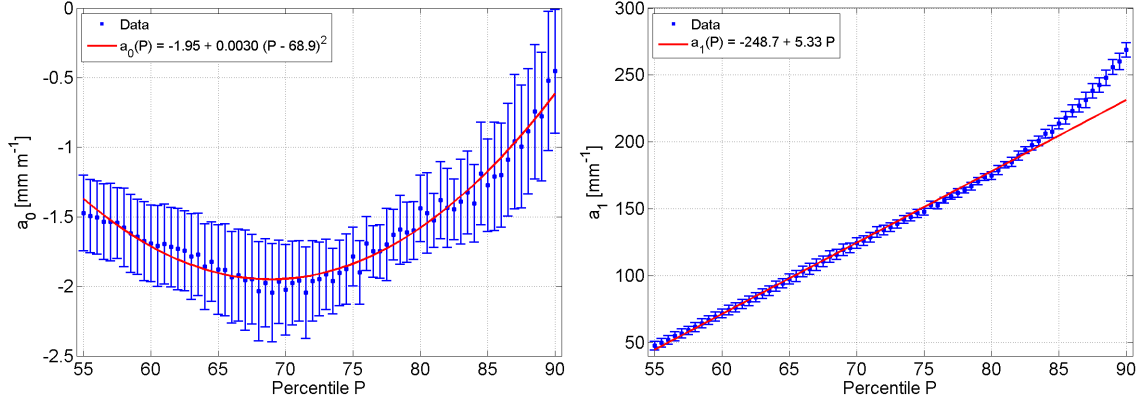


Fig. D.4: Fitted parameters from the hyperbolic fits as a function of P_c . The left panel shows the parabolic fit for a_0 , the right panel shows the linear fit for a_1 . For fitting a_1 , the range of P_c was restricted to $P_c \leq 85\%$. The values of a_0 and a_1 were given in the same unit as s_c . The error bars reflect the uncertainties from the hyperbolic fits to the values of s_c (95 % confidence level).

D.3 Intercomparison of particle size from CAS and HALOHolo

Table D.2: As in Table 5.2 for the CAS compared with HALOHolo at particle sizes larger than $15 \mu\text{m}$.

Quantity	CAS	minsiz	majsiz	eqsiz	OED
Flight 2					
\overline{D} [μm]	19.8	16.1	20.2	18.1	16.6
\overline{D}_g [μm]	19.5	15.6	19.8	17.8	16.1
$\sigma(D)$ [μm]	3.4	4.2	3.7	3.8	3.9
σ_g [μm]	1.2	1.3	1.2	1.2	1.3
Flight 5					
\overline{D} [μm]	19.3	14.1	18.5	16.3	15.0
\overline{D}_g [μm]	19.0	13.4	18.2	15.9	14.5
$\sigma(D)$ [μm]	3.9	4.8	4.0	4.2	4.4
σ_g [μm]	1.2	1.4	1.2	1.2	1.3
Flight 6					
\overline{D} [μm]	18.5	16.3	19.8	18.0	16.8
\overline{D}_g [μm]	18.4	16.0	19.6	17.8	16.4
$\sigma(D)$ [μm]	2.4	3.2	3.0	2.9	3.1
σ_g [μm]	1.1	1.2	1.2	1.2	1.2

D.4 Performance analysis of the sign-matched filter algorithm

Table D.3: As in Table 5.3 for particle sizes of 7.5 μm , 8.5 μm and 9.5 μm .

Quantity	$D_p = 7.5 \mu\text{m}$	$D_p = 8.5 \mu\text{m}$	$D_p = 9.5 \mu\text{m}$
z_0 [mm]	86.5 ± 2.6	141.4 ± 2.2	209.5 ± 32.6
z_1 [mm]	12.7 ± 2.3	12.9 ± 2.2	14.0 ± 8.5
r^2	0.988	0.980	0.736
$RMSE$	0.045	0.036	0.004
z_{90} [mm]	58.6	113.0	> 160.0
$z_{max}(D_p)$ [mm]	137.6	156.0	174.3

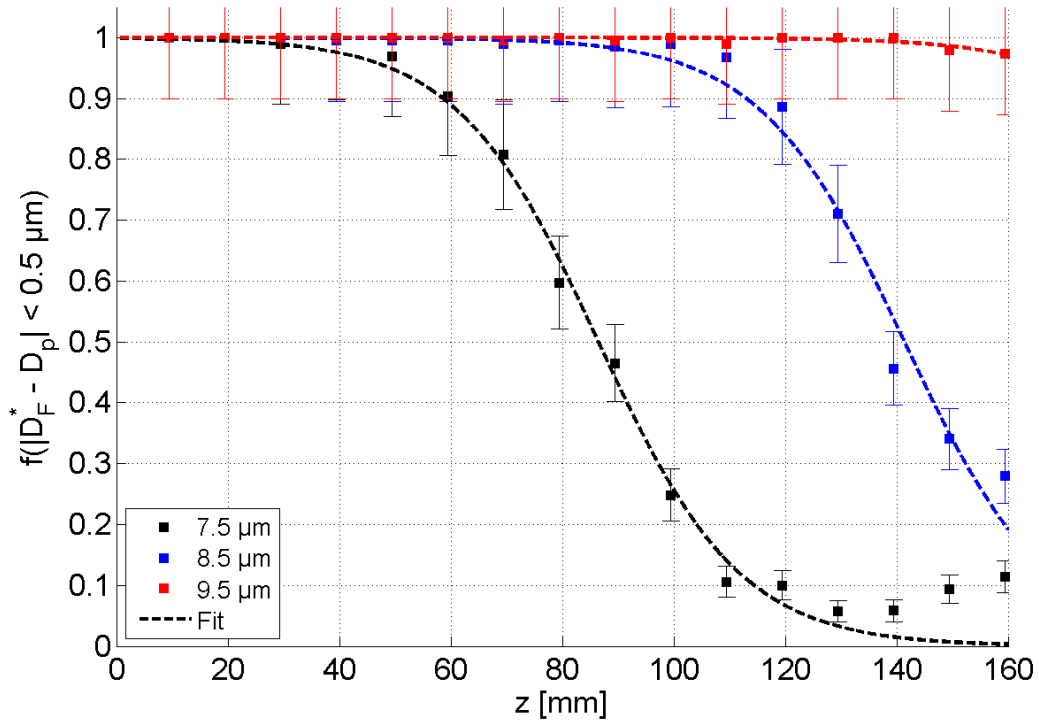


Fig. D.5: As in Fig. 5.10 for particle sizes of 7.5 μm , 8.5 μm and 9.5 μm .

E

RACEPAC campaign overview and additional data

E.1 Overview of the aircraft instrumentation

Table E.1: Specifications of cloud microphysical instruments aboard the Polar 6 aircraft during the RACEPAC field campaign. Described are the measurement principle, the volume sampling rate (VSR) for a TAS of $v_a = 60 \text{ m s}^{-1}$, the size range (D), the size resolution (dD), the distance along flight path between two measured size distributions (L) and the range of number concentrations N . CAS and CIP in Rows 2 and 3 belong to NIXE-CAPS (1), CDP and CIP in Rows 4 and 5 belong to the Cloud Combination Probe (CCP) (2). The PIP VSR is given in liters per second (3).

Instrument	Principle	VSR [$\text{cm}^{-3} \text{s}^{-1}$]	D [μm]	dD [μm]	L [m]	N [cm^{-3}]
HALOHolo	Holographic imaging	232	10 - 10000	1.5	10	$10^{-2} - 10^3$
CAS(1)	Light scattering	80	0.6 - 50	typ. 5	60	$10^{-2} - 10^3$
CIP(1)	1D imaging	31 - 5760	15 - 960	15	60	$10^{-4} - 10^3$
CDP(2)	Forward scattering	13 - 16	2 - 50	typ. 2	60	$10^{-2} - 10^3$
CIP(2)	1D imaging	31 - 5760	15 - 960	15	60	$10^{-4} - 10^3$
PIP	1D imaging	9.1 - 99.5(3)	100 - 6200	100	60	$10^{-5} - 10^2$

The correlation between the measured time series of number concentration N , geometric mean particle diameter \overline{D}_g , geometric standard deviation $\sigma_g(D)$ and liquid water content LWC was examined for HALOHolo, the CDP and the CAS instrument with the results summarized in Table E.2. As expected, the same property measured by another instrument shows a strong correlation with a correlation coefficient $R(x, y) > 0.8$ for all properties except for the number concentration measured by CAS and HALOHolo ($R(x, y) = 0.43$). The weak correlation of N can be explained by the difference in the size distributions of the two instruments where the CAS shows a significantly higher concentration of particles smaller than $12 \mu\text{m}$ than HALOHolo or CDP (see Fig. E.1). Another peculiarity, which is still unresolved, is the weak negative correlation between N measured by CAS and \overline{D}_g and $\sigma_g(D)$ measured by HALOHolo.

Table E.2: Correlation coefficients between microphysical parameters of HALOHolo (columns) and CDP (rows in first table) or CAS (rows in second table) for RACEPAC Flight 2.

CDP	HALOHolo				CAS	HALOHolo			
	N	\overline{D}_g	$\sigma_g(D)$	LWC		N	\overline{D}_g	$\sigma_g(D)$	LWC
N	0.866	0.502	0.357	0.745	N	0.430	-0.172	-0.099	0.184
\overline{D}_g	0.657	0.975	0.587	0.850	\overline{D}_g	0.694	0.983	0.656	0.875
$\sigma_g(D)$	0.501	0.863	0.904	0.659	$\sigma_g(D)$	0.473	0.751	0.901	0.577
LWC	0.894	0.829	0.534	0.949	LWC	0.904	0.801	0.522	0.955

E.2 Instrument intercomparison

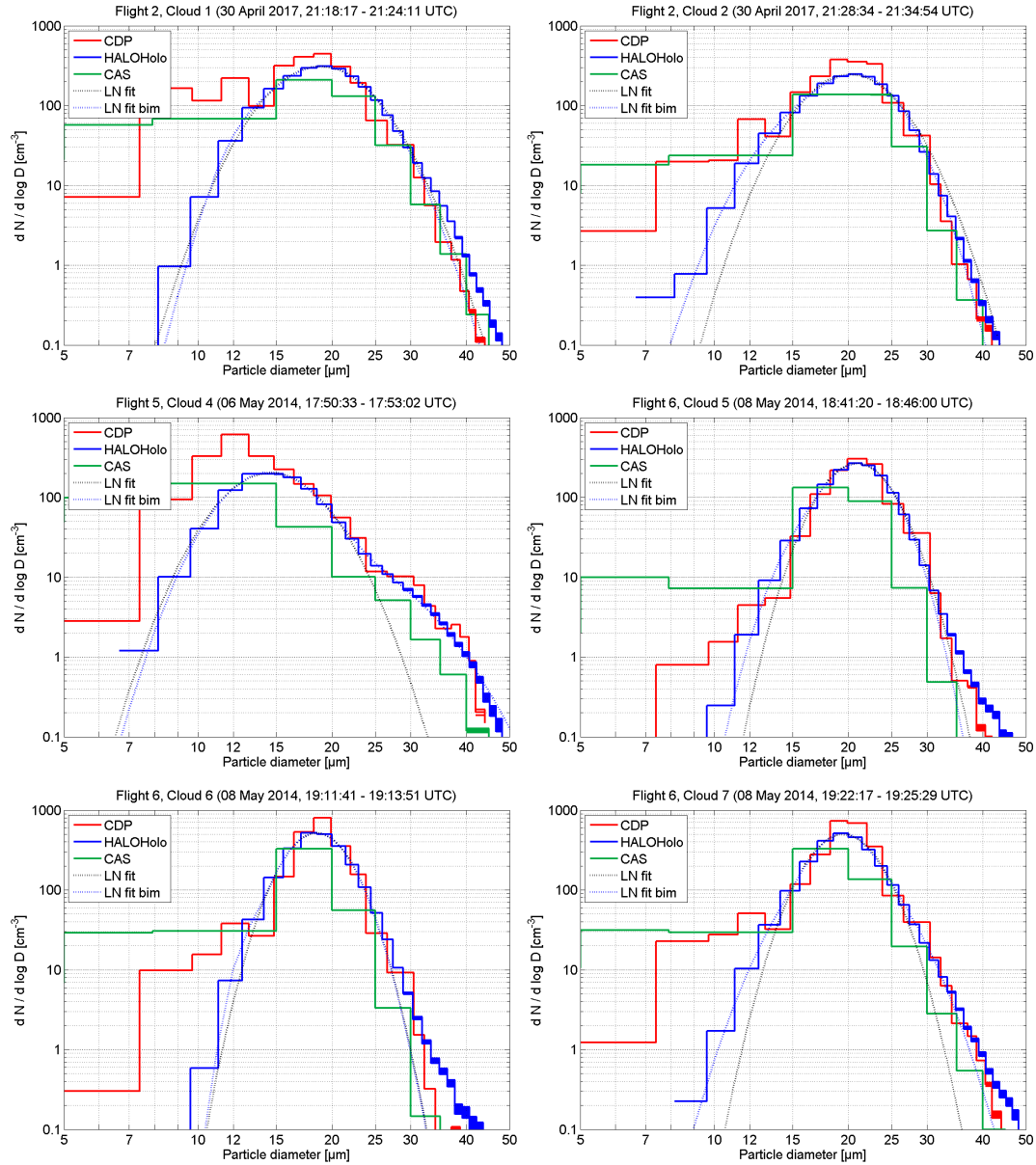


Fig. E.1: Particle size distributions from Flight 2 (upper row), Flight 5 (middle left) and Flight 6 (middle right and bottom row) measured by the CDP (red), CAS (green) and HALOHolo (blue). In addition, monomodal log-normal fits (LN fit, black dotted curve) and bimodal log-normal fits (LN fit bim, blue dotted curve) to the HALOHolo size distributions are shown. Six different cloud passes with a length of more than 5 km in cloud were selected for this intercomparison. The size of the error bars is indicated by the height of the filled stair steps for relative errors of 2 % or larger.

E.3 Flight overview

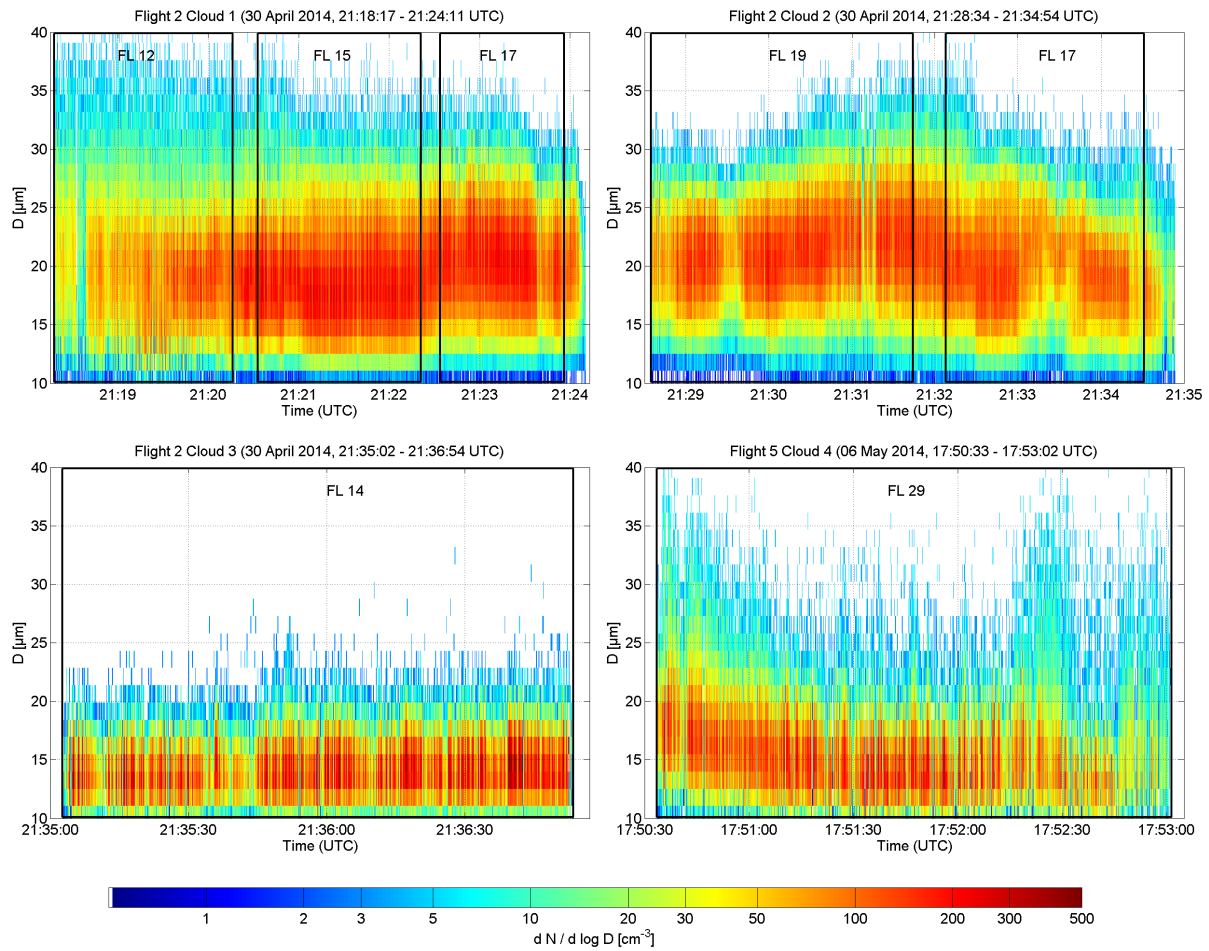


Fig. E.2: Particle size distributions as a function of time along flight path from RACEPAC Flight 2 (top row and bottom left) and Flight 5 (bottom right). The number density of droplets per bin is color-coded using the color bar in the bottom row. The denoted flight levels (FL) are 366 m for FL12, 426 m for FL14, 457 m for FL15, 518 m for FL17, 579 m for FL19 and 884 m for FL29.

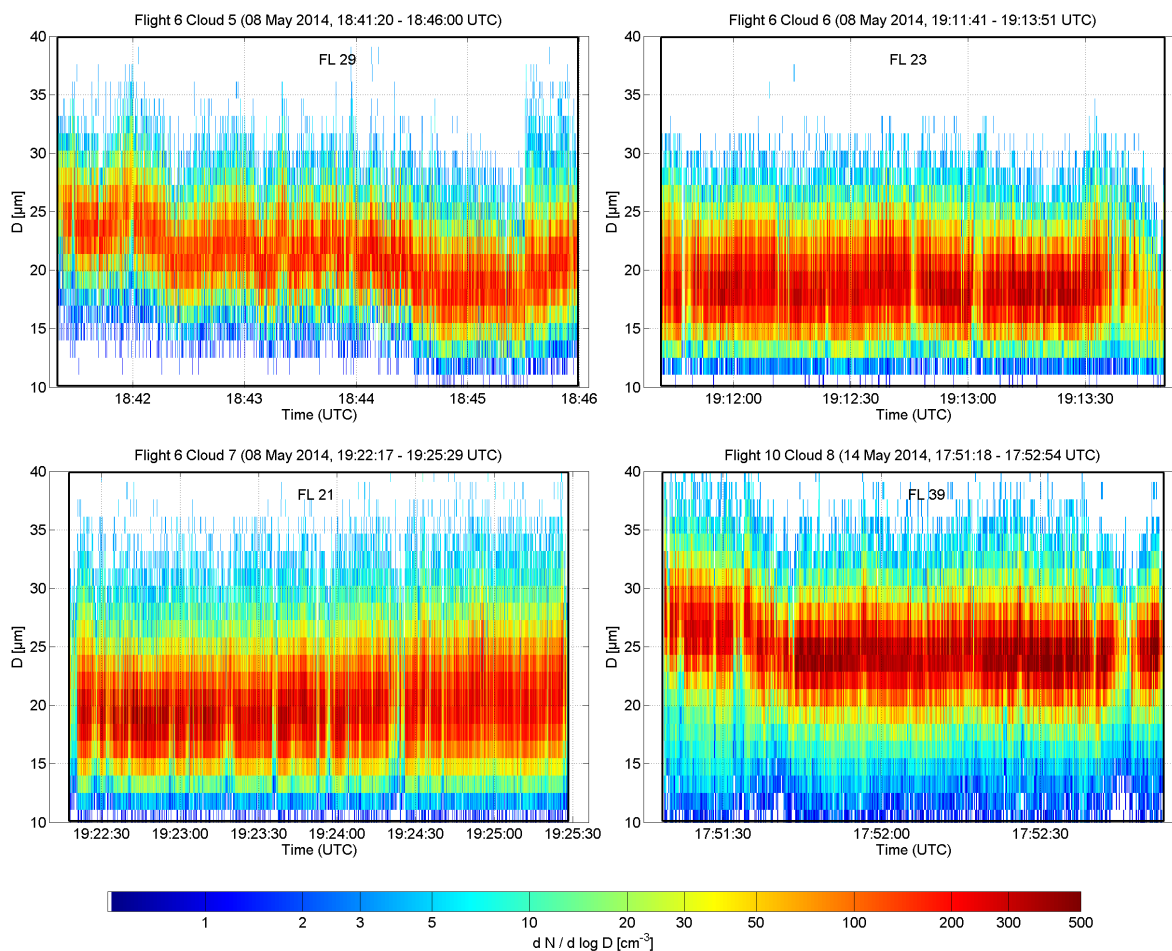


Fig. E.3: As in Fig. E.2 for Flight 6 (top row and bottom left) and Flight 10 (bottom right). The denoted flight levels (FL) are 640 m for FL21, 701 m for FL23, 884 m for FL29 and 1189 m for FL39

E.4 The impact of sampling on noise in HALOHolo power spectra

To investigate the hypothesis from Davis et al. (1996) that the high-frequency signal is caused by the effect of sampling, a synthetic time series with $f^{-\frac{5}{3}}$ noise was generated. From the generated time series of N with a defined mean concentration, a random population of particles at the given concentration with superimposed Poisson fluctuations was generated in a cubical volume which captures 8 liters of air ($20 \times 20 \times 20 \text{ cm}^3$) which includes the HALOHolo sample volume ($2 \times 1.3 \times 15.6 \text{ cm}^3$). To emulate the effect of sampling, the geometry of HALOHolo was used to capture an adequate sample of particles within the larger volume. From the time series of N in the entire volume and from the time series of the sample volume embedded in the larger volume, power spectra were calculated. The length of the time series was 5400 points, which is equal to 15 minutes of

in-cloud flight with HALOHolo, longer than any cloud sample in RACEPAC. Time series and power spectra are presented in Fig. E.4 and E.5.

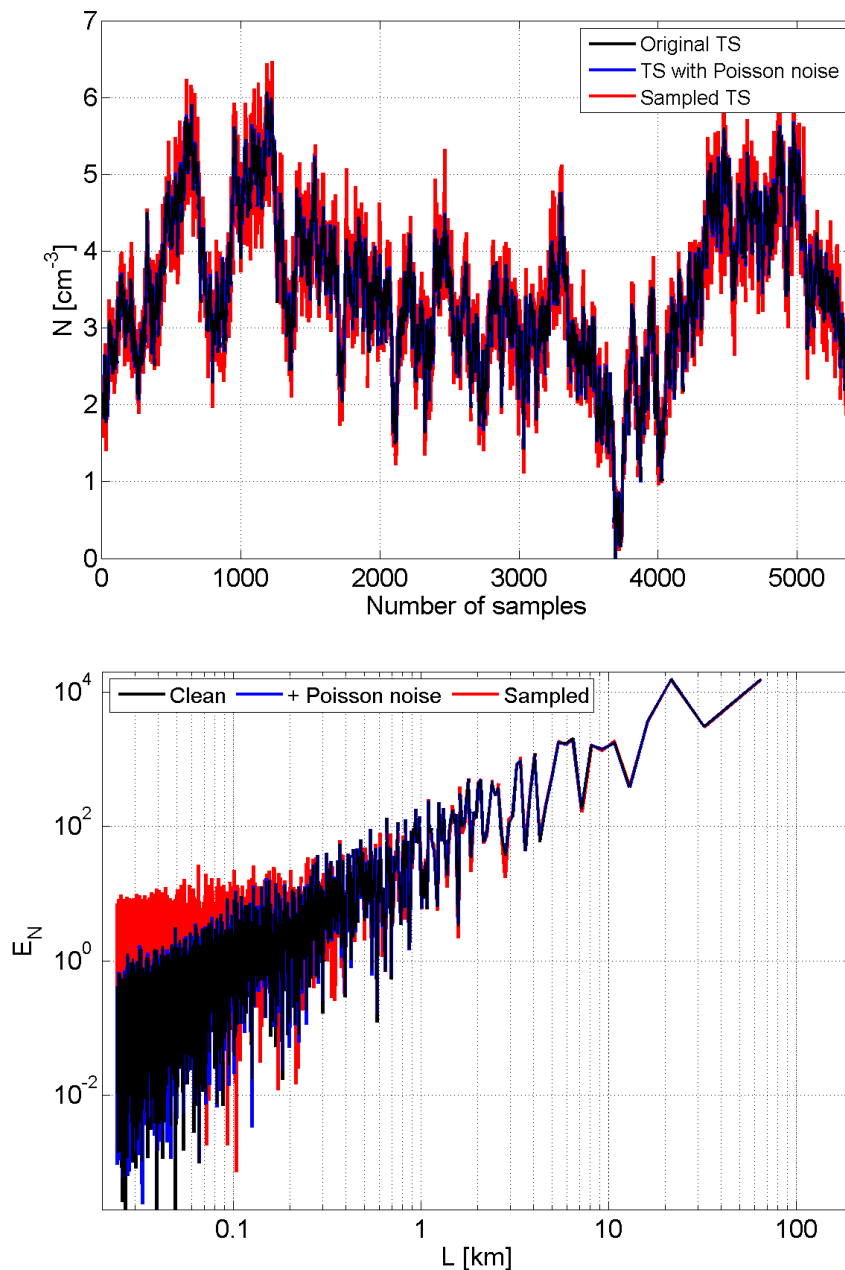


Fig. E.4: Time series data (top row) and power spectra (bottom row) of number concentration from a synthetically generated data set resembling effects from 3D turbulence. The black curves indicate the original time series (TS) data, the blue ones contained random (Poisson) fluctuations when creating the particle sample in the large volume, and the red curves show the data for sampling particles with a HALOHolo geometry within the large volume. The mean number concentration was 3.2 cm^{-3} .

Fig. E.4 shows an example of both the time series data of N and the power spectra of the theoretical and sampled N . The high-frequency noise induced by sampling has little effect on the power spectrum in case of the higher concentration (compare the red and black lines in the bottom row of Fig. E.4). In case of lower number concentration (Fig. E.4), the red signal is significantly higher than the blue signal for $L < 300$ m. The mean N in Fig. E.4 was $N = 3.2 \text{ cm}^{-3}$, the mean N in Fig. E.5 was $N = 32 \text{ cm}^{-3}$. For this test, two different realizations of the synthetic turbulence signal were used.

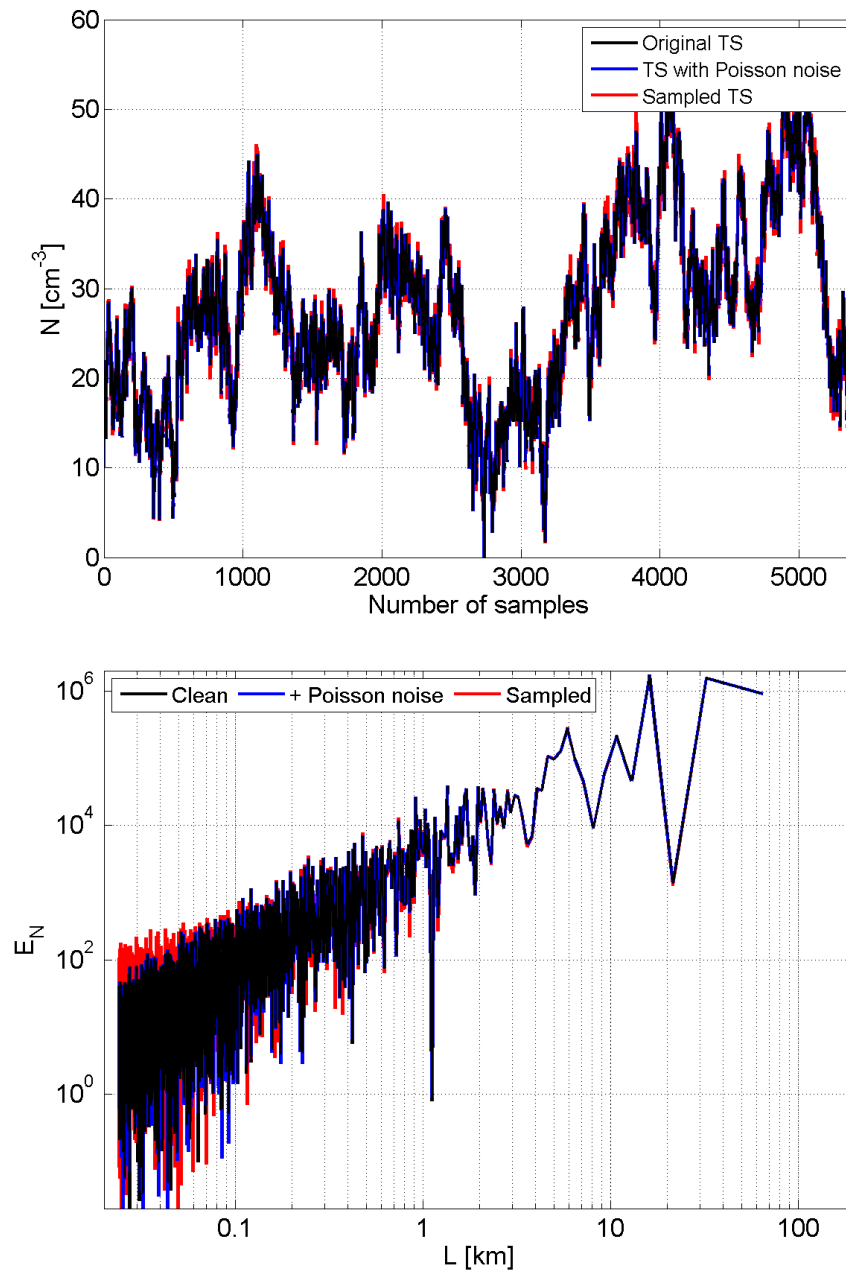


Fig. E.5: As in Fig. E.4 for a number concentration of 32 cm^{-3} .

E.5 Calculation of neighbor distance statistics from two distinct particle modes

We assume a number of $n_1 \geq 1$ particles in Mode 1 and a number of $n_2 \geq 1$ particles in Mode 2. The total number of particles is $n = n_1 + n_2$. Via conditional probability the expected number of particles and first neighbors which are both in Mode 1 can be calculated via Eq. E.1 as $\overline{n_{1,1}}$ where the $\overline{\dots}$ indicates the expectation value of $n_{1,1}$, which is not to be confused with the observed $n_{1,1}$. The same holds for $\overline{n_{2,2}}$.

$$\overline{n_{1,1}} = n \frac{n_1}{n_1 + n_2} \frac{n_1}{n_1 + n_2} = \frac{n_1^2}{n} \quad (\text{E.1})$$

The "mixing term", which is $\overline{n_{1,2}} = \overline{n_{2,1}}$ is calculated in a similar way in Eq. E.2. Here, it needs to be considered that this term occurs twice (as in the Binomial Theorem for the square of the sum of two variables).

$$\overline{n_{1,2}} = 2n \frac{n_1}{n_1 + n_2} \frac{n_2}{n_1 + n_2} = 2 \frac{n_1 n_2}{n} \quad (\text{E.2})$$

The derivation of the statistical uncertainty of each expectation value from Poisson statistics is somewhat more complicated. Here, it needs to be considered that n is a *dependent* variable of n_1 and n_2 and so each expectation value needs to be expressed in terms of n_1 and n_2 rather than n . The corresponding errors are $\Delta n_1 = \sqrt{n_1}$ and $\Delta n_2 = \sqrt{n_2}$. After error propagation and a few lines of algebra, the uncertainties $\Delta n_{1,1}$, $\Delta n_{1,2}$ and $\Delta n_{2,2}$ can be derived, shown in Eq. E.3 - E.5.

$$\Delta n_{1,1} = \frac{\overline{n_{1,1}}}{n} \sqrt{n + 4n_2 + 4 \frac{n_2^2}{n_1}} \quad (\text{E.3})$$

$$\Delta n_{2,2} = \frac{\overline{n_{2,2}}}{n} \sqrt{n + 4n_1 + 4 \frac{n_1^2}{n_2}} \quad (\text{E.4})$$

$$\Delta n_{1,2} = \frac{\overline{n_{1,2}}}{n} \sqrt{\frac{n_1^3 + n_2^3}{n_1 n_2}} \quad (\text{E.5})$$

E.6 Mixing diagrams from other flights

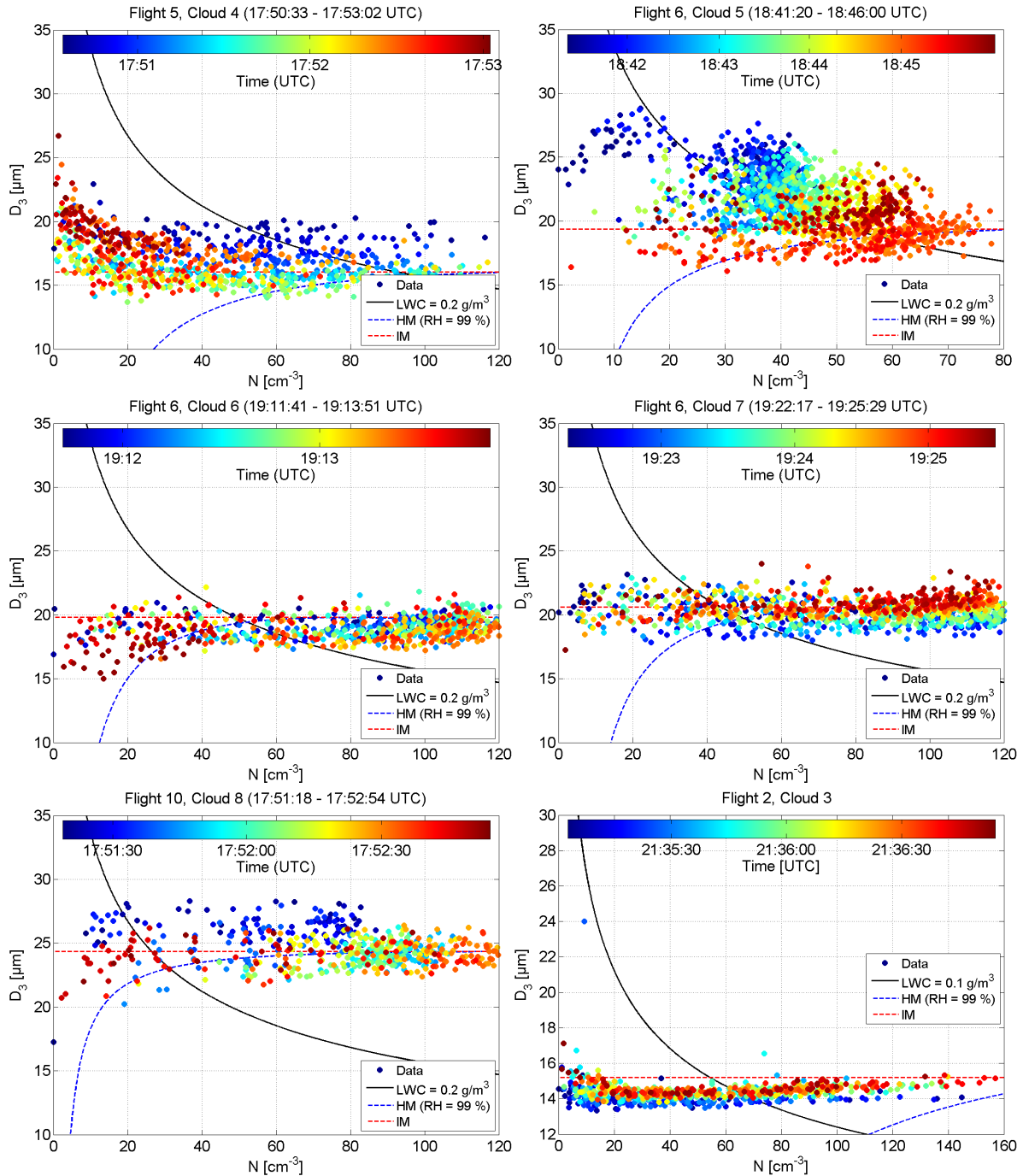


Fig. E.6: Mixing diagrams as in Fig. 6.12 for Flight 5, 6 and 10 from RACEPAC. The bottom right event (Cloud 3) is a good example of inhomogeneous mixing near the cloud base. In general, all these cloud passes are dominated by the signature of inhomogeneous mixing. The example of Cloud 5 (top right) shows an increasing D_3 for decreasing N in the beginning, which is likely due to the presence of larger droplets forming drizzle.

E.7 Spatial distribution analysis of selected cloud passes

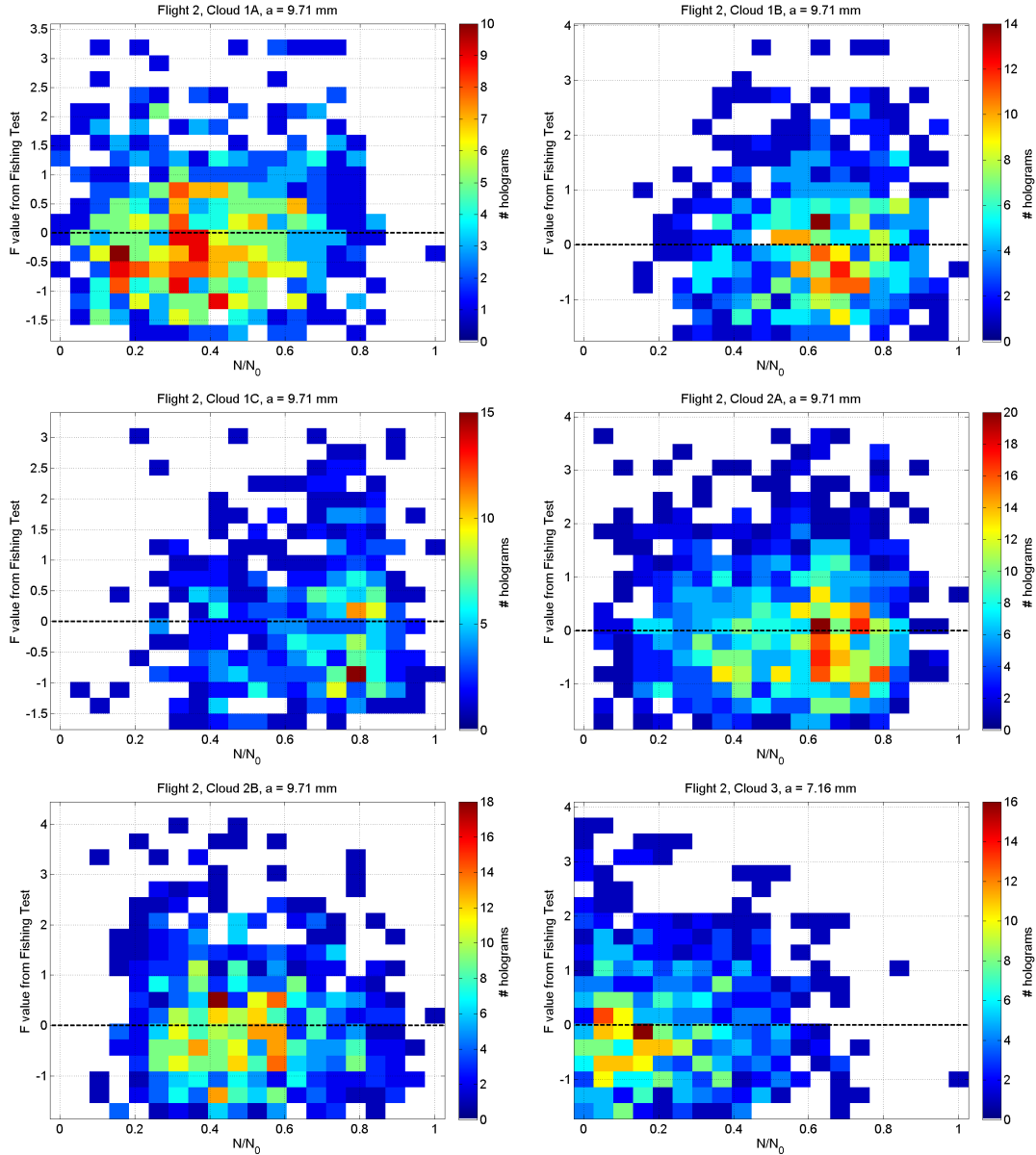


Fig. E.7: Joint frequency distribution plots showing the F value from the Fishing test as defined in Eq. 4.13 as a function of the relative particle number concentration N/N_0 . The dashed line indicates $F = 0$, which is the expectation value for a Poisson distribution. The color code reflects the number of holograms with the particular combination of the F value and the relative number concentration. The particular flight and cloud is mentioned in the title of each plot. From the perspective of these plots, the two quantities F and N/N_0 seem to be uncorrelated. This means that the probability of observing a clustered or filamented droplet population does not depend on the particle number concentration or the position relative to the cloud edge.

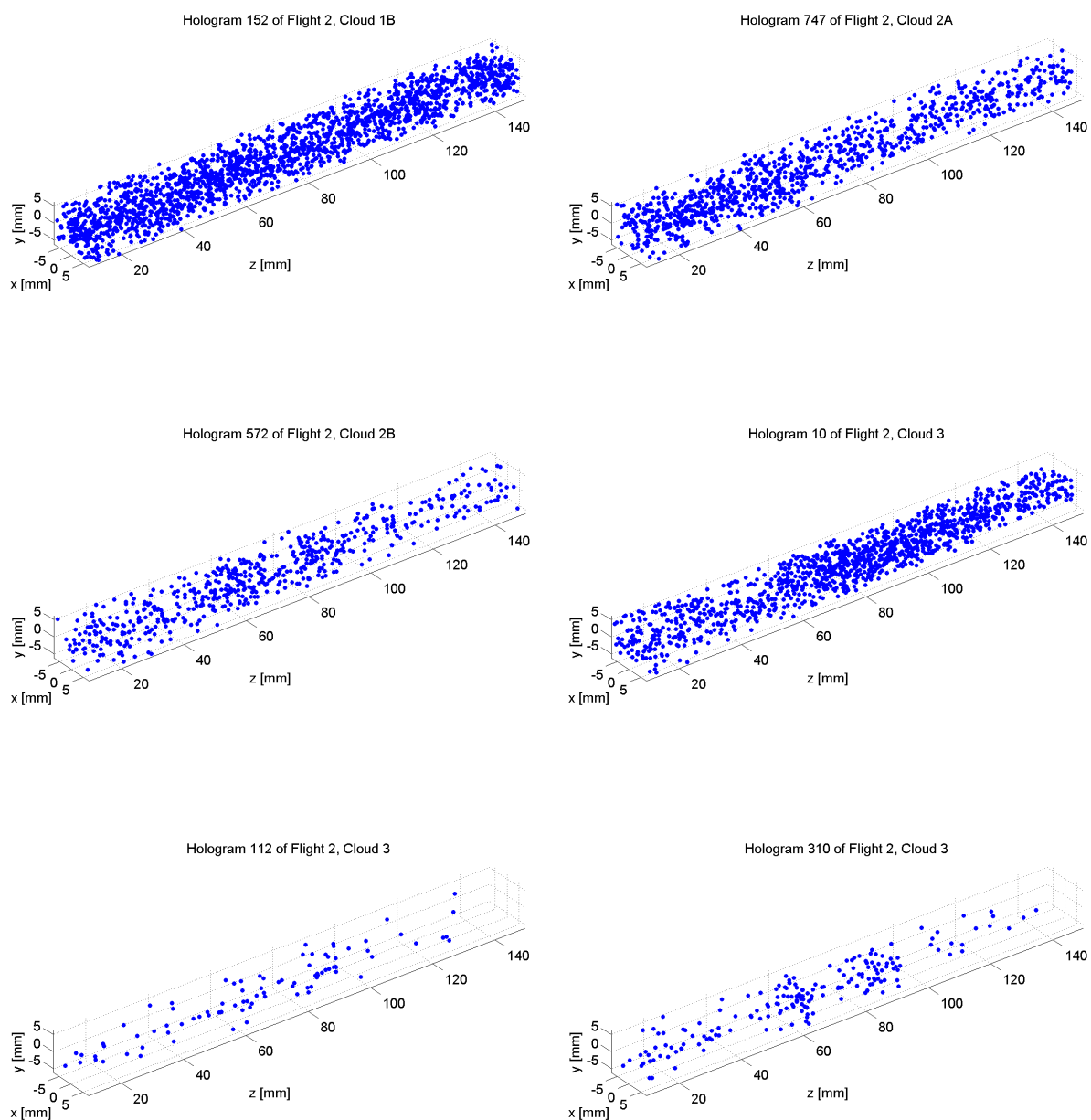


Fig. E.8: Pseudo-3D display of droplet positions in holograms from Flight 2 (Clouds 1, 2 and 3) where the F value from the Fishing test was greater than 6. Shown are one hologram from Cloud 1B (top left), Cloud 2A (top right) and Cloud 2B (middle left) and three holograms from Cloud 3 (middle left and bottom row). All of the selected holograms were at least 100 m away from the horizontal cloud edge. A non-uniform spatial distribution of the particles is visible in the middle and bottom row. Particle clustering in the holograms shown in the top row is revealed by the Fishing test but difficult to see in the 3D plots.

F

ICE-D campaign overview and additional data

F.1 Determining the spatial overlap of the cloud passes

From the geographic latitude and longitude of the cloud passes in Flight B926 on 14 August 2015 it was examined whether the same cloud was measured in subsequent cloud passes. This analysis was done by plotting the cloud passes in different colors on a horizontal map. As the clouds are expected to move with the mean wind at the corresponding pressure or altitude level, the time between two cloud passes needs to be considered as well as the mean of the horizontal wind components u and v to estimate the motion of the cloud between two cloud passes. This estimation was done via forward calculation (indicated by FFP for "Forward From Precursor" in Fig. F.1) and backward calculation (indicated by BFS for "Backward From Successor"). The meaning of these tracks is discussed for an arbitrary cloud pass i . Ideally, the "forward trajectory" of the precursor (Cloud Pass $i - 1$, which yields $FFP(i - 1)$), the "backward trajectory" of the successor (Cloud Pass $i + 1$, which yields $BFS(i + 1)$) and the current cloud pass track $T(i)$ have at least one common intersection point if they belong to the same cloud. This case is only observed for Pass 8 in Fig. F.1 (the actual cloud pass track in solid red intersects with the dashed red FFP and the dotted red BFS in the same point ($x = 2.75$ km, $y = 3.82$ km)). To account for local differences in the mean wind and also cloud growth in the horizontal, a less strict criterion for "Cloud Pass i and j are from the same cloud" is used. Here, the minimum distance between the actual cloud pass track $T(i)$ and the $FFP(i - 1)$ or the $BFS(i + 1)$ has to be small enough to be interpreted as the same cloud. Table F.1 lists the distances for the cloud passes and their corresponding FFP and BFS projections. The maximum distance found in Table F.1 is 1.1 km, which is still within the expected range of differences to consider the two passes as the same cloud. Thus, all cloud passes 1-9 are likely from the same cloud.

Table F.1: Minimum horizontal distance between actual cloud track and its corresponding forward projection from precursor (FFP) and backward projection from successor (BFS).

Pass	$\min (FFP(i - 1) - T(i))$ [km]	$\min (BFS(i + 1) - T(i))$ [km]
1	N/A	< 0.01
2	0.21	0.41
3	0.41	1.10
4	0.88	< 0.01
5	< 0.01	0.37
6	1.09	< 0.01
7	< 0.01	< 0.01
8	0.31	< 0.01
9	< 0.01	N/A

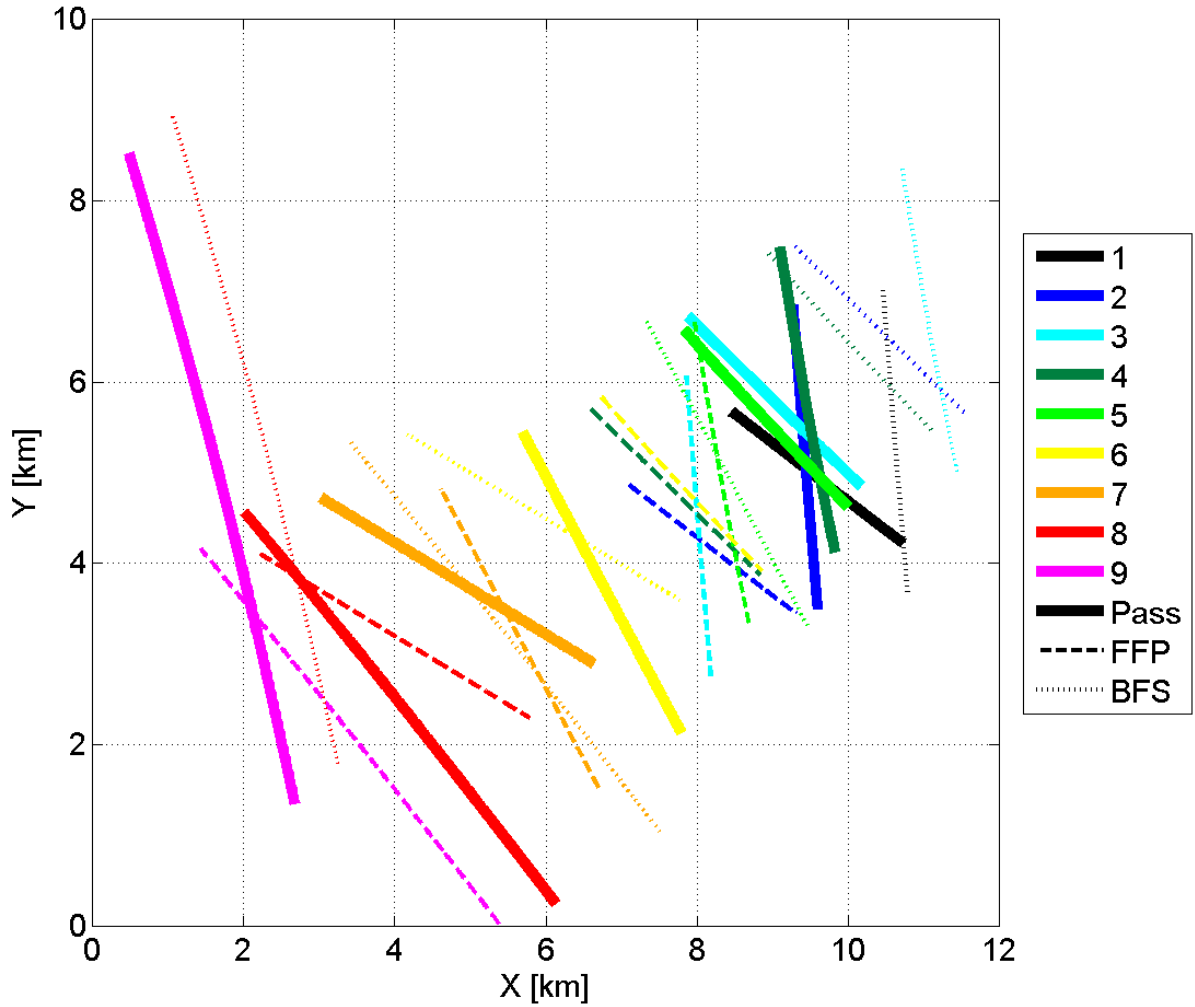


Fig. F.1: Relative position of the cloud passes projected on the $x - y$ plane. The cloud passes are indicated by thick colored lines. By using the mean horizontal wind speed components u and v and the time difference between two cloud passes, the cloud motion was estimated. The dashed lines (FFP, for "forward from precursor") are the "forward trajectories" of the cloud passes and indicate where the following cloud pass should be located if it was the same cloud. A similar calculation was done for the dotted lines (BFS, for "backward from successor"), which are "backward trajectories" of the following cloud pass that should intersect the actual cloud pass. A more detailed explanation is given in the text on the previous page.

F.2 Meteorological overview of Flight B926

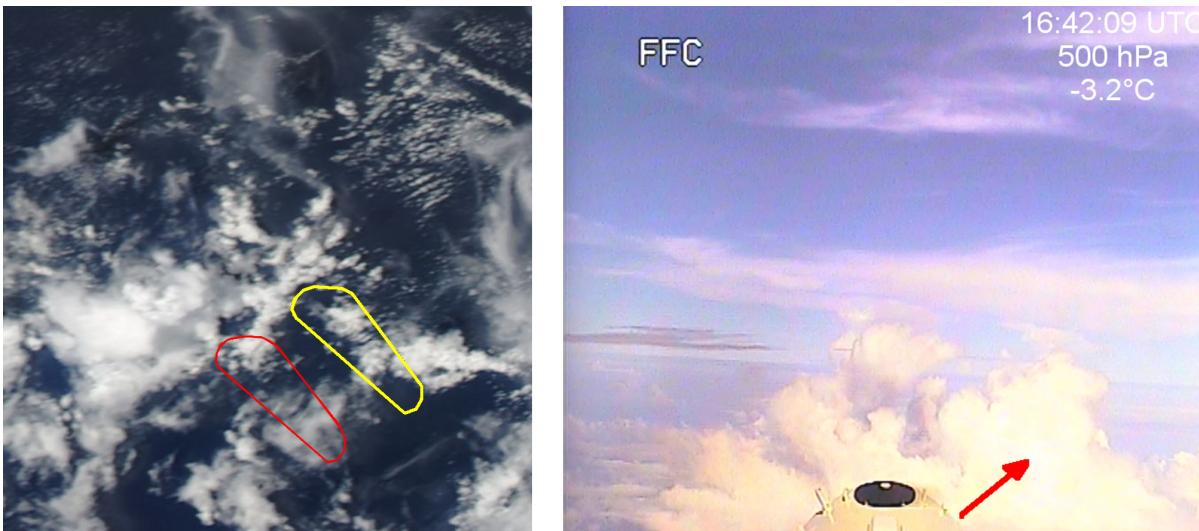


Fig. F.2: Left: Image in the visible spectrum from the MODIS instrument on the polar orbiting satellite Aqua on 14 August 2015, 14:40 UTC. Marked are the flight region (red) and the estimated region of the sampled convective system at the time of the satellite overpass (yellow). Right: Video still of the forward-facing camera of the BAe146 aircraft. The sampled convective storm, which is embedded in a larger system, is indicated by the red arrow.

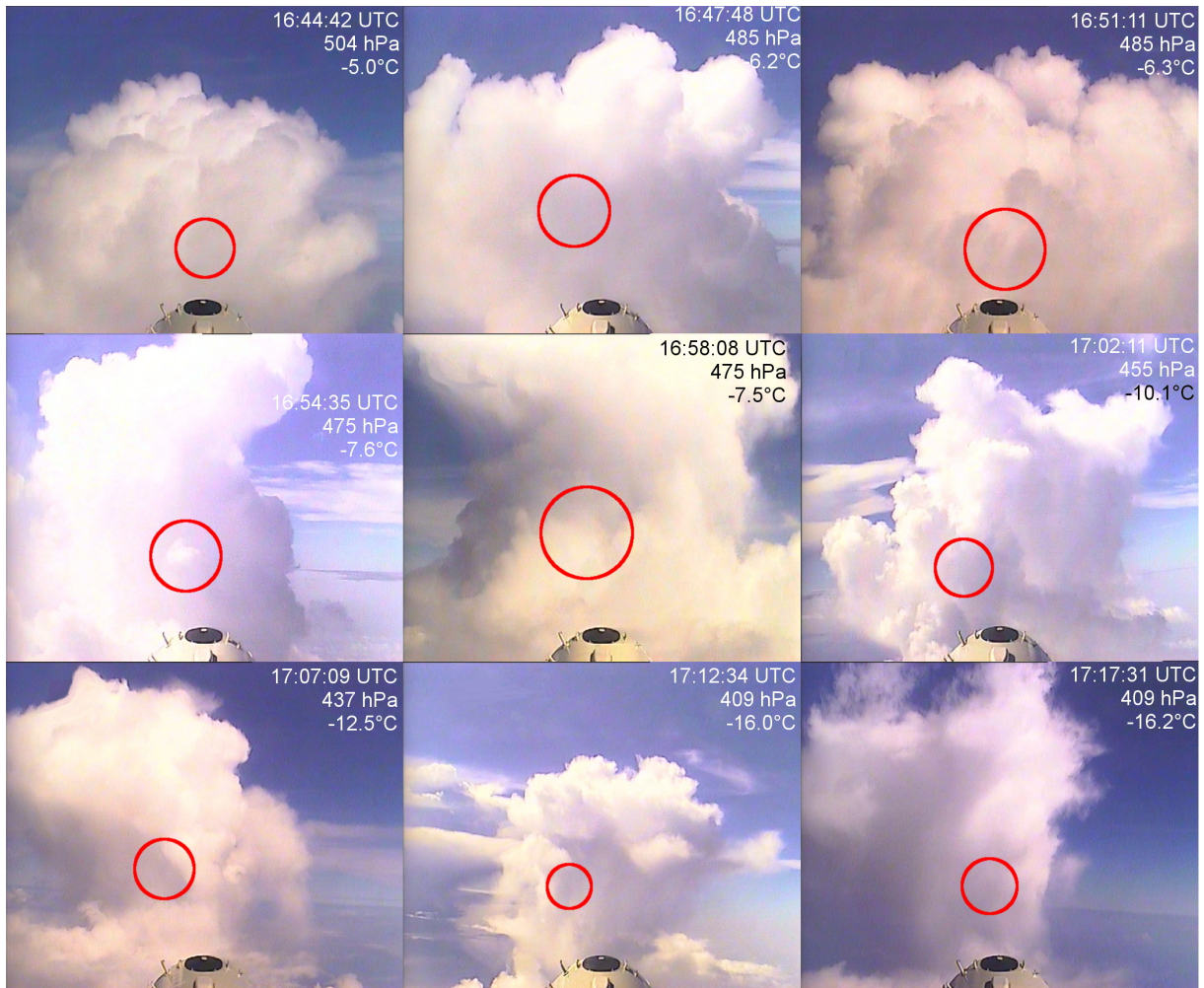


Fig. F.3: Video stills shortly before the cloud passes 1, 2 and 3 (top row), 4, 5 and 6 (middle row) and 7, 8 and 9 (bottom row). The time stamps, average temperature and average pressure are displayed in the upper right edge. Red circles mark the region where the aircraft entered the cloud.

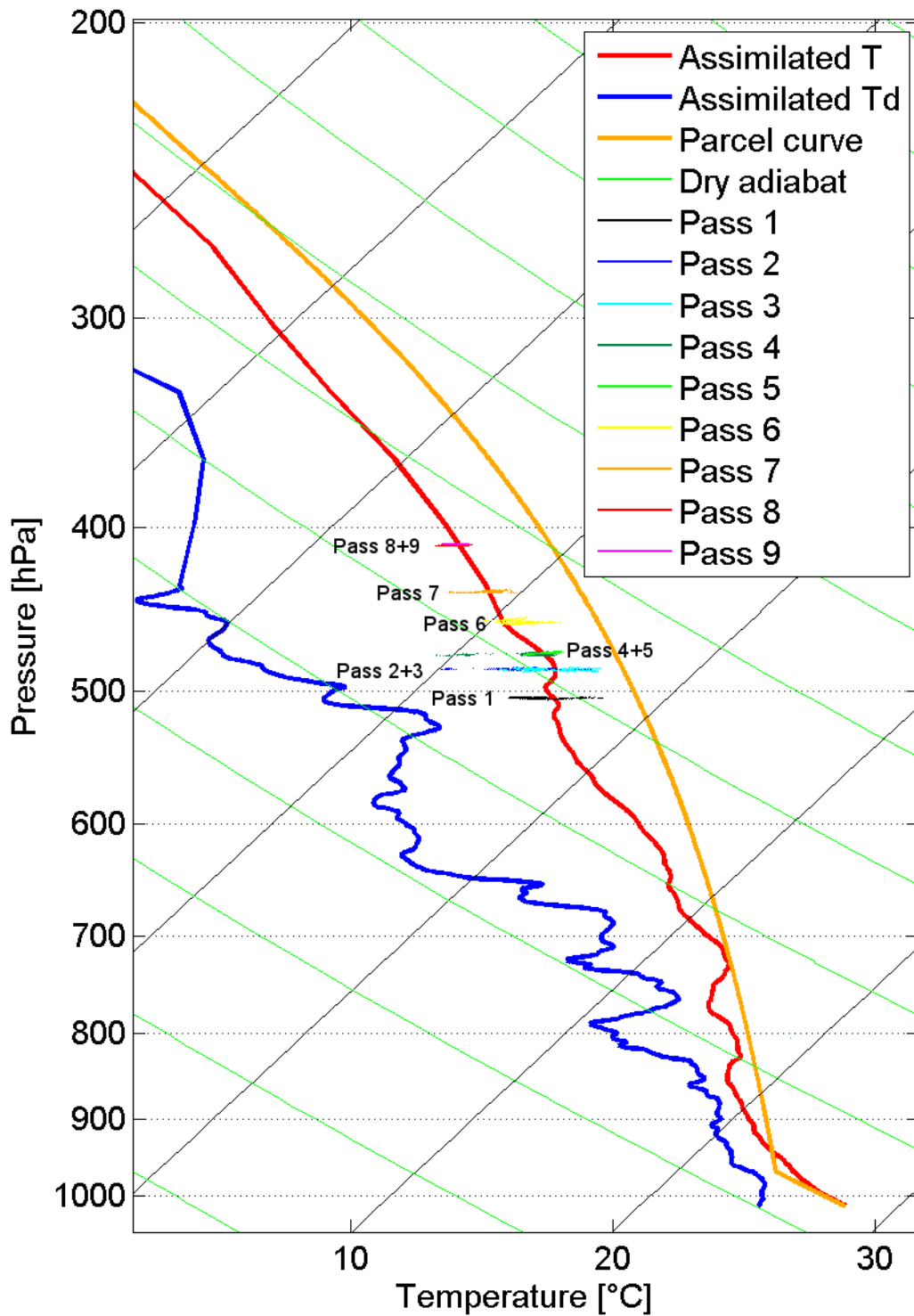


Fig. F.4: Skew-T / log p diagram with combined dropsonde data from 17:22 UTC and Global Data Assimilation System (GDAS) model data at 15:00 UTC. The assimilation method is described in the text of Chapter 7. In addition, the aircraft temperature and pressure measurements from the cloud passes (color-coded plus text) are shown.

F.3 Additional figures of the cloud passes

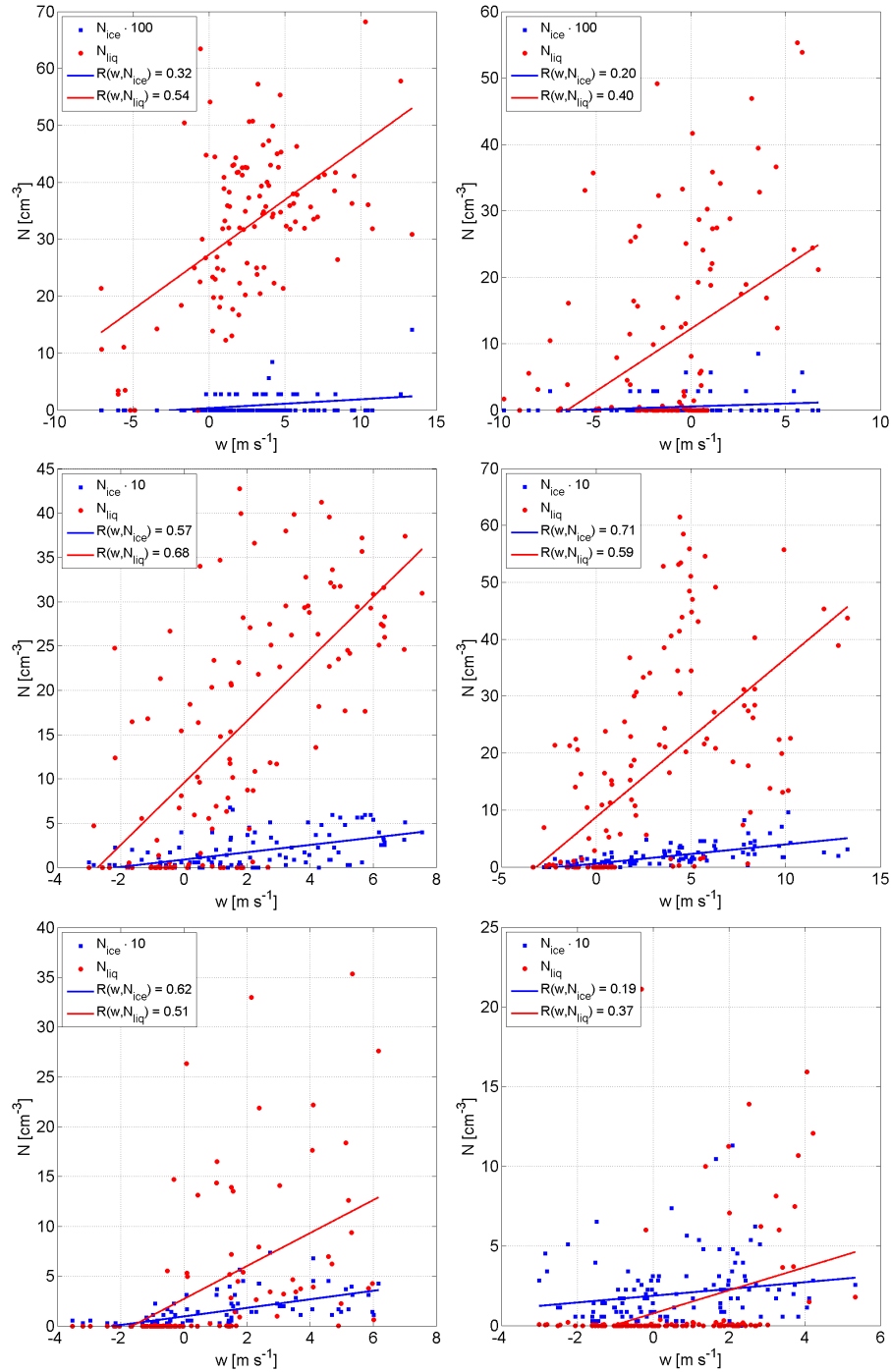


Fig. F.5: Particle number concentration N for ice (blue) and droplets (red) as a function of vertical velocity w for Pass 1 and 3 (top row), Pass 4 and 6 (middle row) and Pass 7 and 8 (bottom row). The cross correlation $R(w, N_{liq})$ and $R(w, N_{ice})$ is mentioned in the legend of each plot. For each cloud pass, a linear least-squares fit of N_{ice} and N_{liq} as a function of w is shown.

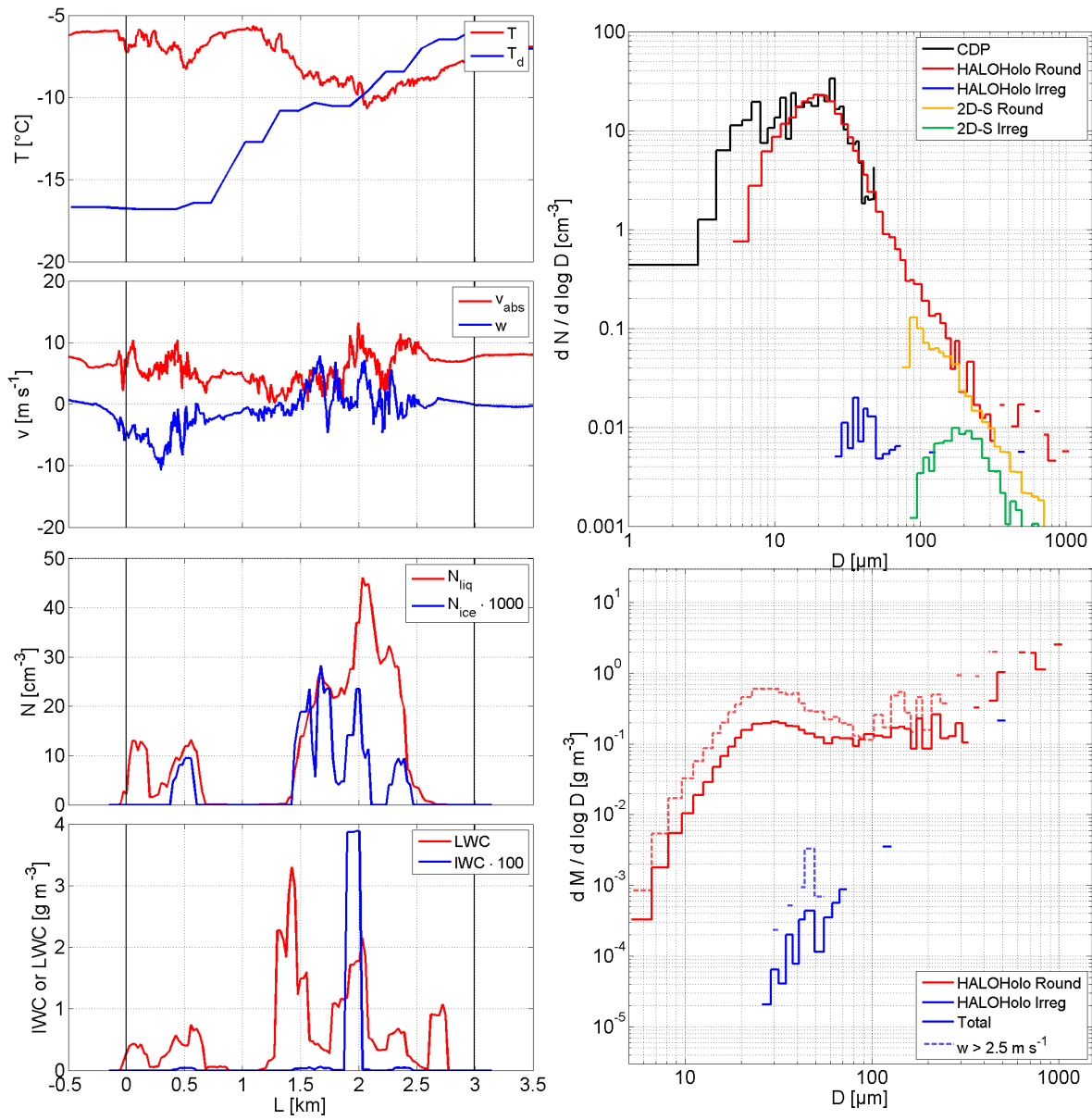


Fig. F.6: As in Fig. 7.2 for Pass 3.

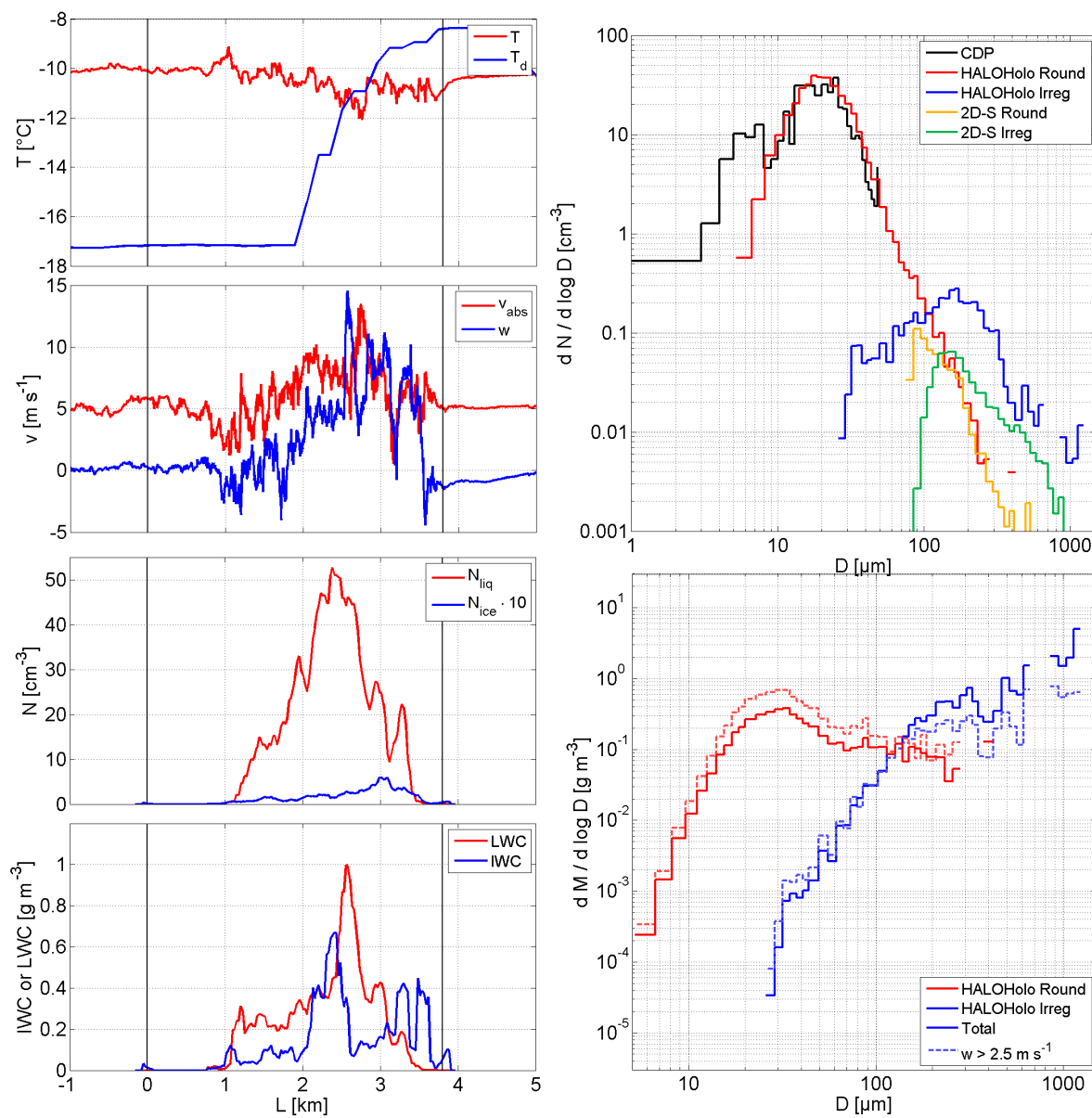


Fig. F.7: As in Fig. 7.2 for Pass 6.

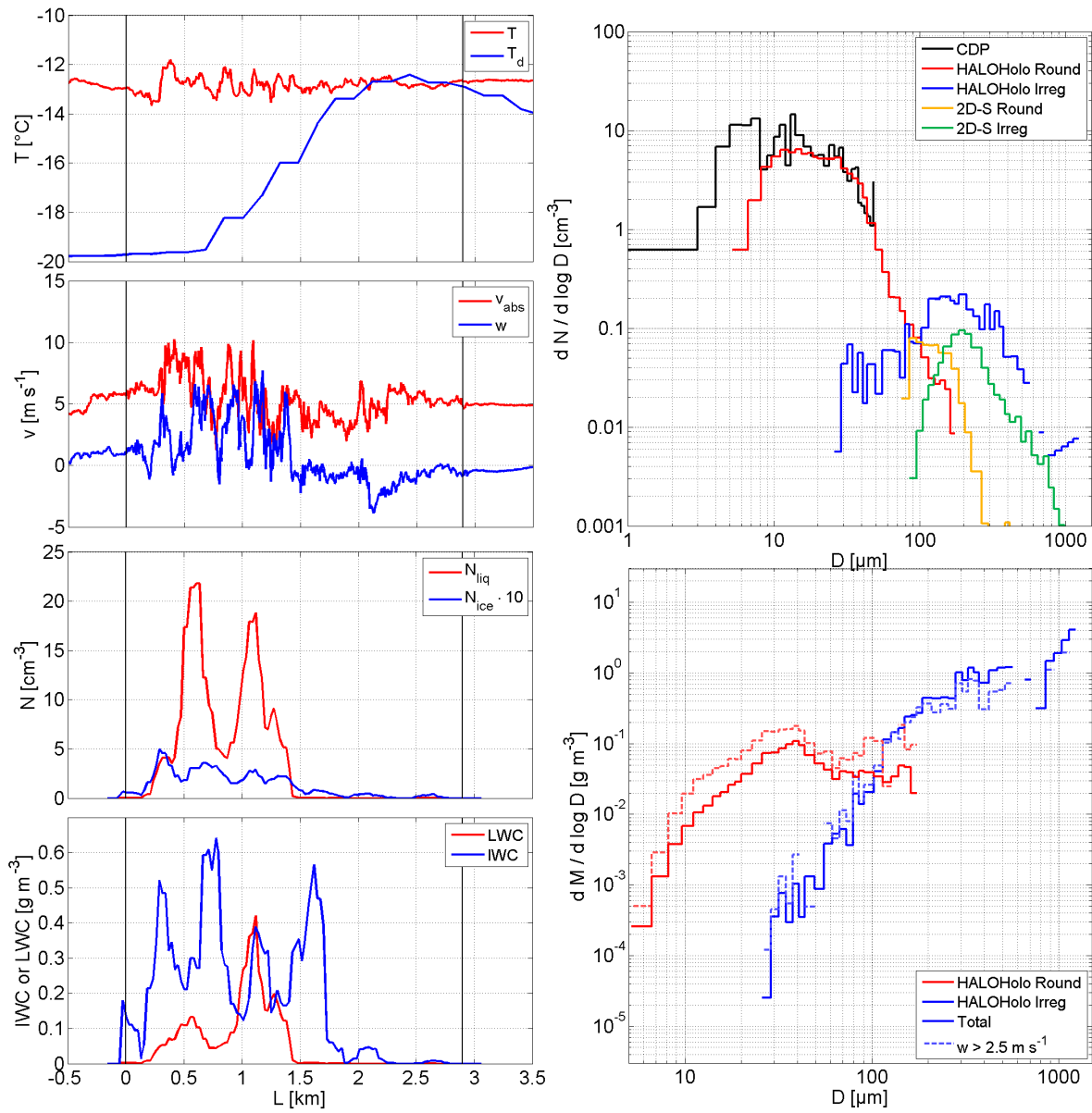


Fig. F.8: As in Fig. 7.2 for Pass 7.

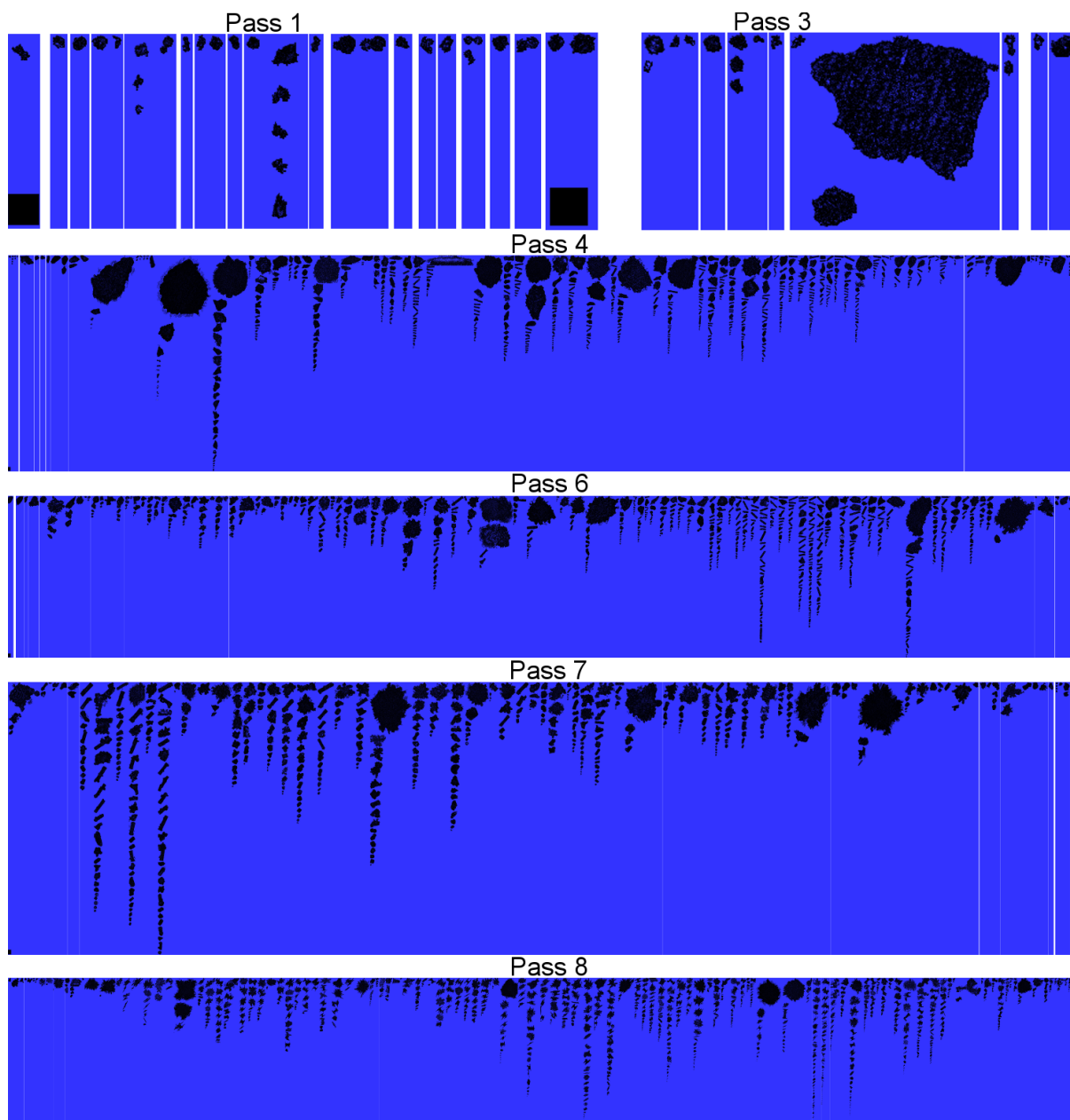


Fig. F.9: Particle images of particles with $D \geq 100\mu\text{m}$ classified as aspherical particles from Pass 1 until Pass 7. Each vertical column represents one hologram. Particles are sorted by their size and vertically stacked. White bars indicate empty holograms between two holograms containing particles. The black square in the lower left edges is 100 microns wide and acts as a scale reference. The number of holograms is 111 for Pass 1, 120 for Pass 3, 122 for Pass 4, 140 for Pass 6, 107 for Pass 7 and 128 for Pass 8.

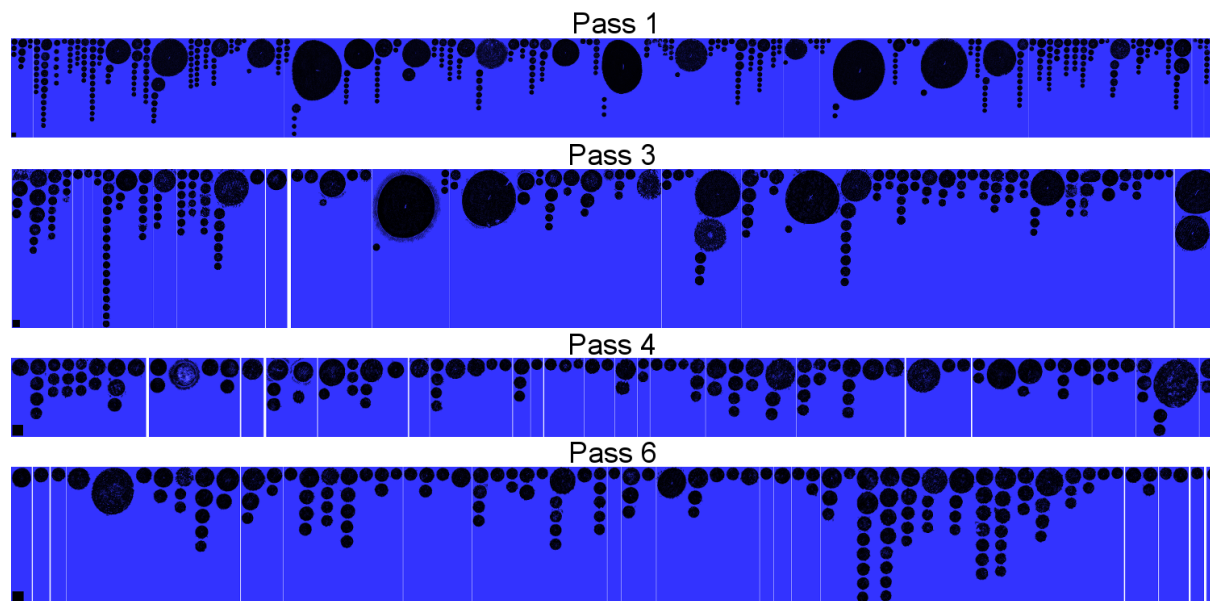


Fig. F.10: As in Fig. F.9 for particles classified as spherical.

F.4 Estimation of particle terminal velocity

The terminal velocity v_t is the equilibrium velocity of a falling hydrometeor, which means that gravitational acceleration and hydrodynamic drag cancel out each other. There are many parameterizations found in the literature for different ice crystal habits and size ranges. Here, the chosen parameterizations are the parameterization for dense graupel after Locatelli and Hobbs (1974) (Eq. F.1) and the parameterization for small pristine columns after Bürgesser et al. (2016) (Eq. F.2). v_t is the terminal velocity in m s^{-1} , D is the particle maximum dimension in μm , L is the length of a columnar crystal in μm and W is the width of a columnar crystal in μm .

Eq. F.1 is valid for $500 \mu\text{m} \leq D \leq 1 \text{ mm}$ and Eq. F.2 is valid for $20 \mu\text{m} \leq L \leq 200 \mu\text{m}$. The results of the calculated v_t for all rimed particles and frozen drops (treated as graupel) and the columnar crystals in Flight B926 are shown in Fig. F.11.

$$v_t(D) = 1.5(D/1000)^{0.37} \quad (\text{F.1})$$

$$v_t(L, W) = 3.886 \cdot 10^{-4} W \left(1 + 0.95 \left(\frac{L}{W} \right)^{0.75} \right) \quad (\text{F.2})$$

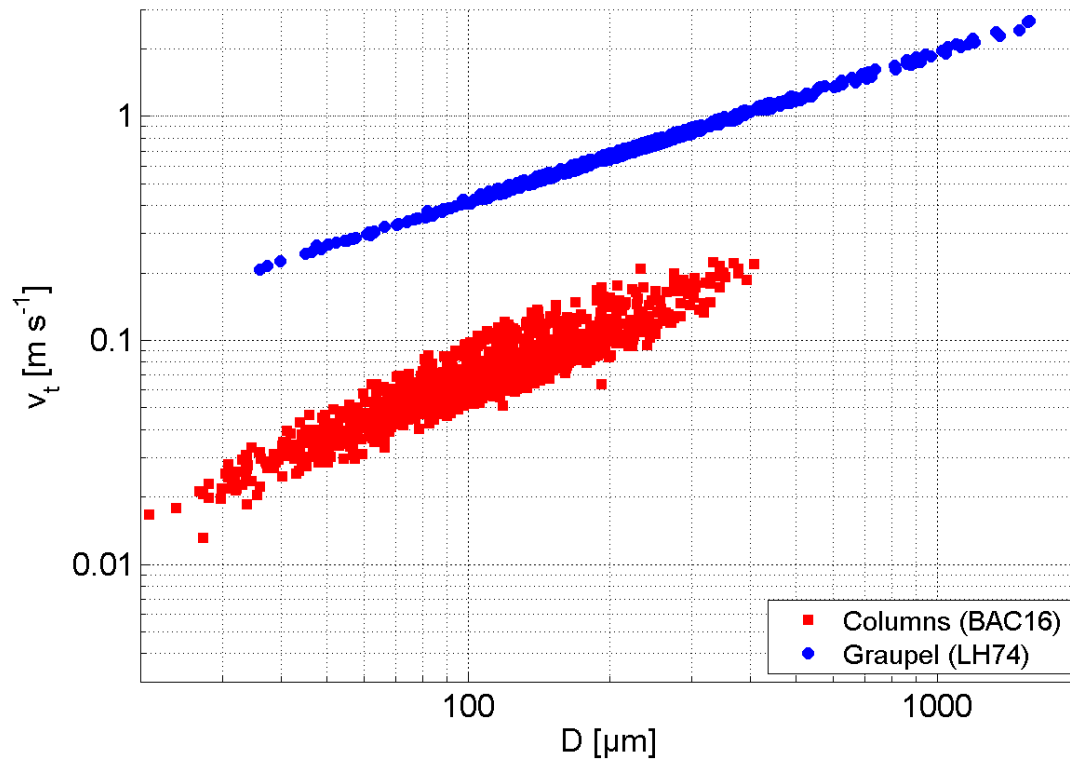


Fig. F.11: Terminal velocity v_t estimated from the parameterization of Locatelli and Hobbs (1974) (LH74) and Bürgesser et al. (2016) (BAC16) as a function of particle maximum dimension D for columns and rimed particles / frozen drops measured in Flight B926.

F.5 Spatial distribution of ice among droplets

Table F.2: First neighbor statistics of holograms from Pass 4 containing at least two ice particles and at least two droplets. Shown are the hologram number, the observed number of ice particles n_{ice} , the observed number of droplets n_{liq} , the ice-ice neighbors $n_{ice,ice}$, the ice-liquid neighbors $n_{ice,liq}$, the liquid-liquid neighbors $n_{liq,liq}$ and the vertical velocity w . Bold-face values indicate $n_{ice,ice}$, $n_{ice,liq}$ or $n_{liq,liq}$ larger than the expectation value plus its error bar (calculated after the equations in Appendix E.5). Bold-face red values indicate that the observed value is smaller than the expectation value plus its error bar.

Hologram	n_{ice}	n_{liq}	$n_{ice,ice}$	$n_{ice,liq}$	$n_{liq,liq}$	w [m s ⁻¹]
6	2	498	1	1	498	-0.40
43	5	293	0	10	288	-0.59
44	7	175	1	11	170	-1.98
46	3	239	0	7	235	-1.08
47	4	258	0	7	255	1.29
48	2	261	0	3	260	0.93
49	3	19	1	3	18	-1.19
50	3	90	0	6	87	0.85
51	5	68	0	8	65	1.72
52	2	104	0	5	101	1.83
55	5	70	1	7	67	1.75
56	4	145	0	7	142	2.30
57	6	222	0	13	215	2.41
58	8	160	1	16	151	3.02
59	6	118	0	13	111	2.72
60	5	149	0	13	141	4.36
61	7	182	0	13	176	5.67
62	5	155	0	12	148	5.66
63	7	208	0	11	204	4.85
64	9	229	0	14	224	1.75
65	6	256	0	14	248	6.04
66	5	350	0	15	340	6.19
67	6	352	0	11	347	4.13
68	6	398	0	9	395	4.51
69	5	357	0	10	352	5.65
70	5	461	0	13	453	5.20
71	5	613	0	13	605	7.42
72	9	575	0	19	565	5.80
73	4	373	0	6	371	5.18
74	5	481	0	10	476	4.07
75	7	445	0	11	441	4.55
76	3	472	0	5	470	5.33
77	2	419	0	3	418	4.36

Table F.3: Table F.2 continued.

Hologram	n_{ice}	n_{liq}	$n_{ice,ice}$	$n_{ice,liq}$	$n_{liq,liq}$	w [m s ⁻¹]
78	9	504	0	15	498	6.02
79	3	458	0	8	453	6.30
81	6	431	0	16	421	6.73
82	2	432	0	3	431	7.86
83	5	404	2	10	397	6.09
84	6	344	0	12	338	5.03
85	5	458	0	10	453	3.36
86	6	446	0	13	439	3.84
87	5	395	0	8	392	3.23
88	3	377	0	3	377	4.96
90	3	426	0	3	426	0.46
95	3	182	0	5	180	0.11
103	3	414	0	4	413	2.43
108	3	617	0	8	612	5.09
110	2	587	0	4	585	6.27
111	2	486	2	0	486	-1.65
114	2	392	0	4	390	1.65

Table F.4: As in Table F.2 for Pass 6.

Hologram	n_{ice}	n_{liq}	$n_{ice,ice}$	$n_{ice,liq}$	$n_{liq,liq}$	w [m s ⁻¹]
34	3	23	0	7	19	-2.51
38	2	13	0	5	10	0.34
40	2	37	0	3	36	0.30
41	2	178	0	5	175	1.27
47	2	215	0	3	214	-0.83
49	2	235	0	2	235	2.17
52	2	130	0	4	128	0.07
55	5	207	0	8	204	-1.46
57	4	258	0	9	253	-0.30
61	4	338	0	7	335	1.04
63	2	348	0	4	346	1.87
68	2	458	0	2	458	3.95
69	2	548	0	5	545	6.22
70	2	470	0	4	468	5.05
71	2	318	0	3	317	3.88
73	4	276	0	6	274	4.28
74	4	245	0	9	240	4.95

Table F.5: Table F.4 continued.

Hologram	n_{ice}	n_{liq}	$n_{ice,ice}$	$n_{ice,liq}$	$n_{liq,liq}$	w [m s ⁻¹]
75	2	313	0	4	311	5.98
76	2	923	0	6	919	4.59
77	4	674	0	7	671	4.41
78	5	826	0	14	817	4.70
79	3	759	0	3	759	4.01
80	4	422	0	9	417	4.30
81	3	627	0	6	624	5.51
83	3	827	0	9	821	4.57
85	2	751	0	3	750	4.76
86	2	731	0	5	728	5.05
89	2	717	0	3	716	12.52
90	3	635	0	7	631	12.82
91	3	690	0	6	687	12.28
92	3	554	0	4	553	10.70
93	5	678	0	10	673	8.71
94	5	656	0	12	649	5.90
96	2	601	0	3	600	4.29
97	4	618	0	10	612	4.83
99	2	483	0	3	482	5.71
100	2	475	0	4	473	10.68
101	4	335	0	8	331	10.38
102	5	292	0	9	288	10.05
103	4	209	0	10	203	8.90
104	7	364	0	12	359	8.04
105	7	328	0	10	325	8.11
106	4	407	0	9	402	8.38
107	13	425	3	16	419	8.60
109	7	469	0	14	462	10.29
110	8	451	1	17	441	8.39
111	8	267	0	14	261	8.67
112	13	207	3	20	197	4.22
113	5	201	1	7	198	2.96
114	5	128	0	9	124	1.53
115	6	22	0	9	19	3.89
116	9	70	3	13	63	6.71
117	6	196	0	9	193	7.24
118	3	374	0	6	371	8.08
119	7	382	0	12	377	7.99
120	2	302	0	6	298	8.41
121	4	282	0	11	275	8.00
122	4	477	0	6	475	5.14

Table F.6: Table F.5 continued.

Hologram	n_{ice}	n_{liq}	$n_{ice,ice}$	$n_{ice,liq}$	$n_{liq,liq}$	w [m s ⁻¹]
123	5	161	0	13	153	4.33
126	2	5	0	3	4	4.34
127	7	19	2	6	18	0.87
128	2	25	0	4	23	-3.42
129	2	3	2	1	2	-2.67

Table F.7: As in Table F.2 for Pass 7.

Hologram	n_{ice}	n_{liq}	$n_{ice,ice}$	$n_{ice,liq}$	$n_{liq,liq}$	w [m s ⁻¹]
10	4	21	1	5	19	4.09
11	5	14	1	8	10	4.04
12	5	135	0	11	129	2.87
13	7	61	0	11	57	-0.25
14	5	48	0	9	44	-0.05
15	13	54	2	18	47	0.91
17	2	69	0	3	68	1.15
20	2	238	0	5	235	5.69
21	3	234	0	5	232	4.86
23	2	545	0	3	544	4.92
24	4	144	0	9	139	5.51
25	6	368	0	13	361	5.99
26	4	309	0	10	303	4.35
27	3	207	0	6	204	2.73
28	4	64	0	8	60	-1.18
29	9	119	0	20	108	1.24
30	7	81	1	13	74	2.67
31	2	92	0	3	91	4.06
32	9	78	0	15	72	5.04
33	2	57	0	2	57	6.31
35	2	32	0	3	31	3.37
38	2	229	0	4	227	0.29
41	4	375	0	8	371	3.78
43	6	387	0	12	381	0.91
44	2	249	0	3	248	2.58
45	2	11	0	5	8	-0.97
47	2	42	0	4	40	0.74

Table F.8: Table F.7 continued

Hologram	n_{ice}	n_{liq}	$n_{ice,ice}$	$n_{ice,liq}$	$n_{liq,liq}$	w [m s ⁻¹]
48	2	223	0	6	219	2.21
49	4	67	0	8	63	2.74
50	6	260	0	8	258	5.13
51	2	199	0	3	198	2.01
52	7	17	4	7	13	-1.20

Table F.9: As in Table F.2 for Pass 8.

Hologram	n_{ice}	n_{liq}	$n_{ice,ice}$	$n_{ice,liq}$	$n_{liq,liq}$	w [m s ⁻¹]
29	2	8	0	5	5	-0.03
31	2	2	2	0	2	1.74
33	4	341	0	8	337	3.40
34	5	166	0	8	163	4.04
35	2	251	0	4	249	2.58
36	4	124	0	7	121	4.00
40	4	211	0	7	208	3.35
41	5	48	0	7	46	5.47
42	2	131	0	4	129	4.28
44	3	30	1	3	29	1.86
45	3	30	2	2	29	1.82
48	2	177	0	3	176	-0.87
64	2	4	1	1	4	2.07

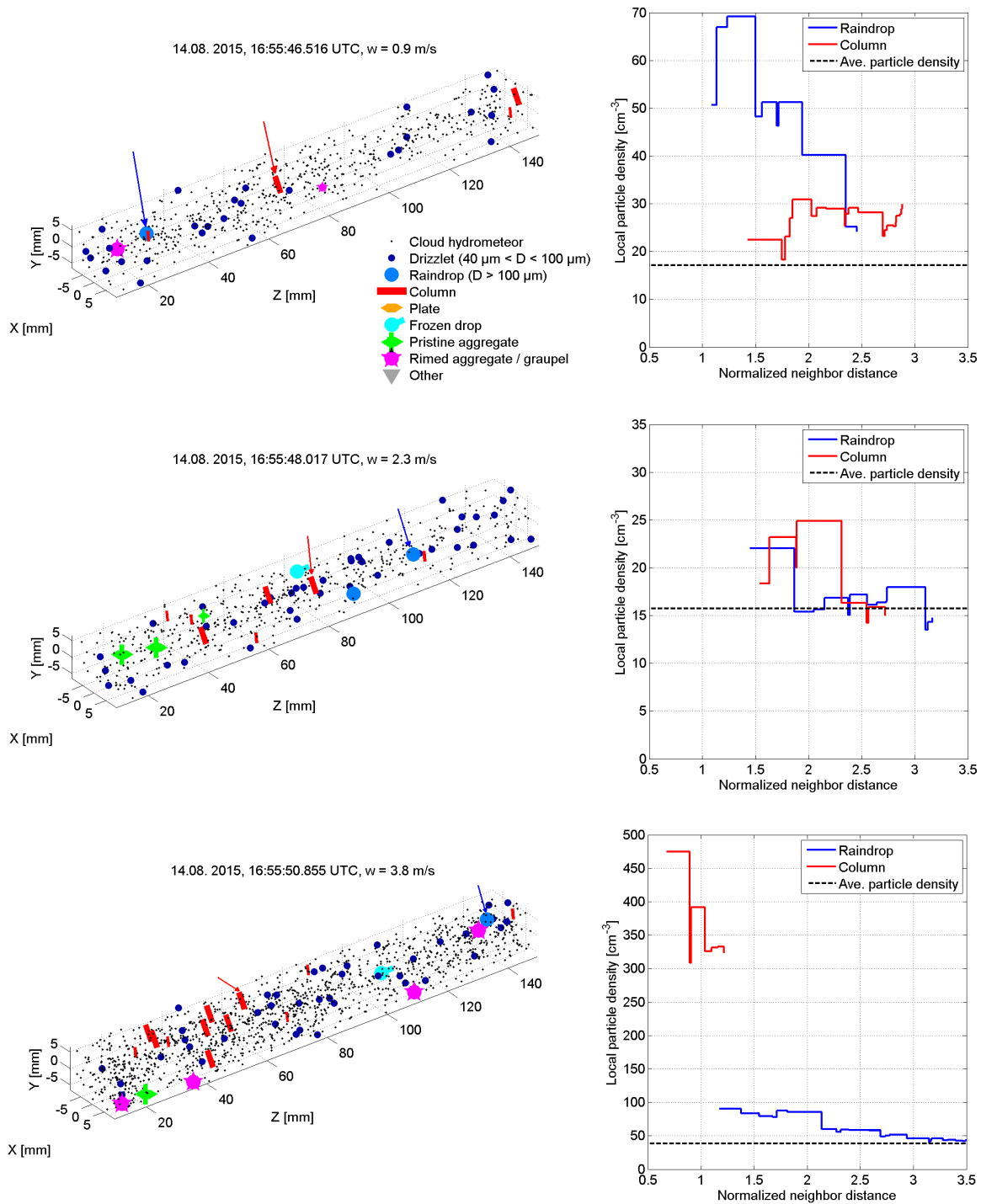


Fig. F.12: Pseudo-3D display of ice crystals and droplets in three holograms at different vertical velocities as in Fig. 7.6 with additional plots of the local particle concentration of a selected ice crystal and a selected raindrop (marked with arrows).

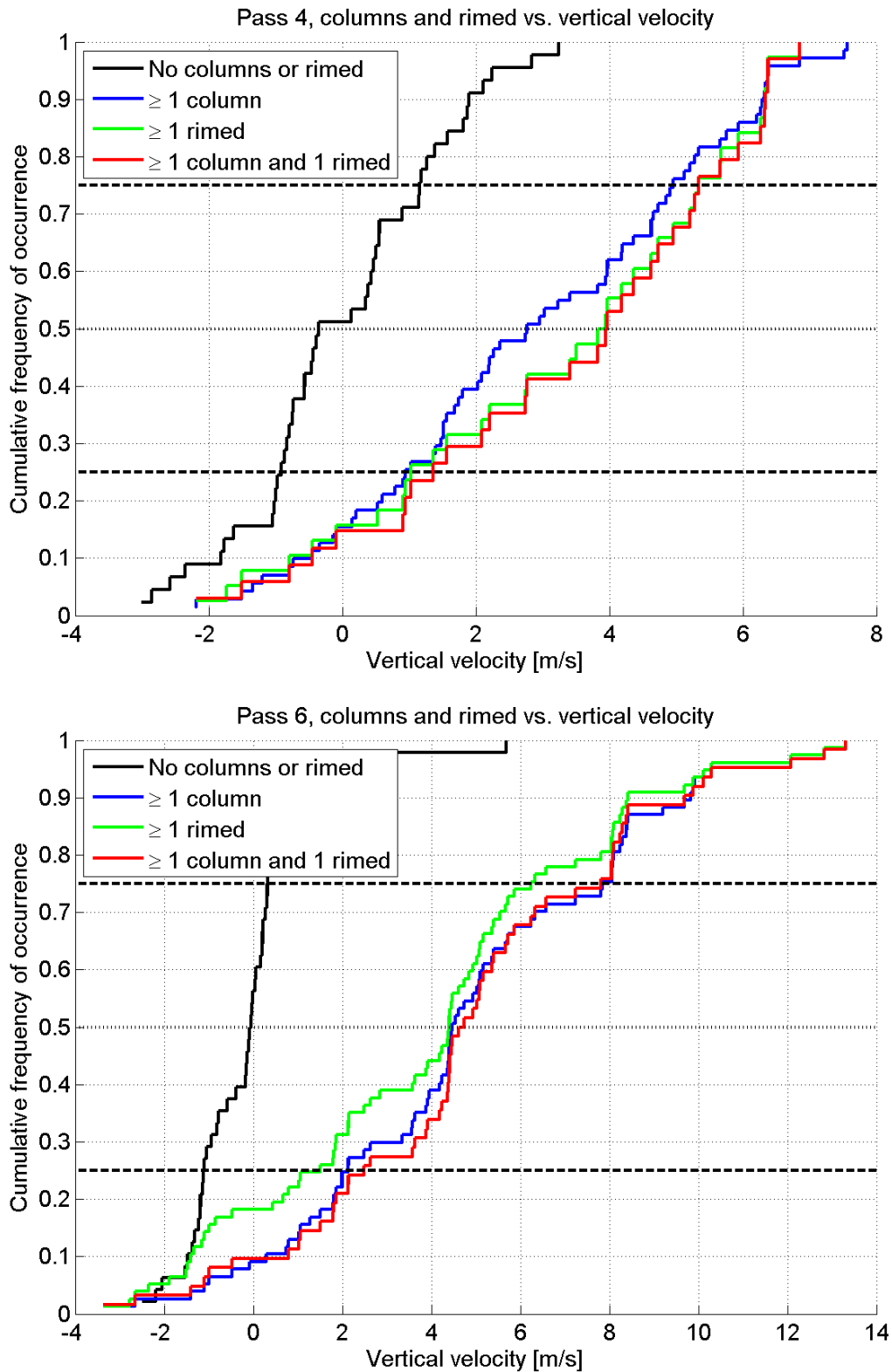


Fig. F.13: Cumulative distribution of vertical velocity in Pass 4 (top) and Pass 6 (bottom) of holograms containing no columnar ice crystal or rimed aggregate (black), at least one columnar ice crystal (blue), at least one rimed aggregate or frozen drop (green) and at least one column and one frozen drop or rimed aggregate (red).

G

COSMICS campaign overview and additional data

G.1 Meteorological overview of COSMICS Flight B889, B890 and B895

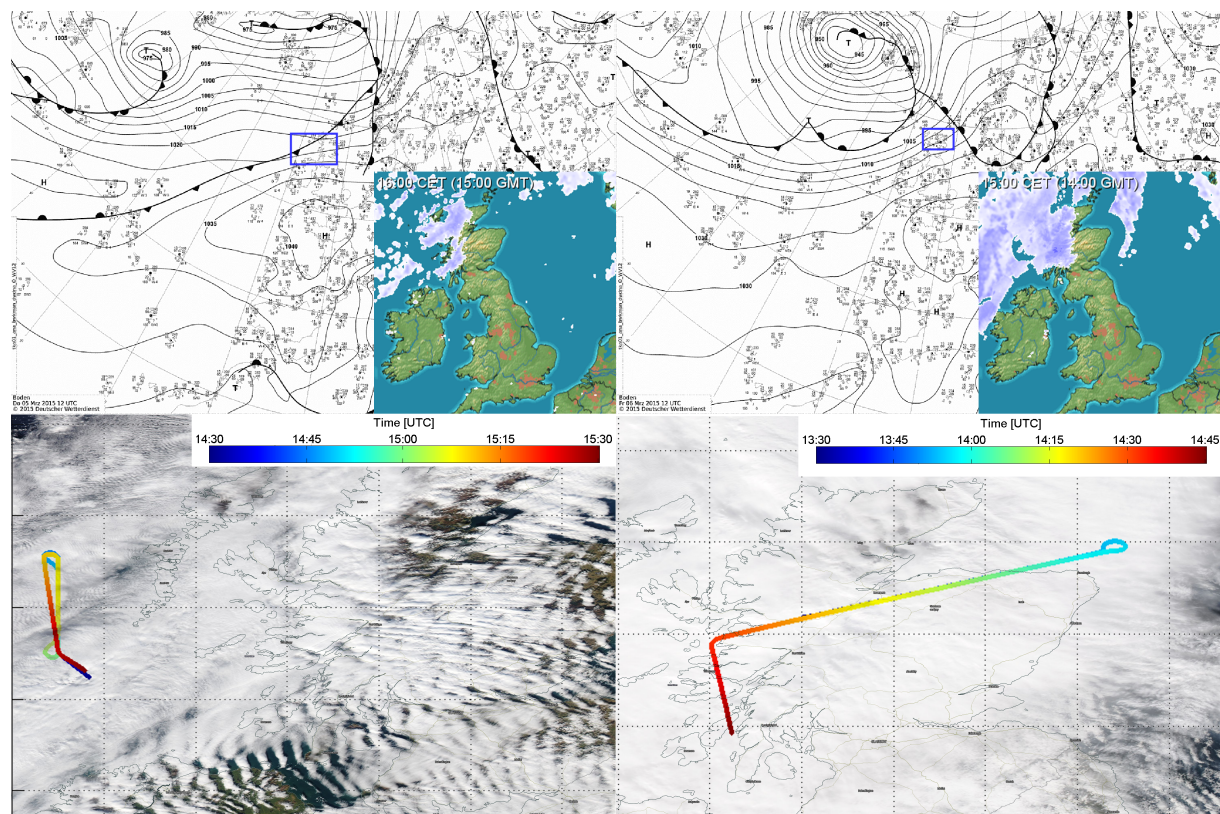


Fig. G.1: Top row: Surface analysis map from Deutscher Wetterdienst (DWD) on 05 March 2015, 12:00 UTC (left) and 06 March 2015, 12:00 UTC (right). The blue frame marks the approximate region which is shown in the bottom row. In the bottom left corners, the radar reflectivity is shown (images taken from <http://www.meteox.com>). Bottom row: Satellite image from the MODIS instrument on Aqua with overlay of the flight track (time is color-coded) on 05 March 2015, 13:20 UTC (left) and 06 March 2015, 12:25 UTC (right). The grid spacing is 1 degree latitude / longitude. The time of the satellite overpass and the time of the in-situ measurement differ by a maximum of 140 minutes. Possible advection is not considered.

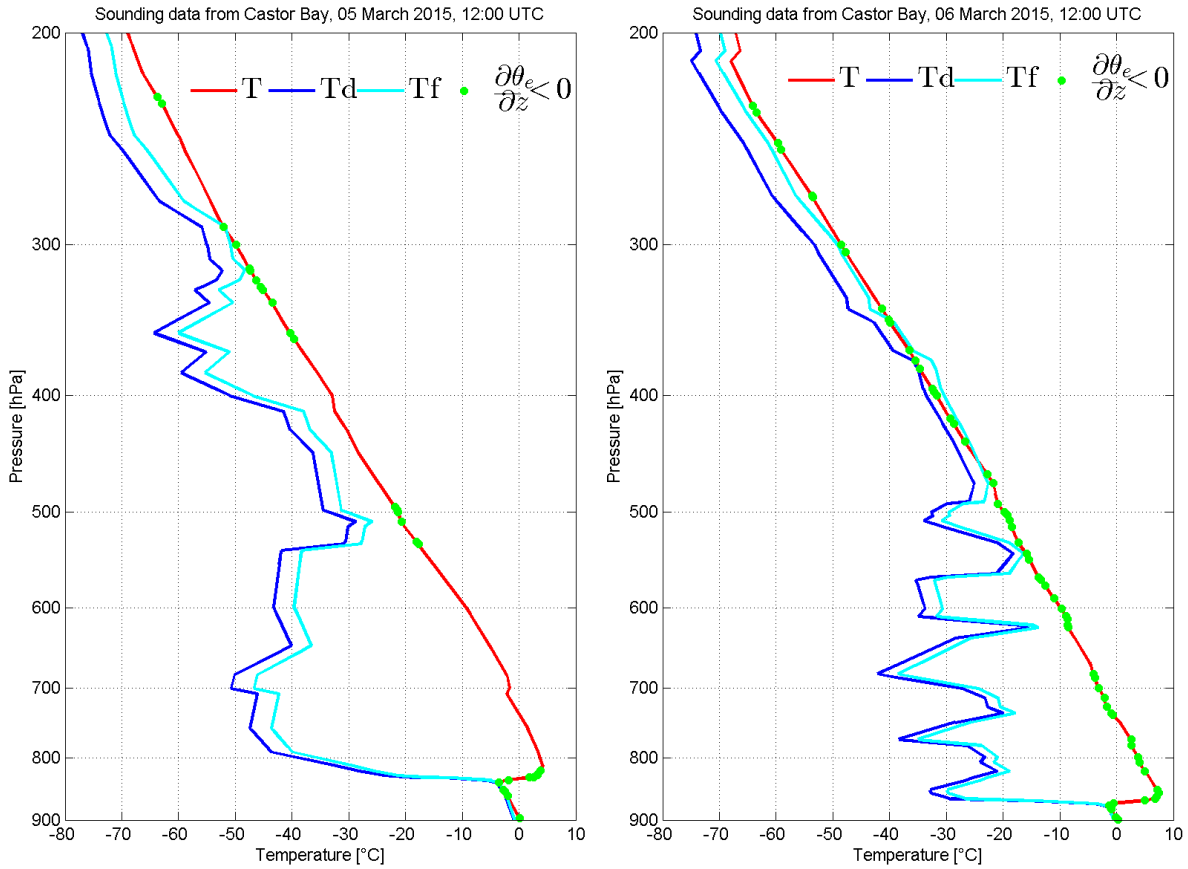


Fig. G.2: Radiosonde data from Castor Bay on 05 March 2015 12:00 UTC (left) and 06 March 2015 12:00 UTC (right). Shown are temperature (red), dewpoint (blue) and frostpoint (cyan) as a function of pressure. Dewpoint and frostpoint were calculated from the measured temperature and relative humidity via the saturation water vapor parameterization after Murphy and Koop (2005). The green circles mark regions with a potentially unstable stratification calculated from the vertical gradient of θ_e .

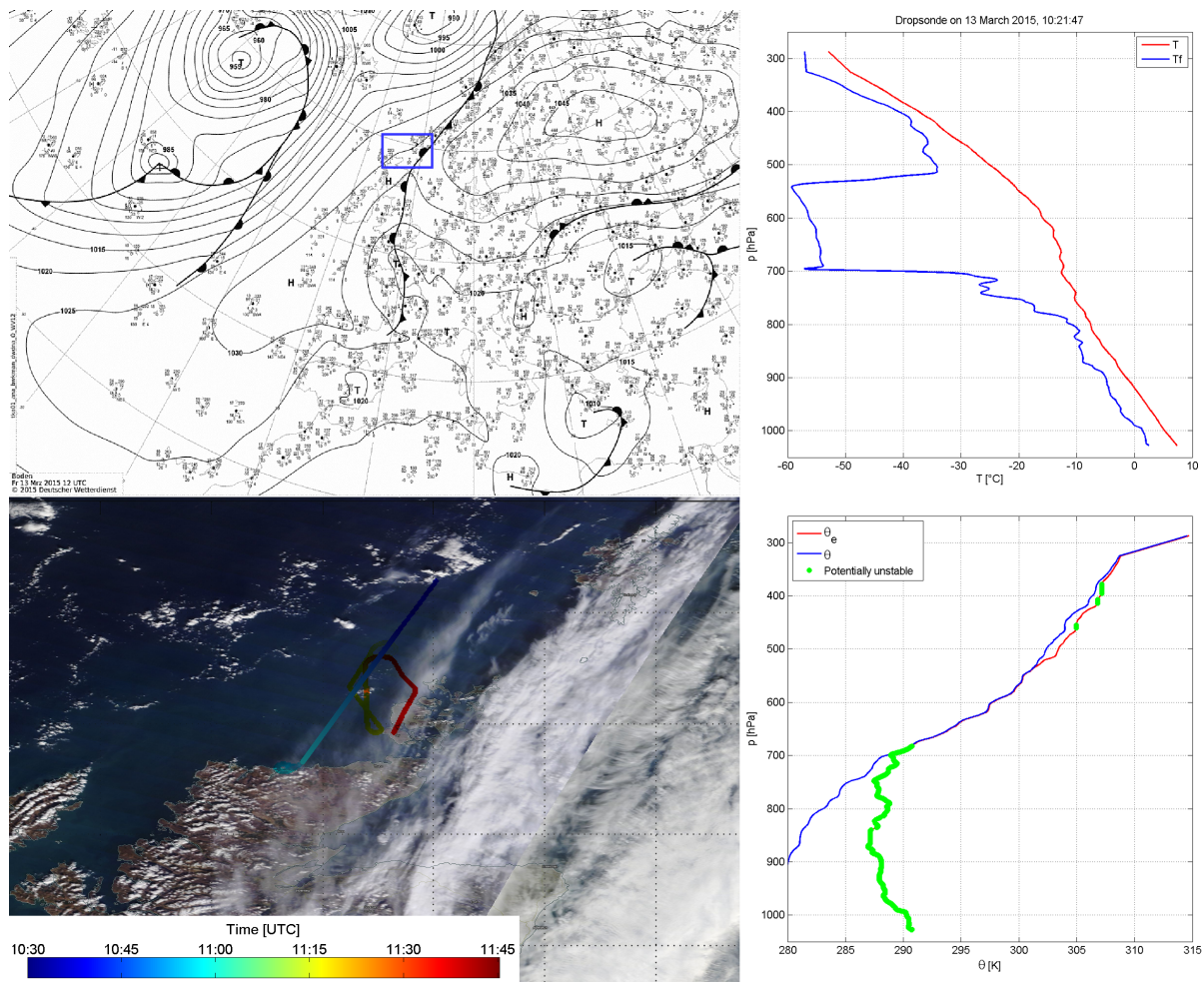


Fig. G.3: Left column: Surface weather analysis map from DWD at 13 March 2015, 12:00 UTC (top) and MODIS Terra satellite image from 13 March 2015, 10:40 UTC (bottom). Right column: Vertical profile of temperature and frostpoint (top) and potential / equivalent potential temperature (bottom) from a dropsonde released near the starting point of the flight track at 10:21:47 UTC. At a temperature below -20°C , three potentially unstable layers (marked in green) could be identified. In accordance with the aircraft data, the moisture sensor from the dropsonde indicates ice-subsaturated conditions from 300 hPa downwards.

G.2 Horizontal and vertical structure of the flights

Table G.1: Overview of the cloud events in Flight B889. Shown are the corresponding pass or run, time, pressure p , temperature T , minimum and maximum altitude h and the length of the cloud pass L .

Cloud	Event	Time (UTC)	p [hPa]	T [°C]	h [km]	L [km]
1	Profile 1	14:38:38 - 14:40:26	297 ± 2	-51.5 ± 0.3	9.17 - 9.31	15.4
2	Run 1	14:43:52 - 14:44:07	288 ± 1	-53.2 ± 0.1	9.40 - 9.42	2.6
3	Run 1	14:47:16 - 14:47:48	288 ± 1	-53.0 ± 0.1	9.43 - 9.44	5.8
4	Run 1	14:48:50 - 14:49:14	288 ± 1	-53.0 ± 0.1	9.43 - 9.44	4.3
5	Run 1	14:52:29 - 14:54:40	288 ± 1	-53.4 ± 0.1	9.45 - 9.46	24.2
6	Run 1	14:59:57 - 15:01:13	289 ± 1	-53.0 ± 0.1	9.46 - 9.47	13.0
7	Run 1	15:02:22 - 15:05:11	288 ± 1	-53.2 ± 0.1	9.45 - 9.47	30.2
8	Profile 2	15:16:16 - 15:17:08	363 ± 4	-41.2 ± 0.7	7.74 - 8.02	8.7
9	Profile 2	15:17:13 - 15:19:16	391 ± 11	-37.1 ± 1.3	7.05 - 7.71	20.4

Table G.2: As in Table G.1 for Flight B895.

Cloud	Event	Time (UTC)	p [hPa]	T [°C]	h [km]	L [km]
1	Run 1	10:32:37 - 10:37:34	322 ± 1	-49.9 ± 0.1	8.65 - 8.71	50.0
2	Profile 1	10:37:34 - 10:42:24	340 ± 11	-46.7 ± 1.9	7.94 - 8.66	48.9
3	Run 2	10:42:24 - 10:47:47	360 ± 1	-43.2 ± 0.1	7.93 - 7.94	52.5
4	Profile 2	10:47:47 - 10:51:15	377 ± 9	-40.8 ± 1.4	7.35 - 7.93	33.0
5	Run 3	10:51:15 - 11:01:09	393 ± 1	-38.5 ± 0.2	7.33 - 7.35	91.6
6	Profile 3	11:01:09 - 11:04:50	408 ± 10	-36.4 ± 1.3	6.75 - 7.34	35.5
7	Run 4	11:04:50 - 11:15:12	428 ± 1	-33.4 ± 0.2	6.74 - 6.75	92.5
8	Profile 4	11:15:12 - 11:19:29	451 ± 14	-30.3 ± 1.8	6.00 - 6.74	39.0
9	Run 5	11:19:29 - 11:28:25	475 ± 1	-27.6 ± 0.3	6.00 - 6.03	76.6

Table G.3: As in Table G.1 for Flight B890.

Cloud	Event	Time (UTC)	p [hPa]	T [°C]	h [km]	L [km]
1	Profile 1	13:46:36 - 13:51:15	478 ± 27	-21.9 ± 3.3	5.27 - 6.70	42.6
2	Run 1a	13:51:15 - 13:51:45	429 ± 1	-28.4 ± 0.2	6.70 - 6.77	4.7
3	Run 1b	13:51:45 - 13:55:37	429 ± 1	-28.4 ± 0.1	6.73 - 6.78	37.5
4	Profile 2	13:55:37 - 14:06:05	360 ± 36	-38.2 ± 5.8	6.78 - 9.21	111.5
5	Run 2	14:06:05 - 14:31:43	301 ± 1	-48.3 ± 0.4	9.19 - 9.24	296.0
6	Profile 3	14:31:43 - 14:44:21	410 ± 69	-30.0 ± 9.8	5.00 - 9.18	126.5

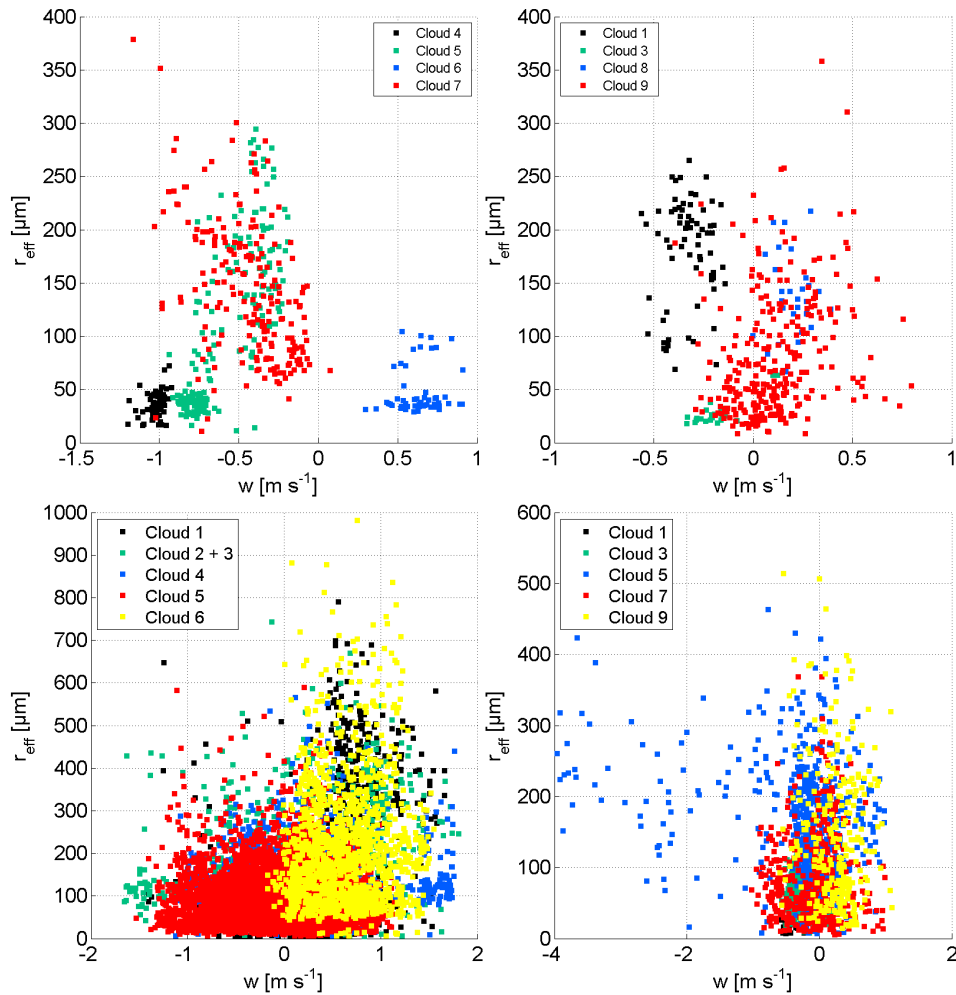


Fig. G.4: Scatter plots between w and r_{eff} for the holograms containing particles in Flight B889 on 05 March 2015 (top row), Flight B890 on 06 March 2015 and Flight B895 on 13 March 2015 (bottom row). Shown are Cloud 4,5,6 and 7 (top left) and Cloud 1,3,8 and 9 (top right) from Flight B889, all cloud events from Flight B890 (left) and Cloud 1,3,5,7 and 9 from Flight B895. Each symbol represents one hologram containing particles, the individual cloud events are color-coded.

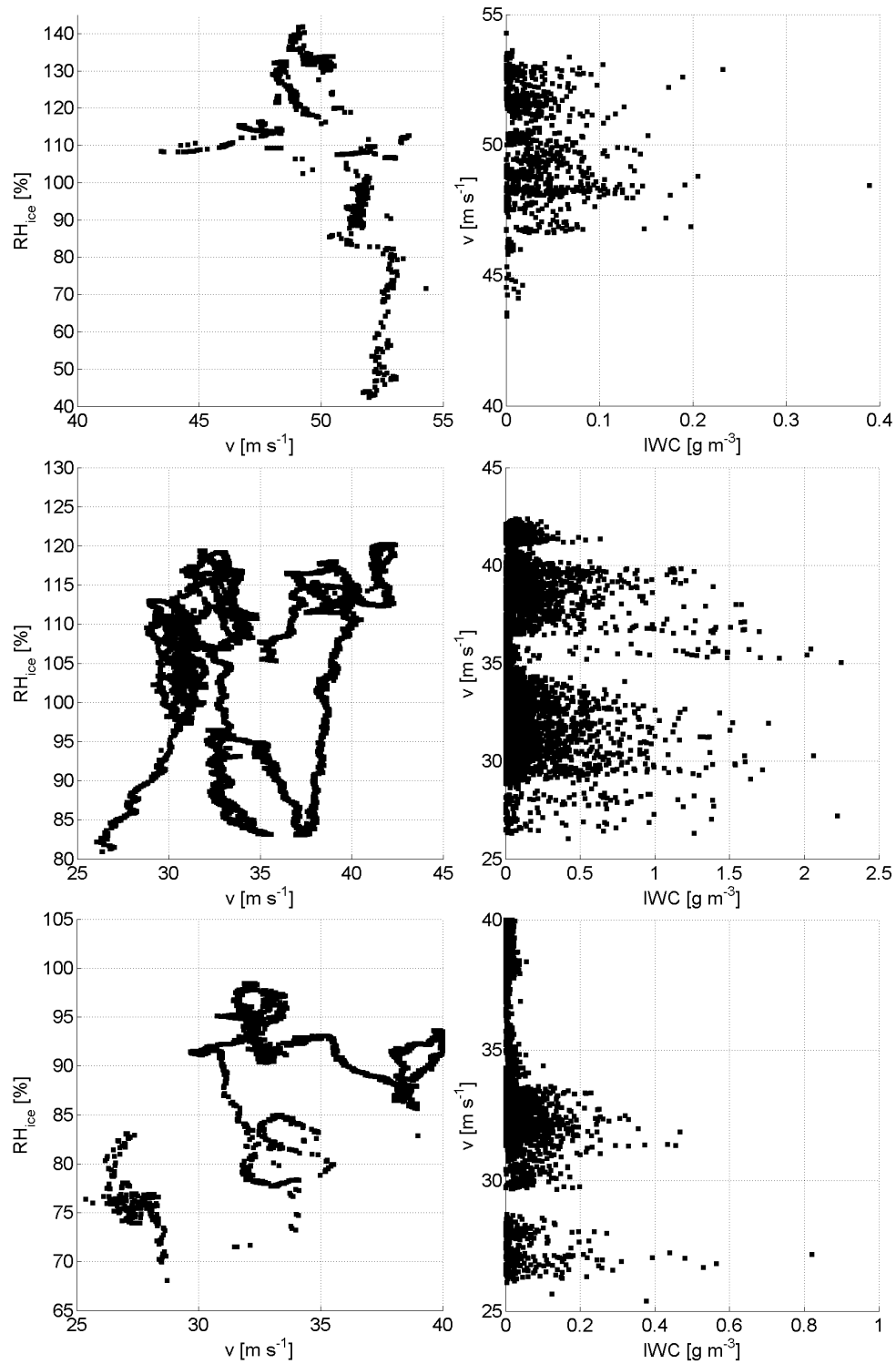


Fig. G.5: Horizontal wind speed v as a function of relative humidity over ice RH_{ice} (left) for all holograms containing ice particles in Flight B889 (top row), B890 (middle row) and B895 (bottom row). The right panels show the ice water content IWC as a function of horizontal wind speed v for the same flights.

G.3 Time series data of COSMICS Flight B889, B890 and B895

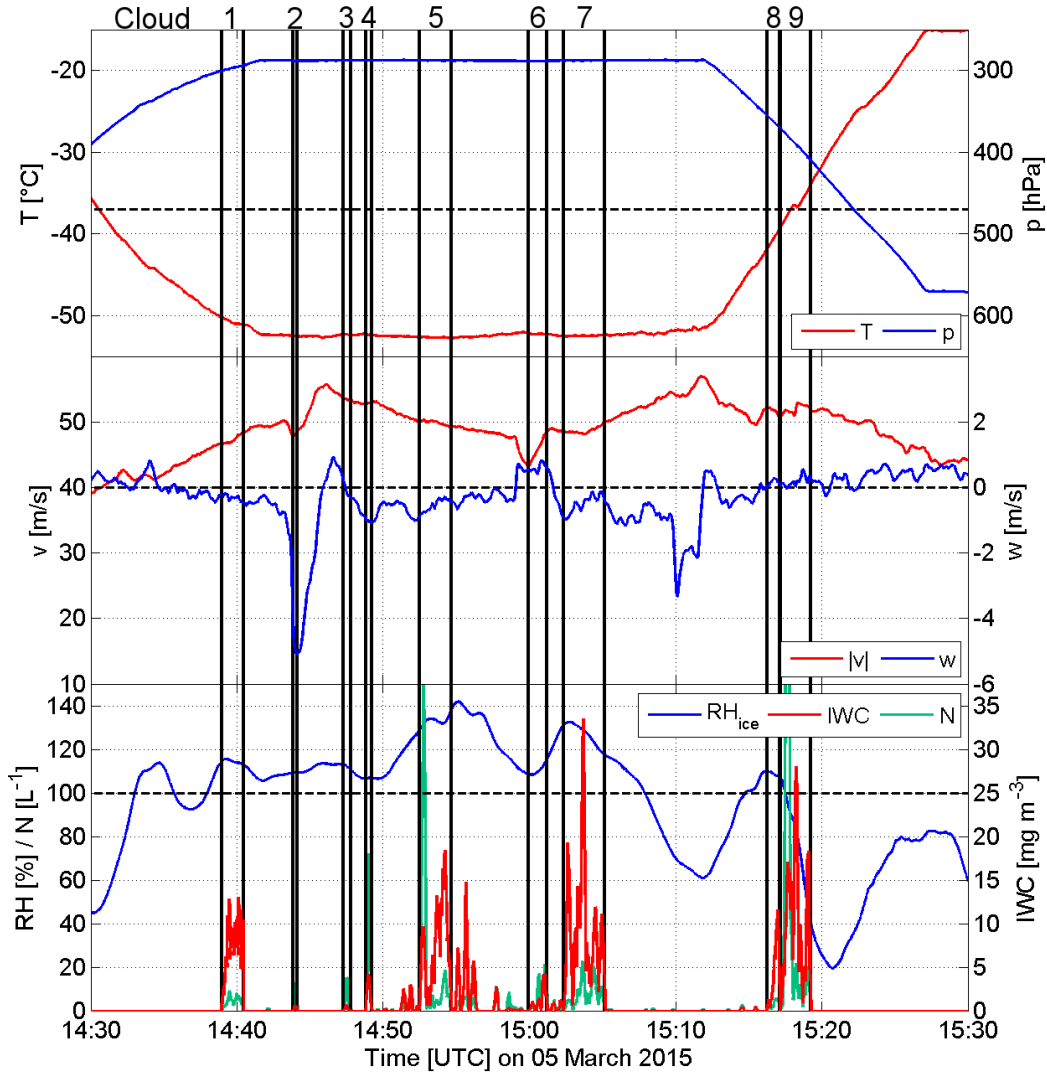


Fig. G.6: Time series of Flight B889 with temperature (right) and pressure (left) in the top panel, horizontal (left) and vertical (right) wind speed in the middle panel, and relative humidity w.r.t. ice and HALOHolo particle number concentration (left) as well as HALOHolo IWC (right) in the bottom panel. Each plotted time series resembles a 10 second running average of the original data. The relative humidity data taken from the General Eastern chilled mirror hygrometer (the dewpoint in the data record was interpreted as frostpoint) were 150 second running averages in order to remove oscillations caused by heating / cooling from the time series. The dotted black lines represent the homogeneous freezing temperature below which all hydrometeors are considered as ice (upper panel), zero vertical velocity (middle panel) and 100 % relative humidity (bottom panel). The estimated accuracy is $\Delta T = \pm 0.3$ K, $\Delta w = \pm 0.5$ m s⁻¹ and $\Delta RH_{ice} = \pm 10$ %. The cloud passes are marked by black lines with their corresponding numbers written on top.

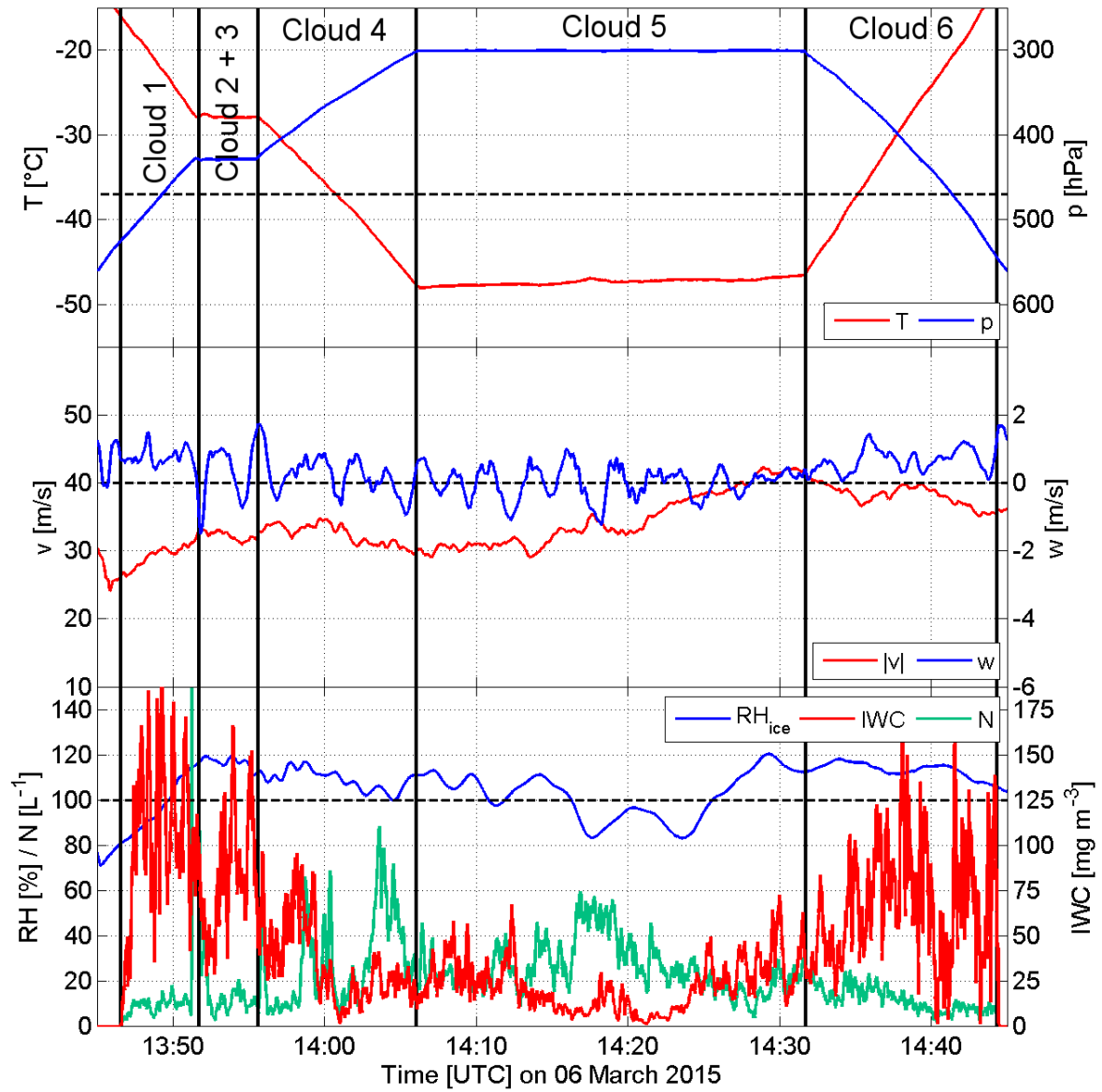


Fig. G.7: As in Fig. G.6 for Flight B890 on 06 March 2015.

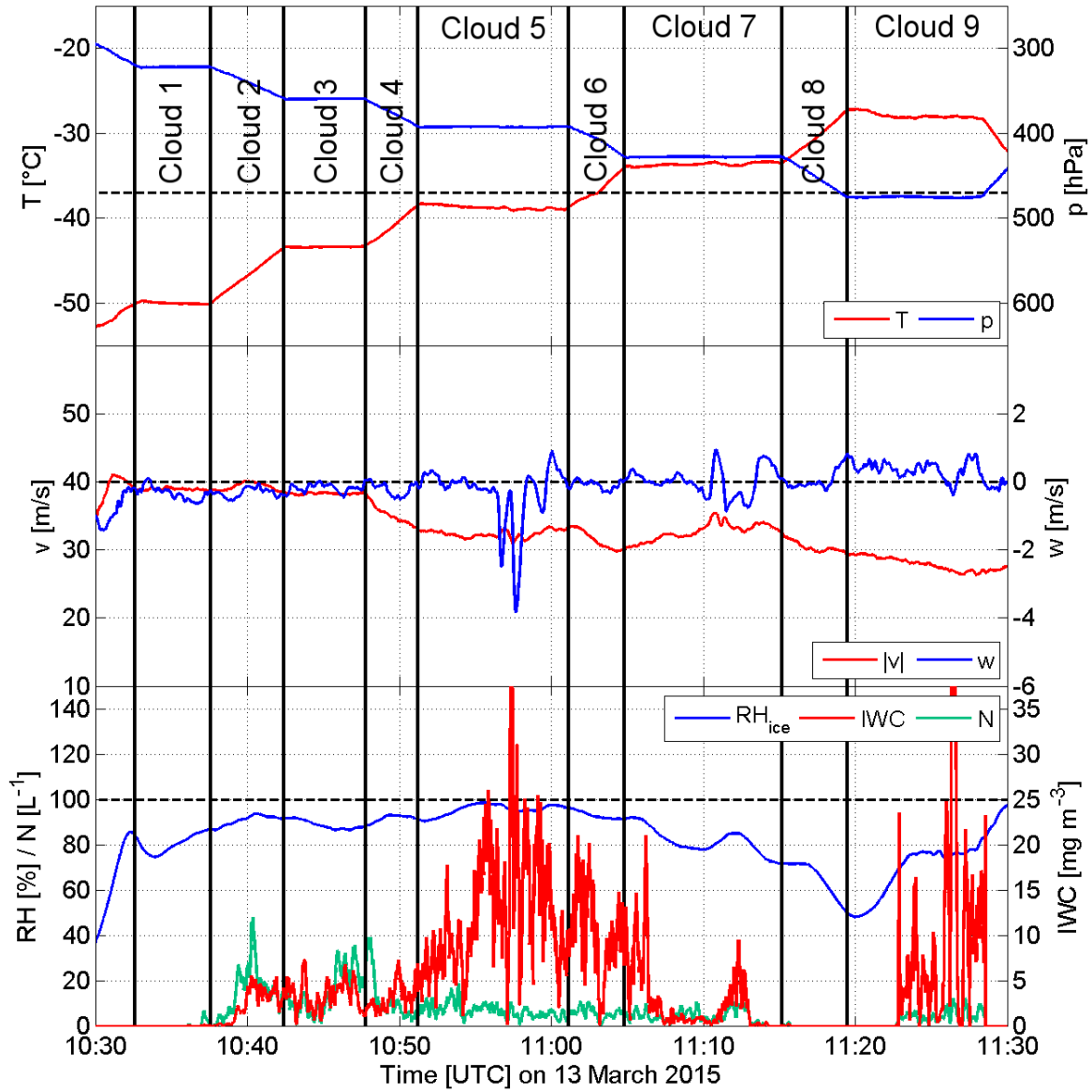


Fig. G.8: As in Fig. G.6 for Flight B895 on 13 March 2015.

G.4 Size distribution intercomparison

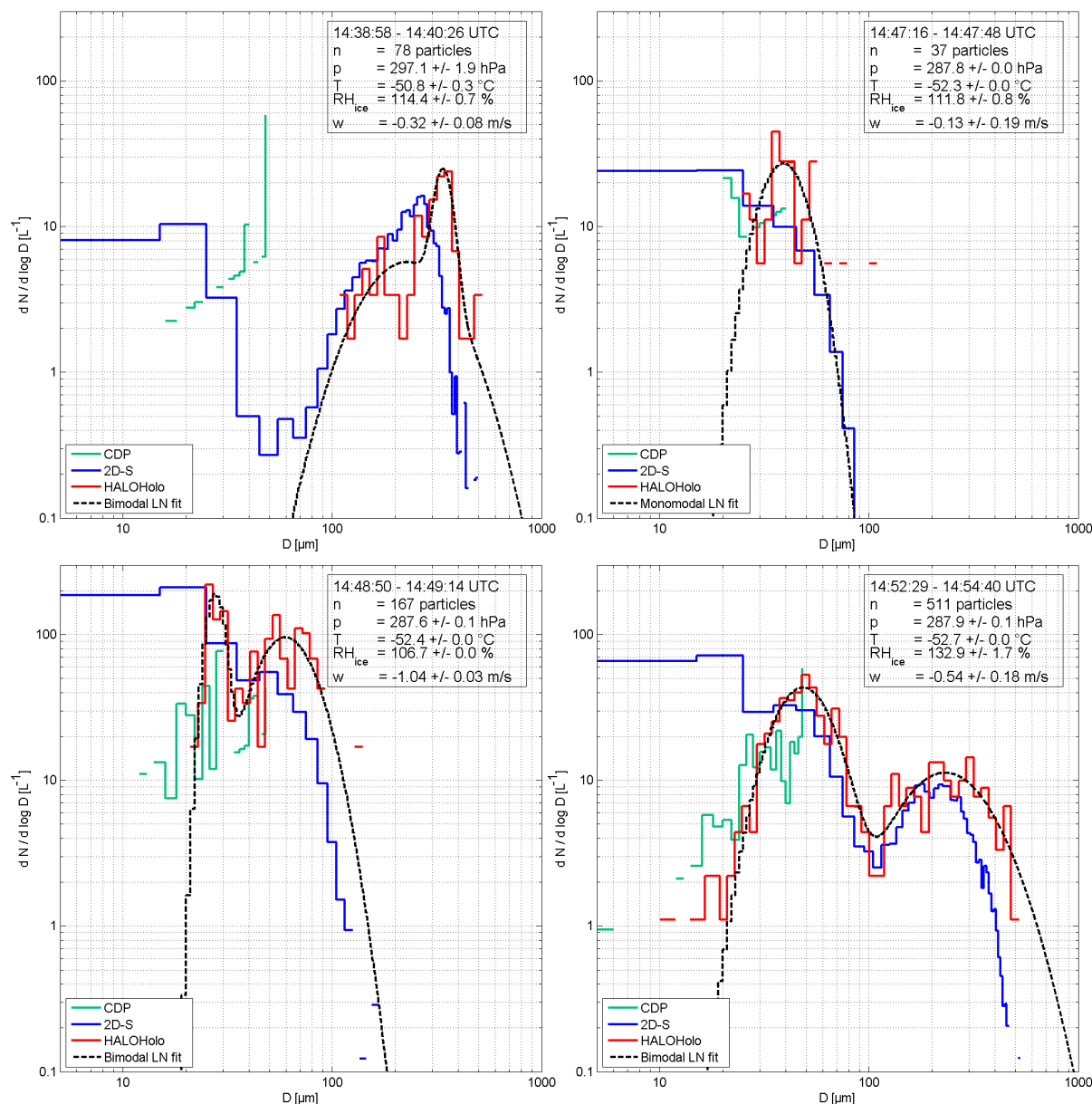


Fig. G.9: Particle size distributions for Flight B889 on 05 March 2015. Shown are the number-weighted particle size distributions for the FAAM CDP (green), the University of Manchester 2D-S (blue), and HALOHolo (red) for Cloud 1 (top left), Cloud 3 (top right), Cloud 4 (bottom left) and Cloud 5 (bottom right). No distinction between spherical and aspherical objects was applied here. Additional information is shown in the top right corner of each panel with the start and end time of the cloud event, the number of particles in HALOHolo, the temperature (mean ± std), the relative humidity over ice (mean ± std), and the vertical velocity (mean ± std).

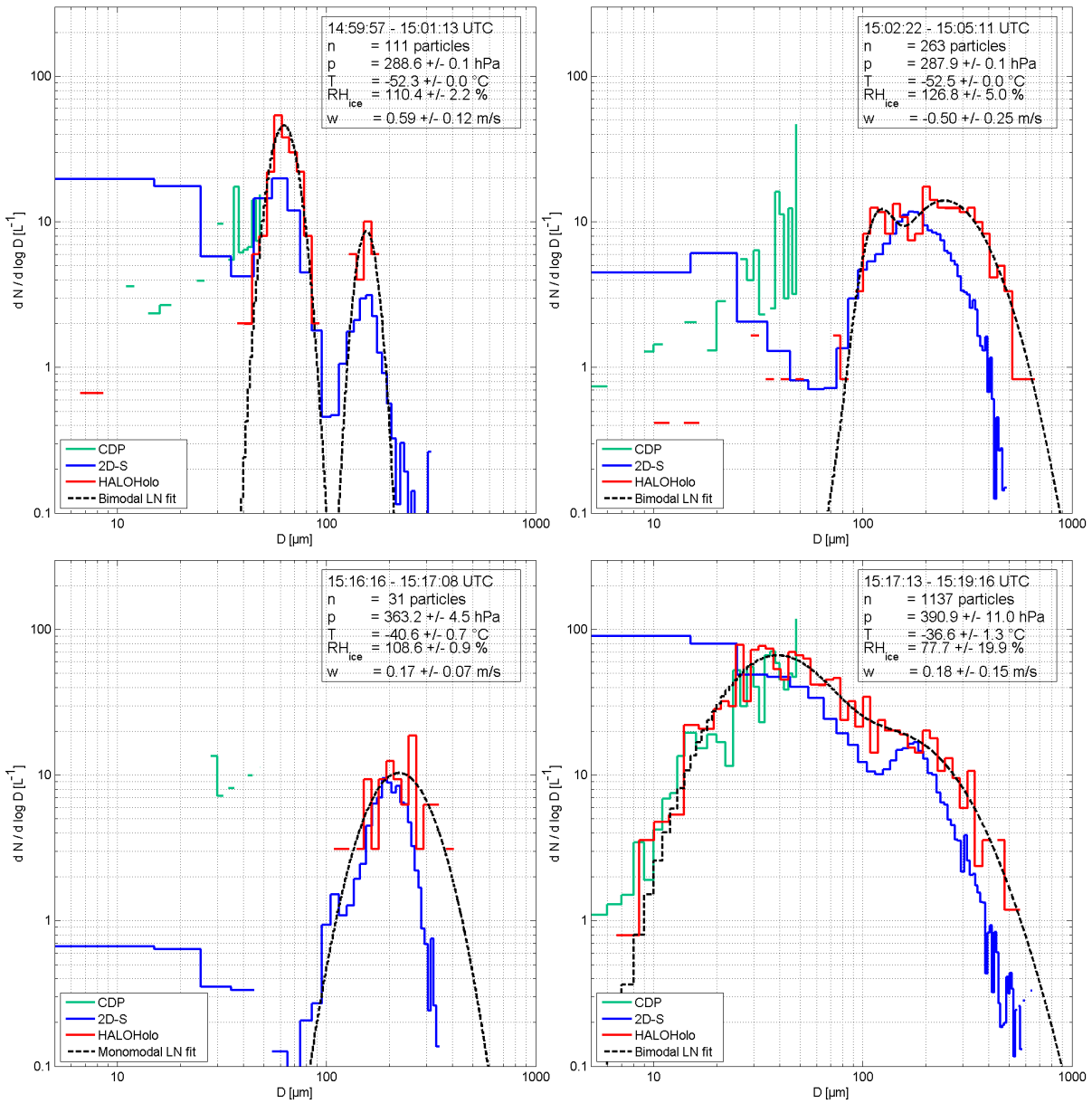


Fig. G.10: As in Fig. G.9 for Cloud 6 (top left), Cloud 7 (top right), Cloud 8 (bottom left) and Cloud 9 (bottom right).

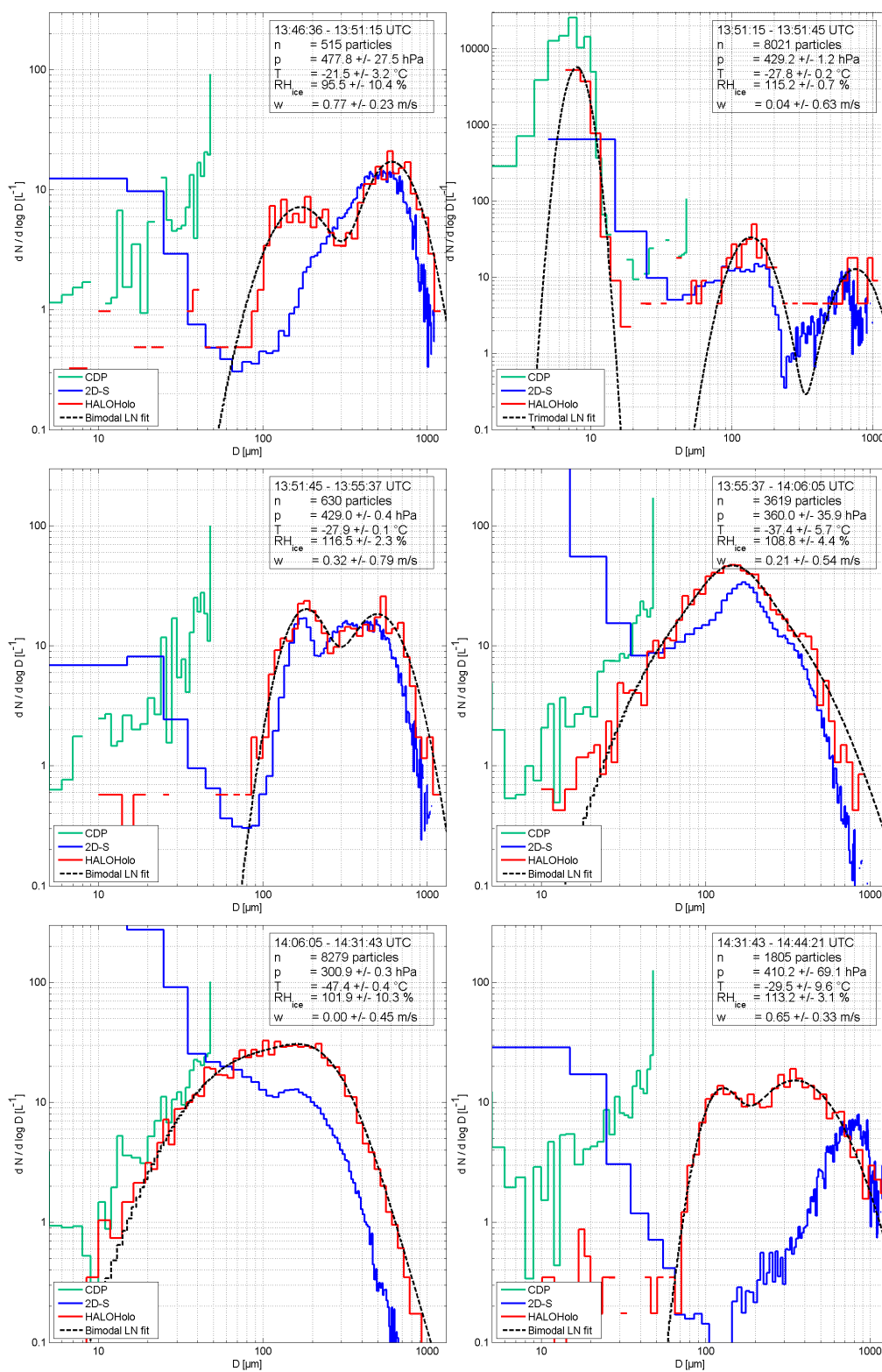


Fig. G.11: As in Fig. G.9 for Clouds 1-6 in Flight B890 on 06 March 2015.

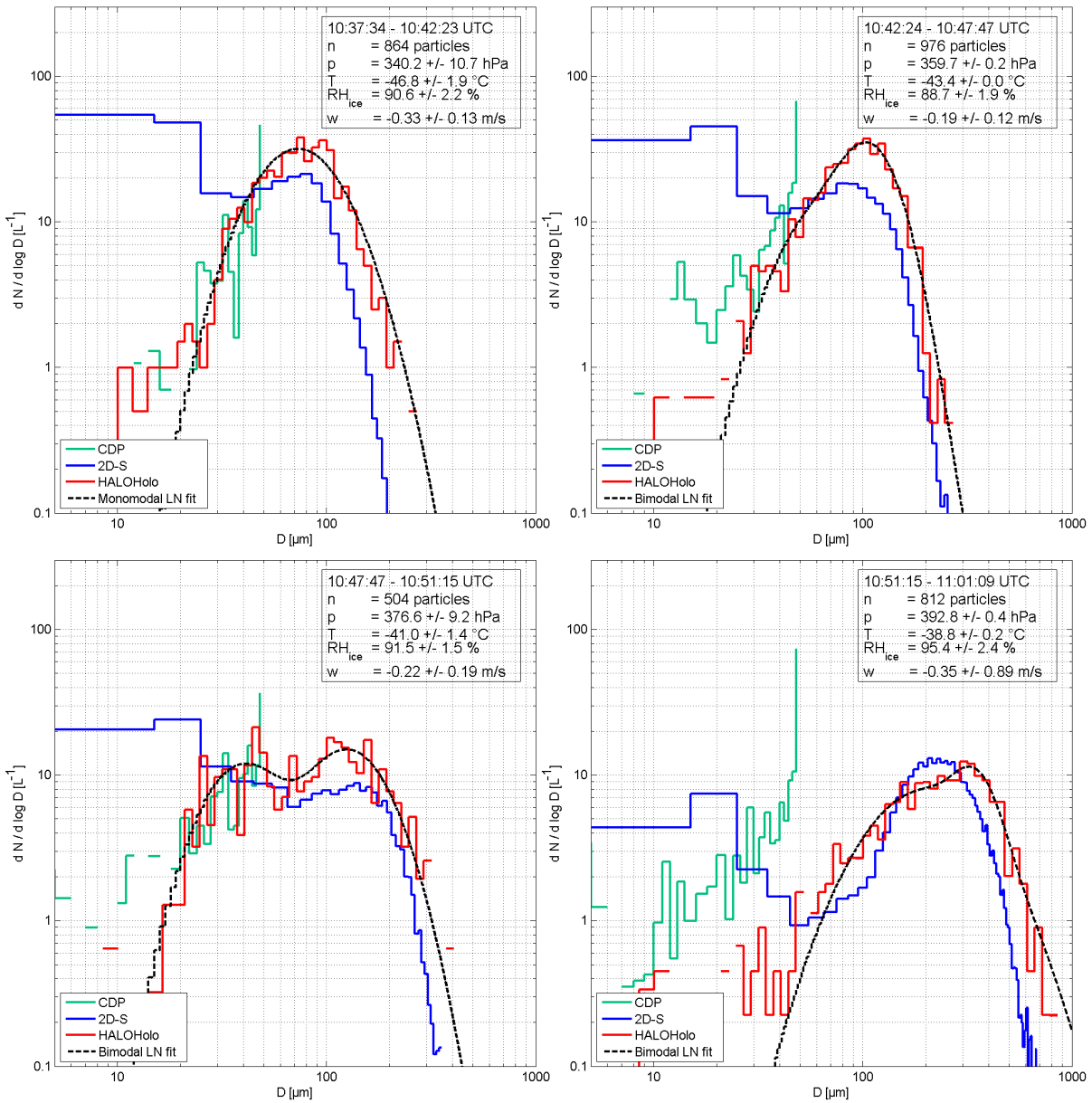


Fig. G.12: As in Fig. G.9 for Flight B895 on 13 March 2015. The cloud events displayed are

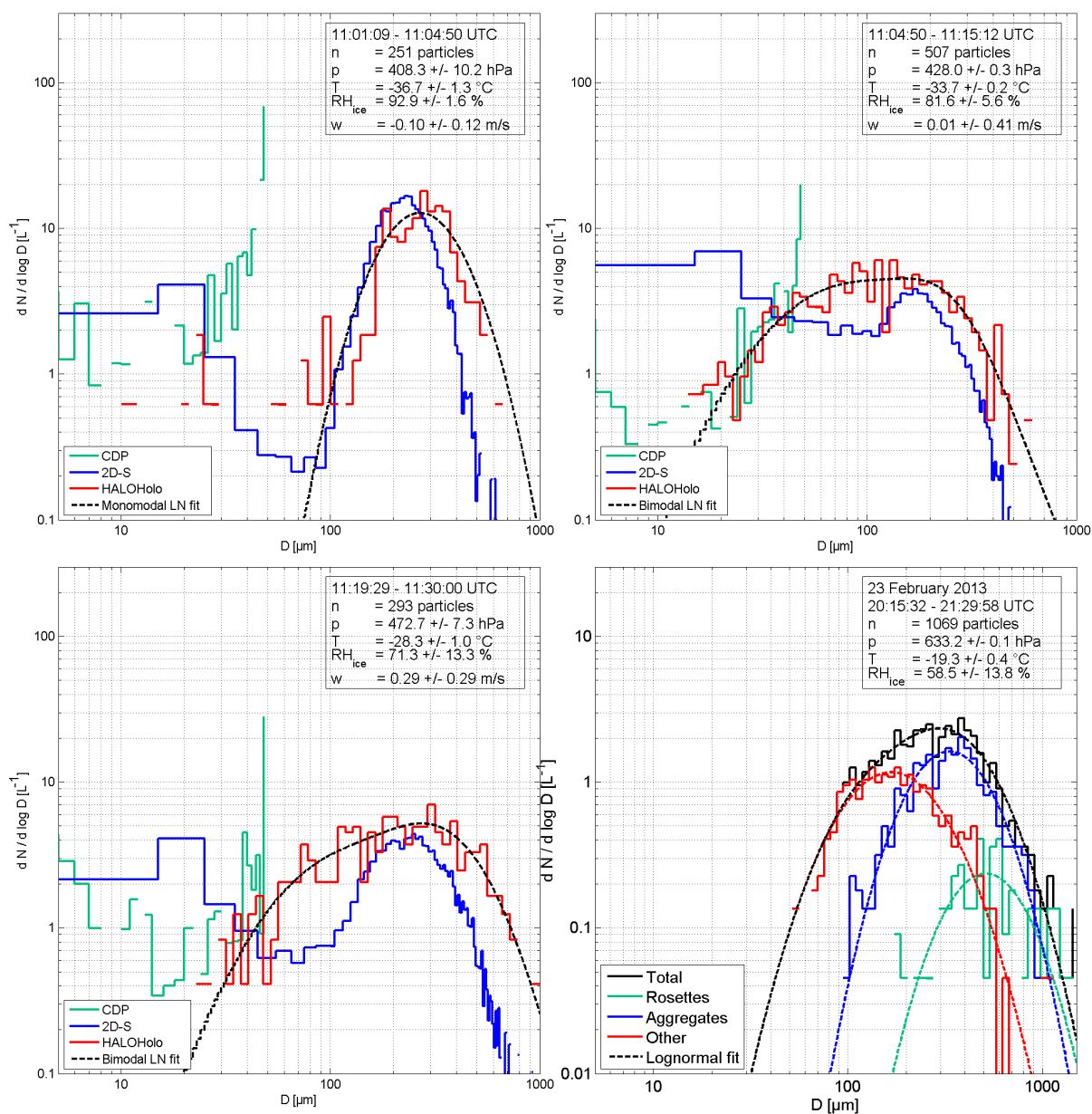


Fig. G.13: As in Fig. G.12 for Cloud 6 (top left), Cloud 7 (top right), Cloud 8 (bottom left) in Flight B895 on 13 March 2015 and ground-based measurements from the Jungfraujoch station obtained by GipefHolo 2 on 23 February 2013 (bottom right).

G.5 Particle size distributions and fit parameters

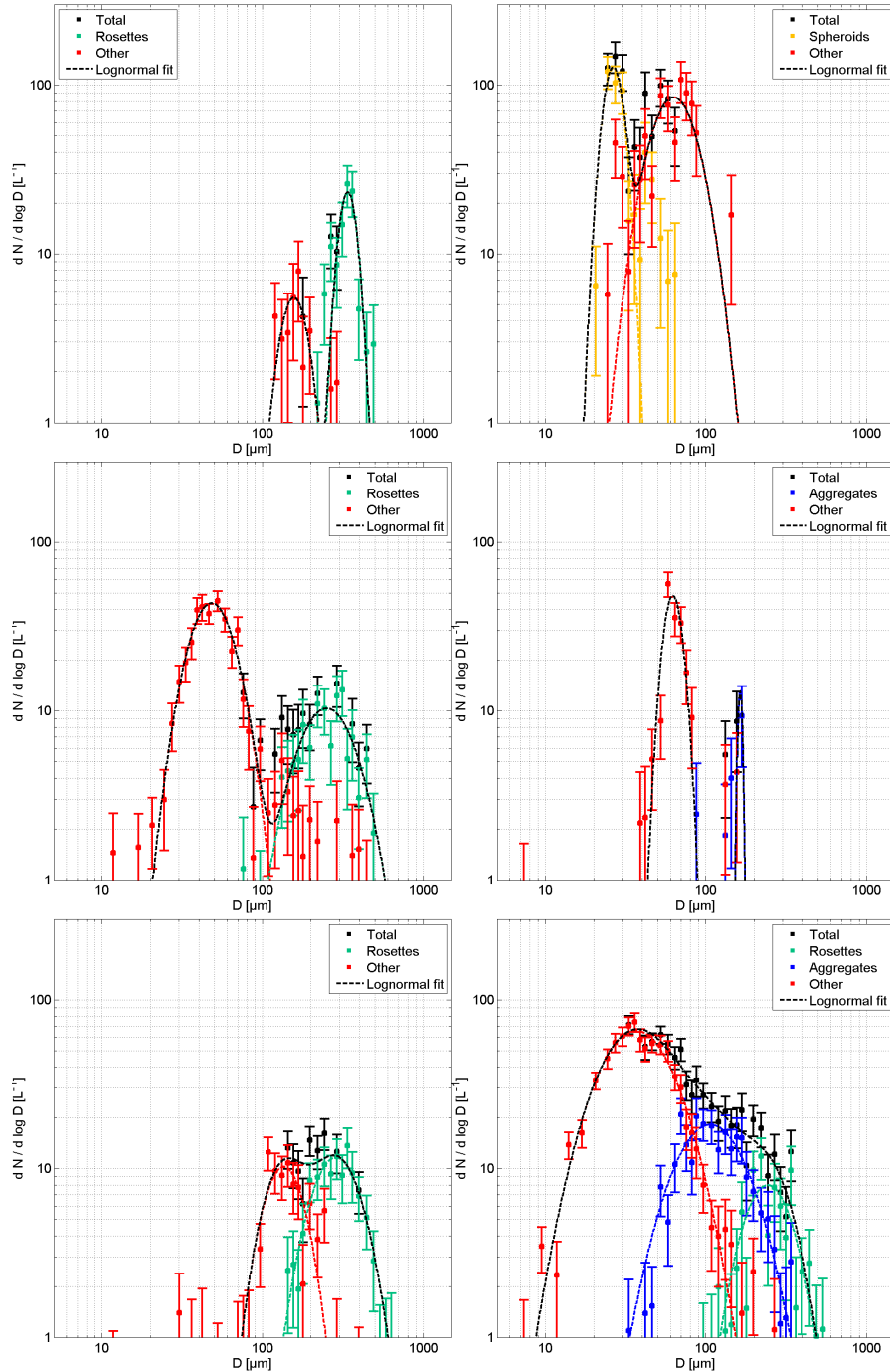


Fig. G.14: As in Fig. G.9 for Cloud 1, 4, 5, 6, 7 and 9 with a distinction between different ice crystal habits (HALOHolo data only). The term "Other" means the total size distribution minus the size distributions for the habits which are explicitly declared. The colored dashed lines represent the individual log-normal fits, the black dashed line is the sum of the individual fits.

Table G.4: Fit parameters of the cloud events in Flight B889 on 05 March 2015. The fit function is defined in Eq. 8.1. Bold-face values indicate an issue with this fit and should not be used in any parameterization. The fits are either bimodal (BM) or monomodal (MM). Individual habit classes are Spheroids (Sph), Aggregates (Agg) and Rosettes (Ros). "Other" means the remaining habit classes after subtracting the explicitly declared ones.

Event	Fit type	$D_0[\mu\text{m}]$	σ_0	$N_0[\text{L}^{-1}]$	$D_1[\mu\text{m}]$	σ_1	$N_1[\text{L}^{-1}]$	$RMSE$	r^2
B889-1	Total BM	339	0.914	-4.75	227	1.561	6.36	1.52	0.909
B889-1	Ros MM	331	1.144	7.29				1.56	0.897
B889-1	Other MM	158	1.214	2.62				0.80	0.736
B889-2	Total MM	46	1.297	48.45				16.8	0.601
B889-3	Total MM	39	1.263	15.96				5.06	0.673
B889-4	Total BM	59	1.355	72.72	27	1.103	45.72	20.6	0.810
B889-4	Sph MM	27	1.108	38.84				14.0	0.800
B889-4	Other BM	63	1.327	60.83				15.2	0.716
B889-5	Total BM	230	1.586	13.01	48	1.354	32.87	3.51	0.921
B889-5	Ros MM	250	1.481	9.95				1.37	0.853
B889-5	Other BM	48	1.361	33.27				3.24	0.938
B889-6	Total BM	155	1.107	2.20	62	1.144	15.52	2.46	0.941
B889-6	Agg MM	158	1.095	1.52				0.41	0.894
B889-6	Other MM	62	1.144	15.46				2.43	0.942
B889-7	Total BM	245	1.501	14.23	119	1.162	3.40	8.17	0.879
B889-7	Ros MM	284	1.400	9.87				0.76	0.958
B889-7	Other MM	136	1.342	7.64				1.37	0.826
B889-8	Total MM	222	1.335	7.93				1.90	0.740
B889-9	Total BM	151	1.737	24.14	38	1.691	86.39	8.17	0.879
B889-9	Ros MM	238	1.371	6.84				1.16	0.833
B889-9	Agg MM	107	1.600	21.49				2.16	0.893
B889-9	Other MM	37	1.627	80.64				7.19	0.910

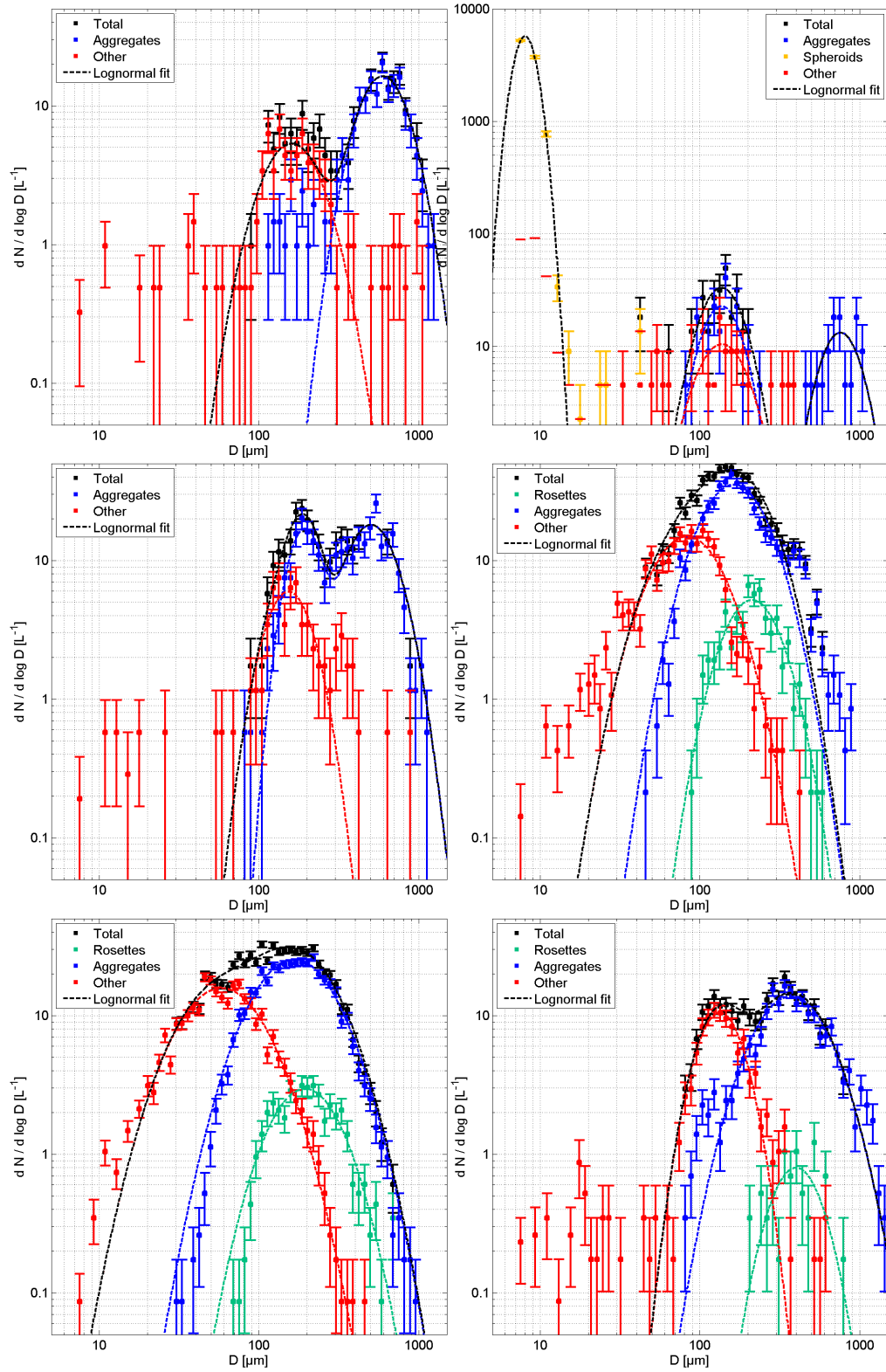


Fig. G.15: As in Fig. G.14 for Flight B890. The class of "Spheroids" in Cloud 2 is likely due to supercooled droplets.

Table G.5: As in Table G.4 for Flight B890 on 06 March 2015. Case B890-2 contains a trimodal (TM) fit.

Event	Fit type	$D_0[\mu\text{m}]$	σ_0	$N_0[\text{L}^{-1}]$	$D_1[\mu\text{m}]$	σ_1	$N_1[\text{L}^{-1}]$	$RMSE$	r^2
B890-1	Total BM	608	1.362	13.20	169	1.483	7.06	1.44	0.921
B890-1	Agg MM	595	1.379	13.16				1.37	0.925
B890-1	Other MM	159	1.467	5.12				0.81	0.794
B890-2	Total TM	136	1.311	22.69	751	1.313	8.74	6.29	0.999
B890-2	TM cont'd	8	1.165	2183				6.29	0.999
B890-2	Sph MM	8	1.165	2183				3.19	0.999
B890-2	Agg BM	136	1.295	14.69	756	1.290	8.41	4.73	0.651
B890-2	Other MM	137	1.38	8.42				2.99	0.441
B890-3	Total BM	497	1.398	15.40	182	1.318	13.84	2.14	0.918
B890-3	Agg BM	192	1.243	9.13	501	1.390	14.91	1.98	0.912
B890-3	Other MM	153	1.351	4.49				0.87	0.783
B890-4	Total BM	143	2.030	47.37	146	1.371	15.75	1.95	0.983
B890-4	Ros MM	211	1.455	4.86				0.51	0.914
B890-4	Agg MM	162	1.544	38.28				2.59	0.952
B890-4	Other MM	83	1.597	17.44				1.40	0.925
B890-5	Total BM	204	1.496	15.20	92	2.076	43.70	1.88	0.972
B890-5	Ros MM	194	1.586	3.42				0.23	0.953
B890-5	Agg MM	166	1.701	33.79				1.12	0.985
B890-5	Other MM	58	1.742	21.93				1.25	0.952
B890-6	Total BM	122	1.265	6.57	348	1.661	19.33	1.13	0.960
B890-6	Ros MM	399	1.401	0.67				0.16	0.699
B890-6	Agg MM	369	1.614	16.48				1.10	0.945
B890-6	Other MM	133	1.355	7.97				0.57	0.965

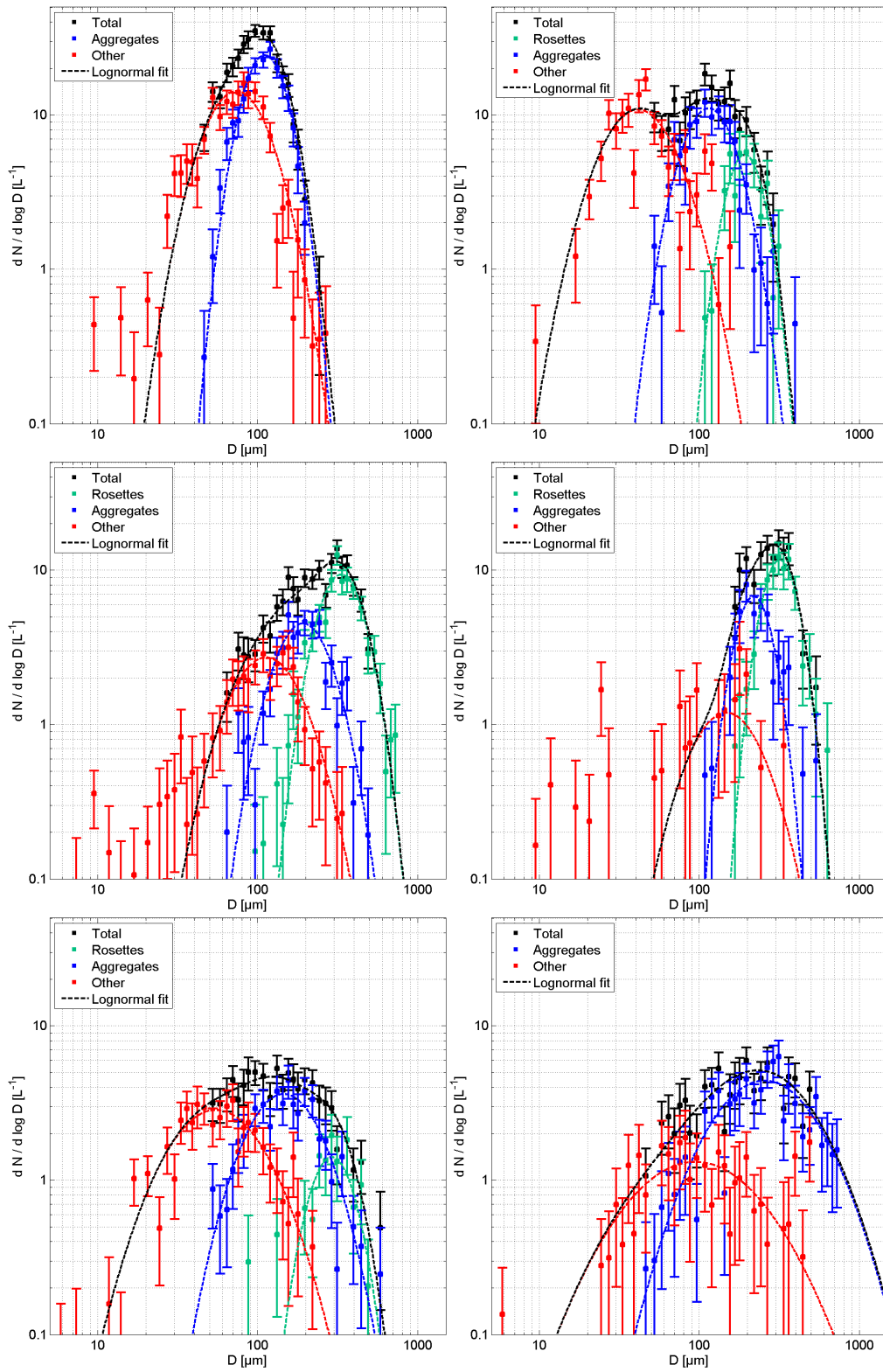


Fig. G.16: As in Fig. G.14 for Flight B895 on 13 March 2015. The cloud events displayed are Cloud 3, 4 and 5 (top row) and Cloud 6, 7 and 9 (bottom row).

Table G.6: As in Table G.4 for Flight B895.

Event	Fit type	$D_0[\mu\text{m}]$	σ_0	$N_0[\text{L}^{-1}]$	$D_1[\mu\text{m}]$	σ_1	$N_1[\text{L}^{-1}]$	$RMSE$	r^2
B895-1	Total MM	25	1.387	2.78				0.83	0.586
B895-2	Total MM	76	1.521	34.46				2.60	0.945
B895-2	Agg MM	111	1.214	7.13				0.97	0.935
B895-2	Other MM	67	1.439	26.91				2.35	0.940
B895-3	Total BM	108	1.314	17.82	71	1.565	15.14	1.58	0.979
B895-3	Agg MM	111	1.340	17.63				1.28	0.969
B895-3	Other MM	74	1.531	15.20				1.57	0.899
B895-4	Total BM	40	1.495	11.85	126	1.488	14.75	2.76	0.788
B895-4	Ros MM	193	1.265	3.34				0.62	0.862
B895-4	Agg MM	115	1.410	9.60				0.94	0.931
B895-4	Other MM	41	1.602	13.34				2.45	0.706
B895-5	Total BM	341	1.230	3.05	203	1.779	11.46	0.76	0.958
B895-5	Ros MM	330	1.356	7.01				0.57	0.959
B895-5	Agg MM	193	1.442	4.20				0.39	0.932
B895-5	Other MM	112	1.606	3.18				0.35	0.860
B895-6	Total MM	273	1.402	12.04				1.51	0.892
B895-6	Ros MM	315	1.245	6.55				0.47	0.978
B895-6	Agg MM	218	1.295	4.16				0.78	0.844
B895-6	Other MM	145	1.628	1.41				0.61	0.200
B895-7	Total BM	213	1.464	1.71	88	2.212	8.33	0.71	0.854
B895-7	Ros MM	294	1.359	1.06				0.28	0.679
B895-7	Agg MM	147	1.644	4.53				0.51	0.862
B895-7	Other MM	55	1.868	4.45				0.40	0.870
B895-8	Total MM	68	1.132	1.98				0.89	0.685
B895-9	Total BM	133	2.062	5.98	327	1.590	4.00	0.78	0.846
B895-9	Agg MM	246	1.886	7.14				0.76	0.817
B895-9	Other MM	101	2.452	2.90				0.46	0.486

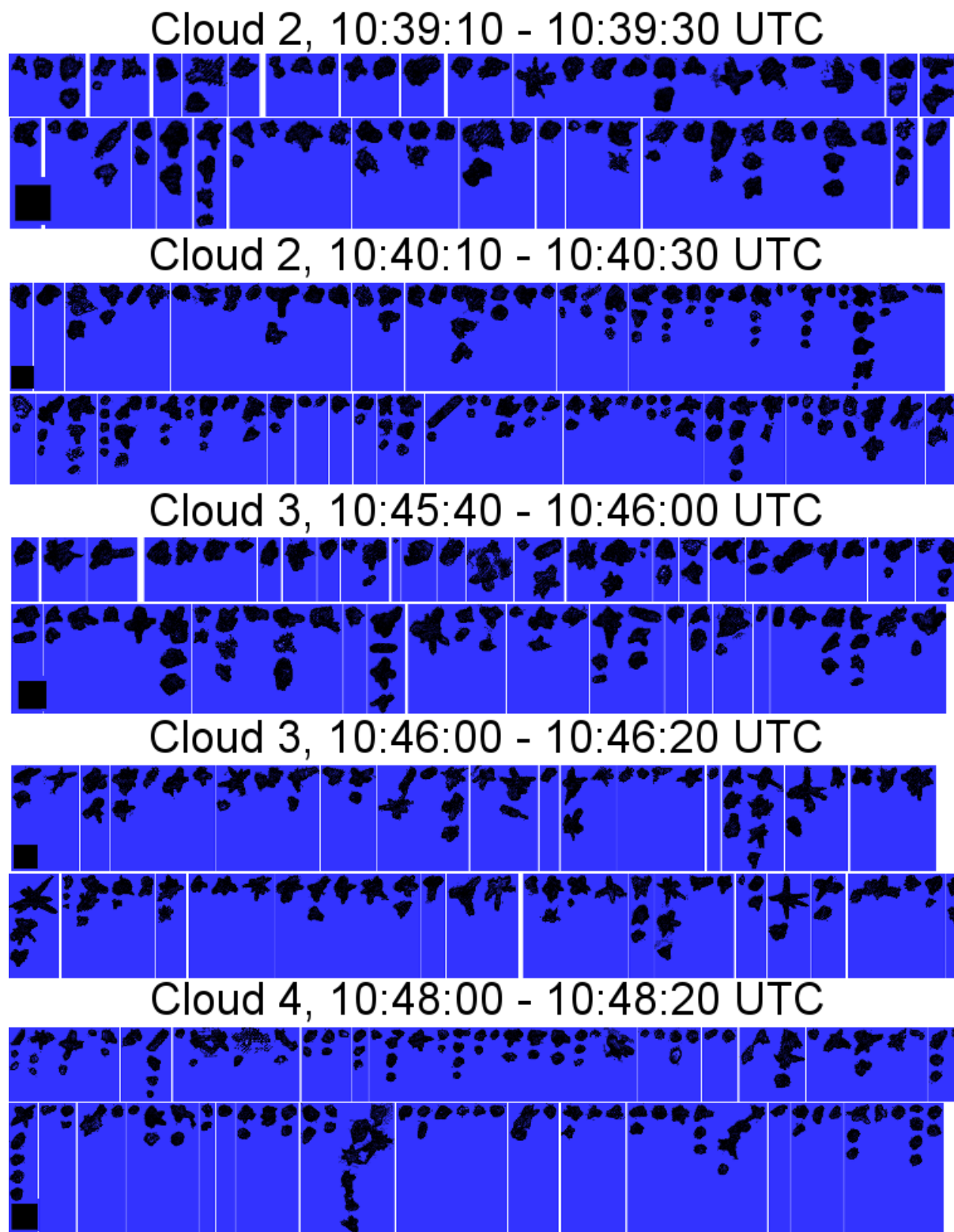


Fig. G.17: As in Fig. 8.2 for Flight B895 on 13 March 2015.

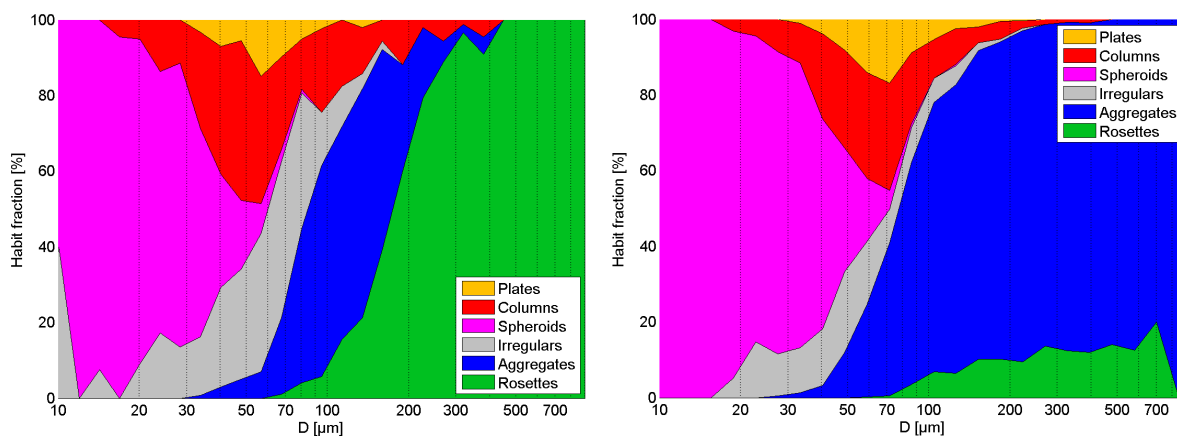


Fig. G.18: Fractional distribution of the classified particle habits in the near-tropopause flight legs of Flight B889 on 05 March 2015 on the 287 hPa level at -53°C (left) and B890 on 06 March 2015 on the 300 hPa level at -47°C (right). Only the size ranges with more than one particle per size bin are shown here. The habits are color-coded and explained in the legend.

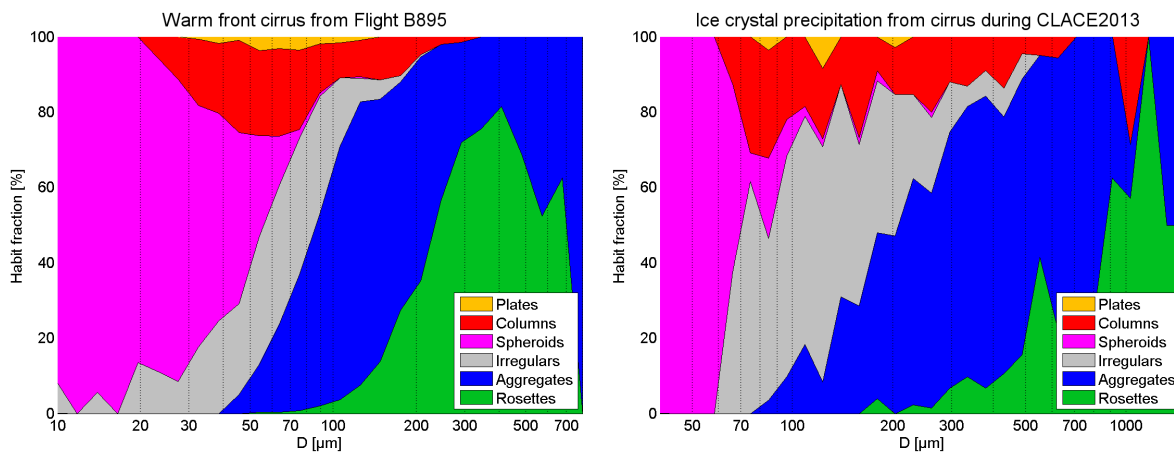


Fig. G.19: As in Fig. G.18 for Flight B895 on 13 March 2015 (left) and ice crystal precipitation from cirrostratus during CLACE2013 on 23 February 2013 (right).

List of Publications

The following list contains articles in peer-reviewed journals written during the time of my doctorate that have been submitted or already published. These articles reflect some of the results and methods from this thesis. A list of conference contributions (oral or poster presentations) is shown on the following page.

Research articles

O. Schlenker, J. Fugal, G. Lloyd, K. Bower, T. Choulaton, M. Flynn, J. Crosier and S. Borrmann (2017): Microphysical properties of ice crystal precipitation and surface-generated ice crystals in a High Alpine environment in Switzerland. *J. Appl. Meteor. Clim.* **15** (2), 433-453, doi:10.1175/JAMC-D-16-0060.1.

A. Korolev, G. McFarquhar, P. R. Field, C. Franklin, P. Lawson, Z. Wang, E. Williams, S. Abel, D. Axisa, S. Borrmann, J. Crosier, J. Fugal, M. Krämer, U. Lohmann, O. Schlenker, M. Schnaiter and M. Wendisch (2017): Mixed-Phase Clouds: Progress and Challenges. *Meteor. Monogr.* **58**, 5.1-5.50.

S. O'Shea, T. Choulaton, G. Lloyd, J. Crosier, K. Bower, M. Gallagher, S. Abel, R. Cotton, P. Brown, J. Fugal, O. Schlenker, S. Borrmann and J. Pickering (2016): Airborne observations of the microphysical structure of two contrasting cirrus clouds. *J. Geophys. Res. - Atmospheres* **121**, doi: 10.1002/2016JD025278.

G. Lloyd, T. Choulaton, K. Bower, M. Gallagher, P. Connolly, M. Flynn, R. Farrington, J. Crosier, O. Schlenker, J. Fugal and J. Henneberger (2015): The origins of ice crystals measured in mixed-phase clouds at the high-alpine site Jungfraujoch. *Atmos. Chem. Phys.* **15**, 15953-12969, doi: 10.5194/acp-15-12953-2015.

Conference contributions

S. Glienke, O. Schlenzcek, J. Fugal, R. A. Shaw and S. Borrmann (2016): Variability of Local Droplet Size Distributions in Marine Stratocumulus Clouds Observed with Airborne Digital Holography. 17th International Conference on Clouds and Precipitation, Manchester, United Kingdom, July 2016.

O. Schlenzcek, J. Fugal, K. Bower, J. Crosier, M. Flynn, J. Henneberger, G. Lloyd, U. Krieger and S. Borrmann (2015): Atmospheric ice crystals over complex terrain: Pure ice cloud conditions observed in CLACE 2013 at Jungfrauoch, Switzerland. European Geosciences Union General Assembly, Vienna, Austria, April 2015.

O. Schlenzcek, J. Fugal and S. Borrmann: The local environment of ice particles in arctic mixed-phase clouds during RACEPAC. European Geosciences Union General Assembly, Vienna, Austria, April 2015.

O. Schlenzcek, J. Fugal, K. Bower, J. Crosier, M. Flynn, G. Lloyd and S. Borrmann: Properties of pure ice clouds in an alpine environment. 14th AMS Conference on Cloud Physics, Boston, USA, July 2014.

J. Fugal, M. Beals, O. Schlenzcek, R. A. Shaw, S. Spuler and J. Stith (2012): Ice particle size distributions measured with a holographic airborne instrument. 16th International Conference on Clouds and Precipitation, Leipzig, Germany, August 2012.

List of Acronyms

<i>2D – S</i>	Two-Dimensional Stereo Probe (from SPEC Inc.)
<i>3V – CPI</i>	Three-View Cloud Particle Imager (from SPEC Inc.)
<i>AC</i>	Alternating Current
<i>ACTOS</i>	Airborne Cloud Turbulence Observation System
<i>AIMMS</i>	Aircraft Integrated Meteorological Measurement System
<i>AWI</i>	Alfred Wegener Institute
<i>BL</i>	Background amplitude level
<i>CAS</i>	Cloud and Aerosol Spectrometer (from DMT)
<i>CCD</i>	Charge Coupled Device
<i>CDF</i>	Cumulative Distribution Function
<i>CDP</i>	Cloud Droplet Probe (from DMT)
<i>CIP</i>	Cloud Imaging Probe (from DMT)
<i>CIRCCREX</i>	Cirrus Coupled Cloud-Radiation Experiment
<i>COLD</i>	Cryogenically Operated Laser Diode
<i>COSMICS</i>	Cold-air Outbreak and sub-Millimetre Ice Cloud Study
<i>CPI</i>	Cloud Particle Imager (from SPEC Inc.)
<i>CPU</i>	Central Processing Unit
<i>CSI</i>	Critical Success Index
<i>DC</i>	Direct Current
<i>d2ne</i>	Distance to Nearest Edge
<i>DMT</i>	Droplet Measurement Technologies Inc.
<i>eqsiz</i>	Equivalent Size, arithmetic mean of minsiz and majsiz
<i>FAAM</i>	Facility for Airborne Atmospheric Measurements
<i>FAR</i>	False Alarm Rate
<i>FFT</i>	Fast Fourier Transform
<i>FL</i>	Flight Level
<i>FND</i>	First Neighbor Distance
<i>GDAS</i>	Global Data Assimilation System
<i>HDD</i>	Hard Disk Drive
<i>ICAO</i>	International Civil Aviation Organization

<i>ICE – D</i>	Ice in Clouds Experiment - Dust
<i>IWC</i>	Ice Water Content
<i>LWC</i>	Liquid Water Content
<i>LED</i>	Light Emitting Diode
<i>majsiz</i>	Major Axis Length of a particle
<i>MDB</i>	Myasishchev Design Bureau
<i>minsiz</i>	Minor Axis Length of a particle
<i>MODIS</i>	Moderate Resolution Imaging Spectroradiometer
<i>NA</i>	Numerical Aperture
<i>NIXE – CAPS</i>	Novel Ice Experiment - Cloud, Aerosol and Precipitation Spectrometer
<i>NTP</i>	Network Time Protocol
$OED = \sqrt{4A/\pi}$	Optical Equivalent Diameter (see also D_A)
<i>P5/P6</i>	Polar research aircraft 5 / 6 from AWI
<i>PDF</i>	Probability Density Function
<i>PIP</i>	Precipitation Imaging Probe (from DMT)
<i>PMS</i>	Particle Measurement Systems Inc.
<i>PL</i>	Particle amplitude level
<i>POD</i>	Probability of Detection
<i>PSD</i>	Particle Size Distribution
<i>PSDE</i>	Power Spectral Density Estimate
<i>RACEPAC</i>	Radiation and Cloud Experiment in the Arctic Circle
<i>RAID</i>	Redundant Array of Independent Disks
<i>RAM</i>	Random-Access Memory
<i>RH</i>	Relative Humidity
<i>RMSE</i>	Root Mean Square Error
<i>SSD</i>	Solid State Drive
<i>SND</i>	Second Neighbor Distance
<i>SNR</i>	Signal to Noise Ratio
<i>STD</i>	Standard Deviation
<i>StratoClim</i>	Stratospheric and Upper Tropospheric Processes for Better Climate Predictions
<i>SV</i>	Sample volume
<i>TAS</i>	True Air Speed
<i>TEM</i>	Transverse Electromagnetic Mode
<i>UCSE</i>	Unit for Connection with Scientific Equipment
<i>USAF</i>	United States Air Force
<i>USB</i>	Universal Serial Bus
<i>UTC</i>	Universal Time Coordinated

VSR Volume Sampling Rate

List of Symbols

A (Particle) area
 a_k k-th fit coefficient
 $C(x)$ Cumulative distribution function of sample x
 c Speed of light in vacuum
 D (Particle) Diameter or Size
 D_A Area-equivalent particle diameter, same as OED
 D_F Filter diameter in sign-matched filter algorithm
 D_m Arithmetic mean of D_x and D_y
 D_p Particle diameter in sign-matched filter algorithm
 D_S Diameter of smallest sphere enclosing the particle
 D_x Maximum dimension in x direction
 D_y Maximum dimension in y direction
 \overline{D} Arithmetic Mean Diameter
 \overline{D}_3 Mean Volume Diameter
 \overline{D}_g Geometric Mean Diameter
 dx Detector pixel width
 dy Detector pixel height
 dz Distance between two reconstruction planes
 d Distance
 $E = U \exp(j\phi)$ Complex optical field in hologram reconstruction
 E_x Power spectral density of x
 f Frequency
 $H(x)$ Histogram of sample x
 h Altitude
 I Intensity
 j Imaginary unit
 K Test statistics from Kolmogorov-Smirnov Test
 L Length
 $\ln(x)$ Natural logarithm of x
 $\log(x)$ Decadal logarithm of x

M	Molar mass
m	(Particle) Mass
N	Number concentration
N_x	Detector width (in pixels)
N_y	Detector length (in pixels)
N_z	Number of reconstruction planes
n	(Particle) Number counts
n_{opt}	Index of refraction in the optical electromagnetic spectrum
P	Particle perimeter
P_c	Percentile cutoff
p	Pressure
$\vec{r} = (x, y, z)^T$	Position vector in 3D space
$R(X, Y)$	Cross correlation between sample X and sample Y
r_{eff}	Particle effective radius
r^2	Coefficient of determination in (non-) linear least-squares fitting
r_{eff}	Particle effective radius
r	Radius
s_c	Cutoff slope from detectability analysis
T	Temperature
T_d	Dewpoint temperature
$TH(x)$	Threshold of x
t	Time
\vec{u}	3D (wind) velocity vector
U	Amplitude of complex field E
u	First component of \vec{v}
\vec{v}	Horizontal (wind) velocity vector
V	(Sample) Volume
v	Second component of \vec{v}
v_a	Speed of aircraft (TAS)
$ v $	Euclidean norm of \vec{v}
w	Vertical component of \vec{u}
\bar{X}	Arithmetic mean of sample X
\bar{X}_g	Geometric mean of sample X
x	First Cartesian coordinate (here: Position along detector width)
y	Second Cartesian coordinate (here: Position along detector height)
z	Third Cartesian coordinate (here: Position along optical axis)
α	Angle
α_L	Linear thermal expansion coefficient
β	Angle
γ	Angle

ΔX	Uncertainty / error of X
δ	Particle aspect ratio
λ	Wavelength
π	Ratio of perimeter to diameter of a circle
ρ	Density
ϕ	Phase of complex field H
ψ	Particle major axis orientation relative to x axis
$\sigma(X)$	Empirical standard deviation of X
$\sigma^2(X)$	Empirical variance of X
$\sigma_g(X)$	Empirical geometric standard deviation of X
τ	Time
θ	Potential temperature
θ_e	Equivalent potential temperature
∂	Partial derivative of an arbitrary function

List of Figures

- 2.1 Illustration of hologram recording. The reference wave is diffracted by the particle located at $z = z_p$. Both waves interfere and the interference pattern (which is the hologram) is recorded at $z = z_H$. The interference pattern contains all information necessary to reconstruct the 2D particle image and the 3D particle position. The pattern in blue resembles the intensity distribution at the hologram plane along x . The y axis is pointing out of the page. 7
- 2.2 Illustration of the conventional sampling strategy (here: a CDP) in contrast to holographic measurements (here: HALOHolo). Data were taken from Flight 6 of the airborne field campaign RACEPAC in Inuvik, Canada on 06 May 2014. The sample volume geometry as defined in the previous paragraph was rotated to allow for better visibility. The colors of the particles indicate particle size (blue / turquoise for small particles, green / yellow / orange for larger particles). A gap between 12 and 16 μm in the dashed black line (top right) indicates that particles of this size were not measured by the CDP. 8
- 3.1 Left: Photograph with description of GipfelHolo 1 on Mt. Zugspitze in September and October 2012. Right: Example of reconstructed hydrometeors from 01 October 2012 during a snow shower. Scale bar increments are 1 mm each. 17
- 3.2 Top left: Photograph with description of GipfelHolo 2 on Jungfrauoch in January and February 2013. Top right: Example of size distributions of cloud droplets and ice particles from a precipitating Nimbostratus cloud and corresponding particle images of droplets (black frame), small ice (blue frame) and larger ice (red frame). Scale bar increments are 100 μm each. Bottom panel: Spatial distribution of frozen hydrometeors and droplets from the same hologram. Modified from Schlenczek et al. (2017). . . 18

- 3.3 Photograph of HALOHolo with labeled components of the instruments. A schematic of the optical components is overlaid to illustrate the working principle of the laser side and camera side lens system. The colored rays in the camera side lens system indicate that the magnified image is not inverted. 20
- 3.4 Minimum resolvable size of HALOHolo as a function of distance along the optical axis for horizontal positioning (dark blue) and vertical positioning (violet) of a USAF 1951 test target placed at various z positions. In the lower right corner, a reconstructed hologram of the test target at the laser window position ($z = 158$ mm) is shown along with the clearly resolved (green), barely resolved (yellow) and barely not resolved (red) line triads (elements). The distances between a pair of lines in the green and red element define the error bars. The expected resolution limit from reconstruction $D_{res,rec}$ (solid line) and its range of uncertainties (dashed lines) is shown in blue. Further constraints shown in the plot are the resolution limit from the imaging lens system (turquoise), the pixel size (red) and the smallest allowed particle diameter in the reconstruction settings (black). 24
- 3.5 Glass beads under the microscope. Left: 8 microns. Middle: 15 microns. Right: 30 microns. The scale increments of the ruler are $25\ \mu\text{m}$. For each of the images, the same magnification factor was used. The black boxes are closeups of 1 or 2 beads (marked with blue circles), digitally magnified by a factor of ten. 26
- 3.6 Reconstruction results of holograms with calibration glass spheres. The spheres had a nominal diameter of $8\ \mu\text{m}$ (top row), $15\ \mu\text{m}$ (middle row) and $30\ \mu\text{m}$ (bottom row) as described in Tab. 3.3. Their corresponding size distributions given by the manufacturer (green) are shown in comparison with the "Equivalent Size" (black) and the "Area-derived diameter" (blue), explained in Chapter 4. The "sign-matched filter" (red) is used as a threshold-independent reference method if the particle is larger than $5.9\ \mu\text{m}$ (SMF lower limit, yellow lines). The filter accuracy was set at $0.74\ \mu\text{m}$ (0.25 pixels). A typical value of the particle sizing uncertainty via determining the number of pixels for the object is $1.5\ \mu\text{m}$ (0.5 pixels). The mean z position of the beads in the sample volume increases from left to right where the mean and STD of z are given in the title of each plot. . . . 27

- 3.7 Box plots of particle position uncertainties determined from synthetic holograms. Left: Error in y position for the holograms at short distance (blue) and long distance (red) to the hologram plane. Right: Error in z position with same color code as in the left panel. The wide boxes represent the inner 50 % of the distribution, the narrow boxes represent the inner 90 % of the distribution. The white circles / black squares indicate the median of each distribution. The x position error (not shown) looks the same as the y position error. 28
- 4.1 Flow chart illustrating the data processing from the raw products leaving the instrument (HALOHolo, HOLODEC,...) to quality-checked high accuracy data products. The green boxes denote data products, the black boxes denote the processes involved to create them. There exist intermediate products in the chain from *classified particle data* to the *quality-checked data products*, which are not specified in the figure. 34
- 4.2 Flow diagram of the hologram reconstruction software. The reconstruction software consists of a preparation segment (blue box), the main reconstruction segment (red box) and a post-reconstruction segment (green box). 35
- 4.3 Raw hologram (top left) and filtered hologram (top right) from measurements in a cumulonimbus cloud (Flight B926 of ICE-D). The particles which are marked with a red, green and blue circle are shown at their in-focus position in the bottom row. The left particle image in each panel shows the amplitude of the hologram field, the right shows the phase information. The image width of each particle image in the bottom row is 1.5 mm. Shown are a frozen raindrop with an attached columnar ice crystal (left), an irregular ice particle (middle) and a graupel (right). The focus position of each particle is written on top. 37

- 4.4 Threshold calculated from the histogram of the amplitude reconstructed at a fixed z from a hologram containing large raindrops (Flight B926 of ICE-D). The histogram $H(U)$ is shown in the two left panels, the logarithmic histograms $\log(H(U))$ are shown in the two right panels. The threshold calculation in the top row was done via Eq. 4.2. For the bottom row, the range of the histogram to fit has been restricted to 80 % of the global maximum and greater ($H(U)$ above the dashed magenta lines). The bimodality in the logarithmic histograms is due to a significant number of dark pixels, probably from the raindrops. The actual threshold TH_{act} used for particle detection is shown in green, the corresponding threshold for the actual histogram (either TH_{lin} or TH_{log}) is shown in red. Apparently, the probability of missing particles or underestimating their size is reduced in the restricted case due to a less strict threshold (bottom row)..... 41
- 4.5 Images of the amplitude of three particles measured in the laboratory. The yellow dots represent the pixels below the threshold if the standard threshold is used. The red squares represent the pixels with $U_{new} < 0.5$. All three particles were located close to the edge and at large distance to the detector, which led to the darker background pixels along the y axis. . . . 43
- 4.6 Top row: Traces of STD of Amplitude Gradient (stdampg, black), STD of Amplitude (stdamp, red) and STD of Complex Gradient (stdcomp, blue) along z of a particle with approx. 60 μm diameter (left), x-z cross section of the reconstructed amplitude (middle) and the in-focus amplitude image (right). Bottom row: Traces of STD of Phase Gradient (stdphg, black) and STD of Phase (stdph, red) in the left panel, x-z cross section of reconstructed phase (middle) and in-focus phase image (right). The estimated focal plane in the left and middle panels is shown in green. 44
- 4.7 As in Fig. 4.6 for an out-of-focus particle with the estimated focal position at the beginning of the reconstructed block (green line). The in-focus position would be located at $z = 62.7$ mm. One possible hint at the correct position of the focal plane (magenta line) is provided by the phase traces: Stdph and stdphg show a local minimum near the global maximum where the focal plane is located. 45
- 4.8 Measures of particle diameter applied on particles of different habits. Shown are the thresholded pixels (blue circles), the fitted ellipse which defines $majsiz$ and $minsiz$ (red), the smallest enclosing circle which defines D_s (yellow), the smallest enclosing rectangle which defines D_x and D_y (green) and the area-equivalent circle (blue). The displayed habit categories are Spheroids (top left, top middle), Plates (top right), Columns (bottom left), Aggregates (bottom middle) and Rosettes (bottom right). . . 46

- 4.9 Sizing performance of the Equivalent size (black) and Area-derived diameter (blue) from the standard threshold, the Equivalent size with modified threshold (cyan) and the sign-matched filter algorithm (red) for two holograms taken in the laboratory with 15 μm and 30 μm glass beads (top row, estimated bead size from manufacturer information in green), for one hologram from airborne measurements aboard Polar 6 (RACEPAC Flight 6, bottom left) and for one hologram from airborne measurements aboard the BAe-146 aircraft (ICE-D Flight B933, bottom right). While the "standard" and "modified" threshold seem to perform equally well on the airborne data, this is not the case for the laboratory measurements. . . . 48
- 4.10 Examples of columns (top left), plates and dendrites (top right), rosettes (bottom left) and spheroids (bottom right). The scale is only preserved within the individual panels. Scale bar increments are 100 μm each. Data taken from ICE-D Flight B926 and COSMICS Flight B889. 52
- 4.11 Example of rimed aggregates vs. pristine (unrimed) aggregates. The rimed particles show numerous spherical protuberances on their outline, which are absent in case of pristine aggregates and dendritic plates. Data taken from ICE-D Flight B926. 52
- 4.12 Examples of frozen drops (top left), irregular particles (top right), pristine aggregates (bottom left) and rimed aggregates (bottom right). The scale is only preserved within the individual panels. Scale bar increments are 100 μm each. Data taken from ICE-D Flight B926. 53
- 4.13 Simulated shadowgraphs of columnar (top row) and plate-type (bottom row) crystals viewed under different angles. The rotational angle α around the z axis and the rotational angle β around the y axis were kept constant ($\alpha = 60^\circ$, $\beta = 0^\circ$) while the rotational angle γ around the x axis was 0° (left), 45° (middle) and 90° (right). The geometry is similar to the geometry of HALOHolo (the z axis points into the plane spanned by x and y). The pixel size used for the simulations was $dx = dy = 5.5 \mu\text{m}$ as in GipfelHolo. 54
- 4.14 Left: Major axis and minor axis length shown in box and whisker plots as a function of the c axis length for simulated hexagonal prisms with $a = 25 \mu\text{m}$. The three orientation angles α , β and γ were varied such that each angle had a uniform random distribution within its respective range (180° for α and β , 90° for γ). The median of the major axis length (white circles) and minor axis length (black squares) are shown along with the inner 50 % of each distribution (wide boxes), the inner 90 % of each distribution (thick lines) and the minimum and maximum (thin lines). Right: Estimated particle mass (white circles and blue boxes and whiskers) versus actual particle mass calculated from hexagonal geometry for the same simulated particles as in the left panel. 55

- 4.15 Spatial distributions (top row), neighbor distance statistics (middle row) and F statistics from a Fishing test (bottom row) of two selected holograms. The hologram in the left column was obtained from RACEPAC Flight 2 (airborne hologram from a stratocumulus cloud in the Arctic) and the hologram in the right column was from a laboratory experiment in WINK where a jet flow was investigated. The two contrasting examples demonstrate the ability of the previously described algorithms of detecting spatial inhomogeneities. 58
- 4.16 Examples of shattering near the laser window at $z = 160$ mm (top row) and near the camera window at $z = 6$ mm (bottom row). The location of particles is shown in a pseudo-3D distribution plot in the first column. The particle image galleries are shown in the second column. Each image gallery has a height scale of 1 mm, the particle sizes are true to scale. All these images are images of shards. Data taken from COSMICS Flight B890. 60
- 4.17 Intercomparison of two shattering removal techniques for number-weighted (left column) and mass-weighted (right column) particle size distributions from COSMICS Flight B890. The top row shows the ascending flight leg where a zone with possible supercooled droplets was encountered, the bottom row shows the flight leg at constant altitude (at $p = 300$ hPa, $T = -45^\circ\text{C}$). Shown are raw data (which include shattering, black curve), shattering removed with Method 1 ("chop-off", blue curve) and shattering removed with Method 3 ("SV surgery", red curve). 62
- 4.18 Flow diagram of the instrument model main routine. Starting with optical parameters, sample volume parameters and particle parameters, synthetic holograms with realistic signal to noise ratio are created. The added low frequency noise in the background field emulate the effect of imperfect background filtering. 64
- 5.1 Normalized number concentration as a function of particle z position and distance to nearest edge $d2ne$ for different cloud passes in RACEPAC Flight 2, Flight 5, Flight 6 and Flight 10 sorted by particle size in ascending order. The black line marks the cutoff threshold used to assure uniform detectability for the given size distribution. The calculation of the reference concentration is explained in the text. The ordinate axis is plotted in reverse direction, so the slope appears reversed in sign. 71

- 5.2 Left panel: Cutoff slope s_c as a function of D_g for six cloud cases in RACEPAC. The actual values (blue symbols, error bars from fit parameters according to Eq. 5.2) are compared with a linear least-squares fit (black line, fit parameters given in the legend). Right panel: Effective sample volume V as a function of D_g calculated from the actual values (blue symbols, error bars from Gaussian error propagation) shown along with the sample volume calculated from s_c (black line) and a linear fit of the actual values (green line, fit parameters in the legend). The red line shows the unrestricted (maximum available) sample volume. 73
- 5.3 Normalized signal strength I/I_0 as a function of $d2ne$ and z for synthetic monodisperse 10 μm (left) and 20 μm (right) single-particle holograms. I_0 is the reference intensity at $d2ne = 6.4\text{ mm}$ and $z = 10\text{ mm}$ 74
- 5.4 Linear (left) and double logarithmic plot (right) of the cutoff slope s_c as a function of particle size D for five different cutoff percentiles P_c . The solid lines show a fitted hyperbola according to Eq. 5.5. Error bars are calculated from the 95 % confidence level of s_c determined from the individual fit. 75
- 5.5 Number of small particles vs. number of large particles for a separation diameter of 50 microns (top left) and 100 microns (top right) from ICE-D Flight B926, cloud pass 1. In addition to the data from 108 holograms (each data point belongs to one hologram), a linear fit (black line) is shown along with the correlation coefficient between the two quantities (text box in upper right corner). In the bottom row, the number concentration is shown as a function of maximum particle size per hologram (left) and the minimum particle diameter per hologram is shown as a function of maximum particle diameter (right). 78
- 5.6 Left: Distance between a possible shader and another particle in the same hologram along the optical axis z . Right: Cumulative distribution function of the particle diameter for large particles with another smaller particle in the same lateral range (blue) and others with no smaller particle in the projected area (red). The cumulative distribution functions reflect the overall number of particles of diameter D_{Shader} with and without other particles in the same lateral range. 79
- 5.7 Results from first neighbor distance analysis (top row) and Fishing test (bottom row) for synthetic data with $N = 20\text{ cm}^{-3}$ (left) and $N = 80\text{ cm}^{-3}$ (right). The effect of shading was simulated by artificially placing two spheres with 2.5 mm radius randomly in the projected plane and removing all particles within the lateral range of the sphere. No visible blue markers in the bottom row indicate that there is no difference between "unperturbed" and "with shading". 80

5.8	Particle size distribution from a cloud pass during StratoClim 2017 Flight 8 (10 August 2017, 09:48:48 - 09:49:48 UTC). Shown are the number densities per bin for HALOHolo (blue squares), the CDP (black triangles), the stand-alone CIP (green triangles), the CIPgs (red circles) and the PIP (magenta stars) along with their error bars from counting statistics. In addition, pressure p , temperature T and altitude H are shown in the upper right corner and the number of particles detected by HALOHolo and the sampled volume of air are shown in the bottom line. White circles indicate that the concentrations measured by HALOHolo are likely underestimated due to detectability issues. The scale bar of the particle image gallery is 100 μm long.	86
5.9	Estimated particle size from sign-matched filter, equivalent size from reconstruction and equivalent size with relative threshold as a function of distance to nearest edge for synthetic particles with a diameter of 9 μm . Each panel shows a small range of z positions from 50 mm (top left) to 150 mm (bottom right). The black solid line marks the expected particle size, the symbols represent the sizing result from each valid particle. A bimodal size distribution in the sizes from the sign-matched filter (apparent in the middle panels) is indicative of a violation of the conditions for accurate size estimation.	88
5.10	Fraction of correctly sized particles with the sign-matched filter as a function of distance along the optical axis. The error bars were calculated from counting statistics and Gaussian error propagation, the fits were performed using Eq. 5.12.	89
6.1	Typical appearance of boundary layer clouds. Depicted are stratus (top row), stratocumulus (middle row) and cumulus (bottom row). The degree of stability decreases from top to bottom, the degree of organization increases from left to right. Photos taken from private collection of O. Schlenczek.	95
6.2	Left: Mixing at a cumulus cloud edge. The red arrows indicate the position where cloud filaments were detrained by some ten to hundred meter large eddies. Right: Horizontal cloud structures mainly due to shallow convection in an altocumulus layer as seen from an aircraft. The clouds resemble the typical appearance of closed cell convection. Photos taken from private collection of O. Schlenczek.	96
6.3	Illustration of the sampling strategy during RACEPAC. While P5 is equipped with remote sensing instruments scanning the cloud layer from above and releasing dropsondes (DS), P6 performs in-situ measurements inside the clouds. Figure adapted after Ehrlich et al. (2015).	99

6.4	Video stills from a GoPro camera aboard Polar 6 on RACEPAC Flight 10 (14 May 2014). Broken stratocumulus (top left) turns into overcast stratocumulus (top right) and later on, the cloud looks much more like a stratus (bottom left). Inside the cloud (bottom right), no structures are visible.	101
6.5	Time series of N (top row) and r_{eff} (bottom row) from RACEPAC Flight 6 Cloud 5 (left) and Cloud 7 (right). Compared are the time series data of the 1 Hz CDP data (black), the 1 Hz HALOHolo data accumulated over one second (blue) and the full resolution HALOHolo data (red). The CDP data of each time series contain approx. 200,000 particles, the HALOHolo data contain approx. 1.4 million particles. Individual pieces of the time series data with strong variability are magnified (black boxes).	105
6.6	As in Fig. 6.5 for the power spectra of N and r_{eff} . Shown are the power spectral densities $P(N)$ and $P(r_{eff})$ as a function of the length scale L . The high frequency structures show a nearly constant value of the power spectral density, which is indicative of white noise.	106
6.7	Excerpt of a cloud pass from Flight 6 shortly before entering Cloud 5. Shown are the hologram by hologram particle size distribution from HALOHolo (top) and the particle by particle diameter along the flight path from the CDP (bottom) with color-coded first neighbors in same mode (red) or in the other mode (black) as in Fig. 8 of Klingebiel et al. (2015). The time axes were calibrated such that both instruments were synchronized and then converted into a length scale by multiplication with the aircraft TAS. The black box marks the bimodal feature observed in this flight segment. The mode separation diameter was found to be 21 microns for HALOHolo and 20 microns for the CDP.	108
6.8	Particle counts per subvolume (left) and Pseudo-3D display of particles in the sample volume of the holograms A, B and C of Fig. 6.7. The dispersion among the two modes appears to be close to a uniform random distribution in the first hologram, it appears clustered for the second hologram and filamented for the third hologram. At this time, the first neighbors in the CDP particle by particle data were close to a uniform random distribution in terms of dispersion among the two modes.	109
6.9	Top row: Latitude and longitude of the flight track from RACEPAC Flight 2 with the cloud passes 1A - 3 highlighted. Bottom row: Number-weighted (left) and mass-weighted (right) particle size distributions of the six cloud passes from HALOHolo. Thick stairs indicate errors from counting statistics which are 5 % or larger. Black lines indicate the flight track below or above the cloud.	112

- 6.10 Cumulative distribution of the distance ΔL between two holograms consistent in N (top left) and consistent in LWC (top right) of each cloud pass. In addition, the cumulative distributions of ΔL are shown for the size distribution agreement from the KS test between two holograms (bottom left) and the size distribution agreement from the normalized RMSE test (bottom right). The cloud passes are color-coded. Steps starting at values greater than zero on the ordinate (e.g. the red curve in the bottom left panel) indicate that there were holograms which did not agree with any of the others in terms of consistency in N , consistency in LWC or statistical equality of the size distributions. 113
- 6.11 Top left: Comparison of the inter-hologram pairwise agreement of N , r_{eff} , LWC , $\sigma_g(D)$ and the particle size distribution via KS test (PSD(KS)) and $nRMSE$ test (PSD(nRMSE)). Top right: Comparison of the agreement of the first and second neighbor distances with a uniform random distribution (FND_r, SND_r), the first, second and third neighbor distance among adjacent hologram pairs (FND, SND, TND) and maximum F values from the Fishing test below 3 ($\max(F) < 3$). Bottom row: Cumulative distribution functions of the F value from a Fishing test with $a = 2$ mm (left) and $a = 10$ mm (right). 115
- 6.12 Particle mean volume diameter as a function of particle number concentration for each hologram in Cloud 1A - 3. The time of measurement is color-coded. In addition, a black solid line of constant LWC is shown together with the calculated homogeneous mixing line (HM, dashed blue line) and the inhomogeneous mixing line (IM, dashed red line). The normalization diameter $D_3(N_0)$ used for rescaling the mixing lines was the median of D_3 from the holograms with $N/N_0 \geq 75$ % where N_0 is the maximum observed number concentration in the particular cloud pass. Other examples can be found in Fig. E.6 of Appendix E.6. 118
- 7.1 Convective storms during their life cycle. Upper image: Summertime convection with a developing storm (cumulus congestus, A1), a developing storm at glaciation (cumulonimbus calvus, B2) and a mature storm (cumulonimbus capillatus incus, C3). Lower image: Wintertime convection with a developing storm (cumulus congestus, A5), two mature storms (cumulonimbus capillatus incus, B3 and B4) and two dissipating storms (cumulonimbus capillatus, turning into cirrus spissatus cumulonimbogenitus, B1 and B2). Photos taken from private collection of O. Schlenczek. 125

- 7.2 Meteorological variables and cloud properties as a function of length along flight track (left column) and particle size distributions (right column) from Pass 1 of Flight B926. Shown are the temperature T (32 Hz) and dewpoint T_d (1 Hz, top row left, $T_d > T$ indicates water-supersaturated conditions), horizontal and vertical wind speed v_{abs} and w (second row left), number concentration of ice and droplets N_{ice} and N_{liq} (third row left, 1 s running average) and LWC / IWC (bottom row left, 1 s running average) along the cloud pass. The number-weighted size distribution (top right) includes data from the CDP (black), spherical particles from HALOHolo (red), aspherical particles from HALOHolo (blue), round particles from the 2D-S (orange) and irregular particles from the 2D-S (green). The mass-weighted size distribution (bottom right) is shown for spherical (red) and aspherical (blue) particles from HALOHolo. The solid lines represent the average size distribution over the entire cloud pass (Total), the dashed lines represent the stronger updrafts ($w > 2.5 \text{ m s}^{-1}$)... 130
- 7.3 As in Fig. 7.2 for Pass 4 as an example of the Hallett-Mossop zone. 132
- 7.4 As in Fig. 7.2 for Pass 8 as an example of the rapid glaciation. 133
- 7.5 Concentration of ice nuclei calculated from the PCASP aerosol measurements and the ambient temperatures via the parameterization of DeMott et al. (2010) (blue circles) vs. concentration of ice crystals larger than 40 microns measured by HALOHolo (red squares). Database and error bar calculation are explained in the text. A notable change of regimes is seen between $T = -6^\circ\text{C}$ and $T = -8^\circ\text{C}$ where the Hallett-Mossop process is activated. 134
- 7.6 Pseudo-3D display of frozen hydrometeors and cloud droplets, drizzlets and raindrops in two holograms from Pass 4 with two ice particles being neighbors of each other. The habits are expressed in different symbols and colors (see legend). The term "cloud hydrometeor" means spherical objects which are smaller than 40 microns. Other hydrometeor classes are explained in the legend. Vertical velocity and time of measurement are displayed in the title. Black arrows mark two ice particles being first neighbors of each other. 136
- 7.7 As in Fig. 7.6 for two examples from Pass 6. Here, the number of drizzlets is considerably higher and the total number of ice particles is also larger. ... 137
- 7.8 Ice particle images from an excerpt of Pass 4. The particles which are stacked belong to the same hologram. The order in which the particles from the same hologram appear is from sorting the particles by their x size. 141

- 7.9 Left: Cumulative distribution of the width and length of columns (black and blue curve) and the width of spicules on the surface of frozen drops or rimed aggregates (red). Right: Number of spicules as a function of particle size for frozen drops and rimed aggregates. The red line represents a linear least-squares fit of the data truncated by the three smallest and three largest values of D in the sample. The data were obtained from Pass 4 of Flight B926. 142
- 8.1 Examples of natural cirrus clouds that may contain bimodal size distributions. Shown are wave cirrus (*cirrocumulus stratiformis undulatus*) with wave breaking visible in the lower third of the first image (top left), a combination of wave structures and shallow convection in *cirrocumulus castellanus undulatus* (top right), another example of shallow convection in *cirrocumulus floccus* (bottom left), and mixing due to large eddies in *cirrus fibratus* (bottom right). Each of the underlying mesoscale processes is capable of producing a secondary mode in the particle size distribution. Photos taken from private collection of O. Schlenczek. 148
- 8.2 Particle image gallery time series of Cloud Event 4, 5, 6 and 7 from Flight B899 on 05 March 2015. The time direction is from left to right, the thickness of the white lines is proportional to the number of empty holograms between two particle holograms. Particles occurring in the same hologram are vertically stacked. The black square in the bottom left of each image strip is 100 μm wide for size reference. A red frame marks events with simultaneous occurrence of particles in both modes of the size distribution. The selected segments contain 96 holograms (Cloud 4), 120 holograms (Cloud 5), 420 holograms (Cloud 6) and 280 holograms (Cloud 7). 152
- 8.3 One second combined particle size distributions (top row) and vertical velocity, relative humidity over ice and temperature as a function of distance along the flight path. The left case is Cloud 4 of Flight B889 on 05 March 2015 (14:48:50 - 14:49:14 UTC), the right case is Cloud 6 of Flight B889 (14:59:57 - 15:01:13 UTC). The regions of interest are marked with arrows. 154
- 8.4 As in Fig. 8.3 for Cloud 5 (14:52:29 - 14:54:40 UTC, left) and Cloud 7 (15:02:22 - 15:05:11 UTC, right) from Flight B899 on 05 March 2015. The direction of the abscissa in Cloud 7 was reversed to match the coordinates of Cloud 5 as Cloud 7 was the return flight along approximately the same line. The arrow marks the occurrence of the small mode in Cloud 5. 155

8.5	Habit-segregated particle size distributions with individual monomodal or bimodal log-normal fits. The fit parameters are shown in Appendix G, Table G.5. The cases shown are Cloud Pass 1a (top left), Cloud Pass 1b (top right), Cloud Pass 2 (bottom left) and Cloud Pass 3 (bottom right) from COSMICS Flight B890 on 06 March 2015.....	157
8.6	As in Fig. 8.2 for Flight B890 on 06 March 2015 at the 300 hPa level (Cloud Pass 3). Each image strip represents 10 seconds of flight (60 holograms). Possibly rimed particles are marked with a green frame.	158
8.7	Number-weighted particle size distribution from holograms combined over 10 seconds as a function of length along the flight track of Cloud 5 in Flight B890. Shown are the size distribution of all particles (top left), aggregates and rosettes (top right), spheroids (bottom left) and the remaining habits (bottom right). The color code shown for the Spheroids is valid for all four panels.	159
8.8	Meteorological data along the flight path as in Fig. 8.3 for Cloud 5 of Flight B890.	160
8.9	Vertical profiles obtained from the microphysical properties measured by HALOHolo. Shown are IWC (left column), r_{eff} (middle column) and N (right column). In the bottom row, the vertical profiles of RH_{ice} , $ v $ and w , obtained from the aircraft, are shown. The bin sizes for T were 0.5 K. The error bars in N are calculated from counting statistics, typical uncertainties of IWC are a factor of two smaller / larger than the displayed value. The corresponding flights were Flight B889 (05 March 2015), B890 (06 March 2015) and B895 (13 March 2015).	162
8.10	As in Fig. 8.9 for θ as vertical coordinate. The direction of the ordinate is opposite to the direction of the ordinate in Fig. 8.9 such that the upper end of the ordinate resembles higher altitude. The corresponding flights were Flight B889 (05 March 2015), B890 (06 March 2015) and B895 (13 March 2015).....	163
8.11	Images of ice particles from StratoClim Flight 8 (10 August 2017) around 09:50 UTC. The black square in the middle left is 100 microns wide.....	166
8.12	Spatial structure of a cirrus cloud in a convective outflow region over Northern India measured during StratoClim Flight 8 (10 August 2017). Shown are the IWC (top), number concentration (middle) and effective radius (bottom) in the top panel and the color-coded particle size distribution in the bottom panel. The error bars of number concentration N were calculated from counting statistics over a sampling distance of approximately 170 m.	167

8.13	Size distribution intercomparison of StratoClim Flight 8 (10 August 2017) 09:48 - 09:50 UTC (HALOHolo in black, CDP in violet, CIP in dark blue) and ice particles in a convective outflow on 16 August 2006 (top panel, data from Frey et al. (2011), OF3 in light green at 11.5 to 11.8 km, OF4 in red at 12.1 to 12.4 km and OF5 in light blue at 13.6 to 13.7 km altitude). Bottom panel: The same data from StratoClim Flight 8 compared with subvisual cirrus measurements over West Africa from Frey et al. (2011). Error bars of CDP, CIP and HALOHolo are shown for relative errors of 10 % or larger.	168
B.1	Optical design of the camera-side imaging system. The beam originates from the sapphire window before entering the prism (right) and then passes the system of nine lenses and a 355 nm interference filter before arriving on the detector (left). The lenses are spherical lenses. All optical elements are shown with their corresponding number as in Table B.1.	182
B.2	The electronics inside HALOHolo: The fuse block distributes the power to the components (110 VAC for the heater cartridges, 28 VDC for the other components). Ten independent temperature sensors measure the temperature of the instrument components and the components are switched off by the corresponding relay if the temperature range for safe operation is exceeded. The hologram sequences (captured by the camera and processed by the PC-104 computer) are stored on the SSD RAID.	183
B.3	Cumulative size distributions from the glass beads examined under the microscope. The manufacturer info is shown as thin solid lines, the fitted Gaussian (Normal) distribution is shown as dashed lines. Each sample consists of 225 particles, which yields an overall error from counting statistics of 1/15.	185
D.1	Spatial dependence of the relative signal strength for synthetic particles with diameters of 6 and 7 microns (top), 8 and 9 microns (middle) and 10 and 11 microns (bottom). The blue line (Fit 90 %) represents a linear fit of the 90 % signal strength threshold with forced zero offset. The white line (Fit RACEPAC, black in legend) represents the fit as obtained from airborne measurements during RACEPAC, using the equation in Fig. 5.2.	192
D.2	As in Fig. D.1 for particle sizes from 12 to 17 microns.	193
D.3	As in Fig. D.1 for particle sizes from 18 to 23 microns.	194
D.4	Fitted parameters from the hyperbolic fits as a function of P_c . The left panel shows the parabolic fit for a_0 , the right panel shows the linear fit for a_1 . For fitting a_1 , the range of P_c was restricted to $P_c \leq 85\%$. The values of a_0 and a_1 were given in the same unit as s_c . The error bars reflect the uncertainties from the hyperbolic fits to the values of s_c (95 % confidence level).	196

D.5	As in Fig. 5.10 for particle sizes of 7.5 μm , 8.5 μm and 9.5 μm	197
E.1	Particle size distributions from Flight 2 (upper row), Flight 5 (middle left) and Flight 6 (middle right and bottom row) measured by the CDP (red), CAS (green) and HALOHolo (blue). In addition, monomodal log-normal fits (LN fit, black dotted curve) and bimodal log-normal fits (LN fit bim, blue dotted curve) to the HALOHolo size distributions are shown. Six different cloud passes with a length of more than 5 km in cloud were selected for this intercomparison. The size of the error bars is indicated by the height of the filled stair steps for relative errors of 2 % or larger.	200
E.2	Particle size distributions as a function of time along flight path from RACEPAC Flight 2 (top row and bottom left) and Flight 5 (bottom right). The number density of droplets per bin is color-coded using the color bar in the bottom row. The denoted flight levels (FL) are 366 m for FL12, 426 m for FL14, 457 m for FL15, 518 m for FL17, 579 m for FL19 and 884 m for FL29.	201
E.3	As in Fig. E.2 for Flight 6 (top row and bottom left) and Flight 10 (bottom right). The denoted flight levels (FL) are 640 m for FL21, 701 m for FL23, 884 m for FL29 and 1189 m for FL39	202
E.4	Time series data (top row) and power spectra (bottom row) of number concentration from a synthetically generated data set resembling effects from 3D turbulence. The black curves indicate the original time series (TS) data, the blue ones contained random (Poisson) fluctuations when creating the particle sample in the large volume, and the red curves show the data for sampling particles with a HALOHolo geometry within the large volume. The mean number concentration was 3.2 cm^{-3}	203
E.5	As in Fig. E.4 for a number concentration of 32 cm^{-3}	204
E.6	Mixing diagrams as in Fig. 6.12 for Flight 5, 6 and 10 from RACEPAC. The bottom right event (Cloud 3) is a good example of inhomogeneous mixing near the cloud base. In general, all these cloud passes are dominated by the signature of inhomogeneous mixing. The example of Cloud 5 (top right) shows an increasing D_3 for decreasing N in the beginning, which is likely due to the presence of larger droplets forming drizzle.	206

- E.7 Joint frequency distribution plots showing the F value from the Fishing test as defined in Eq. 4.13 as a function of the relative particle number concentration N/N_0 . The dashed line indicates $F = 0$, which is the expectation value for a Poisson distribution. The color code reflects the number of holograms with the particular combination of the F value and the relative number concentration. The particular flight and cloud is mentioned in the title of each plot. From the perspective of these plots, the two quantities F and N/N_0 seem to be uncorrelated. This means that the probability of observing a clustered or filamented droplet population does not depend on the particle number concentration or the position relative to the cloud edge. 207
- E.8 Pseudo-3D display of droplet positions in holograms from Flight 2 (Clouds 1, 2 and 3) where the F value from the Fishing test was greater than 6. Shown are one hologram from Cloud 1B (top left), Cloud 2A (top right) and Cloud 2B (middle left) and three holograms from Cloud 3 (middle left and bottom row). All of the selected holograms were at least 100 m away from the horizontal cloud edge. A non-uniform spatial distribution of the particles is visible in the middle and bottom row. Particle clustering in the holograms shown in the top row is revealed by the Fishing test but difficult to see in the 3D plots. 208
- F.1 Relative position of the cloud passes projected on the $x - y$ plane. The cloud passes are indicated by thick colored lines. By using the mean horizontal wind speed components u and v and the time difference between two cloud passes, the cloud motion was estimated. The dashed lines (FFP, for "forward from precursor") are the "forward trajectories" of the cloud passes and indicate where the following cloud pass should be located if it was the same cloud. A similar calculation was done for the dotted lines (BFS, for "backward from successor"), which are "backward trajectories" of the following cloud pass that should intersect the actual cloud pass. A more detailed explanation is given in the text on the previous page. 211
- F.2 Left: Image in the visible spectrum from the MODIS instrument on the polar orbiting satellite Aqua on 14 August 2015, 14:40 UTC. Marked are the flight region (red) and the estimated region of the sampled convective system at the time of the satellite overpass (yellow). Right: Video still of the forward-facing camera of the BAe146 aircraft. The sampled convective storm, which is embedded in a larger system, is indicated by the red arrow. 212
- F.3 Video stills shortly before the cloud passes 1, 2 and 3 (top row), 4, 5 and 6 (middle row) and 7, 8 and 9 (bottom row). The time stamps, average temperature and average pressure are displayed in the upper right edge. Red circles mark the region where the aircraft entered the cloud. 213

F.4	Skew-T / log p diagram with combined dropsonde data from 17:22 UTC and Global Data Assimilation System (GDAS) model data at 15:00 UTC. The assimilation method is described in the text of Chapter 7. In addition, the aircraft temperature and pressure measurements from the cloud passes (color-coded plus text) are shown.	214
F.5	Particle number concentration N for ice (blue) and droplets (red) as a function of vertical velocity w for Pass 1 and 3 (top row), Pass 4 and 6 (middle row) and Pass 7 and 8 (bottom row). The cross correlation $R(w, N_{liq})$ and $R(w, N_{ice})$ is mentioned in the legend of each plot. For each cloud pass, a linear least-squares fit of N_{ice} and N_{liq} as a function of w is shown.	215
F.6	As in Fig. 7.2 for Pass 3.	216
F.7	As in Fig. 7.2 for Pass 6.	217
F.8	As in Fig. 7.2 for Pass 7.	218
F.9	Particle images of particles with $D \geq 100\mu\text{m}$ classified as aspherical particles from Pass 1 until Pass 7. Each vertical column represents one hologram. Particles are sorted by their size and vertically stacked. White bars indicate empty holograms between two holograms containing particles. The black square in the lower left edges is 100 microns wide and acts as a scale reference. The number of holograms is 111 for Pass 1, 120 for Pass 3, 122 for Pass 4, 140 for Pass 6, 107 for Pass 7 and 128 for Pass 8.	219
F.10	As in Fig. F.9 for particles classified as spherical.	220
F.11	Terminal velocity v_t estimated from the parameterization of Locatelli and Hobbs (1974) (LH74) and Bürgesser et al. (2016) (BAC16) as a function of particle maximum dimension D for columns and rimed particles / frozen drops measured in Flight B926.	221
F.12	Pseudo-3D display of ice crystals and droplets in three holograms at different vertical velocities as in Fig. 7.6 with additional plots of the local particle concentration of a selected ice crystal and a selected raindrop (marked with arrows).	227
F.13	Cumulative distribution of vertical velocity in Pass 4 (top) and Pass 6 (bottom) of holograms containing no columnar ice crystal or rimed aggregate (black), at least one columnar ice crystal (blue), at least one rimed aggregate or frozen drop (green) and at least one column and one frozen drop or rimed aggregate (red).	228

- G.1 Top row: Surface analysis map from Deutscher Wetterdienst (DWD) on 05 March 2015, 12:00 UTC (left) and 06 March 2015, 12:00 UTC (right). The blue frame marks the approximate region which is shown in the bottom row. In the bottom left corners, the radar reflectivity is shown (images taken from <http://www.meteox.com>). Bottom row: Satellite image from the MODIS instrument on Aqua with overlay of the flight track (time is color-coded) on 05 March 2015, 13:20 UTC (left) and 06 March 2015, 12:25 UTC (right). The grid spacing is 1 degree latitude / longitude. The time of the satellite overpass and the time of the in-situ measurement differ by a maximum of 140 minutes. Possible advection is not considered. 230
- G.2 Radiosonde data from Castor Bay on 05 March 2015 12:00 UTC (left) and 06 March 2015 12:00 UTC (right). Shown are temperature (red), dewpoint (blue) and frostpoint (cyan) as a function of pressure. Dewpoint and frostpoint were calculated from the measured temperature and relative humidity via the saturation water vapor parameterization after Murphy and Koop (2005). The green circles mark regions with a potentially unstable stratification calculated from the vertical gradient of θ_e 231
- G.3 Left column: Surface weather analysis map from DWD at 13 March 2015, 12:00 UTC (top) and MODIS Terra satellite image from 13 March 2015, 10:40 UTC (bottom). Right column: Vertical profile of temperature and frostpoint (top) and potential / equivalent potential temperature (bottom) from a dropsonde released near the starting point of the flight track at 10:21:47 UTC. At a temperature below -20°C , three potentially unstable layers (marked in green) could be identified. In accordance with the aircraft data, the moisture sensor from the dropsonde indicates ice-subsaturated conditions from 300 hPa downwards. 232
- G.4 Scatter plots between w and r_{eff} for the holograms containing particles in Flight B889 on 05 March 2015 (top row), Flight B890 on 06 March 2015 and Flight B895 on 13 March 2015 (bottom row). Shown are Cloud 4,5,6 and 7 (top left) and Cloud 1,3,8 and 9 (top right) from Flight B889, all cloud events from Flight B890 (left) and Cloud 1,3,5,7 and 9 from Flight B895. Each symbol represents one hologram containing particles, the individual cloud events are color-coded. 234
- G.5 Horizontal wind speed v as a function of relative humidity over ice RH_{ice} (left) for all holograms containing ice particles in Flight B889 (top row), B890 (middle row) and B895 (bottom row). The right panels show the ice water content IWC as a function of horizontal wind speed v for the same flights. 235

G.6	Time series of Flight B889 with temperature (right) and pressure (left) in the top panel, horizontal (left) and vertical (right) wind speed in the middle panel, and relative humidity w.r.t. ice and HALOHolo particle number concentration (left) as well as HALOHolo IWC (right) in the bottom panel. Each plotted time series resembles a 10 second running average of the original data. The relative humidity data taken from the General Eastern chilled mirror hygrometer (the dewpoint in the data record was interpreted as frostpoint) were 150 second running averages in order to remove oscillations caused by heating / cooling from the time series. The dotted black lines represent the homogeneous freezing temperature below which all hydrometeors are considered as ice (upper panel), zero vertical velocity (middle panel) and 100 % relative humidity (bottom panel). The estimated accuracy is $\Delta T = \pm 0.3$ K, $\Delta w = \pm 0.5$ m s ⁻¹ and $\Delta RH_{ice} = \pm 10$ %. The cloud passes are marked by black lines with their corresponding numbers written on top.	236
G.7	As in Fig. G.6 for Flight B890 on 06 March 2015.	237
G.8	As in Fig. G.6 for Flight B895 on 13 March 2015.	238
G.9	Particle size distributions for Flight B889 on 05 March 2015. Shown are the number-weighted particle size distributions for the FAAM CDP (green), the University of Manchester 2D-S (blue), and HALOHolo (red) for Cloud 1 (top left), Cloud 3 (top right), Cloud 4 (bottom left) and Cloud 5 (bottom right). No distinction between spherical and aspherical objects was applied here. Additional information is shown in the top right corner of each panel with the start and end time of the cloud event, the number of particles in HALOHolo, the temperature (mean \pm std), the relative humidity over ice (mean \pm std), and the vertical velocity (mean \pm std).	239
G.10	As in Fig. G.9 for Cloud 6 (top left), Cloud 7 (top right), Cloud 8 (bottom left) and Cloud 9 (bottom right).	240
G.11	As in Fig. G.9 for Clouds 1-6 in Flight B890 on 06 March 2015.	241
G.12	As in Fig. G.9 for Flight B895 on 13 March 2015. The cloud events displayed are	242
G.13	As in Fig. G.12 for Cloud 6 (top left), Cloud 7 (top right), Cloud 8 (bottom left) in Flight B895 on 13 March 2015 and ground-based measurements from the Jungfraujoch station obtained by GipfelHolo 2 on 23 February 2013 (bottom right).	243

G.14	As in Fig. G.9 for Cloud 1, 4, 5, 6, 7 and 9 with a distinction between different ice crystal habits (HALOHolo data only). The term "Other" means the total size distribution minus the size distributions for the habits which are explicitly declared. The colored dashed lines represent the individual log-normal fits, the black dashed line is the sum of the individual fits.	244
G.15	As in Fig. G.14 for Flight B890. The class of "Spheroids" in Cloud 2 is likely due to supercooled droplets.	246
G.16	As in Fig. G.14 for Flight B895 on 13 March 2015. The cloud events displayed are Cloud 3, 4 and 5 (top row) and Cloud 6, 7 and 9 (bottom row).	248
G.17	As in Fig. 8.2 for Flight B895 on 13 March 2015.	250
G.18	Fractional distribution of the classified particle habits in the near-tropopause flight legs of Flight B889 on 05 March 2015 on the 287 hPa level at -53°C (left) and B890 on 06 March 2015 on the 300 hPa level at -47°C (right). Only the size ranges with more than one particle per size bin are shown here. The habits are color-coded and explained in the legend.	251
G.19	As in Fig. G.18 for Flight B895 on 13 March 2015 (left) and ice crystal precipitation from cirrostratus during CLACE2013 on 23 February 2013 (right).	251

List of Tables

3.1	Pixel size calibration of HALOHolo using a ruler at different positions along the optical axis. The measured length and pixel counts are presented along with their uncertainties. The uncertainty of the effective pixel size was determined by using Gaussian error propagation.	21
3.2	Pixel size calibration of HALOHolo on 10 February 2016 under consideration of both x and y direction	22
3.3	Measured bead size in comparison with the manufacturer information. The mean and standard deviation values (STD) as well as the corresponding uncertainties were obtained from Normal distributions fitted to the cumulative particle size distributions. n is the number of particles in each sample. Additional parameters are listed in Table B.3 of Appendix B.3 ...	25

4.1	Explanation of a contingency table. The columns contain the information of the predicted class of the actual object, the lines contain the information about the actual class of the actual object. The combination "Predicted Particle" = "Particle" is called <i>hit</i> , the combination of "Predicted Particle" = "Artifact" is called <i>false alarm</i> , the combination of "Predicted Artifact" = "Particle" is called <i>miss detection</i> and the case of "Predicted Artifact" = "Artifact" is called <i>null event</i>	49
4.2	Short description of shattering removal techniques. The method names and corresponding numbers are used in the further discussion of each method. As the labor required from the user increases from left to right, the typical speed decreases (Method 1 is the fastest, Method 4 is the slowest).	61
5.1	Maximum relative signal strength I/I_0 at the maximum z position within the sample volume as a function of particle size D . In addition, the actual z position is given at which a value of $I/I_0 > 90\%$ can be found.	75
5.2	Comparison of different diameter estimators for HALOHolo in RACEPAC Flights 2, 5 and 6 against each other and against a CDP. For all HALOHolo data, the sample volume was restricted according to the 70% detectability threshold as described in Fig. 5.1. "majsiz" is major axis length, "minsiz" is minor axis length, "eqsiz" is equivalent size and "OED" is area-derived optical equivalent diameter. The times of the flights with data were 20:40 - 21:51 UTC for Flight 2, for Flight 5 and for Flight 6. The sample sizes were larger than 1 million particles for HALOHolo, which yields error bars less than 0.1% of the value. Errors for \bar{D} , $\sigma(D)$, etc. could be provided but, based on the number of particles, were negligible.	84
5.3	Fit parameters of Eq. 5.12 applied on the frequency of correctly sized particles of size D with $ D - D_{test} < 1\mu\text{m}$. In addition, the values of z for 90% correctly sized particles (hereafter z_{90}) and the optical resolution limit $z_{max}(D)$ are shown. For $D = 7\mu\text{m}$, the value at $z = 90\text{ mm}$ was ignored for fitting as it is obviously an outlier due to the resolution limit effect. The error bars of z_0 and z_1 were estimated from the 95% confidence interval of the fit parameters.	90
6.1	Cloud passes of the analyzed RACEPAC flights. Shown are Cloud number, date and time t , flight type, altitude h , temperature T , pressure p and cloud pass length L . For temperature and pressure, the mean and standard deviation are given. Clouds 1-3 were measured during Flight 2, Cloud 4 was measured during Flight 5, Clouds 5-7 were measured during Flight 6 and Cloud 8 was measured during Flight 10.	100

- 6.2 Hologram by hologram and CDP particle number in the first mode (n_1), particle number in the second mode (n_2) and particle neighborhood counts for particle and first neighbor in the primary mode ($n_{1,1}$), particle and first neighbor in secondary mode ($n_{2,2}$) and particle and neighbor in different modes ($n_{1,2} = n_{2,1}$). Results are shown for unrestricted (U) and restricted (R) sample volume ("restricted" means that only particles closer to their neighbors than to the nearest edge were counted to avoid wall proximity effects). The values in brackets denote the expectation value plus / minus uncertainty range from counting statistics after error propagation as derived in Appendix E.5. Bold-face values mark outliers that exceed the uncertainty from counting statistics. Hologram 2 is denoted as "A" in Fig. 6.7 110
- 6.3 Thermodynamic variables used for calculation of the homogeneous mixing lines. The relative humidity was fixed at $RH = 99\%$ for all six cloud cases. Listed are the mean and standard deviation of LWC , in-cloud temperature T_c and pressure p for the six cloud passes of RACEPAC Flight 2. The out of cloud temperature T_a was estimated from the vertical profile obtained from the aircraft where a value for below cloud base was used for Cloud 3 and values for above cloud top were used for the other five events. 117
- 7.1 Overview of the meteorological data of the cloud passes in ICE-D Flight B926. Listed are the cloud pass number, the time of the cloud pass, pressure p , temperature T , altitude z , cloud pass length L and number of holograms in cloud n_H . The temperature data are mean value and standard deviation before entering the cloud to avoid errors from a wet sensor which lead to measured temperatures that are by up to 5 K too low. The temperature after exiting the cloud was approximately 0.2°C lower than the mean temperature before entering the cloud. Temperature values marked with an asterisk (*) were taken from the non-deiced Rosemount RM 102 sensor due to a temperature drift of the deiced sensor. Altitude and pressure values are mean and standard deviation during the cloud pass. Each measurement of temperature, pressure and altitude used for calculating the mean and STD contains approximately 6,000 data points. . 128
- 7.2 Hydrometeor number and mass concentration for the cloud passes with data from HALOHolo. The number concentration of cloud droplets is given in cm^{-3} , the number concentration of the other hydrometeors is given in L^{-1} . In addition, the sampled volume of air V , the IWC/TWC fraction and the temperature are shown. 131

7.3	Hydrometeor number and mass concentration for the cloud passes with data from HALOHolo. $R(X, Y)$ denotes the cross correlation of the two samples X and Y	139
7.4	Habit fractions from particle habit classification of the same cloud passes as in Table 7.3. Displayed are spheroids greater than 40 microns (sph), columns (col), plates (plt), frozen drops (FD), irregular particles (irr), rimed aggregates (RA) and pristine aggregates (PA).	139
B.1	Optical parameters of the elements within the laser side tube and camera side tube of HALOHolo. Displayed are the element type (lens, window, prism), element number (starting on the laser side, pinhole = element 0), center distance z to pinhole, the radius of curvature r_1 for the incident beam and r_2 for the exiting beam and the center thickness d . The two values of z marked with an asterisk correspond to the hologram plane (the first one at $z = 535.5$ mm equals $z = 0$ mm in hologram reconstruction). Positive values of r_1 indicate a concave curvature, positive values of r_2 indicate a convex curvature. Additionally, the lens diameter D and the glass type are listed. For the prisms and the windows, the aperture diameter is given for D instead. Unless otherwise noted, the surfaces have an accuracy of at least $\lambda/10$ w.r.t. 633 nm.	181
B.2	Parameters of the optical glasses as given in Table B.1 used for the optics of HALOHolo. Shown are the index of refraction n_{opt} and the linear thermal expansion coefficient α_L for each individual glass type. The data are valid for temperature $T = 20$ °C and pressure $p = 1013$ hPa.	182
B.3	Calibration results for HALOHolo using three different particle size estimators. The bead sizes displayed in the first line of each block (identical for "Far", "Middle" and "Near") were measured under a microscope via visual inspection and pixel counting (0.9 μ m pixel height / width). The displayed Mean and STD as well as the error bars, r^2 and $RMSE$ were obtained from a nonlinear least-squares fit using a Normal distribution. n is the number of particles in each sample. The different size measures are the sign-matched filter algorithm (threshold-independent), Equivalent size (using a relative threshold) and Area-equivalent diameter (using a relative threshold) as defined in Subsection 3.3.3. The terms "Far", "Middle" and "Near" refer to the average z position where the beads have been dispersed in the sample volume. This table only lists the results for the 8 μ m and 15 μ m beads, the 30 μ m beads are in Table B.4 . . .	184
B.4	As in Table B.3 for the 30 μ m glass beads.	185

C.1	List of the recently used particle metrics (in alphabetical order). Along with the acronym and the source where the metric is calculated from, a description of each metric is given. Table C.1 contains only the basic metrics. Metrics combined from other metrics are listed in Table C.3.....	187
C.2	Table C.1 continued.	188
C.3	As in Table C.1 for the combined metrics.....	189
D.1	Fit parameters for the 90 % relative signal strength threshold obtained from synthetic holograms.	195
D.2	As in Table 5.2 for the CAS compared with HALOHolo at particle sizes larger than 15 μm	196
D.3	As in Table 5.3 for particle sizes of 7.5 μm , 8.5 μm and 9.5 μm	197
E.1	Specifications of cloud microphysical instruments aboard the Polar 6 aircraft during the RACEPAC field campaign. Described are the measurement principle, the volume sampling rate (VSR) for a TAS of $v_a = 60 \text{ m s}^{-1}$, the size range (D), the size resolution (dD), the distance along flight path between two measured size distributions (L) and the range of number concentrations N . CAS and CIP in Rows 2 and 3 belong to NIXE-CAPS (1), CDP and CIP in Rows 4 and 5 belong to the Cloud Combination Probe (CCP) (2). The PIP VSR is given in liters per second (3).	199
E.2	Correlation coefficients between microphysical parameters of HALOHolo (columns) and CDP (rows in first table) or CAS (rows in second table) for RACEPAC Flight 2.	199
F.1	Minimum horizontal distance between actual cloud track and its corresponding forward projection from precursor (FFP) and backward projection from successor (BFS).	210
F.2	First neighbor statistics of holograms from Pass 4 containing at least two ice particles and at least two droplets. Shown are the hologram number, the observed number of ice particles n_{ice} , the observed number of droplets n_{liq} , the ice-ice neighbors $n_{ice,ice}$, the ice-liquid neighbors $n_{ice,liq}$, the liquid-liquid neighbors $n_{liq,liq}$ and the vertical velocity w . Bold-face values indicate $n_{ice,ice}$, $n_{ice,liq}$ or $n_{liq,liq}$ larger than the expectation value plus its error bar (calculated after the equations in Appendix E.5). Bold-face red values indicate that the observed value is smaller than the expectation value plus its error bar.	222
F.3	Table F.2 continued.	223
F.4	As in Table F.2 for Pass 6.	223
F.5	Table F.4 continued.	224
F.6	Table F.5 continued.	225

F.7	As in Table F.2 for Pass 7.	225
F.8	Table F.7 continued	226
F.9	As in Table F.2 for Pass 8.	226
G.1	Overview of the cloud events in Flight B889. Shown are the corresponding pass or run, time, pressure p , temperature T , minimum and maximum altitude h and the length of the cloud pass L	233
G.2	As in Table G.1 for Flight B895.	233
G.3	As in Table G.1 for Flight B890.	234
G.4	Fit parameters of the cloud events in Flight B889 on 05 March 2015. The fit function is defined in Eq. 8.1. Bold-face values indicate an issue with this fit and should not be used in any parameterization. The fits are either bimodal (BM) or monomodal (MM). Individual habit classes are Spheroids (Sph), Aggregates (Agg) and Rosettes (Ros). "Other" means the remaining habit classes after subtracting the explicitly declared ones.	245
G.5	As in Table G.4 for Flight B890 on 06 March 2015. Case B890-2 contains a trimodal (TM) fit.	247
G.6	As in Table G.4 for Flight B895.	249

References

- Bader, M., J. Gloster, J. L. Brownscombe and P. Goldsmith (1974). The production of sub-micron ice fragments by water droplets freezing in free fall or on accretion upon an ice surface. *Quart. J. R. Met. Soc.* 100, 420–426.
- Bailey, M. P. and J. Hallett (2009). A Comprehensive Habit Diagram for Atmospheric Ice Crystals: Confirmation from the Laboratory, AIRS II, and Other Field Studies. *J. Atmos. Sci.* 66, 2888–2899.
- Baker, B. A. (1992). Turbulent Entrainment and Mixing in Clouds: A New Observational Approach. *J. Atmos. Sci.* 49(5), 387–404.
- Baker, B. A. and R. P. Lawson (2006). Improvement in Determination of Ice Water Content from Two-Dimensional Particle Imagery. Part I: Image-to-Mass Relationships. *J. Appl. Meteorol. Climatol.* 45, 1282–1290.
- Beals, M. J. (2013). *Investigations of Cloud Microphysical Response to Mixing Using Digital Holography*. Michigan Tech. University (dissertation).
- Beals, M. J., J. P. Fugal, R. A. Shaw, J. Lu, S. M. Spuler and J. L. Stith (2015). Holographic measurements of inhomogeneous cloud mixing at the centimeter scale. *Science* 50, 87–90.
- Bevington, P. R. (1969). *Data Reduction and Error Analysis for the Physical Sciences*. McGraw-Hill, New York.
- Borrmann, S. (1991). *On Sizes and Spatial Distributions of Cloud Droplets Measured In-Situ by Fraunhofer In-Line Holography*. University of Mainz (dissertation).
- Borrmann, S. and R. Jaenicke (1993). Application of Microholography for Ground-based In Situ Measurements in Stratus Cloud Layers: A Case Study. *J. Atmos. Ocean. Tech.* 10, 277–293.
- Borrmann, S., R. Jaenicke, R. Maser and B. Arends (1994). Instrument Intercomparison Study on Cloud Droplet Size Distribution Measurements: Holography vs. Laser Optical

- Particle Counter. *J. Atmos. Chem.* *19*, 253–258.
- Borrmann, S., R. Jaenicke, R. Maser and B. G. Arends (1993). Droplet Size Distributions and Liquid Water Contents in Stratus Clouds: Instrument Intercomparison between Holography, FSSP-100 Optical Particle Counter and Particulate Volume Monitor PVM-100. *J. Aerosol Sci.* *24*, S577–S578.
- Borrmann, S., R. Jaenicke and P. Neumann (1993). On spatial distributions and interdroplet distances measured in stratus clouds with in-line holography. *Atmos. Res.* *29*, 229–245.
- Brenguier, J.-L. (1993). Observations of Cloud Microstructure at the Centimeter Scale. *J. Appl. Meteorol.* *32*, 783–793.
- Brenguier, J.-L., D. Trevarin, R. Peytavi and P. Wechsler (1993). New electronics for the FSSP: The fast FSSP. *J. Atmos. Ocean. Technol.* *10*, 27–33.
- Bronstein, I., K. Semendjajew, G. Musiol and H. Mühling (2001). *Taschenbuch der Mathematik* (5. Ed.). Harri Deutsch, Thun.
- Brown, P. R. A. (1989). Use of Holography for Airborne Cloud Physics Measurements. *J. Atmos. Ocean. Tech.* *6*, 293–306.
- Bürgesser, R. E., E. E. Avila and N. E. Castellano (2016). Laboratory measurements of sedimentation velocity of columnar ice crystals. *Quart. J. R. Met. Soc.* *142*, 1713–1720.
- Conway, B. J., S. J. Caughey, A. N. Bentley and J. D. Turton (1982). Ground-based and airborne holography of ice and water clouds. *Atmos. Env.* *16*, 1193–1207.
- Cooper, W. A. and G. Vali (1981). The Origin of Ice in Mountain Cap Clouds. *J. Atmos. Sci.* *38*, 1244–1259.
- Davis, A., A. Marshak, W. Wiscombe and R. Cahalan (1996). Scalar Invariance of Liquid Water Distributions in Marine Stratocumulus. Part I: Spectral Properties and Stationarity Issues. *J. Atmos. Sci.* *53*(11), 1538–1558.
- Davis, A. B., A. Marshak, H. Gerber and W. J. Wiscombe (1999). Horizontal structure of marine boundary layer clouds from centimeter to kilometer scales. *J. Geophys. Res.* *104*(D6), 6123–6144.
- DeMott, P. J., A. J. Prenni, X. Liu, S. M. Kreidenweis, M. D. Petters, C. H. Twohy, M. S. Richardson, T. Eidhammer and D. C. Rogers (2010). Predicting global atmospheric ice nuclei distributions and their impacts on climate. *PNAS* *107*(25), 11217–11222.
- Ehrlich, A., E. Bierwirth, T. Carlsen, M. Schäfer, M. Wendisch, A. Herber, R. Neuber, J. Graeser, L. Schmidt, A. Afchine, U. Bundke, M. Krämer, A. Luebke, J. Meyer, A. Petzold, A. Abdelmonem, C. Hoose, M. Schnaiter, P. Vochezer, K. Weixler, H. Bozem,

- P. Hoor, S. Molleker, M. Klingebiel, R. Weigel, J. Fugal, O. Schlenczek, S. Borrmann, J. Schneider, C. Schulz, A. Roth, G. Mioche, O. Jourdan, M. Dollner, A. Walser, B. Weinzierl, A. Minikin, P. Herenz, F. Stratmann and A. de Lozar (2015). Investigation of Arctic mixed-phase clouds during VERDI and RACEPAC: Combined airborne remote sensing and in situ observations. General Assembly of the European Geosciences Union, Vienna, 12-17 April 2015.
- Frey, W. (2011). *Airborne in situ measurements of ice particles in the tropical tropopause layer*. University of Mainz (dissertation).
- Frey, W., S. Borrmann, D. Kunkel, R. Weigel, M. de Reus, H. Schlager, A. Roiger, C. Voigt, P. Hoor, J. Curtius, M. Krämer, C. Schiller, C. M. Volk, C. D. Homan, F. Fierli, G. Di Donfrancesco, A. Ulanovsky, F. Ravegnani, N. M. Sitnikov, S. Viciani, F. D'Amato, G. N. Shur, G. V. Belyaev, K. S. Law and F. Cairo (2011). In situ measurements of tropical cloud properties in the West African Monsoon: upper tropospheric ice clouds, Mesoscale Convective System outflow, and subvisual cirrus. *Atmos. Chem. Phys.* 11(12), 5569–5590.
- Fugal, J. P., T. J. Schulz and R. A. Shaw (2009). Practical methods for automated reconstruction and characterization of particles in digital in-line holograms. *Meas. Sci. Technol.* 20, 14 pp.
- Fugal, J. P. and R. A. Shaw (2009). Cloud particle size distributions measured with an airborne digital in-line holographic instrument. *Atmos. Meas. Tech.* 2, 259–271.
- Fugal, J. P., R. A. Shaw, E. W. Saw and A. V. Sergeev (2004). Airborne digital holographic system for cloud particle measurements. *Appl. Opt.* 43, 5987–5995.
- Gabor, D. (1948). A new microscopic principle. *Nature* 161, 777–778.
- Gerber, H., J. B. Jensen, A. B. Davis, A. Marshak and W. J. Wiscombe (2001). Spectral Density of Cloud Liquid Water Content at High Frequencies. *J. Atmos. Sci.* 58, 497–503.
- Gilles, S. V. (2016). *Laboruntersuchung von Tropfen an der Wolkenobergrenze der Wolkenkammer WINK*. University of Mainz (Diplom thesis).
- Glienke, S., A. Kostinski, J. Fugal, R. A. Shaw, S. Borrmann and J. Stith (2017). Cloud droplets to drizzle: contribution of transition drops to microphysical and optical properties of marine stratocumulus clouds. *Geophys. Res. Lett.* 44, 1–9.
- Goodman, J. W. (2005). *Introduction to Fourier Optics, Third Edition*. Roberts & Company Publishers, Eaglewood.
- Grabowski, W. W. and G. C. Abade (2017). Broadening of Cloud Droplet Spectra through Eddy Hopping: Turbulent Adiabatic Parcel Simulations. *J. Atmos. Sci.* 74(5), 1485–

1493.

- Guildenbecher, D. R., J. Gao, P. L. Reu and J. Chen (2013). Digital holography simulations and experiments to quantify the accuracy of 3D particle location and 2D sizing using a proposed hybrid method. *Appl. Opt.* *52*(16), 3790–3801.
- Hallett, J. and S. C. Mossop (1974). Production of secondary ice during the riming process. *Nature* *249*, 26–28.
- Henneberger, J., J. P. Fugal, O. Stetzer and U. Lohmann (2013). HOLIMO II: a digital holographic instrument for ground-based in situ observations of microphysical properties of mixed-phase clouds. *Atmos. Meas. Tech.* *6*, 2975–2987.
- Henneberger, J. F.-W. (2013). *Mountain-top in-situ observations of mixed-phase clouds with a digital holographic instrument*. ETH Zurich (dissertation).
- Houze, R. (1993). *Cloud Dynamics*. International Geophysics Series. Academic Press, San Diego.
- Klingebiel, M., A. de Lozar, S. Molleker, R. Weigel, A. Roth, L. Schmidt, J. Meyer, A. Ehrlich, R. Neuber, M. Wendisch and S. Borrmann (2015). Arctic low-level boundary layer clouds: in-situ measurements and simulations of mono- and bimodal supercooled droplet size distributions at the top layer of liquid phase clouds. *Atmos. Chem. Phys.* *15*, 617–631.
- Klingebiel, M., A. Ehrlich, F. Finger, T. Rösenthaller, S. Jakirlić, M. Voigt, S. Müller, R. Maser, M. Wendisch, P. Hoor, P. Spichtinger and S. Borrmann (2017). A tandem approach for collocated measurements of microphysical and radiative cirrus properties. *Atmos. Meas. Tech.* *10*(9), 3485–3498.
- Korolev, A. (2006). Limitations of the Wegener-Bergeron-Findeisen Mechanism in the Evolution of Mixed-Phase Clouds. *J. Atmos. Sci.* *64*, 3372–3375.
- Korolev, A. and G. A. Isaac (2006). Relative Humidity in Liquid, Mixed-Phase, and Ice Clouds. *J. Atmos. Sci.* *63*, 2865–2880.
- Korolev, A., G. McFarquhar, P. R. Field, C. Franklin, P. Lawson, Z. Wang, E. Williams, S. J. Abel, D. Axisa, S. Borrmann, J. Crosier, J. Fugal, M. Krämer, U. Lohmann, O. Schlenczek, M. Schnaiter and M. Wendisch (2017). Mixed-Phase Clouds: Progress and Challenges. *Meteor. Monogr.* *58*, 5.1–5.50.
- Korolev, A. V., E. F. Emery, J. W. Strapp, S. G. Cober, G. A. Isaac, M. Wasey and D. Marcotte (2011). Small Ice Particles in Tropospheric Clouds: Fact or Artifact? *Bull. Am. Meteorol. Soc.* *92*(8), 967–973.

- Kozikowska, A., K. Haman and J. Supronowicz (1984). Preliminary results of an investigation of the spatial distribution of fog droplets by a holographic method. *Quart. J. R. Met. Soc.* *110*, 65–73.
- Krämer, M., C. Rolf, A. Luebke, A. Afchine, N. Spelten, A. Costa, J. Meyer, M. Zöger, J. Smith, R. L. Herman, B. Buchholz, V. Ebert, D. Baumgardner, S. Borrmann, M. Klingebiel and L. Avallone (2016). A microphysics guide to cirrus clouds – part 1: Cirrus types. *Atmos. Chem. Phys.* *16*(5), 3463–3483.
- Krämer, M., C. Schiller, A. Afchine, R. Bauer, I. Gensch, A. Mangold, S. Schlicht, N. Spelten, N. Sitnikov, S. Borrmann, M. de Reus and P. Spichtinger (2009). Ice supersaturations and cirrus cloud crystal numbers. *Atmos. Chem. Phys.* *9*(11), 3505–3522.
- Kumar, B., J. Schumacher and R. A. Shaw (2014). Lagrangian Mixing Dynamics at the Cloudy-Clear Air Interface. *J. Atmos. Sci.* *71*, 2564–2580.
- Kunkel, B. A. (1971). Fog Drop-Size Distributions Measured With a Laser Hologram Camera. *J. Appl. Meteorol.* *10*, 482–486.
- Lance, S., C. A. Brock, D. Rogers and J. A. Gordon (2010). Water droplet calibration of the Cloud Droplet Probe (CDP) and in-flight performance in liquid, ice and mixed-phase clouds during ARCPAC. *Atmos. Meas. Tech.* *3*, 1683–1706.
- Lawson, R. P., B. A. Baker, P. Zmarzly, D. O. Connor, Q. Mo, J.-F. Gayet and V. Shcherbakov (2006). Microphysical and Optical Properties of Atmospheric Ice Crystals at South Pole Station. *J. Appl. Meteorol. Climatol.* *45*, 1505–1524.
- Lawson, R. P. and A. R. Rodi (1992). A New Airborne Thermometer for Atmospheric and Cloud Physics Research. Part I: Design and Preliminary Flight Tests. *J. Atmos. Ocean. Technol.* *9*, 556–574.
- Lawson, R. P., S. Woods and H. Morrison (2015). The Microphysics of Ice and Precipitation Development in Tropical Cumulus Clouds. *J. Atmos. Sci.* *72*, 2429–2445.
- Leisner, T., T. Pander, P. Handmann and A. Kiselev (2014). Secondary ice processes upon heterogeneous freezing of cloud droplets. 14th Conference on Cloud Physics and Atmospheric Radiation, Boston, MA, Amer. Meteor. Soc., 2.3.
- Liljequist, G. H. and K. Cihak (1984). *Allgemeine Meteorologie* (3 Ed.). Vieweg, Braunschweig.
- Lin, Y.-L. (2007). *Mesoscale Dynamics*. Cambridge University Press, Cambridge.
- Locatelli, J. D. and P. V. Hobbs (1974). Fall Speeds and Masses of Solid Precipitation Particles. *J. Geophys. Res.* *79*(15), 2185–2197.

- Lu, J., R. A. Shaw and W. Yang (2012). Improved particle size estimation in digital holography via sign matched filtering. *Opt. Express* 20(12), 12666–12674.
- Lüttmer, T. (2017). *Einfluss der Mikrophysik auf Eiskristallgrößenverteilungen*. University of Mainz (M.Sc. thesis).
- Malkiel, E., J. N. Abras and J. Katz (2004). Automated scanning and measurements of particle distributions within a holographic reconstructed volume. *Meas. Sci. Technol.* 15, 601–612.
- Mason, B. J. (1973). Production of Ice Crystals in Slightly Supercooled Cumulus. *Nature* 245, 451–453.
- McFarquhar, G. M. and A. J. Heymsfield (1998). The Definition and Significance of an Effective Radius for Ice Clouds. *J. Atmos. Sci.* 55, 2039–2052.
- Mossop, S. C. (1985). The Origin and Concentration of Ice Crystals in Clouds. *Bull. Am. Meteorol. Soc.* 66(3), 264–273.
- Mossop, S. C., J. L. Brownscombe and G. J. Collins (1974). The production of secondary ice particles during riming. *Quart. J. R. Met. Soc.* 100, 427–436.
- Murphy, D. M. and T. Koop (2005). Review of the vapour pressures of ice and supercooled water for atmospheric applications. *Quart. J. R. Met. Soc.* 131, 1539–1565.
- Nielsen, J. K., C. Maus, D. Rzesanke and T. Leisner (2011). Charge induced stability of water droplets in subsaturated environment. *Atmos. Chem. Phys.* 11(5), 2031–2037.
- O’Shea, S. J., T. W. Chouarton, G. Lloyd, J. Crosier, K. N. Bower, M. Gallagher, S. J. Abel, R. J. Cotton, P. R. A. Brown, J. P. Fugal, O. Schlenzcek, S. Borrmann and J. C. Pickering (2016). Airborne observations of the microphysical structure of two contrasting cirrus clouds. *J. Geophys. Res.: Atmospheres* 121(22), 13,510–13,536. 2016JD025278.
- Pitter, R. L. and H. R. Pruppacher (1973). A wind tunnel investigation of freezing of small water drops falling at terminal velocity in air. *Quart. J. R. Met. Soc.* 99(421), 540–550.
- Prabhakaran, P., S. Weiss, A. Krekhov, A. Pumir and E. Bodenschatz (2017). Can Hail and Rain Nucleate Cloud Droplets? *Phys. Rev. Lett.* 119, 128701.
- Pruppacher, H. R. and J. D. Klett (1997). *Microphysics of Clouds and Precipitation* (Second Revised Ed.). Kluwer, Dordrecht.
- Raasch, J. and H. Umhauer (1989). Computation of the Frequency Distributions of Distances Between Particles Randomly Dispersed in a Fluid Flow. *Part. Part. Syst. Charact.* 6, 13–16.

- Rangno, A. L. (2008). Fragmentation of Freezing Drops in Shallow Maritime Frontal Clouds. *J. Atmos. Sci.* 65, 1455–1466.
- Raupach, S. M. F. (2009a). Cascaded adaptive-mask algorithm for twin-image removal and its application to digital holograms of ice crystals. *Appl. Opt.* 48, 287–301.
- Raupach, S. M. F. (2009b). Observation of interference patterns in reconstructed digital holograms of atmospheric ice crystals. *J. Atmos. Ocean. Tech.* 26, 2691–2693.
- Raupach, S. M. F., H. J. Voessing, J. Curtius and S. Borrmann (2006). Digital crossed-beam holography for in situ imaging of atmospheric ice particles. *J. Opt. A Pure Appl. Opt.* 8, 796–806.
- Schledewitz, W. (2016). *Holographische Messungen von Eis in Stratus-/ Stratocumuluswolken*. University of Mainz (Diplom thesis).
- Schlenczek, O., J. P. Fugal, G. Lloyd, K. N. Bower, T. W. Choulaton, M. Flynn, J. Crosier and S. Borrmann (2017). Microphysical properties of ice crystal precipitation and surface-generated ice crystals in a High Alpine environment in Switzerland. *J. Appl. Meteorol. Clim.* 56(2), 433–453.
- Seinfeld, J. H. and S. N. Pandis (2012). *Atmospheric Chemistry and Physics: From Air Pollution to Climate Change*. Wiley.
- Siebert, H., R. A. Shaw, J. Ditas, T. Schmeissner, S. P. Malinowski, E. Bodenschatz and H. Xu (2015). High-resolution measurement of cloud microphysics and turbulence at a mountaintop station. *Atmos. Meas. Tech.* 8, 3219–3228.
- Silverman, B. A., B. J. Thompson and J. H. Ward (1964). A laser fog distrometer. *J. Appl. Meteorol.* 3, 792–801.
- Spichtinger, P. (2014). Shallow cirrus convection - a source for ice supersaturation. *Tellus A: Dynamic Meteorology and Oceanography* 66(1), 19937.
- Spuler, S. M. and J. P. Fugal (2011). Design of an in-line, digital holographic imaging system for airborne measurement of clouds. *Appl. Opt.* 50, 1–9.
- Stephens, M. A. (1970). Use of the Kolmogorov-Smirnov, Cramer-Von Mises and Related Statistics Without Extensive Tables. *J. Roy. Statist. Soc.* 32(1), 115–122.
- Ström, J., B. Strauss, T. Anderson, F. Schröder, J. Heintzenberg and P. Wendling (1997). In Situ Observation of the Microphysical Properties of Young Cirrus Clouds. *J. Atmos. Sci.* 54, 2542–2553.
- Thompson, B. J., G. B. Parrent, J. H. Ward and B. Justii (1966). A readout technique for the laser fog disdrometer. *J. Appl. Meteorol.* 5, 343–348.

- Trolinger, J. D. (1976). Airborne holography techniques for particle field analysis. *Ann. N. Y. Acad. Sci.* 267, 448–459.
- Uhlig, E.-M., S. Borrmann and R. Jaenicke (1998). Holographic in-situ measurements of the spatial droplet distribution in stratiform clouds. *Tellus* 50 B, 377–387.
- Ulanowski, Z., P. H. Kaye, E. Hirst, R. S. Greenaway, R. J. Cotton, E. Hesse and C. T. Collier (2014). Incidence of rough and irregular atmospheric ice particles from Small Ice Detector 3 measurements. *Atmos. Chem. Phys.* 14, 1649–1662.
- Vali, G. (1980). Ice multiplication by rime breakup. Preprints 8th Int. Conf. Cloud Phys., Clermont-Ferrand, France, 227–228.
- Vaughan, G., C. Schiller, A. R. MacKenzie, K. Bower, T. Peter, H. Schlager, N. R. P. Harris and P. T. May (2008). SCOUT-O3/ACTIVE High-altitude Aircraft Measurements around Deep Tropical Convection. *Bull. Am. Meteorol. Soc.* 89(5), 647–662.
- Voigt, C., U. Schumann, A. Minikin, A. Abdelmonem, A. Afchine, S. Borrmann, M. Boettcher, B. Buchholz, L. Bugliaro, A. Costa, J. Curtius, M. Dollner, A. Dörnbrack, V. Dreiling, V. Ebert, A. Ehrlich, A. Fix, L. Forster, F. Frank, D. Fütterer, A. Giez, K. Graf, J.-U. Grooß, S. Groß, K. Heimerl, B. Heinold, T. Hüneke, E. Järvinen, T. Jurkat, S. Kaufmann, M. Kenntner, M. Klingebiel, T. Klimach, R. Kohl, M. Krämer, T. C. Krisna, A. Luebke, B. Mayer, S. Mertes, S. Molleker, A. Petzold, K. Pfeilsticker, M. Port, M. Rapp, P. Reutter, C. Rolf, D. Rose, D. Sauer, A. Schäfler, R. Schlage, M. Schnaiter, J. Schneider, N. Spelten, P. Spichtinger, P. Stock, A. Walser, R. Weigel, B. Weinzierl, M. Wendisch, F. Werner, H. Wernli, M. Wirth, A. Zahn, H. Ziereis and M. Zöger (2017). ML-CIRRUS: The Airborne Experiment on Natural Cirrus and Contrail Cirrus with the High-Altitude Long-Range Research Aircraft HALO. *Bull. Am. Meteorol. Soc.* 98(2), 271–288.
- Vössing, H. J., S. Borrmann and R. Jaenicke (1998). In-line holography of cloud volumes applied to the measurement of raindrops and snowflakes. *Atmos. Res.* 49, 199–212.
- Wendisch, M. and J.-L. Brenguier (2013). *Airborne Measurements for Environmental Research*. Wiley-VCH, Weinheim.
- WMO (2017). *International Cloud Atlas*. World Meteorological Organization (Online publication, available from <https://cloudatlas.wmo.int>). WMO-No. 407.
- Wu, W. and G. M. McFarquhar (2016). On the Impacts of Different Definitions of Maximum Dimension for Nonspherical Particles Recorded by 2D Imaging Probes. *J. Atmos. Ocean. Tech.* 33(5), 1057–1072.
- Young, M. V., G. A. Monk and K. A. Browning (1987). Interpretation of Satellite Imagery of A Rapidly Deepening Cyclone. *Quart. J. R. Met. Soc.* 113(478), 1089–1115.

Acknowledgments

This part has been removed from the online version of this thesis due to data protection regulations.

Curriculum vitae

Name: Oliver Schlenczek

Date of birth: 18 August 1985

Place of birth: Bad Hersfeld, Germany

Citizenship: German

Education

- since 02/2012 Graduate Studies in Meteorology to obtain a PhD degree
PhD thesis: “*Airborne and ground-based holographic measurement of hydrometeors in liquid-, mixed-phase and ice clouds*” at Max Planck Institute for Chemistry and Johannes Gutenberg University, Mainz, Germany
- 09/2013 INUIT summer school on ice nucleation, Braunfels, Germany
- 01/2012 Diplom (M.Sc. equivalent) in Meteorology
Diplom thesis: “*Automatische Identifikation von Gewitterformen aus Radardaten*” at Karlsruhe Institute of Technology, Karlsruhe, Germany, and Johannes Gutenberg University, Mainz, Germany
- 10/2005 – 01/2012 Student of Atmospheric Physics at Johannes Gutenberg University, Mainz, Germany
- 06/2005 Abitur (school-leaving exam), main subjects Mathematics and Chemistry, Werratalsschule, Heringen, Germany

Positions

- since 10/2017 Research scientist at Max Planck Institute for Dynamics and Self-Organization, Laboratory for Fluid Dynamics, Pattern Formation and Biocomplexity, Göttingen, Germany
- 02/2015 – 09/2017 Research associate at Max Planck Institute for Chemistry, Mainz, Germany
- 02/2012 – 01/2015 Research associate at Institute for Atmospheric Physics, Johannes Gutenberg University, Mainz, Germany
- 10/2007 – 01/2012 Teaching assistant at the Department of Physics, Johannes Gutenberg University, Mainz, Germany

Awards

- 02/2008 – 09/2010 Merit scholarship of the Studienstiftung des deutschen Volkes e.V.
- 10/2011 EMS Young Scientist Travel Award for a poster presentation at the 6th European Conference on Severe Storms, Palma de Mallorca, Spain, October 2011. Poster title: “Automatic identification of convective modes based on radar data”.

Erklärung zur Dissertation

Hiermit erkläre ich, die vorliegende Dissertation selbstständig und nur mit den angegebenen Quellen und Hilfsmitteln angefertigt sowie noch keinen Promotionsversuch unternommen zu haben.

Mainz, den _____

Unterschrift